Dheeraj Kumar Singh
Sanjay Singh
Prabhakar Singh *Editors*

Nanomaterials

Advances and Applications

Springer

Nanomaterials

Dheeraj Kumar Singh · Sanjay Singh ·
Prabhakar Singh
Editors

Nanomaterials

Advances and Applications

Springer

Editors
Dheeraj Kumar Singh
Department of Basic Sciences
Institute of Infrastructure Technology
Research And Management
Ahmedabad, Gujarat, India

Prabhakar Singh
Department of Physics
Indian Institute of Technology BHU
Varanasi, India

Sanjay Singh
National Institute of Animal Biotechnology
Hyderabad, Telangana, India

ISBN 978-981-19-7962-0 ISBN 978-981-19-7963-7 (eBook)
https://doi.org/10.1007/978-981-19-7963-7

This Springer imprint is published by the registered company Springer Nature Singapore Pte Ltd.
The registered company address is: 152 Beach Road, #21-01/04 Gateway East, Singapore 189721, Singapore

Dedicated to my grandfather Late Shri Parmanand Singh

Preface

In the last two decades, nanoscience and nanotechnology have attracted tremendous research attention towards technological developments that are based on the outstanding and appealing intrinsic features of nanomaterials. A variety of nanomaterials are being synthesized that display better performances than their bulk counterparts; therefore, a wide range of applications are envisaged. Recently, significant effort has been devoted to realize applications of nanomaterials in the area of science, engineering, and medical field. Considering the technological importance of nanomaterials, this book has been designed to provide comprehensive information about the recent progress and applications shown by various nanomaterials. Editors of this book opine to provide the necessary background of nanoscience and nanotechnology to the researchers and readers to build strong fundamentals and deep knowledge about the subject. Certain emerging and well-established nanomaterials such as carbon and graphene-based nanomaterials, metal, nanometal oxides, layered chalcogenides, MXenes, ceramic nanomaterials, polymer nanocomposites, metal nanoparticles, nanofluids, etc., are discussed. For the reader, this book covers detailed information about the different nanomaterials sources of synthesis roots and their characterization techniques. Additionally, this book also provides detailed information on fundamental applications of emerging nanomaterials in a variety of fields of science and technology, including energy, electronics, medical, sensing, etc.

This book consists of 12 chapters and provides the fundamentals to advance discussion regarding the capabilities of nanomaterials and their potential applications and limitations. Chapter 1 provides a general overview of different nanomaterials. In this chapter, Dr. Dheeraj K. Singh and co-workers from IITRAM, Ahmedabad, India, have discussed the history of nanomaterials from the prehistoric era to the modern age. They also cover the properties of materials at the nanoscale, classifications of nanomaterials based on their origin, compositions, and dimensions, as well as various synthesis routes, and applications in different fields including energy, electronics, food, medical, sensing, defense, etc. Chapter 2 is based on carbon nanomaterials. In this chapter, Dr. Rajesh Kumar Singh, CUHP, Dharamshala, India, and his team have briefly discussed the various synthesis routes of carbon nanomaterials including carbon nanotubes, fullerene, and carbon dots. The discussed synthesis

methods include chemical vapor deposition (CVD), arc discharge, laser ablation, etc. A separate section in this chapter is dedicated to the various applications of carbon-based nanomaterials including energy storage, biomedical, and sensing applications. In Chap. 3, Dr. Pawan Kumar Dubey from the University of Connecticut, USA, provided a detailed discussion regarding the recent development in the synthesis and applications of graphene-based nanomaterials. Chapter 4 is written by Dr. Puneet Khandelwal from JHU, Maryland, United States, that presents various synthesis approaches, characterization techniques, and applications of metal nanoparticles. In Chap. 5, Dr. Dheeraj K. Singh and his group from IITRAM, Ahmedabad, India, have summarized the synthesis routes, characterization techniques, and physiochemical properties of metal oxide-based nanoparticles (MONPs) and their applications in a variety of fields, including solar cells, batteries, biomedicines, wastewater, pollutant treatment, etc.

A summary of nanocrystalline high entropy alloys (HEAs) and high entropy oxides (HEOs) materials is provided in Chap. 6 written by the group of Dr. Rohit R. Shahi from CUSB, Bihar, India. A thorough description of the various synthesis techniques for nanocrystalline HEAs and HEOs is included along with the understanding of their remarkable properties and some of the advanced functional applications. Further, Chap. 7 provides an overview of two-dimensional (2D) transition-metal dichalcogenides (TMDCs) materials. Here, Prof. Ashish K. Mishra of IIT-BHU, India covered several synthesis techniques and briefly emphasized the characteristics of TMDs for their numerous applications in the fields of optoelectronics, energy, and biomedicine. In Chap. 8, Dr. Jeevan Jyoti, PDPU, Chandigarh, and Dr. Bhanu Pratap Singh, CSIR-NPL, New Delhi, India, provide in-depth information regarding MXene-based nanomaterials. This chapter includes a detailed discussion of the different MXene synthesis techniques, their properties, and their applications in a variety of fields. Moreover, nowadays, ceramic nanocomposite is widely used in a variety of electrochemical devices owing to their great applications in the field of energy. Therefore, in Chap. 9, Dr. Raghvendra Pandey and Prof. Prabhakar Singh describe the key concepts behind nanocomposite ceramics and explore their various types. This chapter also reveals the various fabrication techniques for the preparation and processing of nanocomposites ceramics as well as their physical properties and applications along with the benefits and flaws of nanocomposites. Polymer nanocomposites have a wide range of applications in a variety of fields because of their low toxicity and biocompatibility. Hence, Chap. 10 is devoted exclusively to polymer composite nanomaterials by Dr. Amaresh Kumar Sahoo, IIIT, Allahabad, India, where a thorough understanding of the various synthesis approaches, characterization approaches, and applications of polymer nanocomposites is developed. Chapter 11 covers the biomedical applications of advanced nanotechnologies. In this chapter, Dr. Chandraiah Godugu from NIPER, Hyderabad, India, outlines the uses and applications of several nanotechnologies and advanced nanomaterials for diagnosis and therapy. The primary focus of this chapter is on the biomedical applications of inorganic (metal and metal oxide) and organic (carbon nanotubes and liposomes) nanoparticles and their nanopattern surfaces for diagnostics, biosensing, and bioimaging applications, as well as drug delivery, theranostic systems, and bone

replacing implants. In Chap. 12, Dr. Sanjay Singh from DBT-NIAB, Telangana, India, addresses the recent developments and uses of nanomaterials as nutritional supplements and therapeutic agents for animal nutrition and the treatment of various animal diseases causing microbes, parasites, and fungi as well as vaccine adjuvant made by nanotechnology. He also discusses the limitations of nanoparticles for animal health and nutrition.

It is expected that this book will make the readers enthusiastic about the recent advancement and importance of nanoscience and nanotechnology by providing a thorough understanding of the various synthesis and characterization techniques along with the fundamental applications of nanomaterials. Additionally, the outlined merits and demerits together with possible solutions will also encourage young scientists and researchers to make new discoveries in this field.

Ahmedabad, India — Dheeraj Kumar Singh
Hyderabad, India — Sanjay Singh
Varanasi, India — Prabhakar Singh

Acknowledgements

I would like to express my sincere gratitude to Almighty God Prabhu Shree Ram, Bajarang Balee, and Maa Saraswati to give me strength for the successful collections of quality book chapters on nanomaterials. The book entitled "Nanomaterials: Advances and Applications" consists of 12 chapters from various reputed institutions across India and abroad. The execution of the book was possible with the unconditional support and help of many individuals, scientists, and academicians. I would like to express my sincere thanks to all of them. First, I would like to show my heartfelt gratitude and thanks to all contributors for providing a quality chapter on the recent developments of nanomaterails. I extend my heartfelt gratitude to IITRAM family for their motivation and good infrastructure.

I owe my deepest gratitude towards the Springer publisher team, especially Loyola D'Silva, Sivananth S Siva Chandran, Anindya Bose, books production team, editorial team, etc., for their guidance to complete the book. I do take the opportunity to thank my seniors and collaborators Prof. Prabhakar Singh and Prof. Sanjay Singh for their enormous support and scientific discussions.

I am grateful to the Science and Engineering Research Board (SERB), DST, Government of India, for financial support to conduct research work at IITRAM which makes a basis to collaborate with the expert researchers and exchange our ideas. My heartfelt and special thanks to my Ph.D. students Hardik, Amit, Deepak, and Nirav for their valuable time to help me during editing the book. Last but not least, I would like to thank my family, my wife Dr. Shweta Singh, my daughter Drishti Singh, my father Jamuna Prasad Singh, and my mother Pramila Singh for their valuable support and sacrifices during the preparations of the book.

Dr. Dheeraj Kumar Singh
IITRAM Ahmedabad, India

Contents

Editors and Contributors

About the Editors

Dr. Dheeraj Kumar Singh (Alexander von Humboldt Fellow, Germany & JSPS Fellow, Japan), Assistant Professor of Physics IITRAM Ahmedabad, Gujarat, India—380026, Office: +91-7967775459, Mobile: +91-9415114778, Home Page: https://dsinghmscrl.wixsite.com/mysite.

He received his Ph.D. degree in Physics from Banaras Hindu University (BHU), Varanasi, India, in 2010. He was subsequently a CSIR-Nehru postdoc at NCL Pune, an NRF postdoc at Seoul, South Korea, and a prestigious Alexander von Humboldt (AvH) postdoc Fellow in Germany. He was also awarded the prestigious international award of JSPS Fellowship, Japan, Dr. DS Kothari Postdoc Fellowship, CSIR-SRF, UGC-Meritorious Fellowship (RFSMS), etc. Currently, he is working as an Assistant Professor of Physics at IITRAM Ahmedabad. His research group is mainly focused on frequency and time domain spectroscopic techniques, their development, and applications on ionic liquids, biomolecules, functionalized nanomaterials, molecular interactions, renewable energy-based materials, etc. Moreover, he has written many book chapters and has the patent granted by the USA. He has organized many workshops and conferences on functional molecules and materials. He has edited two Books in Springer Nature as a corresponding editor. He has been awarded the prestigious ECR Project grant by SERB-DST, Government of India, and DST-Inspire Project for his Ph.D. student.

He has published more than 75 research papers in an international journal of repute. e-mail: dheerajsingh@iitram.ac.in

Dr. Sanjay Singh Scientist—FDBT-National Institute of Animal Biotechnology Hyderabad—500032, Telangana, India, Phone (off): 040-23120135, Webpage: https://www.niab.res.in/peoplesanjaysingh/.

He is currently working as a Scientist—F at DBT-National Institute of Animal Biotechnology (NIAB), Hyderabad, India. He has obtained his Ph.D. degree from CSIR—National Chemical Laboratory, Pune, India. He worked as a postdoctoral research fellow at the Burnett School of Biomedical Sciences, University of Central Florida, Orlando, and at the Department of Pharmacology, College of Medicine, Pennsylvania State University, Hershey Pennsylvania, USA. Subsequently, he worked at Ahmedabad University, Ahmedabad, India, as an Assistant Professor (2012–2017) and Associate Professor (2017–2021) and worked on novel inorganic nanozymes exhibiting catalytic activities and multifunctional drug-delivering nanocarriers. He has published 95 international peer-reviewed scientific research papers, 19 book chapters, and 4 edited books in the area of Nanobiotechnology and Nanomedicines. He has been bestowed with several international awards including the prestigious Endeavour Research Fellowship, Yamagiwa-Yoshida Memorial International Grant Award, International Association of Advanced Materials Scientist Medal, and EMBO Fellowship. He has also attracted several research grants from national and international funding agencies. e-mail: sanjay@niab.org.in

Dr. Prabhakar Singh Indian Institute of Technology, Banaras Hindu University (IIT BHU) Varanasi-221005 (India).

Prabhakar Singh, Ph.D. (University of Muenster Germany), is a Professor in the Department of Physics, Indian Institute of Technology (Banaras Hindu University), Varanasi. He completed his M.Sc. in Physics and M.Tech. in Materials Science and Technology from Banaras Hindu University, Varanasi. He graduated from Udai Pratap College, Varanasi. He has served as an Assistant Professor in Udai Pratap College, Varanasi, and Indira Gandhi National Open University (IGNOU), New Delhi, for more than 8 years. He joined the Institute of Technology, Banaras Hindu University in 2007 as a Reader/Associate Professor. He became a Professor of Physics in September 2015 at IIT (BHU) Varanasi. With more than two decades of teaching and research experience, he has more than 130 peer-reviewed international publications, 7 book chapters, and 1 monograph to his credit. His research interests include physics of materials for energy applications such as solid oxide fuel cells, solar cells, and piezoelectric/dielectric. He has supervised 12 Ph.D. and 15 master's students for their Ph.D. and master's theses, respectively, and mentored several postdoctoral fellows under various national fellowship schemes. He has completed successfully six externally funded projects as principal investigator and currently two externally funded projects are running under his principal investigatorship. He has visited several countries to carry out his academic and research works and has many international collaborations. He is a member of many national and international professional societies. He has attended more than 50 national and international conferences and delivered invited talks. e-mail: psingh.app@iitbhu.ac.in

Contributors

Stuti Bhagat DBT-National Institute of Animal Biotechnology (NIAB), Gachibowli, Hyderabad, Telangana, India;
DBT-Regional Centre for Biotechnology (RCB), Faridabad, Haryana, India

Amit K. Bhojani Department of Basic Sciences, Institute of Infrastructure Technology Research And Management, Ahmedabad, Gujarat, India

Pradeep Kumar Bolla Department of Biomedical Engineering, College of Engineering, The University of Texas at El Paso, El Paso, TX, USA

Raviteja Bulusu College of Pharmacy and Pharmaceutical Sciences, Florida A&M University, Tallahassee, FL, USA

Yong-Song Chen Department of Mechanical Engineering and Advanced Institute of Manufacturing With High-Tech Innovations, National Chung Cheng University, Chiayi, Taiwan

Nitika Devi Department of Mechanical Engineering and Advanced Institute of Manufacturing With High-Tech Innovations, National Chung Cheng University, Chiayi, Taiwan

Pawan Kumar Dubey Center for Clean Energy Engineering, Department of Materials Science and Engineering, University of Connecticut, Storrs, CT, USA

Chandraiah Godugu Department of Regulatory Toxicology, National Institute of Pharmaceutical Education and Research (NIPER), Balanagar, Hyderabad, Telangana, India

Amit K. Gupta Functional Materials Research Laboratory, Department of Physics, Central University of South Bihar, Gaya, Bihar, India

Jay Deep Gupta School of Materials Science and Technology, Indian Institute of Technology (Banaras Hindu University), Varanasi, India

Junsung Hong Center for Clean Energy Engineering, Department of Materials Science and Engineering, University of Connecticut, Storrs, CT, USA

Priyanka Jangra School of Materials Science and Technology, Indian Institute of Technology (Banaras Hindu University), Varanasi, India

Nirav Joshi Department of Basic Sciences, Institute of Infrastructure Technology Research And Management, Ahmedabad, Gujarat, India

Jeevan Jyoti Centre of Advanced Studies, Physics Department, Panjab University, Chandigarh, India

Hardik L. Kagdada Department of Basic Sciences, Institute of Infrastructure Technology Research And Management, Ahmedabad, Gujarat, India

Shabari Girinath Kala Department of Pharmaceutical Sciences, Jawaharlal Nehru Technological University, Ananthapuramu, Andhra Pradesh, India

Puneet Khandelwal Department of Radiology, School of Medicine, Johns Hopkins University, Baltimore, MD, USA

Nagavendra Kommineni Center for Biomedical Research, Population Council, New York, NY, USA

Rajesh Kumar Department of Mechanical Engineering, Indian Institute of Technology, Uttar Pradesh, Kanpur, India

Priyanka Kumari Functional Materials Research Laboratory, Department of Physics, Central University of South Bihar, Gaya, Bihar, India

Kevin Lee Center for Clean Energy Engineering, Department of Materials Science and Engineering, University of Connecticut, Storrs, CT, USA

Divya Mehta DBT-National Institute of Animal Biotechnology (NIAB), Gachibowli, Hyderabad, Telangana, India;
DBT-Regional Centre for Biotechnology (RCB), Faridabad, Haryana, India

Ashish Kumar Mishra School of Materials Science and Technology, Indian Institute of Technology (Banaras Hindu University), Varanasi, India

Bhavita G. Mistry Macromolecular Materials Laboratory, Applied Chemistry Department, Faculty of Technology and Engineering, The Maharaja Sayajirao University of Baroda, Vadodara, India

Shashi Kant Mohapatra Functional Materials Research Laboratory, Department of Physics, Central University of South Bihar, Gaya, Bihar, India

Deepak K. Pandey Department of Basic Sciences, Institute of Infrastructure Technology Research And Management, Ahmedabad, Gujarat, India

Raghvendra Pandey Department of Physics, ARSD College, University of Delhi, New Delhi, India

Shashank Reddy Pasika Department of Biotechnology, National Institute of Pharmaceutical Education and Research – Raebareli (NIPER-R), Raebareli, India

Sivasankar Putta Department of Chemistry and Biochemistry, University of California, Santa Cruz, CA, USA

Sneha Ranjan Department of Biotechnology, Babasaheb Bhimrao Ambedkar University, Lucknow, UP, India

Balaga Venkata Krishna Rao Department of Pharmaceutical Sciences & Technology, Birla Institute of Technology, Mesra, Ranchi, Jharkhand, India;
School of Pharmacy, Suresh Gyan Vihar University, Jagatpura, Jaipur, Rajasthan, India

Amaresh Kumar Sahoo Department of Applied Sciences, Indian Institute of Information Technology, Allahabad, Prayagraj, UP, India

Manjit Sandhu School of Mechanical Engineering Department, Indian Institute of Technology Ropar, Rupnagar, Punjab, India

Rohit R. Shahi Functional Materials Research Laboratory, Department of Physics, Central University of South Bihar, Gaya, Bihar, India

Raj Kumar Sharma Department of Radiology, School of Medicine, Johns Hopkins University, Baltimore, MD, USA

Saurabh Shivalkar Department of Applied Sciences, Indian Institute of Information Technology, Allahabad, Prayagraj, UP, India

Ankita Singh School of Materials Science and Technology, Indian Institute of Technology (Banaras Hindu University), Varanasi, India

Bhanu Pratap Singh Advanced Carbon Products and Metrology, CSIR-National Physical Laboratory, New Delhi, India

Dheeraj K. Singh Department of Basic Sciences, Institute of Infrastructure Technology Research And Management, Ahmedabad, Gujarat, India

Prabhakar Singh Center for Clean Energy Engineering, Department of Materials Science and Engineering, University of Connecticut, Storrs, CT, USA;
Department of Physics, Indian Institute of Technology (BHU), Varanasi, India

Rajesh Kumar Singh School of Physical and Material Sciences, Central University of Himachal Pradesh (CUHP), Dharamshala, HP, India

Sanjay Singh DBT-National Institute of Animal Biotechnology (NIAB), Gachibowli, Hyderabad, Telangana, India;
DBT-Regional Centre for Biotechnology (RCB), Faridabad, Haryana, India

Surya Kant Tripathi Centre of Advanced Studies, Physics Department, Panjab University, Chandigarh, India

Chapter 1
An Overview of Nanomaterials: History, Fundamentals, and Applications

Hardik L. Kagdada, Amit K. Bhojani, and Dheeraj K. Singh

Abstract Nanomaterials exhibit the tendency to alter the fundamental properties with the size in the range of nanometers. The fascinating nanomaterials exhibit excellent fundamental properties and possess numerous applications in the fields of science and technology. However, the concept of nanomaterials already existed in prehistoric times unknowingly. Therefore, the present chapter discusses the historical overview, usage, and development of nanomaterials from the prehistoric time to the modern age. The scientific milestones achieved for the development of nanomaterials and nanotechnology have also been covered. Further, the properties at the nanoscale have been discussed in terms of confinement effect and the surface-to-volume ratio. The classification of nanomaterials based on several factors such as origin, composition, and dimensionality are elaborated. This chapter also included the possible synthesis approaches along with their benefits and disadvantages. Moreover, we briefly explore the general overview of nanomaterials for a variety of applications in the fields of energy, medicine, electronics, sensing, defense, etc.

Keywords Nanomaterials · Historical overview · Classification of nanomaterials · Synthesis approaches · Applications

1.1 Historical Overview

Nanomaterials are arising as a revolutionary class of materials, unfolding a wide range of applications, by possessing the size or one or all of the dimensions in the nanometer range with unique properties. The word "Nano" is originated from the Greek phrase "nanos," which is defined as very short men. The astonishing history of nanomaterials reveals that they have existed naturally in ancient times. The history of nanomaterials is flabbergasting and long, which includes naturally occurred and man-made nanomaterials. Natural sources of nanomaterials consist the forest fire products, ocean spray, volcanic ash, etc. Moreover, from the meteorites, nanodiamonds have

H. L. Kagdada · A. K. Bhojani · D. K. Singh (✉)
Department of Basic Sciences, Institute of Infrastructure Technology Research And Management, Ahmedabad, Gujarat 380026, India
e-mail: dheerajsingh@iitram.ac.in; dheerajsingh84@gmail.com

D. K. Singh et al. (eds.), *Nanomaterials*,
https://doi.org/10.1007/978-981-19-7963-7_1

been obtained, also known as the most abundant presolar grain [1], which suggests that the nanomaterials may have originated from the big bang process. One example of nature's nano assembly is the Nacre, where the mollusks are formed from calcium carbonate through the nanopatterning process and provide outstanding hardening [2]. Another attraction of nature's nanomaterials is spider silk, prepared from the polymer consisting of protein and exhibits strength more than that of high-tensile steel [3].

Since, prehistoric times, humans have synthesized and utilized nanomaterials for several purposes. Specifically, artists from ancient times have strategically used nanomaterials for cave paintings. From Sulawesi, Indonesia, cave paintings consisting of hand stencils have been found dated back to 40,000 BCE, which were prepared from fat, charcoal, and plant pigments [4]. Date back to 34,000 BCE, another piece of work of the hand stencil and wild mammals have been discovered in the Chauvet Pont-d'Arc Cave, France, where graphene and other nanocomposites have been used unknowingly [5, 6]. Further, for cloth bleaching purpose Cyprus clay have been utilized since 5000 BCE [7].

In ancient times, humans are not known that soot exhibits carbon-based nanomaterials. Before 4500 years, humans utilized asbestos nanofibers having a diameter of 50–200 nm to the reinforcement of ceramic matrix materials [8]. The PbS nanoparticles (also known as galena) have been used for the hair dye material, where the PbS change the optical properties of the hair shaft with no effect on the mechanical properties of the hairs [9]. This concept provided the development of the hair dye formula 2000 years ago [9]. The azure pigment exhibits a hydrophobic nature, also known as the Maya blue used for corrosion resistance, manufactured using the indigo dye and nanoporous clay in the Mayan city of Chichen Itza [10, 11]. One of the ancient artworks from the Roman time was the Lycurgus Cup (~400 CE), which changes its color from green to red under the illumination of light (See Fig. 1.1). The material of the cup consists of the doping of silver and gold nanoparticles modifies the color according to the light [12]. In medieval times, the bright red and yellow colors of the glass windows in the churches appeared due to the presence of gold and silver nanoparticles [13]. Between 300 and 1700 AD, nanoparticles have been extensively used for manufacturing steel (also known as damascus steel) swords, where nanoparticles play a vital role in the strength, sharpness, and shatter resistance [14]. In 900 AD, the Indian civilization used cementites nanowires and carbon nanotubes in the microstructure of wootz steel [15].

The scientific report for nanomaterials started in 1857, by Michael Faraday, synthesized the colloidal solution of gold nanoparticles, called "activated gold." Faraday discussed this work at the royal society of London with the statement, "Gold reduced in exceedingly fine particles, which becoming diffused, produce a ruby red fluid, the various preparations of gold, whether ruby, green, violet or blue consist of that substance in a metallic divided state" [16]. Figure 1.2 depicts the major milestones of the developments in the field of nanomaterials and nanotechnology. Moreover, in the 1940s, silica nanoparticles have been used as a replacement for carbon black in rubber reinforcement [17]. The concept of nanotechnology and nanoscience was boosted in 1959 through the revolutionary statement "There's plenty of room

Fig. 1.1 Lycurgus cup, left size is reflected and right side shows the transmission of light (adapted with permission from [8]). Copyright (2013) (Elsevier)

at the bottom" by physicist Richard Feynman during his talk at the American Physical Society meeting at the California Institute of Technology [18]. In the same talk, Feynman asked and discussed that "W*hy cannot we write the entire 24 volumes of the Encyclopedia Brittanica on the head of the pin.*" Moreover, Feynman suggested the possibility of modulation in materials at the atomic level, where the properties are drastically different from the large scale. Furthermore, Feynmann also depicted that smaller and smaller sizes neglect gravity, while van der Waals interactions and surface tension parameters would be more dominant. Due to his revolutionary statements and discussion, Richard Feynmann is also known as the "Father of nanotechnology," although he never mentioned explicitly the word Nanotechnology [17]. In 1974, Japanese scientist, Norio Taniguchi was the first to define the term Nanotechnology as the process of atomic-level deformation and separation of materials [19]. However, the term nanotechnology was not famous till 1986, when the American engineer Eric Drexler published a book named *Engines of creation: the Coming Era of Nanotechnology*, which brings spans the revolutionary field of nanotechnology [20]. After that, the great inventions in experimental techniques such as scanning tunneling microscopy (STM) by Heinrich Rohrer and Gerd Binnig in 1981, which allowed to see the materials at the atomic scale leads to a boost in the awareness of nanotechnology. For such an invention, Rohner and Binning were awarded the Nobel prize in physics [21]. After that, the growth in the carbon allotropes towards the nano dimensions fuels the development of nanomaterials. Started with the discovery of fullerenes by Harold W. Kroto, Richard E. Smalley, and Robert F. Curl Jr. in 1985 [22], and all three scientists were awarded the Nobel prize in 1996. Further, the IBM scientists successfully orchestrated the logo of IBM by moving the Xenon atoms on the surface using STM tips [23]. Such exceptional work moves one step closer to the Feynmann hypothesis. For carbon nanotubes, Japanese inventor and physicist Sumio Iijima is often cited as the inventor of carbon nanotubes [24]. After

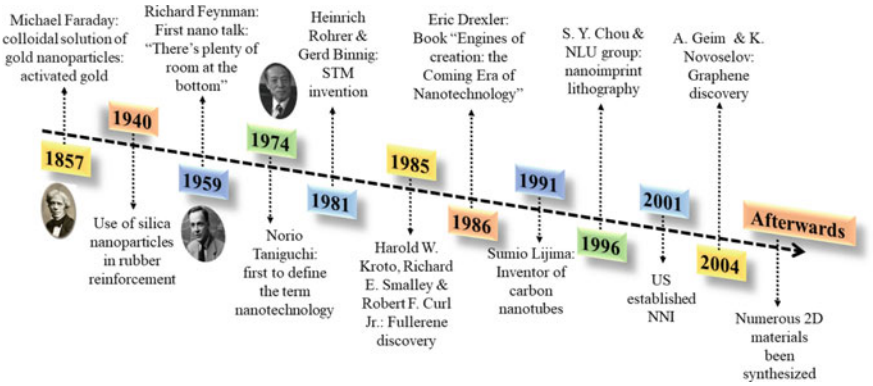

Fig. 1.2 Scientific milestones of nanomaterials and nanotechnology from the year 1857

that, the concept of nanoimprint lithography has been proposed for the first time by Chou and the group at the Nanostructure Laboratory of the University of Minnesota [25]. The transformation of integrated chips (ICs) also can be considered a part of the historical development of nanotechnology in the field of electronics. In 1947, the single transistor size was in the range of micro-objects, based on the demands of miniaturization and maintaining the pace with Moore's law, the size of transistor deduced significantly and in the year 2002, it further reduced to 90 nm [17]. Currently, the size of transistors is reduced to below 10 nm. In 2001, the United States established the national nanotechnology initiative (NNI) for the systematic and scientific development of nanomaterials and nanotechnology [26]. With novel properties and remarkable applications, the most eminent carbon-based nanomaterial, single-layer graphene has been synthesized successfully by Andre Geim and Konstantin Novoselov and awarded the Nobel prize in Physics in the year of 2010 [27]. The discovery of graphene further leads to the development of numerous two-dimensional materials. There are several specific journals devoted to nanotechnology and nanomaterials such as the International Journal of nanotechnology, Journal of nanoscience and nanotechnology, Journal of nanoparticle research, Nano letters, etc., have been started [26].

1.2 What Happened at the Nanoscale?

The nanometer is the distance, which is equal to the 1 billionth part of the one-meter distance (1 nm = 10^{-9} m). The properties of nanomaterials show a drastic change when one of the dimensions or sizes belongs to the nanometer range. Now, the question is: why the properties of materials are so different at the nanometer scale compared to their bulk structure? The classical mechanics or thermodynamics failed to reveal the proper explanation of the properties of nanomaterials. While quantum

mechanics unveil the fundamental aspects of the materials at the nanoscale region, where the motion of the electron is confined. The size or dimension of materials is analogous to the de Broglie wavelengths of electrons, phonons, or excitons, the confinement effect originated, which leads to the dramatic variations in the properties of the materials. Based on the amount of confinement, the materials can be distinguished into (i) quantum dots or zero-dimensional materials (0D), (ii) quantum wires or one-dimensional (1D) materials, and (iii) two-dimensional (2D) materials or thin films. The detailed classification of nanomaterials is discussed in the next section. Due to the confinement effects, the density of states (DOS) plays an important role in the fundamental understanding of the transport, spectroscopic and optical properties of materials at the nanoscale region [28]. The density of states is defined as the number of energy states for the range of unit energy. For each dimensionality of the particles, the density of states related to the energy is presented in Fig. 1.3. It is clear that the DOS for 0D materials has discrete energy levels and is represented by the Dirac delta function. In the case of 1D materials or nanowires, the energy states are inversely proportional to the square root of the energy. However, for 2D materials or thin films, the density of states becomes constant as a function of energy, while the same is proportional to the square root of the energy for the case of 3D materials, where no quantum confinement is probed [28]. Moreover, reducing the particle size increases the portion of atoms at the surface of the nanomaterials. Therefore, the nanomaterials exhibit a larger surface area to volume ratio, compared to the bulk materials, which results in anomalous changes in the fundamental properties. Furthermore, at the surface region, the atoms may possess unsatisfied dangling bonds, which exhibit lower stability than that of the bulk materials. The interaction of materials occurred at the surface, and therefore, due to unsatisfied bonds and large surface-to-volume ratio, the nanomaterials reveal a higher chemical activity compared to the 3D materials. The fascinating impact of the quantum confinement on the physical properties is the variation in the band gap with the size of the nanomaterials [29, 30]. Here, the confinement leads to an increase in the band gap of nanomaterials. Figure 1.4 shows the schematic diagram of the particle size-dependent band gap variation. For the weak confinement region, the coulomb energy is stronger than the confinement energy, which results in the electron–hole as a pair product, while, for the strong confinement regime, the energy of confinement overcomes the Coulomb energy and the electron and hole exhibit separate confinement in the spherical potential [31–33]. The optical absorption spectrum of the nanomaterials responds according to the size confinement of the nanoparticles, which provides the tunning of the light-absorbing properties at the nanoscale. For example, the photoluminescence peak of the CdSe quantum dots reduces with increasing size and exhibits the shifting of the peak toward blue light [34]. The optoelectronic properties of the graphene have been significantly tunned by preparing graphene nanosheet using the bottom-up approach, where hydrocarbons covered the graphene to maintain the sp^2 configuration [35].

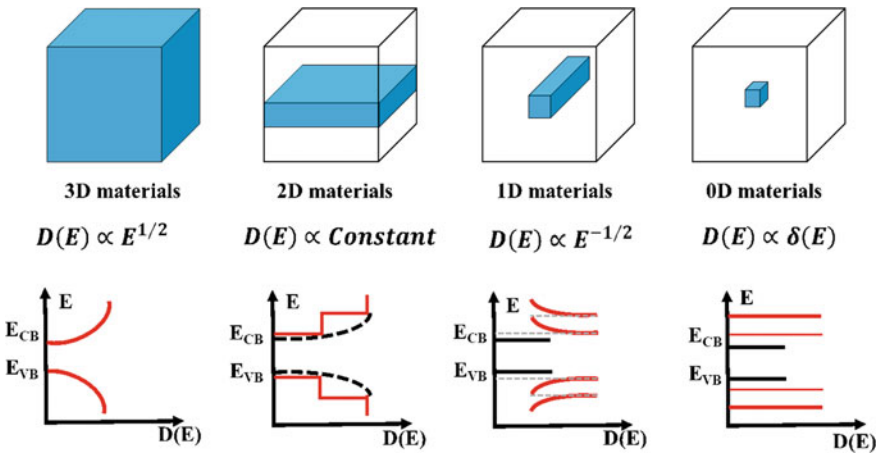

Fig. 1.3 Upper panel represents the schematic presentation of confinement effect. While lower panel depicts the nature of density of states with increasing the confinement in each dimension

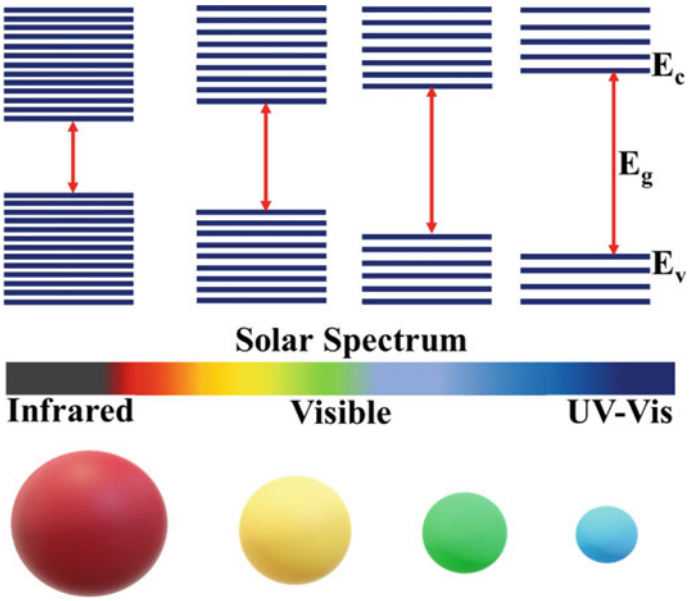

Fig. 1.4 Schematic presentation of the electronic properties of the nanoparticles with various sizes

1.3 Classification of Nanomaterials

The most studied materials of the current century, nanomaterials, gave birth to the new field of science and technology, often called nanotechnology. This class of materials is

manufactured or fabricated at the nanometer scale and the properties of nanomaterials are drastically changed compared to that of bulk materials. The classification of nanomaterials depends on several factors such as the origin, size, shape, chemical composition, characteristics, and applications. Based on the origin, there are two types of nanomaterials, naturally originated which are produced non-intentionally and belong to the environment, while another class consisting the nanomaterials made up of defined purpose through the systematic synthesis or fabrication process such as top-down and bottom-up approaches.

On the other hand, based on composition, the nanomaterials are classified into majorly four categories, carbonaceous, organic, inorganic, and composite-based nanomaterials. The carbonaceous nanomaterials exhibit the sp^2 hybridization in their orbital configuration. Graphene, nanodiamond, carbon nanotubes, fibers, nanowires, and nanographite are examples of carbonaceous nanomaterials. Chapter 2 consisting a detailed discussion of carbon-based nanomaterials. The organic category includes bioinspired nanomaterials such as micelles, dendrimers, ferritin, liposomes, etc., and exhibits a size ranging from 10 to 1000 nm [36]. On the other hand, the inorganic nanomaterials consisting of non-carbon elements such as metal and metal oxides (Chaps. 4 and 5), metallic nanoclusters, magnetic nanomaterials (Chap. 6), nanoclay, zeolite, groups IV–VII-based nanomaterials (specifically the chalcogenides, Chap. 7), MXenes (Chap. 8), etc. The majority of the inorganic nanomaterials exhibit a crystalline nature and different sizes and shapes (spheres, cubes, stars, ellipsoids, cylinders, etc.) in their structure, resulting in a wide range of desired properties for various fields of science and technology. The fourth category in this section includes the composite-based nanomaterials (Chaps. 9 and 10), which exhibit the matrix-based structure, where the metal, polymer, hydrogel, or ceramic are considered as the matrix in the nanostructure. The hydrogels depict biocompatible activities in precise surroundings and have been utilized for drug delivery applications [37].

Based on the dimensionality the nanomaterials have been classified into three types; zero-dimensional (0D), one-dimensional (1D), and two-dimensional (2D) nanomaterials. The size and morphology change according to the dimensionality of the nanomaterials, which provides a significant tunning of the properties.

0D nanomaterials: All three dimensions are confined to the nanometer scale, consisting of a few tens to thousands of atoms in the range of 2–100 nm. The 0D materials include fullerenes, quantum dots, nanoclusters, nanoparticles (magnetic and metallic), etc. Fullerenes having 60 carbon atoms, named buckminsterfullerene (C_{60}), honor the American architect Buckminster Fuller who is known to bring geodesic structures into the field of architecture [22]. The cage-like structure has the shape of a soccer and a diameter of ~1 nm, fullerenes consisting of the bonds of each carbon atom to the other three carbon atoms similar to graphite. Despite having a sphere-like structure all carbon atoms in the structure exhibit the sp^2 hybridization and possess a higher surface-to-volume ratio for broad applications in the field of science and technology. Other 0D nanomaterials are the quantum dots (QDs), which exhibit a semiconducting nature having a size in the range of 2–10 nm and consisting the 10–50 atoms. The optical properties of the quantum dots are quite different than that of the bulk materials as QD emits various colors of light with the size and surface

morphology. Due to its very small size, the optical properties are highly sensitive to the number of atoms. For example, the carbon quantum dots having a size <1.2 nm possess the emission of ultraviolet (UV) light, while the same has emitted visible light with a size between 1.5 and 3 nm, which further provides the infrared light for the size of ~3.8 nm [38, 39]. On the other hand, metal and metal oxide nanoparticles exhibit a similar nature of size-dependent optical properties, which is also known as surface plasmon resonance (SPR) [40, 41]. The silver and gold nanoparticles were studied most for the SPR phenomena, where the electric field inside the particle will be significantly enhanced through the coupling of plasmon with the external incident light and provides the scattering and absorption of light [42–51]. Both gold and silver nanoparticles exhibit potential applications in medical science, diagnostics, sensors, and solar cells. Specifically, silver nanoparticles possess promising usability as antibacterial and anti-microorganisms [52, 53]. Similarly, metal oxide nanoparticles such as ZnO, TiO_2, Fe_2O_3, etc., possess excellent size and shape-dependent physicochemical properties and broad applications in renewable energy and medical sectors [54–56].

1D nanomaterials: This class of nanomaterials exhibits the two dimensions in the nanoscale range. Examples are nanotubes, nanofibers, and nanowires, which are heavily attractive for usage in thin film-based devices [57–59]. One of the most studied 1D nanomaterials is the carbon nanotubes (CNTs), which are the elongation of the fullerenes in one of the dimensions with a cylindrical shape, consisting of the micron to the millimeter of length and nanometer range of diameter. CNTs are of two types, one is single-walled CNTs (SWCNTs), while another is multi-walled CNTs (MWCNTs), which exhibit an interlayer distance similar to that of graphite [60]. Based on the chirality and diameter of the nanotubes the desired range of physical properties can be achieved. For example, the bandgap of the CNTs is highly sensitive to the diameter, where the larger the bandgap results from the smaller diameter and vice versa [61]. CNTs possess exceptional mechanical properties among all carbon materials, whereas Young's modulus of CNTs is approximately five times higher than that of steel [62, 63]. Apart from carbon-based 1D nanomaterials, metal chalcogenides and boron nitride-based 1D nanomaterials are also reported significantly for their physical properties and variety of applications with the size and length of the nanoribbon and nanotubes [64].

2D nanomaterials: With the plane-like structure in two dimensions, 2D nanomaterials have one dimension in the nanometer range, where electrons are confined to move. This class of materials includes graphene and graphene oxides (Chap. 3), transition metal dichalcogenides and oxides, boron nitride and pnictides, group-IV chalcogenides, group-IV-based elemental 2D nanomaterials, and MXenes. The 2D materials revealed the prospective applications in the electronic, optoelectronic and sensing devices, energy and environmental sector as well as in biomedicine, attributed to their exceptional physical properties such as high mechanical strength, electronic and optical tunability and flexibility in the structure [65–67].

1.4 Synthesis of Nanomaterials

Over the decades, nanostructured materials have captivated a significant research interest due to their size and shape depending on physical, chemical, electronic, and magnetic properties. The performance of nanomaterials depends on their properties, which mainly depend on the structure, composition, defects, and interfaces, and are directed by synthesis root. Therefore, several synthesis techniques have been developed to construct different types of nanomaterials with controlled size, shape, structure, and dimension. Such available synthesis techniques are used to fabricate the various form of nanomaterials like nanocolloids, powders, clusters, roads, tubes, and so on. The synthesis methods of nanomaterials (nanoparticles) are categorized into two parts: (i) top-down, and (ii) bottom-up approaches. The first approach is a breakdown method in which a solid material is converted into nano-sized particles in the presence of external force. In the second approach, the nanoparticles build by assembling atoms and molecules from atomic to the nanoscale, also called as build-up method. Figure 1.5 classified the top-down and bottom-up techniques.

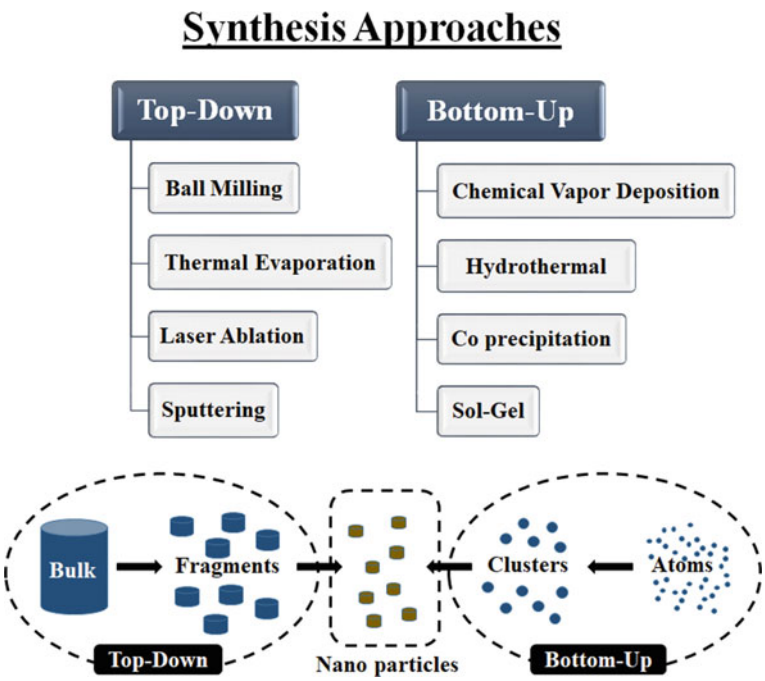

Fig. 1.5 Nanomaterials synthesis techniques: top-down and bottom-up approaches

1.4.1 Top-Down Approach

The top-down approach is easy to use for the transformation of bulk materials into nano-sized structures/particles via wet and dry grinding techniques. Presently, at the industry level, the top-down approach is dominant for the fabrication of man-made nanomaterials. For example, in the semiconductor industry, the photolithography procedure has been used to imprint the metal oxide semiconductor field–effect transistor (MOSFET) onto a silica wafer [68, 69]. In this approach, several operations have been performed on large-scale materials to convert them into nanoscale particles. However, these approaches required a large installation area for setup which makes them quite expensive. Further, the slow growth rate makes them impropriate for the production of large-scale amounts. Top-down approaches are also not suitable methods for soft materials because the mechanical parts used in these devices to grind the materials are rigid and hard. The major downside of these techniques is the irregularity in the shape and particle size of constructed nanomaterials, e.g., the fabricated nanowires using the lithography technique contain lots of structural defects and impurities. Some of the well-known top-down approaches are ball milling, thermal evaporation, laser ablation, and sputtering techniques.

Ball milling. Ball milling is a well-known top-down grinding approach for the fabrication of nanoparticles in powder form. It is one of the easiest and most productive mechanical processes used to create a variety of nanoparticles and metal alloys by transferring the kinetic energy of the grinding medium into the sample material. Ball milling works on the principle of impact and attrition (i.e., friction). As demonstrated in Fig. 1.6, the ball mill consists of a hollow cylindrical shell rotating around its axis horizontally or at a small angle with a horizontal line. Based on the rotation of the ball mill, the ball milling process is divided into various types: planetary, attrition, horizontal, rotatory, and vibratory mill. The grinding medium partially filled inside the ball mill is the hard sphere balls made from steel (chrome and stainless), rubber, flint pebbles, or ceramic materials. The sample material is also placed inside the ball mill along with the grinding medium. As the ball mill rotates, the grinding balls lift near the top of the mill and then drop down to the ground, resulting in the reduction in the size of the target materials by impact. The impact between the grinding balls, mill wall, and target materials creates a fine powder of sample material. The ball milling process is also used for several purposes such as mixing two or more materials, compression of particle size, change in particle structure, agglomeration, modifying the material characteristics, and so on [70]. Some examples of synthesized nanomaterials using different ball milling processes are ZnO nanoparticles (10–30 nm) using high-energy ball milling [71], GR oxide nanoparticles (40 nm) [72], CuO nanoparticles (13.8 nm) [73], and graphite oxide nanoparticles using planetary ball milling process [74].

The ball milling technique possesses several advantages and benefits. Such as, it is a low expensive process, suitable for continuous operation, nanoparticles with the size of 2–20 nm can be produced, simple in serving, reliable and safe, long lifetime, helpful for thickness reduction of various materials, and high capacity, for open and

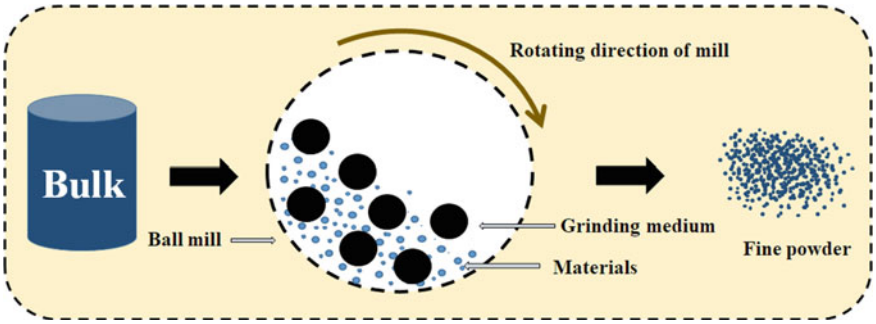

Fig. 1.6 Schematic diagram of ball milling top-down approach

close circuit grinding, to synthesize few milligrams to kilogram nanoparticles within a short time interval of few minutes to few hours [28, 76–78]. The ball milling technique also possesses several drawbacks like low surface, irregular shape nanoparticles, formation of disordered crystal structure, and grinding needs a bunch of energy, noise, and heavyweight [28, 75, 76].

Thermal evaporation. Around the 1850s, Faraday [16] construct an endothermic process known as thermal evaporation in which heat is used for the chemical breakdown of a molecule [79]. Thermal evaporation is also a popular top-down approach for the production of various nanomaterials such as inorganic nanoparticles [80], thin films [81], etc. Figure 1.7 demonstrates the schematic representation of the thermal evaporation technique. As shown in Fig. 1.7, the metal crucible containing the target material is placed inside a high vacuum chamber having pressure below 10^{-4} Torr. In this process, the atoms/clusters/molecules are gets ejected from the target material in vapor form by heating or passing the electrical current from the metal crucible. The generated vapor flux condensed on the surface of the substrate. In electron beam evaporation, when an electron beam is bombarded on the target material it generates the vapor flux. While in the case of thermal evaporation, the joule effect with a suitable temperature has been used to heat the target material. By contacting the target materials with hot surface evaporation can be achieved, known as resistive heating, and used for materials that get vaporized below 1500 °C temperature. Carbon, tungsten, boron nitride and TiB_2 composite ceramics, and molybdenum are well-known resistive heating elements [82]. Some examples of synthesized nanomaterials by thermal evaporation technique are MoS_2 nanowafers (0.7 nm thick) [83], Zn_2GeO_4 nanocrystals (10 nm thick) [84], thin films of SnS (720 nm thick) [85], Ga_2O_3 (350 nm thick) [86].

In comparison with other techniques, the thermal evaporation process acquires numerous advantages. Some of the major advantages are high deposition rate, low-cost apparatus/cost-effective, no need for solvent, suitable for low melting point materials, monitoring and controlling of deposition rate, vapors, and thickness of the film are easy, ultrathin layer materials can be deposited [87, 88]. The thermal evaporation technique also exhibits a few disadvantages. It is incompatible with

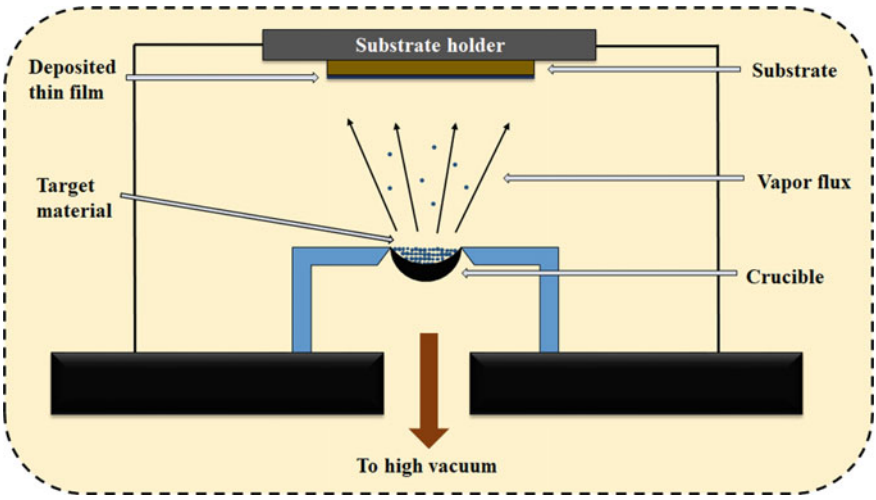

Fig. 1.7 Schematic diagram of thermal evaporation top-down approach

multicomponent thin film production, limited processing variables to control film properties, poor source material, and deposition of various alloys together is also difficult.

Laser ablation (vaporization). Laser ablation is a top-down vaporization method used to fabricate multi-component nanocrystals using high-intensity laser pulses. Laser means high power beam of electromagnetic radiation amplified by stimulated emission which has various applications in the field of medicine, industry, printing, and military [89]. Laser ablation is one of the easiest techniques presented for the synthesis of nanoparticles from multiple solvents by controlling the evaporation process in a short period of time [79]. In this process, a pulsed laser beam has been focused and bombarded on the target interest to vaporize the atoms and molecules from the surface of the target material and fabricates nanostructures as illustrated in Fig. 1.8. When a focused laser beam is targeted on the surface material, it produces vapor/plasma/liquefied metal, which interacts with the liquid medium and generates specific nanoparticles [90] The structure and properties of produced nanoparticles can be tuned by laser and liquid medium (water, ethanol, etc.) [91]. The ablation process only takes place when a target material starts evaporating or melting through absorbing a sufficient amount of energy. It means ablation is a process associated with both evaporation and melting [92].

Usually, the synthesis rate of nanoparticles depends on the energy of the laser pulse. Laser is classified into two types (Infrared and UV/excimer laser) according to their wavelengths, in which excimer is a pulsed gas laser used to generate UV light with power efficiency in the range of 0.2–2% [92]. Laser ablation has applications in numerous fields of ceramics, polymer, and glass industries as well as in cutting,

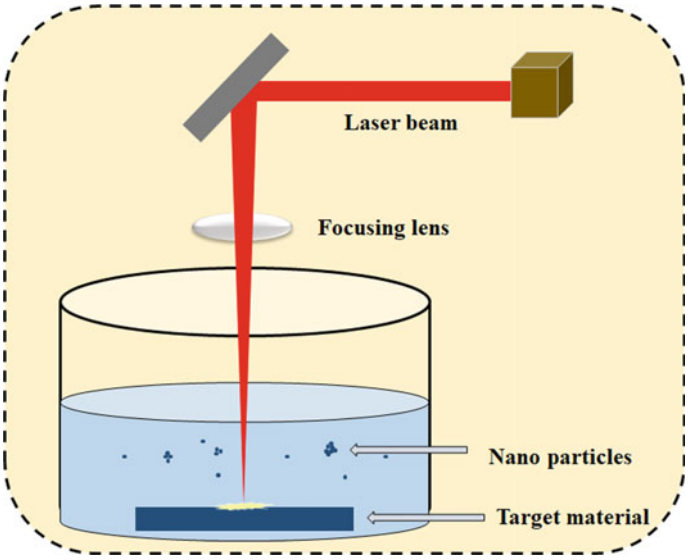

Fig. 1.8 Schematic diagram of laser ablation top-down approach

drilling, and milling through a laser beam. Some examples of synthesized nanoparticles by laser ablation process are carbon nanomaterials [93], ZnO [89, 90]-, SnO [91]-, TiO_2 [90, 94]-, CdO [95]-, and Ag [96]-based nanoparticles.

Some advantages of the laser ablation technique are the ability to produce novel and multicomponent nanoparticles, and energy loss is low during the generation of nanoparticles. There are a few disadvantages of the laser ablation process such as, it needs a large amount of energy to obtain high ablation efficiency, and the increase in the ablation time reduces the effectiveness of the process [97].

Sputtering. Sputtering is a non-thermal vaporization technique, widely used for surface coating, etching, and deposition of thin layers [98, 99]. Sputtering works under low pressure (<0.67 Pa) [100], is controlled by using a vacuum pump, and contains various components like an isolated chamber, sputtering gas source, etc. The high-energy inert gas ions are used to deposit the nanomaterials on the surface of the substrate ejected from the target material as depicted in Fig. 1.9. The interaction mechanism between the ions and target material mainly depends on the ratio of ions–target atomic mass and the energy of incident ions. When the ions get to interact with the surface of the target material, various phenomenon takes place such as generating photons, sputtering out the atoms and molecules from the surface of the target material, secondary electrons, and the creation of vacancy and defects in the target material. Therefore, it is a very effective method for spintronic applications to deposit multilayer films [28]. Depending on their source materials, the sputtering technique is divided into the following types: (i) direct current (DC) sputtering, (ii) reactive sputtering, (iii) radio frequency (RF) sputtering, and (iv) magnetron sputtering. The efficiency of the sputtering technique can be improved by increasing

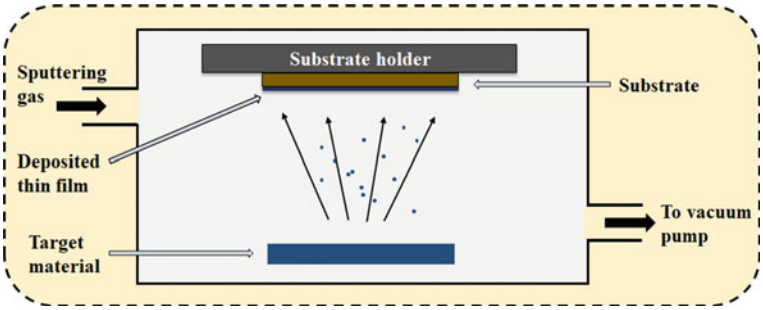

Fig. 1.9 Schematic diagram of a sputtering top-down approach

the efficiency of ions, deposition rate, and plasma ionization, and by decreasing the area of the deposition chamber [101].

Some advantages of the sputtering deposition technique are working efficiency at low temperature, uniform coating of a large area possible, and sputtering and deposition of various compounds and alloys possible [102]. A few disadvantages of this technique are the low sputtering rate of thermal evaporation technique, low purity of deposited films, generates a large amount of heat [103].

1.4.2 Bottom-Up Approach

The bottom-up approach is a constructive technique for the fabrication of nanomaterials through the self-assembling of atoms and molecules. This approach is referring to the growth of nanomaterials via atom-by-atom, molecule-by-molecule, and cluster-by-cluster. It is generally divided into two phases: gaseous and liquid phase methods. It works on the principle of self-assembly also known as molecular recognition. The term self-assembly indicates the more and more growth of one's kind from itself of materials. Self-assembly also refers to the shaking and baking, shaking means gathering precursors from various positions and baking means applying energy in the desired space to allow the configuration of nanomaterial. Several biological systems such as proteins, RNA, and some virus exhibits extraordinary self-assembling capabilities by transforming the randomly arranged coil into a linear polymer chain. The major advantage of this approach is the less generation of waste, the capability of parallel device production, and the more economical than the top-down approach. However, it gets difficult as the size of the assembly increases. Further, the bottom-up approach also provides fewer defects, short- and long-range and homogenous nanomaterials. Some of the well-known bottom-up approaches are chemical vapor deposition, hydrothermal, co-precipitation, and sol–gel synthesis routes.

Chemical vapor deposition (CVD). Over the decades, CVD is a powerful appealing technique available for the construction of nanostructures. Generally, CVD has been used for coating purposes of several organic and inorganic materials with the

help of the vapor phase of suitable chemicals. Due to their easy instrumentation and processing, cost-effectiveness, and possible deposition of various materials, CVD has been a broadly used technique at the industry level. The fabrication of certain nanocrystalline films has been done using the CVD technique under various deposition conditions. CVD has been classified into different types according to their gas pressure, working temperature, and geometrical arrangement of instruments: metallo-organic, plasma-enhanced CVD, vapor phase, and atomic layer epitaxy methods. The basic step of the CVD technique for the synthesis of nanomaterials are as follows: transport of reacting gas ions to the surface of a material and their absorption on the surface, surface diffusion, growth of nucleation process, and formation of thin films. Basic CVD techniques have been used to deposit the ceramic, semiconducting, and metallic thin films. Some examples of synthesized nanostructures by CVD are graphene films [104], nanoplatelets [105], carbon nanotubes [106], and ZnO films [107].

Several advantages of the CVD technique for the growth and fabrication of nanostructures are a large amount of good quality two-dimensional nanomaterials that can be fabricated, controllable growth rate, low processing cost, pure, excellent homogeneity, dense, and rigid production of nanostructures, crystal structure, and surface morphology process can be controlled, the synthesis process can be repeated multiple times, shaped coating possible. Apart from the various advantages, CVD also consists few drawbacks such as costly precursors, they can be flammable, poisonous, and explosive, some deposition takes place at high temperature, and sometimes creates poisonous by-products [108].

Hydrothermal. Hydrothermal is the most common solution reaction-based bottom-up approach for the preparation of nanostructured materials. In this process, the reaction between the solid material and aqueous solution inside a reaction vessel leads to the deposition of small particles in the presence of high pressure and temperature. Further, this process also works from the room to very high temperatures during the formation of nanomaterials. Here, water is used as solvent material which refers to the term hydrothermal. The morphology of prepared material can be controlled by varying the pressure from low to high, depending on the vapor pressure of the main compositions used in the reaction. Therefore, the synthesis of several types of nanomaterials has been possible by this method and exhibits significant advantages over the other synthesis roots. Nanomaterials that are not stable at a raised temperature and also have high vapor pressure can be synthesized by a hydrothermal process with minor loss of material. The synthesis rate of deposition can be controlled by the liquid phase and multiple chemical reactions in the hydrothermal process. This process gained tremendous interest in the modern science and technology field due to its low cost, homogeneous precipitation, product purity, and eco-friendly nature. The deposition process of this method is divided into the following parts: synthesis, treatment, growth of the crystal, organic waste treatment, and preparation of nanopowder. Some examples of synthesized nanoparticles by using hydrothermal are Ag [109], Au [110], CuO [111], NiO [112], and ZrO_2 [113] nanoparticles.

The hydrothermal technique possesses few advantages over the other synthesis roots. Such as high crystallinity nanocrystal is produced, size control of nanoparticles

possible, and nanomaterials having low melting point will be obtained [114]. Some limitations of this technique are difficult to control, the growth of crystal cannot be observed directly, and expensive autoclave [114].

Co-precipitation. Co-precipitation is a wet chemical bottom-up method used for the synthesis of a wide range of nanomaterials. In the co-precipitation method, inorganic salts like nitrate, sulfate, etc., are used as a precursor to achieving desirable compositions of cations in a homogeneous medium of clusters and ions. In this process, filtration and washing methods are used to easily separate the generated impurities during the precipitation process. Homogenous and small-size nanoparticles can be produced by performing several chemical reactions inside the solution of this method. In co-precipitation, it is very important to maintain the pH of the initial solution, therefore to retain the essential pH of the solution during the precipitation process, another solution carrying the precipitation agents is added drop-wise or directly which results in the production of nanoparticles. Some of the widely used precipitants are chlorides, hydroxides, carbonates, and many more. Further, to obtain high-purity nanocrystals and morphology of nanoparticles, processes like annealing, sintering, and calcination are used. The size of synthesized nanoparticles depends on the concentration and nucleation rate of the process. Such as smaller size nanoparticles are fabricated through high concentration and fast nucleation and vice versa. Therefore, this process is used to synthesize the various nanotubes, nanoparticles, and nanorings. Some of them are $CoMn_2O_4$ nanoparticles [115], and Mn_3O_4 nanograins [116].

This technique is easy to prepare and quick can work at low temperature, and homogeneity in particle size, and can be modified, and cost-effective [117, 118]. This technique acquires several drawbacks such as it is not suitable for the reactants that own different precipitation rates, the presence of impurities in the final product and the presence of several chemicals generate risky waste and can affect the purity of the final product [118, 119].

Sol–Gel. Sol–gel technique is the most common bottom-up approach used for liquid phase synthesis of nanomaterials started nearly the 1970s. The sol–gel involves the two terms sol and gel, which means two different materials or components. The term sol means the colloidal solution of solid particles in a solvent, while the gel term refers to the formation of semi-rigid mass when the solvent of sol creates a continuation network by joining particles through evaporation. Similar to the co-precipitation method, the pH control of the initial solution in sol–gel is also needed and can be achieved by adding an acidic or base solution to form a homogenous gel and also to avoid precipitations. Sol–gel is a widely used multi-step wet chemical solution process to fabricate the thin films, fibers, and nanopowders of ceramic and glass materials. The synthesis process of sol–gel is generally divided into the following parts: (i) hydrolysis, (ii) condensation, (iii) aging, (iv) drying, and (v) calcination. In the first step, a suitable precursor (metal oxide or alkoxides) is chosen to form an appropriate gel. To obtain a hydroxide solution, hydrolysis can be done with a reaction medium of water or alcohol. Afterward, condensation takes place between the neighboring molecules, resulting in the formation of a metal oxide bond and the removal of water or alcohol. This further leads to the formation of a porous structure

(gel-like liquid phase) due to polycondensation which increases the viscosity of the solvent. In the next step, the continuous polycondensation reduces the porosity and increases thickness, resulting formation of a gel structure called aging. At last, the gel is dried with the help of different drying methods and then the calcination process is executed to remove the water molecules from the sample. Here, temperature plays an important role to maintain the porous size and material density. This process leads to the fabrication of a variety of nanomaterials including glass and ceramic-based nanoparticles, thin films, and many more. Some examples of synthesized nanomaterials by sol–gel techniques are Cu-doped TiO_2 nanoparticles [119], Co_3O_4 [120], and ZnO [121] nanoparticles.

The advantages of a sol–gel technique are low cost, can work under low temperature, high-purity products, homogeneous material production, and easy fabrication of complicated nanomaterials [122, 123]. Some disadvantages of sol–gel are the long reaction time, sample purification needed, and health risks due to the presence of some organic materials [122, 123].

1.4.3 Characterization of Nanomaterials

The physicochemical features of nanomaterials such as size, shape, surface behavior, composition, crystal structure, defects, etc., play a vital role in the determination of the structure–property relation. Therefore, the characterization of nanomaterials is essential for understanding the fundamental aspects and basis for applications in the discrete area of science and technology. X-ray diffraction (XRD) technique is used to determine the crystal structure and lattice parameters of the nanomaterials, while the size, shape, and morphology of the nanomaterials are characterized through microscopy-based techniques such as transmission electron microscopy (TEM), scanning electron microscopy (SEM), high-resolution TEM, and atomic force microscopy (AFM) [124]. Further, dynamic laser scattering (DLS) has been used to determine the size distribution and aggregation states of the nanoparticles [124, 125]. The electronic structure, elemental composition, and oxidation states are identified by using X-ray photoemission spectroscopy (XPS). Vibrational spectroscopic techniques such as Raman and infrared (IR) spectroscopy are widely utilized to determine the structural composition, functionalization, and functional group binding in the nanomaterials [126, 127]. For example, the Raman spectra presented in Fig. 1.10a clearly show the differences between the bulk graphite and defect-less graphene structures as well as the displacement of the G peak towards the low wavenumber [128]. Similarly, Fig. 1.10b reveals a notable variation in the intensity of the D peak as the number of layers grows, demonstrating the significance of Raman spectroscopy for differentiating the single and multilayer structures [128].

Further, surface-enhanced Raman spectroscopy (SERS) allows the enhancement of the weak Raman signal up to 10^8 times or greater through localized plasmon resonance excitation [129]. With the aid of the SERS technique, the surface phenomena of nanomaterials, ligand assembly, and the detection of hazardous or explosive

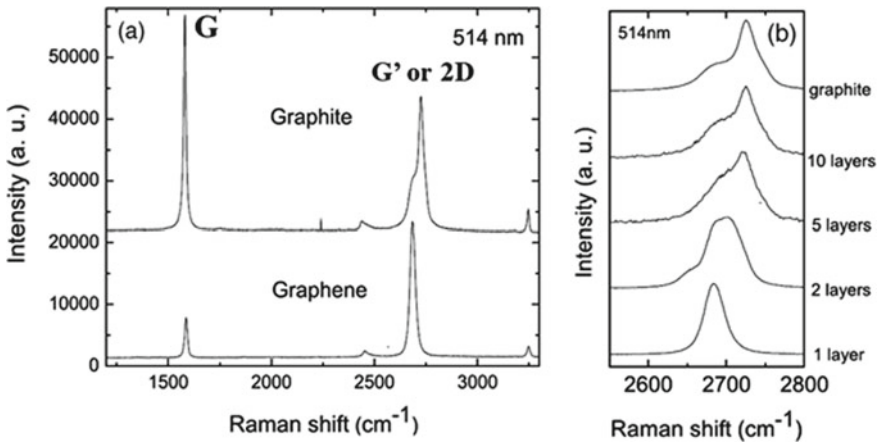

Fig. 1.10 Raman spectra comparison of **a** bulk graphite and defectless graphene, and **b** for different numbers of layers at 514 nm (adapted with permission from [128]). Copyright (2006) (Americal Physical Society)

molecules can be carried out. Furthermore, the surface charge exhibits importance in the colloidal stability of the nanomaterials [130]. The zeta potential characterization technique is the most common and widely used for the surface charge analysis and surface modification of nanomaterials [125]. The excited state electronic structure and optical properties of the nanomaterials are characterized by using UV–Visible spectroscopy and photoluminescence (PL), where the size-dependent electronic states, the change in bandgap, and binding energy of excitons can be measured [126, 127]. The mass distribution in the nanomaterials can be explored through the thermogravimetric analysis (TGA) method [125], while the chemical and molecular composition, chemical shift, and ligand density are offered by the qualitative nuclear magnetic resonance (NMR) technique [131]. Superconducting quantum interference device magnetometry (SQUID) is utilized to measure the magnetic properties such as magnetization, remanence as well as the blocking temperature of the nanomaterials [132]. Furthermore, nano-SQUID was recently developed to determine the magnetic spectroscopy and imaging of the nanomaterials [124]. For each type of nanomaterial and its specific property analysis and perspective, a detailed discussion of the characterization is presented in the subsequent chapters.

1.5 Applications of Nanomaterials

Nanomaterials possess unique physical, chemical, electrical, optical, and magnetic properties, which attract researchers for a wide variety of applications in diverse fields from science to engineering. At the nanoscale, the material properties are size-dependent, which has opened the path for making new instruments, and devices

to improve the quality of life and facilities. Figure 1.11 describes the broad range of applications of nanomaterials. A few of them are briefly discussed as follows. Further, subsequent chapters consist of an in-depth discussion regarding different types of nanomaterials applications in the different fields of science and technology.

Electronics: Nanoparticle-incorporated electronic components aim to take advantage of nanoproperties of materials for several potential applications. Nanocomponent-based devices are useful in many ways such as providing fast process, better printing, more information storage, flexible displays, energy efficiency, and longer lifetime. Nanomaterial-based transistors are faster and more powerful. Electronic devices such as television, laptop, computer, camera, and mobile phones have used nanomaterials to gain better performance, lightweight, and low-cost manufacturing. Nanoelectronics-based products include transistors, diodes, LED and plasma displays that improve the display screen, and capabilities of data storage, reduce the size, and procedures, less power consumption [133, 134].

Sensors: Nanomaterial-based sensors exhibit many advantages at the micro- and macro-scale level due to their novel properties. Such as reduction in size, weight, and cost, less power consumption, increases sensitivity, mass production, and integration level will be higher, in medical sensors. Based on the sensing applications, nanosensors are classified as transduction, measurand, and technological aspects. It can be further classified according to the use of nanostructured materials like tubes, wires, particles, composites, etc. Nanosensors also possess industrial applications in communications, transportation, medicine, safety, and security, for detecting chemicals, and radiation damage in the human body, detecting and destroying tumors, and defense and military [135]. Gold nanoparticles and quantum clusters bear the potential application for the sensing of hazardous metal ions [136–138]. Silver nanoparticles have been used to detect various fungi using the SERS technique [139–141].

Catalysts: Nanocatalysts are more efficient than conventional catalysts due to the large surface-volume ratio of nanomaterials and significantly enhancing the chemical

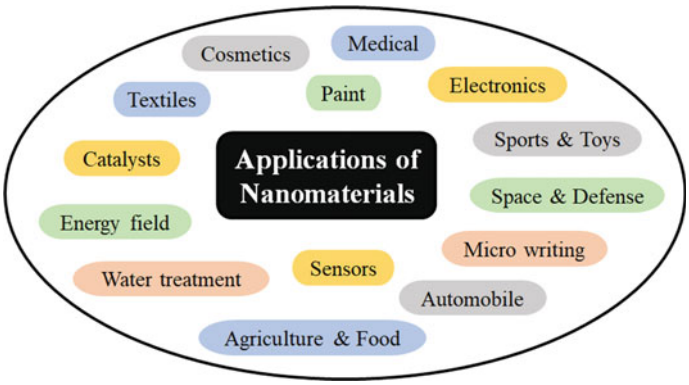

Fig. 1.11 Applications of nanomaterials in diverse fields

reaction ability. Nano-based catalysts are cost-saving, have low waste and environmental impact, as well as highly selective. Due to the nanosize of particles, the nanostructured catalysts provide a large surface area to significantly enhance the chemical reactivity. Several nanocatalysts made from metal, carbon, quantum dot, thin layer, ceramic, etc., are currently available in the commercial market [142].

Textiles: The incorporation of nanomaterials introduces multifunctional properties and applications of fabrics for the textile industry like strain resistivity, water absorption capability, antibacterial, light emitting, etc. Further, the antimicrobial property can also be introduced into fabrics by inserting nylon and other polymer-based nanoparticles. The zinc oxide-based nanoparticles can also be imparted for an antimicrobial property without changing the gloss and color of fabrics. Plasma technology is also a useful method to obtain antifungal, antibacterial, and water-repellent properties in textiles. In addition, the presence of nanomaterial helps to gain heat resistivity, sensing ability, mechanical flexibility, color changing, sensor network, pressure detection, temperature measurement, etc. Integrating optical fiber sensors with fabrics and composites helps to measure the strength of buildings and bridges. Moreover, the nanoparticle-fabricated fibers will help soldiers during the night patrolling and attack [135, 143].

Agriculture & Food Industry: Agriculture and the food industry also have potential applications for nanomaterials. Some of them are present here: nanoporous zeolites and fertilizers for water release and plants, nanosensors to check soil quality and plant health, nanocomposites and antimicrobial nanoemulsions for food packaging, nanobarcodes for food and agriculture identification, food supplements, color additives, organic dyes, photocatalytic materials to disinfect the food and agriculture products, less unhealthy and attractive food, enhancing the nutritional contents of food and increasing the shelf life of food products and many more [143, 144].

Medical: The medical field achieves a great revolution and is more patient-friendly after the introduction of nanomaterials in the biotechnology field. The smaller size and huge variety of nanoparticles show their potential for diagnosis and treatment. The nanoparticle-based treatments have significant applications such as drug delivery, disease diagnosis, TB and cancer therapy, health monitoring via biosensors, disease detection, tissue engineering, repairing neurological damages, etc. The gold and silver nanoparticles have been widely investigated for their antioxidant, antibacterial, and anti-cancer [136, 145–151]. For cancer treatment, nanomedibots have been used to release anti-cancer pharmaceuticals on the cancer cell to penetrate the tissue and remove them mechanically with minimum side effects. Gold-coated nanoshells are also useful in the treatment of tumors [143].

Paint: The performance of paints can be improved by modifying their properties through the incorporation of nanomaterials. The presence of nanoparticles makes paint lighter, reduces the coating weight, is cost-effective, increases the durability, reduces the impact on health and the environment, long lifetime, anti-fouling surface for heat exchange, and leads the energy saving [152].

Energy: Nanomaterials play an important role in the green energy field owing to their great efficiency and low-cost manufacturing process. Some of the well-known nanostructured technologies for the energy field are photovoltaic systems, fuel cells,

hydrogen storage and conversion, thermoelectric, light-emitting devices, and many more. The nanomaterial-based solar cell also gained higher efficiencies and better performances. Nanomaterials also play an important role in the enhancement of the performance of Li-ion batteries [153]. Such as nanomaterials-based Li batteries exhibit a long lifetime and have the potential to operate under extreme conditions [153]. Further, the ultracapacitor electrodes made up of nanomaterials increase the energy storage capacity of capacitors [135].

Space & Defence: Nanomaterials are important for space and defense fields due to their lightweight, small size, and great power consumption abilities which enhance the system intelligence of wireless networks. There are various potential applications of nanomaterials for space and defense systems such as, the lighter weight of vehicles increases the fuel economy and their capacity for covering the long distance, better thermal control due to the adaptive structure of nanomaterials, lightweight clothes, for tracking and tracing applications, in motion sensors, high energetic propellants, biometric sensing for face, DNA and fingerprint identification, wireless sensor networks, bulletproof clothes, improving the sensitivities of detectors, smaller size satellites with better communication, navigation, and data processing [135].

Sports & Toys: Nanomaterials also possess potential applications in sports instruments and toys. Nanoclays-based tennis balls increase the lifetime of the ball by filling the pores and air pressure inside. Carbon nanotube-based racquets are having high strength or toughness, and are lighter weight. In the toy industry, nanomaterial-based motors, dolls, and robots are also very popular among children by making the toys much smoother, natural-looking, and attractive [154].

Cosmetics: Nanomaterials are also very popular in cosmetic products like sunscreen, personal care, and anti-aging due to their potential features. In sunscreen, titanium and zinc oxide-based nanomaterials are used to block UV rays and prevent sunburn. Further, the presence of such nanoparticles in creams makes them transparent and after applying the skin will be much more clear and more visible. The use of nanoparticles in other products like powder, spray, gel, and hair care makes them anti-fungal, anti-oxidant, anti-odor, and anti-bacterial and also increases the smoothness of the skin. Nanomaterial-based contact lenses are also becoming popular in fashion statements [155].

Water Treatment: Our earth contains almost around 1% freshwater for living things, suggesting the need for effective water management facilities. Among the available various standard water treatment methods like mechanical separation, UV radiation, and chemical and biological treatments, the nanomaterial-enabled products are more economical and have better efficiencies. Further, nanomaterial-based devices also contribute in many ways to water management. Some of them are listed here: purification of wastewater through nanoparticles, carbon nanotubes, nano clays, and membranes for water filtration and softening, checking water quality by nanosensors, magnetic and titanium dioxide nanoparticles to remove heavy metals, salts, toxins, and impurities from water, helpful in the removal of pathogens responsible for the waterborne diseases [156, 157].

1.6 Conclusions

Nanomaterials exhibit dimensions in the range of 1–100 nm, where the properties can be tuned with the size variation. Conventional physics failed to explain the phenomenological behaviors of nanomaterials, and therefore, quantum mechanics provides a significant explanation. Nanomaterials existed since prehistoric times and become the key to the development of revolutionary technology in the modern era. The synthesis approaches, top-down and bottom-up, for the production of nanomaterials, have been briefly glanced at in the present chapter. The detailed synthesis procedures and unique fundamental characteristics such as physical, biological, and chemical properties of a variety of nanomaterials are devoted in the subsequent chapters. The scientific advancement in technology leads to the rapid growth in the development of nanomaterials with numerous applications in almost all sectors including energy, catalysts, defense, space, electronics, optoelectronics, medical, pharmacy, biotechnology, food industries, etc.

References

1. Z.R. Dai, J.P. Bradley, D.J. Joswiak, D.E. Brownlee, H.G.M. Hill, M.J. Genge, Nature **418**, 157–159 (2002)
2. X. Li, W.C. Chang, Y.J. Chao, R. Wang, M. Chang, Nano Lett. **4**, 613–617 (2004)
3. S. Keten, M.J. Buehler, Appl. Phys. Lett. **96**, 153701 (2010)
4. M. Aubert, A. Brumm, M. RamlI, T. Sutikna, E.W. Saptomo, B. Hakim, A. Dosseto, Nature **514**, 223–227 (2014)
5. H. Valladas, J. Clottes, J.-M. Geneste, M.A. Garcia, M. Arnold, H. Cachier, N. Tisnérat-Laborde, Nature **413**, 479 (2001)
6. A.K. Yetisen, A.F. Coskun, G. England, S. Cho, H. Butt, J. Hurwitz, S.H. Yun, Adv. Mater. **28**, 1724–1742 (2016)
7. G. Rytwo, Macla. **9**, 15–17 (2008)
8. F.J. Heiligtag, M. Niederberger, Mater. Today **16**, 262–271 (2013)
9. P. Walter, E. Welcomme, P. Hallégot, N.J. Zaluzec, C. Deeb, J. Castaing et al., Nano Lett. **6**, 2215–2219 (2006)
10. P. Gomez-Romero, C. Sanchez, New J. Chem. **29**, 57–58 (2005)
11. L.A. Polette-Niewold, F.S. Manciu, B. Torres, M. Alvarado Jr., R.R. Chianelli, J. Inorg. Biochem. **101**, 1958–1973 (2007)
12. I. Freestone, N. Meeks, M. Sax, C. Higgitt, Gold Bull. **40**, 270–277 (2007)
13. J. J. Kunicki-Goldfi nger, I. C. Freestone, I. McDonald, J. A. Hobot, H. Gilderdale-Scott, T. Ayers, J. Archaeol. Sci. **41**, 89–105 (2014)
14. M. Reibold, N. Pätzke, A. Levin, W. Kochmann, I. Shakhverdova, P. Paufler, D. Meyer, Structure of several historic blades at nanoscale. Crys. Res. Technol. **44**, 1139–1146 (2009)
15. M. Reibold, P. Paufler, A.A. Levin, W. Kochmann, N. Pätzke, D.C. Meyer, Nature **444**, 286–286 (2006)
16. M. Faraday, Phil. Trans. R. Soc. Lond. **147**, 145–181 (1857)
17. N. Kumar, S. Kumbhat, *Essentials in Nanoscience and Nanotechnology*, 1st edn. (Wiley, Hoboken, NJ, United States, 2010)
18. R.P. Feynman, Eng. Sci. **23**, 22–36 (1960)
19. N. Taniguchi, On the basic concept of "nano-technology," in *Proceedings of the International Conference on Production Engineering, Part II* (Japan Society of Precision Engineering, Tokyo, Japan, 1974) pp. 18–23

20. S. Kaplan, J. Radin, Soc. Stud. Sci. **41**, 457–485 (2011)
21. G. Binning, H. Rohrer, IBM. J. Res. Dev. **30**, 355–369 (1986)
22. H.W. Kroto, J.R. Heath, S.C. Obrien, R.F. Curl, R.E. Smalley, Nature **318**, 162–163 (1985)
23. CNET, IBM's 35 atoms and the rise of nanotech (2017). [online] Available from: https://www.cnet.com/news/ibms-35-atoms-and-the-rise-of-nanotech/
24. S. Iijima, Nature **354**, 56–58 (1991)
25. F. Hadef, in *Environmental Nanotechnology*, ed. by N. Dasgupta, S. Ranjan, E. Lichtfouse, (Springer, Cham. 2018) pp. 1–58.
26. M.J. Eckelman, J.B. Zimmerman, P.T. Anastas, J. Ind. Ecol. **12**, 316–328 (2008)
27. K.S. Novoselova, K. Geims, V. Morozovd, J. Zhangs, V. Dubonosi, V. Grigorieva, A. A. Firsov, Science, **306**, 666–669 (2004)
28. S. K. Kulkarni (ed.), *Nanotechnology: Principles and Practices book* (Springer, Cham 2015)
29. S. Baskoutas, A. Terzis, J. Appl. Phys. **99**, 013708 (2006)
30. X. Lan, S. Masala, E. Sargent, Nat. Mater. **13**, 233–240 (2014)
31. Y. Kayanuma, Solid State Commun. **59**, 405–408 (1986)
32. T. Takagahara, Phys. Rev. Rev. B **36**, 9293–9296 (1987)
33. P.N. Sudha, K. Sangeetha, K. Vijayalakshmi, A. Barhoum, in *Emerging Applications of Nanoparticles and Architecture Nanostructures* (Springer, 2018), pp. 341–384
34. P. Gupta, M. Ramrakhiani, Open Nanosci. J. **3**, 15–19 (2009)
35. J. Wu, W. Pisula, K. Müllen, Chem. Rev. **107**, 718–747 (2007)
36. P. Bhattacharya, D. Du, Y. Lin, J.R. Soc, Interface **11**, 20131067 (2014)
37. D.K. Pandey, M. Kuddushi, A. Kumar, D.K. Singh, Colloids Surf. A Physicochem. Eng. **650**, 129631 (2022)
38. H. Li, X. He, Z. Kang, Angew. Chem. Int. Ed **49**, 4430–4434 (2010)
39. R.P. Choudhary, S. Shukla, K. Vaibhav, Mater. Res. Express **2**, 095024–095028 (2015)
40. G.V. Naik, V.M. Shalaev, A. Boltasseva, Adv. Mat. **25**, 3264–3294 (2013)
41. S. Peng, J.M. McMahon, G.C. Schatz, S.K. Gray, Y. Sun, Proc. Natl. Acad. Sci. **107**, 14530–14534 (2010)
42. A. Otto, I. Mrozek, H. Grabhorn, W. Akemann, J. Phys.: Condens. Matter **4**, 1143 (1992)
43. Z.Q. Tian, B. Ren, D.Y. Wu, J. Phys. Chem. **106**, 9463–9483 (2002)
44. S. Eustis, M.A. El-Sayed, Chem. Soc. Rev. **35**, 209–217 (2006)
45. E. Hao, G.C. Schatz, J. Chem. Phys. **120**, 357–366 (2004)
46. K. Kneipp, H. Kneipp, J. Kneipp, Acc. Chem. Res. **39**, 443–450 (2006)
47. J. Plaickner, E. Speiser, S. Chandola, N. Esser, D.K. Singh, J. Raman Spectrosc. **51**, 788–794 (2020)
48. E.M. Cho, E.O. Ganbold, A.T.N. Lam, D.K. Singh, D. Kim, S.I. Yang, S.W. Joo, Colloids Surf. A Physicochem. Eng. **486**, 45–52 (2015)
49. E.-M. Cho, D.K. Singh, E.-O. Ganbold, U. Dembereldorj, S.-W. Jang, D. Kim, J. Choo, S. Kim, C.M. Lee, S.I. Yang, S.-W. Joo, Appl. Spectrosc. **68**, 307–314 (2014)
50. V. Kaushik, H.L. Kagdada, D.K. Singh, S. Pathak, Appl. Surf. Sci. **574**, 151724 (2022)
51. Q. Wang, Z.H. Ren, W.M. Zhao, L. Wang, X. Yan, A. Zhu, F. Qiu, K.K. Zhang, Nanoscale **14**, 564–591 (2022)
52. P. Gong, H. Li, X. He, K. Wang, J. Hu, W. Tan, Nanotechnology **18**, 285604 (2007)
53. I. Sondi, B. Salopek-Sondi, J. Colloid. Interface. Sci. **275**, 177182 (2004)
54. X. Liu, J. Locozzia, Y. Wang, X. Cui, Y. Chen, S. Zhao, Z. Lin, Energy Environ. Sci. **10**, 402–434 (2017)
55. D.K. Pandey, H.L. Kagdada, A. Materny, D.K. Singh, J. Phys. Chem. A **125**, 2653–2665 (2021)
56. D.K. Pandey, H.L. Kagdada, A. Materny, D.K. Singh, J. Mol. Liq. **322**, 114538 (2021)
57. H.A. Abdelsalam, A.Y. Abdelaziz, Electr Power Components Syst. **42**, 306–314 (2014)
58. S. Lu, J.A. Cardenas, R. Worsley, N.X. Williams, J.B. Andrews, C. Casiraghi, A.D. Franklin, ACS Nano **13**, 11263–11272 (2019)
59. Y. Xing, E. Speiser, D.K. Singh, P.S. Dittrich, N. Esser, J. Phys. Chem. C **121**, 23200–23206 (2017)

60. Y.T. Ong, A.L. Ahmad, S.H. Sharif Zein, S.H. Tan, Braz. J. Chem. Eng. **27**, 227–242 (2010).
61. J.A. Elliott, J.K.W. Sandler, A.H. Windle, Phys. Rev. Lett. **92**, 095501–095504 (2004)
62. M.F. Yu, B.S. Files, S. Arepalli, Phys. Rev. Lett. **84**, 5552–5555 (2000)
63. S. Xie, W. Li, Z. Pan, J. Phys. Chem. Solids **61**, 1153–1158 (2000)
64. S.S. Sinha, L. Yadgarov, S.B. Aliev, Y. Feldman, I. Pinkas, P. Chithaiah, R. Tenne, J. Phys. Chem. C **125**, 6324–6340 (2021)
65. J. Lee, J. Shin, G. Lee, C. Lee, Nanomater **6**, 193 (2016)
66. D. Vaughn, S. In, R. Schaak, ACS Nano **5**, 8852–8860 (2011)
67. A. VahidMohammadi, J. Rosen, Y. Gogotsi, Sci. **372**, 6547 (2021)
68. Y. Xia, G.M. Whitesides, Angew. Chem. Int. Ed. **16**, 3997 (2006)
69. H.J. Kim, K.J. Kim, D.S. Kwok, Qual. Reliab. Eng. Int. **26**, 765 (2010)
70. O.D. Neikov, N. A. Yefimov, S. Naboychenko (ed.) *Handbook of Non-ferrous Metal Powders* (Elsevier Ltd 2009) pp. 45–62
71. A.E.D. Mahmoud, A. Stolle, M. Stelter, A.C.S. Sustain, Chem. Eng. **6**, 6358–6369 (2018)
72. G. Otis, M. Ejgenberg, Y. Mastai, Nanomater. **11**, 238 (2021)
73. X. Wei, X. Wang, B. Gao, W. Zou, L. Dong, ACS Omega Mar. **5**, 5748–5755 (2020)
74. F.M.C. Caicedo, E.V. López, A. Agarwal, V. Drozd, A. Durygin, A.F. Hernandez, C. Wang, Diamond and related materials. Diamond Relat. Mater Nov. **109**, 108064 (2020)
75. O.D. Neikov, Mechanical crushing and grinding, in *Handbook of Non-ferrous Metal Powders* (Elsevier, 2009) pp. 45–62
76. L.H. Li, Y. Chen, G. Behan, H. Zhang, M. Petravic, A.M. Glushenkov, J. Mater. Chem. Aug. **21**, 11862–11866 (2011)
77. R. Janot, D. Guérard, Carbon N. Y. **40**, 2887–2896 (2022)
78. L.H. Li, Y. Chen, A.M. Glushenkov, Nanotechnology **21**, 105601 (2010)
79. I. Ijaz, E. Gilani, A. Nazir, A. Bukhari, Chem. Lett. Rev. **13**, 59–81 (2020)
80. M. Salavati-Niasari, F. Davar, N. Mir, Polyhedron **27**, 3514–3518 (2008)
81. N. Abid, A.M. Khan, S. Shujait, K. Chaudhary, M. Ikram, M. Imran, J. Haider, M. Khan, Q. Khan, M. Maqbool, Adv. Colloid Interface Sci. **300**, 102597 (2021)
82. G. Wei, Z. Zhengwei, S. Nigel, *An Introduction to Electronic Materials for Engineers*, 2nd edn. (World Scientific, River Edge, NJ, USA, 2011)
83. Y. Guo, X. Fu, Z. Peng, J. Mater. Sci. **53**, 8098–80107 (2018)
84. R. Zahra R, J. Jacob, N. Bano, A. Ali, K. Mahmood, S. Ikram, S. Hussain, Phys. B Condens. Matter **564**, 143–146 (2019)
85. A. Basak, A. Hati, A. Mondal, U.P. Singh, S.K. Taheruddin, Thin Solid Films Jan. **645**, 97–101 (2018)
86. Q. Shi, Q. Wang, D. Zhang, Q. Wang, S. Li, W. Wang, J. Zhang, J. Lumin **206**, 53–58 (2019)
87. D.M. Mattox, Met. Finish. **100**, 394–408 (2002)
88. S. Wang, X. Li, J. Wu, W. Wen, Y. Qi, Curr. Opin. Electrochem. **11**, 130–140 (2018)
89. H. Huang, J. Lai, J. Lu, Z. Li, AIP Adv. **9**, 015307 (2019)
90. N. Mintcheva, S. Yamaguchi, S.A. Kulinich, liquid. Materials **13**, 719 (2020)
91. N. Mintcheva, A.A. Aljulaih, S. Bito, M. Honda, T. Kondo, S. Iwamori, S. Kulinich, J. Alloys Compd. **747**, 166–175 (2018)
92. S. Ravi-Kumar, B. Lies, X. Zhang, H. Lyu, H. Qin, In: Polym. Int. **68**, 1391–1401 (2019)
93. E.A. Ganash, G.A. Al-Jabarti, R.M. Altuwirqi, Mater. Res. Expr. **7**, 015002 (2020)
94. G.G. Guillén, S. Shaji, M.M. Palma, D. Avellaneda, G.A. Castillo, T.D. Roy, B. Krishnan, Appl. Surf. Sci. **405**, 183–194 (2017)
95. A.M. Mostafa, S.A. Yousef, W.H. Eisa, M.A. Ewaida, E.A. Al-Ashkar, Optik **144**, 679–684 (2017)
96. A.A. Menazea, Radiat. Phys. Chem. **168**, 108616 (2020)
97. M.C. Sportelli, M. Izzi, A. Volpe, M. Clemente, R.A. Picca, A. Ancona, N. Cioffi, Antibiotics, **7**, 67 (2018)
98. A.M. Ealias, M.P. Saravanakumar, I.O.P. Conf, Ser. Mater. Sci. Eng. **263**, 032019 (2017)
99. M.T. Nguyen, T. Yonezawa, Sci. Technol. Adv. Mater. **19**, 883–898 (2018)

100. O.O. Abegunde, E.T. Akinlabi, O.P. Oladijo, S. Akinlabi, A.U. Ude, A.I.M.S. Mater, Sci. **6**, 174–199 (2019)
101. A. Baptista, F. Silva, J. Porteiro, J. Míguez, G. Pinto, Coatings **8**, 402 (2018)
102. P.A. Savale, Asian J. Res. Chem. **11**, 195–205 (2018)
103. W. Zeng, N. Chen, W. Xie, Cryst. Eng. Comm. **22**, 851–869 (2020)
104. D. Ji, X. Wen, T. Foller, Y. You, F. Wang, R. Joshi, Nanomater **10**, 1–9 (2020)
105. M.A. Azam, N. Mudtalib, R. Seman, Mater. Today Commun. **15**, 81–97 (2018)
106. O. Aberefa, K. Bedasie, S. Madhi, M.O. Daramola, S.E. Iyuke, Adv. Nat. Sci. Nanosci. Nanotechnol. **9**, 035009 (2018)
107. J. Ding, S. Chen, N. Han, Y. Shi, P. Hu, H. Li, J. Wang, Ceram Int. **46**, 15152–15158 (2020)
108. I. Sayago, E. Hontãnón, M. Aleixandre, Tin Oxide Mater. 247–280, (2020)
109. X. Zhang, H. Sun, S. Tan, J. Gao, Y. Fu, Z. Liu, Inorg. Chem. Commun. **100**, 44–50 (2019)
110. S.P. Vinay, G. Nagaraju, C.P. Chandrappa, N. Chandrasekhar, Chem. Phys. Lett. **748**, 137402 (2020)
111. R. Jana, A. Dey, M. Das, J. Datta, P. Das, P.P. Ray, Appl. Surf. Sci. **452**, 155–164 (2018)
112. M.Z. Nakhjiri, S. Asadi, A. Hasan, M.M.N. Babadaei, Y. Vahdani, B. Rasti, M. Falahati, J. Mol. Liq. **317**, 113893 (2020)
113. C.V. Reddy, B. Babu, I.N. Reddy, J. Shim, Ceram Int. **44**, 6940–6948 (2018)
114. P.G. Jamkhande, N.W. Ghule, A.H. Bamer, M.G. Kalaskar, J. Drug Deliv. Sci. Technol. **53**, 101174 (2019)
115. J.A.M. Mark, A. Venkatachalam, A. Pramothkumar, N. Senthilkumar, K. Jothivenkatachalam, J. prince Jesuraj, Phys. B Condens. Matteri. **601**, 412349 (2021)
116. B.J. Rani, M. Ravina, G. Ravi, S. Ravichandran, V. Ganesh, R. Yuvakkumar, Surf. Interfaces **11**, 28–36 (2018)
117. N. Wang, J.Y.H. Fuh, S.T. Dheen, A. Senthil Kumar, Bio-Design Manufact. **4**, 379–404 (2021)
118. L.A. Kolahalam, I.K. Viswanath, B.S. Diwakar, B. Govindh, V. Reddy, Y.L.N. Murthy, Mater. Today **18**, 2182–2190 (2019)
119. M. Ikram, E. Umar, A. Raza, A. Haider, S. Naz, D.A. Ul-Hamid, S. Ali, RSC Adv. **10**, 24215–24233 (2020)
120. A.B. Vennela, D. Mangalaraj, N. Muthukumarasamy, S. Agilan, K.V. Hemalatha, Int. J. Electrochem. Sci. **14**, 3535–3542 (2019)
121. R. Bekkari, L. Laˆanab, D. Boyer, R. Mahiou, B. Jaber, Mater. Sci. Semicond. Process. **71**, 181–187 (2017)
122. M. Parashar, V.K. Shukla, R. Singh, J. Mater. Sci. Mater. Electron. **31**, 3729–3749 (2020)
123. N. Baig, I. Kammakakam, W. Falath, I. Kammakakam, Mater. Adv. **2**, 1821–1871 (2021)
124. S. Mourdikoudis, R.M. Pallares, N.T.K. Thanh, Nanoscale **10**, 12871–12934 (2018)
125. H. Surangi, N. Jayawardena, S.H. Liyanage, K. Rathnayake, U. Patel, M. Yan, Anal. Chem. **93**, 1889–1911 (2021)
126. D.K. Singh, S. Das, A. Materny (eds.), *Advances in Spectroscopy: Molecules to Materials* (Springer Nature Singapore 2019)
127. D.K. Singh, M. Pradhan, A. Materny (eds.) *Modern Techniques of Spectroscopy* (Springer Nature Singapore 2021)
128. A.C. Ferrari, J.C. Meyer, V. Scardaci, C. Casiraghi, M. Lazzeri, F. Mauri, S. Piscanec, D. Jiang, K.S. Novoselov, S. Roth, A.K. Geim, Phys. Rev. Lett. **97**, 187401 (2006)
129. J. Langer, D.J. Aberasturi, J. Aizpurua, R.A. Alvarez-Puebla, B. Auguié, J.J. Baumberg et al., ACS Nano **14**, 28–117 (2020)
130. S.R. Neufeldt, M.S. Sanford, Acc. Chem. Res. **45**, 317–326 (2012)
131. S. Akoka, G.S. Remaud, Prog. Nucl. Magn. Reson. Spectrosc. **120–121**, 1–24 (2020)
132. J. Clarke, A.I. Braginski (eds.), *The SQUID Handbook* (Wiley-VCH, Weinheim, 2004)
133. K. Liu, B. Ouyang, X. Guo, Y. Guo, Y. Liu, NPJ Flexible Electron. **6**, 1–19 (2022)
134. H.P. Phan, Micromachines **12**, 157 (2021)
135. B.S. Murty, P. Shankar, B. Raj, B.B. Rath, J. Murday, *Textbook of nanoscience and nanotechnology* (Springer, Berlin, Heidelberg, 2013)
136. P. Khandelwal, D.K. Singh, S. Sadhu, P. Poddar, Nanoscale **7**, 19985–20002 (2015)

137. P. Khandelwal, D.K. Singh, S. Sadhu, P. Poddar, Chem. Plus Chem. **79**, 134–142 (2014)
138. D.K. Pandey, H.L. Kagdada, A. Materny, D.K. Singh, J. Mol. Liquid **384**, 119957 (2022)
139. D.K. Singh, E.-O. Ganbold, E.-M. Cho, K.-H. Cho, D. Kim, J. Choo et al., J. Hazard. Mater **265**, 89–95 (2014)
140. D.K. Singh, E.-O. Ganbold, E.-M. Cho, C.M. Lee, S.I. Yang, S.-W. Joo, J. Mol. Struct. **1049**, 464–472 (2013)
141. J.C. Ramirez-Perez, T.A. Reis, C.L.P. Olivera, M.A. Rizzutto, Spectrochim. Acta Part A Mol. Biomol. Spectrosc. **272**, 120980 (2022)
142. S.B. Somwanshi, S.B. Somvanshi, P.B. Kharat, J. Phys: Conf. Ser. **1644**, 012046 (2020)
143. P. Makvandi, S. Iftekhar, F. Pizzetti, A. Zarepour, E.N. Zare, M. Ashrafizadeh, T. Agarwal, V.V.T. Padil, R. Mohammadinejad, M. Sillanpaa, T.K. Maiti, G. Perale, A. Zarrabi, F. Rossi, Environ. Chem. Lett. **19**, 583–611 (2021)
144. H. Chen, L. Zhang, Y. Hu, C. Zhou, W. Lan, H. Fu, Y. She, Sens. Actuators B Chem. **329**, 129135 (2021)
145. P. Khandelwal, D.K. Singh, P. Poddar, Chemistry Select **4**, 6719–6738 (2019)
146. D.K. Singh, R. Jagannathan, P. Khandelwal, P.M. Abraham, P. Poddar, Nanoscale **5**, 1882–1893 (2013)
147. M. Hosny, A.S. Eltaweil, M. Mostafa, Y.A. El-Badry, E.E. Hussein, A.M. Omer, M. Fawzy, ACS Omega **7**(3), 3121–3133 (2022)
148. I.G. Antropova, A.A. Revina, P.M. Oo, E.S. Kurakina, I.A. Butorova, E.P. Magomedbekov, ACS Omega **6**, 8313–8321 (2021)
149. Z. Li, W. Ma, I. Ali, H. Zhao, D. Wang, J. Qiu, ACS Omega **5**, 32632–32640 (2020)
150. A.T.N. Lam, J. Yoon, E.-O. Ganbold, D.K. Singh, D. Kim, K.-H. Cho, S.Y. Lee, J. Choo, K. Lee, S.-W. Joo, Colloids Surf. B **123**, 61–67 (2014)
151. A.T.N. Lam, J. Yoon, E.-O. Ganbold, D.K. Singh, D. Kim, K.-H. Cho, S.J. Son, J. Choo, S.Y. Lee, S. Kim, S.-W. Joo, J. Colloid Interface Sci. **425**, 96–101 (2014)
152. R. Solano, D. Patino-Ruiz A. Herrera, Nanomater. Nanotechnol., **10**, (2020)
153. Y. Liu, G. Zhou, K. Liu, Y. Cui, Acc. Chem. Res. **50**, 2895–2905 (2017)
154. M.N. Shalaby, M.M. Saad, Int. J. Psychosoc. Rehabil. **24**, 2314–2322 (2020)
155. S. Nafisi, H.I. Maibach, in *Cosmetic science and technology: theoretical principles and applications*, ed. by K. Sakamoto, H. Lochhead, H. Maibach, Y. Yamashita (Elsevier 2017), p. 337
156. M. Nasrollahzadeh, M. Sajjadi, S. Iravani, R.S. Varma, J. Hazar. Mat. **401**, 123401 (2021)
157. S. Iravani, Inorg. Nano-Met. Chem **51**, 1615–1645 (2021)

Chapter 2
Carbon-Based Nanomaterials: Carbon Nanotube, Fullerene, and Carbon Dots

Nitika Devi, Rajesh Kumar, Yong-Song Chen, and Rajesh Kumar Singh

Abstract Carbon nanomaterials are special materials with remarkable properties which have high potential to use in material science. Carbon nanomaterials are the most explored ones as their different isotopes have interestingly unique properties. Carbon nanomaterials include carbon nanotubes (CNTs), fullerene, carbon dots (CDs), graphene, etc., which vary in their dimensionality and characteristic properties. This chapter describes the most common synthesis routes for these carbon nanomaterials. The synthesis process has a substantial influence on defining the properties of carbon nanomaterials materials. Chemical vapor deposition (CVD), arc discharge, laser ablation, microwave-assisted, pyrolysis, and some other chemical methods have been generally used for synthesizing carbon nanomaterials. A detail of each method has been summarized along with its merits and demerits. Properties of a material defined its application area as CNTs are prominently used in electronic area, whereas CDs are popular for optical applications. Here, a brief description is given on the prime characteristics of CNTs, CDs, and fullerenes. Also, some published reports and their salient outcomes have been discussed for few fields like energy storage, biomedical, and sensing applications.

Keywords Carbon nanomaterials · Synthesis · Properties · Applications

N. Devi · Y.-S. Chen
Department of Mechanical Engineering and Advanced Institute of Manufacturing With High-Tech Innovations, National Chung Cheng University, Chiayi 621301, Taiwan

R. Kumar
Department of Mechanical Engineering, Indian Institute of Technology, Uttar Pradesh, Kanpur 208016, India

R. K. Singh (✉)
School of Physical and Material Sciences, Central University of Himachal Pradesh (CUHP), Kangra, Dharamshala, HP 176215, India
e-mail: rksbhu@gmail.com

D. K. Singh et al. (eds.), *Nanomaterials*,
https://doi.org/10.1007/978-981-19-7963-7_2

2.1 Introduction

Carbon nanomaterials are unusual, due to their exceptional performance in various application areas. Nanomaterials' extraordinary features are due to their size in 1–100 nm range. The nature of a nanomaterial is characterized by its composition. Examples include metal, semiconductor, metal oxide, polymer, carbon, and liquid nanomaterials [1]. Some of the carbon nanomaterials are of significant importance because of their high electrical and mechanical properties, high surface area, and excellent optical properties. Carbon allotropy results in different useful forms of carbon, especially on a nanometer scale like carbon nanotubes (CNTs), graphene, fullerene, carbon dots (CDs), etc. Although, all these are examples of carbon allotropes, they have different properties respective to their dimension and arrangement of atoms [2]. CNTs are one-dimensional (1-D) allotrope of carbon which was discovered by Sumio Iijima in 1991 [3]. It can be of two types that are multi-wall CNTs (MWCNTs) and single-wall CNTs (SWCNTs). An SWCNT is rolled sheet of a single layer of carbon atoms but MWCNT consists of multiple layers of rolled sheets of carbon atoms. SWCNTs have a dimension of 1–10 nm diameters with a length of a few μm and MWCNTs have a length of 10 μm with a diameter ranging from 10 to 100 nm. The direction of rolled graphite sheets also classified the CNTs into two types that are zig-zag and armchair arrangements [4, 5]. Graphene is a two-dimensional (2-D) material which is an isolated single sheet of graphite. Zero-dimensional (0-D) carbon materials are categorized by example such as CDs in which confinement is in all the three-dimensional (3-D). The discovery of CDs was an accidental incident by Xu et al. [6] in 2004 during the purification of CNTs. The size of a CD is less than 10 nm [7, 8]. Fullerene was invented by three researchers, Harold W. Kroto and Richard E. Smalley and Robert F. Curl Jr. in 1985 in Smalley's lab at Rice University [9]. Fullerene is also a type of carbon allotrope which can exist in different shapes and sizes formed by a closed mesh of singly and doubly bonded carbon atom rings. A single ring comprises five or seven carbon atoms and the fullerene name is designated as C_n. Here, n represents the no of carbon atoms and is $n > 20$ and accordingly, there are different types of fullerene-like C_{60}, C_{70}, $C_{82,}$ etc. According to shape, fullerene can be of closed buckyballs and open-ended CNTs shapes [10]. All discussed carbon nanomaterials have been explored for diverse applications like energy storage [11–13], biomedical [14–16], sensing [17–19], environmental [20–22], etc. This chapter summarizes the important aspects of carbon nanomaterials like their synthesis routes, characteristics, and key applications.

2.2 Synthesis of Carbon Nanomaterials

2.2.1 CNT Synthesis

CNTs can be synthesized by using different methods like arc discharge, chemical vapor deposition (CVD), laser ablation, electrolysis, and hydrothermal as shown in Fig. 2.1 [23–31]. Critical factors involved in CNT synthesis are related to final yield such that purification and consumed carbon source. Arc discharge is the oldest method used for CNT synthesis. In this method, current (AC or DC) is used for CNTs generation. The reaction chamber consists of a carbon precursor anode and a graphite cathode which is filled with gas or submerged in a liquid. A current supply causes the electrode to move toward each other and is kept at a min. distance of 1–2 mm so that a constant discharge can occur. A constant arc is required to get a non-fluctuating output so a closed loop and a constant current is maintained throughout the experiment so that distance between the electrode can be automatically adjusted with constant arc discharge.

The schematic representation for arc discharge process is shown in Fig. 2.2. Carbon at the anode evaporates at high temperatures (∼4000–6000 K) plasma formed due to constant current. Due to temperature gradient at the cathode, gas-phase carbon vapors drift towards the cathode and are deposited onto the cathode. This deposited material is CNTs and can be obtained after a few minutes. Deposit material needs to be further purified as it may consist of carbon soot along with the CNTs [32].

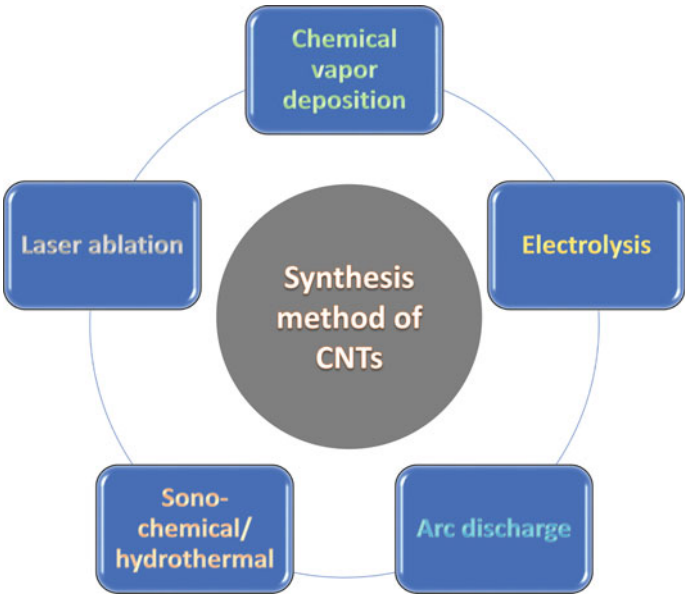

Fig. 2.1 Different synthesis methods of CNTs

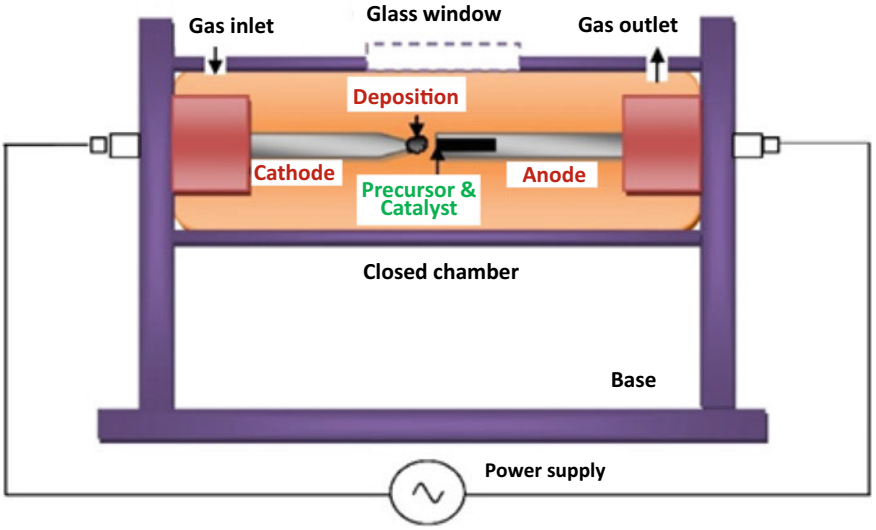

Fig. 2.2 Schematic diagram representing synthesis method for arc discharge CNTs [32]. Adapted with permission from [32]. Copyright (2014) (Elsevier)

Arc discharge synthesis can be a catalyst insisted or can occur without the catalyst as described above. Usually, SWCNTs are synthesized in presence of a catalyst like iron, nickel, and cobalt metals. Other than this, the nature of inert gas and the pressure of the chamber can also significantly affect the product quality.

Shi et al. [33] studied the quality and production of SWCNTs under various helium gas pressure (500–700 Torr), using a different catalyst and at varying arc discharge currents. It was concluded from the study that all these conditions are critical for good quality SWCNTs. Cadek et al. [34] also optimized the synthesis parameters for the production of MWCNTs and found that the best results are found for 195 A cm^{-2} and 500 Torr of helium current density and pressure. There are many studies which summarize and studied the various factors affecting the arc discharge synthesis of CNTs [35–37]. Laser ablation is another synthesis technique which can be used for CNTs fabrication. It is found that laser ablation is usually used for synthesizing the SWCNTs and the schematic used in this synthesis is shown in Fig. 2.3. In laser ablation a laser beam is used to vaporize the graphite carbon source and a catalyst such as nickel–cobalt in a high-temperature furnace under high helium and argon gases pressure. These conditions result in vaporized carbon with catalyst vapor which is then collected onto a substrate. Nd:YAG and CO_2 lasers are mainly used for vaporizing the target and laser wavelength, and laser power considerably affects the final product [36]. Munoz et al. [38] studied the CNT synthesis in presence of nitrogen, helium, and argon gases for a pressure range of 50–500 Torr. The study summarizes that both argon and nitrogen in the pressure range of 200–400 Torr are suitable for obtaining SWCNTs. Laser wavelength is also a crucial factor for CNT synthesis as described by Chrzanowska et al. [39]. Merits of using laser ablation methods are its capability

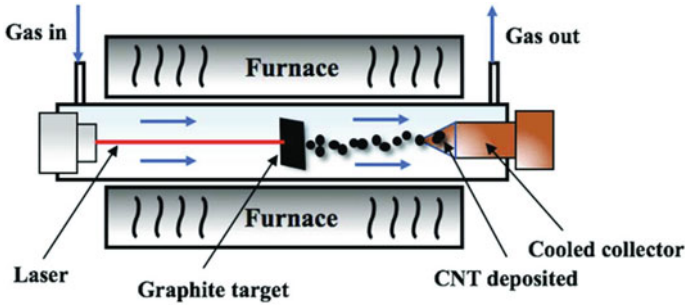

Fig. 2.3 Laser ablation-assisted CNT synthesis setup [40]. Adapted with permission from [40]. Copyright (2019) (Frontiers Media S.A.)

of forming SWCNTs with high quality and also the method provides easy control over reaction conditions. But for large-scale production, this method is not suitable because of the high cost involve for laser and other experimental arrangements [36].

CVD method involves the decomposition of hydrocarbons in the presence of a catalyst. CVD synthesis is simpler as compared to laser ablation and arc discharge with the scope of large-scale production. CVD can be used for the synthesis of SWCNTs as well as MWCNTs. Ethylene and acetylene are usually used as carbon sources which enter the reaction quartz tube along with some inert gases. The major catalysts used in the synthesis of CNTs are Fe, Co, and Ni; CNTs growth mechanism also depends upon the used catalyst. Tip growth and base growth are two different mechanisms for CNTs growth [41]. Figure 2.4 represents the schematic of CVD synthesis. CVD can be further classified into different types depending upon the reaction conditions like plasma-enhanced CVD, liquid pyrolysis, microwave-assisted CVD, low-pressure CVD, etc. [42]. The advantages of CVD also include product quality as 90% of CVD-synthesized CNTs are of high quality, so most do not need additional purification steps as in the case of other synthesis methods. The type of catalyst, temperature of the reaction chamber, and reaction conditions can significantly affect the final product as described in the CNTs CVD synthesis review by Öncel et al. [43]. Large-scale production of carbon nanomaterials is always been a researcher's goal and they are continuously working toward this goal. Recently, Wang et al. [44] reported a large-scale production of graphene nanoribbons/CNTs composite using the CVD synthesis technique. The amount of CNTs was 26 gm yield with per gm of catalyst was achieved in 30 min. reaction time and further composite was analyzed for capacitive benefits. Composite offered a maximum 23.43 mg g^{-1} desalination capacity for the highest specific capacitance of 242.3 F g^{-1} at 0.5 A g^{-1}. A different kind of variation has been made to CVD synthesis approach for getting desirable CNT product. For instance, a study concluded that, in the presence of gamma radiation, the final CNTs are surrounded by a moss-like coating of organic impurities [45]. Likewise, thermal CVD has been used for synthesizing the

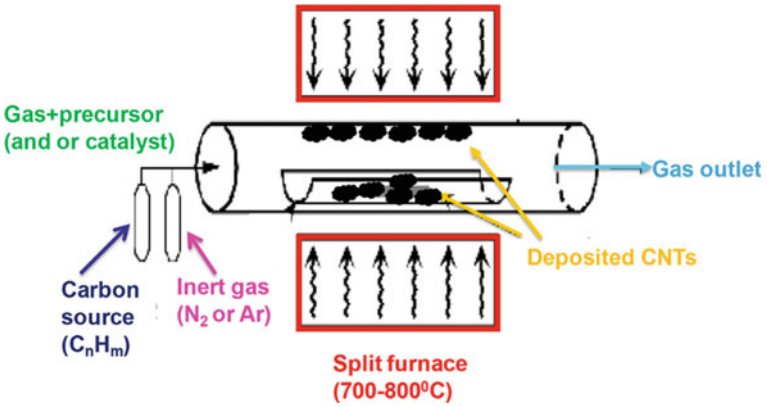

Fig. 2.4 CVD setup for CNT synthesis [47]. Adapted with permission from [47]. Copyright (2016) (Intech)

composite of carbon nanospheres and CNTs [46]. CVD synthesis of CNTs is a low-cost efficient technique which also gave an easy way of controlling and varying the reaction parameters.

Electrolysis is a less-known technique for CNT synthesis as compared to vastly discussed CVD, laser ablation, and arc discharge. Graphite is used as a carbon source electrode and sometimes the reaction is performed in graphite crucible which itself provides carbon for CNT formation. In a typical electrolysis process, alkali metal chlorides are electrolyzed in a graphite crucible. During this reaction, carbon constituents are produced at the graphitic surface due to erosion, and CNT is formulated in the liquid phase. After the completion of reaction, solidified cooled salt can be separated by washing with water through which suspended CNTs can be filtered. A different mechanism has been proposed for explaining this reaction and CNT formation like oxidation, reduction, formation of some intermediate compounds, etc. [48]. Novoselova et al. [49] reported CNT synthesis by an electrolytic method using some altered reaction conditions. The electrolytic reaction was controlled by applying current and potential and molten salts were dissolved in CO_2. Obtained CNTs were MWCNTs type with curbed shape and agglomerated bundles form.

Scientists also explored sonochemical and hydrothermal methods for CNT synthesis. Hydrothermal synthesis involves the reaction of precursors in a closed vessel at high temperature and pressure [50]. In the case of sonochemical synthesis, reaction is initiated by powerful ultrasound radiation (20 kHz–10 MHz) [51]. Clemens et al. [52] utilized these mentioned techniques for preparing anatase titanium dioxide-coated SWCNTs. Low cost is the advantage of this method which can be explored for large-scale production. Similarly, Manafi et al. [53] prepared MWCNTs by sonochemical and hydrothermal reactions under low-temperature conditions. In this work, dichloromethane, cobalt chloride, and metallic lithium were used as starting materials and ultrasonic pre-treatment was found to be an important step

in this synthesis. Dimensional analysis showed that MWCNTs had a length of 2–5 μm and diameters of 60 ± 20 nm. Flower-like MoS_2/CNTs nanocomposite was synthesized by hydrothermal treatment in which reaction is assisted with ultrasonic irradiations. Nanocomposite was further employed for the degradation of hydroxychloroquine and was found to be efficient [54]. There are other reports on nanocomposite synthesis such as MWCNT/MnO_2/rGO [55], and MWCNTs/TiO_2 [56] which showed that hydrothermal and sonochemical synthesis can be successfully used for CNT and its composite formation.

2.2.2 *Fullerene Synthesis*

Fullerene can be synthesized in four ways as shown in Fig. 2.5. Laser irradiation of carbon was the first method which successfully synthesized fullerene but the product amount was very less so researchers have explored other methods like laser irradiation of polyaromatic hydrocarbons (PAHs), electric arc heating of graphite, and resistive arc heating of graphite.

In laser irradiation method, graphite carbon source is vaporized by using laser in an inert atmosphere such as helium gas. Krätschmer et al. [57] were the first group who reported the lab-scale synthesis of fullerene by this method. Although the method was evident in obtaining C_{60} fullerene yield was found to be very low at ~ 1% and reaction conditions were very harsh like high temperature and pressure. Also, the completion of the process involves many steps like separation, purification, and functionalization. C_{60} and C_{70} fullerene thin film was prepared by laser irradiation

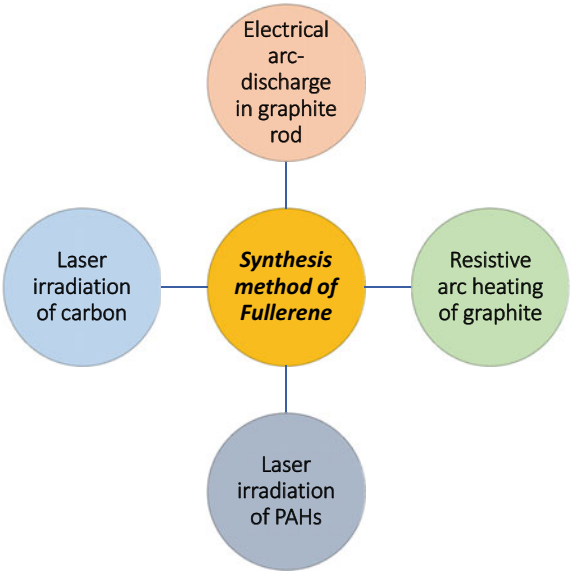

Fig. 2.5 Various synthesis methods for fullerene

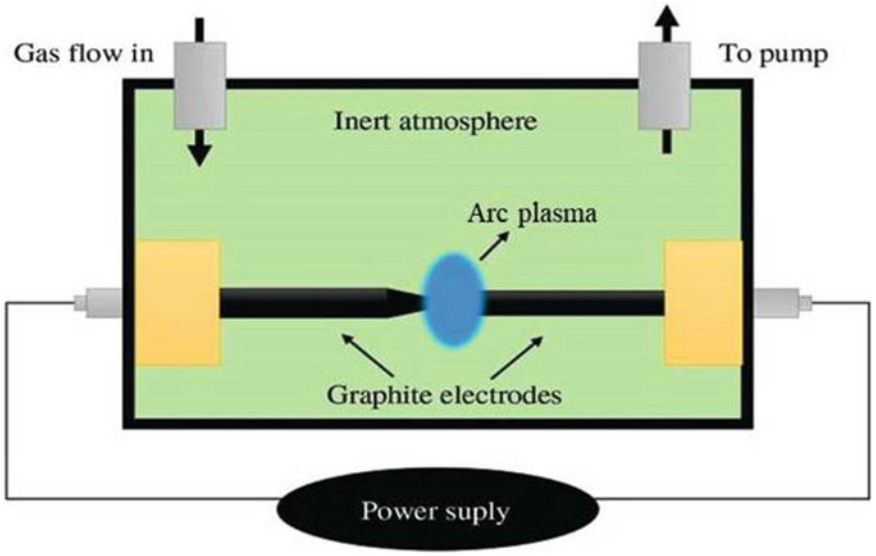

Fig. 2.6 Schematic of fullerene synthesis by electric arc heating of graphite [59]. Adapted with permission from [59]. Copyright (2019) (De Gruyter)

of graphite powder. A continuous wave CO_2 laser beam with a power of 45 KW was used under Ar or He gas atmospheres at 30 or 200 Torr pressure [58].

In electric arc heating of graphite synthesis method, a potential difference is applied between the electrodes in an inert atmosphere under low pressure. The carbon atom from the anode passes through the ionized gas or plasma and is then deposited on to cathode. All this reaction process occurred inside a steel chamber and till now this process of obtaining fullerene is one of the widely employed methods [59]. A schematic of the process and setup is shown in Fig. 2.6.

Kikuchi et al. [60] used this method for obtaining different forms of fullerenes that were C_{60}, C_{70}, C_{76}, C_{78}, C_{82}, C_{84}, $C_{90,}$ and C_{96}. Few of these forms like C_{82} and C_{96} were first time reported by this group. Nerushev et al. [61] explained the kinetics of fullerene formation by electric arc heating of graphite. Optimization of reaction conditions was done by Kareev et al. [62] for getting a high yield of fullerene and 11.4 wt% was the highest amount of obtained extract. Resistive heating was used for evaporating graphite under the partial pressure of helium. The evaporating material was in the form of soot which forms the fullerene and was collected on the glass shields around the carbon rods [63]. A study on different parameters of resistive heating concludes that graphite with hexagonal lattice showed the best result in terms of fullerene yield and best He pressure for the best yield amount was reported for 0.7×10^4–8.0×10^4 Pa [64]. Kyesmen et al. [65] combined resistive heating and arc discharge for the synthesis of fullerene. Results summarized that the combination of these two processes results in high yield and thus can be employed for large-scale production. Fullerene derivative can also be prepared by using resistive heating as

reported by Funasaka et al. [66]. This work involves the synthesis of endohedral fullerenes (LaC_{82}, La_2C_{80}) and exohedral fullerenes ($C_{60}(C_mO_n)$).

In laser irradiation of PAHs method, laser irradiation is used for heating the aromatic hydrocarbon which converts into fullerene. These polycyclic hydrocarbons contained carbon frameworks which under suitable heating conditions convert into fullerene [63]. A continuous wave CO_2 laser beam was used for detecting fullerene production from benzene (+cyclopentadiene), acetylene, or ethylene hydrocarbon. Benzene/oxygen or acetylene/oxygen mixture results in the fullerene soot [67]. Cyclodehydrogenation of a $C_{60}H_{30}$ polyarene by laser irradiation results in C_{60} fullerene as reported by Booram et al. [68]. C_{60} and C_{70} types of fullerene can be extracted by pyrolysis of perchlorofulvalene. This pyrolysis method involves two steps of pyrolysis at 450 °C and 750 °C [69]. Other than this, the combustion of benzene and ethylene was also used for fullerene synthesis and this approach provides a good quantity of fullerene [70]. There are a few more reports which summarize different manipulations in synthesis methods for the production of fullerene [71–74].

2.2.3 Carbon Dot Synthesis

CDs can be synthesized by different synthesis routes like microwave-assisted, hydrothermal synthesis, arc discharge, laser ablation, etc. [75–77]. A complete summary of the type of synthesis routes is shown in Fig. 2.7. Synthesis approaches can be divided into two classifications that are top-down and bottom-up approaches. Difference is the starting materials' dimensions as the top-down approach starts with a big-size material tailored to the nanoscale with various techniques. In the case of bottom-up approach, one needs to start frm scratch and process toward getting desirable size materials.

Microwave-assisted synthesis is getting popularity due to its less time-consuming approach, ease of controlling reaction conditions, cost efficiency, and, most importantly, its eco-friendly nature. In this approach, carbonization takes place in a very short period with microwave heating. Zhu et al. [78] report was the first which reported a microwave-assisted method for preparing fluorescent CDs. Lactose was treated with the concentrated HCl assisted with the microwave heat treatment at 160 °C for 15 min. with a power of 750 W. Prepared CDs were used for detecting four heterocyclic aromatic amines and results suggested that they can be useful for chemical sensing[79]. Glutamine and glucose along with ionic liquid 1-ethyl-3-methylimidazolium ethyl sulfate can be utilized for CD synthesis. Resulting CDs have great potential toward H_2O_2 production due to their selectivity for oxygen reduction reaction (ORR) and large potential range of 0.8 V [80]. Microwave-assisted synthesized CDs can also be powerful for biomedical application like in vivo and in vitro antimicrobial photodynamics. This was a one-step approach in which citric acid was dissolved in distilled water and microwave heated for 8 min [81]. Microwave synthesis also provides an easy way for forming the doped and other derivatives of CDs. Li et al. [82] prepared the N and P doped CDs by microwave heating of

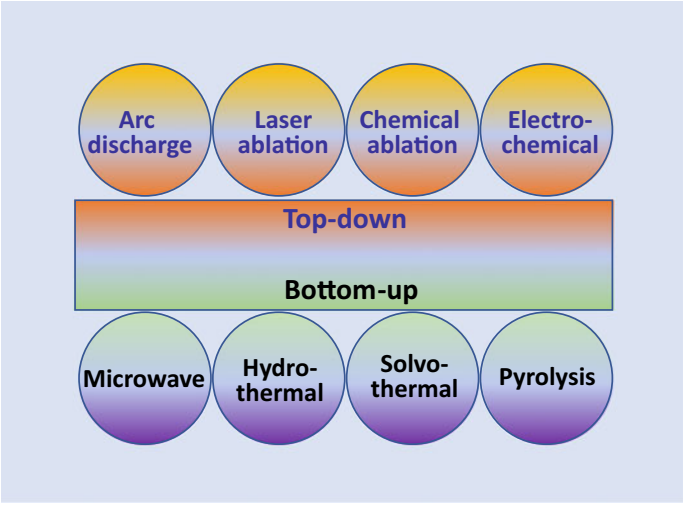

Fig. 2.7 Different top-down and bottom-up approaches applied for the synthesis of CDs

N-phosphonomethyl iminodiacetic acid and ethylenediamine and the product was further used for fluorescent cell imaging. A green natural material like kelp has been treated with microwave irradiation for CDs' formation. CDs were used for the detection of CO^{2+} in the real water sample and it was efficient enough for this application [83]. There are many reports which are evidence of successful microwave-assisted synthesis of CDs.

Hydrothermal and solvothermal synthesis involve the reactions of reactants using water and a solvent, respectively, inside a closed vessel at high temperature and pressure. This procedure can also be applied for preparing CDs and it is the most promising method due to its simple operational technique, low-cost and eco-friendly procedure [75]. Wang et al. [84] developed nitrogen CDs by hydrothermal synthesis in which water was used as a solvent for dissolving mandelic acid and ethylenediamine. The reaction was carried out at 200 °C for 5 h and the final product was obtained by centrifugation. This reaction was capable of giving a 41.5% reaction yield which was significant with a simple process. Using citric acid and L-histidine as precursors for hydrothermal synthesis of CDs yield obtained was 22% [85]. Another work used citric acid with polyethylenimine and did the hydrothermal treatment at 110 °C for 2 h which result in high photoluminescence quantum yield of 48.3 ± 5.3% [85]. Graphene oxide can also act as a starting material for the synthesis of CDs as reported by Wang et al. [86]. In this procedure, graphene oxide and HNO_3 solution were treated with microwave-assisted hydrothermal treatment at 800 W for 15–16 min. N- and P-doped CDs have been synthesized by hydrothermal approach and were further used for Cd(II) analyses [87]. Citric acid, ethylenediamine, and methyl blue were hydrothermally heated at 240 °C for 4 h resulting in sulfur and N-doped CDs. N- and S-doped CDs were found efficient for sensing mercuric (Hg^{2+}) and

hypochlorite ions [88]. Solvothermal synthesis is also capable of synthesizing CDs as reported by Huang et al. [89]. In this study, tea residue was used as starting material which was treated with choline chloride/urea then the mixture was heated in a closed vessel at 200 °C for 8 h. Vanillin can also be used as a carbon source for the solvothermal synthesis of CDs. C_2H_5OH solvent and vanillin carbon source result in water-soluble CDs which have a size of ~10 nm [90]. Deng et al. [91] studied the effect of using different alcohol (CH_3OH, C_2H_5OH, $(CH_2OH)_2$, and C_3H_8O) as a solvent for L-ascorbic acid starting carbon source. C_2H_5OH-treated CDs were the most effective in terms of their fluorescence applications. So, like hydrothermal synthesis, solvothermal synthesis method are also capable of synthesizing CDs and doped CDs [89].

Pyrolysis synthesis involves the decomposition of reactants at high temperature in the presence of strong acids or bases [75]. Scientists have explored this technique for the preparation of CDs and established that technique can be successfully used for CDs formation. Stan et al. [92] prepared the CDs by pyrolytic treatment of *N*-hydroxysuccinimide and synthesized material can be used in different applications like sensing and optoelectronic devices. Sago waste has been utilized as starting product for the synthesis of carbon quantum dots. In this synthesis, sago waste was firstly heated at 450 °C for 1 h. Then obtained material is mixed with distilled water and homogenized with ultrasonication for 2 h then centrifugation results in the final product [93]. Another study took guanidinium chloride and citric acid as a starting material for synthesizing the N-doped CDs by the pyrolysis method [94]. For drug release and cell imaging applications, CDs were prepared by pyrolysis of glycerol by Lai et al. [95]. Some modified forms of CDs such as CDs@SiO_2 and CDs@mSiO_2-PEG were also prepared in the same way. Danger et al. [96] reported CD synthesis by fennel seeds; schematic of the synthesis process is shown in Fig. 2.8. The steps involved in synthesis are given in Fig. 2.8a–g, which started from powder formation then followed by pyrolysis at 500 °C for 3 h and sonication, centrifugation. Figure 2.8h shows transmission electron microscopic image of CDs [96].

Using lactic acid–ionic liquid (IL) gel as a precursor for CD synthesis resulted in a high yield that was 34.9 wt% [97]. Li et al. [98] also reported a large-scale pyrolysis process which was capable of giving a yield of 65.5% and the material was further used for sensing Fe(III). So, pyrolysis can be successfully used for CD preparation with good yield. Electrochemical synthesis of CDs is a type of top-down approach, in which electrodes of material like CNTs, carbon fiber, and graphite are electrolytically treated for getting CDs. It was found that this process gives ultrapure CDs and an example of such process can be seen in schematic Fig. 2.9. In this schematic, there are two electrodes, in which one is a carbon material electrode and the other is the counter electrode, and it is treated with some potential difference in presence of an electrolyte. Here, in this particular case, platinum electrode was used as a counter electrode, pure graphite was used as the working electrode, and sodium phytate was chosen as an electrolyte. After 12 h under a constant voltage of 5 V, the solution contained the required CDs which can be filtered using filter paper. The last image in this schematic is cthe olor of solution containing P-doped CDs in UV light due to fluorescence [99].

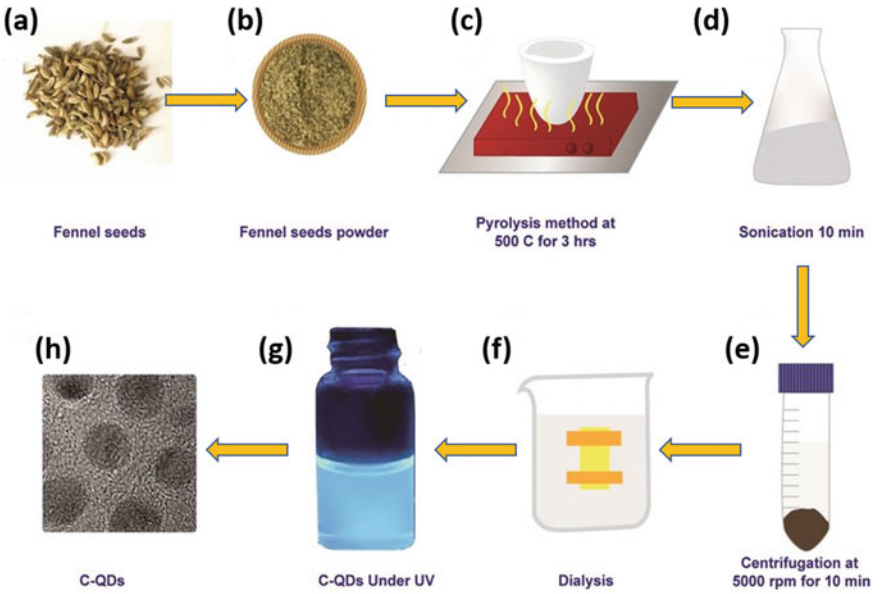

Fig. 2.8 Schematic of the pyrolysis process involved in CD synthesis [96]. Adapted with permission from [96]. Copyright (2019) (Nature Portfolio)

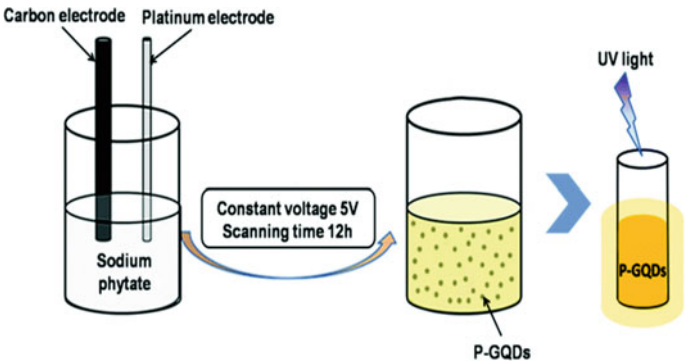

Fig. 2.9 Schematic of synthesis of P-CDs by electrochemical method along with their yellow fluorescence under the 365 nm UV light [99]. Adapted with permission from [99]. Copyright (1999) (Royal Society of Chemistry)

Hou et al. [100] synthesized a composite of CDs/TiO_2 using an electrochemical process using P25 powder, anhydrous C_2H_5OH, C_2H_7NO, $C_{16}H_{40}O_4Ti$, and NaOH starting materials. The prepared material showed excellent visible photocatalytic activity. Red fluorescent CDs were synthesized by electrochemical treatment of graphite in $K_2S_2O_8$ solution [101]. Sodium citrate and urea were used with distilled water for synthesizing functionalized CDs. The electrochemical treatment of two

platinum electrodes with a potential of 5 V for 1 h. CDs were efficient for Hg^{2+} sensing with a low detection limit of 3.3 mM [102]. Ming et al. [103] reported a large-scale synthesis of CDs with the electrochemical treatment of graphite rod immersed in pure water. Another counter electrode was also the graphite electrode and electrochemical treatment was done at static potential applied of 15–16 V DC. Electrochemical treatment is efficient enough for giving pure CDs but scientists are exploring new ways for finding the large-scale electrochemical preparation.

Laser ablation is a top-down approach in which a continuous or pulsed laser beam is used for CD preparation. In this process, a large organic macromolecule is attacked by a laser beam for ejecting the CDs. Kang et al. [104] developed N-doped CDs from graphite flakes in the liquid medium of C_2H_5OH. The ND:YAG laser system was used with a wavelength of 355 nm at a pulse width of 10 nm, and the ablation energy was 1 W. This reaction took 30 min to complete and then filtered CDs were dried at 80 °C in the oven. Laser ablation of graphite in polyethylenimine and ethylenediamine with Nd:YAG laser results in CDs. A laser beam was used at 532 nm wavelength with a 10 ns pulse duration and at 10 Hz frequency [105]. Graphite plates in a mixture of polyethylene glycol and water solution were laser treated at conditions of energy = 40 mJ, pulse duration = 6 ns, and frequency = 10 Hz with 1064 nm wavelength. Obtained CDs had efficient for the use of in vivo imaging applications [106]. S atom-sincorporated graphene quantum dots using pulsed laser ablation were prepared following a process as shown in Fig. 2.10. In this process, graphite flakes were immersed in 3-mercaptopropionic and C_2H_5OH mixed solution. Q-Switch Nd:YAG laser was used for 30 min. in room temperature and air atmosphere. The wavelength of laser was 355 nm at a repetition rate of 10 Hz. After completion of the reaction, S-incorporated CDs were obtained after overnight drying at 80 °C [104].

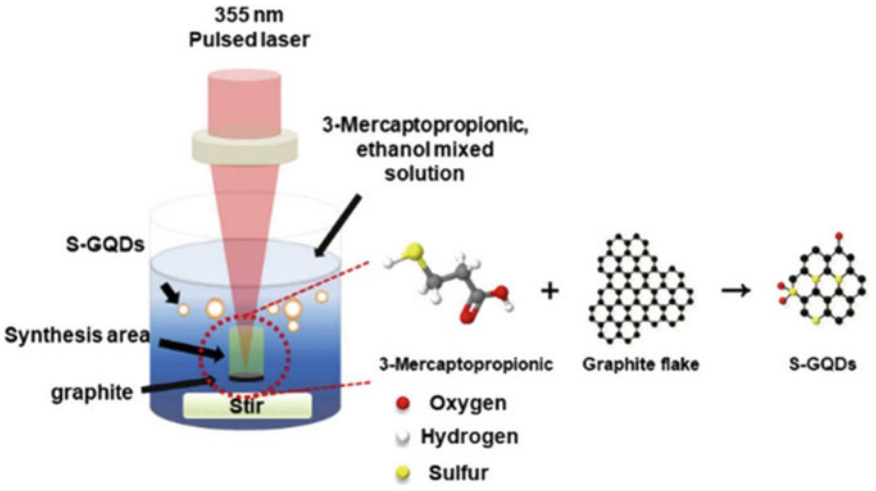

Fig. 2.10 Schematic of laser ablation process for preparing Sulfur-incorporated CDs [104]. Adapted with permission from [104]. Copyright (2020) (Optica Publishing Group)

There are more reports which developed the CDs using a similar approach reported by Russo et al. [107] and Kang et al. [108]. In these reports, graphite oxide liquid dispersion was used for laser ablation and resulted in CDs. Arc discharge method is processed in the same way as discussed for CNT synthesis. CD synthesis by arc discharge was observed accidentally during the CNT synthesis. There are not that many reports on the synthesis of CDs by arc discharge but a few reports are evident enough that it is capable of synthesizing CDs. Dey et al. [109] developed B- and N-doped graphene quantum dots synthesized by arc discharge method. Arc chamber was filled with H and He at a pressure of 200 Torr and 500 Torr, respectively, which flowed B_2H_6 vapors to the arc chamber. The graphite electrode was treated at a discharge current of 100–150 A with a voltage of 60 V. This resulted in 2–3 layers of graphene which further undergoes different chemical exposure for getting the final CDs. DC arc discharge in liquid was used for synthesizing CD/TiO_2 nanostructures which were further analyzed for visible light photocatalytic application [110].

2.3 Properties of Carbon Nanomaterials

CNT is a unique form of carbon made up of a single graphite sheet rolling. CNT has sp^2 hybridization and, due to its structural arrangement and energy bang gap, it can exhibit semiconducting and metallic properties. 1-D energy dispersion relation of CNT is defined according to graphene electronic properties which can be written as

$$E_{CNT}^{\upsilon}(K) = E_{g-2D}(k\frac{K_2}{|K_2|} + \upsilon K_1)$$

$$\text{where} K_1 = \frac{1}{N}(-t_2 b_1 + t_1 b_2),\ K_2 = \frac{1}{N}(m b_1 - n b_2)$$

$-\frac{\pi}{T} < K < \frac{\pi}{T}$ is a 1-D wave vector along the CNT axis and $\upsilon = 1 \ldots N$. The periodic boundary condition for a CNT gives N discrete K values in the circumferential direction. The theoretical electric current density reported for metallic CNTs is 4×10^9 A cm^{-2}. Electron transport exists only along the tube axis which causes a quantum effect and CNTs can be considered as 1-D conductors [57]. Carbon atom sp^2 boding gives exceptional mechanical strength to CNTs. In terms of young's modulus and tensile strength, the value for SWCNT is 0.65–5.5 TPa and 126 GPa, respectively. Mechanical strength varied in the case of MWCNTs and was found of the order of 0.2–0.95 TPa = young's modulus and >63(300) = tensile strength [111]. Thermal conductivity of SWCNTs varied according to direction as along the axis of the tube and across the axis of tubes values are 3500 W m^{-1} K^{-1} and 1.52 W m^{-1} K^{-1}, respectively [112].

In the case of fullerene, their properties are not that much explored still there are few reports related to the absorption and fluorescence nature of these materials. C60

and C70 both types of fullerene showed strong UV absorption but a weak absorption in the visible region. For UV absorption, E_{max} ~10^5 M^{-1} cm^{-1}, and, for visible region, λ_{max} ~540 nm, E_{max} ~710 M^{-1} cm^{-1} for C_{60} and λ_{max} ~468 nm, E_{max} ~15,000 M^{-1} cm^{-1} for C_{70}. No fluorescence emission was shown by $C_{60,}$ but there is a very weak fluorescence emission corresponding to C_{70} [113].

In CDs, optical properties are more interesting and appreciated for their use in different applications. CDs showed absorption in the UV and visible regions of the electromagnetic spectra. This absorption is happening because of different transitions in different bondings like the $\pi-\pi^*$transition of the C=C bonds, and the $n-\pi^*$transition of C=O. Other than absorption CDs also have properties of fluorescence, phosphorescence, and different type of luminescence. Emission wavelength defined the λ_{ex} in the PL of a CD which may be possible because of the quantum confinement or maybe due to the trap emissive surface of CDs. Phosphorescence of CDs arises due to their triple excited states and because of the presence of aromatic carbonyls group on the surface of CDs. Luminescence of CDs can be of many types chemiluminescence, electrochemical luminescence, and up-conversion photoluminescence. These all properties have been utilized in various application areas, especially in sensing and biomedical applications [114].

2.4 Application of Carbon Nanomaterials

2.4.1 Energy Storage Application

Carbon nanomaterials have been widely applied for energy storage applications due to their good conductivity and surface area properties. In recent years, CNTs have been explored in various energy storage devices like lithium-ion batteries (LIBs), supercapacitors, hydrogen storage, etc. The synergetic effect of using CNTs features results in a good-performing device [90, 115, 116]. CNT's length also affects its performance and it was reported that a smaller length results in a good performance as LIB anode because of the easy insertion and extraction of the Li-ions [117]. CVD synthesis was used for synthesizing the 3-D MWCNTs which were used for LIBs. These 3-D anodes offered a high specific capacity and large and cyclic stability [118]. Bulusheva et al. [119] reported a CVD-grown nitrogen-doped MWCNTs for LIBs electrode as it shows reversible capacity of 270 mAh g^{-1} at a current density of 0.2 mA cm^{-2}. Nanocomposites of CNTs with Sb and $SnSb_{0.5}$ has been used for LIB anode. Composite was prepared by chemical method and the highest reversible capacity was 518 mAh g^{-1} for the composition of CNT–56 wt.% $SnSb_{0.5}$ [120].

Chen et al. [121] prepared the nanocomposite of hollow CNTs/carbon–nanofiber hybrid for LIBs anode. A schematic of the nanocomposite and the important outcome of the report is shown in Fig. 2.11. CNTs are grown on carbon fiber by CVD using C_2H_2 as a carbon source which was obtained from the calcination of the polymer under Ni nanoparticle. Figure 2.11b and c reveal the charge/discharge

capacities and cyclic performance of the hollow CNTs/carbon–nanofiber hybrid at different conditions. Reversible capacities ~940, 700, 500, 380, and 320 mAh g^{-1} were recorded at current densities of 0.5, 1, 3, 5, and 8 A g^{-1}, respectively (Fig. 2.11c). Charge/discharge capacities and coulombic efficiencies graphs showed that the coulombic efficiencies remain above 95% for each cycle and even after a 70% cycle only ~20% of coulombic efficiency faded. The highest reversible capacity was 1530 mAh g^{-1} at 0.1A g^{-1} because of its high surface area and hollow structure [109]. Fullerene and CDs also have been used for the supercapacitor and LIBs applications. Hu et al. [122] developed CD-based high current density lithium–sulfur batteries. Poly(ethyleneimine)-functionalized CDs were prepared by carbonization process and a specific capacity offered was 712 mAh g^{-1} at a current density of 2 mA cm^{-2}. CDs derived from glucose oxidation can act as an anode for LIBs and SIBs. The performance shown as anode for LIBs and SIBs were 864.9 mAh g^{-1} at 0.5 C and 323.9 mAh g^{-1} at 0.5 C, respectively. CD–Bi_2O_3 nanocomposite synthesized by hydrothermal synthesis and offered a high discharge capacity of 1500 mA h g^{-1} at 0.2 C. Fullerene can also be used for various purposes in batteries applications like in anode [123, 124], interfacial stabilization of Ni-rich cathodes [125]. Few reports on such kinds of research work are summarized in Table 2.1.

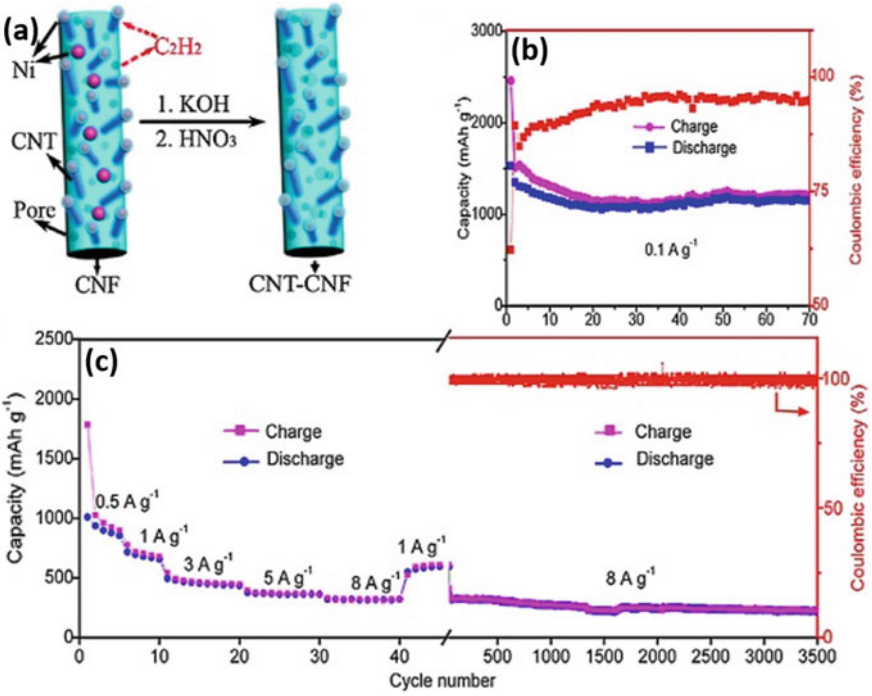

Fig. 2.11 **a** Schematic image of hollow CNTs/carbon–nanofiber hybrid, **b** charge/discharge capacities at different rates, and **c** cycling performances of hybrid electrodes tested between 3 and 0 V [121]. Adapted with permission from [121]. Copyright (2013) (The American Chemical Society)

Table 2.1 Summarized results of some reports on the energy storage application of CNTs, fullerene, and CDs

Nanomaterials	Synthesis method	Morphology	Application	Study outcomes	Ref
Pt/CNT/PANI	CVD	CNT yarn with a diameter of ~16 μm	Supercapacitor	35.27 Wh kg^{-1} at 100 mV s^{-1}	[126]
SWCNTs	Arc discharge	CNT with a diameter of 10–20 nm	Supercapacitor	20 kW kg^{-1} at 6.55 Wh kg^{-1}	[127]
Fe_3O_4–CNTs	Chemical synthesis	CNTs were decorated with nanoparticles	Supercapacitor	145.4 F g^{-1} at 2 mV s^{-1}	[128]
Ferrocenylpyrrolidine C_{60}	Precipitation	Cross-like 3-D hierarchical lamellae	Supercapacitor	505.4 F g^{-1} at 0.1 A g^{-1}	[129]
Macaroni fullerene C_{60}–CNTs	Precipitation	Macaroni fullerene-mesoporous CNTs	Supercapacitor	422 F g^{-1} at 1 A g^{-1}	[130]
Polyaniline/fullerene /emeraldine base hybrids	Copolymerization	Coral-like porous morphology	Supercapacitor	776 F g^{-1} at 1 mA cm^{-2}	[131]
Polyaniline/fullerene	Polymerization	Spongy irregular shaped	Supercapacitor	2201 F g^{-1} at 2 A g^{-1}	[132]
Iron oxide-mesoporous fullerene	Nano-hard templating	Doughnut-shaped morphology	Supercapacitor	65 F g^{-1} at 2 A g^{-1}	[133]
C_{70} microtubes	Precipitation	Macropores of several micrometers	Supercapacitor	362.0 F g^{-1} at 0.1 A g^{-1}	[134]
CNTs/carbon fiber	Thermal CVD	30 nm in diameter, with a bamboo structure	LIBs	643 mAh g^{-1} at 0.05 mA cm^{-2}	[135]
Fluorine-doped CDs	Hydrothermal	Stockade-like etching patterns	Li-ion storage	297.3 mAh g^{-1} at 100 mA g^{-1}	[136]
CDs/holey Graphene	Electrolyzing	CDs of 5–10 nm on the surface of graphene sheets	Li-CO_2 batteries	12,300 mAh g^{-1} at 0.5 A g^{-1}	[137]

(continued)

Table 2.1 (continued)

Nanomaterials	Synthesis method	Morphology	Application	Study outcomes	Ref
C_{24} fullerene	DFT calculation	–	LIBs	Cell voltage 1.70 V	[138]
CDs	pyrolysis	–	LIBs	~165 mAh g^{-1} at 0.1 C	[139]
CDs/MnO_2/graphene aerogel	Hydrothermal	Porous structure	Supercapacitor	38.2 W h kg^{-1} at 1 k W kg^{-1}	[140]
NiS/CDs	Hydrothermal	Flower-like structure	Supercapacitor	880 F g^{-1} at 2 A g^{-1}	[124]
CDs/layered carbon	Heat treatment of C_{60} powder	Sponge consists of interconnected sheet-like assembly of CDs	Supercapacitor	157.4 F cm^{-3} at 0.5 A g^{-1}	[141]

2.4.2 Biomedical Applications

Carbon nanomaterials show a crucial role in the biomedical field for different uses and development. Different biomedical applications of CNTs were reviewed by Yang et al. [142]. Chen et al. [143] developed functionalized CNTs for targeted drug delivery for treated tumors. The study concluded that prepared material is efficient in drug delivery and making a binding of the drug with microtubules. CNTs were used for preparing doxorubicin and mitoxantrone drug delivery in cancer treatment. It was reported that the high surface area of CNTs gave high loading drug delivery efficiency and CNTs showed a unique bonding with cellular membranes [144]. Molecular dynamics with computer simulation help in understanding the CNTs' interactions with cellular membranes because if the physical properties of CNTs are not compatible, then CNTs can be toxic to the body [145]. CNTs can also be used as detection probes in medical applications. Sapna et al. [146] used anti-LipL32 CNTs as an immunofluorescence probe for early detection of leptospirosis. Full-body penetrating clinical modalities of MRI, PET, SPECT, and X-ray CT can also be assisted with CNTs agents [147]. Like CNTs, CDs and fullerenes also have been explored for medical applications. Hyaluronan-conjugated nitrogen-doped CDs for tumor imaging have been developed by Karakoçak et al. [148]. This was possible because of the dependency of CD fluorescence on the wavelength of excitation. N-, P-, and S-doped CDs can be successfully used for the antibacterial assay, particularly for Escherichia coli (*E. coli*) and Staphylococcus aureus (*S. aureus*) [149]. CDs were synthesized by dimethyl diallyl ammonium chloride and glucose as reaction precursors which have been further used for wounds affected by bacteria [150]. Ding et al. [151] developed the CDs by using a green precursor by hydrothermal treatment. In this synthesis, lemon juice was treated with formamide in autoclave at 200 °C for 6 h and then purified by silica column chromatography. CDs were utilized for in vitro cell imaging as shown in Fig. 2.12. Figure 2.12a, b show the confocal laser scanning microscope image of HeLa cells which was under incubation for 5 h with 30 $\mu g\ mL^{-1}$ CDs. Figure 2.12c, d show in vivo imaging of subcutaneous injected mouse which showed the effective luminescence of CDs. Figure 2.12d shows an image of the nude mouse after 15 min. in which bright fluorescence of CDs indicates the body circulation of CD aqueous solution [151].

Fluorescent fullerene (C_{60}-TEG-COOH)-coated mesoporous silica nanoparticles were found to be efficient for pH-sensitive drug release and fluorescent cell imaging [152]. Liu et al. [153] developed C_{70}-based poly(L-lactide) (PLLA) composite nanofibers loaded with water-soluble fullerene C_{70} nanoparticles and paclitaxel for the application of drug delivery, bioimaging, etc. Table 2.2 summarized some reports on the biomedical application of CNTs, CDs, and fullerenes.

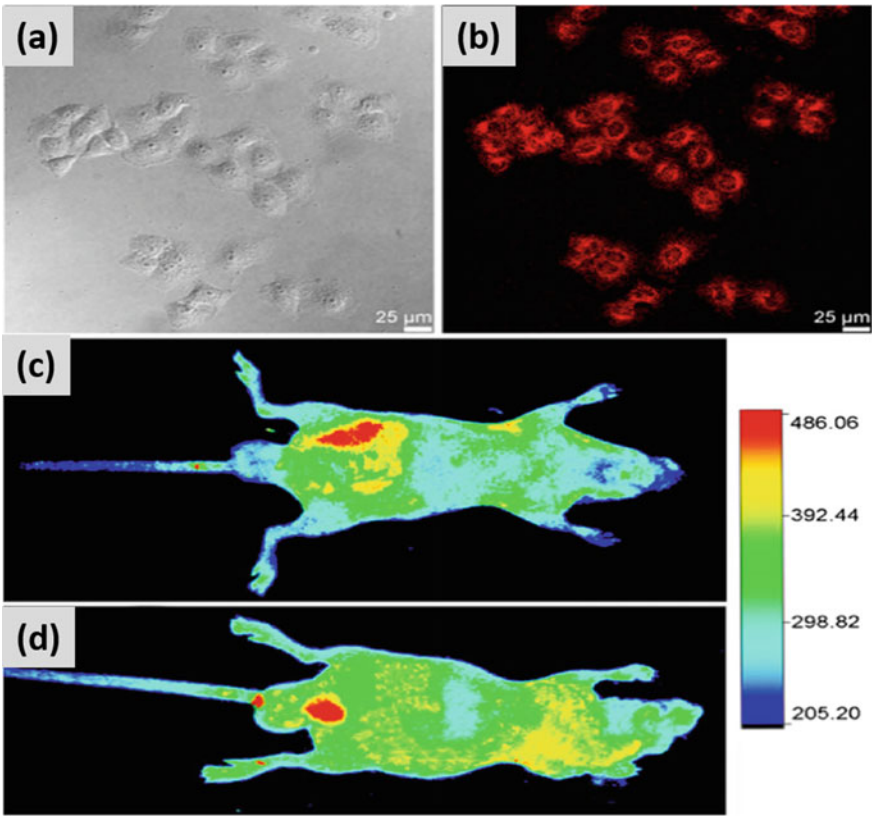

Fig. 2.12 **a** Confocal fluorescence micrographs of HeLa cells incubated with CDs (30 μg mL^{-1} for 0.5 h) in bright field and **b** at 578 nm excitation. **c** In vivo PL image of a nude mouse treated with subcutaneous injection and **d** intravenous injection of 50 μL of CDs aqueous solution (color bars: fluorescence intensity) [151]. Adapted with permission from [151]. Copyright (2019) (Elsevier)

2.4.3 Electrochemical Sensing

Electrochemical sensing also becomes efficient and advanced with the use of carbon nanomaterials. CNTs can be used in sensing due to their good strength, high conductivity, and surface area. Functionalization of CNTs can improve their adsorption which is an important aspect of sensing applications.

Congo red functionalized MWCNTs were prepared by a simple solution-phase method which improves the sensitivity and antifouling capacity of MWCNTs [171]. Wisitsoraat et al. [172] developed CNT-based microfluidic device for cholesterol detection. The device was successfully used for more than 60 samples and exhibited linear detection from 50 to 400 mg dl^{-1}. CNTs' electrochemical sensor for Sudan I offered a detection from 0.01 mg L^{-1} to 1.0 mg L^{-1} with a detection limit

Table 2.2 Summarized results of some reports on the biomedical applications of CNTs, fullerene, and CDs

Nanomaterials	Synthesis method	Morphology	Application	Reference
CNTs	Vacuum filtration	1.5–4 nm size	For treatment of breast cancer	[154]
CNTs–Ag nanohybrid	Mussel-inspired coating approach	Ag nanoparticles distributed on the CNTs surface	Antibacterial	[155]
MWCNTs	CVD	Large agglomerates and closely packed CNTs	Antibacterial agent	[156]
SWCNTs	–	200−500 nm length	Targeted killing of cancer cells in vivo and in vitro	[157]
Pollen typhae crbonisata–CDs	Pyrolysis	spherical, 2–8 nm	in the field of hemorrhage control	[158]
CDs	Solvothermal method	Uniform size with 3.3 nm	Drug delivery in cancer stem cells	[159]
CDs	Hydrothermal method	3.8 ± 0.5 nm size	Imaging and nucleus-targeted drug delivery	[160]
CDs–quinic acid	Hydrothermal method	7.55 ± 1.04 nm size	Drug delivery of gemcitabine to breast cancer cells	[161]
CO–CDs	Hydrothermal method	Particle size of around 2 nm	Drug delivery system	[162]
Chitosan/CDs/aptamer complex	Magnetic stirring	122.7 nm	anticancer drug delivery system	[163]
CDs	Hydrothermal method	0.75–2.75 nm	Antimicrobial activity	[159]
CDs	Chemical synthesis	Mean size of 2.5 nm	wound healing with mixed bacterial infection	[162]
CDs	Microwave-assisted synthesis	6.99 ± 2.50 nm	Bioimaging and anti-inflammation	[164]
F- and Cl-doped CDs	hydrothermal method	5 ± 2 nm	bioimaging	[165]
Fluorescent ultrafine C_{60}	Electrochemical	Size distribution around 5 nm	Bioimaging	[166]

(continued)

Table 2.2 (continued)

Nanomaterials	Synthesis method	Morphology	Application	Reference
Perfluorohexane-encapsulated fullerene	Vacuum ultrasonic emulsification and centrifugation	average size 278.3 ± 51.0 nm	Dual-modality US/CT imaging and synergistic high-intensity focused ultrasound ablation	[167]
Fullerene-rhodamine	Acid/base treatment	diameter of ~95 nm	Cancer diagnosis and treatment	[168]
PEGylated fullerene/iron oxide nanocomposites	Solvothermal	163.8 ± 3.7 nm	Drug delivery and MR imaging	[169]

of 5.0 μg L^{-1}[173]. Figure 2.13 reveals the schematic and electrochemical results of Cu nanoparticle/fullerene-C_{60}/MWCNT composite-based sensor. Carbon paste electrode (CPE) was modified with 1 mg of MWCNTs:C_{60} (2:1) mixture which was dissolved in 10 ml toluene. Cu nanoparticles deposition on the modified CPE was done by electrochemical deposition by applying a potential range of -0.3 to 1.0 V. Developed sensor was used for paracetamol detection with a detection limit of 7.3×10^{-11} M. Sensor had a linear detection limit of with a recovery of 99.21–103% for paracetamol detection in biological samples [170]. Kachoosangi et al. [174] fabricated a MWCNT-based sensor for detecting capsaicin in real samples of chili pepper sauces. The detection limit of the sensor was 0.31 μM with two linear ranges of 0.5–15 μM and 15–60 μM. CDs and fullerene also have been used for electrochemical sensing. Wu et al. [175] reported a CD-based electrochemical sensor for detecting dopamine in human serum. The lowest detection limit of the sensor toward dopamine was 0.08 μM with a linear sensing range of 0.25–76.81 μM. CDs, chitosan, and gold nanoparticles were used for preparing the modified electrochemical sensor for detecting patulin with the lowest detection limit of 7.57×10^{-13} mol L^{-1} [176]. Liu et al. [176] developed F- and N-doped CDs decorated laccase for sensing catechol. Functionalized fullerene C_{60}-based sensor was successfully used for the analysis of primaquine for which the lowest detection limit observed was 0.80 nM [177]. Fullerene and its composites can be utilized for the detection of *p*-nitrophenol [178], vanillin [179], catechol, and hydroquinone [180]. Table 2.3 shows the summary of few reports on the electrochemical sensing using carbon nanomaterials.

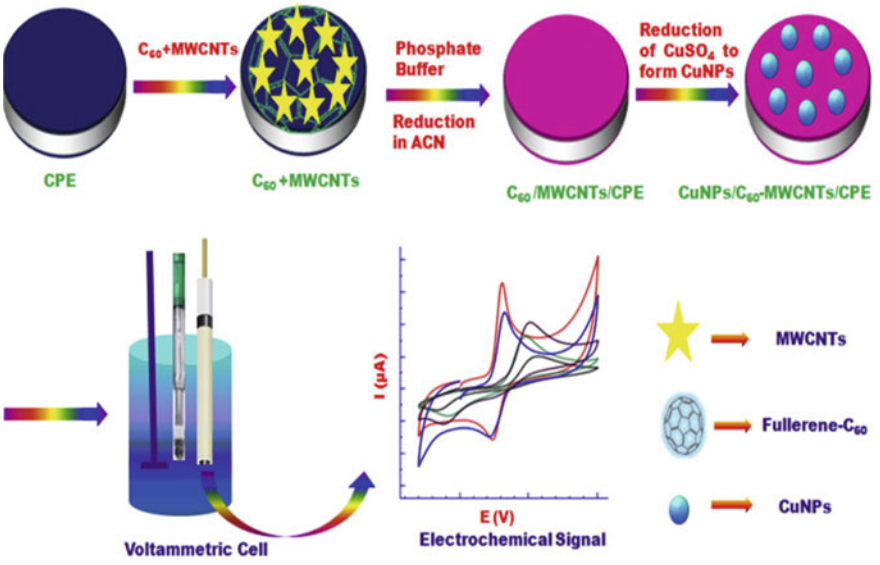

Fig. 2.13 Schematic fabrication of Cu nanoparticles/fullerene-C_{60}/MWCNTs composites-based electrochemical sensor [170]. Adapted with permission from [170]. Copyright (2016) (Elsevier)

Table 2.3 Summarized results of few reports on the electrochemical sensing by CNTs, CDs, and fullerenes

Nanomaterials	Morphology	Sensing	Lowest detection limit	Ref
Zinc porphyrin-fullerene-derivative	Granular morphology	H_2O_2 and nitrite	0.81 μM and 1.44 μM	[181]
Fullerene-functionalized CDs/ionic liquid	Nanoclusters of C_{60} and CNTs	Catecholamines	18 ± 2 nM, 22 ± 2 nM and 15 ± 2 nM in various samples	[182]
Fullerene nanorods	Linear hexagonal cross-sectional rods crimpled to form star-shaped structures	Paraben	3.8 nM	[183]
Fullerene-C_{60} coated Gold electrode	Small bundles and single fullerene particles	Dopamine	0.26×10^{-9} M	[184]
Fullerene C_{60}-enzyme	–	Glucose	1.6×10^{-6} M	[185]
Gold nanoparticles/CNTs	10 nm Au nanoparticles were on the wall of CNTs	Arsenic (III)	0.1 μg L^{-1}	[186]
CNTs–chitosan	–	Dehydrogenase enzymes	3 μM	[187]
Ni nanoparticles/CNTs	Ni nanoparticles distributed on CNTs	Glucose	500 nM	[188]
Polyaniline–CNTs	Core–shell arrangement of composite	Carbaryl and methomyl	1.4 and 0.95 μmol L^{-1}	[189]
MWCNTs@molecularly imprinted polymer	Porous structure	Chloramphenicol	1.0×10^{-10} mol L^{-1}	[190]
CDs/MWCNTs nanocomposites	CDs (6.5 nm) distributed on CNTs	H_2O_2	0.25 μM	[191]
CDs	particle size 2–5 nm	Glucose	0.09 μM	[192]
NCDs/cuprous oxide	Sphere-like morphology	Chlorpromazine	25 nM	[193]
CDs/hexadecyl trimethyl ammonium bromide/chitosan	1.55 ± 0.25 nm spherical nanoparticles	2,4-dichlorophenol	0.01 μmol L^{-1}	[194]

(continued)

Table 2.3 (continued)

Nanomaterials	Morphology	Sensing	Lowest detection limit	Ref
N-CDs/manganese oxide	4.089 nm nanosphere	p-aminophenol and paracetamol	0.0303 μM and 0.046 μM	[195]

2.5 Conclusion and Future Perspective

CNTs, CDs, and fullerenes are three different dimensionality carbon nanomaterials. CNTs are 1-D materials with high electronic conductivity, superior mechanical strength, and high surface area. CDs and fullerenes are 0-D carbon nanomaterials, but fullerenes existing in other forms called CNTs are cylindrical fullerenes. C_{60}, C_{70}, $C_{84,}$ etc., are different fullerene family members, they all differ in their number of carbon atoms. CDs have unique optical properties like fluorescence, luminescence, and phosphorescence which make them suitable particularly for the use of biomedical applications like sensing, in vitro and in vivo imaging, catalysis, etc. CNTs can be synthesized using laser ablation, arc discharge, and CVDs, but CVD method is more useful in terms of large production. Similar kinds of approaches can be applied for synthesizing CDs and fullerenes. CNTs, CDs, and fullerenes can be excellent materials for electronic use, electrochemical sensing, biomedical application, and in many other fields. Good synthesis approaches and different derivatives could be the ways for further enhancing the performance of these materials. Different composites formed by combining these with others can generate multifunctional advanced materials.

References

1. N. Gupta, S.M. Gupta, S.K. Sharma, Carbon Lett. **29**, 419–447 (2019)
2. D. Maiti, X. Tong, X. Mou, K. Yang, Front. Pharmacol. **9**, 1401 (2019)
3. S. Iijima, Nature **354**, 56–58 (1991)
4. M. Monthioux, P. Serp, E. Flahaut, M. Razafinimanana, C. Laurent, A. Peigney, W. Bacsa, J.-M. Broto, in *Springer handbook of nanotechnology*. ed. by B. Bhushan (Springer, Berlin Heidelberg, Berlin, Heidelberg, 2010), pp.47–118
5. D. Tománek, A. Jorio, M. S. Dresselhaus, and G. Dresselhaus, in *Carbon Nanotubes: Advanced Topics in the Synthesis, Structure, Properties and Applications*, edited by A. Jorio, G. Dresselhaus, and M. S. Dresselhaus (Springer Berlin Heidelberg, Berlin, Heidelberg, 2008), pp. 1–12
6. X. Xu, R. Ray, Y. Gu, H.J. Ploehn, L. Gearheart, K. Raker, W.A. Scrivens, J. Am. Chem. Soc. **126**, 12736–12737 (2004)
7. S.Y. Lim, W. Shen, Z. Gao, Chem. Soc. Rev. **44**, 362–381 (2015)
8. D.L. Zhao, T.-S. Chung, Water Res. **147**, 43–49 (2018)
9. H.W. Kroto, J.R. Heath, S.C. O'Brien, R.F. Curl, R.E. Smalley, Nature **318**, 162–163 (1985)
10. W.O.J. Boo, J. Chem. Educ. **69**, 605 (1992)
11. L. Sun, X. Wang, Y. Wang, Q. Zhang, Carbon **122**, 462–474 (2017)
12. J. Xiao, R. Momen, C. Liu, Electrochem. Commun. **132**, 107143 (2021)

13. T. Xu, W. Shen, W. Huang, X. Lu, Mater. Today Nano **11**, 100081 (2020)
14. S. Goodarzi, T. Da Ros, J. Conde, F. Sefat, M. Mozafari, Mater. Today **20**, 460–480 (2017)
15. X. Li, X. Liu, J. Huang, Y. Fan, F.-Z. Cui, Surf. Coat. Technol. **206**, 759–766 (2011)
16. M.J. Molaei, RSC Adv. **9**, 6460–6481 (2019)
17. A. Merkoçi, M. Pumera, X. Llopis, B. Pérez, M. del Valle, S. Alegret, TrAC Trends Anal. Chem. **24**, 826–838 (2005)
18. M.J. Molaei, Anal. Methods **12**, 1266–1287 (2020)
19. S. Pilehvar, K. De Wael, in *Nanocarbons for Electroanalysis*, ed. by S. Szunerits, R. Boukherroub, A. Downard, J. J Zhu (Wiley Online Library, Hoboken, New Jersey, U.S. 2017), p. 173.
20. M.S. Mauter, M. Elimelech, Environ. Sci. Technol. **42**, 5843–5859 (2008)
21. C.W. Tan, K.H. Tan, Y.T. Ong, A.R. Mohamed, S.H.S. Zein, S.H. Tan, Environ. Chem. Lett. **10**, 265–273 (2012)
22. Y. Yao, H. Zhang, K. Hu, G. Nie, Y. Yang, Y. Wang, X. Duan, S. Wang, J. Environ. Chem. Eng. **10**, 107336 (2022)
23. R. Kumar, R.K. Singh, P.K. Dubey, P. Kumar, R.S. Tiwari, I.-K. Oh, J. Nanoparticle Res. **15**, 1847 (2013)
24. R. Kumar, R.K. Singh, P.K. Dubey, R.M. Yadav, D.P. Singh, R.S. Tiwari, O.N. Srivastava, J. Nanoparticle Res. **17**, 24 (2015)
25. R. Kumar, R.S. Tiwari, O.N. Srivastava, NANO **06**, 215–223 (2011)
26. R. Kumar, R.S. Tiwari, O.N. Srivastava, Nanoscale Res. Lett. **6**, 92 (2011)
27. R. Kumar, R.K. Singh, P.K. Dubey, D.P. Singh, R.M. Yadav, R.S. Tiwari, Adv. Mater. Interfaces **2**, 1500191 (2015)
28. K. Awasthi, R. Kumar, R.S. Tiwari, O.N. Srivastava, J. Exp. Nanosci. **5**, 498–508 (2010)
29. R. Kumar, R.K. Singh, R.S. Tiwari, Mater. Des. **94**, 166–175 (2016)
30. R. Kumar, R.K. Singh, V.S. Tiwari, A. Yadav, R. Savu, A.R. Vaz, S.A. Moshkalev, J. Alloys Compd. **695**, 1793–1801 (2017)
31. R. Kumar, R.K. Singh, P. Kumar, P.K. Dubey, R.S. Tiwari, O.N. Srivastava, Sci. Adv. Mater. **6**, 76–83 (2014)
32. N. Arora, N.N. Sharma, Diam. Relat. Mater. **50**, 135–150 (2014)
33. Z. Shi et al., J. Phys. Chem. Solids **61**, 1031–1036 (2000)
34. M. Cadek, R. Murphy, B. McCarthy, A. Drury, B. Lahr, R.C. Barklie, M. in het Panhuis, J. N. Coleman, and W.J. Blau, Carbon **40**, 923–928 (2002)
35. S. Cui, P. Scharff, C. Siegmund, D. Schneider, K. Risch, S. Klötzer, L. Spiess, H. Romanus, J. Schawohl, Carbon **42**, 931–939 (2004)
36. C.E. Baddour, C. Briens, Int. J. Chem. React. **3**, 1–20 (2005)
37. M. Keidar, Phys. D: Appl. Phys. **40**, 2388–2393 (2007)
38. E. Muñoz, W.K. Maser, A.M. Benito, M.T. Martínez, G.F. de la Fuente, Y. Maniette, A. Righi, E. Anglaret, J.L. Sauvajol, Carbon **38**, 1445–1451 (2000)
39. J. Chrzanowska, J. Hoffman, A. Małolepszy, M. Mazurkiewicz, T.A. Kowalewski, Z. Szymanski, L. Stobinski, Phys. Status Solidi B **252**, 1860–1867 (2015)
40. Z. Lu, R. Raad, F. Safaei, J. Xi, Z. Liu, J. Foroughi, Front. Mater. Sci. **6**, 138 (2019)
41. R. Andrews, D. Jacques, D. Qian, T. Rantell, Acc. Chem. Res. **35**, 1008–1017 (2002)
42. J. Prasek, J. Drbohlavova, J. Chomoucka, J. Hubalek, O. Jasek, V. Adam, R. Kizek, J. Mater. Chem. **21**, 15872–15884 (2011)
43. Ç. Öncel, Y. Yürüm, Fuller. Nanotub. Carbon Nanostruct. **14**, 17–37 (2006)
44. H. Wang, W. Sun, Y. Liu, H. Ma, T. Li, K.A. Lin, K. Yin, S. Luo, J. Electroanal. Chem **904**, 115907 (2022)
45. A.G. Ryabenko, D.P. Kiryukhin, G.A. Kichigina, V.G. Basu, O.M. Zhigalina, N.N. Dremova, High Energy Chem. **56**, 50–53 (2022)
46. V. Sivamaran, V. Balasubramanian, M. Gopalakrishnan, V. Viswabaskaran, A.G. Rao, Chem. Phys. **4**, 100072 (2022)
47. W. Khan, R. Sharma, P. Saini, in *Carbon Nanotubes-Current Progress of their Polymer Composites* ed. by M. R. Berber, I. H. Hafez (Intech Open, Vienna, Austria, 2016), p. 1

48. S. Abbasloo, M. Ojaghi-Ilkhchi, M. Mozammel, in *5th International Biennial Conference on Ultrafine Grained and Nanostructured Materials* (2015), pp. 1–6
49. I.A. Novoselova, N.F. Oliinyk, S.V. Volkov, A.A. Konchits, I.B. Yanchuk, V.S. Yefanov, S.P. Kolesnik, M.V. Karpets, Physica E Low Dimens. Syst. Nanostruct. **40**, 2231–2237 (2008)
50. K. Byrappa, T. Adschiri, Prog. Cryst. Growth Char. **53**, 117–166 (2007)
51. H. Xu, B.W. Zeiger, K.S. Suslick, Chem. Soc. Rev. **42**, 2555–2567 (2013)
52. P. Clemens, X. Wei, B.L. Wilson, R.L. Thomas, Open. J. Compos. Mater. **3**, 30686 (2013)
53. S. Manafi, H. Nadali, H.R. Irani, Mater. Lett. **62**, 4175–4176 (2008)
54. M. Dastborhan, A. Khataee, S. Arefi-Oskoui, Y. Yoon, Ultrason. Sonochem. **87**, 106058 (2022)
55. B.J. Choudhury, V.S. Moholkar, Ultrason. Sonochem. **82**, 105896 (2022)
56. M. Krishnaveni, A.M. Asiri, S. Anandan, Ultrason. Sonochem. **66**, 105105 (2020)
57. W. Krätschmer, K. Fostiropoulos, D.R. Huffman, Chem. Phys. Lett. **170**, 167–170 (1990)
58. S. Kano, M. Kohno, K. Sakiyama, S. Sasaki, N. Aya, H. Shimura, Chem. Phys. Lett. **378**, 474–480 (2003)
59. L. S. Porto, D. N. Silva, A. E. F. d. Oliveira, A. C. Pereira, K. B. Borges, Rev. Anal. Chem. **38** (2019)
60. K. Kikuchi, N. Nakahara, T. Wakabayashi, M. Honda, H. Matsumiya, T. Moriwaki, S. Suzuki, H. Shiromaru, K. Saito, K. Yamauchi, I. Ikemoto, Y. Achiba, Chem. Phys. Lett. **188**, 177–180 (1992)
61. O. Nerushev, G. Sukhinin, Tech. Phys. **42**, 160–167 (1997)
62. I.E. Kareev, V.M. Nekrasov, V.P. Bubnov, Tech. Phys. **60**, 102–106 (2015)
63. A. Nimibofa, E.A. Newton, A.Y. Cyprain, W. Donbebe, J. Mater. Sci. **7**, 22–23 (2018)
64. R. Otsuki, S. Nasu, R. Fujimori, K. Anada, K. Ohhashi, R. Yamamoto, K. Fujii, K. Ohkubo, Powder Metall. **51**, 622–625 (2004)
65. P.I. Kyesmen, A. Onoja, A.N. Amah, Springerplus **5**, 1323 (2016)
66. H. Funasaka, K. Yamamoto, K. Sakurai, T. Ishiguro, K. Sugiyama, T. Takahashi, Y. Kishimoto, Fullerene Sci. Technol. **1**, 437–448 (1993)
67. X. Armand, N. Herlin, I. Voicu, M. Cauchetier, J. Phys. Chem. Solids **58**, 1853–1859 (1997)
68. M.M. Boorum, Y.V. Vasil'ev, T. Drewello, L.T. Scott, Science **294**, 828–831 (2001)
69. K.Y. Amsharov, M. Jansen, Carbon **45**, 117–123 (2007)
70. S. Mitra, C.J. Pope, K.K. Gleason, Y. Makarovsky, A.L. Lafleur, J.B. Howard, MRS Proc. **270**, 149 (2011)
71. I. Voicu, X. Armand, M. Cauchetier, N. Herlin, S. Bourcier, Chem. Phys. Lett. **256**, 261–268 (1996)
72. L. Becker, T.E. Bunch, Meteorit. Planet. Sci. **32**, 479–487 (1997)
73. H. Suematsu, C. Minami, R. Kobayashi, Y. Kinemuchi, T. Hirata, R. Hatakeyama, S.-C. Yang, W. Jiang, K. Yatsui, Jpn. J. Appl. Phys. **42**, L1028–L1031 (2003)
74. Q. Tang, S. Zhang, X. Liu, M. Sumita, S. Ishihara, H. Fuchs, Q. Ji, L.K. Shrestha, K. Ariga, Phys. Chem. Chem. Phys. **19**, 29099–29105 (2017)
75. B. Gayen, S. Palchoudhury, J. Chowdhury, J. Nanomater. **2019**, 3451307 (2019)
76. R. Kumar, R.K. Singh, S.K. Yadav, R. Savu, S.A. Moshkalev, J. Alloy. Compd. **683**, 38–45 (2016)
77. R.K. Singh, R. Kumar, D.P. Singh, R. Savu, S.A. Moshkalev, Mater. Today Chem. **12**, 282–314 (2019)
78. H. Zhu, X. Wang, Y. Li, Z. Wang, F. Yang, X. Yang, Chem. Commun. 5118–5120 (2009)
79. C. López, M. Zougagh, M. Algarra, E. Rodríguez-Castellón, B. B. Campos, J. C. G. Esteves da Silva, J. Jiménez-Jiménez, A. Ríos, Talanta **132**, 845–850 (2015)
80. T.-N. Pham-Truong, T. Petenzi, C. Ranjan, H. Randriamahazaka, J. Ghilane, Carbon **130**, 544–552 (2018)
81. M.P. Romero, F. Alves, M.D. Stringasci, H.H. Buzzá, H. Ciol, N.M. Inada, V.S. Bagnato, Front. Microbiol. **12**, 1455 (2021)
82. H. Li, F.-Q. Shao, S.-Y. Zou, Q.-J. Yang, H. Huang, J.-J. Feng, A.-J. Wang, Mikrochim. Acta **183**, 821–826 (2016)
83. C. Zhao, X. Li, C. Cheng, Y. Yang, Microchem. J. **147**, 183–190 (2019)

84. Y. Wang, X. Chang, N. Jing, Y. Zhang, Anal. Methods **10**, 2775–2784 (2018)
85. Z. Han, L. He, S. Pan, H. Liu, X. Hu, J. Lumin. **35**, 989–997 (2020)
86. Q. Wang, H. Zheng, Y. Long, L. Zhang, M. Gao, W. Bai, Carbon **49**, 3134–3140 (2011)
87. L. Lin, Y. Wang, Y. Xiao, W. Liu, Mikrochim. Acta **186**, 147 (2019)
88. H. Lee, Y.-C. Su, H.-H. Tang, Y.-S. Lee, J.-Y. Lee, C.-C. Hu, T.-C. Chiu, J. Nanomater. **11**, 1831 (2021)
89. Z. Pang, Y. Fu, H. Yu, S. Liu, S. Yu, Y. Liu, Q. Wu, Y. Liu, G. Nie, H. Xu, S. Nie, S. Yao, Ind. Crops Prod. **183**, 114957 (2022)
90. X. Lai, L. Gao, J. Li, P. Zhang, Integr. Ferroelectr. **228**, 272–280 (2022)
91. Y. Deng, Y. Zhou, S. Ye, J. Qian, S. Cao, J. Wuhan Univ. Technol. Mater. Sci. Ed. **37**, 23–27 (2022)
92. C.S. Stan, C. Albu, A. Coroaba, M. Popa, D. Sutiman, J. Mater. Chem. C **3**, 789–795 (2015)
93. X.W. Tan, A.N.B. Romainor, S.F. Chin, S.M. Ng, J. Anal. Appl. Pyrolysis **105**, 157–165 (2014)
94. M. Rong, Y. Feng, Y. Wang, X. Chen, Sens. Actuators B Chem. **245**, 868–874 (2017)
95. C.-W. Lai, Y.-H. Hsiao, Y.-K. Peng, P.-T. Chou, J. Mater. Chem. **22**, 14403–14409 (2012)
96. A. Dager, T. Uchida, T. Maekawa, M. Tachibana, Sci. Rep. **9**, 14004 (2019)
97. W. Tang, B. Wang, J. Li, Y. Li, Y. Zhang, H. Quan, Z. Huang, J. Mater. Sci. **54**, 1171–1183 (2019)
98. Y. Li, J. Chen, Y. Wang, H. Li, J. Yin, M. Li, L. Wang, H. Sun, L. Chen, Appl. Surf. Sci. **538**, 148151 (2021)
99. Y. Li, S. Li, Y. Wang, J. Wang, H. Liu, X. Liu, L. Wang, X. Liu, W. Xue, N. Ma, Phys. Chem. Chem. Phys. **19**, 11631–11638 (2017)
100. Y. Hou, Q. Lu, H. Wang, H. Li, Y. Zhang, S. Zhang, Mater. Lett. **173**, 13–17 (2016)
101. Y.-S. Lee, C.-C. Hu, T.-C. Chiu, J. Environ. Chem. Eng. **10**, 107413 (2022)
102. Y. Hou, Q. Lu, J. Deng, H. Li, Y. Zhang, Anal. Chim. Acta **866**, 69–74 (2015)
103. H. Ming, Z. Ma, Y. Liu, K. Pan, H. Yu, F. Wang, Z. Kang, Dalton Trans. **41**, 9526–9531 (2012)
104. S. Kang, Y.K. Jeong, K.H. Jung, Y. Son, W.R. Kim, J.H. Ryu, K.M. Kim, Opt. Express **28**, 21659–21667 (2020)
105. A. Kaczmarek, J. Hoffman, J. Morgiel, T. Mościcki, L. Stobiński, Z. Szymański, A. Małolepszy, Materials **14**, 729 (2021)
106. A.K. Narasimhan, T.S. Santra, M.R. Rao, G. Krishnamurthi, RSC Adv. **7**, 53822–53829 (2017)
107. P. Russo, R. Liang, E. Jabari, E. Marzbanrad, E. Toyserkani, Y.N. Zhou, Nanoscale **8**, 8863–8877 (2016)
108. S. Kang, Y.K. Jeong, K.H. Jung, Y. Son, S.-C. Choi, G.S. An, H. Han, K.M. Kim, RSC Adv. **9**, 38447–38453 (2019)
109. S. Dey, A. Govindaraj, K. Biswas, C.N.R. Rao, Chem. Phys. Lett. **595–596**, 203–208 (2014)
110. N. Biazar, R. Poursalehi, H. Delavari, in *AIP Conference Proceedings* (AIP Publishing LLC, 2018), p. 020033
111. J.-P. Salvetat, J.-M. Bonard, N. Thomson, A. Kulik, L. Forro, W. Benoit, L. Zuppiroli, Int. J. Appl. Phys **69**, 255–260 (1999)
112. J. Hone, Dekker Encycl. Nanosci. Nanotechnol. **7**, 603–610 (2004)
113. C.S. Foote, (Springer Berlin Heidelberg, Berlin, Heidelberg, 1994), pp. 347–363
114. Y. Wang, A. Hu, J. Mater. Chem. C **2**, 6921–6939 (2014)
115. G.X. Wang, J.-H. Ahn, J. Yao, M. Lindsay, H.K. Liu, S.X. Dou, J. Power Sources **119–121**, 16–23 (2003)
116. K.K. Singh, B. Kachhi, A. Singh, D.K. Sharma, Int. J. New Chem. **9**, 348–360 (2022)
117. X.X. Wang, J.N. Wang, H. Chang, Y.F. Zhang, Adv. Funct. Mater. **17**, 3613–3618 (2007)
118. C. Kang, I. Lahiri, R. Baskaran, W.-G. Kim, Y.-K. Sun, W. Choi, J. Power Sources **219**, 364–370 (2012)
119. L.G. Bulusheva, A.V. Okotrub, A.G. Kurenya, H. Zhang, H. Zhang, X. Chen, H. Song, Carbon **49**, 4013–4023 (2011)
120. W.X. Chen, J.Y. Lee, Z. Liu, Carbon **41**, 959–966 (2003)

121. Y. Chen, X. Li, K. Park, J. Song, J. Hong, L. Zhou, Y.-W. Mai, H. Huang, J.B. Goodenough, J. Am. Chem. Soc. **135**, 16280–16283 (2013)
122. Y. Hu, W. Chen, T. Lei, B. Zhou, Y. Jiao, Y. Yan, X. Du, J. Huang, C. Wu, X. Wang, Y. Wang, B. Chen, J. Xu, C. Wang, J. Xiong, Adv. Energy Mater. **9**, 1802955 (2019)
123. A.A. Arie, J.K. Lee, Phys. Scr. **T139**, 014013 (2010)
124. S. Sahoo, A.K. Satpati, P.K. Sahoo, P.D. Naik, ACS Omega **3**, 17936–17946 (2018)
125. C. Park, E. Lee, S.H. Kim, J.G. Han, C. Hwang, S.H. Joo, K. Baek, S.J. Kang, S.K. Kwak, H.K. Song, N.S. Choi, J. Power Sources **521**, 230923 (2022)
126. D. Zhang, M. Miao, H. Niu, Z. Wei, ACS Nano **8**, 4571–4579 (2014)
127. K.H. An, W.S. Kim, Y.S. Park, Y.C. Choi, S.M. Lee, D.C. Chung, D.J. Bae, S.C. Lim, Y.H. Lee, Adv. Mater. **13**, 497–500 (2001)
128. M. Nawwar, R. Poon, R. Chen, R.P. Sahu, I.K. Puri, I. Zhitomirsky, Carbon Energy **1**, 124–133 (2019)
129. Z. Peng, Y. Hu, J. Wang, S. Liu, C. Li, Q. Jiang, J. Lu, X. Zeng, P. Peng, F.F. Li, Adv. Energy Mater. **9**, 1802928 (2019)
130. S. Maji, R.G. Shrestha, J. Lee, S.A. Han, J.P. Hill, J.H. Kim, K. Ariga, L.K. Shrestha, Bull. Chem. Soc. Jpn. **94**, 1502–1509 (2021)
131. S. Xiong, F. Yang, H. Jiang, J. Ma, X. Lu, Electrochim. Acta **85**, 235–242 (2012)
132. A. Ramadan, M. Anas, S. Ebrahim, M. Soliman, A.I. Abou-Aly, Int. J. Hydrog. Energy **45**, 16254–16265 (2020)
133. M.R. Benzigar et al., Microporous Mesoporous Mater. **285**, 21–31 (2019)
134. S. Zheng, H. Ju, X. Lu, Adv. Energy Mater. **5**, 1500871 (2015)
135. J. Chen, J.Z. Wang, A.I. Minett, Y. Liu, C. Lynam, H. Liu, G.G. Wallace, Energy Environ. Sci. **2**, 393–396 (2009)
136. D.-Y. Shin, K.-W. Sung, H.-J. Ahn, Chem. Eng. J. **413**, 127563 (2021)
137. Y. Jin, C. Hu, Q. Dai, Y. Xiao, Y. Lin, J.W. Connell, F. Chen, L. Dai, Adv. Funct. Mater. **28**, 1804630 (2018)
138. Z. Bagheri, Appl. Surf. Sci. **383**, 294–299 (2016)
139. Z. Li, F. Liu, S. Chen, F. Zhai, Y. Li, Y. Feng, W. Feng, Nano Energy **82**, 105698 (2021)
140. H. Lv, Y. Yuan, Q. Xu, H. Liu, Y.-G. Wang, Y. Xia, J. Power Sources **398**, 167–174 (2018)
141. G. Chen, S. Wu, L. Hui, Y. Zhao, J. Ye, Z. Tan, W. Zeng, Z. Tao, L. Yang, Y. Zhu, Sci. Rep. **6**, 19028 (2016)
142. W. Yang, P. Thordarson, J.J. Gooding, S.P. Ringer, F. Braet, Nanotechnology **18**, 412001 (2007)
143. J. Chen, S. Chen, X. Zhao, L.V. Kuznetsova, S.S. Wong, I. Ojima, J. Am. Chem. Soc. **130**, 16778–16785 (2008)
144. E. Heister, V. Neves, C. Lamprecht, S.R.P. Silva, H.M. Coley, J. McFadden, Carbon **50**, 622–632 (2012)
145. M.N. Al-Qattan, P.K. Deb, R.K. Tekade, Drug Discov. **23**, 235–250 (2018)
146. K. Sapna, M. Tarique, A. Asiamma, T. N. Ravi Kumar, V. Shashidhar, A. B. Arun, K. S. Prasad, J. Biosci. Bioeng. **130**, 424–430 (2020)
147. M. Hernández-Rivera, N.G. Zaibaq, L.J. Wilson, Biomaterials **101**, 229–240 (2016)
148. B.B. Karakoçak, A. Laradji, T. Primeau, M.Y. Berezin, S. Li, N. Ravi, A.C.S. Appl, Mater. Interfaces **13**, 277–286 (2021)
149. K.M. Tripathi, H.T. Ahn, M. Chung, X.A. Le, D. Saini, A. Bhati, S.K. Sonkar, M.I. Kim, T. Kim, A.C.S. Biomater, Sci. Eng. **6**, 5527–5537 (2020)
150. C. Zhao, X. Wang, L. Yu, L. Wu, X. Hao, Q. Liu, L. Lin, Z. Huang, Z. Ruan, S. Weng, A. Liu, X. Lin, Acta Biomater. **138**, 528–544 (2022)
151. H. Ding, X. Zhou, B. Qin, Z. Zhou, Y. Zhao, J. Lumin. **211**, 298–304 (2019)
152. L. Tan, T. Wu, Z.-W. Tang, J.-Y. Xiao, R.-X. Zhuo, B. Shi, C.-J. Liu, Nanotechnology **27**, 315104 (2016)
153. W. Liu, J. Wei, Y. Chen, New J. Chem. **38**, 6223–6229 (2014)
154. B. Panchapakesan, S. Lu, K. Sivakumar, K. Taker, G. Cesarone, E. Wickstrom, J. Nanobiotechnology **1**, 133–139 (2005)

155. C. Nie, Y. Yang, C. Cheng, L. Ma, J. Deng, L. Wang, C. Zhao, Acta Biomater. **51**, 479–494 (2017)
156. Y. Bai, I.S. Park, S.J. Lee, T.S. Bae, F. Watari, M. Uo, M.H. Lee, Carbon **49**, 3663–3671 (2011)
157. A.A. Bhirde, V. Patel, J. Gavard, G. Zhang, A.A. Sousa, A. Masedunskas, R.D. Leapman, R. Weigert, J.S. Gutkind, J.F. Rusling, ACS Nano **3**, 307–316 (2009)
158. X. Yan, Y. Zhao, J. Luo, W. Xiong, X. Liu, J. Cheng, Y. Wang, M. Zhang, H. Qu, J. Nanobiotechnol. **15**, 60 (2017)
159. S. Pandiyan, L. Arumugam, S.P. Srirengan, R. Pitchan, P. Sevugan, K. Kannan, G. Pitchan, T.A. Hegde, V. Gandhirajan, ACS Omega **5**, 30363–30372 (2020)
160. X.-W. Hua, Y.-W. Bao, F.-G. Wu, A.C.S. Appl, Mater. Interfaces **10**, 10664–10677 (2018)
161. S. Samimi, M.S. Ardestani, F.A. Dorkoosh, J. Drug Delivery Sci. Technol. **61**, 102287 (2021)
162. X. Hao, L. Huang, C. Zhao, S. Chen, W. Lin, Y. Lin, L. Zhang, A. Sun, C. Miao, X. Lin, M. Chen, S. Weng, Mater. Sci. Eng. C. **123**, 111971 (2021)
163. H.S. Zavareh, M. Pourmadadi, A. Moradi, F. Yazdian, M. Omidi, Int. J. Biol. Macromol. **165**, 1422–1430 (2020)
164. Z. Qu, L. Liu, T. Sun, J. Hou, Y. Sun, M. Yu, Y. Diao, S. Lu, W. Zhao, L. Wang, Nanotechnology **31**, 175102 (2020)
165. Z.M. Marković, M. Labudová, M. Danko, D. Matijašević, M. Mičušík, V. Nádaždy, M. Kováčová, A. Kleinová, Z. Špitalský, *V.* Pavlović, D.D. Milivojević, M. Medić, M.B. Todorović Marković, ACS Sustain. Chem. Eng. **8**, 16327–16338 (2020)
166. E. Yifeng, L. Bai, L. Fan, M. Han, X. Zhang, S. Yang, J. Mater. Chem. **21**, 819–823 (2011)
167. K. He, H. Ran, Z. Su, Z. Wang, M. Li, L. Hao, Int. J. Nanomed. **14**, 519 (2019)
168. Q. Tang, W. Xiao, J. Li, D. Chen, Y. Zhang, J. Shao, X. Dong, J. Mater. Chem. B **6**, 2778–2784 (2018)
169. J. Shi, X. Yu, L. Wang, Y. Liu, J. Gao, J. Zhang, R. Ma, R. Liu, Z. Zhang, Biomaterials **34**, 9666–9677 (2013)
170. P.K. Brahman, L. Suresh, V. Lokesh, S. Nizamuddin, Anal. Chim. Acta **917**, 107–116 (2016)
171. C. Hu, C. Yang, S. Hu, Electrochem. Commun. **9**, 128–134 (2007)
172. A. Wisitsoraat, P. Sritongkham, C. Karuwan, D. Phokharatkul, T. Maturos, A. Tuantranont, Biosens. Bioelectron. **26**, 1514–1520 (2010)
173. T. Gan, K. Li, K. Wu, Sens. Actuators B Chem. **132**, 134–139 (2008)
174. R.T. Kachoosangi, G.G. Wildgoose, R.G. Compton, Analyst **133**, 888–895 (2008)
175. R. Wu, S. Yu, S. Chen, Y. Dang, S.-H. Wen, J. Tang, Y. Zhou, J.-J. Zhu, Anal. Chim. Acta **1229**, 340365 (2022)
176. W. Guo, F. Pi, H. Zhang, J. Sun, Y. Zhang, X. Sun, Biosens. Bioelectron. **98**, 299–304 (2017)
177. B.B. Prasad, A. Kumar, R. Singh, Carbon **109**, 196–207 (2016)
178. J.A. Rather, P. Debnath, K. De Wael, Electroanalysis **25**, 2145–2150 (2013)
179. L. Taouri, M. Bourouina, S. Bourouina-Bacha, D. Hauchard, J. Food Compost. Anal. **100**, 103811 (2021)
180. Y. Zhu, S. Huai, J. Jiao, Q. Xu, H. Wu, H. Zhang, J. Electroanal. Chem. **878**, 114726 (2020)
181. H. Wu, S. Fan, X. Jin, H. Zhang, H. Chen, Z. Dai, X. Zou, J. Anal. Chem. **86**, 6285–6290 (2014)
182. M. Mazloum-Ardakani, A. Khoshroo, Electrochem. Commun. **42**, 9–12 (2014)
183. J. A. Rather, A. J. Al Harthi, E. A. Khudaish, A. Qurashi, A. Munam, P. Kannan, Anal. Methods **8**, 5690–5700 (2016)
184. R.N. Goyal, V.K. Gupta, N. Bachheti, R.A. Sharma, Electroanalysis **20**, 757–764 (2008)
185. L.-H. Lin, J.-S. Shih, J. Chin. Chem. Soc. **58**, 228–235 (2011)
186. L. Xiao, G.G. Wildgoose, R.G. Compton, Anal. Chim. Acta **620**, 44–49 (2008)
187. M. Zhang, A. Smith, W. Gorski, J. Anal. Chem. **76**, 5045–5050 (2004)
188. H. Nie, Z. Yao, X. Zhou, Z. Yang, S. Huang, Biosens. Bioelectron. **30**, 28–34 (2011)
189. I. Cesarino, F.C. Moraes, M.R.V. Lanza, S.A.S. Machado, Food Chem. **135**, 873–879 (2012)
190. G. Yang, F. Zhao, Biosens. Bioelectron. **64**, 416–422 (2015)
191. J. Bai, C. Sun, X. Jiang, Anal. Bioanal. Chem. **408**, 4705–4714 (2016)

192. W. Zheng, H. Wu, Y. Jiang, J. Xu, X. Li, W. Zhang, F. Qiu, Anal. Biochem. **555**, 42–49 (2018)
193. V.N. Palakollu, R. Karpoormath, L. Wang, J.-N. Tang, C. Liu, J. Nanomater. **10**, 1513 (2020)
194. L. Yu, X. Yue, R. Yang, S. Jing, L. Qu, Sens. Actuators B Chem. **224**, 241–247 (2016)
195. Y. Feng, Y. Li, S. Yu, Q. Yang, Y. Tong, B.-C. Ye, Analyst **146**, 5135–5142 (2021)

Chapter 3
Graphene-Based Materials: Synthesis and Applications

Pawan Kumar Dubey, Junsung Hong, Kevin Lee, and Prabhakar Singh

Abstract Graphene, a two-dimensional (2D) material, has fascinated the scientific world thanks to its remarkable electrical, mechanical, optical, biological, and thermal properties. Graphene-based materials have been used in a variety of new applications, including next-generation electronics, sensors, solar energy conversion, energy storage, batteries, field-emitting devices, and more. Commercialization of graphene-based materials and their novel application necessitate the development of synthesis methods capable of fabricating high-quality, large-scale graphene. Various methods for synthesizing graphene have emerged over a duration of few decades, and it will be noteworthy to compile a list of the most notable approaches and applications. This chapter mainly focuses on recent progress in the production of graphene and their applications, as well as attempts to summarize and document advancements in graphene research and future prospects.

Keywords Graphene · 2D materials · CVD · Solar cell

3.1 Introduction

Carbon is a distinctive and versatile element found in the periodic table, capable of forming a variety of nanoscale designs. Carbon exists as various allotropes, the most well known of which being graphite, diamond, and amorphous carbon since ancient times. In addition to the three-dimensional carbon allotropes (3D; diamond, and graphite), the one-dimensional (1D; CNTs) and zero-dimensional (0D; fullerenes) ones were known to the scientific at the end of the twentieth century. Fullerenes and carbon nanotubes were discovered by Kroto et al. in 1985 and Iijima in 1991, respectively, and have become significant in the science and technology fields

P. K. Dubey (✉) · J. Hong · K. Lee · P. Singh (✉)
Center for Clean Energy Engineering, Department of Materials Science and Engineering, University of Connecticut, 44 Weaver Road, Storrs, CT 06269-5233, USA
e-mail: dubey.pawan@yahoo.com

P. Singh
e-mail: singh.prabhakar@uconn.edu

D. K. Singh et al. (eds.), *Nanomaterials*,
https://doi.org/10.1007/978-981-19-7963-7_3

[1, 2]. Then, graphene, a two-dimensional carbon allotrope composed of sp^2 carbon atoms packed closely into a two-dimensional honeycomb lattice [3], was first unambiguously produced and identified experimentally by Geim and Novoselov [4] in the first decade of this century while it had been predicted theoretically by Wallace in 1947 [5]. It is supposed to be the future of electronics and materials science due to its remarkable electrical/thermal conductivity, mechanical flexibility, and optical transparency [6]. The Nobel Prize in Physics was awarded upon recognition of its significance in 2010. Graphene is considered "mother of all carbon forms" since it serves as the fundamental building unit of other graphitic carbon allotropes, such as "graphite," which is a stack of graphene sheets (separated by an interlayer distance of 3.37 Å) [7]. "Fullerenes" and "CNTs" also can be fabricated by wrapping and rolling graphene sheets [8]. A schematic diagram in Fig. 3.1 shows the graphene sheet as the building block for fullerene, CNTs, and graphite.

Graphene has revolutionized various research fields such as materials science, physics, chemistry, nanotechnology, and biotechnology, and currently used in a variety of novel applications thanks to its incomparable physical and chemical properties [9]. For instance, graphene has semi-metallic feature with zero bandgap, high specific surface area of ~2600 m^2g^{-1}, optical transparency, exceptional thermal conductivity (~2000–5000 Wm^{-1} K^{-1}), and very high Young's modulus (~1 TPa), as well as excellent electrical conductivity, making it an attractive material for applications in catalysis, energy conversion and storage [10], biochemical sensing, and drug delivery [11, 12]. 2D honeycomb framework morphological structure of Graphene is also favored for retaining the stable structures for battery anode materials in the

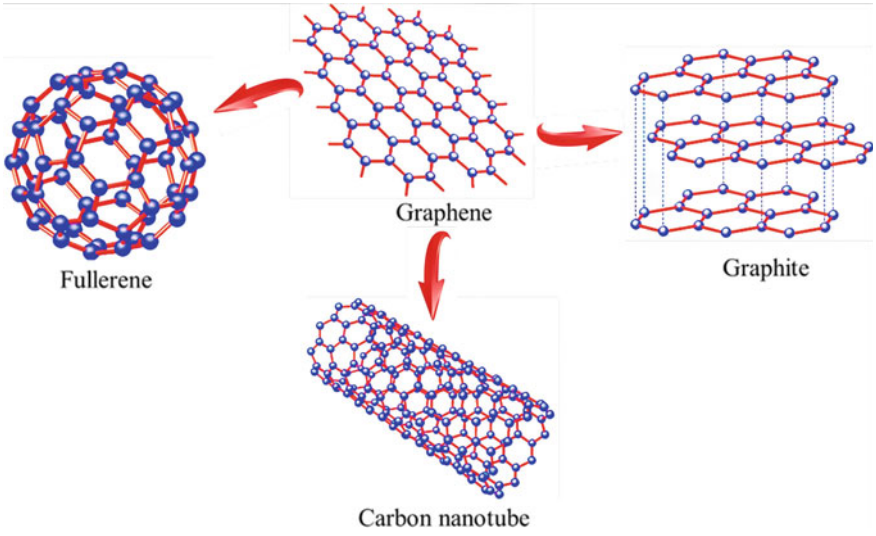

Fig. 3.1 Graphene as a two-dimensional building block for carbonaceous materials of all other dimensions

charging and discharging processes [13] and for promising additives to nanocomposite battery electrodes [14]. Graphene is frequently labeled as a "Wonder Material" due to its remarkable properties, but some of its characteristic properties were perceived only in certain conditions or very high-quality samples, e.g., graphene deposited on specific substrates like hexagonal boron nitride [15–17]. With graphene research increasingly leaning toward industrial applications, it is critical to achieve large-scale manufacturing of high-quality graphene to commercialize it.

Despite exceptional properties of Graphene, large-scale manufacture of high-quality graphene has been delayed owing to several obstacles [18, 19]. Graphene and its related 2D materials, such as graphene oxide (GO), reduced graphene oxide (RGO), functionalized graphene, and graphene nanocomposites, are synthesized from top-down or bottom-up approach. Physical and chemical methods can be used to tune and tailor graphene to meet specific requirements [20–22]. The appropriate method of preparation is selected to prepare the graphene with application-specific qualities such as purity, type, and extent of functionalization [23, 24]. Each preparation method has its advantages and disadvantages. For example, mechanical exfoliation of graphene, known as the "scotch tape" method, is allowed to produce high-quality single-layer graphene nanosheets; however, the approach is somewhat time-consuming and has scalability issues [25]. On the other hand, graphene grown by chemical vapor deposition (CVD) requires transfer onto desirable substrates for applications and thus direct growth of homogeneous graphene sheets on appropriate substrates (i.e., Si, SiO_2, Al_2O_3, and GaN). Attempts have been made to guide the formation of uniform and high-quality graphene on the dielectric substrates [18, 26–30]. However, the technique needs extensive research to produce continuous and highly conductive graphene films.

Graphene has demonstrated its capacity to revolutionize a wide range of industries, from electronics to body armor and paper. Even future space elevators may utilize graphene as a basic material. Graphene's unique two-dimensional structure makes it a promising candidate for sensing applications. Because of the large surface area, its sensitivity to the surrounding gases can be maximized. Specifically, a change in resistance during gas adsorption and desorption can be used to detect certain gas phases. The outstanding electrical and optical properties of graphene make it an excellent choice for the use of transparent and conductive electrodes particularly in touch screens, liquid crystal displays, organic photovoltaic cells, and organic light-emitting diodes. In fact, graphene is seen to be a perfect option for nanoelectronics with the potential to replace Si-based microelectronics. Moreover, since its discovery in 2004, graphene has shown enormous potential in various applications such as light processing, sensors, plasmonics, energy production, and storage [31]. This chapter will discuss how graphene and related 2D nanomaterials are made and how they are used in energy conversion, storage, sensors, field emission, and biomedical applications.

3.2 Synthesis of Graphene

Graphene has received the most focused research spotlight for its excellent properties and rapidly developed production technology. Its high potential has endorsed the rapid progress of graphene fabrication technology. Graphene synthesis methods are divided into two categories: top-down and bottom-up approaches. A schematic explaining the top-down and bottom-up technique for graphene synthesis is depicted in Fig. 3.2. The top-down approach mainly focuses on the decomposition of graphene precursor (graphite) from the stack into atomic layers, which includes mechanical exfoliation [32], ball milling [33], sonication [34], and electrochemical exfoliation [35], The bottom-up approach uses carbon molecules as building blocks [36], which contains chemical vapor deposition [37], epitaxial growth on silicon carbide (SiC) [38], growth from metal–carbon melts [39], and deposition [40]. Examples of a few important top-down and bottom-up approaches to graphene synthesis are described in the following section.

3.2.1 Mechanical Exfoliation

Sustainable and wide application of graphene poses the prerequisites for mass production and commercial availability. Graphene is a novel material discovered in 2004. Geim and Novoselov was succeeded to separate graphene, for the first time, from highly oriented pyrolytic graphite (HOPG) with transparent sticky scotch tape until they found a one-atomic layer thick graphitic sheet [41]. Exfoliating graphite to obtain graphene is one of the simplest methods for achieving graphene sheets at a low cost. They demonstrated the existence of the two-dimensional crystal structure at ambient temperature. The mechanical stripping process is simple to apply and produces very high-quality samples; it is now the most common method for making high-quality single-layer graphene. However, its controllability is limited, so that the graphene produced by this process is quantitatively small and qualitatively unreliable. Furthermore, the method is time-consuming and suffers from low productivity and high cost, making it unsuitable for large-scale production (Fig. 3.3).

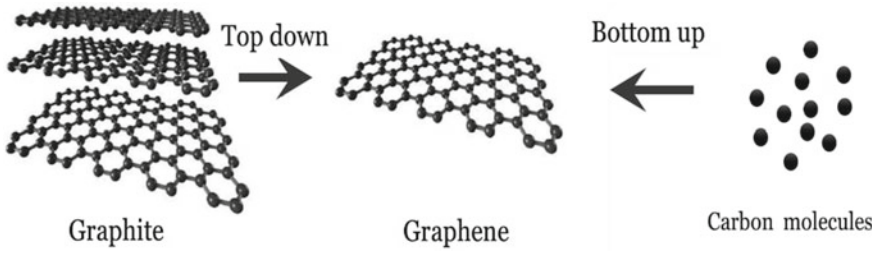

Fig. 3.2 Schematics of top-down and bottom-up approaches for graphene fabrication

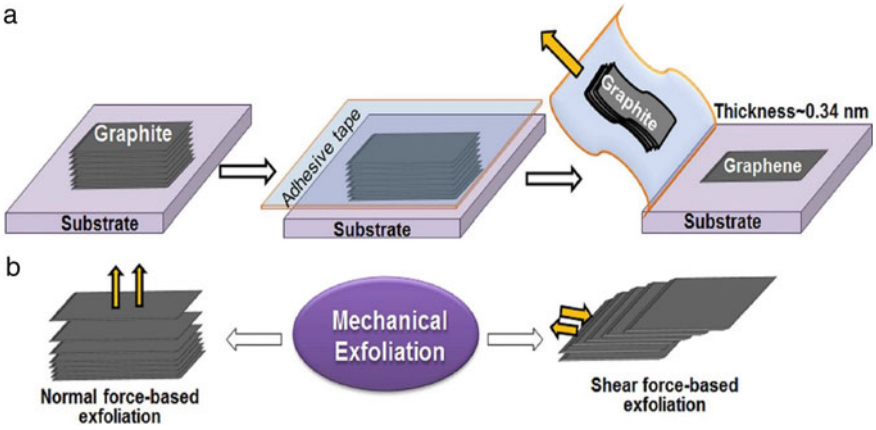

Fig. 3.3 **a** Schematic illustration of the exfoliation of graphene from bulk graphite using scotch tape [42]. **b** Normal-force- and shear-force-based mechanical exfoliation for graphene preparation. Adapted with permission from [43] Copyright (2020) (Elsevier)

3.2.2 Graphite Intercalation

Graphene can be obtained by the intercalation of graphite. Graphite intercalation may be achieved in two ways: one is by inserting tiny molecules into graphite layers while the other is by affixing molecules or polymers onto the sheets via noncovalent bonds, which is supposed to form graphite intercalation compounds (GICs). For instance, An et al. used sulfuric acid and hydrogen peroxide as intercalant and oxidant, respectively, for GIC formation [42]. Both expanded graphite and graphene nanoplatelets (GNPs) were successfully produced by conversion of spheroidized natural graphite (SNG). Bae et al. investigated the influence of polymer intercalation on sound absorption and found that the sound transmission loss was reduced [45]. The graphite layers in GICs remain unchanged with guest molecules positioned in the interlayer galleries [45]. GICs showed different properties depending on intercalants, which considerably benefit applications concentrating on electrical [46, 47], thermal [48], chemical [49, 50], and magnetic [51] performance. Horie et al. [51] investigated the conversion and selectivity of cinnamaldehyde (CAL) between graphite layers using platinum nanosheet intercalants, demonstrating the unique role of intercalants. Figure 3.4 shows the schematics of graphene synthesis through intercalation of graphite [52].

3.2.3 Chemical Synthesis

The chemical conversion of graphite to graphene oxide (GO), followed by chemical reduction, has shown to be an effective method for producing large scale of

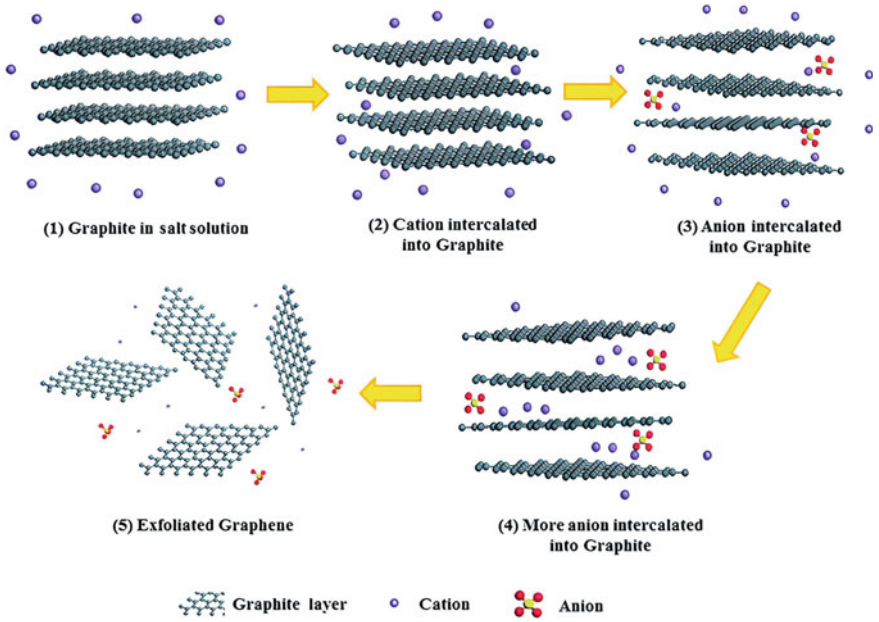

Fig. 3.4 Schematics of graphene exfoliation via graphite intercalation. Adapted with permission from Ref. [52]. Copyright (2017) (Royal Society of Chemistry)

graphene nanosheets [53]. For the large-scale production of graphene, this top-down route is more viable than the bottom-up approach. Reducing GO has preferably been used for graphene because graphite and expandable graphite produce a less degree of exfoliation [21]. This choice is simple, affordable, and scalable for large-scale graphene synthesis. For example, exfoliation of graphite oxide can be easily obtained by sonication. Another advantage of this approach is that it may create functionalized graphene and GO, which have vast application potential. GO can be produced utilizing several ways [53–57]. Hummers' method is one of the most widely used method for graphene synthesis, and it has been further modified by many other researchers [58, 59]. A typical synthesis method involves the oxidation of graphite into graphite oxide by strong oxidizers such as strong sulfuric acid, nitric acid, and potassium permanganate [60]. During the oxidation process, oxygen functional groups are intercalated in between the graphitic layers, which increases the layer separation. With the increase in layer spacing, it becomes easier to separate the layers to generate graphene oxide sheets during ultrasonic treatment. This procedure yields single or several layers of GO, which are further reduced to graphene using strong reductants such as hydrazine hydrate or aqueous sodium borohydride ($NaBH_4$). However, this method has several drawbacks. For instance, the conductivity and specific surface area of graphene decrease by graphene aggregations because of its low thickness, limiting its application for optoelectronic equipment. Furthermore, structural defects such as the loss of carbon atoms can occur during this process,

reducing the quality of products. Peng et al. used strong oxidant K_2FeO_4, to obtain graphene oxide powder (GO), a precursor material for graphene synthesis, avoiding the polluting heavy metals and toxic gases in preparation [61] (Fig. 3.5).

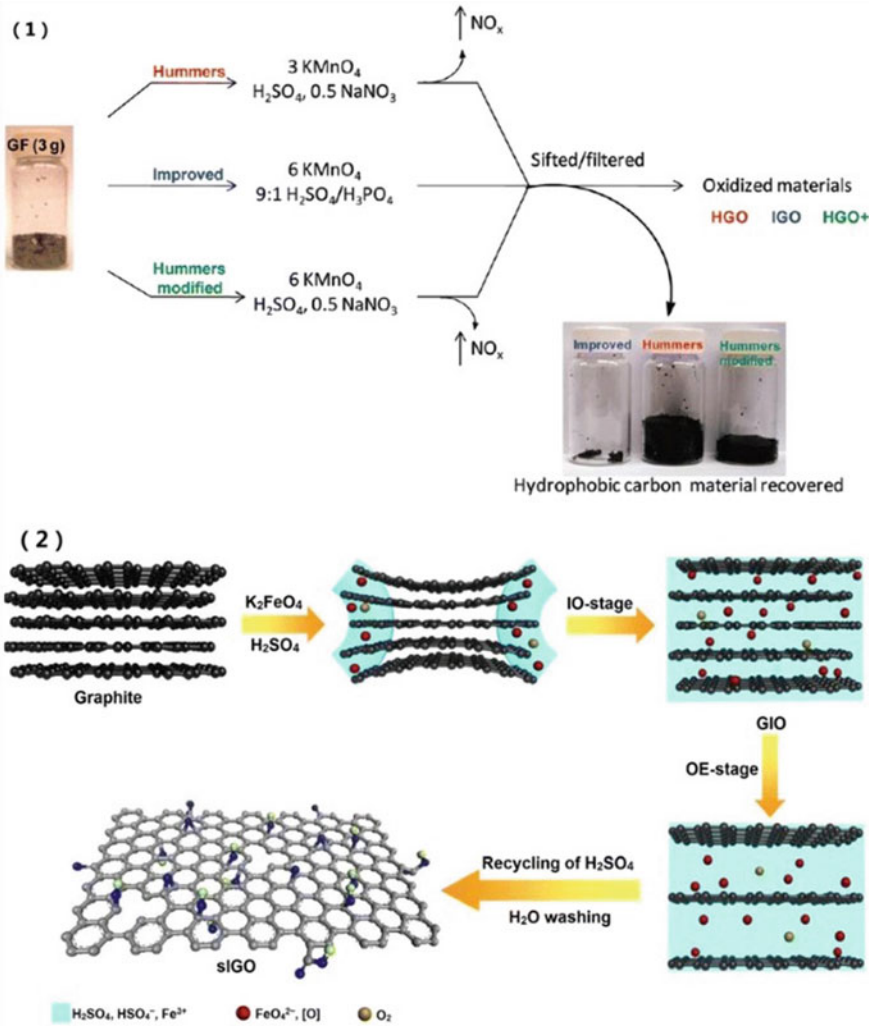

Fig. 3.5 **a** Oxidation procedures of graphite flakes (GF) by Hummers method, improved Hummers method, and modified Hummers method. **b** Synthesis of single-layer graphene oxide (GO) by K_2FeO_4. Adapted with permission from Ref. [62] (Copyright 2015) (Springer Nature)

3.2.4 Chemical Vapor Deposition

Chemical vapor deposition (CVD) can be employed for graphene synthesis where a chemical reaction takes place between substrates and carbon-containing organic gas chosen as a source material [63]. In this CVD process, thermally disintegrated precursors are diffused onto the substrate at high temperatures and deposit graphene layers. For high-quality graphene deposition by CVD process, various transition-metal substrates such as Copper [64], Nickel [65], Palladium [66], Ruthenium [67], and Iridium [68] have been used. The CVD approach is ideal for industrially manufacturing graphene films [69] because of its capability to produce high-quality, large-area graphenes. CVD methods can be classified into two major categories [65]: thermal CVD and plasma CVD. Unlike thermal CVD used at high temperatures, plasma-enhanced chemical vapor deposition (PECVD) provides another approach for graphene synthesis at lower temperatures [36]. Rybin et al. [70] have controlled the details of the CVD process utilized in real-time experiments for graphene sheet fabrication on nickel foils. They showed graphene films of various thicknesses (from 3 to 53 layers and more) in their report. The typical CVD process consists of the following steps [66]: (a) flowing hydrocarbon gases such as methane and ethanol onto the surface of metal substrates at high temperatures and (b) cooling the substrate once the continuous reaction is done. During the cooling process, mono or several layers of graphene are formed on the surface of the substrate. This procedure is divided into two stages: dissolution and diffusion of carbon atoms on the substrate. Dong's group [71] studied grain boundaries (GBs) of graphene film and found several key parameters that control the grain boundaries, providing us with a deep insight into CVD graphene growth. It can be utilized to build capacitors with high-quality graphene as electrodes on an ultrathin Ti catalytic layer [72]. The benefits of this method for graphene synthesis include the capability for large-area, high-quality graphene formation and low energy consumption (e.g., low-temperature operation). The graphene can be readily separated from the substrate using a chemical corrosion metal method, which is advantageous and favorable for continuous graphene processing. However, the cost is significant and the process conditions should be fully controlled. The large-area graphene sheets cannot be employed independently because of their thinness. Thus, it must be coupled to macro-devices for utilization, such as touch screens, heating devices, and so on (Fig. 3.6).

3.2.5 Epitaxial Growth on Silicon Carbide (SiC)

Epitaxial thermal growth particularly on a single-crystalline silicon carbide (SiC) substrate is one of the most promising methods of graphene synthesis. The term "*epitaxy*" comes from Greek, where the prefix *epi-* means "over" or "upon" and *taxis* means "order" or "arrangement." Epitaxial growth occurs when a single-crystalline film is deposited on a single-crystalline substrate, resulting in epitaxial film. It is

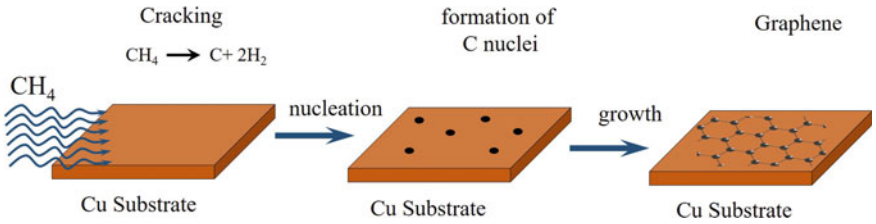

Fig. 3.6 A single layer of graphene is deposited onto a copper substrate and can then be etched to obtain the single-layer graphene

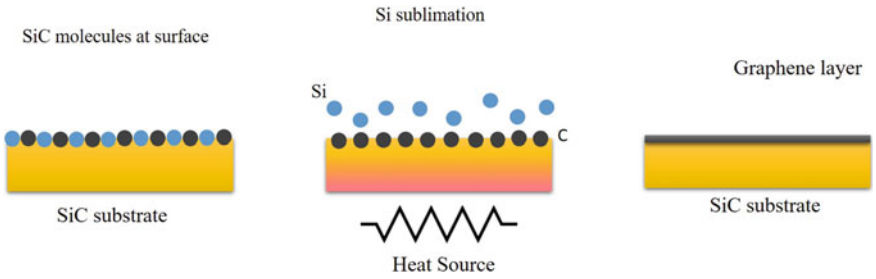

Fig. 3.7 Illustration of the epitaxial graphene growth on SiC substrate. After the sublimation of silicon, carbon remains on the surface and becomes graphene

capable of producing high-crystalline graphene on single-crystalline SiC substrates. In this approach, silicon atoms are released from the SiC surface during heat treatment of the SiC single crystals. The leftover carbon atoms are self-assembled and rebuilt, resulting in graphene layer on SiC substrates. The epitaxial growth method on SiC substrates yields thin graphene sheets larger than 50 μm, which is ideal for usage in transistors and circuits. However, because the size of graphene flakes is still determined by the size of SiC wafers, it is very important to prepare substrates in the desired dimension. Also, stringent equipment requirements are needed for high-quality graphene production (Fig. 3.7).

3.2.6 Growth from Metal–Carbon Melts

Graphene can be grown on the furnace of metal–carbon melts. The procedure includes dissolving carbon in a molten metal at certain temperatures, enabling the dissolved carbon to nucleate and develop on top of the melt at lower temperatures. Also, metal-catalyzed epitaxial growth can occur at specific conditions by passing hydrocarbon over catalytically active transition-metal substrates such as Pt, Ir, Ru, and Cu under ultra-high vacuum. The adsorbed gas is subsequently dehydrogenated under heat, resulting in graphene. The metal-catalyzed epitaxial growth requires ultra-high

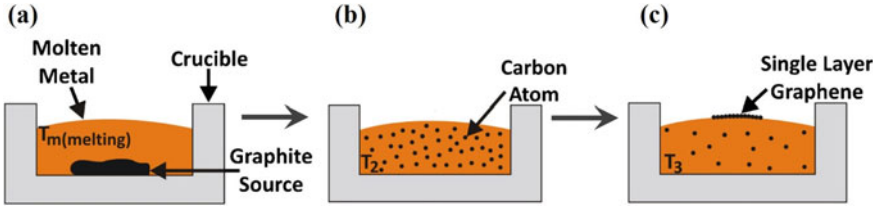

Fig. 3.8 Schematic of graphene growth from molten nickel **a** melting nickel in contact with graphite as carbon source, **b** carbon dissolution inside the melt at high temperatures, **c** temperature reduction for graphene formation, and **d** temperature–time diagram of the process. Adapted with permission from Ref. [73]. Copyright (2010) (AIP Publishing)

vacuum condition, compared with the epitaxial growth on SiC. The gas covers the entire metal substrate during the adsorption process. The growth is a self-limiting process, indicating that the substrate does not absorb another layer of hydrocarbon once adsorbing the first layer of gas. As a result, the graphene prepared by this method is primarily monolayer. Furthermore, the uniform graphene layer can be produced on a vast scale (Fig. 3.8).

3.2.7 Other Methods

Apart from the aforementioned synthesis methods, there are several other methods which are capable of graphene synthesis. Some of these include the ion-implantation, high-temperature growth under high pressure, blast method, and organic compound synthesis method. However, it may be pointed out that despite the availability of several methods of graphene synthesis, production of high-quality graphene at industrial level still appears far-fetched. Current synthesis techniques still suffer to meet the key requirements of industrial manufacturing of graphene which include the synthesis technique capable of producing economically cheaper, large-scale, and reproducible high-quality graphene with large surface area. These key technical issues are still not resolved till date and remain a roadblock in pathway to commercialization of graphene. Numerous important and unique properties of graphene have been observed with the high quality and high purity of graphene specimens. However, for the graphene with multilayers and internal defects, these superior properties get diminished. The industrialization of graphene would be realized only after a suitable production process is revealed (Table 3.1).

Table 3.1 Advantages and disadvantages of major graphene synthesis techniques. Adapted from Ref. [74]

Synthesis procedure	Advantages	Limitations	References
Micromechanical exfoliation	• Easy procedure • Excellent quality • Suitable for fundamental research	• Poor reproducibility • Not amenable to large-scale production	[18]
CVD	• Large surface area (up to ~1 cm^2) • Low defects • Large-scale production • High quality	• Costly process • Poor scalability	[64]
Epitaxial growth	• High quality • Less defects	• Very expensive • High-temperature process	[18]
Unzipping of CNTs	• Scalable • Controlled growth • Control on functionalization and edge quality	• Low yield • Costly	[75]
Reduction of GO	• Low cost • Easy procedure	• Higher defects	[76]

3.3 Characterization of Graphene-Related Materials

Several investigative and analysis technologies have emerged in the last few decades to characterize the structural and microstructural study, surface morphology, defect structure, and properties of graphene. In this section, the most common and frequently used characterization techniques such as X-ray diffraction (XRD), scanning electron microscopy (SEM), transmission electron microscopy (TEM), ultraviolet–visible spectroscopy (UV–Visible), and Raman spectroscopy will be described in brief.

3.3.1 X-Ray Diffraction (XRD)

X-ray diffraction is one of the basic fingerprint characterization techniques that provide information related to the phase, crystal structure, and crystallinity of the material. The intense and narrow peaks in the XRD pattern represent a high degree of crystallinity; in other words, stacking of a large number of graphitic layers. In the contrast, broad and low-intensity peaks characterized by stacking of a few layers. A representative XRD pattern of graphite, graphene, and graphite oxide is depicted in Fig. 3.9. A typical X-ray diffraction pattern of graphite shows sharp and intense diffraction peak at $2\theta = 26.35°$ corresponding to interplanar spacing $d = 3.34$ Å. Graphite oxide peak found to be shifted left at $2\theta = 13.9°$ due to the intercalation of

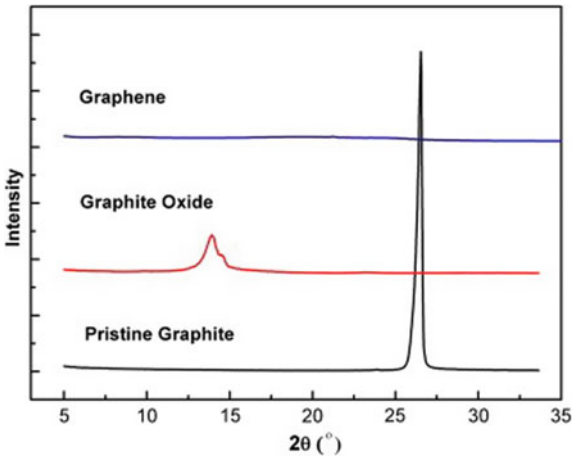

Fig. 3.9 XRD pattern of graphite, graphite oxide, and graphene specimen. Adapted with permission from Ref. [78]. Copyright (2010) (Elsevier)

oxygen functional groups in between graphitic layers after oxidation [77]. Graphene does not show any diffraction peak due to lack of stacking or layers (as shown in Fig. 3.9) [78].

3.3.2 Scanning Electron Microscopy (SEM)

Morphological characterization of graphene and its derivatives such as form, structure, folds, impurities, and defects are analyzed by SEM. Graphene synthesized through different processes requires the effective identification of number of layers, structure, and morphology for the evaluation of quality of graphene. However, imaging of few layer and single-layer graphene sheets is limited by the low resolution of SEM. Graphene with different number of layers is grown on porous alumina substrate by Seekaew et al. [79] and shown in Fig. 3.10. The SEM micrographs (a and b) show the images of monolayer and bilayer graphene which appears transparent as porous alumina substrate can be seen in the background. Three-layer graphene and multi-layer graphene are shown in SEM image (c and d). The porous alumina is not visible in case of graphene with three or higher numbers of layers as evident by SEM images shown in Fig. 3.10.

3.3.3 Transmission Electron Microscope (TEM)

Transmission Electron Microscope (TEM) is one of the most versatile methods utilized for the investigation of materials at atomic level. TEM equipped with Scanning Transmission Electron Microscope (STEM) is frequently utilized for studying

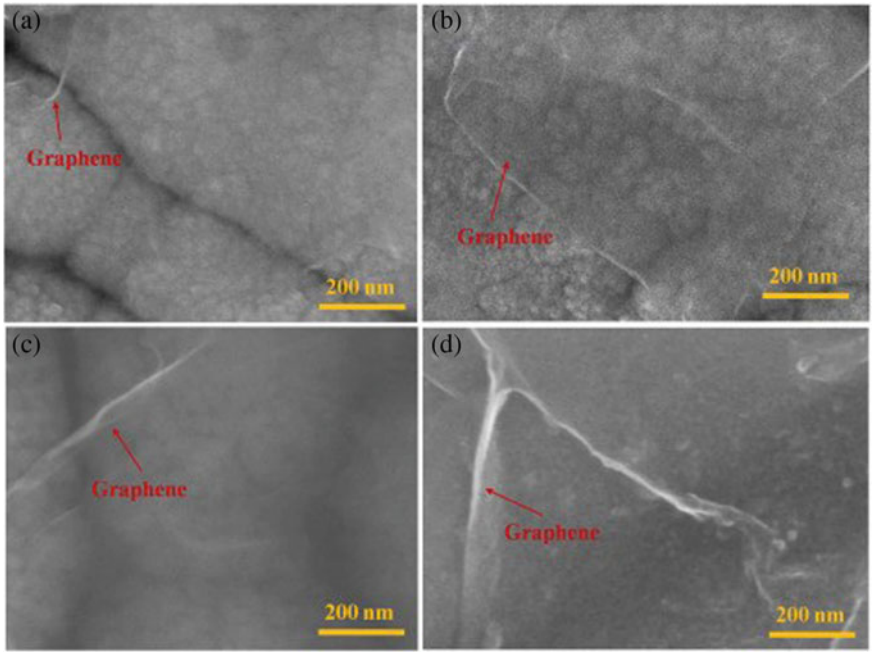

Fig. 3.10 SEM image of the SEM images of **a** monolayer, **b** bilayer, **c** three-layer, and **d** multi-layer graphene films on porous alumina substrate. Adapted with permission from Ref. [79]. Copyright (2017) (Elsevier)

the quality of graphene, number of layers, defects, and atomic arrangement. Electron beam transmitted through a very thin material specimen and used to produce images. Figure 3.11 shows the TEM images of graphene. Figure 3.11a–c shows the atomic-resolved images of graphene whereas a typical TEM image of multi-layer graphene is shown in Fig. 3.11d. High-resolution TEM images produce the dark fringes when graphene layers are aligned parallel to the incident electron beam. These fringes are used in the estimation of number of layers in the graphene sample.

3.3.4 Ultraviolet Visible Spectroscopy (UV–Vis)

UV–visible spectroscopy is often applied to investigate the layers and type of graphene such as graphene, graphene oxide, and few layers graphene. The absorbance spectra resulted from irradiating the specimen by UV–visible possesses the information about the electronic transition due to π–π^* transition. Virgin graphene displays an absorption peak around 260 nm, whereas single-layer graphene containing oxygen functional groups exhibit peak about 230 nm [77, 82]. The transmittance mode of measurement is utilized for the estimation of number of layers in the graphene

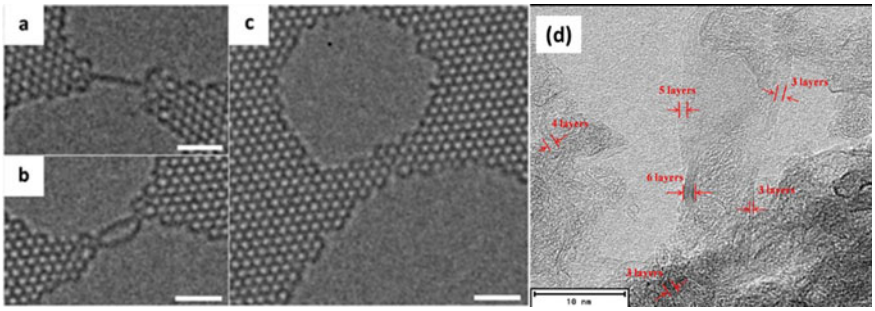

Fig. 3.11 Smoothed AC-TEM images of **a** a carbon chain (graphene), **b** adjacent carbon chains, and **c** large field view of atomic-scale-resolved graphene. Scale bars are 1 nm. Adapted with permission from Ref. [80]. Copyright (2013) (Royal Society of Chemistry). **d** TEM image multi-layer graphene. Fringes represent the number of layers. Adapted with permission from Ref. [81]. Copyright (2014) (Elsevier)

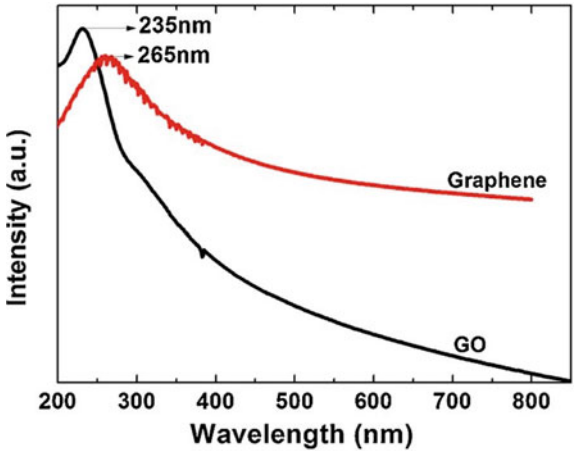

Fig. 3.12 The UV–visible absorption spectra of the graphene oxide as well as the synthesized graphene samples. Adapted with permission from [83]. Copyright (2014) (Elsevier)

specimen. The single layer of graphene shows approximately 97% of transmittance at 550 nm. The transmittance decreases with increase in number of layers in the graphene specimen. Figure 3.12 shows the typical UV–visible spectrum of graphene oxide and graphene.

3.3.5 Atomic Force Microscopy (AFM)

Atomic force microscopy (AFM) is also one of the most utilized techniques in characterization of graphene surface, structure, and number of layer. A cantilever tip is used to scan the whole surface or along a line to generate an AFM image. AFM

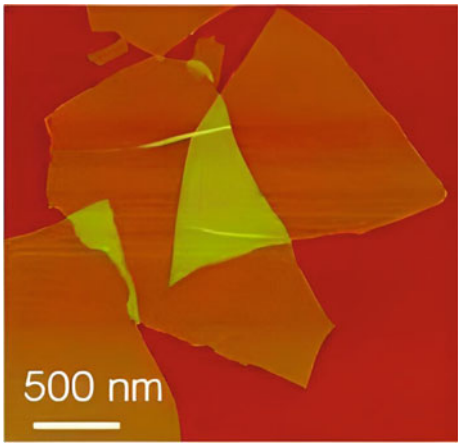

Fig. 3.13 AFM image of graphene showing the layer thickness. Adapted with permission from Ref. [84]. Copyright (2010) (Royal Society of Chemistry)

typically uses the force of interaction between the sharp nanotip at the end of the cantilever and specimen surface. A laser system is used to measure the amount of bending by the tip during the scanning and processed by computer program and generate the image of sample topography. A representative AFM image of graphene is depicted in Fig. 3.13.

3.3.6 Raman Spectroscopy

Raman spectroscopy is the most important and useful technique for the characterization of quality of graphene, nature of defects, and numbers of layers. Monochromatic laser is used to record the scattering pattern from the graphene specimen. Despite the fact that only few layers or single layer of atoms are probed, significantly strong signals are detected due to the resonance of light with the phonon mode (lattice vibration) [85, 86]. A typical Raman spectrum of graphene represents the three peaks mainly known as D, G, and 2D mode. The D mode peak appears at approximately 1350 cm^{-1} and represents the disorder or defect in sp^2 carbon atom. The E2g mode at the Γ-point gives rise to G band peak about 1583 cm^{-1} due to stretching vibration of C–C bond [87, 88]. The second-order Raman scattering which involves the two-phonon process near the Dirac point gives rise to emergence of 2D band peak. The ratio of the intensities of D band and G band (I_D/I_G) represents the elastic scattering graphene and assists in assessment of disorder in graphene [89, 90]. Figure 3.14 shows Raman spectra of monolayer graphene and graphite.

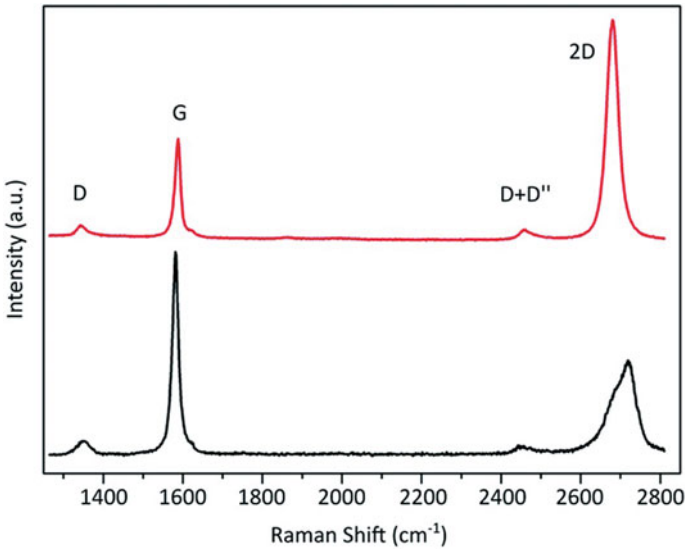

Fig. 3.14 Raman spectra from single-layer graphene and graphite sample. Adapted with permission from Ref. [91]. Copyright (2019) (Royal Society of Chemistry)

3.4 Applications of Graphene Materials

Graphene is considered to be a wonder material due to its properties like high electrical conductivity, large carrier mobility, 2D atomic layer structure, large surface area, optical transmittance, high mechanical, chemical stability, etc. These properties make graphene the most potential candidate for ultrafast and low-cost device fabrication such as sensing gases and biomolecules, making LCD displays, solar cells, energy storage, ultrafast electronics, Li–ion batteries, making composite systems, etc. (Fig. 3.15).

3.4.1 Field-Effect Transistors (FET)

Graphene is intensively employed in the manufacture of field-effect transistors (FETs) because 2D graphene has various advantages over bulk semiconductors such as silicon [93, 94]. Interestingly, graphene is a zero-gap semiconductor, which limits the direct use of graphene in FET applications. Novosolov et al. discovered the electric field effect in graphene for the first time in 2004 [95]. In that report, the electric field effect was demonstrated by single-atom thick film with electrons and holes in concentrations up to 10^{13} cm^{-2}, and room-temperature mobilities of ~10,000 cm^2 v−s can be induced by applying gate voltage. Theoretical calculation predicted that graphene nanoribbons (GNRs), 1D form of graphene, possess useful energy gap,

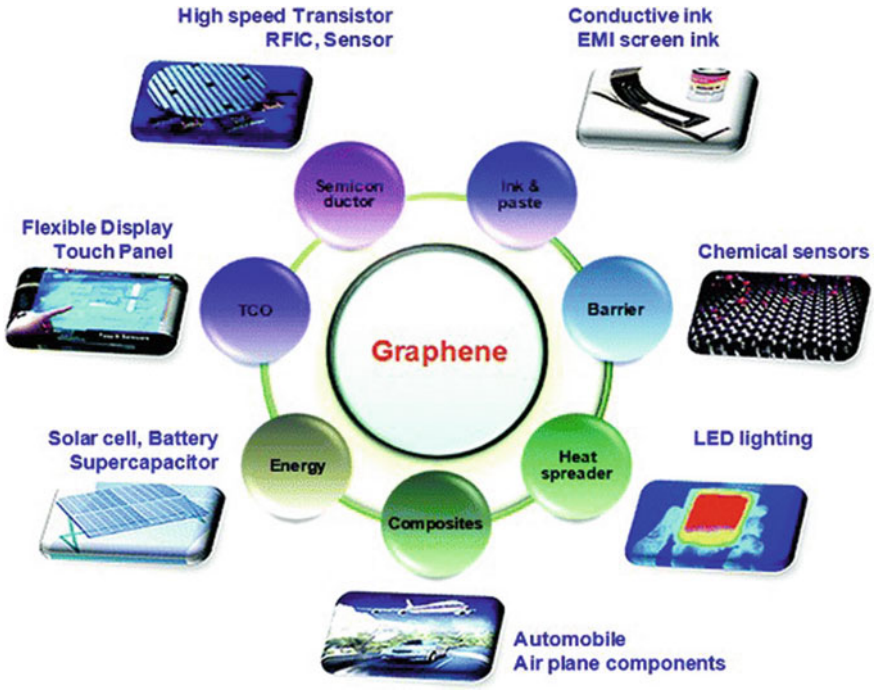

Fig. 3.15 Overview of applications of graphene in different sectors. Adapted with permission from Ref. [92] Copyright (2015) (Royal Society of Chemistry)

excellent toggling speed (changing the logic state), and higher charge carrier mobility which is suitable for room-temperature field-effect applications. Owing to the 1D nature of GNR, electrons get confined to 1D due to splitting of graphene energy dispersion levels in one dimension. Although bandgaps have been demonstrated in GNRs, they were found to be substantially different from graphene in terms of charge carrier transport and challenges of assembling the device.

The bandgap has also been produced by applying electric fields to bilayer graphene structures. These gaps, however, have been seen to be smaller than 400 meV, resulting in considerable tunneling across bands. Several researchers have demonstrated several ways for fabricating GNRs for FET application, including chemical and lithographic approaches. The use of lithographic patterning successfully fabricated GNRs with widths ranging from 20 to 30 nm while chemical routes produced GNRs with widths ranging from 10 to 15 nm. Chen et al. studied FET properties of GNRs as a function of their widths and found that the resistivity of GNRs increased as the width decreased owing to the edge states. Furthermore, at low frequency, the electrical current noise of GNR devices was dominated by 1/f noise. Since the initial demonstration of graphene-based FETs, various theoretical studies have been reported that predict the performance of GNR FETs as functions of their chirality, chemical doping, edge roughness, carrier scattering, and contacts.

Furthermore, numerous models for predicting the performance of GNR FETs have also been devised [96]. The theoretical investigations gave a better understanding of the performance and characteristics of GNR-based FETs; moreover, they can be useful tools for designing efficient FETs. Despite the demonstration of the potential of graphene FETs, it may take long to fabricate commercially viable logic devices from graphene because of its reliability and reproducibility.

3.4.2 Sensors

Graphene has surface adsorption property, large specific surface area, and low Johnson noise, which enables it as one of the most potential and promising materials for the fabrication of gas and bio-sensors [97]. The sensing property of gases and biomolecules is owing to the electrical conductivity of graphene that varies upon surface adsorption of different molecules, such as gases and biomolecule. The change in electrical conductivity of graphene is related to charge transfer between graphene and adsorbed molecules acting as donor or acceptor. Furthermore, sensitivity of graphene-based sensors can be enhanced to single-atom- or molecule-level detection. For instance, Schedin et al. in 2007 reported graphene-based sensors that have superior sensitivities to NO_2, NH_3, H_2O, and CO gases [98].

In a very short period of time, graphene has achieved considerable success in biological and chemical sensing [99–105]. The availability of a diverse range of graphene materials, as well as their exceptional sensing properties, enables the widespread use of graphene-based sensors for the detection of various chemicals and ions including gaseous molecules, biological molecules, and bacterial and animal cells (e.g., sugars, proteins, DNAs). These graphene-based sensors outperformed previous sensors in many aspects, such as sensitivity, selectivity, detection range, temporal resolution, response time, and cost. These improvements are significant advances toward the commercialization of graphene-based sensors although there remain hurdles such as mass-scale production and handling of graphene properties. While the overall capability of graphene-based sensors has not been explored, some novel graphene nanomaterials and structures are still being developed, such as graphene (a hydrogenated twin material of graphene) and CVD-grown three-dimensional graphene foam. Hybridizing and compositing graphene materials with diverse organic and inorganic systems (e.g., polymers, carbon nanotubes, and nanoparticles) are also expanding the capability of graphene sensor. A graphene sensor with multiple sensing modalities (e.g., electronic and optical) should be attainable by combing its various capabilities and merits. Furthermore, it will not be long until a graphene sensor capable of detecting a single biomolecule is developed. Currently, the development and application of graphene sensors are largely hindered by the lack of methods suitable for controllable, reproducible, scalable, and facile production of graphene materials with defined structures and properties. Furthermore, a deeper knowledge of graphene characteristics, interactions with molecules/cells, and sensing (or signal transduction) mechanisms is necessary.

Collaborations between diverse disciplines and technologies are required to progress forward. Given their rapid technical development, we anticipate that upcoming graphene sensors will have a significant influence on environmental and safety monitoring, diagnostics, biological investigations, and drug screening in the near future.

3.4.3 Transparent Conductive Films

Indium-doped tin oxide (ITO) is extensively used in the production of transparent conductive oxide coatings to be utilized in liquid crystal displays (LCD), touch sensitive screens, solar cells, and electromagnetic interference (EMI) shielding. However, high cost, sparse availability, and fragile nature of Indium limit its utilization in flexible substrate. These shortcomings of Indium thus encourage the quest for enormously high transparent and highly conductive thin-film alternatives. Graphene is considered as one of the most suitable and potential candidates for future optoelectronic devices, such as transparent electrodes for solar cells and liquid crystal displays, thanks to its high electrical charge conductivity, mechanical stability, monoatomic layer thickness, and high optical transparency in the visible range of the spectrum [106–108]. The impermeable, chemically inert, and stable thin layers of graphene act like transparent extreme thin film and better than any metal due to remarkable heat and electrical conductivity. Therefore, graphene can be envisaged as the future of next-generation transparent conducting electrode materials for miscellaneous applications, such as solar cells, light-emitting diodes (LED), organic light-emitting diodes (OLED) touch screens, and photovoltaic cells [109]. Monolayer graphene is extremely both conductive and transparent (absorbing just 2.3% of white light). Owing to the properties, such as high hole mobility, high surface area, and chemical inertness to oxygen and water, graphene remains one of the most viable choices for solar applications.

3.4.4 Battery

Li–ion batteries have become a key component of hand-held gadgets, portable electronic devices, electric vehicles (EV), and many other different and diversified power devices due to its high output voltage, high energy and power density, and renewable and clean nature. Many promising and potential electrode materials (e.g., metal electrodes, graphite-based electrodes, transition-metal oxide, phosphide electrodes, etc.) in Li–ion batteries are constrained by slow Li–ion diffusion and low electron transport in electrodes. These electrodes also suffer with the increase in resistance with time at the electrode and electrolyte interface at high charge–discharge rates. For this reason, there has been a lot of interest in designing and developing novel electrode materials for Li–ion batteries with improved lithium storage ability, coulombic

charge efficiency, and long charge–discharge cyclability life. Graphene-based anodes have been proposed as one of the promising alternative electrodes for Li–ion batteries because of excellent electrical conductivity, high specific surface area, and chemical tolerance [94–98]. Though there are few studies on the application of graphene as an electrode material in batteries, forthcoming research should focus on developing the knowledge and understanding of operational principle of the electrochemical process in graphene-based electrodes in Li–ion batteries. It is also important to recognize the application of a range of graphene-based electrodes in Li–ion batteries.

3.4.5 Solar Cell

In recent years, there has been growing consensus among most countries around the world to supplement and replace fossil fuels with clean and sustainable energy resources to fulfil their growing energy demands. Solar energy harvesting and its conversion in useful energy form such as electricity or chemical fuel through solar-power-assisted electrolysis by solar cells represents most potential and promising future prospects. Dye-sensitized solar cells (DSSC) have gained substantial attention among various solar energy conversion technologies because of their comparatively high solar to electricity conversion efficiencies. Graphene has a high potential for use in DSSC owing to its exceptional properties [115–118]. Particularly, graphene thin-film electrodes with high optical transparency, higher electrical conductivity, and superior chemical and thermal stabilities have the potential to replace expensive indium tin oxide (ITO) and fluorine tin oxide (FTO) for DSSC. Graphene may also be utilized in conjunction with photoanodes (TiO_2, ZnO, etc.) to improve charge carrier separation ability. Organic solar cells, on the other hand, have been recommended as an economically cheaper solar energy conversion source owing to their simplicity of fabrication, light weight, and compatibility with the flexible substrates. For organic solar cell applications, graphene might serve as an effective acceptor material, promoting electron–hole separation and hole transport layer efficiency. Also, graphene could be used to improve photo-generated charge transfer in quantum dot (QD)-sensitized solar cells or silicon-material-based solar cell applications.

3.5 Conclusion and Future Perspective

Graphene is one of the most extensively explored in application-oriented researches at lab and industrial scale among all 2D materials, with great commercial possibilities. Over the last several decades, graphene-based materials have made amazing progress in terms of production and application. However, specific fundamental characteristics including the structure–property relationship must be discovered for better device design. Nevertheless, mass manufacturing of low-cost, high-quality graphene remains a significant hurdle. Substantial efforts have been undertaken to

mass-produce high-quality graphene using CVD and chemically generated graphene. Thermal methods have been also attempted to grow very large graphene sheets with minimal defects. These top-down approaches are typically implemented to produce graphene-related 2D materials for energy storage applications and wearable devices. However, a great control of size, shape, and purity must be accomplished through the synthetic chemical approaches. Graphene's exceptional and fascinating electrochemical and mechanical capabilities have led to the development of flexible and superior batteries, supercapacitors, and sensors. Graphene materials are used in cutting-edge energy gadgets because of its high stability. Graphene-based supercapacitor electrodes demonstrated intrinsic capacitance, mechanical stability, great performance, and extremely low resistance. Moreover, optimizing the storage (packing) density of graphene-based materials is critical for flexible devices to achieve high gravimetric and volumetric capacitance. Graphene-based sensors have demonstrated high efficiency, improved sensitivity, and fast response time compared to previously reported bio-sensors though its reliability as an implanted device should be scrutinized due to the cytotoxic effects. On an innovative approach, functionalized graphene nanosheets have shown increased interfacial contact and adhesion with proteins, human cells, and microbes, making it a potential system for next-generation biomedical devices. Nevertheless, the development of high-quality graphene employing low-cost manufacturing techniques is required to meet industrial needs. Finally, it is expected that an improved understanding of the ongoing cutting-edge research on graphene may enable the scientific community to appropriately take advantage of the technological applications.

References

1. H.W. Kroto, J.R. Heath, S.C. O'Brien, R.F. Curl, R.E. Smalley, C60: buckminsterfullerene. Nature **318**, 162 (1985)
2. S. Iijima, Helical microtubules of graphitic carbon. Nature **354**, 56 (1991)
3. G. Yang, L. Li, W.B. Lee, M.C. Ng, Structure of graphene and its disorders: a review. Sci. Technol. Adv. Mater. **19**, 613 (2018)
4. A.K. Geim, K.S. Novoselov, The rise of graphene. Nat. Mater. **6**, 183 (2007)
5. P.R. Wallace, The band theory of graphite. Phys. Rev. **71**, 622 (1947)
6. D.P. Hansora, N.G. Shimpi, S. Mishra, Graphite to graphene via graphene oxide: an overview on synthesis. Prop. Appl. JOM **67**, 2855 (2015)
7. A. Fasolino, J.H. Los, M.I. Katsnelson, Intrinsic ripples in graphene. Nat. Mater. **6**, 858 (2007)
8. M. Antonietti, K. Müllen, Carbon: the sixth element. Adv. Mater. **22**, 787 (2010)
9. A. Martín, A. Escarpa, Graphene: the cutting-edge interaction between chemistry and electrochemistry. TrAC Trends Anal. Chem. **56**, 13 (2014)
10. H. Bi, J. Chen, W. Zhao, S. Sun, Y. Tang, T. Lin, F. Huang, X. Zhou, X. Xie, M. Jiang, Highly conductive, free-standing and flexible graphene papers for energy conversion and storage devices. RSC Adv. **3**, 8454 (2013)
11. X. Fan, G. Jiao, W. Zhao, P. Jin, X. Li, Magnetic Fe_3O_4–graphene composites as targeted drug nanocarriers for PH-activated release. Nanoscale **5**, 1143 (2013)
12. T. Hwang, J.A. Kim, A. Kulkarni, T. Kim, Graphene photo detector with integrated waveguide biochemical sensors. Sens. Actuators B Chem. **187**, 319 (2013)

13. B.H. Nguyen, V.H. Nguyen, Promising applications of graphene and graphene-based nanostructures. Adv. Nat. Sci. Nanosci. Nanotechnol. **7**, 023002 (2016)
14. D. Wang et al., Self-assembled TiO_2–graphene hybrid nanostructures for enhanced Li-ion insertion. ACS Nano **3**, 907 (2009)
15. M. Yankowitz, J. Xue, B.J. LeRoy, Graphene on hexagonal boron nitride. J. Phys. Condens. Matter **26**, 303201 (2014)
16. T. Iwasaki et al., Bubble-free transfer technique for high-quality graphene/hexagonal boron nitride van der Waals heterostructures. ACS Appl. Mater. Interfaces **12**, 8533 (2020)
17. L. Banszerus, H. Janssen, M. Otto, A. Epping, T. Taniguchi, K. Watanabe, B. Beschoten, D. Neumaier, C. Stampfer, *Identifying suitable substrates for high-quality graphene-based heterostructures.* 2D Mater. **4**, 025030 (2017)
18. K.S. Novoselov, V.I. Fal′ko, L. Colombo, P.R. Gellert, M.G. Schwab, K. Kim, A roadmap for graphene. Nature **490**, 192 (2012)
19. J.A. Torres, R.B. Kaner, Graphene closer to fruition. Nat. Mater. **13**, 328 (2014)
20. F.V. Ferreira, L.D.S. Cividanes, F.S. Brito, B.R.C. de Menezes, W. Franceschi, E.A. Nunes Simonetti, G.P. Thim, *Functionalizing Graphene and Carbon Nanotubes* (Springer International Publishing, Cham, 2016)
21. M. Raji, N. Zari, A. el kacem Qaiss, R. Bouhfid, Chemical preparation and functionalization techniques of graphene and graphene oxide, in *Functionalized Graphene Nanocomposites and Their Derivatives* (Elsevier, 2019), pp. 1–20
22. F. Wang, K. Wang, B. Zheng, X. Dong, X. Mei, J. Lv, W. Duan, W. Wang, Laser-induced graphene: preparation, functionalization and applications. Mater. Technol. **33**, 340 (2018)
23. A. Dey, A. Chroneos, N.S.J. Braithwaite, R.P. Gandhiraman, S. Krishnamurthy, Plasma engineering of graphene. Appl. Phys. Rev. **3**, 021301 (2016)
24. M.S.A. Bhuyan, M.N. Uddin, M.M. Islam, F.A. Bipasha, S.S. Hossain, Synthesis of graphene. Int. Nano Lett. **6**, 65 (2016)
25. Z. Wang, Progress on preparation of graphene and its application. IOP Conf. Ser. Mater. Sci. Eng. **242**, 012032 (2017)
26. S.K. Jerng, D.S. Yu, Y.S. Kim, J. Ryou, S. Hong, C. Kim, S. Yoon, D.K. Efetov, P. Kim, S.H. Chun, Nanocrystalline graphite growth on sapphire by carbon molecular beam epitaxy. J. Phys. Chem. C **115**, 4491 (2011)
27. K.-B. Kim, C.-M. Lee, J. Choi, Catalyst-free direct growth of triangular nano-graphene on all substrates. J. Phys. Chem. C **115**, 14488 (2011)
28. X. Ding, G. Ding, X. Xie, F. Huang, M. Jiang, Direct growth of few layer graphene on hexagonal boron nitride by chemical vapor deposition. Carbon N. Y. **49**, 2522 (2011)
29. L. Zhang, Z. Shi, Y. Wang, R. Yang, D. Shi, G. Zhang, Catalyst-free growth of nanographene films on various substrates. Nano Res. **4**, 315 (2011)
30. C.M. Lee, J. Choi, Direct growth of nanographene on glass and postdeposition size control. Appl. Phys. Lett. **98**, 183106 (2011)
31. S. Ray, *Applications of Graphene and Graphene-Oxide Based Nanomaterials*, 1st ed. (Elsevier, 2015)
32. A. Martinez, K. Fuse, S. Yamashita, Mechanical exfoliation of graphene for the passive mode-locking of fiber lasers. Appl. Phys. Lett. **99**, 121107 (2011)
33. I.-Y. Jeon et al., Edge-carboxylated graphene nanosheets via ball milling. Proc. Natl. Acad. Sci. **109**, 5588 (2012)
34. Z. Lin, P. Karthik, M. Hada, T. Nishikawa, Y. Hayashi, Simple technique of exfoliation and dispersion of multilayer graphene from natural graphite by ozone-assisted sonication. Nanomaterials **7**, 125 (2017)
35. W. Dai, C.-Y. Chung, F.E. Alam, T.-T. Hung, H. Sun, Q. Wei, C.-T. Lin, S.-K. Chen, T.-S. Chin, Superior field emission performance of graphene/carbon nanofilament hybrids synthesized by electrochemical self-exfoliation. Mater. Lett. **205**, 223 (2017)
36. S.S. Shams, R. Zhang, J. Zhu, Graphene synthesis: a review. Mater. Sci. **33**, 566 (2015)
37. M.R. Habib, T. Liang, X. Yu, X. Pi, Y. Liu, M. Xu, A Review of theoretical study of graphene chemical vapor deposition synthesis on metals: nucleation, growth, and the role of hydrogen and oxygen. Reports Prog. Phys. **81**, 036501 (2018)

38. S. Forti et al., Electronic properties of single-layer tungsten disulfide on epitaxial graphene on silicon carbide. Nanoscale **9**, 16412 (2017)
39. N.L.V. Carreño et al., Metal-carbon interactions on reduced graphene oxide under facile thermal treatment: microbiological and cell assay. J. Nanomater. **2017**, 1 (2017)
40. C. Trudeau, L.-I. Dion-Bertrand, S. Mukherjee, R. Martel, S. Cloutier, Electrostatic deposition of large-surface graphene. Materials (Basel). **11**, 116 (2018)
41. J.-C. An, E.J. Lee, I. Hong, Preparation of the spheroidized graphite-derived multi-layered graphene via GIC (graphite intercalation compound) method. J. Ind. Eng. Chem. **47**, 56 (2017)
42. V. M. G. S. Shmavonyan, G.G. Sevoyan, Aroutiounian, Armen. J. Phys. **6**, 1 (2013)
43. A. Agrawal, G.-C. Yi, *Sample Pretreatment with Graphene Materials* (2020), pp. 21–47
44. Y.-H. Bae, T.-S. Kwon, M.-J. Yu, B.-C. Lee, S.-R. Kim, Acoustic characteristics and thermal properties of polycarbonate/(graphite intercalation compound) composites. Polym. Korea **41**, 189 (2017)
45. V. Singh, D. Joung, L. Zhai, S. Das, S.I. Khondaker, S. Seal, Graphene based materials: past, present and future. Prog. Mater. Sci. **56**, 1178 (2011)
46. I. Ovsiienko, L. Matzui, I. Berkutov, I. Mirzoiev, T. Len, Y. Prylutskyy, O. Prokopov, U. Ritter, Magnetoresistance of graphite intercalated with cobalt. J. Mater. Sci. **53**, 716 (2018)
47. S. Maruyama, T. Fukutsuka, K. Miyazaki, T. Abe, Observation of the intercalation of dimethyl sulfoxide-solvated lithium ion into graphite and decomposition of the ternary graphite intercalation compound using in situ Raman spectroscopy. Electrochim. Acta **265**, 41 (2018)
48. L. Poláková, Z. Sedláková, P. Ecorchard, E. Pavlova, J. Peter, B. Paruzel, H. Beneš, Poly(meth)acrylate nanocomposite membranes containing in situ exfoliated graphene platelets: synthesis, characterization and gas barrier properties. Eur. Polym. J. **94**, 431 (2017)
49. T. Rozmanowski, P. Krawczyk, Influence of chemical exfoliation process on the activity of $NiCl_2$-$FeCl_3$-$PdCl_2$-graphite intercalation compound towards methanol electrooxidation. Appl. Catal. B Environ. **224**, 53 (2018)
50. I. Jeon, B. Yoon, M. He, T.M. Swager, Hyperstage graphite: electrochemical synthesis and spontaneous reactive exfoliation. Adv. Mater. **30**, 1704538 (2018)
51. M. Horie, K. Takahashi, H. Nanao, M. Shirai, Selective hydrogenation of cinnamaldehyde over platinum nanosheets intercalated between graphite layers. J. Nanosci. Nanotechnol. **18**, 80 (2018)
52. S. Wang, C. Wang, X. Ji, Towards understanding the salt-intercalation exfoliation of graphite into graphene. RSC Adv. **7**, 52252 (2017)
53. D.C. Marcano, D.V. Kosynkin, J.M. Berlin, A. Sinitskii, Z. Sun, A. Slesarev, L.B. Alemany, W. Lu, J.M. Tour, Improved synthesis of graphene oxide. ACS Nano **4**, 4806 (2010)
54. N. Justh, B. Berke, K. László, I.M. Szilágyi, Thermal analysis of the improved hummers' synthesis of graphene oxide. J. Therm. Anal. Calorim. **131**, 2267 (2018)
55. X. Wu, L. Ma, S. Sun, K. Jiang, L. Zhang, Y. Wang, H. Zeng, H. Lin, A versatile platform for the highly efficient preparation of graphene quantum dots: photoluminescence emission and hydrophilicity-hydrophobicity regulation and organelle imaging. Nanoscale **10**, 1532 (2018)
56. P. Mandal, M.J.P. Naik, M. Saha, Room temperature synthesis of graphene nanosheets. Cryst. Res. Technol. **53**, 1700250 (2018)
57. V. Mazánek, S. Matějková, D. Sedmidubský, M. Pumera, Z. Sofer, One-step synthesis of B/N co-doped graphene as highly efficient electrocatalyst for the oxygen reduction reaction: synergistic effect of impurities. Chem. A Eur. J. **24**, 928 (2018)
58. R. Hack, C. H. G. Correia, R. A. de S. Zanon, S. H. Pezzin, Characterization of graphene nanosheets obtained by a modified Hummer's method. Matéria (Rio Janeiro) **23**, (2018)
59. O.V. Sinitsyna, G.B. Meshkov, A.V. Grigorieva, A.A. Antonov, I.G. Grigorieva, I.V. Yaminsky, Blister formation during graphite surface oxidation by hummers' method. Beilstein J. Nanotechnol. **9**, 407 (2018)
60. R. Yuan, J. Yuan, Y. Wu, P. Ju, L. Ji, H. Li, L. Chen, H. Zhou, J. Chen, Graphene oxide-monohydrated manganese phosphate composites: preparation via modified hummers method. Colloids Surfaces A Physicochem. Eng. Asp. **547**, 56 (2018)

61. L. Peng, Z. Xu, Z. Liu, Y. Wei, H. Sun, Z. Li, X. Zhao, C. Gao, An iron-based green approach to 1-h production of single-layer graphene oxide. Nat. Commun. **6**, 5716 (2015)
62. F. Lin, X. Tong, Y. Wang, J. Bao, Z.M. Wang, Graphene oxide liquid crystals: synthesis, phase transition, rheological property, and applications in optoelectronics and display. Nanoscale Res. Lett. **10**, 435 (2015)
63. X. Li et al., Large-area synthesis of high-quality and uniform graphene films on copper foils. Science **324**(80), 1312 (2009)
64. A. Reina, X. Jia, J. Ho, D. Nezich, H. Son, V. Bulovic, M.S. Dresselhaus, J. Kong, Large area, few-layer graphene films on arbitrary substrates by chemical vapor deposition. Nano Lett. **9**, 30 (2009)
65. K.S. Kim, Y. Zhao, H. Jang, S.Y. Lee, J.M. Kim, K.S. Kim, J.-H. Ahn, P. Kim, J.-Y. Choi, B.H. Hong, Large-scale pattern growth of graphene films for stretchable transparent electrodes. Nature **457**, 706 (2009)
66. M. Choucair, P. Thordarson, J.A. Stride, Gram-scale production of graphene based on solvothermal synthesis and sonication. Nat. Nanotechnol. **4**, 30 (2009)
67. P.W. Sutter, J.-I. Flege, E.A. Sutter, Epitaxial graphene on ruthenium. Nat. Mater. **7**, 406 (2008)
68. J. Coraux, A. T. N'Diaye, C. Busse, T. Michely, Structural coherency of graphene on Ir(111). Nano Lett. **8**, 565 (2008)
69. M.H. Ani, M.A. Kamarudin, A.H. Ramlan, E. Ismail, M.S. Sirat, M.A. Mohamed, M.A. Azam, A critical review on the contributions of chemical and physical factors toward the nucleation and growth of large-area graphene. J. Mater. Sci. **53**, 7095 (2018)
70. M.G. Rybin, I.I. Kondrashov, A.S. Pozharov, V.C. Nguyen, N.M. Phan, E.D. Obraztsova, In situ control of CVD synthesis of graphene film on nickel foil. Phys. Status Solidi **255**, 1700414 (2018)
71. J. Dong, H. Wang, H. Peng, Z. Liu, K. Zhang, F. Ding, Formation mechanism of overlapping grain boundaries in graphene chemical vapor deposition growth. Chem. Sci. **8**, 2209 (2017)
72. B.-J. Park, J.-S. Choi, J.-H. Eom, H. Ha, H.Y. Kim, S. Lee, H. Shin, S.-G. Yoon, Defect-free graphene synthesized directly at 150 °C via chemical vapor deposition with no transfer. ACS Nano **12**, 2008 (2018)
73. S. Amini, J. Garay, G. Liu, A.A. Balandin, R. Abbaschian, Growth of large-area graphene films from metal-carbon melts. J. Appl. Phys. **108**, 094321 (2010)
74. L. Karuppasamy, L. Gurusamy, G.-J. Lee, J. J. Wu, *Synthesis of Metal/Metal Oxide Supported Reduced Graphene Oxide (RGO) for the Applications of Electrocatalysis and Supercapacitors*, (2019), pp. 1–48
75. L. Jiao, L. Zhang, X. Wang, G. Diankov, H. Dai, Narrow graphene nanoribbons from carbon nanotubes. Nature **458**, 877 (2009)
76. P.T. Yin, S. Shah, M. Chhowalla, K.-B. Lee, Design, synthesis, and characterization of graphene-nanoparticle hybrid materials for bioapplications. Chem. Rev. **115**, 2483 (2015)
77. W.-W. Liu, S.-P. Chai, A.R. Mohamed, U. Hashim, Synthesis and characterization of graphene and carbon nanotubes: a review on the past and recent developments. J. Ind. Eng. Chem. **20**, 1171 (2014)
78. H.-B. Zhang, W.-G. Zheng, Q. Yan, Y. Yang, J.-W. Wang, Z.-H. Lu, G.-Y. Ji, Z.-Z. Yu, Electrically conductive polyethylene terephthalate/graphene nanocomposites prepared by melt compounding. Polymer (Guildf). **51**, 1191 (2010)
79. Y. Seekaew, D. Phokharatkul, A. Wisitsoraat, C. Wongchoosuk, Highly sensitive and selective room-temperature NO_2 gas sensor based on bilayer transferred chemical vapor deposited graphene. Appl. Surf. Sci. **404**, 357 (2017)
80. A.W. Robertson, J.H. Warner, Atomic Resolution Imaging Of Graphene By Transmission Electron Microscopy. Nanoscale **5**, 4079 (2013)
81. Y. Seekaew, S. Lokavee, D. Phokharatkul, A. Wisitsoraat, T. Kerdcharoen, C. Wongchoosuk, Low-cost and flexible printed graphene–PEDOT:PSS gas sensor for ammonia detection. Org. Electron. **15**, 2971 (2014)

82. U.K. Sur, A. Saha, A. Datta, B. Ankamwar, F. Surti, S.D. Roy, D. Roy, Synthesis and characterization of stable aqueous dispersions of graphene. Bull. Mater. Sci. **39**, 159 (2016)
83. F.T. Johra, J.-W. Lee, W.-G. Jung, Facile and safe graphene preparation on solution based platform. J. Ind. Eng. Chem. **20**, 2883 (2014)
84. J. Zhang, H. Yang, G. Shen, P. Cheng, J. Zhang, S. Guo, Reduction of graphene oxide via L-ascorbic acid. Chem. Commun. **46**, 1112 (2010)
85. P. Vandenabeele, *Practical Raman Spectroscopy—An Introduction* (Wiley, 2013)
86. D.J. Gardiner, P.R. Graves (eds.), *Practical Raman Spectroscopy* (Springer, Berlin Heidelberg, Berlin, Heidelberg, 1989)
87. P.C. Eklund, J.M. Holden, R.A. Jishi, Vibrational modes of carbon nanotubes; spectroscopy and theory. Carbon N. Y. **33**, 959 (1995)
88. M.J. Allen, V.C. Tung, R.B. Kaner, Honeycomb carbon: a review of graphene. Chem. Rev. **110**, 132 (2010)
89. Y. Ying Wang, Z. Hua Ni, T. Yu, Z. X. Shen, H. Min Wang, Y. Hong Wu, W. Chen, A. T. Shen Wee, Raman studies of monolayer graphene: the substrate effect. J. Phys. Chem. C **112**, 10637 (2008)
90. A.C. Ferrari, J. Robertson, Interpretation of raman spectra of disordered and amorphous carbon. Phys. Rev. B **61**, 14095 (2000)
91. S. Roscher, R. Hoffmann, O. Ambacher, Determination of the graphene-graphite ratio of graphene powder by Raman 2D band symmetry analysis. Anal. Methods **11**, 1224 (2019)
92. A.C. Ferrari et al., Science and technology roadmap for graphene, related two-dimensional crystals, and hybrid systems. Nanoscale **7**, 4598 (2015)
93. Y.-M. Lin, C. Dimitrakopoulos, K.A. Jenkins, D.B. Farmer, H.-Y. Chiu, A. Grill, P. Avouris, 100-GHz transistors from wafer-scale epitaxial graphene. Science **327**, 662 (2010)
94. Y.-M. Lin et al., Wafer-scale graphene integrated circuit. Science **332**, 1294 (2011)
95. K.S. Novoselov, A.K. Geim, S.V. Morozov, D. Jiang, Y. Zhang, S.V. Dubonos, I.V. Grigorieva, A.A. Firsov, Electric field effect in atomically thin carbon films. Science **306**, 666 (2004)
96. Q. Yan, B. Huang, J. Yu, F. Zheng, J. Zang, J. Wu, B.-L. Gu, F. Liu, W. Duan, Intrinsic current-voltage characteristics of graphene nanoribbon transistors and effect of edge doping. Nano Lett. **7**, 1469 (2007)
97. W. Yang, K.R. Ratinac, S.P. Ringer, P. Thordarson, J.J. Gooding, F. Braet, Carbon nanomaterials in biosensors: should you use nanotubes or graphene? Angew. Chem. Int. Ed. Engl. **49**, 2114 (2010)
98. F. Schedin, A.K. Geim, S.V Morozov, E.W. Hill, P. Blake, M.I. Katsnelson, K.S. Novoselov, Detection of individual gas molecules adsorbed on graphene. Nat. Mater. **6**, 652 (2007)
99. K. Zhou, Y. Zhu, X. Yang, J. Luo, C. Li, S. Luan, A novel hydrogen peroxide biosensor based on Au–graphene–HRP–chitosan biocomposites. Electrochim. Acta **55**, 3055 (2010)
100. T.Z. Cui, B. Zhang, A. Simple, Flexible, low-cost acetylcholine biosensor based on nano self assembly of graphene. Sens. Lett. **9**, 4 (2011)
101. W. Hong, H. Bai, Y. Xu, Z. Yao, Z. Gu, G. Shi, Preparation of gold nanoparticle/graphene composites with controlled weight contents and their application in biosensors. J. Phys. Chem. C **114**, 1822 (2010)
102. B. Zhang, Q. Li, T. Cui, Ultra-sensitive suspended graphene nanocomposite cancer sensors with strong suppression of electrical noise. Biosens. Bioelectron. **31**, 105 (2012)
103. H. Chang, Z. Sun, K.Y.-F. Ho, X. Tao, F. Yan, W.-M. Kwok, Z. Zheng, A highly sensitive ultraviolet sensor based on a facile in situ solution-grown ZnO nanorod/graphene heterostructure. Nanoscale **3**, 258 (2011)
104. W. Li et al., Reduced graphene oxide electrically contacted graphene sensor for highly sensitive nitric oxide detection. ACS Nano **5**, 6955 (2011)
105. U. Lange, T. Hirsch, V.M. Mirsky, O.S. Wolfbeis, Hydrogen sensor based on a graphene—palladium nanocomposite. Electrochim. Acta **56**, 3707 (2011)
106. X. Li, Y. Zhu, W. Cai, M. Borysiak, B. Han, D. Chen, R. D. Piner, L. Colombo, R. S. Ruoff, Transfer of large-area graphene films for high-performance transparent conductive electrodes. Nano Lett. **9**, 4359 (2009)

107. S. De, P.J. King, M. Lotya, A. O'Neill, E.M. Doherty, Y. Hernandez, G.S. Duesberg, J.N. Coleman, Flexible, transparent, conducting films of randomly stacked graphene from surfactant-stabilized, oxide-free graphene dispersions. Small **6**, 458 (2010)
108. J. Zhao, S. Pei, W. Ren, L. Gao, H.-M. Cheng, Efficient preparation of large-area graphene oxide sheets for transparent conductive films. ACS Nano **4**, 5245 (2010)
109. F. Bonaccorso, Z. Sun, T. Hasan, A.C. Ferrari, Graphene photonics and optoelectronics. Nat. Photonics **4**, 611 (2010)
110. H. Wang, Y. Yang, Y. Liang, J.T. Robinson, Y. Li, A. Jackson, Y. Cui, H. Dai, Graphene-wrapped sulfur particles as a rechargeable lithium-sulfur battery cathode material with high capacity and cycling stability. Nano Lett. **11**, 2644 (2011)
111. A.L.M. Reddy, A. Srivastava, S.R. Gowda, H. Gullapalli, M. Dubey, P.M. Ajayan, Synthesis of nitrogen-doped graphene films for lithium battery application. ACS Nano **4**, 6337 (2010)
112. J.K. Lee, K.B. Smith, C.M. Hayner, H.H. Kung, Silicon nanoparticles-graphene paper composites for li ion battery anodes. Chem. Commun. (Camb). **46**, 2025 (2010)
113. E. Yoo, H. Zhou, Li-air rechargeable battery based on metal-free graphene nanosheet catalysts. ACS Nano **5**, 3020 (2011)
114. Y.J. Mai, J.P. Tu, C.D. Gu, X.L. Wang, Graphene anchored with nickel nanoparticles as a high-performance anode material for lithium ion batteries. J. Power Sources **209**, 1 (2012)
115. X. Miao, S. Tongay, M.K. Petterson, K. Berke, A.G. Rinzler, B.R. Appleton, A.F. Hebard, High efficiency graphene solar cells by chemical doping. Nano Lett. **12**, 120503132902000 (2012)
116. Y.-B. Tang et al., Incorporation of graphenes in nanostructured TiO(2) films via molecular grafting for dye-sensitized solar cell application. ACS Nano **4**, 3482 (2010)
117. L. Kavan, J.-H. Yum, M. Grätzel, Graphene nanoplatelets outperforming platinum as the electrocatalyst in co-bipyridine-mediated dye-sensitized solar cells. Nano Lett. **11**, 5501 (2011)
118. N. Yang, J. Zhai, D. Wang, Y. Chen, L. Jiang, Two-dimensional graphene bridges enhanced photoinduced charge transport in dye-sensitized solar cells. ACS Nano **4**, 887 (2010)

Chapter 4
Metal Nanoparticles: Synthesis, Characterization, and Biomedical Applications

Sivasankar Putta, Raj Kumar Sharma, and Puneet Khandelwal

Abstract Metallic nanoparticles have attracted the attention of researchers worldwide because of their fascinating optical, electrical, magnetic, and catalytic properties. Metallic nanoparticles have an easy surface modification chemistry to attach various molecules such as ligands, targeting agents, biomolecules, drugs, and antibodies. Because of the different properties and easy modification chemistry, these nanoparticles have wide-ranging applications, including biomedical, solar, catalysis, etc. This chapter will focus on metallic nanoparticles, specifically gold nanoparticles, for biomedical applications.

Keywords Metal nanoparticles · Gold nanoparticles · Nanomedicine · Gene silencing · Phototherapy · Immunotherapy · CRISPR–Cas9 · Radiotherapy

4.1 Introduction

Metals have been a center of attraction over the last two centuries because of their fascinating physical and biological properties. A PubMed search shows the presence of around 1.5 million research documents on metals since 1800. The metals in their nano form, known as bhasma, have been used in India since ancient times to treat various diseases. However, the concept of nanotechnology was introduced in the last century (1959) by physics Nobel laureate Richard P. Feynman in his famous lecture titled "There's Plenty of Room at the Bottom" at the meeting of the American Physical Society [1, 2]. The terminology "nanotechnology" was introduced by Norio Taniguchi in 1974.

Gold nanoparticles have unique physical, chemical, and optical properties, which leads to their excellent biocompatibility, easy synthesis in a broad range of sizes

S. Putta
Department of Chemistry and Biochemistry, University of California, Santa Cruz, CA 95064, USA

R. K. Sharma · P. Khandelwal (✉)
Department of Radiology, School of Medicine, Johns Hopkins University, Baltimore, MD 21202, USA
e-mail: pkhande3@jhmi.edu

D. K. Singh et al. (eds.), *Nanomaterials*,
https://doi.org/10.1007/978-981-19-7963-7_4

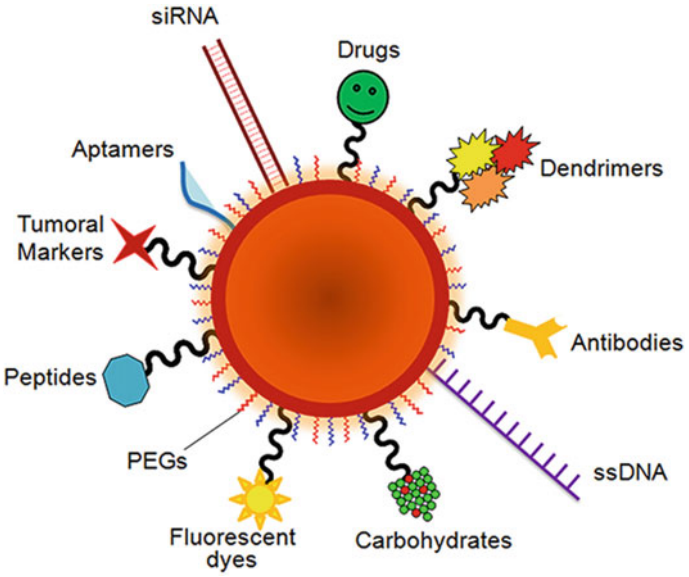

Fig. 4.1 Various biomolecules can be attached to the gold nanoparticle's surface, providing enhanced biocompatibility, chemical stability, functionality, and specificity for targeted therapy and imaging applications. Adapted with permission from Ref. [3] (Copyright 2014 Frontiers Media)

and shapes in an aqueous medium, easy surface functionalization, and photostability, and photo-thermal activity (Fig. 4.1) [3]. Due to their strong optical properties originating from the localized surface plasmon resonance and their high surface-to-volume ratio, these nanoparticles have been used for efficient light-to-heat conversion (photo-thermal therapy), sensors (sensing biomolecules and heavy metal ions), and imaging applications [4]. In 1857, Faraday described the synthesis of colloidal gold nanoparticles for the first time by reducing gold chloride ($AuCl^{4-}$) using phosphorus and their stabilization by carbon disulfide. Later, Turkevich et al. reported the colloidal gold nanoparticle synthesis by trisodium citrate to reduce gold chloride in the aqueous medium [5, 6].

4.2 Synthesis of Metal Nanoparticles

The metal nanoparticles can be synthesized by two main methods: (1) The top-down approach and (2) the bottom-up approach. Both of these methods differ mainly by starting material. In the top-down process, the starting material is bulk, the size of which is reduced to nano dimension by various physical, chemical, or mechanical methods. On the other hand, the bottom-up approach uses atoms and molecules as the starting materials [7]. The synthesis of nanoparticles is based on the decrease in the size of the initial material by different physical, chemical, and biological treatments.

Although the top-down approach is easy to operate, it is not appropriate for preparing informally shaped and microscopic particles. The major challenge with this method is the change in surface chemistry and physicochemical properties of synthesized nanoparticles [8, 9].

The bottom-up approach is based on the formation of nanoparticles from smaller molecules and/or atoms, including joining atoms, molecules, or small particles. In this process, the nanostructured building blocks are first synthesized, followed by their assembly to synthesize the final nanoparticles [10–13].

Mechanical milling method

Mechanical milling is a kind of grinding method which uses high-speed rotating balls to reduce the particle size of the bulk material. The bulk material is introduced into a rolling hollow cylinder with high-speed rotating balls dropping from the top of the cylinder to the bulk material, reducing particle size. This method is environment-friendly and cost-effective; therefore, it has wide applications in industries.

Laser ablation method

Laser ablation, also known as the photoablation method, is used to make nanoparticles from bulk material. The bulk material is irradiated with a pulse laser such as Nd:YAG, Ti:Sapphire, and copper vapor laser, resulting in nanoparticle suspension. The time duration, wavelength, and fluency of the laser and surrounding medium affect the synthesized nanoparticles. The laser ablation method is suitable for making homogenous and monodisperse nanoparticles with a high production rate.

Physical vapor deposition method

In this method, the metal vapor is deposited on an electrically conductive material either as a thin film or as nanoparticles. The ion beam sputtering method uses inert gas ions (such as argon) to make the plasma surrounding the target material. The argon ions then strike the target material (at high voltage), which will eject the atoms from the target material and deposit them onto the substrate. The entire process is performed at a very high pressure of about 10^{-1} to 10^{-3} mbar. Magnetron sputtering has been used successfully to synthesize various nanoparticles [14].

Chemical vapor deposition method

Unlike the physical vapor method, the chemical vapor deposition approach involves the reaction of chemical vapors containing more volatile precursors with the target material. The thin film of the target material is deposited on a substrate [15]. This approach is widely used in semiconductors to make thin films.

Sol–gel method

The sol–gel nanoparticle synthesis method involves the synthesis of metal alkoxide precursors in solution (sol phase), which further acts as a building block for an integrated metal oxide network (gel phase) [16]. This method is generally used for the synthesis of metal oxide nanoparticles.

Chemical reduction method

The metal salt is reduced in an aqueous medium using different chemical reducing agents in the presence of a surfactant. Examples of reducing agents are sodium borohydride, sodium citrate, and ascorbic acid. Formed metal nanoparticles are capped with stabilizing or capping agents such as long-chain alkylates and long-chain fatty acids, including sodium lauryl sulfate and hexadecyltrimethylammonium bromide. Sometimes, a stabilizing agent can also act as a reducing agent, such as sodium citrate and ascorbic acid. Many biomolecules containing amine, oxide, or thiol groups may act as reducing and capping agents [17–20]. This is one of the most popular methods for synthesizing metal nanoparticles.

Hydrothermal method

The hydrothermal approach to synthesizing nanoparticles involves the growth of a single crystal in high vapor pressure and high-temperature environment. This environment is created in specially designed thick-walled vessels of high corrosion and temperature-resistant steel [21–27].

Solvothermal method

The solvothermal method is similar to the hydrothermal method in most ways which also uses a high-temperature and high-pressure environment developed inside a thick-walled steel vessel. The significant difference in both approaches is that the latter uses organic solvents instead of aqueous solvents [28].

Pyrolysis

Pyrolysis is the process of chemical transformation or decomposition of material in an inert atmosphere at a high temperature. The spray pyrolysis approach involves the delivery of nanoparticle precursors in vapor form using a nebulizer into the hot reactor. On the other hand, the laser pyrolysis method involves the precursors absorbing laser energy for the preparation of nanoparticles. In the flame pyrolysis approach, the liquid precursors are directly sprayed into the flame [29].

Biological method

The biological method is a cost-effective, eco-friendly, green synthesis approach involving the use of different microorganisms and plant products for nanoparticle synthesis. The biological process has an advantage over other methods because this method doesn't require high temperature, pressure, and toxic chemicals [30].

Electrochemical deposition

The electrochemical method is a process in which a thin metal layer has been deposited on the conducting material surface. The metal precursor ions get reduced at the conducting surface and make a thin layer of metal coating in the presence of sufficient electric current [31].

Microwave-assisted synthesis

Microwave-assisted synthesis is preferred over the thermal approach because of its fast, homogenous heating and high product yield. Microwave frequency of 300 MHz to 300 GHz leads to the polar molecule orientation with the electric field. In contrast, re-orientation with an alternating electric field triggers molecular friction and energy loss in the form of heat [32–34].

Ultrasound-assisted synthesis

The ultrasound approach uses the cavitation process, which is the formation and collapse of the bubble by intense ultrasound waves, producing an enormous amount of kinetic energy which converts into heat. This process has an advantage over other conventional methods in that it produces a high yield, requires low energy, doesn't need toxic chemicals, and produces low waste [35].

4.3 Characterization of Metal Nanoparticles

Several technologies have been used to characterize the physical, chemical, and optical properties of nanoparticles, such as shape, size, crystal structure, elemental composition, and stability.

4.3.1 Spectroscopic Characterization

The metallic nanoparticles show characteristic optical properties due to the oscillations of the conduction band of electrons at the surface of nanoparticles, known as surface plasmon resonance. The color of gold nanoparticle suspension changes from deep red to purple depending on the size of the nanoparticles. Due to LSPR, some portion of the electromagnetic spectrum is absorbed while others get reflected, leading to their visible colors. The absorption of the electromagnetic spectrum can be detected in UV–Vis spectrophotometer as a strong peak between 520 and 800 nm depending upon the size of nanoparticles.

4.3.2 SEM Analysis

Scanning electron microscopy is used to characterize nanoparticle size, shape, and agglomeration. In SEM imaging, a focused electron beam is allowed to react with the sample, which produces many signals required to obtain the shape and composition of the nanoparticles. The sample processing for SEM is very straightforward in that

the sample must be drop-casted on the conductive substrate and dried thoroughly to remove any solvent traces.

4.3.3 TEM Analysis

Transmission electron microscopy is used to characterize the structural properties of nanoparticles. TEM can be used to produce the images, diffraction patterns, and microanalytical data of the nanomaterial to get a complete insight into the different properties and behavior of nanomaterials. Unlike SEM, TEM sample preparation includes a diluted sample drop cast on the carbon-coated copper grid.

4.3.4 AFM Analysis

The atomic force microscope uses phosphorus-doped silicon probes, which scan the entire nanoparticle surface and provide 3D projection images of nanoparticles. AFM can also give extensive qualitative and quantitative data depending on the type of nanomaterial. The sample preparation for AFM is very similar to the SEM.

4.3.5 FTIR Analysis

The Fourier transform infrared (FTIR) spectroscopy utilizes infrared waves to analyze the chemical structure of the nanomaterial at the molecular scale, especially the bonding of capping agents to the nanoparticle surface. The sample preparation includes mixing and grinding of completely dried nanomaterial with KBr powder.

4.3.6 XRD Analysis

X-ray diffraction utilizes the constructive interference between X-ray radiation and the nanomaterials, which generates information about the structure of nanomaterials, especially the crystal structure, crystallite size, nature of phase, lattice parameters, and strain.

4.4 Metal Nanoparticles for Biomedical Applications

4.4.1 Chemotherapy

The ease of surface functionalization of gold nanoparticles through various biomolecules made them an attractive delivery agent for chemotherapy. There are different methods developed for the functionalization of gold nanoparticles. In one method, prodrugs can be coupled covalently to the gold nanoparticles via cleavable linkers [36–39]. In another approach, hydrophobic drug molecules can be non-covalently attached to gold nanoparticles, allowing delivery without any structural change of the drug molecules [10–13]. Gold nanoparticles can release the drugs by either internal (e.g., glutathione) or external (e.g., light) stimuli [40–46]. The diversity of the gold nanoparticle monolayer is crucial to both release mechanisms, offering tunability for endogenous delivery processes and a functional platform for external delivery approaches [47].

4.4.2 Phototherapy

Sunlight has been used in medicine from ancient Egypt, Greece, India, and China to treat various diseases [48]. The disorders such as psoriasis and vitiligo were treated using vegetal-derived substances in the presence of sunlight in ancient Egypt [49]. In ancient times, light therapies had also been used to treat several other disorders, such as physiological illnesses, sleep, skin diseases, neonatal jaundice, retinal correction, and cancer.

However, the use of light irradiation has recently been shown for the precision therapy of cancer treatment. The light can be used directly to initiate physiological changes or endogenous biochemical reactions, which leads to cell damage [50]. The light can also be used indirectly to initiate the production of effector molecules as byproducts [49, 51, 52]. According to the method, the use of light can be broadly divided into two different categories: (a) Photodynamic therapy—in this method, sensitizer molecules absorb the light and initiate a chemical alteration reaction that leads to the therapeutic outcome, and (b) Photo-thermal therapy—in this method, gold nanoparticles have been used which convert the light to heat and damage the cells (Fig. 4.2) [49, 51–55].

Phototherapy uses lasers as a light source that generates monochromatic light and can be transported through an optical fiber. The light source selection depends on the absorption of photosensitizers, location of the disease, lesion size, exposure time, total light dose, and light delivery type. The wavelength of phototherapy is chosen in the range 600–800 nm, the NIR region known as the therapeutic window. In this range of wavelength, photosensitizer molecules get excited. The significant advantage of

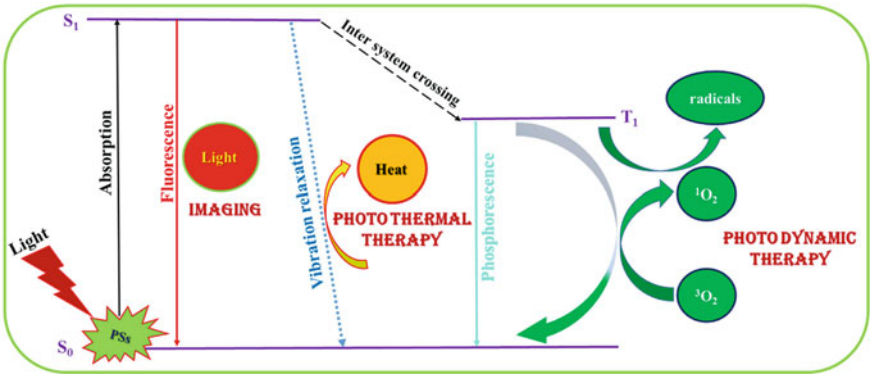

Fig. 4.2 Light-induced therapy—**a** photodynamic (PDT) and **b** photo-thermal (PTT) treatment. Schematic representation of the crucial steps of PDT and PTT used as a therapeutic approach against cancer. Adapted with permission from Ref. [50] (Copyright 2021 MDPI)

phototherapy is minimal invasiveness, tumor specificity, reduced systemic cytotoxicity, and spatiotemporally controlled illumination via focused irradiation only at the diseased lesion [56].

Gold nanoparticles have been used effectively to deliver photosensitizer molecules benefitting from the easy surface modifications of the nanoparticles. Gold nanoparticles can efficiently deliver different biomolecules, such as proteins, DNA, and drug molecules, which may act as sensitizers. The gold nanoparticles and photosensitizer conjugates can effectively transfer the energy or electrons between sensitizer and nanoparticles, making them suitable for effective PDT [51, 54, 57, 58].

Photo-thermal therapy is another minimally invasive alternative to photodynamic therapy, which utilizes the generation of controlled local heat with extreme precision. Since the early 1900s, it has been very well-known that cancer cells are more susceptible to heat than normal cells. Photo-thermal therapy utilizes photo-thermal agents and generates heat to raise the local temp as high as 40–45 °C, which is higher than the physiological temperature (36–37 °C). The photo-thermal therapy kills cancer cells by affecting several cellular and molecular mechanisms such as direct cell membrane damage, inhibition of DNA synthesis, and cytoskeleton damage. Hyperthermia therapy is not free from side effects. Hyperthermia can cause side effects because of the disproportionate photo-thermal agent's distribution throughout the body and extreme laser power [56, 59].

4.4.3 Immunotherapy

Vaccination is a kind of immunotherapy that utilizes adjuvant molecules to make the response highly efficient [60]. The development of vaccines is crucial, including the long-lasting induction of robust immune response, antigen-specific CD8+ T cell, and

stimulating antibody response to existing tumors [61]. The critical factor in developing vaccines is the delivery of antigens to antigen-presenting cells with subsequent activation and maturation. This will, in response, maximize cross-presentation for inducing cytotoxic CD8+ T cell response [62]. For this purpose, the vaccine delivery to the lymph node can be one of the best strategies because lymph nodes contain many APCs and immune cells responsible for both humoral and cellular immunity [61, 63–66].

Nanoparticles have evolved as a potential candidate for antigen delivery because they can easily be targeted to the lymph node via a lymphatic vessel in a size-dependent manner [61, 63]. Small particles around 25 nm have higher accumulations in lymph nodes than the larger ones with a size equal to or more than 100 nm [67]. Therefore, there are some critical considerations for developing nanoparticles for antigen delivery, such as (a) the nanoparticles should be smaller than 50 nm, (b) the antigen or adjuvant should be versatile to be functionalized on the nanoparticle surface, (c) the antigen should effectively activate antigen-presenting cells to induce humoral and cellular immunity, and (d) nanoparticles should be trackable non-invasively throughout the body. Given these considerations, gold nanoparticles can fit the best because of the following properties: (a) easy to control the size of gold nanoparticles from 1 nm to hundreds of nanometers, (b) various biomolecules, including protein, peptide, and oligonucleotides, can be easily attached to the gold nanoparticles surface, (c) gold nanoparticles are biocompatible, biologically inert, and non-toxic, (d) gold nanoparticles can easily be tracked throughout the body using imaging techniques such as computed tomography which is readily available in most of the hospitals or clinical centers.

Lee et al. prepared a vaccine based on gold nanoparticles (size = 7 nm) for targeted delivery to lymph nodes (Fig. 4.3). The gold nanoparticles were functionalized by red fluorescence protein (which works as an antigen), and thiol-modified CpG 1668 oligodeoxynucleotide (ODN; CpG 1668 is an ODN that contains CpG motifs, which works as a potent stimulator of the immune response). The red fluorescence protein was modified to have two cysteines at its c-terminus, which enables its coupling to the surface of gold nanoparticles via Au–S bonding [68]. The CpG 1668 with a spacer consisting of ten adenine nucleotides (A10) can effectively trigger immune responses through the activation of toll-like receptor 9 (TLR-9) [69].

Ahn et al. used the extra domain B (EDB) of fibronectin for the vaccine formulation. EDB is a tumor-associated self-antigen overexpressed in fetal and tumor tissues and is therefore known as an oncofetal antigen [70]. Moreover, EDB is also an excellent angiogenesis marker as it accumulates explicitly in the basement membrane of the neovascular structures present in aggressive tumors. AuNP/EDB-$OVA_{257–269}$ efficiently facilitated cross-presentation of the antigen in professional dendritic cells, eventually stimulating antigen-specific cytotoxic T-lymphocyte reactions. Following administration of AuNP/EDB-$OVA_{257–269}$, the vaccine efficiently reached the local lymph nodes, causing a high-level EDB-specific antibody production and finally preventing tumor growth in an EDB-overexpressing breast tumor model [70].

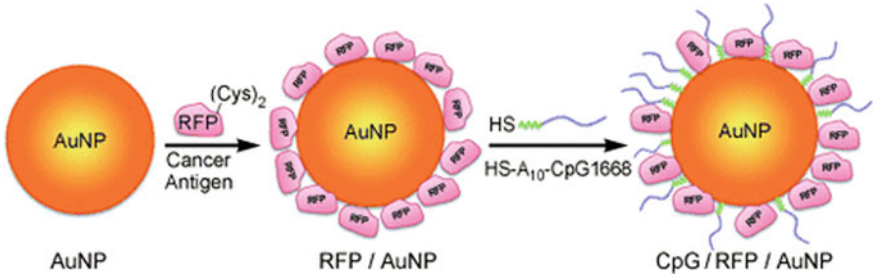

Fig. 4.3 Schematic representation of CpG/RFP/AuNPs preparation. Adapted with permission from Ref. [68] (Copyright 2014 Elsevier)

4.4.4 Radiotherapy

Due to its high-level tissue penetration, radiotherapy is one of the most extensively used non-surgical therapies for cancer patients in clinics. Various metals with high atomic numbers, such as gold, bismuth, gadolinium, and hafnium, have been widely explored as radiosensitizers. Gold has been extensively studied among these metals because of its intrinsic radiosensitivity property (due to its higher atomic number) and biocompatibility compared to other high atomic number materials [71, 72].

However, high-energy radiation, like X-rays, can damage genetic material. Therefore, delivery agents (radiosensitizers) are needed that can interact with X-rays to confine the radiation dosage into desired cells/tissues. Nanoparticles have the advantage over traditional molecular radiosensitizers because nanoparticles can be tailored to facilitate selective delivery into tumor tissues due to the enhanced permeability and retention (EPR) effect [71, 73–79].

Gold nanoparticles can be selectively delivered to the tumors, leading to higher absorption of X-rays into the tumors than in normal tissues. As per the calculations, this dose enhancement can be considerably more significant than normal tissues, even 200% or higher [71, 76]. Additional advantages of Au NPs are that they can be used as contrast for image-guided therapy and are appropriate for combinatorial therapy to deliver more than one drug molecule.

Ding et al. reported gold nanoparticles conjugated with a responsive peptide (Tat-R-EK) [80]. This responsive peptide consists of three main components: a cell and nuclear-penetrating component derived from human immunodeficiency virus-1 transactivator of transcription protein (Tat), a cathepsin B cleavable linker, and a zwitterionic antifouling component (Fig. 4.4). The peptide covered the gold nanoparticles via the Au–S bonding between gold and thiol groups from cysteine.

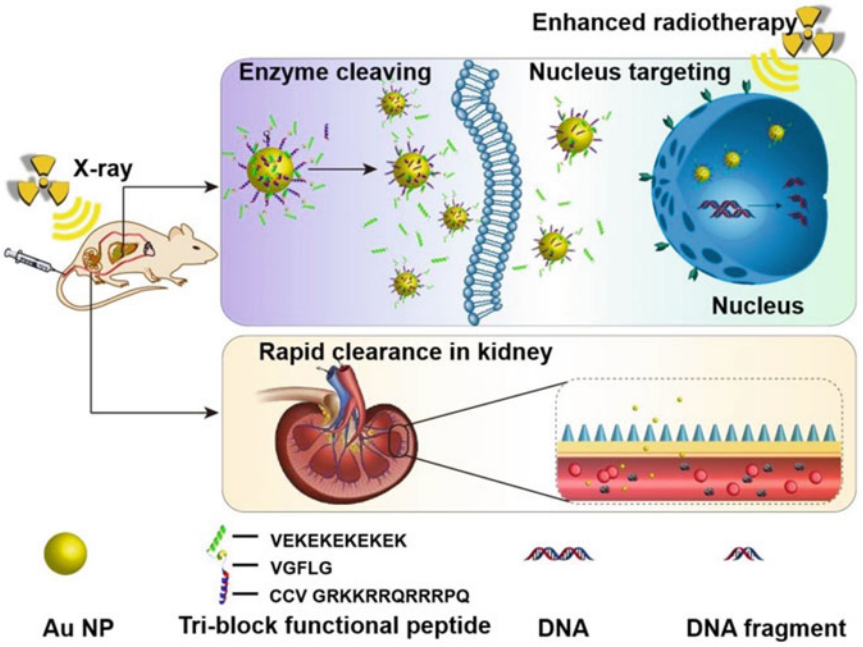

Fig. 4.4 Schematic shows the gold nanoparticle delivery in tumor tissues and cell nuclei for improved radiotherapy in vivo and fast clearance via the kidney. Adapted with permission from Ref. [80] (Copyright 2020 Ivyspring International Publisher)

4.4.5 Gene Silencing

4.4.5.1 RNAi

The gold nanoparticles have been extensively studied to deliver siRNA for gene knockdown purposes. There are two ways to attach the siRNA with gold nanoparticles: (a) via Au–S chemistry or (b) via electrostatic interactions.

Au–S bonding has been used to bind thiol-containing ligands to the surface of gold nanoparticles. In a study by Giljohann et al., 13 nm gold nanoparticles were co-loaded with SH–PEG400 and SH–siRNA (Fig. 4.5). In this system, the PEG was significantly smaller than the siRNA, so the nanoparticle surface displayed to the cells exhibits almost entirely siRNA [81].

Electrostatic interactions have also been used for attaching the negatively charged siRNA molecules to the surface of gold nanoparticles via positively charged polymers such as polyethyleneimine (Fig. 4.6). For example, Elbakry et al. reported a complex with a 15 nm gold nanoparticle core followed by layers of PEI, siRNA, and PEI [82].

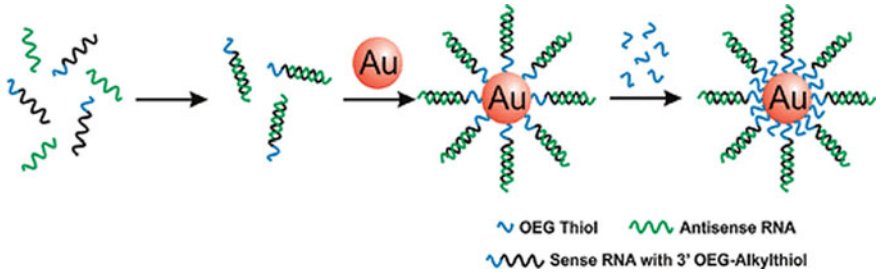

Fig. 4.5 Preparation of siRNA conjugated gold nanoparticles. The RNA duplex was formed first, followed by the addition of gold nanoparticles and OEG-alkylthiol. Adapted with permission from Ref. [81]. Copyrights 2009 American Chemical Society

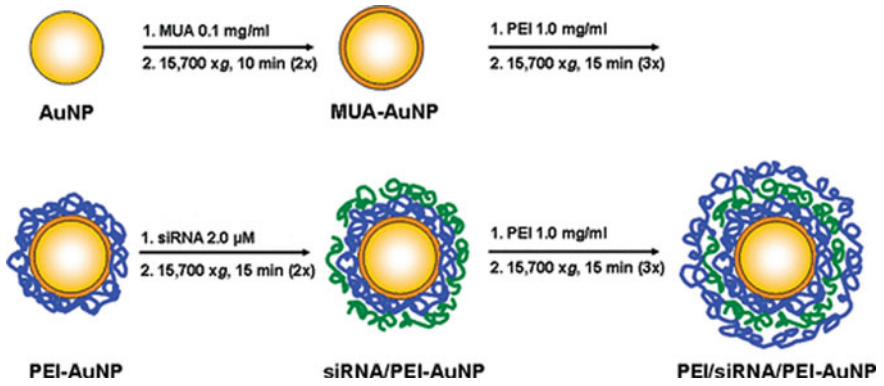

Fig. 4.6 Flowchart illustrating the layer-by-layer deposition applied to gold nanoparticles. After each coating step, gold nanoparticles were purified by centrifugation and resuspended in unbuffered 10 mM NaCl. Adapted with permission from Ref. [82]. Copyrights 2009 American Chemical Society

4.4.5.2 CRISPR–Cas9

The discovery and translation of clustered regularly interspaced short palindromic repeats (CRISPR)/Cas9 from bacteria to mammalian cells demonstrated a milestone for genome engineering due to its robustness, simplicity, and versatility [83–85]. There are two main types of gene-editing therapies that have been used for the CRISPR–Cas9 system: (1) non-homologous end joining (NHEJ), which completely silences disease-producing genes by introducing indel mutations, and (2) homology-directed repair (HDR), which reverts disease-producing gene mutations to their wild-type form. HDR-based therapies can treat most genetic diseases. Therefore, there is considerable interest in advancing HDR-based therapeutics. However, in vivo gene editing via HDR is difficult due to the targeted delivery of Cas9, guide RNA (gRNA), and donor DNA [86–90].

Gene therapy using adeno-associated viruses (AAVs) is presently the highly developed and used approach for delivering Cas9 in vivo. However, in vivo AAV delivery is difficult because a substantial portion of the human population has pre-existing immunity toward AAV, making them disqualified for therapeutics [91]. Moreover, the AAV-based Cas9-delivery system also generates considerable off-target genomic modifications because of the constant expression of Cas9. AAV also has a smaller packing size and may need several viruses to deliver Cas9 ribonucleoprotein (RNP) and donor DNA in vivo, which may reduce the HDR efficiency of the AAV-based Cas9-delivery system. Finally, the viral titers required to produce curative amounts of editing have been way higher than the clinically accepted levels [92–96]. Therefore, the reliable and effective delivery of CRISPR/Cas9 remains a significant challenge restricting its wide applications. For this reason, gold nanoparticles have been explored for efficient delivery [91, 97–100].

Lee et al. developed "CRISPR–Gold," which can deliver Cas9 RNP and donor DNA in vivo and stimulate HDR [90]. CRISPR–Gold is composed of gold nanoparticles coupled with DNA, which are complexed with donor DNA, Cas9 RNP, and poly(N-(N-(2-aminoethyl)-2-aminoethyl) aspartamide) (PAsp(DET)) which is an endosomal-disruptive polymer. CRISPR–Gold is created to be internalized by cells via endocytosis due to the cationic PAsp(DET), which complexes with the components of CRISPR–Gold (Fig. 4.7). After endocytosis, the cationic polymer on CRISPR–Gold activates endosomal disruption and triggers the delivery of CRISPR–Gold into the cytoplasm. Importantly, once in the cytoplasm, glutathione releases the DNA from the gold core of CRISPR–Gold, which causes the rapid release of Cas9 RNP and donor DNA.

CRISPR–Gold was capable of targeting CXCR4 in human embryonic stem cells, human-induced pluripotent stem cells, bone-marrow-derived dendritic cells, and the dystrophin gene in myoblasts with an HDR efficiency between 3 and 4%. CRISPR–Gold can also deliver Cas9 RNP and generate gene deletions in Ai9 mice. CRISPR–Gold was capable of correcting the mutated dystrophin gene in mdx mice to the wild-type sequence after a single dose and restoring dystrophin protein expression in muscle tissue. CRISPR–Gold can stimulate HDR in the dystrophin gene. In particular, 5.4% of the dystrophin gene in mdx mice was corrected back to the wild-type after CRISPR–Gold therapy. This correction rate was around 18 times higher than treatment with Cas9 RNP and donor DNA alone, with only a 0.3% correction rate.

Wang et al. used lipids such as DOTAP, DOPE, cholesterol, and PEG2000-DSPE to coat TAT-modified gold nanoparticles to deliver the Cas9-sgPlk-1 plasmid [101]. The lipids can facilitate the entry of gold nanoparticles into the cells, while TAT peptides can take the plasmid into the nucleus. A laser-triggered thermal effect caused the release of plasmid from nanoparticles. On day 20, the tumor volume decreased to about 42% with the nanoparticles and 20% with the nanoparticles and laser irradiation compared to the control group.

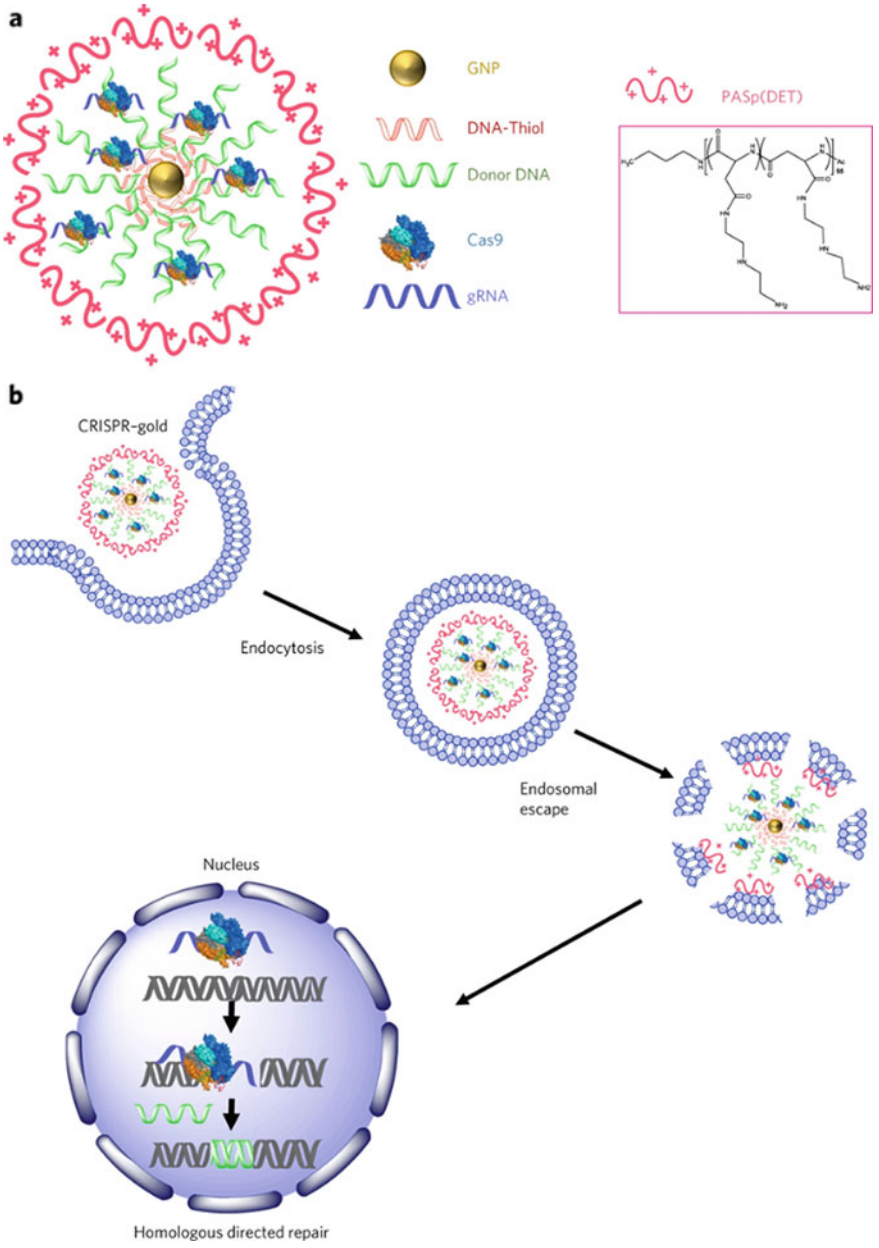

Fig. 4.7 **a** The components of CRISPR–Gold; **b** the working principle of CRISPR–Gold. Adapted with permission from Ref. [90]. Copyrights 2017 Springer Nature Limited

4.5 Conclusion and Future Perspective

This book chapter provides a summary of recent developments in the field of gold nanoparticles. Gold nanoparticles have been one of the most studied delivery systems because of their exciting physical, optical, chemical, and biological properties. Due to their biocompatibility, stability, and easy surface modifications, metal nanoparticles provide a promising platform for numerous biological applications, including the delivery of biomolecules, therapy, and diagnosis.

However, there are several critical issues that need to be addressed before their clinical applications. These issues may include the size and surface-dependent cytotoxicity, immune response, biodistribution, and targeting of a specific organ or tissue. These investigations will help design new delivery systems and enhance the understanding of nanomaterials' interaction with biological systems.

References

1. E.C. Dreaden, A.M. Alkilany, X. Huang, C.J. Murphy, M.A. El-Sayed, Chem. Soc. Rev. **41**, 2740 (2012)
2. R. Sardar, A.M. Funston, P. Mulvaney, R.W. Murray, Langmuir **25**, 13840 (2009)
3. J. Conde, J.T. Dias, V. GrazÃº, M. Moros, P.v. Baptista, J. M. de la Fuente, Front. Chem. **2** (2014)
4. P. Khandelwal, P. Poddar, J. Mater. Chem. B **5**, 9055 (2017)
5. S.S. Shankar, S. Bhargava, M. Sastry, J. Nanosci. Nanotech. **5**, 1721 (2005)
6. F. Kettemann, A. Birnbaum, S. Witte, M. Wuithschick, N. Pinna, R. Kraehnert, K. Rademann, J. Polte, Chem. Mater. **28**, 4072 (2016)
7. P.G. Jamkhande, N.W. Ghule, A.H. Bamer, M.G. Kalaskar, J. Drug Deliv. Sci. Technol. **53**, 101174 (2019)
8. C. Sharan, P. Khandelwal, P. Poddar, RSC Adv. **5**, 1883 (2015)
9. C. Sharan, P. Khandelwal, P. Poddar, RSC Adv. **5**, 91785 (2015)
10. P. Khandelwal, D.K. Singh, S. Sadhu, P. Poddar, Nanoscale **7**, 19985 (2015)
11. P. Khandelwal, D.K. Singh, S. Sadhu, P. Poddar, ChemPlusChem **79**, 134 (2014)
12. P. Khandelwal, A. Alam, A. Choksi, S. Chattopadhyay, P. Poddar, ACS Omega **3**, 4776 (2018)
13. D.K. Singh, R. Jagannathan, P. Khandelwal, P.M. Abraham, P. Poddar, Nanoscale **5**, 1882 (2013)
14. P.A. Pandey, G.R. Bell, J.P. Rourke, A.M. Sanchez, M.D. Elkin, B.J. Hickey, N.R. Wilson, Small **7**, 3202 (2011)
15. H. Nonomura, M. Nagata, H. Fujisawa, M. Shimizu, H. Niu, K. Honda, Appl. Phys. Lett. **86**, 163106 (2005)
16. T. Sugimoto, F. Shiba, T. Sekiguchi, H. Itoh, Colloids Surf. A Physicochem. Eng. Asp. **164**, 183 (2000)
17. T.S. Rodrigues, M. Zhao, T. Yang, K.D. Gilroy, A.G.M. da Silva, P.H.C. Camargo, Y. Xia, Chem. A Eur. J. **24**, 16944 (2018)
18. G. Su, C. Yang, J.-J. Zhu, Langmuir **31**, 817 (2015)
19. X. Ji, X. Song, J. Li, Y. Bai, W. Yang, X. Peng, J. Am. Chem. Soc. **129**, 13939 (2007)
20. J.D.S. Newman, G.J. Blanchard, Langmuir **22**, 5882 (2006)
21. Q. You, Y. Chen, J. Mater. Chem. C Mater. (2018)
22. D. Pan, J. Zhang, Z. Li, M. Wu, Adv. Mater. **22**, 734 (2010)
23. R.L. Penn, J.F. Banfield, Geochim. Cosmochim. Acta **63**, 1549 (1999)

24. Z. Liu, Y. Wang, Y. Zu, Y. Fu, N. Li, N. Guo, R. Liu, Y. Zhang, Mater. Sci. Eng. C **42**, 31 (2014)
25. N.-D. Tan, J.-H. Yin, Y. Yuan, L. Meng, N. Xu, Bull. Korean Chem. Soc. **1** (2018)
26. J. Liu, X. Ren, X. Meng, Z. Fang, F. Tang, Nanoscale **5**, 10022 (2013)
27. N. Xu, H. Li, Y. Wu, Anal. Chim. Acta **958**, 51 (2017)
28. J. Choi, S. Park, Z. Stojanović, H. Han, J. Lee, H.K. Seok, D. Uskoković, K.H. Lee, Langmuir **29**, 15698 (2013)
29. M. Carmen Bautista, O. Bomati-Miguel, M. del Puerto Morales, C. J. Serna, S. Veintemillas-Verdaguer, J. Mag. Mag. Mater. **293**, 20–27 (2005)
30. M. Gajbhiye, J. Kesharwani, A. Ingle, A. Gade, M. Rai, Nanomedicine **5**, 382 (2009)
31. Y. Zhou, Y. Yu, Y. Chai, R. Yuan, Talanta **181**, 32 (2018)
32. L. Shang, L. Yang, F. Stockmar, R. Popescu, V. Trouillet, M. Bruns, D. Gerthsen, G.U. Nienhaus, Nanoscale **4**, 4155 (2012)
33. K.-T. Chuang, Y.-W. Lin, J. Phys. Chem. C **121**, 26997 (2017)
34. Y. Liu, G.-F. Tian, X.-W. He, W.-Y. Li, Y.-K. Zhang, J. Mater. Chem. B **4**, 1276 (2016)
35. J.K.-J. Li, J. Med. Biol. Eng. **33**, 23 (2013)
36. F. Zhou, B. Feng, H. Yu, D. Wang, T. Wang, J. Liu, Q. Meng, S. Wang, P. Zhang, Z. Zhang, Y. Li, Theranostics **6**, 679 (2016)
37. T.C. Johnstone, K. Suntharalingam, S.J. Lippard, Chem. Rev. **116**, 3436 (2016)
38. X. Ling, J. Tu, J. Wang, A. Shajii, N. Kong, C. Feng, Y. Zhang, M. Yu, T. Xie, Z. Bharwani, B.M. Aljaeid, B. Shi, W. Tao, O.C. Farokhzad, ACS Nano Acsnano 8b06400 (2018)
39. Y. Shi, J. Goodisman, J.C. Dabrowiak, Inorg. Chem. **52**, 9418 (2013)
40. D. Pornpattananangkul, S. Olson, S. Aryal, M. Sartor, C. Huang, K. Vecchio, L. Zhang, ACS Nano **4**, 1935 (2010)
41. J. Li, X. Qu, G.F. Payne, C. Zhang, Y. Zhang, J. Li, J. Ren, H. Hong, C. Liu, Adv. Funct. Mater. **25**, 1404 (2015)
42. G. Liu, J. Li, D.-Q. Feng, J. Zhu, W. Wang, Anal. Chem. **89**, 1002 (2017)
43. H.S. El-Sawy, A.M. Al-Abd, T.A. Ahmed, K.M. El-Say, V.P. Torchilin, ACS Nano **12**, 10636 (2018)
44. F. Zhu, G. Tan, Y. Jiang, Z. Yu, F. Ren, Biomater Sci **6**, 2905 (2018)
45. X. Wang, X. Cai, J. Hu, N. Shao, F. Wang, Q. Zhang, J. Xiao, Y. Cheng, J. Am. Chem. Soc. **135**, 9805 (2013)
46. L. Qiu, Y. Zhao, N. Cao, L. Cao, L. Sun, X. Zou, Sens. Actuators B Chem. **234**, 21 (2016)
47. C.K. Kim, P. Ghosh, V.M. Rotello, Nanoscale **1** (2009)
48. C.W. Ng, J. Li, K. Pu, Adv. Funct. Mater. **28**, 1804688 (2018)
49. E.S. Shibu, M. Hamada, N. Murase, V. Biju, J. Photochem. Photobiol. C **15**, 53 (2013)
50. B.S. Dash, S. Das, J.-P. Chen, Int. J. Mol. Sci. **22**, 6658 (2021)
51. Z. Sun, L.-P. Zhang, F. Wu, Y. Zhao, Adv. Funct. Mater. **27**, 1704079 (2017)
52. A. Amendoeira, L.R. García, A.R. Fernandes, P.v. Baptista, Adv. Ther. (Weinh) **3**, 1900153 (2020)
53. L.v. Nair, S.S. Nazeer, R.S. Jayasree, A. Ajayaghosh, ACS Nano **9**, 5825 (2015)
54. S.S. Lucky, K.C. Soo, Y. Zhang, Chem. Rev. **115**, 1990 (2015)
55. S. Bhana, G. Lin, L. Wang, H. Starring, S.R. Mishra, G. Liu, X. Huang, ACS Appl. Mater. Interfaces **7**, 11637 (2015)
56. D. de Melo-Diogo, C. Pais-Silva, D.R. Dias, A.F. Moreira, I.J. Correia, Adv. Healthc. Mater. **6**, 1700073 (2017)
57. M.B.A. Nanocluster **102**, 2328 (2015)
58. W. Li, H. Zhang, X. Guo, Z. Wang, F. Kong, L. Luo, Q. Li, C. Zhu, J. Yang, Y. Lou, Y.-Z. Du, J. You, ACS Appl. Mater. Interfaces **9**, 3354 (2017)
59. M. Kim, J. Lee, J. Nam, Adv. Sci. **6**, 1900471 (2019)
60. L.C.W. Lin, S. Chattopadhyay, J.C. Lin, C.M.J. Hu, Adv. Healthc. Mater. **1701395**, 1 (2018)
61. S.T. Reddy, A.J. van der Vlies, E. Simeoni, V. Angeli, G.J. Randolph, C.P. O'Neil, L.K. Lee, M.A. Swartz, J.A. Hubbell, Nat. Biotechnol. **25**, 1159 (2007)

62. U. Sahin, P. Oehm, E. Derhovanessian, R.A. Jabulowsky, M. Vormehr, M. Gold, D. Maurus, D. Schwarck-Kokarakis, A.N. Kuhn, T. Omokoko, L.M. Kranz, M. Diken, S. Kreiter, H. Haas, S. Attig, R. Rae, K. Cuk, A. Kemmer-Brück, A. Breitkreuz, C. Tolliver, J. Caspar, J. Quinkhardt, L. Hebich, M. Stein, A. Hohberger, I. Vogler, I. Liebig, S. Renken, J. Sikorski, M. Leierer, V. Müller, H. Mitzel-Rink, M. Miederer, C. Huber, S. Grabbe, J. Utikal, A. Pinter, R. Kaufmann, J.C. Hassel, C. Loquai, Ö. Türeci, Nature **585**, 107 (2020)
63. A. Schudel, A.P. Chapman, M.K. Yau, C.J. Higginson, D.M. Francis, M.P. Manspeaker, A.R.C. Avecilla, N.A. Rohner, M.G. Finn, S.N. Thomas, Nat. Nanotechnol. **15**, 491 (2020)
64. C. Bourquin, D. Anz, K. Zwiorek, A.-L. Lanz, S. Fuchs, S. Weigel, C. Wurzenberger, P. von der Borch, M. Golic, S. Moder, G. Winter, C. Coester, S. Endres, J. Immunol. **181**, 2990 (2008)
65. L. Jeanbart, M. Ballester, A. de Titta, P. Corthesy, P. Romero, J.A. Hubbell, M.A. Swartz, Cancer Immunol. Res. **2**, 436 (2014)
66. S.N. Thomas, E. Vokali, A.W. Lund, J.A. Hubbell, M.A. Swartz, Biomaterials **35**, 814 (2014)
67. T. Fifis, A. Gamvrellis, B. Crimeen-Irwin, G.A. Pietersz, J. Li, P.L. Mottram, I.F.C. McKenzie, M. Plebanski, J. Immunol. **173**, 3148 (2004)
68. J.P.M. Almeida, E.R. Figueroa, R.A. Drezek, Nanomedicine **10**, 503 (2014)
69. I.H. Lee, H.K. Kwon, S. An, D. Kim, S. Kim, M.K. Yu, J.H. Lee, T.S. Lee, S.H. Im, S. Jon, Angewandte Chemie Int. Edn. **51**, 8800 (2012)
70. S. Ahn, I.H. Lee, S. Kang, D. Kim, M. Choi, P.E. Saw, E.C. Shin, S. Jon, Adv. Healthc. Mater. **3**, 1194 (2014)
71. K. Haume, S. Rosa, S. Grellet, M.A. Śmiałek, K.T. Butterworth, A.v. Solov'yov, K.M. Prise, J. Golding, N.J. Mason, Cancer Nanotechnol. **7**, 8 (2016)
72. D. Luo, A. Johnson, X. Wang, H. Li, B.O. Erokwu, S. Springer, J. Lou, G. Ramamurthy, C.A. Flask, C. Burda, T.J. Meade, J.P. Basilion, Nano Lett. **20**, 7159 (2020)
73. N. Goswami, Z. Luo, X. Yuan, D.T. Leong, J. Xie, Mater. Horiz. **4**, 817 (2017)
74. N. Ma, F. Wu, X. Zhang, Y. Jiang, H.-R. Jia, H. Wang, Y. Li, P. Liu, N. Gu, Z. Chen, ACS Appl. Mater. Interfaces **9**, 13037 (2017)
75. X. Fang, Y. Wang, X. Ma, Y. Li, Z. Zhang, Z. Xiao, L. Liu, X. Gao, J. Liu, J. Mater. Chem. B **5**, 4190 (2017)
76. J.F. Hainfeld, F.A. Dilmanian, D.N. Slatkin, H.M. Smilowitz, J. Pharm. Pharmacol. **60**, 977 (2010)
77. F. Ghahremani, D. Shahbazi-Gahrouei, A. Kefayat, H. Motaghi, M.A. Mehrgardi, S.H. Javanmard, RSC Adv. **8**, 4249 (2018)
78. Q. Chen, J. Chen, Z. Yang, J. Xu, L. Xu, C. Liang, X. Han, **1802228**, 1 (2019)
79. D. Huo, S. Liu, C. Zhang, J. He, Z. Zhou, H. Zhang, Y. Hu, ACS Nano **11**, 10159 (2017)
80. Y. Ding, Z. Sun, Z. Tong, S. Zhang, J. Min, Q. Xu, L. Zhou, Z. Mao, H. Xia, W. Wang, Theranostics **10**, 5195 (2020)
81. D.A. Giljohann, D.S. Seferos, A.E. Prigodich, P.C. Patel, C.A. Mirkin, J. Am. Chem. Soc. **131**, 2072 (2009)
82. A. Elbakry, A. Zaky, R. Liebl, R. Rachel, A. Goepferich, M. Breunig, Nano Lett. **9**, 2059 (2009)
83. I. Kaushik, S. Ramachandran, S.K. Srivastava, Semin. Cell Dev. Biol. **96**, 4 (2019)
84. M. Chen, A. Mao, M. Xu, Q. Weng, J. Mao, J. Ji, Cancer Lett. **447**, 48 (2019)
85. F.J. Sánchez-Rivera, T. Jacks, Nat. Rev. Cancer **15**, 387 (2015)
86. F.A. Ran, P.D. Hsu, J. Wright, V. Agarwala, D.A. Scott, F. Zhang, Nat. Protoc. **8**, 2281 (2013)
87. H. Nishimasu, X. Shi, S. Ishiguro, L. Gao, S. Hirano, S. Okazaki, T. Noda, O.O. Abudayyeh, J.S. Gootenberg, H. Mori, S. Oura, B. Holmes, M. Tanaka, M. Seki, H. Hirano, H. Aburatani, R. Ishitani, M. Ikawa, N. Yachie, F. Zhang, O. Nureki, Science (1979) **9129**, eaas9129 (2018)
88. C. Arnold, Nat. Med. **27**, 184 (2021)
89. H. Shivram, B.F. Cress, G.J. Knott, J.A. Doudna, Nat. Chem. Biol. **17**, 10 (2021)
90. K. Lee, M. Conboy, H.M. Park, F. Jiang, H.J. Kim, M.A. Dewitt, V.A. Mackley, K. Chang, A. Rao, C. Skinner, T. Shobha, M. Mehdipour, H. Liu, W.C. Huang, F. Lan, N.L. Bray, S. Li, J.E. Corn, K. Kataoka, J.A. Doudna, I. Conboy, N. Murthy, Nat. Biomed. Eng. **1**, 889 (2017)

91. Z. Glass, Y. Li, Q. Xu, Nat. Biomed. Eng. **1**, 854 (2017)
92. X. Tian, T. Gu, S. Patel, A.M. Bode, M.-H. Lee, Z. Dong, NPJ Precis. Oncol. **3**, 8 (2019)
93. F.A. Khan, N.S. Pandupuspitasari, H. Chun-Jie, Z. Ao, M. Jamal, A. Zohaib, F.A. Khan, M.R. Hakim, Z. ShuJun, Oncotarget **7**, 52541 (2016)
94. C. Jiang, X. Lin, Z. Zhao, Trends Mol. Med. **25**, 1039 (2019)
95. M.K. White, K. Khalili, Oncotarget **7**, 12305 (2016)
96. M. Martinez-Lage, P. Puig-Serra, P. Menendez, R. Torres-Ruiz, S. Rodriguez-Perales, Biomedicines **6**, 105 (2018)
97. S. Aghamiri, S. Talaei, A.A. Ghavidel, F. Zandsalimi, S. Masoumi, N.H. Hafshejani, V. Jajarmi, J. Drug Deliv. Sci. Technol. **56**, 101533 (2020)
98. F. Chen, M. Alphonse, Q. Liu, WIREs Nanomed. Nanobiotechnol. **12** (2020)
99. Y. Xu, R. Liu, Z. Dai, Nanoscale **12**, 21001 (2020)
100. B.E. Givens, Y.W. Naguib, S.M. Geary, E.J. Devor, A.K. Salem, AAPS J. **20**, 108 (2018)
101. P. Wang, L. Zhang, W. Zheng, L. Cong, Z. Guo, Y. Xie, L. Wang, R. Tang, Q. Feng, Y. Hamada, K. Gonda, Z. Hu, X. Wu, X. Jiang, Angew. Chem. **130**, 1507 (2018)

Chapter 5
Metal Oxide Nanoparticles: Synthesis, Properties, Characterization, and Applications

Nirav Joshi, Deepak K. Pandey, Bhavita G. Mistry, and Dheeraj K. Singh

Abstract Metal oxide nanoparticles (MONPs) are a substantial category of nanomaterials that have numerous implications in science and technology owing to their distinctive characteristics such as high surface-to-volume ratio, large surface area, and abundance on earth. The present book chapter attempts to present a brief summary of research on MONPs, including available synthesis routes, techniques for characterization, and some of the unique nanoscale physicochemical features. Further, we provided an overview of the defining specific applications of MONPs in a variety of applied nanotechnology domains. We anticipate that this chapter will contribute to an increase in understanding and the recent developments in the utilizations of MONPs in specific industrial sectors.

Keywords Metal oxide nanoparticles · Synthesis · Characterization techniques · Properties · Wastewater treatment · Solar cells · Batteries

5.1 Introduction

Nanotechnology paves the way for a plethora of opportunities and has the potential to provide answers to some of the most pressing challenges confronted by human civilization on a global scale through the utilization of technologically advanced nanoparticles. It is only possible by the exceptional properties of nanosized particles, which they possess as a result of their one-of-a-kind size and shape [1, 2]. New nanotechnology applications in energy generation, conversion, storage, optics, microelectronics, mechanical, and ceramics engineering are becoming more commonplace every day [2]. Among the multitude of nanoparticles, metal oxide nanoparticles (MONPs) stand out and are receiving considerable attention from both academia

N. Joshi · D. K. Pandey · D. K. Singh (✉)
Department of Basic Sciences, Institute of Infrastructure Technology Research And Management, Ahmedabad, Gujarat 380026, India
e-mail: dheerajsingh84@gmail.com; dheerajsingh@iitram.ac.in

B. G. Mistry
Macromolecular Materials Laboratory, Applied Chemistry Department, Faculty of Technology and Engineering, The Maharaja Sayajirao University of Baroda, Vadodara 390001, India

D. K. Singh et al. (eds.), *Nanomaterials*,
https://doi.org/10.1007/978-981-19-7963-7_5

and industry [3–8]. In addition, the distinctive physicochemical characteristics, such as relatively large specific surface area and the surface-to-volume ratio [2, 9] as compared to their bulk counterparts, play a key role in many areas of science and industry. Another crucial factor contributing to their increased interest and extensive investigation is that they are abundant on earth, environmentally benign, inexpensive, and, in certain instances, chemically robust with appropriate electrical and optical properties [10–17]. Further notable characteristics of these materials comprise their excellent high dielectric constant, optical transparency, wide bandgap, high carrier mobility, and superior superconductivity [17, 18].

Many different synthesis processes allow metals to produce a wide range of oxide compounds [9, 19]. When it comes to metal oxides, the *d*-shell is usually partially filled, whereas the *s*-shell is always completely filled with electrons [20]. MONPs can display semiconductor, metallic, or insulator properties [21] due to their distinctive electronic structure, which is made up of positive metallic and negative oxygen ions [17]. In transition metal oxides, the energy difference between the two possible configurations of the cation d^n and the electron configuration d^{n+1} or d^{n-1} is known to be minimal, allowing for rapid transitions between the various forms, albeit with unstable structures. Metal oxides having electronic configurations of d^0 and d^{10} are regarded as stable materials. Transition-metal oxides like V_2O_5, TiO_2, and WO_3 have the d^0 configuration, but post-transition-metal oxides like SnO_2 and ZnO have the d^{10} configuration. Pre-transition metal oxides are anticipated to be inactive in a number of applications due to their high bandgaps, which make it difficult for electrons and holes to create [22].

Small size and a high density of corner or edge surface sites make MONPs particularly interesting in terms of their unique physical and chemical characteristics [23]. Three significant classes of fundamental characteristics in any material are anticipated to be influenced by particle size. The first category includes the structural properties, specifically the cell parameters and lattice symmetry [24]. Typically, bulk oxides are stable and have crystal structures that are clearly characterized. However, when particle size decreases, surface free energy and stress become increasingly important. It is necessary for a nanoparticle to have a low surface free energy to show mechanical or structural stability. As a result of such necessity, phases with low stability in bulk substances can attain high stability in nanostructures. TiO_2, VO_x, Al_2O_3, and MoO_x oxides have all been found to have this structural phenomenon [25–27]. The electrical characteristics of the oxide are connected to the second noteworthy influence of size. The existence of distinct, atom-like electronic states causes the nanostructure to create the so-called quantum confinement effects in any material. The optical bandgap and exciton levels shift as a result of quantum confinement in oxides, which can be observed experimentally [28, 29]. The long-range impacts of the Madelung fields, which are a crucial consideration when dealing with the electrical characteristics of a bulk oxide surface, are absent or constrained in a nanostructured oxide [30–32]. The solid's physical and chemical properties, which make up the third category of properties affected by size in a basic classification, are primarily driven by its structural and electrical properties. A reduced average oxide particle size alters the bandgap's size [32, 33], which has a significant impact on the chemical reactivity

and conductivity [34, 35]. When it comes to 2D-infinite surfaces, surface properties of nanostructured metal oxides are significantly altered, resulting in solids with novel sorption or acid/base properties [36]. Additionally, the existence of O vacancies or undercoordinated atoms (such as edges or corners) in an oxide nanoparticle should result in particular geometrical arrangements and occupied electronic states that are above the valence band of the bulk counterparts [37–39], increasing the chemical activity of the system [36, 40–42]. The aforementioned facts reveal how nanometal oxides' structure, size, and arrangements of electrons in shells play a crucial part in determining their unique properties appropriate for a wide range of applications.

Further, nanometal oxides display distinctive and controllable optoelectronic, magnetic, mechanical, optical, electrical, thermal, photochemical properties, and catalytic applications [43]. Metal oxides' size, structure, composition, stoichiometry, and doping all allow for the engineering of their electrical, physical, and chemical properties [44, 45]. In addition, transition metal oxides can take on ferromagnetic and semiconductive states at different temperatures. Metal oxides can be recognized from other materials and employed in a variety of applications because of all these distinctive qualities. Due to the aforementioned unique characteristics, nanostructured metal oxides are regarded as one of the most exciting functional materials and are still an active research area even after more than three decades since their emergence. Additionally, a thorough understanding of the surface and core properties is crucial for building innovative nanoproducts. The present chapter, therefore, attempts to portray the state-of-the-art progress of nanometal oxides with the existing synthesis methods, characterization techniques, their characteristics, and various types of applications. The main aim of the chapter is to give a thorough overview to new researchers of the most recent developments in the field of metal oxides as well as how they are used in a number of applications, including solar cells, water purification, energy storage, sensor technology, biomedical applications, etc. In this chapter, the impact of MONPs' characteristics and how these affect their industrial uses will receive special focus.

5.2 Synthesis of MONPs

This section will cover detailed synthesis methods available to produce a variety of MONPs including different shapes and sizes. As the surface-to-volume ratio of the synthesized products is the most crucial factor responsible for their tremendous use in mechanics, optics, electronics, biotechnology, energy storage industry, sensor, solar and fuel cells, cosmetics, food, paints, personal care products, microbiology, environmental remediation, wastewater treatment, catalysis, medicine, numerous engineering fields, and material science. Therefore, the purpose behind the synthesis of MONPs is not only its great properties but also to change the nanomaterials' morphologies with high performance, understand its phenomenon in different dimensional systems, and make a new generation of nanodevices. In this direction, various

physical, chemical, biological, and hybrid methods exist to synthesize these nanomaterials. The physical process involved flame spray pyrolysis, chemical vaporization, laser ablation, etc., co-precipitation/precipitation, hydrothermal, sol–gel, ultrasonication, vapor deposition, etc., methods for chemical processes [46, 86]. Some materials prepared in nature by microorganisms, animals, and plants can be replicated in laboratories, even on a wide scale. It is seen as a very appealing option for achieving environmentally or so-called green synthesis of MONPs [47, 48]. As it is not possible to cover the synthesis of each NP by each synthesis method in this overview, only a few examples of MONPs' preparation using each method are presented in this section.

5.2.1 Physical Methods

Spray pyrolysis/Flame spray pyrolysis

This simple method is a continuous and single-step process, providing economic viability and does not require high-level equipment, producing fine MONPs particles and thin films [49]. The solution-containing precursor is injected or sprayed onto a hot substrate in the furnace using a nano-porous nebulizer, causing the precursor to decompose and form the final desired material on the substrate. To begin, the precursor solution's chemical composition must include compounds that, after pyrolysis, will yield the required different chemical composition. Second, the acceptable range of synthesis temperatures is used to produce the final material's morphological characteristics. The aerosol droplet size distribution and aerosol generation mechanism will determine this. The carrier gas and its flux rate will either increase or decrease the likelihood of a reactive interaction with the precursor compound. Finally, the chemical reaction in the gas phase or on a hot substrate determines whether the synthesized material is a powder or a film coating. Zinc oxide (ZnO) is produced through this technique; its morphological study determined by TEM shows hexagonal wurtzite structure and XRD gives its crystal structure [50]. Another successfully synthesized nanoparticle is Fe_2O_3 by the same technique with the particle size 315 to 675 nm with the high surface energy characterized from the SEM analysis at the different temperature ranges [51].

The flame spray pyrolysis (FSP) method employs low-cost, less volatile, and frequently hygroscopic precursors, such as metal nitrates and acetates, dissolved in appropriate solvents. The MONPs are prepared by burning unwanted compounds from the precursor, which is nebulized [52]. Previously, Marshall et al. explained how droplets of an aqueous zinc acetate solution have been fed into the flame of a Meker burner and pyrolyzed into ZnO fumes in a 1971 research article [53]. Titania (TiO_2) is the additional manufacturing aerosol resource in terms of volume and value derived from this technique [54]. Synthesis of bismuth oxide (Bi_2O_3) nanoparticles from bismuth nitrate solutions yielded 10 nm diameter pure, homogenous, and crystalline nanoparticles, exemplifying the FSP approach for producing such nanoparticles.

XRD is typically used to determine the crystallinity of MONPs, and in this case, the same method has been used to determine the crystallinity and crystal structure. The increasing oxygen gas flow rate by increasing the surface area of Bi_2O_3 results in a controlled size and excellent production rate of Bi_2O_3 [55]. A typical schematic illustration of spray pyrolysis and FSP methods is given in Fig. 5.1a.

Sputter deposition

The sputter deposition technique is widely used for the formation of stoichiometric thin films from the given materials and could be an alloy, a ceramic, or a compound. Further, it can also be used to create non-porous compact films. It is an excellent method for depositing layered films for reflectors or magnetic films for electronic and optical applications. An inert gas ion such as Ar^+ is targeted at a high energy level which are depending on the ions mass to target the atom mass ratio. At the ground level, ions become neutral, and at the same time incident ions get rebounded, causing collision effects in target atoms. It disturbs many of the atoms in the target, causing vacant positions, creating interstitials, and other deformities, desorbing some adsorbates, generating particles while burning energy to target atoms, and even sputtering out some target atomic nuclei, clusters, ions, and electrons. Different methods of sputtering are available typically including Direct Current (DC) sputtering, Radio Frequency (RF) sputtering, and magnetron sputtering methods. A general ray diagram of the process is shown in Fig. 5.1b.

The TiO_2 nanoparticles were prepared from the sputter deposition under an Ar-O_2 atmosphere with high power and the diameter of prepared MONPs was found to

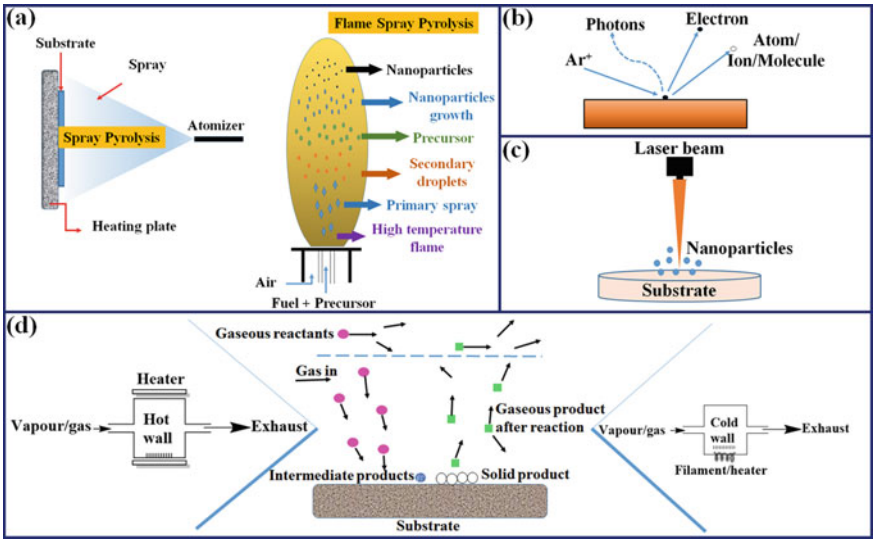

Fig. 5.1 Schematic of (**a**) Spray pyrolysis and flame spray pyrolysis, (**b**) Sputter deposition, (**c**) Laser ablation technique, and (**d**) Chemical vapor deposition

be 25–75 nm with the uniform crystalline phase and different composition of Ti–O [56]. One of the previous investigations detailed the formation of WO_x, MoO_x, NbO_x, and TiO_x MONPs by employing the Sputter deposition technique, and transmission electron microscopy (TEM) analysis verified the particle size of 20 nm. TEM, which employs an electron beam, is frequently used to photograph a sample of nanoparticles and is the preferred technique for accurately determining the particle size [57].

Laser ablation

The laser ablation of the material is achieved using high-power laser pulses which include a high vacuum system with inert gas facilities, target material, laser beam, and cooled surface (substrate). Since certain materials' substrates frequently reflect other wavelengths, like IR or visible light, ultraviolet (UV) lasers, including excited monomer lasers, are typically required in this technique. Here, the intense laser beam evaporates the substrate's atoms, causing a collision between the reactive gases that, when applied to the cooled surface, form clusters (see Fig. 5.1c for ray diagram). When it comes to particle size and distribution, gas pressure is essential. The formation of alloys or compounds is achieved by simultaneously evaporating a further material and mixing the two vaporized materials in inert gas. This technique can create unique phases of components that are not formed usually.

Y_2O_3, Gd_2O_3, $Y_3Al_5O_{12}$, Al_2O_3, and $YAlO_3$ NPs synthesized by this method along with average sizes ranging from 2 to 4.5 nm and narrow size distribution [58]. Some chemical techniques make it extremely difficult to produce MONPs and hydroxides and prepare their layers; laser ablation is a one-spot method that can accomplish this. Sasaki et al. synthesized TiO_2 and SnO_2 NPs via this technique and the particle size was observed to be very small (2–6 nm in diameter) [59].

Chemical vapor deposition

To obtain coatings of various inorganic or organic materials, a hybrid method using chemicals in the vapor phase is traditionally used in industries due to its simple processing. In the basic CVD techniques, reactant gas flows toward the substrate at a high temperature, and various products produced by the reactant crack that spread across the substrate's surface and the formation of the suitable film at the proper region go through a chemical reaction. After the reaction, some impurities are left from the substrate and go to the gaseous phase. Using a carrier gas, given material vapors can be frequently pumped into the reactor vessel, and sometimes reactions proceed in the gas phase. On the substrate, temperatures around 300–1200 °C are required and it is heated by two approaches: Hot and cold walls. In the hot wall, deposition occurred at the wall of the reactor. Furthermore, reactions can occur in the gas phase with a hot wall design, which is suppressed in a cold wall setup. Again, plasma-chemical reaction coupling in a cold wall setup is possible. A schematic diagram of the CVD technique and its working mechanism is shown in Fig. 5.1d. TEM investigation proved that CVD successfully coated MONPs like SiO_2 and TiO_2 on the surface of the gold up to 10 nm in size [60].

5.2.2 Chemical Methods

Sol–gel method

The word "sol" and "gel" comes from M. Ebelman for the first time in 1845 [61]. This is the most reliable approach in the chemical process because it produces less pollution, uses a simple precursor, and does not need any more sophisticated equipment. Here, solid metal precursor particles are added to the sols (a subclass of colloids), which are then incorporated into a gel-like liquid network to produce small particles or thin films through the evaporation process [61]. The schematic illustration of this method is shown in Fig. 5.2.

Zinc 2-ethyl hexanoate, which contains 1% ethylene glycol monomethyl ether, tetramethylammonium ($(CH_3)_4NOH$) aqueous solution, and isopropanol, was used as precursors to create nanocrystalline ZnO powder. The TEM results revealed that the particles created by this investigation ranged in size from 20 to 50 nm [62]. Tin tetrachloride pentahydrate ($SnCl_4.5H_2O$) was used as a precursor to generating the SnO_2 NPs [63]. Tetraethylorthosilicate was used as a precursor in the sol–gel process to create SiO_2 NPs, which were then analyzed by TEM, giving a particle size of 25 nm and an excellent XRD pattern match [64].

Hydrothermal

This method is useful for the preparation of novel nano- and micro-sized MONPs. In this preparation method, an "autoclave" is used as a reaction vessel made of steel or another metal-containing material at a high temperature of around 300 °C and high pressure at 100 bars. During synthesis, the chemical precursor is dissolved in distilled water/solvent and put into an autoclave for a fixed amount of time. Mostly

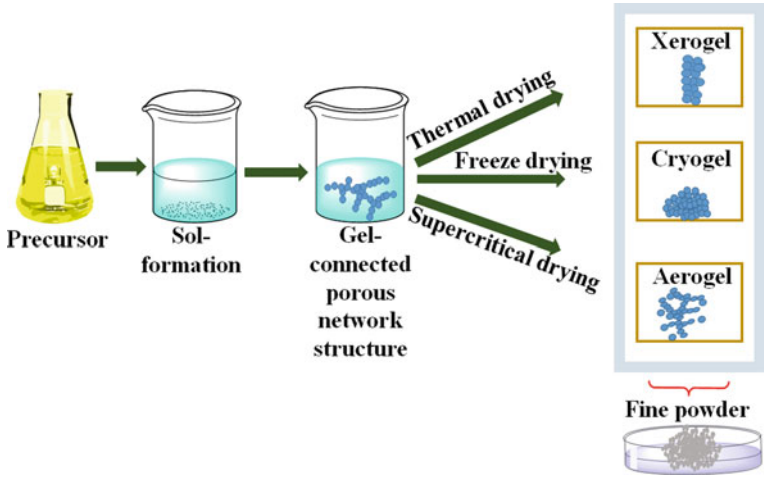

Fig. 5.2 Synthesis of MONPs via sol–gel method

this technique is useful for non-dissolving materials at a lower temperature. "Forced hydrolysis" is a different type of hydrothermal synthesis process in which inorganic metal salts are typically dissolved in dilute solutions (10^{-2} to 10^{-4} M) and hydrolysis is performed at temperatures over 150 °C [61, 65]. The hydrothermal approach was used to vary the particle size of iron oxide nanoparticles as a result of increasing the reaction temperature [66]. The chemical materials' composition was confirmed by FT-IR after the XRD revealed the maghemite's crystalline phase. The aforementioned study indicates that the hydrothermal reaction has a greater role in the development of various particles of different sizes and structures [66]. The schematic overview of various chemical methods for the synthesis of MONPs is depicted in Fig. 5.3.

Sonochemical

In this approach, the ultrasonic waves used to pass in the liquid precursor and the bubbles formed which are small and it is continuously growing to create a certain particle size and burst, releasing high energy ~ 5000 °C and higher pressure (a few hundred times higher than atmospheric pressure). The solute in the liquid must diffuse to the expanding bubble for the reaction to take place in the gas phase. The handling of solute and solvents is quite difficult and only reactants should find their position within the bubble in the form of vapor, non-volatile liquids would hinder bubble formation, which is desired. The solvents must be stable and inert to ultrasonic radiation. The particle size is also affected by the cooling rate, as particles are highly

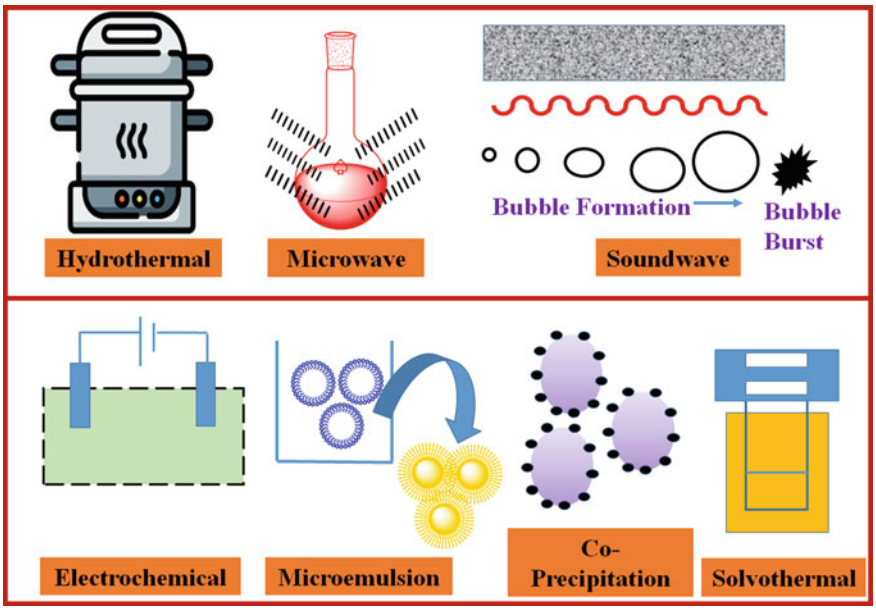

Fig. 5.3 Overview of chemical methods for the synthesis of MONPs

Table 5.1 List of MONPs prepared by sonochemical method

MONPs	Particle size (nm)	References
TiO_2	Smaller size	[68, 69]
ZnO	Nanorod-180 nm Nano cup-250 to 300 nm Nano disks-140 nm	[70]
MoO_3	Micrometer-sized whiskers	[71]
V_2O_5	400–900 nm	[72]

amorphous and these particles are more beneficial to compared crystalline one [61, 67]. Some of the examples of this method are given in Table 5.1.

Solvothermal method

This method is used to prepare a range of nanomaterials by dispersing the starting material in an appropriate solvent and subjecting it to reasonably high temperatures and high pressure which lead to product formation. An organometallics complex of titanium was utilized for the TiO_2 nanoparticle synthesis [67]. Moreover, this method allows for the preparation of ultra-small nanoparticles (<5 nm) such as 2.5×4.3 nm of TiO_2 and 1.6 ± 0.3 nm WO_x nanoparticles [73].

Electrochemical

The two-electrode setup including electrolyte solution is used for the synthesis of MONPs. Here, bulk metals are used as the anode which is transferred into metal clusters. This metal cluster is stabilized by the salt solution in the form of an electrolyte. All the reaction setup is put into the inert atmosphere to avoid oxygen contact. The bulk metal is oxidized at the anode and the metal cations move to the cathode. The role of the stabilizer is to prevent the agglomeration of MONPs. Examples of MONPs prepared by electrochemical processes are CuO and Cr_2O_3 NPs [65].

Microwave

This is the simplest method for the synthesis of MONPs. Here, the precursor is dissolved in distilled water and then continuously stirred for 10 to 15 min at room temperature, and then a white color gel is formed. The mixture receives microwave radiation before cooling naturally at ambient temperature. The precipitate is vacuum-filtered, cleaned with deionized water and pure ethanol, and then dried in a vacuum for 1 h at 80 °C [65, 74]. The anti-bacterial properties of CaO and MgO NPs have been synthesized and tested by this method.

Co-precipitation

The addition of base (commonly ammonium hydroxide and sodium hydroxide) in a precursor salt transforms the metal into its corresponding metal hydroxide in co-precipitation in an aqueous medium. The obtained oxo-hydroxide precipitate is then eliminated by heating and the formation of the desired MONPs takes place [65]. The disadvantage of this method is uncontrolled particle size and it is managed by the use

of the alternate metal salt solution, its ionic nature, and pH. This method has been employed in synthesizing MONPs like ZnO [75], MnO_2 [76], $BiVO_4$ [77], MgO [78], etc.

Microemulsion

In this method, two immiscible phases (oil and water) are separated by the monolayer of surfactant molecules generating two binary systems including oil/surfactant and water/surfactant. Surfactant has a hydrophobic tail dissolved in the oil phase and a head group of hydrophilic chain in the aqueous medium. Surfactant, oil, water, and metal precursor all are mixed and stirred at ambient temperature to make a homogeneous solution. To allow the precipitation of NPs, oxidizing/reducing and precipitating agents are then added to this reaction mixture while being vigorously stirred. After filtering, purifying, and drying properly, the formation of MONPs takes place [79]. For the formation of the nanoparticles, microemulsions serve as nanoreactors. Various MONPs synthesized by this method such as TiO_2 [80], ZnO [81], CuO [82], etc.

5.2.3 Green Synthesis

The green approach is the most pertinent in the field of nanotechnology, aside from physical and chemical methods used in the last decade to create MONPs. Thus, some fundamental ideas of "green synthesis" can be used to describe a number of aspects, including waste prevention/minimization, derivatives/pollution management, the use of safer or non-toxic solvents, as well as sustainable materials. Various biological materials such as bacteria, fungi, algae, plant extract, etc. have been used for the green synthesis of metallic nanoparticles. Among all these materials, the plant extract form is easy and more beneficial than bacteria- and fungi-mediated MONPs.

Plants

Biomolecules found in plants, such as proteins, coenzymes, and carbohydrates, have a remarkable capacity to transform metal salts into nanoparticles. Here, plant extract material is mixed with the metal precursor solution and stirred on the magnetic stirrer to follow various conditions like maintaining its pH, concentration of metal precursor solution, reaction time, and its temperature. These natural sources have both reducing as well as stabilizing agent properties. After the reaction, the smaller particles get centrifuged, and the collected particles are dried and weighed [47]. The general mechanism of the synthesis of MONPs is shown in Fig. 5.4. The spherical shape of the Al_2O_3 NPs can be synthesized through this technique in which a material extract from coffee, tea, and Triphala kind of herbal plants is taken which consists of phenolic compounds. Then it was irradiated with a 540 W microwave [83]. Similarly, Ansari et al. used a 1:4 ratio of metal salt and leaf extracts of *Cymbopogon citratus* (lemongrass) to obtain the same metal oxide particles [112]. Thovhogi et al. used an extract of *Hibiscus sabdariffa* to make green-mediated CeO_2 NPs, which had a

spherical morphology with a size of roughly 3.9 nm. ATR-IR spectroscopy revealed a distinctive band at 483.8 cm^{-1} attributed to CeO stretching mode and face-centered cubic phase was confirmed by XRD [84].

Microorganism

Depending on the kinds of microorganisms used, there are various synthesis procedures available. According to the used microorganisms, metal ions adhere to the surface or become trapped inside the microbial cells. These arrested metal ions are then transformed into MONPs by the activity of enzymes. Microorganisms have the tendency to interact with metals that get into contact with them through their cells and produce MONPs. However, it is still unclear how microorganisms interact with metallic salt ions and produce the consequent metallic nanoparticles through natural decomposition processes [47]. Jha et al. discovered a sustainable, inexpensive, and repeatable *Saccharomyces cerevisiae*-mediated method of producing Sb_2O_3 nanoparticles [85]. The Oluwafemi group has provided a detailed review of the synthesis of MONPs by microorganisms, including plants, with a detailed description of the synthesized particle sizes, their shapes, and possible mechanisms involved [86]. Some of the examples of the synthesis of MONPs from microorganisms are provided in Table 5.2.

Merits and demerits of physical, chemical, and biological methods

The physical method required heavy equipment which is time-consuming and sometimes human errors are also observed. While using chemical methods requires the

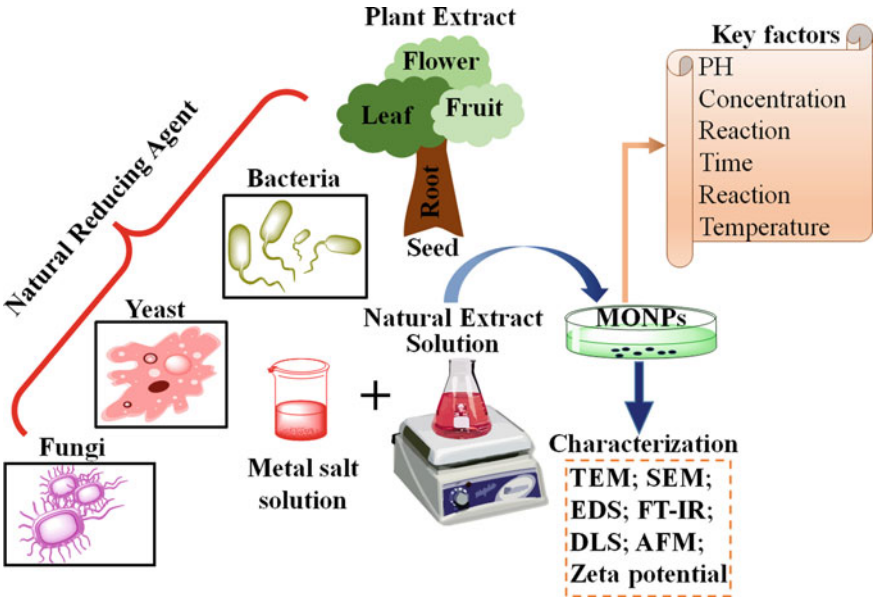

Fig. 5.4 Schematic representation of green synthesis routes available for MONPs

Table 5.2 Examples of synthesis of MONPs from microorganisms

MONPs	Green substrates	Name	References
ZnO	Algae	*Marine macroalgae*	[87]
		Caulerpa peltata	
	Bacteria	*Aeromonas hydrophila*	
		Lactobacillus sporogenes	
	Fungi	*Aspergillus fumigatus*	
		Fusarium spp	
Iron oxide	Fungi	*Alterneria alternata*	[88]
		Phialemoniopsis ocularis	
		A. wentii	
ZnO MnO_2 MgO	Bacteria	*P. polymyxa strain Sx3*	[89]
UO_2	Bacteria	*Desulfosporosinus sp.*	[90]
TiO_2	Bacteria	*Lactobacillus sp.*	[91]
CuO	Algae	*Eichhornia crassipes*	[92]
Bi_2O_3	Fungi	*Fusarium Oxysporum*	[93]

use of basic chemicals, and metal salt solutions, and their handling is rather challenging. However, the advantages of chemical methods are to obtain a large number of products, the liquid product is easily converted into powder form, different sized particles could be synthesized, and some reactions take place at room temperature also. Both the above methods produced good quality MONPs which have applications in varieties of fields. But the next-generation biosynthesis of MONPs provides a strong capping layer on the surface to which additional functional groups can be conjugated if required, which increases the NPs' biocompatibility and efficacy [94]. During the conventional synthesis of MONPs, the prime cost of nanoparticles is mainly determined by the cost of both the metal salts and stabilizing agents. While in the case of "green" synthesis, the major cost is determined by the metal salts and plant wastes from other industries such as food and agriculture which can serve as stabilizing agents [86].

5.3 Characterizations of MONPs

Comprehensive characterization techniques, such as chemical composition, surface morphology, surface topography, and spatial distribution of the functional groups, are often employed to better comprehend the physicochemical characteristics of MONPs. Fundamental techniques employed to investigate MONPs include X-ray diffraction (XRD) analysis, X-ray photoelectron spectroscopy (XPS), infrared (IR) spectroscopy, transmission electron microscopy (TEM), scanning electron microscopy (SEM), atomic force microscopy (AFM), thermal gravimetric analysis (TGA), dynamic light scattering (DLS), etc. Here, a brief discussion is given of some of the techniques which are initially required to characterize the synthesized MONPs.

X-ray diffraction

X-ray diffraction (XRD) is a versatile non-destructive technique for investigating crystalline structures, nature of phases, crystal lattice parameters, and crystalline grain size of MONPs [95–98]. Since, it is well known that variation in these parameters can result in varied characteristics of MONPs, which pushes us to thoroughly examine these aspects. XRD follows Bragg's law ($n\lambda = 2dsin\theta$) that defines the relationship between the angles for coherent and incoherent scattering from a crystalline lattice [97–99]. In XRD, the position and intensity of the diffractogram peaks for the MONPs are compared with the reference diffractogram available on the International Center for Diffraction Data (ICDD) (formerly, Joint Committee on Powder Diffraction Standards (JCPDS) system), which contains a vast collection of crystal structures from known materials [96, 100]. By applying the Scherrer formula to the experimental diffractogram, the average crystallite size may also be obtained. This method may be used for both crystalline and amorphous materials (some polymers and even biomolecules) by employing a small angular range of typically 0.1–3 ° [96, 101].

Electron microscopy

Electron microscopy is a technique based on a similar principle to optical microscopy, *i.e.*, image formation takes place owing to the interaction of the sample to be analyzed and the source of the illumination. Electron microscopy majorly differs from light microscopy in terms of source of illumination and system of condenser lenses. It has developed into an indispensable tool for scientists who are interested in understanding the properties of nanostructured materials and manipulating their behavior [102–104]. Since electron microscopy provides several hundred times resolving power and several lakhs times magnification than light microscopy, it is widely used for the structural characterization of MONPs. Among different electron microscopy techniques, scanning electron microscopy (SEM) and transmission electron microscopy (TEM) are widely used for the characterization of the MONPs [98, 105–108].

In SEM, when the test sample is scanned with a high-frequency electron beam, various processes occur at the sample surfaces, such as electron backscattering, secondary electron emission, and characteristic X-rays. These processes provide

information about the shape, surface topography, and chemical composition of MONPs [97, 100, 101, 109–111]. Conversely, when an electron beam strikes a test sample, some of the electrons are transmitted through the test sample while the rest are scattered elastically or inelastically in TEM. The intensity of the interaction is controlled by different parameters, including sample size, density, and composition of the test sample. The collected information from the transmitted electrons is used to construct the final image in TEM. Because it offers not only direct images of the sample, TEM is the most often used technique to analyze nanoparticle size and shape [100, 107, 111, 112].

Vibrational Spectroscopy

Vibrational spectroscopy is a non-destructive method widely used for analyzing molecular structures. The vibrational energies are distinct properties of molecular samples and may be thought of as "molecular fingerprints". As a result, their detection facilitates rapid characterization of molecules, providing detailed structural information. In general, infrared (IR) and Raman spectroscopy are two primary vibrational spectroscopy techniques [113]. IR spectroscopy involves the use of vibrational resonances in the infrared energy spectrum and Raman spectroscopy is based on inelastic scattering of higher energy incident photons (usually in the near IR to UV range) from sample molecules [114]. Both methods allow for the relatively quick, label-free, and precise measurement of a wide range of materials, including MONPs [95, 115–118]. Their application ranges from quick functional group identification to an in-depth study of the sample structural condition and modifications [113].

UV–Vis Spectroscopy

UV–visible (UV–Vis) spectroscopy is a simple, non-destructive, and analytical technique that measures the absorption of the incident electromagnetic radiation from the ultraviolet to the visible region on a test sample [119]. Since the optical properties of MONPs are relevant to their various applications, UV–Vis spectroscopy allows us to estimate the optical bandgap of the MONPs [97, 110, 120]. It further offers information on the functional groups present in the specimen including the purity of the test sample [119].

Furthermore, apart from these aforementioned techniques, some other techniques are also accessible that expand our existing knowledge of the given material (specifically MONPs). These techniques include dynamic light scattering (DLS) spectroscopy, zeta potential analysis, atomic force microscopy (AFM), X-ray photoelectron spectroscopy (XPS), energy-dispersive X-ray spectroscopy (EDS), etc. DLS is an immensely helpful tool for studying intensity fluctuations of visible light scattered from the particles while they make random Brownian motion in the liquid solution. This allows for estimating the hydrodynamic radii, which are strongly related to the size and shape of the MONPs [61, 121–123]. Zeta potential analysis is important for assessing the degree of electrostatic interaction at the particle–liquid interface, which influences particle stability in a colloidal system [112, 124]. AFM is a type of scanning probe microscopy technique that involves scanning the specimen using a sharp tip with a typical diameter of 100 Å attached to a small cantilever

to obtain the specimens' topography along with physical, magnetic, or chemical characteristics [125–127]. X-ray Photoelectron Spectroscopy (XPS) is an ultra-high vacuum method based on the basic photoelectric phenomenon. After absorbing the photons that interact with the sample, the electrons within the sample emerge. The measurement of the kinetic energy of these emerging electrons is critical since it reveals information about the sample's elemental composition [61, 128–130]. EDS is another well-known technique for determining the elemental composition of a specimen which helps in identifying the purity of the test sample. It is based on the investigation of the characteristic X-rays produced by the interaction of the high-energy electrons beam with the sample's atom. The elemental composition of the sample is obtained by analyzing the energy and intensities of these characteristic X-rays [61, 97, 110]. Figure 5.5 illustrates a summary of various techniques for the characterization of MONPs.

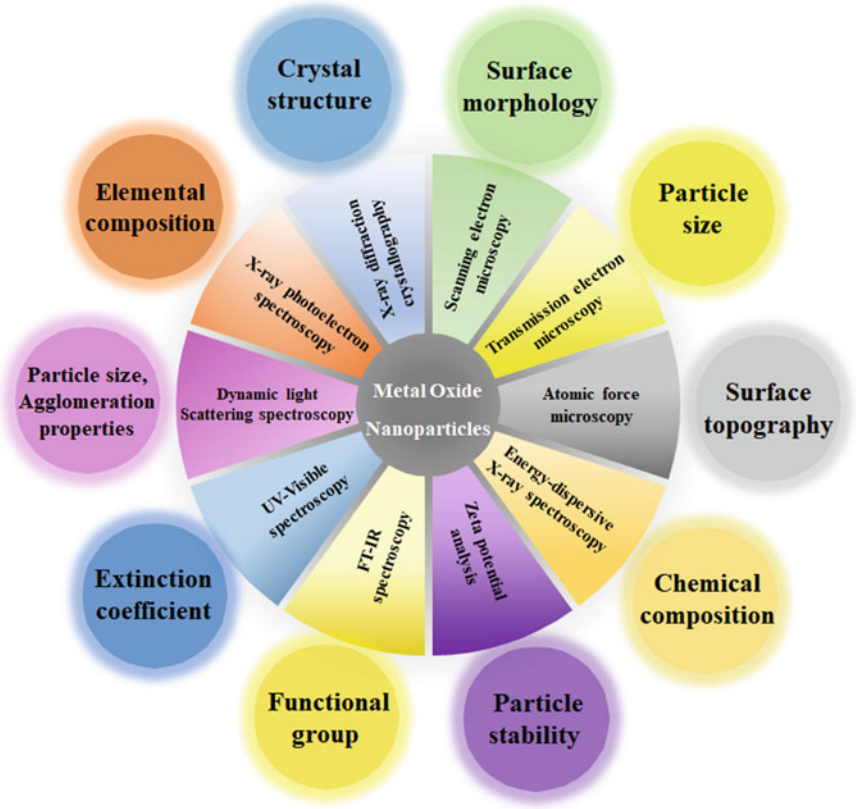

Fig. 5.5 A summary of various MONPs' characterization techniques and the key information they provide

5.4 Properties of MONPs

It is well known that the majority of the physicochemical characteristics of MONPs exhibit a strong size dependence. The commercial usage of MONPs as sensors, absorbents, ceramics, electrode material, and/or photocatalysts is largely related to their physicochemical characteristics. Numerous cutting-edge applications in these domains depend on the oxide nanomaterials' size-dependent optical, (electronic or ionic) transport, mechanical, and surface/chemical characteristics. We should emphasize that structural/electronic quantum size and size defect or non-stoichiometry effects are frequently two linked aspects of size effects in oxide chemistry. Some of their important properties are discussed in the following subsections.

5.4.1 Optical Properties

Specific optical features, including UV absorption, particular color absorption in the visible spectrum, dichroism, and photoluminescence, are offered by MONPs. The quickest approach to ascertain the size dependency in oxide materials is to examine the material's absorption spectrum as a function of the photons' incident wavelength. If the quantum confinement effect drives the bandgap's energy behavior in MONPs, then the optical bandgap energy is predicted to have an inverse squared dependence on the primary particle size [131–133]. Further, "non-stoichiometry" size-dependent defects have an additional impact on the optical absorption characteristics of nanosized oxides. Additionally, applied strain affects optical absorption spectra. The study of Ong et al. for ZnO nicely illustrates the impact of strain on the optical absorption spectra by demonstrating the splitting of the first exciton peak at high values of compressive strain [134].

5.4.2 Transport Properties

It is experimentally well established that MONPs have ionic or mixed ionic/electronic conductivity which is influenced by the nanostructure of the materials. Boltzmann statistics suggest that the electronic charge carrier in MONPs is a function of bandgap energy. Further, the distribution of charge carriers (defects) is also very different from that of bulk materials. This is because the shielding of electrostatic potential depletion at the surface layers of nanosized materials causes charge carriers to be present throughout the whole material [7]. It is documented that CeO_2 has an increased *n*-type conductivity that may be four orders of magnitude better than the corresponding bulk/micro-crystalline ceria and is attributed to a substantial improvement of the electronic contribution as a consequence of these nanoscale-generated effects [135]. WO_3, SnO_2, and In_2O_3 oxides' considerable size dependence for

electrical conductivity is an aspect of gas sensors that have recently been examined [136]. It is interesting to note that Li^+–ion batteries have some of the most striking impacts of the nanostructure on ionic transport in oxides. Employing Li-infiltrated nano-porous Al_2O_3, an exceptional improvement in Li^+–ion conductivity has been accomplished [137].

5.4.3 Mechanical Properties

The yield stress and hardness at low temperatures and the super plasticity at high temperatures are the key mechanical properties of MONPs which are discovered to be strain rate related. With reducing main particle/grain dimension, TiO_2 and ZrO_2 are showing greater strain rate sensitivity at ambient temperature. Despite these facts, it is evident that oxide materials—like Al_2O_3, ZrO_2, CeO_2, and TiO_2—sintered under vacuum or using the spark plasma technique exhibit increased yield strength and hardness in comparison to conventional/bulk ceramic materials. These also have the additional property of being transparent (films), making them potential aerospace industry materials [138, 139]. When the particle size is decreased, the superplasticity strain rate increases at a fixed temperature or the superplasticity temperature decreases at a constant strain rate. The ductility of nanocrystalline oxides at ambient temperature may be slightly greater than that of bulk materials, although these are not superplastic. They appear to have notable strain rate sensitivity and compressive ductility at high temperatures, which are indications of superplasticity [138].

5.4.4 Thermal Properties

It is a well-known fact that some of MONPs in solid form have higher thermal conductivities than those of fluids. For example, alumina has higher thermal conductivity than water. The possible reason for enhanced conductivity is the availability of large surface area in MONPs which is a prerequisite for enhanced thermal conductivity. Therefore, generally, MONPs are used in nanofluids where the base fluids contain suspended solid MONPs and display significantly improved thermal conductivities. Furthermore, nanofluids are expected to exhibit superior properties relative to those of conventional heat transfer fluids containing microscopic-sized particles. Moreover, the large surface area is also responsible for the increase in the stability of NPs suspension [140]. Therefore, due to the higher thermal conductivity of MONPs, various types of nanofluids are being studied consisting of CuO, Al_2O_3, and Fe_2O_3 NPs in a variety of base fluids such as water, ionic liquids, etc. [141].

In addition to the aforementioned properties, we have listed a few MONPs, their morphologies, and individual properties in Table 5.3.

Table 5.3 Summary of various properties of MONPs with their respective morphologies

MONPs	Morphology	Property	Reference
TiO_2	Nanofilms	Wide bandgap, High surface area	[142]
	Nano structures	Low operating voltage	[143]
	Nanowires	Higher charge capacity, Large specific surface area	[144]
	Nanoflower	High surface area	[145]
	Nanoparticles	Mosquitocidal and anti-bacterial activity	[146]
	Nanoparticles	Cytotoxicity and anti-microbial property	[147]
ZnO	Nanofilms	High electron mobility and good optical properties	[148]
	Nanorods	Good photoconversion efficiency	[149]
	Nanostructures	Good photoconversion efficiency	[150]
	Thin film	Good gas-sensing properties and Good thermal conductivity	[151]
	Nanorods	High response, good selectivity, and sensitivity toward low concentration	[152]
	Thin film	High photodetection response	[153]
	Nanoparticles	Cytotoxic and anti-cancer activity	[154]
	Nanorods	Highly crystalline and cytotoxic	[155]
	Quantum dots	Highly photo-luminescent and water dispersible	[156]
	Nanoparticles	Good photocatalytic activity and anti-bactericidal properties	[157]
	Nanoparticles	Good photocatalytic activity	[158]
SnO_2	Mesoporous thin-film	Good electron transport properties	[159]
	Nanowire	High theoretical storage capacity	[160]
	Nanowire	High sensitivity to low gas concentration	[161]
	Single nanowire	Good gas-sensing property	[162]
Fe_2O_3	Nanowire	High theoretical storage capacity	[163]
	Nanoparticles	Magnetic properties, chemical stability, and toxicity	[164]
	Nanoparticles	High surface area, good photocatalytic activity, and adsorption capacity	[165]
	Nanoparticles	High adsorption capacity, larger surface area, and highly active surface sites	[166]

(continued)

Table 5.3 (continued)

MONPs	Morphology	Property	Reference
Fe_3O_4	Nanoparticles	Non-toxicity, low processing cost, and high specific capacity	[167]
	Nanoparticles	Good adsorption and magnetic property	[168]
Co_3O_4	Needle-like nanotubes	High current density, good rate capability, short effective diffusion length, and ultra-high capacity with high-capacity retention	[169]
	Nanopowder	Good electrochemical properties, high storage capacity, and good cyclability	[170]
	Nanocube	Good catalytic activity	[171]
ZrO_2	Nanofilms	Thermally stable, chemical inertness, non-toxicity, higher isoelectric point, stable pH, and affinity for groups containing oxygen	[172]
	Nanoparticles	Superior mechanical and creep properties	[173]
Al_2O_3	Nanoporous templates	Good electrochemical property	[174]
CuO	Nanosheets	Larger surface area, good response toward low concentrations	[175]
	Nanowires	High surface area-to-volume ratio and less agglomerated, high gas sensitivity, and rapid response speed	[176]
	Nanoparticles	Good optical sensitivity	[118]
WO_3	Nanoparticles and nanoplatelets	Good gas-sensing properties	[177]
MoO_2	Nanocrystal	Good electrochemical performance and stability	[178]
MnO_2	Nanoparticles	Narrow bandgap, low toxicity, strong oxidizability large surface area, good adsorptive capabilities, and ecological purification activity	[179]
	Nanoflowers	Good adsorption activity and high stability	[163]

5.5 Applications of MONPs

MONPs can be utilized in a range of technological and industrial domains thanks to their unique physicochemical characteristics, including optical, magnetic, electrical, and catalytic characteristics. Particularly, due to their distinct reactivity, large surface area, and size distribution, MONPs have been extensively investigated in the energy generation and storage, pharmaceuticals, sensor technology, magnetic and optical

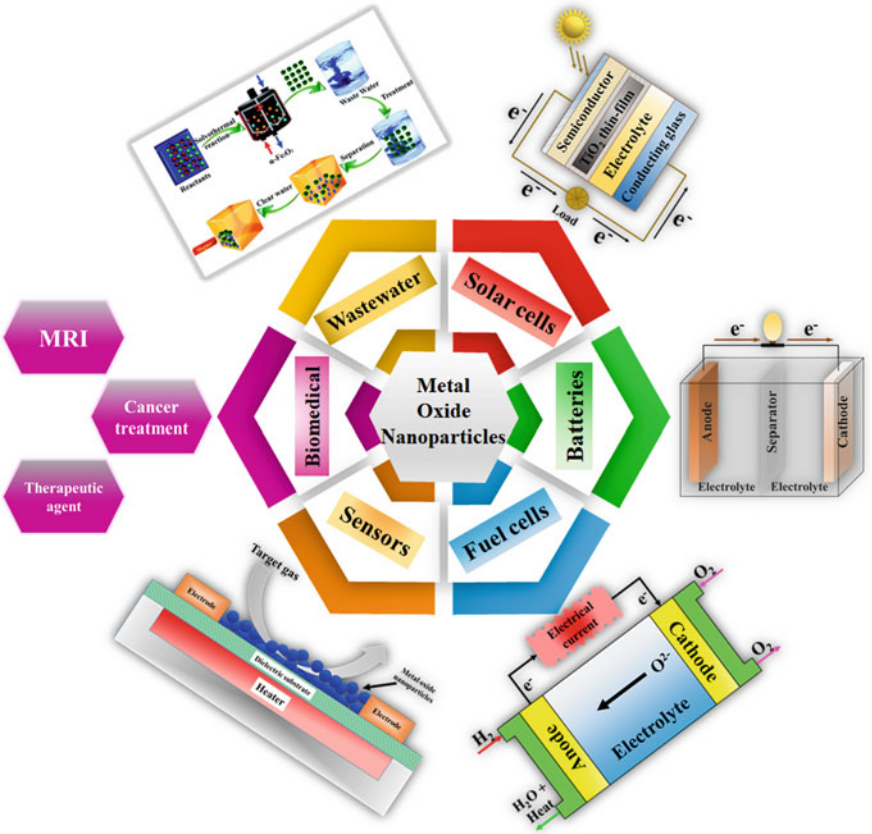

Fig. 5.6 Various applications of MONPs. Figure indicating wastewater treatment is adapted with permission from [192]. Copyright 2017 the Royal Society of Chemistry

devices, and catalysis sectors [126, 150, 159, 181–191]. Only some of the most significant applications of MONPs are included below as it will not be possible to discuss all the applications in this overview. Figure 5.6 illustrates the summary of applications of MONPs in solar cells, batteries, fuel cells, sensors, biomedicine, and wastewater treatment. The following subsections briefly discuss the aforementioned applications of MONPs.

5.5.1 Solar Cells (SCs)

Solar cells (SCs), which convert electromagnetic energy into electrical energy, are the most cost-effective method of generating electricity. Therefore, developing a sustainable and cost-effective approach as well as novel materials is necessary to

enhance the photoconversion efficiency (PCE) of SCs. In this regard, metal oxide semiconductors are the most suitable materials to fulfill this requirement since they are eco-friendly, inexpensive, and stable [2]. In this direction, silicon-wafer-based first-generation SCs offer high efficiency but with high manufacturing cost whereas second-generation thin-film SCs are more cost-effective but are less efficient [193]. Hence, third-generation SCs are being developed to achieve high efficiency with low fabrication costs [194] which include nanocrystalline SCs, polymer-based SCs, dye-sensitized SCs (DSSCs), concentrated SCs, perovskite SCs, polymer: Fullerene SCs, hybrid polymer SCs, quantum dots-sensitized SCs, etc. [194]. Figure 5.7 portrays use of various MONPs in several solar cell technologies.

O'Regan and Grätzel first reported the prospective uses of nano-scaled TiO_2 porous film electrodes in DSSCs and PCE were found to be ~8% in artificial solar conditions and 12% in natural solar conditions [142]. Gopal et al. grew TiO_2 nanotube arrays of 360 nm length, 17 nm wall thickness, and 46 nm pore diameter on a fluorine-doped tin oxide-coated glass substrate (FTO glass) to produce a photocurrent of 7.87 mA/cm^2 with a PCE of 2.9% in DSSCs [195]. Qualities such as low cost, high absorption coefficient, good mobility, availability, and non-toxicity of Cu_2O-based thin films make them a reliable candidate for photovoltaic applications. The authors of [196] demonstrate that the formation of CuO–Cu_2O nanocomposite layer on ZnO photoelectrode in DSSCs leads to improved photocurrent efficiency of 2.31% and

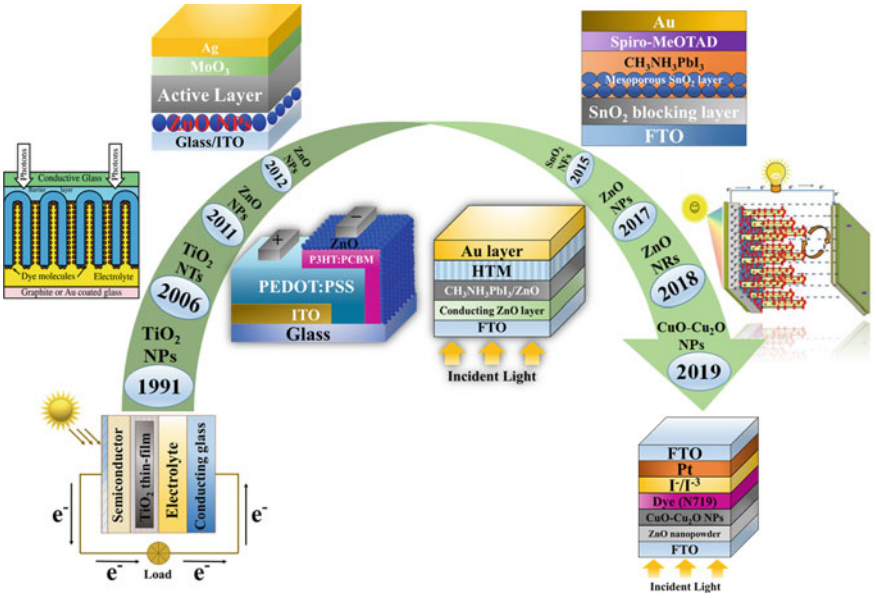

Fig. 5.7 Applications of various MONPs in several types of solar cell technologies, arranged chronologically. Schematic of use of TiO_2 NTs in DSSCs is adapted with permission from [195]. Copyright 2006 American Chemical Society, and schematic of DSSC using ZnO NRs is adapted with permission from [149]. Copyright 2018 Elsevier

current density (J_{sc}) of 7.33 mA.cm^{-2}. Indium tin oxide (ITO) is the most extensively used thin film in photovoltaics in the SC industry as it is optically transparent, chemically inert, electrically conductive, hard, and has high transmittance in the visible region of the electromagnetic spectrum [2]. Jouane et al. introduced ZnO nanostructures as a cathode buffer layer (CBL) in organic solar cells (ITO/PEDOT: PSS/P3HT: PCBM/Al) and obtained an improved PCE from 2.16% to 2.34% depending on the size of ZnO and the thickness of the ZnO CBL [148]. The authors of [197] reported the photon-to-electron conversion efficiency of 4.35% and 3.28% with short-circuit current (J_{sc}) of 8.80 mA/cm^2 and 7.80 mA/cm^2 by using pomegranate-like and hollow spherical structured ZnO nanoparticles as a photoanode in DSSCs, respectively. By using ZnO nanoparticles as an electron-transfer layer in inverted-structure polymer solar cells based on PTB7:$PC_{71}BM$ ([6, 6]-phenyl C71-butyric acid methyl ester), an improved PCE of 7.34% was gained [198]. The efficiency reported by authors of [149] for DSSCs based on ZnO nanorods as photoanodes deposited in 0 mM and 9 mM hexamethylenetetramine (HMTA) solutions was 1.79 and 3.75%, respectively. Duan et al. successfully demonstrated the perovskite solar cells with improved PCE of 13.1% with J_{sc} of 19.7 mA/cm^2 achieved by morphological modifications in ZnO nanostructures [150]. Dai and coworkers reported PCE of 10.18% with J_{sc} of 18 mA/cm^2 in perovskite solar cells with mesoporous SnO_2 nanofilms as an electron-transfer layer combined with $TiCl_4$ treatment [159]. These are only a limited collection of SC applications of specific MONPs; for more information in detail, readers can go through these review papers [199–202].

5.5.2 Batteries

The increased generation capacity from renewable energy sources has necessitated the development of high-capacity energy storage and batteries are one of the several available solutions for energy storage. Therefore, developing high-power, high-energy–density batteries is being seriously considered a viable solution. Due to their unique chemical and structural properties, MONPs have enhanced battery efficiency when utilized as anode materials, cathode materials, and electrolyte additives. Nanostructured metal oxides, such as SnO_2, TiO_2, Fe_2O_3, Co_3O_4, and complex metal oxides, have been used in Li–ion batteries (LIBs) to improve specific capacity, and rate capability, and cycle efficiency [20, 203]. Poizot et al. first developed negative electrodes based on transition MONPs (MO, where M = Co, Ni, Cu, or Fe) for LIBs and estimated a theoretical capacity higher than 700 mAh/g [182]. Tin oxide has been considered a promising graphite alternative in LIBs as it has a higher theoretical capacity (1494 mAh/g vs. 372 mAh/g) [204]. Similarly, Ying et al. prepared the SnO_2 nanowires using the thermal evaporation method (see Fig. 5.8a), which were used as an anode material to manufacture the button-type LIB with improved storage capacity (see Fig. 5.8b) [160]. With a capacity fade rate of 3.89% per cycle and a constant current density of 0.5 mA/cm^2, the authors were able to achieve a storage

capacity of 2133 mAh/g during the initial discharge and a reversible capacity of more than 700 mAh/g for 15 subsequent cycles [160].

Wu et al. demonstrated an LIB with a high initial discharge capacity of 1600 mAh/g and a reversible capacity of 516 mAh/g after 50 cycles at a current density of 400 mAh/g, which consists of 3D hierarchical SnO_2 nanostructures synthesized by a hydrothermal approach used as an anode [183]. TiO_2 NPs have been regarded as a possible graphite alternative material for LIBs as they are abundant, non-toxic, low cost, and extremely safe with a moderate capacity. TiO_2 nanostructures are also a viable anode material in sodium–ion batteries (SIBs) due to the low operating voltage [143, 205]. Han et al. reported rutile-TiO_2 nanowires (synthesized by the hydrothermal process) for LIBs which enhance lithium intercalation properties with a reversible capacity of 173 mAh/g up to 100 cycles [144]. The authors demonstrated that the coating of TiO_2 nanoparticles on sulfur cathode of lithium–sulfur batteries (LSBs) resulted in sulfur–TiO_2 yolk–shell nanoarchitecture which minimized the poly-sulfur dissolution in electrolyte and exhibited high retention capacity [206]. The initial specific capacity and coulombic efficiency reported employing this nanoarchitecture was 1030 mAh/g at 0.5 C and 98.4% and the capacity retention of 67% (capacity decay of 0.033% per cycle) was found after over 1000 cycles [206]. However, due to high abundance, non-toxicity, low cost, and the high theoretical capacity of 745, 1005, and 928 $mAhg^{-1}$, make FeO, Fe_2O_3, and Fe_3O_4 nanoparticles a prominent anode material for LIBs, respectively [167, 207]. Wang and Co-workers synthesized α-Fe_2O_3 nanowires to use as an anode for LIBs whose SEM image is shown in Fig. 5.9a and b [163]. Utilizing these nanowires in LIB at 0.1 C within a voltage range of 0.1–3 V exhibited a high discharge/charge capacity of 1303/974 mAh/g and 456 mAh/g of discharge capacity retained after 100 cycles [163].

Manganese oxides such as MnO, MnO_2, Mn_2O_3, and Mn_3O_4 are attractive anode materials for LIBs due to low electrochemical force, eco-friendliness, cost-effectiveness, and their high specific capacities of 756, 1232, 1018, and 937 mAh/g,

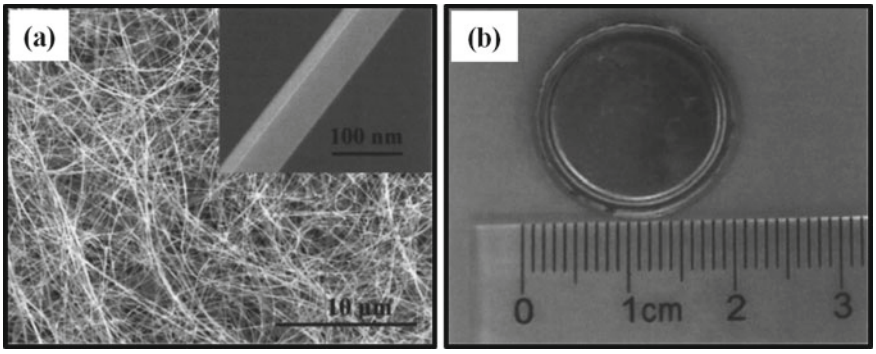

Fig. 5.8 (**a**) SEM image of SnO_2 nanowires synthesized via thermal evaporation, (**b**) Button-type Li–ion battery fabricated using SnO_2 nanowires as an anode material. Adapted with permission from [160]. Copyright 2005 AIP Publishing

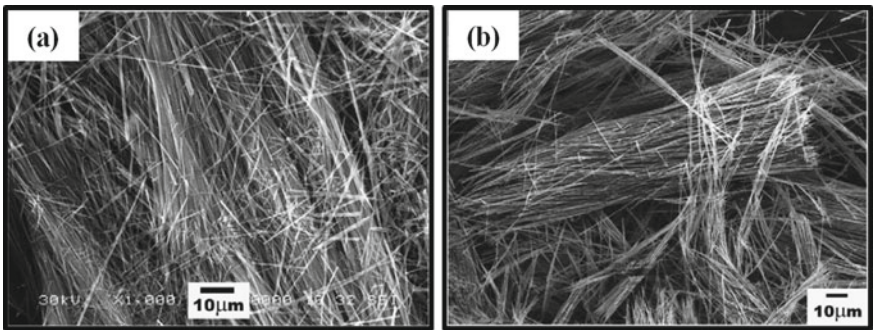

Fig. 5.9 SEM images of Fe_2O_3 nanowires synthesized via hydrothermal images (**a**) Fe_2O_3 nanowire precursors (**b**) Fe_2O_3 nanowires after sintering at 500 °C. Adapted with permission from [163]. Copyright 2009 Elsevier

respectively [167]. Additionally, manganese oxides are integrated with porous carbon, carbon fibers, and carbon nanosheets as anode materials to enhance the LIBs' performance [167]. Zhang et al. incorporated porous Mn_2O_3 nanoplates as an anode in LIBs and achieved a specific capacity of ~ 814 mAh/g at a current density of 0.1 A/g after 50 cycles [208]. Liang et al. developed a sulfur/manganese oxide nanosheet composite to enhance the specific capacity of lithium-sulfide batteries (LSBs) [209]. The reported reversible capacity was 1300 mAh/g at 0.2 C and fading rate of 0.036% per cycle after 2000 cycles at 2 C [209]. Cobalt oxides, including CoO, are also attractive anode materials for LIBs with theoretical specific capacities of 715 and 890 mAh/g, respectively [210, 211]. When needle-like Co_3O_4 nanotubes were used as a negative electrode in LIBs, the charge capacity was 950 mAh/g during the first cycle. With a maintained charge capacity of 918 mAh/g and a fading rate of 0.1% every cycle, nearly 100% retention capacity was attained [169]. Furthermore, after 70 cycles at 0.22 C, Co_3O_4 thin film demonstrates an enhanced reversible capacity of 1000 mAh/g in micro-batteries [212]. The reported storage capacity was 360 mAh/g after thirty cycles, which is very promising for using nano-size Co_3O_4 as anode materials for LIBs [170]. In addition, to increase electrolyte conductivity, metal oxide nanoparticles such as TiO_2, SiO_2, and Al_2O_3 were added as fillers in the poly(ethylene oxide) (PEO)-based electrolyte in LIBs [213, 214]. The authors demonstrated that the use of template electrodeposited PbO_2 nanowires as a positive electrode in lead–acid batteries resulted in an initial specific capacity of 200 mAh/g, which is nearly equivalent to the theoretical specific capacity of 220 mAh/g, and ~90% efficiency was achieved at higher C-rate than 1C after over 1000 cycles [215]. The Ni/NiO nanocomposites were utilized to enhance specific capacity from 75 mAh/g to 100 mAh/g at 2 A/g current density as a cathode in alkaline batteries with 72% of high retention capability for an increased current density from 2 to 40 A/g [216].

5.5.3 Sensors

Sensors are becoming increasingly vital in sectors such as aviation, industrial manufacturing, pollution prevention, marine research, biotechnology, and clinical applications, as there is a great demand for accurate and consistent information [217]. The features of MONPS, such as improved selectivity, ease of implementation, and high specific surface areas with extremely high surface reactivity, make them a popular material for improving the sensing performance of sensors such as gas sensors, biosensors, and optical sensors [2, 118, 218].

Figure 5.10 illustrates schematic representation of a typical MONPs-based gas sensor which consists of a heating element, electrodes, and MONPs as gas-sensing substance. MONPs like ZnO, TiO_2, SnO_2, WO_3, CuO, etc. are commonly used as sensing materials in gas sensors [184]. In 1962, Seiyama et al. developed the first metal oxide gas sensor, a 2–100-nm-thick ZnO thin film that served as a chromatographic detector for gases such as propane, toluene, benzene, carbon dioxide, ethyl ether, and ethyl alcohol [151]. Gas sensors based on ZnO nanorods have shown a good sensing response to a low concentration of H_2S gas (0.05 ppm) at room temperature (RT) [152]. Similarly, Lupan et al. fabricated a hydrogen gas sensor using ZnO nanorods and obtained a sensitivity of ~4% at 200 ppm of H_2 gas at RT [219]. In a similar vein, Yelamaggad and coworkers synthesized ZnO nanoparticles for the CO gas-sensing application and obtained a response of 6% at 25 ppm and RT [220]. Recently, Ding et al. fabricated a ZnO thin film by aerosol-assisted CVD for NO_2 and ethanol gas sensing and obtained a sensitivity of ~41 toward 1 ppm NO_2 at 225 °C and ~236 to 100 ppm ethanol at 350 °C [221]. Moreover, different morphologies of TiO_2 nanostructure had been used in ethanol, acetone, oxygen, carbon monoxide, and hydrogen sulfide gas-sensing applications [222]. Recently, the Hazra group has utilized TiO_2 nanotubes as an efficient detecting material for sensing organic volatile solvent and obtained a response magnitude of 75.4% at 150 °C and 80% at 200 °C toward 100 ppm ethanol with a response time of 155 s [222]. Cao et al. examined the gas sensitivity characteristics of various phases of TiO_2 nanostructures and found that rutile-TiO_2 nanorods-based gas sensors had a high sensitivity of 12.3 toward 100 ppm acetone vapor compared to anatase-TiO_2 nanoparticles (4.1) and brookite-TiO_2 nanorods (2.3) at 320 °C with a faster response time of 3 s as rutile phase had relative narrow bandgap and increased oxygen vacancies [185]. Similarly, SnO_2, WO_3, and CuO nanosheets had been utilized for ethanol, acetone, hydrogen sulfide, and nitrogen dioxide gas sensing [223].

Other MONPs such as TiO_2, SnO_2, ZnO, CeO_2, and ZrO_2 were also generally used in biosensor applications for detecting analytes like glucose, glutamate, urea, hydrogen peroxide, cholesterol, DNA, enzymes, etc. [172, 224–229]. Wang et al. constructed a single-crystal ZnO nanocomb-based biosensor of 15.33 $\mu A/cm^2$ mM high sensitivity for glucose detection [230]. The authors showed that the application of ZnO nanofilms in cholesterol sensors enhances electron-transfer activity between ChOx and electrode [227]. Similarly, Bao et al. synthesized nanostructured porous TiO_2 and upon testing in a glucose sensor, it showed good stability, higher sensitivity,

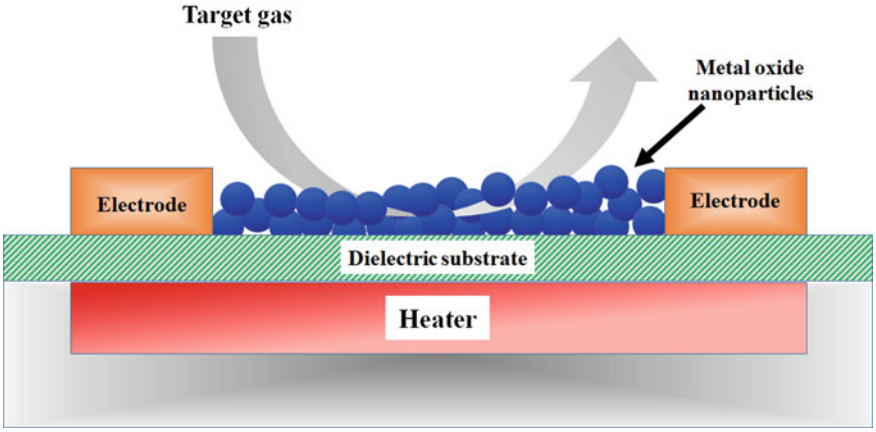

Fig. 5.10 Schematic representation of MONPs-based gas-sensing device

and excellent immobilizing effect [231]. In a similar direction, Das and coworkers performed the electrochemical deposition of ZrO_2 film on the gold surface in DNA biosensors to immobilize 21-mer ssDNA, specific to mycobacterium tuberculosis. The aforementioned fabricated DNA biosensor could be utilized for rapid and early diagnosis with a detection limit of 0.065 ng/μL within 60 s [172].

A typical optical sensor must have higher sensitivity, selectivity, and stability with fast and linear responsivity. To fulfill this purpose, MONPs such as ZnO, Mn_3O_4, Co_3O_4, NiO, etc. were used in optical sensors [153, 232–234]. Mollow firstly observed the UV photoresponse of ZnO material in the 1950s [235]. Alenezi et al. developed the on-chip ZnO nanostructure-based UV detectors with improved sensitivity of ~10^5, a fast response time of 90 ms, and a recovery time of 210 ms [232]. Kobayashi et al. reported MONP-based optical sensors (MONPs were Mn_3O_4, Co_3O_4, and NiO) for detecting reducing gases such as H_2 and CO gas in the atmosphere [233, 234]. The detailed literature discussed above indicates that MONPs are widely used in various types of sensing technologies [236].

5.5.4 Fuel Cells

A typical fuel cell generates electricity with byproducts such as water and heat from the chemical recombination reaction of hydrogen fuel with oxygen present in the air across an electrolyte membrane through anode and cathode [237]. The basic principle of the fuel cell was discovered by *Christan Friedrich Schonbein* in 1838 and the first fuel cell was created by *William Grove* in 1839 by reverse electrolysis of water [238]. This section looks forward to how MONPs are used in fuel cells to make them a highly efficient, clean, and inexpensive source of power. The proton exchange membrane fuel cells also known as polymer electrolyte fuel cells (PEFCs)

had several restraining factors for their commercialization such as high cost, low activity, and short durability of electrocatalysts which could be overcome by using MONPs as electrocatalysts, co-catalysts, and supports for various chemical reactions [187, 239]. Rajalakshmi et al. found that the application of TiO_2 nanofilms as alternative catalyst support instead of carbon for platinum (Pt) in PEMFCs had improved thermal stability and electrochemical activity [240]. The presence of TiO_2 nanofilms in platinum was advisable to avoid the agglomeration of platinum particles, resulting in dispersed platinum atoms in clusters, and offer thermal and oxidation stability concerning corrosion [240]. Yu et al. developed the nanophase ceria (CeO_2)-doped Pt/C cathode for oxygen reduction reaction (ORR) and found that the doping of 1 wt.% CeO_2 with 40% Pt/C increased the oxygen concentration which led to the performance enhancement of direct-methanol fuel cells (DMFC) [241]. Maiyalagan et al. incorporated WO_3 nanorods as a Pt catalyst support and prepared Pt/WO_3 catalyst which exhibited better electrolytic activity than the commercial 20% Pt supported on carbon catalyst (i.e., 62 $mAcm^{-2}$ vs. 29.5 $mAcm^{-2}$), and good stability toward methanol oxidation too. It was ascribed to a synergistic effect between Pt and WO_3 that prevents electrode toxicity [126]. Yan et al. synthesized the molybdenum oxide nanocrystals down to 5 nm on carbon using the ion-exchange principle [178]. The resultant electrocatalyst constructed with Pt nanoparticles supported by C-MoO_2 (Pt/C-MoO_2) exhibited enhanced stability and high mass activity of 187.4 mA mg^{-1} than that of the commercial Pt/C electrocatalyst (98.4 mA mg^{-1}) at 0.9 V for ORR, which was attributed to the synergistic effect of MoO_2 and the strong interaction force between Pt and MoO_2 [178]. Further, the major concern with molten carbonate fuel cells (MCFCs) is the NiO dissolution, which led to the degradation of cathode material, which limits its long-term operation. In this direction, Hong et al. synthesized nanosized TiO_2-coated NiO powder as a cathode material for MCFCs via the sol–gel method to restrain their solubility in the electrolyte. The immersion of this modified NiO powder in molten carbonate ($(Li_{0.62}K_{0.38})CO_3$) led to a steady phase formation of Li_2TiO_3, which reduced their solubility by around 50% compared to pure NiO cathode [242]. Kim et al. prepared NiO powder modified with Co_3O_4 nanoparticles by annealing process at 650 °C, which formed the highly lithiated outer phase on the $Ni_{0.9}Co_{0.1}O$ [243]. This phase acted as a barrier that led to the minimization of NiO dissolution, and the modified cathode exhibited adequate electrochemical activity and better stability under a normal state of operation [243]. Meléndez-Ceballos et al. carried out a deposition of Nb_2O_5 film of different thicknesses (5, 20, 50, and 300 nm) on porous Ni cathode in MCFC by atomic layer deposition (ALD) [244]. They studied the electrochemical properties of this modified cathode at 650 °C in molten Li_2CO_3-K_2CO_3 eutectic carbonates and found the reduced solubility of NiO cathode with a 20-nm-thick Nb_2O_5 layer and satisfactory electrochemical performance confirmed by open-circuit potential (OCP) evolution for the same modification [244]. Furthermore, Accardo and coworkers developed a reinforced NiAl anode with nano-ceria (CeO_2) and nano-zirconia (ZrO_2) for the MCFCs, and they showed that the reinforcement of nanoparticles with an anode improved their mechanical and creep properties [173]. Moreover, MONPs have also been used in solid oxide fuel cells

(SOFCs) to improve cell performance. In this regard, Kwon and coworkers developed micro-SOFC with deposition of nano-porous Al_2O_3 thin film of 20 nm thick by ALD between two layers of yttria-stabilized zirconia (YSZ) electrolyte of 300 nm thickness each. This ALD modification reduced the gas leakage between columnar grains of the YSZ electrolyte and led to a better open-circuit voltage of 1.02 V and the maximal power density of 350 $mWcm^{-2}$ at 500 °C [174]. Xu et al. modified the Sr-doped $LaMnO_3$ cathode of solid oxide fuel cells by the Co_3O_4 nanotubes exposed to the (001) plane, which led to improved cell performance. The modified cell exhibited the highest power density of 500 $mWcm^{-2}$ at 600 °C [171]. Similarly, the researchers deposited the nanoscale ZrO_2 layer of around 5 nm thickness via ADL to improve the stability of the $La_{0.6}Sr_{0.4}CoO_{3-\delta}$ (LSCo) cathode of the intermediate temperature (600–800 °C) SOFC (IT-SOFC). This improvement provided the benefit of an 18 and 19 times reduction in the degradation rate and polarization area-specific resistance (R_p), respectively, over unmodified LSCo cathode, tested for 4000 h at 700 °C in the air [245]. Another type of fuel cell is microbial fuel cell (MFC) which has gained attention in the science community because of its bio-electrochemical activity, *i.e.*, generating electricity by degrading organic material in the wastewater. Air–cathode MFCs are widely investigated over other types of MFCs as designed such that they utilize the free oxygen available in without applying any energy. Therefore, the improvement in ORR leads to the enhancement of the overall performance of MFCs. Fan et al. took a green synthesis route to synthesize a high-performance, long durable, and cost-effective cathode catalyst for ORR. They synthesized the iron oxide nanoparticles embedded with N-doped porous carbon (F/N–C) cathode catalyst through a hydrothermal treatment and successive carbonization procedures using Chlorella pyrenoidosa and got a maximum power density of 48% higher (2740 ± 160 mWm^{-2}) than that of with the commercial 20 wt.% Pt/C (1846 ± 66 mWm^{-2}) at the same catalyst loading [246]. Similarly, Kim and coworkers incorporated a cobalt oxide nanoparticle with cobalt phthalocyanine (CoPc) to develop an efficient and inexpensive CoO_x–CoPc cathode material for MFCs. Using this cathode, the MFC delivered a power density of 780 mWm^{-2}, which was 50% higher than that of a pure catalyst without cobalt oxide. An 80% recovery was attained of its initial voltage under the resistance load of 1 kΩ after 100 days of operation [247].

5.5.5 Biomedical Applications

MONPs have recently been used in a wide range of biomedical applications due to their huge surface area and increased magnetic and catalytic activity [248]. MONPs such as Fe_2O_3, TiO_2, ZrO_2, CeO_2, etc. are most commonly used in biomedical applications such as therapeutic and bioimaging agents, components in medical implants, drug delivery systems, and probes for neurochemical monitoring due to their interesting catalytic, antioxidant, bactericidal activities, mechanical stability, and biocompatibility [189, 249–252]. The highly magnetized iron oxide NPs including magnetite (Fe_3O_4) and maghemite (γ-Fe_2O_3), have been used as contrast agents to distinguish

between healthy and diseased tissue in magnetic resonance imaging (MRI). Kim et al. synthesized extremely small-sized (diameter < 4 nm) iron oxide nanoparticles (ESIONs) which demonstrated a low r_2/r_1 ratio of > 6.2 mM^{-1} s^{-1}, indicating their efficacy as T_1 contrast agents in MRI [253]. Hyeon and coworkers incorporated MnO nanoparticles as a T_1 contrast agent for MRI of various body organs such as the brain, liver, kidney, and spinal cord and obtained sharp MR images [254]. Similarly, Shin et al. developed the hollow manganese oxide nanoparticles (HMONs) and demonstrated their potential use as a dual contrast agent for T_1- and T_2- weighted MRI as well as drug delivery carriers [255].

Titanium dioxide nanoparticles have demonstrated potential anti-bacterial, anti-fungal, and anti-cancer properties. Therefore, they have been integrated into a variety of polymer patches and these patches have exhibited effective anti-bacterial activity against both gram-positive and gram-negative bacteria [256]. The incorporation of curcumin with TiO_2 NPs has been found efficacious in wound healing. Selvi et al. showed that the polymer patches integrated with TiO_2 NPs and curcumin have promising anti-bacterial activity against gram-positive and gram-negative bacteria [256]. Karthik et al. synthesized TiO_2 NPs and studied their anti-bacterial activity against E. coli, P. aeruginosa, S. flexneri, K. pneumoniae, and S. aureus bacteria along with the anti-lung cancer activity for A549 cell line (IC50: 24.96 μg/mL) [257]. In a similar direction, Gowri et al. synthesized biocompatible zirconia NPs and assessed their anti-bacterial activity against S. aureus and E. coli and anti-fungal activity against C. Albicans and A. niger strains [258]. They suggested their potential applicability as an anti-bacterial and anti-fungal agent based on the inhibitory values for S. aureus (13 mm), E. coli (14 mm), C. Albicans (13 mm), and A. niger (12 mm) [258]. Lohbauer et al. incorporated zirconia NPs with the primer (P) or into the adhesive resin component (A) of the Adper Scotchbond Multi-Purpose (SBMP) to investigate the effect on the dentine bone strength and morphological changes at the bond interface [259]. The addition of zirconia nanoparticles into the primer or the adhesive of SBMP significantly increased micro-tensile bond strength (μTBS) to dentin, leading to a reinforcing effect on the resin [259].

ZnO NPs have piqued the interest of researchers for a variety of biomedical applications because of their various advantages, including biocompatibility, biodegradability, low cost, ease of synthesis, and multiple drugs/therapeutic molecule loading [260]. They were often used as drug delivery carriers and for therapeutics of several diseases such as cancer, microbial infection, diabetes, etc. [261–263]. Further, ZnO NPs have been employed for diagnostics due to their bioimaging and biosensing capabilities [264, 265]. Muthuraman et al. investigated the cytotoxic effect of synthesized ZnO NPs on human cervical cancer cells and observed that the ZnO NPs induced an apoptotic process by raising intracellular ROS (reactive oxygen species) production [154]. Moreover, they found that the cytotoxicity of ZnO NPs in HeLa cells by SRB assay caused apoptosis, demonstrating their use as cancer therapeutics [154]. Premanathan et al. employed the MTT [3-(4,5-dimethylthiazol-2-yl)-2,5-diphenyltetrazolium bromide] analysis to assess the cytotoxicity of ZnO NPs against human myeloblastic leukemia cells (HL60) and normal peripheral blood mononuclear cells (PBMCs). The obtained minimum inhibitory concentration (MIC) values

of ZnO NPs against E. coli, P. aeruginosa, and S. aureus were about 500 μg/mL, 500 μg/mL, and 125 μg/mL, respectively, and the obtained cytotoxic concentration (CC50) of ZnO NPs for HL60 cells was 52.80 μg/mL, whereas it was 741.82 μg/mL for PBMCs [266]. Kishwar and coworkers used ZnO nanorods (NRs) grown on the tip (0.5 μm diameter) of borosilicate glass capillaries by aqueous chemical growth technique (ACGT) for the treatment of breast cancer cells (T-47D). These ZnO NRs were conjugated with protoporphyrin dimethyl ester (PPDME), which absorbed the white light emitted from ZnO NRs after being excited by UV light in the cancerous cell. The absorption of white light resulted in the generation of singlet oxygen, which is responsible for the necrosis of breast cancer cells by damaging mitochondria [155]. Zhu and the group employed the ZnO quantum dots (QDs) for targeted anti-cancer drug delivery for the therapy of HeLa cancer cells. The amine-capped ZnO (ZnO-NH_2) QDs were functionalized with folic acid (ZnO-FA QDs), and the anti-cancer drug loading of doxorubicin (DOX) was validated by the drug solution changing color from orange to stunning pink, indicating the development of the Zn^{2+}-DOX complex. The anti-cancer drug release was carried out by the decomposition of the DOX-ZnO-FA complex in the moderate acidic intracellular environment of cancer cells, resulting in synergetic cytotoxicity against cancerous cells [156]. Moreover, most recently, highly thermal conductive α-Fe_2O_3 NPs have been loaded into the three-dimensional (3D) network of hybrid hydrogel for the enhancement of diclofenac drug release performance [267].

5.5.6 Wastewater Treatment

In addition to global warming, air pollution, deforestation, ozone layer depletion, and other major environmental issues, "wastewater" is one of the biggest environmental problems because of its extensive consumption. The commercial/industrial sectors discharge effluent in water containing heavy metals such as Pb (II), Cr (VI), As (V), Mn (II), Hg (II), Ni (II), Cd (II), etc., and other contaminants are causing an increase in water pollution. Therefore, wastewater treatment facilities are intended to handle huge amounts of waste utilizing modern technologies, depending on the kind of waste and the amount of waste released.

In this direction, common types of MONPs employed so far for this purpose include TiO_2-, ZnO-, MnO-, and Fe-based nanomaterials [190]. The usage of MONPs as an absorbent for wastewater treatment is depicted in Fig. 5.11. Due to its low cost, high abundance, chemical and biological inertness, stable photocatalytic, and non-toxic behavior, TiO_2 is a popular and alluring photocatalyst [191, 268]

A variety of organic dyes, including Amido Black 10B, Orange G, Alizarin green, Safranine O'azure II, Indigo carmine, Malachite green, solvent red 23, Rhodamine 6G, Sudan III, and others, were degraded in the presence of TiO_2 photocatalyst [270]. The photocatalytic activity of TiO_2 NPs is shown in Fig. 5.12. Budarz et al. have investigated the photoreactive capability of TiO_2 NPs to degrade the chlorpyrifos (organophosphorus pesticide) during the photodegradation process in the

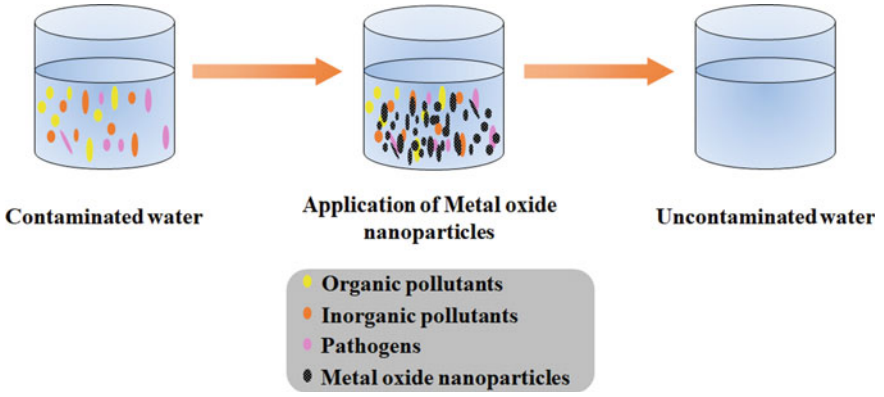

Fig. 5.11 Utilization of MONPs for wastewater treatment

absence and presence of bacteria. The UV-active TiO_2 NPs degraded chlorpyrifos into both chlorpyrifos oxon and 3,5,6-trichloro-2-pyridinol, with 80% degradation of chlorpyrifos after 24 h [271]. Furthermore, the TiO_2 nanocomposites' regeneration and recyclability make them effective photocatalysts for environmental remediation. Gomez and coauthors synthesized TiO_2 supported on zeolitic material (HBETA) which acted as reusable photocatalysts to degrade dichlorvos pesticide. The 20 wt.% loading of TiO_2 in HBETA showed enhanced photocatalytic activity, which was attributable to the high adsorption of dichlorvos pesticide on HBETA [272]. The intrinsic properties of ZnO NPs such as photocatalysis, anti-fungal, anti-bacterial, therapeutic benefits, and UV filtering have made them a versatile agent for wastewater treatment [273]. Owing to these properties, Rambabu et al. synthesized ZnO NPs using phoenix dactylifera waste (PDW) for the effective degradation of hazardous methylene blue and eosin yellow dyes [274]. The DPW-mediated ZnO NPs (DP-ZnO NPs) showed a fast degradation rate with a 90% degradation efficiency. Moreover, in terms of zone-of-inhibition evaluated by the disc diffusion technique, DP-ZnO-NPs exhibited strong anti-bacterial activity on several pathogens [274]. Similarly, Prasad et al. developed the green, facile method for the production of ZnO NPs as a photocatalyst. They tested their photocatalytic activity against organic dyes including methylene blue, rhodamine B, Congo red, and methyl orange in an aqueous solution [158]. By observing UV–Vis spectra at each 10-min interval during the reaction, they discovered the photodegradation capability of ZnO NPs for selective cationic dyes with 95% removal of the methylene blue solution (32 mg/L) in 60 min and 100% removal of the rhodamine B (9.5 mg/L) in 50 min using 125 mg of catalyst (see Fig. 5.13a and b). The percentage degradation efficiency after each 10-min interval is shown in Fig. 5.13c. Moreover, the study of photocatalytic degradation of dye molecules with 25–175 mg of the catalyst was carried out, which showed that the addition of catalyst enhanced the degradation capacity (Fig. 5.13d) [158].

By considering several unique properties such as narrow bandgap, low toxicity, strong oxidizability, abundance, large surface area, adsorptive capabilities, and

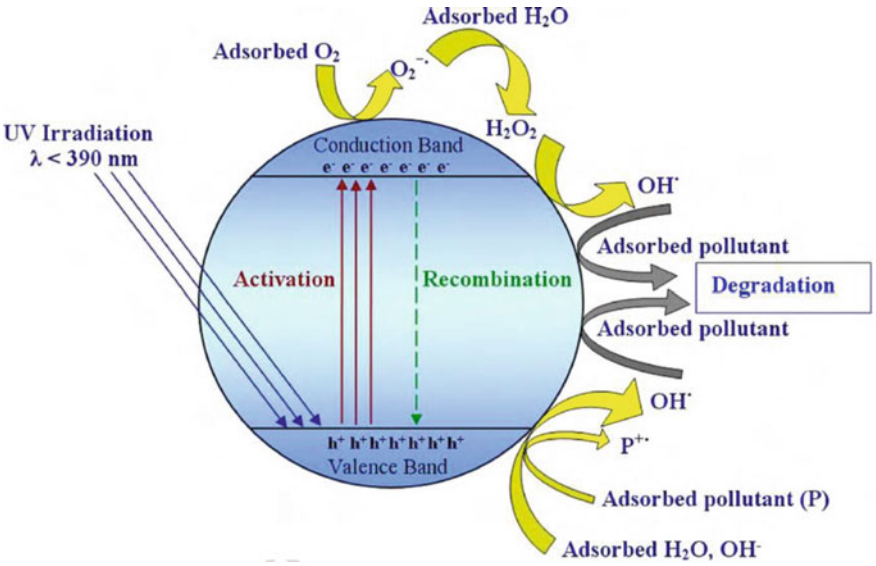

Fig. 5.12 Illustration of photocatalytic activity of TiO_2 NPs. Adapted with permission from [269]. Copyright 2010 Elsevier

ecological purification activity, MnO_2 NPs are widely used as an adsorbent material for the removal of heavy metals, dyes, and as a photocatalyst for the degradation of pollutants [179]. The MnO_2's adsorption capacity for heavy metal ions varies with a crystalline structure, adsorption location, and specific surface morphology. The birnessite MnO_2 structure has the highest adsorption capability among all forms of MnO_2 with different crystalline phases [275]. Li et al. synthesized flower-like and wire-like birnessite MnO_2 for the removal of Thallium from wastewater and found that wire- and flower-like MnO_2 was effective for the removal of Tl(I) (85.4%–99.9%) [275]. Moreover, the adsorption performance of ε-MnO_2 nanoflowers for the removal of Pb (II) ions from groundwater was studied by Lin et al. It was observed that the ε-MnO_2 nanoflowers were able to remove Pb (II) efficiently with a maximum adsorption capacity of 239.7 mg g^{-1} at the dosage of 0.2 g L^{-1} [180]. Kim et al. synthesized hierarchical nano-porous G-MnO_2 (using glucose), F-MnO_2 (using fructose), and S-MnO_2 (using sucrose) by a solution plasma process (SPP) and investigated their adsorption efficiencies for organic dye removal (in this case methylene blue (MB) dye). The MB dye removal efficiencies for all nano-porous MnO_2 obtained were > 99% for an initial MB dye concentration (C_0) of 10 mg L^{-1} within 2 min and > 82% for $C_0 = 50$ mg L^{-1} within 30 min [276]. Iron oxide nanoparticles have been discovered to be the most promising candidates for heavy metal adsorption and dye removal in wastewater treatment because of their high porosity, larger specific surface area, and strong magnetic response [168, 277]. The most commonly used iron oxide NPs are α-Fe_2O_3 (Hematite) [165], γ-Fe_2O_3 (maghemite) [166, 278], and Fe_3O_4 (magnetite) [168, 279, 280] to fulfill the purpose. Nassar performed

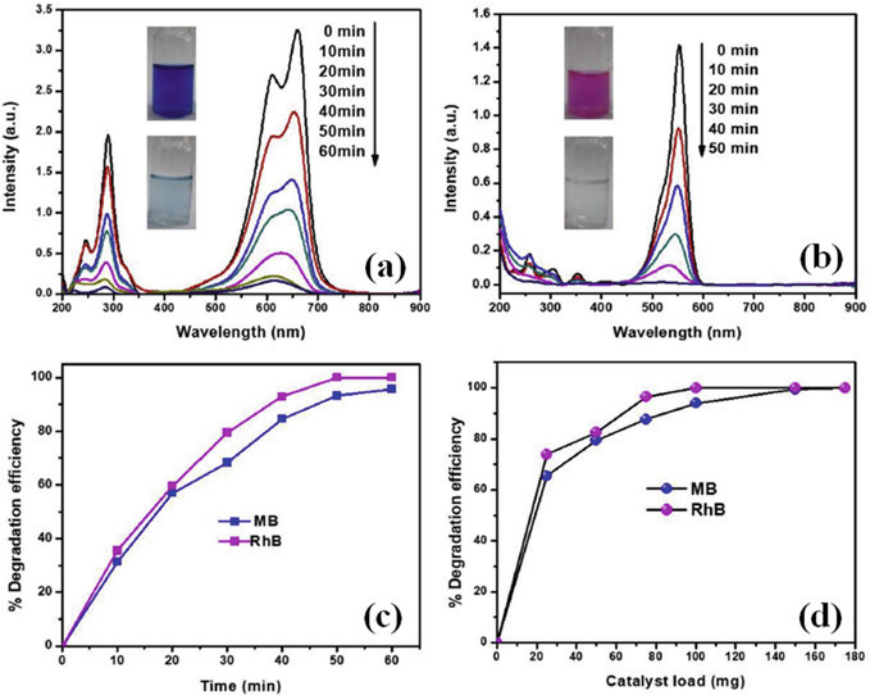

Fig. 5.13 ZnO nanoparticles' photocatalytic activity under UV illumination against (**a**) methylene blue and (**b**) rhodamine B. Degradation efficiency (%) (**c**) at fixed time durations and (**d**) as a function of catalyst loading for both dyes. Adapted with permission from [158]. Copyright 2019 Elsevier

a batch-adsorption technique in which Fe_2O_3 nanoparticles were employed as an absorbent for rapid removal of Pb(II) ions from aqueous solutions and the maximum absorption capacity achieved was 36 mg/g using this technique [281]. Similarly, the Batch experiments were performed by Zhu et al., where the volcanic rock coated with α-Fe_2O_3 NPs is used for efficient removal of Cd(II) ions from water. The obtained maximum absorption capacity of Cd(II) ions was 158.48 mg/g at 313 K [130]. Zuo and coworkers studied the heavy metal adsorption capacity of synthesized Fe_3O_4 NPs of average particle size of 8 nm, 12 nm, and 35 nm via a co-precipitation, the co-precipitation combining a surface decoration, and the polyol process, respectively [282]. These prepared Fe_2O_3 NPs were used to remove metal ions such as Ni(II), Cu(II), Cd(II), and Cr(VI) from wastewater, with removal capacities of toxic ions of 41.86 mg/l, 47.44 mg/l, 45.86 mg/l, and 43.59 mg/l for Ni^{2+}, Cu^{2+}, Cd^{2+}, and Cr^{6+}, respectively. The aforementioned studies indicate that MONPs play a very significant role in treating wastewater both as a photocatalyst and an absorbent.

5.6 Conclusion and Future Perspective

Recent advances in biotechnology, environmental, optics, photocatalysis, electronics, cell energy, and pharmaceutical sciences have enhanced the applicability of MONPs in these fields. As a result, we have included a brief overview of MONPs in this chapter, followed by a comprehensive description of all the recent trends in the possible synthesis routes for the MONPs. Additionally, a summary of various characterization techniques is given, along with information on how the size and morphology of MONPs affect their characteristics. Furthermore, in light of certain recent studies, we discussed the use of MONPs in various industries, including wastewater treatment, sensors, batteries, fuel cells, solar cells, and batteries. This leads to the conclusion that MONPs have played a significant role in applied nanotechnology for a variety of applications.

However, MONPs in nanotechnology also present certain difficulties. It is clear from the analysis that MONPs are harmful to plant life when they are excessive but beneficial to plants when they are present in trace amounts. Therefore, additional research in the field is needed to understand how MONPs affect plants. Further, more work should be put into choosing the right type of nano-oxide, designing hierarchical structures with appropriate morphologies, and selecting the right combination of additives that exhibit the best performance for detecting a specific environmental reductant because MO sensors currently have limited commercial applications. The bandgap energy of the MONPs layer restricts the efficiency of current devices when it comes to light harvesting. Therefore, it is crucial to create solar harvesting devices based on nanostructures that exhibit up-conversion across a wide spectral range when exposed to sunlight. Last but not least, the toxicity of nanoparticles can vary according to the experimental technique used for their preparation. Hence, in order to enhance the properties of MONPs synthesized from plant extracts, researchers should concentrate more on this area of study.

Acknowledgements D. K. S. acknowledges financial support from the SERB-DST ECR project "ECR/2016/001289". D. K. P. is grateful to DST, India for providing financial support under the INSPIRE Fellowship No. IF170625.

References

1. K.E. Sapsford, W.R. Algar, L. Berti, K.B. Gemmill, B.J. Casey, E. Oh, M.H. Stewart, I.L. Medintz, Chem. Rev. **113**, 1904–2074 (2013)
2. M.S. Chavali, M.P. Nikolova, S.N. Appl, Sci. **1**, 607 (2019)
3. C. Noguera, Physics and chemistry at oxide surfaces (Cambridge University Press, 1996).
4. H. H. Kung, Transition metal oxides: surface chemistry and catalysis (Elsevier, 1989).
5. V. E. Henrich, P. A. Cox, the surface science of metal oxides (Willey, 1994).
6. A.F. Wells, *Structural Inorganic Chemistry* (Oxf. Univ. Press., Oxford, 2012)
7. J. A. Rodriguez, M. Fernández-García, Synthesis, properties, and applications of oxide nanomaterials (John Wiley & Sons, 2007).

8. M. Fernández-García, A. Martínez-Arias, J.C. Hanson, J.A. Rodriguez, Chem. Rev. **104**, 4063–4104 (2004)
9. J. A Tanna, R. Gomaji Chaudhary, N. V Gandhare, H. D Juneja, Adv. Mater. Lett. **7**, 933–938 (2016).
10. D. Nunes, A. Pimentel, L. Santos, P. Barquinha, E. Fortunato, R. Martins, Catalysts **7**, 60 (2017)
11. D. Nunes, A. Pimentel, J.V. Pinto, T.R. Calmeiro, S. Nandy, P. Barquinha, L. Pereira, P.A. Carvalho, E. Fortunato, R. Martins, Catal. Today **278**, 262–270 (2016)
12. D. Nunes, A. Pimentel, P. Barquinha, P.A. Carvalho, E. Fortunato, R. Martins, J. Mater. Chem. C **2**, 6097–6103 (2014)
13. H. B. Wu, J. S. Chen, H. H. Hng, X. W. (David) Lou, Nanoscale **4**, 2526 (2012).
14. A. Pimentel, A. Samouco, D. Nunes, A. Araújo, R. Martins, E. Fortunato, Materials **10**, 1308 (2017)
15. A. Pimentel, J. Rodrigues, P. Duarte, D. Nunes, F.M. Costa, T. Monteiro, R. Martins, E. Fortunato, J. Mater. Sci. **50**, 5777–5787 (2015)
16. A. Kolmakov, M. Moskovits, Annu. Rev. Mater. Res. **34**, 151–180 (2004)
17. R.S. Devan, R.A. Patil, J.-H. Lin, Y.-R. Ma, Adv. Funct. Mater. **22**, 3326–3370 (2012)
18. X. Yu, Nat. Mater. **15**, 14 (2016)
19. R.W.G. Wyckoff, *Crystal Structures*, vol. 2 (Wiley, New York, 1964)
20. T. Guo, M.-S. Yao, Y.-H. Lin, C.-W. Nan, CrystEngComm **17**, 3551–3585 (2015)
21. R. A. Scott, John Wiley & Sons, and Wiley Online Library (Online service), Encyclopedia of inorganic and bioinorganic chemistry (2011).
22. C. Wang, L. Yin, L. Zhang, D. Xiang, R. Gao, Sensors **10**, 2088–2106 (2010)
23. S. Phanichphant, Procedia Eng. **87**, 795–802 (2014)
24. P. Ayyub, V.R. Palkar, S. Chattopadhyay, M. Multani, Phys. Rev. B **51**, 6135–6138 (1995)
25. H. Zhang, J.F. Banfield, J. Mater. Chem. **8**, 2073–2076 (1998)
26. V. M. Samsonov, N. Yu. Sdobnyakov, A. N. Bazulev, Surf. Sci. **532–535**, 526-530 (2003)
27. Z. Song, T. Cai, Z. Chang, G. Liu, J.A. Rodriguez, J. Hrbek, J. Am. Chem. Soc. **125**, 8059–8066 (2003)
28. A.D. Yoffe, Adv. Phys. **42**, 173–262 (1993)
29. L. Brus, J. Phys. Chem. **90**, 2555–2560 (1986)
30. G. Pacchioni, A.M. Ferrari, P.S. Bagus, Surf. Sci. **350**, 159–175 (1996)
31. J. A. Mejías, A. M. Márquez, J. Fernández Sanz, M. Fernández-García, J. M. Ricart, C. Sousa, F. Illas, Surf. Sci. **327**, 59–73 (1995).
32. M. Fernández-García, J.C. Conesa, F. Illas, Surf. Sci. **349**, 207–215 (1996)
33. J.A. Rodriguez, S. Chaturvedi, M. Kuhn, J. Hrbek, J. Phys. Chem. B **102**, 5511–5519 (1998)
34. G.J. Miller, Angew. Chem. **101**, 1570–1571 (1989)
35. P. Hofmann, Angew. Chem. **98**, 1037–1038 (1986)
36. P. Jeevanandam, K. J. Klabunde, In synthesis, properties, and applications of oxide nanomaterials (John Wiley & Sons, Ltd, 2007), pp. 381–410.
37. J.L. Anchell, A.C. Hess, J. Phys. Chem. **100**, 18317–18321 (1996)
38. J.A. Rodriguez, J. Hrbek, J. Dvorak, T. Jirsak, A. Maiti, Chem. Phys. Lett. **336**, 377–384 (2001)
39. A.M. Ferrari, G. Pacchioni, J. Phys. Chem. **99**, 17010–17018 (1995)
40. H. Lüth, *Solid Surfaces, Interfaces and Thin Films* (Springer, Berlin Heidelberg Springer e-books, Berlin, Heidelberg, 2010)
41. J.A. Rodriguez, X. Wang, G. Liu, J.C. Hanson, J. Hrbek, C.H.F. Peden, A. Iglesias-Juez, M. Fernández-García, J. Mol. Catal. Chem. **228**, 11–19 (2005)
42. R. Richards, W. Li, S. Decker, C. Davidson, O. Koper, V. Zaikovski, A. Volodin, T. Rieker, K.J. Klabunde, J. Am. Chem. Soc. **122**, 4921–4925 (2000)
43. G. Mavrou, S. Galata, P. Tsipas, A. Sotiropoulos, Y. Panayiotatos, A. Dimoulas, E. K. Evangelou, J. W. Seo, Ch. Dieker, J. Appl. Phys. **103**, 014506 (2008).
44. Q. Zhang, K. Zhang, D. Xu, G. Yang, H. Huang, F. Nie, C. Liu, S. Yang, Prog. Mater. Sci. **60**, 208–337 (2014)

45. S. Walia, S. Balendhran, H. Nili, S. Zhuiykov, G. Rosengarten, Q.H. Wang, M. Bhaskaran, S. Sriram, M.S. Strano, K. Kalantar-zadeh, Prog. Mater. Sci. **58**, 1443–1489 (2013)
46. S. K. Kulkarni, In: *Nanotechnology: Principles and Practices* (Springer International Publishing, Cham, 2015), pp. 77–109.
47. J. Singh, T. Dutta, K.-H. Kim, M. Rawat, P. Samddar, P. Kumar, J. Nanobiotechnology **16**, 84 (2018)
48. Annu, A. Ali, S. Ahmed, In: *Handbook of Ecomaterials*, edited by L. M. T. Martínez, O. V. Kharissova, B. I. Kharisov (Springer International Publishing, Cham, 2018), pp. 1–45.
49. D. Perednis, L.J. Gauckler, J. Electroceramics **14**, 103–111 (2005)
50. H. Reza, M. Ali, A. Morad, Iran J Chem Chem Eng **30**, 6 (2011)
51. B.K. Ozcelik, C. Ergun, Ceram. Int. **41**, 1994–2005 (2015)
52. F. Meierhofer, U. Fritsching, Energy Fuels **35**, 5495–5537 (2021)
53. B.S. Marshall, I. Telford, R. Wood, Analyst **96**, 569–578 (1971)
54. S. Pratsinis, In: *Aerosol Science and Technology: History and Reviews* (2011).
55. L. Madler, S.E. Pratsinis, J. Am. Ceram. Soc. **85**, 6 (2002)
56. R. Gunnarsson, U. Helmersson, I. Pilch, J. Nanoparticle Res. **17**, 353 (2015)
57. T. Suzuki, S. Suzuki, Y. Tomita, K. Okazaki, T. Shibayama, S. Kuwabata, T. Torimoto, Chem. Lett. **39**, 1072–1074 (2010)
58. D. Amans, C. Malaterre, M. Diouf, C. Mancini, F. Chaput, G. Ledoux, G. Breton, Y. Guillin, C. Dujardin, K. Masenelli-Varlot, P. Perriat, J. Phys. Chem. C **115**, 5131–5139 (2011)
59. T. Sasaki, Y. Shimizu, N. Koshizaki, J. Photochem. Photobiol. Chem. **182**, 335–341 (2006)
60. M. Okumura, S. Nakamura, S. Tsubota, N. Toshiko, M. Azuma, M. Haruta, Catal. Lett. **51**, 53–58 (1998)
61. S. K. Kulkarni, *Nanotechnology: Principles and Practices*, 3rd edn. (Springer Nature, Switzerland AG, 2015).
62. M. Ristić, S. Musić, M. Ivanda, S. Popović, J. Alloys Compd. **397**, 4 (2005)
63. S. Gnanam, V. Rajendran, J. Sol-Gel Sci. Technol. **53**, 555–559 (2010)
64. R.S. Dubey, Y.B.R.D. Rajesh, M.A. More, Mater. Today Proc. **2**, 3575–3579 (2015)
65. A. Raghunath, E. Perumal, Int. J. Antimicrob. Agents **49**, 137–152 (2017)
66. F. Ozel, H. Kockar, O. Karaagac, J. Supercond. Nov. Magn. **28**, 823–829 (2015)
67. S. Stankic, S. Suman, F. Haque, J. Vidic, J. Nanobiotechnology **14**, 1–20 (2016)
68. J. C. Yu, J. Yu, W. Ho, L. Zhang, Chem. Commun. 1942–1943 (2001).
69. W. Huang, X. Tang, Y. Wang, Y. Koltypin, A. Gedanken, Chem. Commun. 1415–1416 (2000).
70. S.H. Jung, E. Oh, K.H. Lee, Y. Yang, C.G. Park, W. Park, S.H. Jeong, Cryst. Growth Des. **8**, 265–269 (2008)
71. C.V. Krishnan, J. Chen, C. Burger, B. Chu, J. Phys. Chem. B **110**, 20182–20188 (2006)
72. C.J. Mao, H.C. Pan, X.C. Wu, J.J. Zhu, H.Y. Chen, J. Phys. Chem. B **110**, 14709–14713 (2006)
73. N. Soultanidis, W. Zhou, C.J. Kiely, M.S. Wong, Langmuir **28**, 17771–17777 (2012)
74. M. Baghbanzadeh, L. Carbone, P.D. Cozzoli, C.O. Kappe, Angew. Chem. - Int. Ed. **50**, 11312–11359 (2011)
75. M. Farahmandjou, S. Jurablu, Int. J. Bio-Inorg. Hybr. Nanomater. **3**, 179–184 (2014)
76. C. Kahattha, S. Santhaveesuk, Ferroelectrics **552**, 121–131 (2019)
77. X. Zhang, Z. Ai, F. Jia, L. Zhang, X. Fan, Z. Zou, Mater. Chem. Phys. **103**, 162–167 (2007)
78. K.G. Rao, C.H. Ashok, K.V. Rao, C.S. Chakra, Int. J. Sci. Res. **3**, 43–46 (2014)
79. M. Sanchez-Dominguez, M. Boutonnet, C. Solans, J. Nanoparticle Res. **11**, 1823–1829 (2009)
80. R. Zhang, L. Gao, Mater. Res. Bull. **37**, 1659–1666 (2002)
81. A. Bumajdad, M. Madkour, Nanoscale Res. Lett. **10**, 19 (2015)
82. A. Kumar, A. Saxena, A. De, R. Shankar, S. Mozumdar, RSC Adv. **3**, 5015–5021 (2013)
83. P. Sutradhar, N. Debnath, M. Saha, Adv. Manuf. **1**, 357–361 (2013)
84. N. Thovhogi, A. Diallo, A. Gurib-Fakim, M. Maaza, J. Alloys Compd. **647**, 392–396 (2015)
85. A.K. Jha, K. Prasad, K. Prasad, Biochem. Eng. J. **43**, 303–306 (2009)
86. N. Zikalala, K. Matshetshe, S. Parani, O.S. Oluwafemi, Nano-Struct. Nano-Objects **16**, 288–299 (2018)

87. C. Sharan, P. Khandelwal, P. Poddar, RSC Adv. **5**, 1883–1889 (2015)
88. Priya, Naveen, K. Kaur, A. K. Sidhu, Front. Nanotechnol. **3**, 655062 (2021).
89. S.O. Ogunyemi, M. Zhang, Y. Abdallah, T. Ahmed, W. Qiu, Md.A. Ali, C. Yan, Y. Yang, J. Chen, B. Li, Front. Microbiol. **11**, 588326 (2020)
90. Y. Suzuki, S.D. Kelly, K.M. Kemner, J.F. Banfield, Nature **419**, 134 (2002)
91. D. Kundu, C. Hazra, A. Chatterjee, A. Chaudhari, S. Mishra, J. Photochem. Photobiol. B. **140**, 194–204 (2014)
92. P. Vanathi, P. Rajiv, R. Sivaraj, Bull. Mater. Sci. **39**, 1165–1170 (2016)
93. I. Uddin, S. Adyanthaya, A. Syed, K. Selvaraj, A. Ahmad, P. Poddar, J. Nanosci. Nanotechnol. **8**, 3909–3913 (2008)
94. I. Hussain, N.B. Singh, A. Singh, H. Singh, S.C. Singh, Biotechnol. Lett. **38**, 545–560 (2016)
95. Y. Zhao, C. Li, X. Liu, F. Gu, H. Jiang, W. Shao, L. Zhang, Y. He, Mater. Lett. **61**, 79–83 (2007)
96. I. Bilecka, I. Djerdj, M. Niederberger, Chem. Commun. **0**, 886–888 (2008).
97. L. Gnanasekaran, R. Hemamalini, R. Saravanan, K. Ravichandran, F. Gracia, S. Agarwal, V.K. Gupta, J. Photochem. Photobiol. B **173**, 43–49 (2017)
98. R.S. Dubey, Mater. Lett. **215**, 312–317 (2018)
99. E.N. Kaufmann, *Characterization of Materials* (John Wiley and Sons, Hoboken, NJ, 2003)
100. S. Mourdikoudis, R.M. Pallares, N.T.K. Thanh, Nanoscale **10**, 12871–12934 (2018)
101. A. Polini, F. Yang, in *Nanofiber Composites for Biomedical Applications*, edited by M. Ramalingam and S. Ramakrishna (Woodhead Publishing), pp. 97–115 (2017).
102. E. M. Slayter and H. S. Slayter, *Light and Electron Microscopy* (Cambridge University Press, 1992).
103. D.K. Singh, R. Jagannathan, P. Khandelwal, P.M. Abraham, P. Poddar, Nanoscale **5**, 1882–1893 (2013)
104. P. Khandelwal, D.K. Singh, S. Sadhu, P. Poddar, Nanoscale **7**, 19985–20002 (2015)
105. W. Muhammad, N. Ullah, M. Haroon, B.H. Abbasi, RSC Adv. **9**, 29541–29548 (2019)
106. A. Chanda, K. Rout, M. Vasundhara, S. Ram Joshi, J. Singh, RSC Adv. **8**, 10939–10947 (2018).
107. D. Smith, In: *Nanocharacterization (2),* ed. by A. I. Kirkland, S. J. Haigh (Royal Society of Chemistry, 2015), p. 1.
108. S. Sagadevan, J. Podder, I. Das, J. Mater. Sci. Mater. Electron. **27**, 5622–5627 (2016)
109. Y. Wang, V. Petrova, In: *Nanotechnology Research Methods for Foods and Bioproducts* (John Wiley & Sons, Ltd, 2012), pp. 103–126.
110. P.P.N.V. Kumar, U. Shameem, P. Kollu, R.L. Kalyani, S.V.N. Pammi, BioNanoScience **5**, 135 (2015)
111. F. Chekin, S.M. Vahdat, M.J. Asadi, Russ. J. Appl. Chem. **89**, 816–822 (2016)
112. M.A. Ansari, H.M. Khan, M.A. Alzohairy, M. Jalal, S.G. Ali, R. Pal, J. Musarrat, World J. Microbiol. Biotechnol. **31**, 153–164 (2015)
113. D. K. Singh, M. Pradhan, A. Materny, *Modern Techniques of Spectroscopy*, 1st ed. (Springer Singapore, 2021).
114. D.K. Pandey, H.L. Kagdada, P. Sanchora, D. K. Singh, in *Modern Techniques of Spectroscopy: Basics, Instrumentation, and Applications.* ed. by D.K. Singh, M. Pradhan, A. Materny (Springer, Singapore, 2021), pp.145–184
115. K. Gopinath, V. Karthika, C. Sundaravadivelan, S. Gowri, A. Arumugam, J. Nanostructure Chem. **5**, 295–303 (2015)
116. Y. Liu, L. He, A. Mustapha, H. Li, Z. q. Hu, M. Lin, J. Appl. Microbiol. **107**, 1193–1201 (2009).
117. K.Y. Kumar, H.B. Muralidhara, Y.A. Nayaka, J. Balasubramanyam, H. Hanumanthappa, Powder Technol. **246**, 125–136 (2013)
118. M. Maruthupandy, Y. Zuo, J.-S. Chen, J.-M. Song, H.-L. Niu, C.-J. Mao, S.-Y. Zhang, Y.-H. Shen, Appl. Surf. Sci. **397**, 167–174 (2017)
119. D. K. Singh, S. Das, A. Materny, editors , *Advances in Spectroscopy: Molecules to Materials*, 1st ed. (Springer Singapore, 2019).

120. N.R. Dhineshbabu, V. Rajendran, N. Nithyavathy, R. Vetumperumal, Appl. Nanosci. **6**, 933–939 (2016)
121. J. Stetefeld, S.A. McKenna, T.R. Patel, Biophys. Rev. **8**, 409–427 (2016)
122. T. Ghosh, S.K. Dash, P. Chakraborty, A. Guha, K. Kawaguchi, S. Roy, T. Chattopadhyay, D. Das, RSC Adv. **4**, 15022–15029 (2014)
123. E.N. Taylor, K.M. Kummer, N.G. Durmus, K. Leuba, K.M. Tarquinio, T.J. Webster, Small **8**, 3016–3027 (2012)
124. P.C. Hiemenz, R. Rajagopalan (eds.), *Principles of Colloid and Surface Chemistry, Revised and Expanded*, 3rd edn. (CRC Press, Boca Raton, 2017)
125. B. S. Hameed, C. S. Bhatt, B. Nagaraj, and A. K. Suresh, in *Nanomaterials in Chromatography*, edited by C. M. Hussain (Elsevier, 2018), pp. 503–518.
126. T. Maiyalagan, B. Viswanathan, J. Power Sources **175**, 789–793 (2008)
127. M. Najafi, F. Di Giacomo, D. Zhang, S. Shanmugam, A. Senes, W. Verhees, A. Hadipour, Y. Galagan, T. Aernouts, S. Veenstra, R. Andriessen, Small **14**, 1702775 (2018)
128. R. R. Mather, In: *Surface Modification of Textiles*, edited by Q. Wei (Woodhead Publishing, 2009), pp. 296–317.
129. T. Radu, C. Iacovita, D. Benea, R. Turcu, Appl. Surf. Sci. **405**, 337–343 (2017)
130. X. Zhu, T. Song, Z. Lv, G. Ji, Process Saf. Environ. Prot. **104**, 373–381 (2016)
131. M. Iwamoto, T. Abe, Y. Tachibana, J. Mol. Catal. Chem. **155**, 143–153 (2000)
132. O. Vigil, F. Cruz, A. Morales-Acevedo, G. Contreras-Puente, L. Vaillant, G. Santana, Mater. Chem. Phys. **68**, 249–252 (2001)
133. R. Viswanatha, S. Sapra, B. Satpati, P.V. Satyam, B.N. Dev, D.D. Sarma, J. Mater. Chem. **14**, 661–668 (2004)
134. H.C. Ong, A.X.E. Zhu, G.T. Du, Appl. Phys. Lett. **80**, 941–943 (2002)
135. E.B. Lavik, I. Kosacki, H.L. Tuller, Y.-M. Chiang, J.Y. Ying, J. Electroceramics **1**, 7–14 (1997)
136. M.E. Franke, T.J. Koplin, U. Simon, Small **2**, 36–50 (2006)
137. H. Maekawa, R. Tanaka, T. Sato, Y. Fujimaki, T. Yamamura, Solid State Ion. **175**, 281–285 (2004)
138. S.C. Tjong, H. Chen, Mater. Sci. Eng. R Rep. **45**, 1–88 (2004)
139. Z. Wang, S. Seal, S. Patil, C. Zha, Q. Xue, J. Phys. Chem. C **111**, 11756–11759 (2007)
140. S. Lee, S.U.-S. Choi, S. Li, J.A. Eastman, J. Heat Transf. **121**, 280–289 (1999)
141. T.C. Paul, A. Tikadar, R. Mahamud, A.S. Salman, A.K.M.M. Morshed, J.A. Khan, Processes **9**, 858 (2021)
142. B. O'Regan, M. Grätzel, Nature **353**, 737–740 (1991)
143. M.B. Vazquez-Santos, P. Tartaj, E. Morales, J.M. Amarilla, Chem. Rec. **18**, 1178–1191 (2018)
144. B. Han, S.-J. Kim, B.-M. Hwang, S.-B. Kim, K.-W. Park, J. Power Sources **222**, 225–229 (2013)
145. X. Gao, Y. Li, W. Zeng, C. Zhang, Y. Wei, J. Mater. Sci. Mater. Electron. **28**, 18781–18786 (2017)
146. K. Murugan, D. Dinesh, K. Kavithaa, M. Paulpandi, T. Ponraj, M.S. Alsalhi, S. Devanesan, J. Subramaniam, R. Rajaganesh, H. Wei, S. Kumar, M. Nicoletti, G. Benelli, Parasitol. Res. **115**, 1085–1096 (2016)
147. S. Ranjan, N. Dasgupta, B. Rajendran, G.S. Avadhani, C. Ramalingam, A. Kumar, Environ. Sci. Pollut. Res. **23**, 12287–12302 (2016)
148. Y. Jouane, S. Colis, G. Schmerber, P. Kern, A. Dinia, T. Heiser, Y.-A. Chapuis, J. Mater. Chem. **21**, 1953–1958 (2011)
149. T. Marimuthu, N. Anandhan, R. Thangamuthu, Appl. Surf. Sci. **428**, 385–394 (2018)
150. J. Duan, Q. Xiong, H. Wang, J. Zhang, J. Hu, J. Mater. Sci. Mater. Electron. **28**, 60–66 (2017)
151. T. Seiyama, A. Kato, K. Fujiishi, M. Nagatani, Anal. Chem. **34**, 1502–1503 (1962)
152. C. Wang, X. Chu, M. Wu, Sens. Actuators B Chem. **113**, 320–323 (2006)
153. S.K. Shaikh, S.I. Inamdar, V.V. Ganbavle, K.Y. Rajpure, J. Alloys Compd. **664**, 242–249 (2016)
154. M. Pandurangan, G. Enkhtaivan, D.H. Kim, J. Photochem. Photobiol. B **158**, 206–211 (2016)

155. S. Kishwar, M.H. Asif, O. Nur, M. Willander, P.-O. Larsson, Nanoscale Res. Lett. **5**, 1669–1674 (2010)
156. F. Muhammad, M. Guo, Y. Guo, W. Qi, F. Qu, F. Sun, H. Zhao, G. Zhu, J. Mater. Chem. **21**, 13406–13412 (2011)
157. O. Eskikaya, S. Ozdemir, G. Tollu, N. Dizge, R. Ramaraj, A. Manivannan, D. Balakrishnan, Chemosphere **306**, 135389 (2022)
158. A.R. Prasad, J. Garvasis, S.K. Oruvil, A. Joseph, J. Phys. Chem. Solids **127**, 265–274 (2019)
159. Y. Li, J. Zhu, Y. Huang, F. Liu, M. Lv, S. Chen, L. Hu, J. Tang, J. Yao, S. Dai, RSC Adv. **5**, 28424–28429 (2015)
160. Z. Ying, Q. Wan, H. Cao, Z.T. Song, S.L. Feng, Appl. Phys. Lett. **87**, 113108 (2005)
161. B. Wang, L.F. Zhu, Y.H. Yang, N.S. Xu, G.W. Yang, J. Phys. Chem. C **112**, 6643–6647 (2008)
162. J.D. Prades, R. Jimenez-Diaz, F. Hernandez-Ramirez, S. Barth, A. Cirera, A. Romano-Rodriguez, S. Mathur, J.R. Morante, Sens. Actuators B Chem. **140**, 337–341 (2009)
163. H. Liu, D. Wexler, G. Wang, J. Alloys Compd. **487**, 24 (2009)
164. C. Fang, M. Zhang, J. Mater. Chem. **19**, 6258–6266 (2009)
165. Y.-H. Chen, F.-A. Li, J. Colloid Interface Sci. **347**, 277–281 (2010)
166. J. Hu, G. Chen, I.M.C. Lo, Water Res. **39**, 4528–4536 (2005)
167. K. Cao, T. Jin, L. Yang, L. Jiao, Mater. Chem. Front. **1**, 2213–2242 (2017)
168. S.-H. Huang, D.-H. Chen, J. Hazard. Mater. **163**, 174–179 (2009)
169. X.W. Lou, D. Deng, J.Y. Lee, J. Feng, L.A. Archer, Adv. Mater. **20**, 258–262 (2008)
170. G.X. Wang, Y. Chen, K. Konstantinov, J. Yao, J. Ahn, H.K. Liu, S.X. Dou, J. Alloys Compd. **340**, 5 (2002)
171. X. Xu, C. Wang, M. Fronzi, X. Liu, L. Bi, X.S. Zhao, Mater. Renew. Sustain. Energy **8**, 15 (2019)
172. M. Das, G. Sumana, R. Nagarajan, B.D. Malhotra, Appl. Phys. Lett. **96**, 133703 (2010)
173. G. Accardo, D. Frattini, S.P. Yoon, H.C. Ham, S.W. Nam, J. Power Sources **370**, 52–60 (2017)
174. C.-W. Kwon, J.-W. Son, J.-H. Lee, H.-M. Kim, H.-W. Lee, K.-B. Kim, Adv. Funct. Mater. **21**, 1154–1159 (2011)
175. T. Wang, Q. Xiao, Mater. Chem. Phys. **139**, 603–608 (2013)
176. Y.S. Kim, I.S. Hwang, S.J. Kim, C.Y. Lee, J.H. Lee, Sens. Actuators B Chem. **135**, 298–303 (2008)
177. C.S. Rout, M. Hegde, C.N.R. Rao, Sens. Actuators B Chem. **128**, 488–4293 (2008)
178. Z. Yan, J. Xie, J. Jing, M. Zhang, W. Wei, S. Yin, Int. J. Hydrog. Energy **37**, 15948–15955 (2012)
179. R. Yang, Y. Fan, R. Ye, Y. Tang, X. Cao, Z. Yin, Z. Zeng, Adv. Mater. **33**, 2004862 (2021)
180. M. Lin, Z. Chen, Chemosphere **250**, 126329 (2020)
181. D.K. Pandey, H.L. Kagdada, A. Materny, D.K. Singh, J. Mol. Liq. **322**, 114538 (2021)
182. P. Poizot, S. Laruelle, S. Grugeon, L. Dupont, J.-M. Tarascon, Nature **407**, 496–499 (2000)
183. H. B. Wu, J. S. Chen, X. W. (David) Lou, H. H. Hng, J. Phys. Chem. C **115**, 24605–24610 (2011).
184. D. Nunes, A. Pimentel, A. Gonçalves, S. Pereira, R. Branquinho, P. Barquinha, E. Fortunato, R. Martins, Semicond. Sci. Technol. **34**, 043001 (2019)
185. S. Cao, N. Sui, P. Zhang, T. Zhou, J. Tu, T. Zhang, J. Colloid Interface Sci. **607**, 357–366 (2022)
186. D. K. Pandey, H. L. Kagdada, A. Materny, D. K. Singh, J. Mol. Liq. **364** 119957 (2022)
187. Z. Zhang, J. Liu, J. Gu, L. Su, L. Cheng, Energy Env. Sci **7**, 2535–2558 (2014)
188. D.K. Pandey, H.L. Kagdada, A. Materny, D.K. Singh, J. Phys. Chem. A **125**, 2653–2665 (2021)
189. H.-T. Song, J. Choi, Y.-M. Huh, S. Kim, Y. Jun, J.-S. Suh, J. Cheon, J. Am. Chem. Soc. **127**, 9992–9993 (2005)
190. M. Kamali, K.M. Persson, M.E. Costa, I. Capela, Environ. Int. **125**, 261–276 (2019)
191. U.G. Akpan, B.H. Hameed, J. Hazard. Mater. **170**, 520–529 (2009)
192. R. Zha, T. Shi, Z. Zhang, D. Xu, T. Jiang, M. Zhang, RSC Adv. **7**, 6345–6357 (2017)
193. K.L. Chopra, P.D. Paulson, V. Dutta, Prog. Photovolt. Res. Appl. **12**, 69–92 (2004)

194. J. Yan, B.R. Saunders, RSC Adv **4**, 43286–43314 (2014)
195. G.K. Mor, K. Shankar, M. Paulose, O.K. Varghese, C.A. Grimes, Nano Lett. **6**, 215–218 (2006)
196. D. Wongratanaphisan, K. Kaewyai, S. Choopun, A. Gardchareon, P. Ruankham, S. Phadungdhitidhada, Appl. Surf. Sci. **474**, 85–90 (2019)
197. R. Chauhan, M. Shinde, A. Kumar, S. Gosavi, D.P. Amalnerkar, Microporous Mesoporous Mater. **226**, 201–208 (2016)
198. J. You, C.-C. Chen, L. Dou, S. Murase, H.-S. Duan, S.A. Hawks, T. Xu, H.J. Son, L. Yu, G. Li, Y. Yang, Adv. Mater. **24**, 5267–5272 (2012)
199. C. Thu, P. Ehrenreich, K.K. Wong, E. Zimmermann, J. Dorman, W. Wang, A. Fakharuddin, M. Putnik, C. Drivas, A. Koutsoubelitis, M. Vasilopoulou, L.C. Palilis, S. Kennou, J. Kalb, T. Pfadler, L. Schmidt-Mende, Sci. Rep. **8**, 3559 (2018)
200. R. Jose, V. Thavasi, S. Ramakrishna, J. Am. Ceram. Soc. **92**, 289–301 (2009)
201. Y. Wang, A. B. Djurišić, W. Chen, F. Liu, R. Cheng, S. Ping Feng, A. M. C. Ng, Z. He, J. Phys. Energy **3**, 012004 (2020).
202. N.M. Saidi, F.S. Omar, A. Numan, D.C. Apperley, M.M. Algaradah, R. Kasi, A.-J. Avestro, R.T. Subramaniam, A.C.S. Appl, Mater. Interfaces **11**, 30185–30196 (2019)
203. U. P. M. Ashik, S. Kudo, J. Hayashi, In: *Synthesis of Inorganic Nanomaterials* (Elsevier, 2018), pp. 19–57.
204. M.A. Kebede, Curr. Opin. Electrochem. **21**, 182–187 (2020)
205. X. Yan, Z. Wang, M. He, Z. Hou, T. Xia, G. Liu, X. Chen, Energy Technol. **3**, 801–814 (2015)
206. Z. Wei Seh, W. Li, J. J. Cha, G. Zheng, Y. Yang, M. T. McDowell, P.-C. Hsu, Y. Cui, Nat. Commun. **4**, 1331 (2013).
207. L. Zhang, H.B. Wu, X.W.D. Lou, Adv. Energy Mater. **4**, 1300958 (2014)
208. Y. Zhang, Y. Yan, X. Wang, G. Li, D. Deng, L. Jiang, C. Shu, and C. Wang, Chem.—Eur. J. **20**, 6126–6130 (2014).
209. X. Liang, C. Hart, Q. Pang, A. Garsuch, T. Weiss, L.F. Nazar, Nat. Commun. **6**, 5682 (2015)
210. G. Binitha, A.G. Ashish, D. Ramasubramonian, P. Manikandan, M.M. Shaijumon, Adv. Mater. Interfaces **3**, 1500419 (2016)
211. C. Chen, Y. Huang, H. Zhang, X. Wang, Y. Wang, L. Jiao, H. Yuan, J. Power Sources **314**, 66–75 (2016)
212. M.E. Donders, H.C.M. Knoops, W.M.M. Kessels, P.H.L. Notten, J. Power Sources **203**, 72–77 (2012)
213. P. Lightfoot, M.A. Mehta, P.G. Bruce, Science **262**, 883–885 (1993)
214. J. Guo and C. Wang, in *Functional Metal Oxide Nanostructures*, edited by J. Wu, J. Cao, W.-Q. Han, A. Janotti, H.-C. Kim, Vol. 149 (Springer New York, New York, NY, 2012), pp. 337–363.
215. A. Moncada, S. Piazza, C. Sunseri, R. Inguanta, J. Power Sources **275**, 181–188 (2015)
216. J.B. Wu, X. Xia, R.Q. Guo, X.H. Huang, Y. Lin, Mater. Res. Bull. **96**, 315–319 (2017)
217. J. Bai, B. Zhou, Chem. Rev. **114**, 10131–10176 (2014)
218. J.M. George, A. Antony, B. Mathew, Microchim. Acta **185**, 358 (2018)
219. O. Lupan, G. Chai, L. Chow, Microelectron. Eng. **85**, 2220–2225 (2008)
220. A. Narayana, S.A. Bhat, A. Fathima, S.V. Lokesh, S.G. Surya, C.V. Yelamaggad, RSC Adv. **10**, 13532–13542 (2020)
221. J. Ding, S. Chen, N. Han, Y. Shi, P. Hu, H. Li, J. Wang, Ceram. Int. **46**, 15152–15158 (2020)
222. T. Gakhar, A. Hazra, Nanoscale **12**, 9082–9093 (2020)
223. X. Liu, T. Ma, N. Pinna, J. Zhang, Adv. Funct. Mater. **27**, 1702168 (2017)
224. R. Doong, H. Shih, Biosens. Bioelectron. **25**, 1439–1446 (2010)
225. J. Liu, Y. Li, X. Huang, Z. Zhu, Nanoscale Res. Lett. **5**, 1177–1181 (2010)
226. A.A. Ansari, P.R. Solanki, B.D. Malhotra, Appl. Phys. Lett. **92**, 263901 (2008)
227. P.R. Solanki, A. Kaushik, A.A. Ansari, B.D. Malhotra, Appl. Phys. Lett. **94**, 143901 (2009)
228. M. Ahmad, C. Pan, Z. Luo, J. Zhu, J. Phys. Chem. C **114**, 9308–9313 (2010)
229. Y. Zhuo, Y.-Q. Chai, R. Yuan, L. Mao, Y.-L. Yuan, J. Han, Biosens. Bioelectron. **26**, 3838–3844 (2011)

230. J.X. Wang, X.W. Sun, A. Wei, Y. Lei, X.P. Cai, C.M. Li, Z.L. Dong, Appl. Phys. Lett. **88**, 233106 (2006)
231. S.-J. Bao, C.M. Li, J.-F. Zang, X.-Q. Cui, Y. Qiao, J. Guo, Adv. Funct. Mater. **18**, 591–599 (2008)
232. M.R. Alenezi, S.J. Henley, S.R.P. Silva, Sci. Rep. **5**, 8516 (2015)
233. T. Kobayashi, M. Ando, M. Haruta, Chem. Sens. **9**, 143 (1993). ((in Japanese))
234. T. Kobayashi, M. Haruta, H. Sano, B. Delmon, In: Proc. 3rd Int. Meeting Chemical Sensors, Cleveland, OH, USA, (1990), p. 318.
235. E. Mollow, In: Proceedings of the Photoconductivity Conference, ed. by R.G. Breckenridge (Wiley, New York, 1954) , p. 509.
236. Z. Li, H. Li, Z. Wu, M. Wang, J. Luo, H. Torun, P. Hu, C. Yang, M. Grundmann, X. Liu, Y. Fu, Mater. Horiz. **6**, 470–506 (2019)
237. X. Huang, Z. Zhang, J. Jiang, In: *2006 IEEE International Symposium on Industrial Electronics*, Vol. 2 (2006), pp. 1613–1618.
238. W. R. Grove, Lond. Edinb. Dublin Philos. Mag. J. Sci. **14**, 127–130 (1839).
239. S. Ball, J. Sharman, I. Harkness, Platin. Met. Rev. **55**, 225–228 (2011)
240. N. Rajalakshmi, N. Lakshmi, K. Dhathathreyan, Int. J. Hydrog. Energy **33**, 7521–7526 (2008)
241. H.B. Yu, J.-H. Kim, H.-I. Lee, M.A. Scibioh, J. Lee, J. Han, S.P. Yoon, H.Y. Ha, J. Power Sources **140**, 59–65 (2005)
242. M.Z. Hong, H.S. Lee, M.H. Kim, E.J. Park, H.W. Ha, K. Kim, J. Power Sources **156**, 158–165 (2006)
243. Y.-S. Kim, C.-W. Yi, H.S. Choi, K. Kim, J. Power Sources **196**, 1886–1893 (2011)
244. A. Meléndez-Ceballos, S.M. Fernández-Valverde, V. Albin, V. Lair, J.Á. Chávez-Carvayar, A. Ringuedé, M. Cassir, Int. J. Hydrog. Energy **41**, 18721–18731 (2016)
245. Y. Gong, D. Palacio, X. Song, R.L. Patel, X. Liang, X. Zhao, J.B. Goodenough, K. Huang, Nano Lett. **13**, 4340–4345 (2013)
246. Z. Fan, J. Li, W. Yang, Q. Fu, K. Sun, Y.-C. Song, Z. Wei, Q. Liao, X. Zhu, Chem. Eng. J. **385**, 123393 (2020)
247. J. Ahmed, H.J. Kim, S. Kim, RSC Adv **4**, 44065–44072 (2014)
248. K. Donaldson, A. Seaton, J. Nanosci. Nanotechnol. **7**, 4607–4611 (2007)
249. W.H. Suh, K.S. Suslick, G.D. Stucky, Y.-H. Suh, Prog. Neurobiol. **87**, 133–170 (2009)
250. N.L. Rosi, C.A. Mirkin, Chem. Rev. **105**, 1547–1562 (2005)
251. C.T. Campbell, C.H.F. Peden, Science **309**, 713–714 (2005)
252. A.H. Faraji, P. Wipf, Bioorg. Med. Chem. **17**, 2950–2962 (2009)
253. B.H. Kim, N. Lee, H. Kim, K. An, Y.I. Park, Y. Choi, K. Shin, Y. Lee, S.G. Kwon, H.B. Na, J.-G. Park, T.-Y. Ahn, Y.-W. Kim, W.K. Moon, S.H. Choi, T. Hyeon, J. Am. Chem. Soc. **133**, 12624–12631 (2011)
254. H.B. Na, J.H. Lee, K. An, Y.I. Park, M. Park, I.S. Lee, D.-H. Nam, S.T. Kim, S.-H. Kim, S.-W. Kim, K.-H. Lim, K.-S. Kim, S.-O. Kim, T. Hyeon, Angew. Chem. Int. Ed. **46**, 5397–5401 (2007)
255. J. Shin, R.M. Anisur, M.K. Ko, G.H. Im, J.H. Lee, I.S. Lee, Angew. Chem. Int. Ed. **48**, 321–324 (2009)
256. R.T. Selvi, A.P.S. Prasanna, R. Niranjan, M. Kaushik, T. Devasena, J. Kumar, R. Chelliah, D.-H. Oh, S. Swaminathan, G.D. Venkatasubbu, Appl. Surf. Sci. **449**, 603–609 (2018)
257. K. Karthik, S. Vijayalakshmi, A. Phuruangrat, V. Revathi, U. Verma, J. Clust. Sci. **30**, 965–972 (2019)
258. S. Gowri, R. Rajiv Gandhi, M. Sundrarajan, J. Mater. Sci. Technol. **30**, 782–790 (2014).
259. U. Lohbauer, A. Wagner, R. Belli, C. Stoetzel, A. Hilpert, H.-D. Kurland, J. Grabow, F.A. Müller, Acta Biomater. **6**, 4539–4546 (2010)
260. A. K. Barui, R. Kotcherlakota, C. R. Patra, In: *Inorganic Frameworks as Smart Nanomedicines* (Elsevier, 2018), pp. 239–278.
261. S. Ostrovsky, G. Kazimirsky, A. Gedanken, C. Brodie, Nano Res. **2**, 882–890 (2009)
262. R.D. Umrani, K.M. Paknikar, Nanomed. **9**, 89–104 (2014)

263. X. Bai, L. Li, H. Liu, L. Tan, T. Liu, X. Meng, A.C.S. Appl, Mater. Interfaces **7**, 1308–1317 (2015)
264. H.-M. Xiong, Adv. Mater. **25**, 5329–5335 (2013)
265. K.-Y. Hwa, B. Subramani, Biosens. Bioelectron. **62**, 127–133 (2014)
266. M. Premanathan, K. Karthikeyan, K. Jeyasubramanian, G. Manivannan, Nanomedicine Nanotechnol. Biol. Med. **7**, 184–192 (2011)
267. D.K. Pandey, M. Kuddushi, A. Kumar, D.K. Singh, Colloids Surf. Physicochem. Eng. Asp. **650**, 129631 (2022)
268. J. Schneider, M. Matsuoka, M. Takeuchi, J. Zhang, Y. Horiuchi, M. Anpo, D.W. Bahnemann, Chem. Rev. **114**, 9919–9986 (2014)
269. A.R. Khataee, M.B. Kasiri, J. Mol. Catal. Chem. **328**, 8–36 (2010)
270. T. Aarthi, P. Narahari, G. Madras, J. Hazard. Mater. **149**, 725–734 (2007)
271. J. Farner Budarz, E. M. Cooper, C. Gardner, E. Hodzic, P. L. Ferguson, C. K. Gunsch, M. R. Wiesner, J. Hazard. Mater. **372**, 61–68 (2019).
272. S. Gomez, C.L. Marchena, M.S. Renzini, L. Pizzio, L. Pierella, Appl. Catal. B Environ. **162**, 167–173 (2015)
273. Z. Li, Y. Sun, J. Xing, Y. Xing, A. Meng, J. Hazard. Mater. **352**, 204–214 (2018)
274. K. Rambabu, G. Bharath, F. Banat, P.L. Show, J. Hazard. Mater. **402**, 123560 (2021)
275. K. Li, H. Li, T. Xiao, J. Long, G. Zhang, Y. Li, X. Liu, Z. Liang, F. Zheng, P. Zhang, J. Environ. Manage. **251**, 109563 (2019)
276. H. Kim, A. Watthanaphanit, N. Saito, A.C.S. Sustain, Chem. Eng. **5**, 5842–5851 (2017)
277. Y. Pang, G. Zeng, L. Tang, Y. Zhang, Y. Liu, X. Lei, Z. Li, J. Zhang, Z. Liu, Y. Xiong, Chem. Eng. J. **175**, 222–227 (2011)
278. J. Hu, G. Chen, I.M.C. Lo, J. Environ. Eng. **132**, 709–715 (2006)
279. J. Liu, Z. Zhao, G. Jiang, Environ. Sci. Technol. **42**, 6949–6954 (2008)
280. A.R. Mahdavian, M.A.-S. Mirrahimi, Chem. Eng. J. **159**, 264–271 (2010)
281. N.N. Nassar, J. Hazard. Mater. **184**, 538–546 (2010)
282. Y.F. Shen, J. Tang, Z.H. Nie, Y.D. Wang, Y. Ren, L. Zuo, Sep. Purif. Technol. **68**, 312–319 (2009)

Chapter 6
Nanocrystalline High Entropy Alloys and Oxides as Emerging Materials for Functional Applications

Priyanka Kumari, Amit K. Gupta, Shashi Kant Mohapatra, and Rohit R. Shahi

Abstract Recently, researchers have paid attention to high entropy alloys (HEAs) and high entropy oxides (HEOs) because of their impressive mechanical properties, excellent corrosion resistance, extraordinary thermal stability, and tunable magnetic properties. The unique structure, core effects, and wide range of composing elements make HEAs and HEOs emerging materials for advanced functional applications. A detailed discussion on these emerging materials with their unique core effects is presented herein. Also, an overview of different synthesis methods of nanocrystalline HEAs and HEOs are discussed with their merits and demerits. The impressive mechanical, corrosion resistive, and magnetic properties are also discussed briefly. At the end of the chapter, different advanced functional applications such as electrochemical energy storage, hydrogen storage, waste water treatment, catalytic and microwave absorption applications of these materials are discussed.

Keywords High entropy alloys · High entropy oxides · Synthesis · Applications · Magnetic properties

6.1 Introduction

In the latter half of the eighteenth century, when the industrial revolution began, more and more metals and alloys were developed using different techniques. An alloy has always been mechanically, electrically, magnetically, and thermally superior to pure metals, making it the greatest gift of materials science to humankind. Alloying has been a field of vast interest in metallurgy and materials science as it is for the betterment of humankind. Conventional alloys are developed by combining two or three elements to enhance the desired property. Thus, in the case of conventional alloys, only one or two principal elements are usually present. The number of elements in the periodic table restricts the number of conventional alloys. Moreover, conventional alloys also have limitations regarding the combination of different properties in a

P. Kumari · A. K. Gupta · S. K. Mohapatra · R. R. Shahi (✉)
Functional Materials Research Laboratory, Department of Physics, Central University of South Bihar, Gaya, Bihar 824236, India
e-mail: rohitrshahi@cusb.ac.in

D. K. Singh et al. (eds.), *Nanomaterials*,
https://doi.org/10.1007/978-981-19-7963-7_6

particular alloy. Thinking out of the conventional box, Prof Brian Cantor [1] and Prof Jien-Wei-Yeh [2] independently came up with the new idea of equiatomic and non-equiatomic multicomponent alloys, these alloys later named as High Entropy Alloys (HEAs). Incidentally, they both came up with the first literature on HEA in the same year, 2004, although Cantor had started the research much earlier [2, 3]. Then it has been a dynamic topic for researchers to work on it, and around 5000 research papers have been published since 2004 on this emerging material.

6.1.1 Definition of HEAs

High entropy alloys (HEAs) are generally defined in two ways, i.e., based on composition and entropy. HEAs can be defined as alloys sharing five or more principal elements with a concentration between 5–35%. In addition, some minor elements with concentration <5% can also be added to enhance the desired property of the base HEA. [4] According to statistical thermodynamics, the configurational entropy of a system is given by Boltzmann's equation: $\Delta S_{conf} = K_B \ln w$, where K_B is Boltzmann constant and w is the number of ways in which the available energy can be distributed among the particles of the system. If we consider the equiatomic solid state solution of N elements, the configurational entropy per mole can be given as $\Delta S_{conf} = R \ln N$, where R is the gas constant. [5] This shows that the configurational entropy increases with the number of elements. If we evaluate the $\Delta S_{conf.}$ by selecting different no. of alloying elements, we found that the change in the configurational entropy is not significant with more than 13 alloying elements (shown in Fig. 1a). Moreover, it is found that the configurational entropy in the non-equiatomic case is less than that in the equiatomic case. Based on the above facts, the alloy can be classified into three categories—low entropy alloys (or Conventional alloys) with $\Delta S_{conf} \leq R$, medium entropy alloys with $R < \Delta S_{conf} \leq 1.5R$, and high entropy alloys with $\Delta S_{conf} > 1.5R$ [6]. Figure 1b represents the classification of the alloys on the basis of entropy.

Now, different research articles confirmed that HEAs possess extraordinary properties due to the core effect named (a) High Entropy Effect, (b) Sluggish Diffusion Effect, (c) Severe Lattice Distortion, and (d) Cocktail Effect [7, 8].

6.1.2 High Entropy Effect

Based on definition only, simple solid solution phases of bcc, fcc or hcp structures are formed for HEAs due to the high configurational entropy of these alloys [9–11]. According to Gibb's free energy, $\Delta G_{conf} = \Delta H_{conf} — T\Delta S_{conf}$ (where ΔH_{conf} = configurational enthalpy, T = temperature, and ΔS_{conf} = configurational entropy), the greater the value of ΔS_{conf}, the value of ΔG_{conf} becomes lower, the temperature being constantly high. Therefore, the probability of forming the solid solution rather than intermetallic compounds increases with the increased configurational

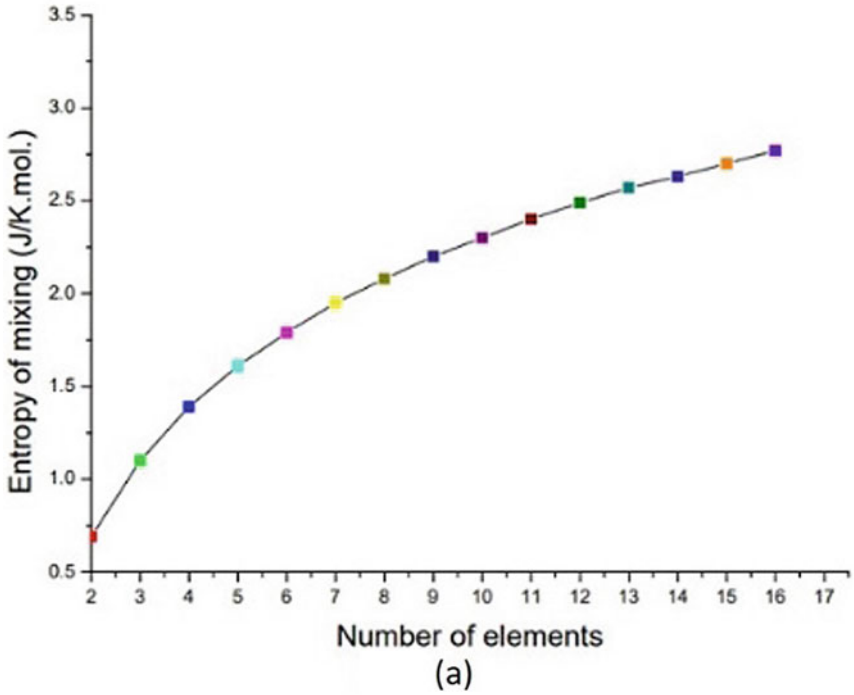

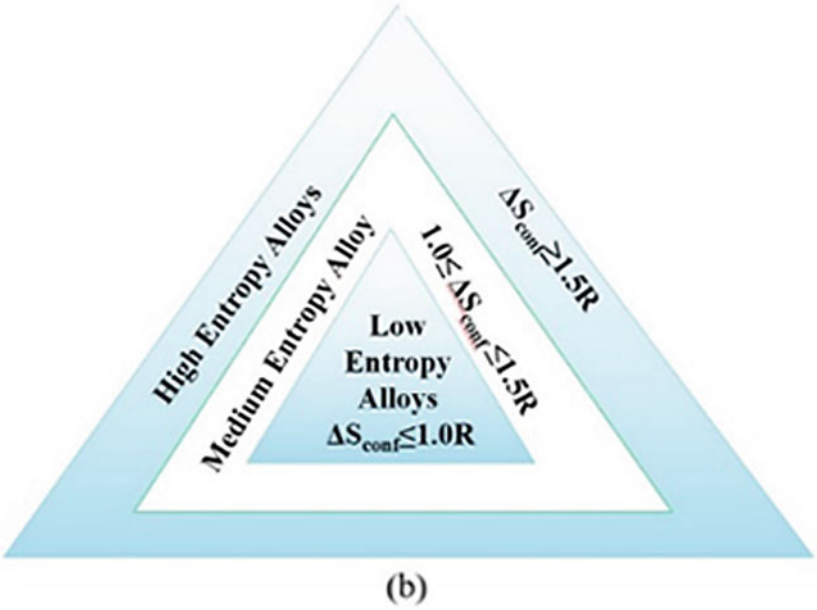

Fig. 6.1 (**a**) Variation of configurational entropy of mixing with an increase in the number of elements, (**b**) Classification of alloys based on configurational entropy. Adapted with permission from [6]. Copyright (2022) (Elsevier)

entropy, especially at high temperatures [2]. Although configurational, vibrational, magnetic dipole and electronic randomness contribute to the total mixing entropy, configurational entropy dominates over the other three contributions [2].

6.1.3 Sluggish Diffusion Effect

HEAs are formed by diffusion of the atoms of their constituent elements in each other lattice. The diffusion of different multi-principal elements for HEAs is quite slow as compared to conventional alloys [12]. This can be understood by considering the two facts. Firstly, each lattice site of HEAs has different neighboring atoms, and hence there is a difference in neighboring atoms before and after an atom jumps into a vacancy which results in different bonding and, thereby, different local energies for each site [2]. There are certain advantages of the sluggish diffusion effect as well. These are: —fine-sized particles, increase in recrystallization temperature, slow grain growth, and grain-coarsening [13, 14]. These benefits increase the toughness of materials, high-temperature strength, structural stability, random nucleation, and enhanced microstructural properties of HEAs.

6.1.4 Severe Lattice Distortion

The atoms in HEA may have irregularly sized neighbors. These size differences necessarily led to lattice distortion. Larger atoms push away their neighbors, and small ones leave extra space around [2]. The overall free energy of the HEA lattice is raised due to the strain energy associated with the lattice distortion, thereby affecting the properties of HEAs. This effect leads to pronounced solid solution strengthening and an increase in the scattering of propagating electrons and phonons, resulting in lower electrical and thermal conductivity of HEA [15].

6.1.5 Cocktail Effect

In 2003, Prof. S Ranganathan wrote an article on “Alloyed pleasures: Multi-metallic cocktails,” where the word “cocktail” was used for the first time in advanced material science [6, 16]. They concluded that the properties of HEAs depend not only on the properties of individual elements but also on the combined effect of the various constituent elements. For example, Al is a soft and low melting element. But experimentally, it is found that the hardness of the $Al_xCoCrCuFeNi$ alloy increases with increase in Al content. This is due to the hard BCC phase and the stronger cohesive bonding between Al and other components and its larger atomic size [2].

6.2 Prediction of Phase Formation Through Thermodynamic Parameters

The properties of the HEAs are highly sensitive to the phase structure [2]. It will be beneficial to theoretically predict the phase of selected HEAs before designing and developing it for a particular application. However, the most common phases that are usually detected in HEAs are disordered/random solid solution (e.g., bcc, fcc etc.), ordered solid solution (Eg:-B2, $L1_2$ etc.), and sometimes complex phases (Eg:-Laves, $\sigma - phase$) [2]. For the synthesis of HEAs, the basic Hume-Rothery rules are always considered along with certain thermodynamical parameters. Zhang [17] and Guo [18] studied and found that enthalpy(ΔH_{conf}) and entropy (ΔS_{conf}) of mixing and atomic size differences(δ) are the most important phase formation parameters for HEAs. We can predict the phase for the selected composition of HEAs using the mentioned thermodynamic parameters. For the formation of the solid solution phase, the conditions $-22 \leq \Delta H_{conf} \leq 7$ kJ/mol, $11 \leq \Delta S_{conf} \leq 19.5$ J/Kmol, and $0 \leq \delta \leq 8.5$ must be satisfied. [18] A larger positive value of ΔH_{conf} arises the probability of phase separation, and a larger negative value of ΔH_{conf} leads to the formation of intermetallic phases or compounds. A large atomic size difference(δ) supports the amorphous phase formation. So δ should be smaller [18]. In addition, the effect of entropy relative to enthalpy(Ω-parameter) must be greater than or equal to 1.1 [18]. Value of valence electron concentration (VEC) gives an idea about the type of simple solid solution phase. Guo et al. suggested that if the value of VEC ≥ 8, then the fcc phase may form [19]. The bcc phase will form if the value is VEC ≤ 6.87. And if the value of VEC is in the range of $6.87 \leq$ VEC ≤ 8, the mixture of fcc and bcc phase may form [19].

6.3 High Entropy Oxides

In 2015, Rost et al. developed the first High Entropy Oxide (HEO) (Mg0.2Co0.2Ni0.2Zn0.2Cu0.2)O system with rock-salt structure [20]. Similar to the concept of HEAs, HEOs are described as multicomponent oxide systems with five or more five constituent cations in an equimolar ratio for the formation of single-phase oxide [20–22]. The entropy stabilization factor is one of the dominant keys which affect the stabilization of HEO, and its value should be greater than 1.5 R (where R is the universal Gas Constant) [20–22]. The configurational entropy S_{config} value is evaluated for $C_xD_yO_z$ type oxide using Eq. (6.1) [22]:

$$S_{config} = -R\left[m \cdot \left(\sum_{a=1}^{C} Inm_{a^*} \cdot m_a \right)_{p\text{ - sites}} + n \cdot \left(\sum_{b=1}^{D} Inn_{b^*} n_b \right)_{Q\text{ - sites}} \right.$$

$$+z \cdot \left(\sum_{o=1}^{P} \mathrm{In} z_{o*} \cdot z_o \right)_{O\text{ - sites}} \Bigg] \tag{6.1}$$

where C, D, P represents the integer cation present in P, Q, O, sites and m_a, n_b, z_o is mole fractions of elements in P, Q, and O-sites. For oxide structure, the configuration entropy value is generally zero for O^{2-} site but in some cases, some extra configuration entropy is found in anion sublattice due to F^- in Oxyfluorides and oxygen defect [23].

There are eight significant classifications of HEOs based on the structure. These are fluorite, rock-salt, pyrochlore, bixbyite, magneto plumbite, spinel, O3-type layered, and perovskite [24]. The vast range structure of HEO endows a broad range of properties such as electrochemical, optical, magnetic, dielectric, mechanical, thermal, and catalytic [6, 25]. These emerging oxide materials showed improved properties as compared to binary and doped conventional oxides [26–28]. Moreover, high configuration disorder has certain advantages in regard to the advanced functional properties of HEOs.

6.4 Synthesis of HEAs and HEOs

High Entropy Materials (HEMs) can be synthesized through various routes, including conventional and novel synthesis methods [11]. These materials can be synthesized through solid state synthesis, liquid state synthesis, and gaseous state synthesis. Figure 6.2 summarizes the different synthesis routes and respective techniques for the synthesis of High Entropy Materials. Nanocrystalline high entropy materials can be synthesized through mechanical alloying followed by SPS and HPS [29], magnetron sputtering [30], electrochemical synthesis [31], carbothermal shock synthesis [32], plasma-related synthesis [33], microwave-assisted synthesis [34] and combustion assisted synthesis [35]. The detail of all the synthesis methods is beyond the scope of this chapter. These methods were also discussed in recent reviews [6, 11]. Here, we discuss only those synthesis methods which are used for the development of nanocrystalline HEAs and HEOs.

6.4.1 Synthesis Through Mechanical Alloying

Mechanical alloying is the top-down synthesis approach for developing homogeneous single-phase HEAs performed through a high-energy ball miller. High-energy ball milling is one of the powerful synthesis techniques to synthesize nanocrystalline high entropy alloys [37]. In this synthesis technique, the mixture of different elemental powders (selected composition of five or more elements) is milled in

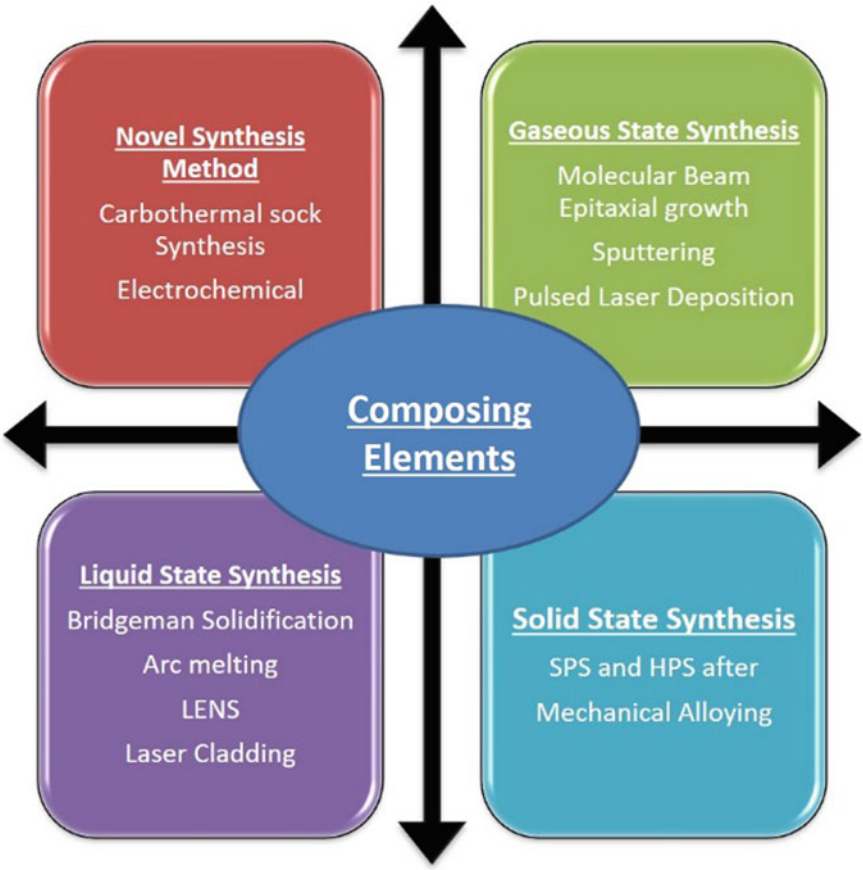

Fig. 6.2 Different synthesis routes of High Entropy Materials. Adapted with permission from [36]. Copyright (2022) (Elsevier)

a high-energy ball mill. Mechanical alloying (MA) is possessed, and a homogeneous distribution of nanoparticles is formed [38]. Further, diffusion is started due to local heat generated by the impact of balls and materials, and homogeneous alloy formation occurs. During high-energy ball milling, the mixture of elemental powders is continuously fractured, cold-welded, flattened, and rewelded, which assures the transformation of micro-size particles to the nano-size and leads to the diffusion of the elemental powders and the formation of the solid solution phase occurred [39]. Thus, the ball milling works two-fold: firstly, it reduces the particles, and secondly, homogeneous diffusion will occur during the milling. MA is one of the efficient ways the synthesis single-phase HEAs. A pictorial representation of the high-energy ball milling process for the synthesis of the HEAs is shown in Fig. 6.3 (i) [39]. The final microstructure and the particle size obtain after the MA depend on the ball to powder weight ratio, process control agent, rotation and revolution speed, milling duration,

and milling atmosphere. In order to reduce the lattice strain and densify the mechanically alloyed powder sample vacuum annealing/sintering is performed. Further, to preserve the nano-size effect of synthesis HEA through MA, Spark Plasma synthesized is performed. Spark plasma sintering is a technique for compacting and densifying the materials at sintering temperature for a certain duration with maintaining the nano-size effect of the synthesized HEA [40].

6.4.2 Synthesis Through Microwave-Assisted Method

Different novel synthesis technique has also been adopted for the synthesis of High Entropy Materials, such as Flame Spray pyrolysis, co-precipitation, Solid state reaction, and Nebulized Spray pyrolysis [20, 41]. These methods prevail some pros and cons in it. These methods' demerits were that they required expensive equipment, long synthesized duration, large particle size, and high energy consumption [41, 42]. The reduction of particle size to the nanosized range has a pronounced influence on the thermal, catalytic, dielectric, and magnetic properties of HEMs [43–47]. The microwave irradiation method is an ideal method for the formation of nanostructured High Entropy Materials [48–52]. The microwave energy interacts with two different modes with the sample. Firstly, it helps in ionic conduction and then dipole rotation. This induces collision, friction, and heat [52]. The multi-metallic ions during collision lead to nucleation of primary amorphous High entropy Oxide with microwave irradiation. The reaction rate increased due to internal heating, leading to the reactant ions' activation. This reduced the synthesis duration of HEO from hours to minutes and to seconds. The advantage of Microwave synthesis methods over conventional methods is that they require a short duration for synthesis, are cost-effective, have high purity, formation of nanosized particles, and are convenient and effortless. (MgCuNiCoZn)O HEO was synthesized by Kheradmandfard et al. and used as anode material for Lithium-Ion batteries [53]. They used microwave radiation of 2.45 GHz frequency. The synthesized nanoparticles were semi-spherical in nature of particle size on the scale of 20–70 nm. Moreover, Veronesi et al. also synthesized $FeCoCrNiAl_{2.5}$, FeCrNiTiAl, and FeCoNiCuAl, High Entropy Alloys through microwave-assisted method at frequency 2450 and 5800 MHz through direct heat of metal powder precursor [54].

6.4.3 Chemical Routes of Synthesis

Sol–gel technique is commonly used for the synthesis of conventional oxide nanoparticles. In this technique, exothermic reactions are evolved, and morphology, particle size, and texture can be easily controlled. This method can also be used for the synthesis of nanoparticles of HEMs. This method has evolved into three steps: Hydrolysis, condensation, and drying. During hydrolysis, the metal percussor is

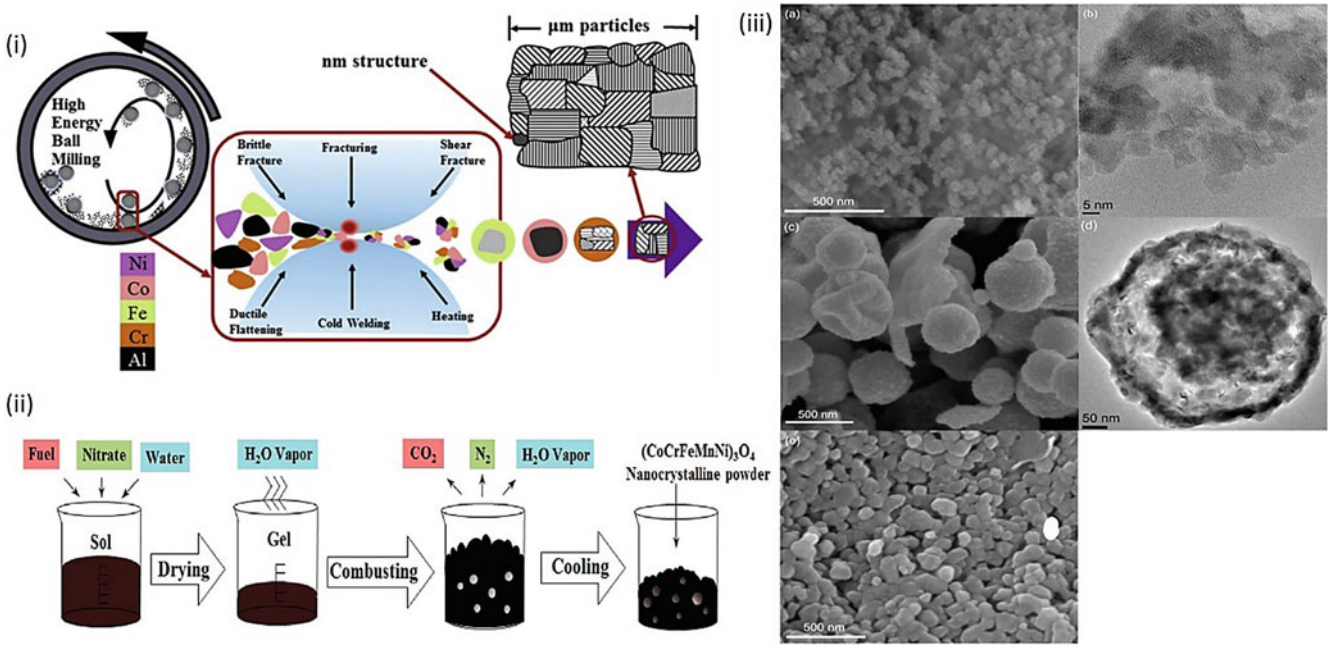

Fig. 6.3 (i) Steps involved in the mechanical alloying technique, Adapted with permission from [39]. Copyright (2018) (Elsevier). (ii) Synthetic scheme for (CoCrFeMnNi)3O4 nanocrystalline powder by SCS method, Adapted with permission from [56]. Copyright (2019) (Elsevier) (iii) SEM (left) and TEM (right) micrographs of (CoCuMgNiZn)O powder synthesized via FSP (**a**, **b**), NSP (**c**, **d**), and RCP (**e**), Adapted with permission from [41]. Copyright (2017) (Elsevier)

transformed into a metal hydroxide solution. In the condensation process, the formation of a 3-dimension gel occurs, and after drying, the products are changed into Xerogel or Aerogel. Sol–gel technique is classified into two forms: Aqueous, in which water is used as a solvent, and non-aqueous, in which organic solvents are used as solvent [55]. Mao et al. proposed a facile synthesis of a Spinel $(CoCrFeMnNi)_3O_4$ HEO by solution combustion synthesis methods (SCS) [56]. They synthesized High Entropy Spinel Oxide (HESO) nanoparticles by using metal nitrates as oxidizers and glycine as a fuel. Figure 3ii represents the systematic steps involved in the synthesis process. (Drying → combusting → cooling). (CoCrCuNiAl) nanocrystalline High Entropy Alloy (HEA) with average grain size of 14 nm is also synthesized by the sol–gel followed by in-situ reduction [35]. The HEA nanoparticles have bcc and fcc phases. Figure 3iii represents the different steps involved in the synthesis of nanocrystalline (CoCrCuNiAl) HEA [35].

The reverse co-precipitation method is also a commonly used method for the synthesis of nanoparticles. In this method, the precipitation of metal nanoparticles occurs when the base is used as a solvent. The nucleation and kinetic of particle growth are affected by the release of cations and anions [57]. Talluri et al. synthesized $(CoCrFeMnNi)_3O_4$ High Entropy Spinel Oxide (HESO) by reverse co-precipitation and studied the super capacitive properties. [58]. Sarkar et al. investigated the possibilities for the synthesis of Transition Metal HEO by two spray pyrolysis techniques, i.e., Flame Spray Pyrolysis (FSP) and Nebulized Spray Pyrolysis (NSP), and a wet chemical technique, i.e., Reverse Coprecipitation methods (RCP) [41]. Among the selected techniques, FSP and NSP are fast synthesis techniques that reduce the synthesis time and may establish the metastable phases. However, RCP is a slow synthesis technique that provides time for proper diffusion, and a single step may form. In FSP, the decomposition takes place in flame; hence, the particle formation time is very short (around 0.01 s) [59]. As a result, fine crystallites are formed (shown in Fig. 3iii a, b). In NSP, the time for the particles in a hot reactor was around 0.15 s (larger than FSP), and hence the formed nanoparticles have a large size as compared to the particles synthesized through FSP (shown in Fig. 3iii c, d). However, for the HEO synthesized through RCP, the morphology and phase are greatly affected by the reaction conditions and PH. Moreover, it is a slow process as compared to NSP and FSP, and hence large dense agglomerated particles are formed (as shown in Fig. 3iii e).

6.4.3.1 Laser-Assisted Synthesis

One of the major drawbacks of synthesizing HEAs through ball milling is chemical inhomogeneity [60]. The Laser-assisted synthesis can remove this shortcoming and able to produce nanoscale particles with chemical homogeneity. Wang et al. synthesized colloidal (CoCrCuFeNi) HEA NPs through the quick Laser synthesis method [61]. In this method, three steps are involved. HEA bulk is exposed to laser pulse for ultrashort durations followed by atomization, allowing the bulk to form a plume. Moreover, the ablate matter is nucleated, condensation occurs in the liquid, and the

colloidal HEA NPs are get stabilized in the ethanol. The colloidal nature of HEA NPs (having less than 5 nm in size) was confirmed with the help of the centrifugal size measurement technique. This synthesis approach is capable of industrial applications having a 3 gh^{-1} yield.

6.5 Properties of HEAs and HEOs

6.5.1 Mechanical Properties

HEAs possessed extraordinary mechanical properties, i.e., hardness, elastic modulus, yield strength, ultimate strength, elongation, fatigue, and creep resistance [62]. The mechanical properties of HEAs are highly sensitive to the composition, alloying elements, annealing treatment, processing rate, and phase structure. The mechanical property of the conventional alloys is dominated by the property of only one principal element. However, HEAs contain at least five principal elements, and the mechanical property can be tuned by the selection of alloying elements and their composition. The high strength for the case of HEA has occurred via the dislocation movement through the alloys and randomness at the atomic scale (the friction stress) [63, 64]. Classification of various structures in accordance with their typical hardness range is shown in Table 6.1, although there are a few exceptions as well.

We can see that the valence compounds have typical high hardness due to their strong covalent bonds. Intermetallic compounds with complex structures remain lower than valence compounds in the hardness range. This is due to the lack of easily accessible slip systems and hence hindered dislocation movements [2]. The ultrahigh yield strength and low plasticity are usually exhibited by bcc-based HEAs, while fcc-based HEAs exhibit low yield strength and high plasticity at room temperature. This is because of the presence of stronger directional bonding and lack of close-packed slip planes in bcc-based structures [65, 66]. The HEAs with bcc + fcc structure possessed balanced mechanical strength (i.e., high yield strength and high ductility). The high melting point of HEAs makes the high yield strength sustainable to ultra-high temperatures. The wear properties of HEAs have also been tested in a number of systems under both abrasive [17, 18] [67–72] and adhesive [73–75] conditions. Experimentally, it is found that the wear properties are effective in simple disordered

Table 6.1 Range for hardness value for different HEAs and Compounds [2]

Phase Types	Valence compounds (Carbides, Borides, etc.)	Intermetallic phases with complex structures (Laves, etc.)	BCC based structures (BCC, B2, etc.)	FCC based structures (FCC, $L1_2$, etc.)
Typical Hardness (Hv)	1000–4000	650–1300	300–700	100–300

phases in comparison to conventional alloys with similar hardness. HEAs with B2 and complex ordered phases as their main phase show outstanding wear properties. Exceptionally high-temperature strength is yet another benefit of HEAs. This originates from their outstanding thermal softening resistance from the sluggish diffusion that affected the HEAs. Above the transition temperature, a diffusion-related mechanism is mainly responsible for deformation. Thus, the sluggish diffusion effect reduces thermal softening [76, 77]. Thus, the HEAs provide great freedom to tune the mechanical properties by selecting a proper alloying element. For the case of HEA, we can develop alloys by considering the multiple mechanisms that hold synergistically and simultaneously contradictory mechanical properties i.e., high strength and ductility in a single alloy.

6.5.2 Magnetic Properties

6.5.2.1 Magnetic Properties of HEAs

The literature review confirmed that the magnetic properties of HEAs are highly sensitive to the phase structure, synthesis route, and alloying element present in a particular HEA [6, 78]. These materials showed prominent magnetic properties and had great potential to overcome the limitation of conventional magnetic materials [6]. Here we summarized the magnetic properties of some recently reported promising nanocrystalline HEAs. Yu et al. synthesized CoCrFeCuNi and CoCrFeMnNi HEAs through the mechanical alloying technique followed by high-pressure sintering (HPS) [79]. CoCrFeCuNi and CoCrFeMnNi HEAs have fcc and minor bcc phases in as milled stage. Metastable bcc phase transformed to single fcc phase and the lattice parameter decreased after the high-pressure sintering of these MAed HEAs. The value of hardness for as-cast CoCrFeCuNi HEA was found to be 133Hv [13] and the same was increased to 494 Hv for MA-HPS (Fig. 4a) [79]. Similarly, for as-cast CoCrFeMnNi HEA, the value of hardness was found to be 300 Hv [1], and the same was increased to 587 Hv for MA-HPS CoCrFeMnNi HEA (shown in Fig. 4a) [79]. The hardness value in these MA-HPS HEAs is increased due to a decrease in the particle size. The value of M_s and H_c was found to be 53.41 emu/g and 166 Oe for CoCrFeCuNi HEA. However, the value of M_s decreased to 1.34 emu/g for CoCrFeMnNi HEA. CoCrFeNiMn HEA was synthesized in another study through MA and exhibited fcc and bcc phases. However, after SPS at 800 ºC the metastable bcc phase disappeared [80]. For synthesized CoCrFeNiMn HEA, the particle size was found to be about 10 nm. Nanoscale grains play an important role in enhancing the hardness and compressive strength, the value of hardness and compressive strength for MA- SPS' ed HEA was found to be 646 Hv and 1987 MPa. The value of M_s, H_c and remanence ratio was found to be 94.29 emu/g, 175.68 Oe, and 2.95%, respectively. However, super-paramagnetic behavior was found in synthesized CoCrFeNiMn HEA (shown in Fig. 4b). It can be seen from the M-H loop (shown in Fig. 4b) that after SPS of CoCrFeNiMn HEA, paramagnetic behavior is observed with $M_s = 32.49$ emu/g

under the applied field of 20,000 Oe. The observed magnetic transitions occurred due to structure coarsening and phase transformation after SPS. A FeCoNiMnV HEA was synthesized through the MA in argon atmosphere, and the effect of milling duration on microstructure and magnetic properties was studied [81]. The developed HEA have a solid solution phase of bcc and fcc structure, and the bcc phase was vanadium rich. The formed phases for FeCoNiMnV HEA were stable even after 96 h of mechanical alloying. The value of M_s and H_c was 100 emu/g and 150 Oe for 48 h milled FeCoNiMnV HEAs. The value of M_s and H_c was reduced with prolonged milling of FeCoNiMnV HEA (Shown in the Fig. 4c), due to declination in the crystallinity and hence disruption in the magnetic exchange interaction. Duan et al. studied the effect of content of Cr and heat treatment on the magnetic properties of $FeCoNiAlCr_x$ (x = 0.1, 0.3, 0.5, 0.7 & 0.9) HEAs synthesized through MA abbreviated as M_x and followed by annealing at 500 ºC under argon atmosphere for 1 h abbreviated as T_x [82]. M_x exhibited a mixture of fcc and bcc structure with a peak corresponding to undissolved Co. However, the peak corresponding to undissolved Co disappeared for $T_{x,}$ and the mixture of bcc, fcc phase, and Fe_3O_4 was formed. With the increase in the Cr content, the value of M_s was decreased, and H_c firstly increased for Cr, x = 0.5, then decreased for a higher concentration of Cr. For annealed HEAs, the value of M_s increased to 98.69 emu/g from 94.89 emu/g when the x is increased to 0.3 from 0.1, respectively. Variation of M_s and H_c with an increase in the content of Cr is shown in Fig. 4d, e). In another study, Zhao et al. investigated the effect of Cr in $CoCr_xCuFeMnNi$ (x = 0, 0.5, 1.0, 1.5, 2.0) HEAs synthesized through MA in Ar atmosphere for 45 h of dry milling and then added 5 h of wet milling in ethanol [83]. Single fcc phase was formed for x = 0, 0.5, 1.0 and the mixture of fcc and bcc phase was found for x = 1.5, 2.0 in $CoCr_xCuFeMnNi$ HEAs. With increased Cr content, the value of M_s lowered due to a decrease in the content of ferromagnetic elements, and H_c increased. The variation of M_s and H_c with increased Cr content is shown in Fig. 4f.

Our research group also extensively studied the magnetic properties of TiFeNiCr-based HEAs. An AlCrFeMnNiTi HEA having fcc and bcc phase structure was synthesized through MA [84]. It was found that these phases remained stable after the vacuum annealing at 700 ºC for one h. However, the fcc phase volume fraction increased, and the bcc phase decreased with annealing. The value of M_s and H_c was found to be 17.5 emu/g and 153.8 Oe. However, the value of M_s decreased to 4.22 emu/g, and H_c increased to 215 Oe for 700 ºC annealed AlCrFeMnNiTi HEA. We also studied the phase formation and magnetic properties of TiFeNiCrM (M = Cr, Co, Mn) HEAs synthesized through MA [85]. Dual fcc and sigma phase was formed for TiFeNiCr, and TiFeNiCrMn HEAs. However single fcc phase was formed for TiFeNiCrCo HEA. The value of M_s and H_c was found to be 13.82 emu/g and 166.93 Oe, 2.28 emu/g and 225.83 Oe, and 24.44 emu/g and 149.54 Oe for TiFeNiCr, TiFeNiCrMn, and TiFeNiCrCo HEAs respectively. The value of M_s decreased from 13.82 emu/g to 2.28 emu/g after the addition of Mn in TiFeNiCr HEA, whereas the value of M_s increased to 24.44 emu/g after the addition of Co in TiFeNiCr HEA. The change in the value of M_s was observed due to the fact that the value of M_s is highly sensitive to the content of ferromagnetic elements present in the particular

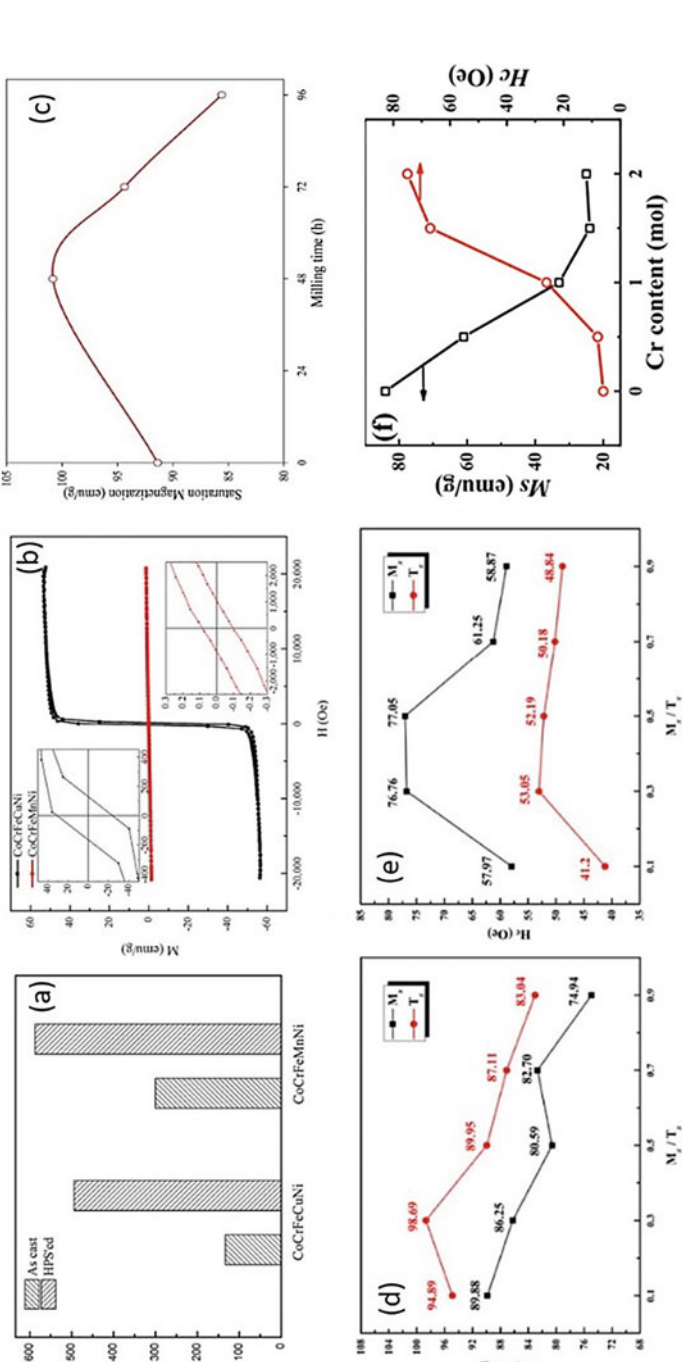

Fig. 6.4 (**a**) Value of hardness of CoCrFeCuNi and CoCrFeMnNi HEAs synthesized through casting and MA-HPS, Adapted with permission from [79]. Copyright (2016) (Elsevier), (**b**) M—H loop of CoCrFeCuNi and CoCrFeMnNi HEAs synthesized through MA- HPS, Adapted with permission from [79]. Copyright (2016) (Elsevier), (**c**) Variation of M_s and H_c with prolonged milling of FeCoNiMnV HEA. "Adapted with permission from [81]. Copyright (2019) (Elsevier). (**d**) Variation of M_s and (**e**) H_c with increase in the content of Cr for $FeCoNiAlCr_x$ (x = 0.1, 0.3, 0.5, 0.7 & 0.9) HEAs. Adapted with permission from [82]. Copyright (2020) (Elsevier). (**f**) variation of M_s and H_c with increase in Cr content for $CoCr_xCuFeMnNi$ (x = 0, 0.5, 1.0, 1.5, 2.0) HEAs. Adapted with permission from [83]. Copyright (2019) (Elsevier)

HEAs. We have also found that the value of M_s decreased after annealing due to an increase in the lattice parameter, which increased the distances between the ferromagnetic elements, and hence the magnetic exchange coupling was disturbed. Our further investigation was focused on the effect of annealing on phase formation and the magnetic properties of TiFeNiCrCo HEA synthesized through the MA [86]. The mixture of fcc, bcc, and minor impure phases was found for as-synthesized TiFeNiCrCo HEA. These phases were stable under vacuum annealing for 500 and 700 ºC. However, a Ti_4Fe_2O phase was formed for 500, and 700 ºC open air annealed TiFeNiCrCo HEA. However, the value of M_s was slightly increased for vacuum-annealed TiFeNiCrCo HEA at 500 and 700 ºC. The value of M_s and H_c was increased to 15.27 emu/g and 164.36 Oe, and 21.93 emu/g and 284.81 Oe for 500 and 700 °C open air annealed TiFeNiCrCo HEA. This increment in the value of M_s was associated with the change in the volume phase fraction of the bcc and fcc phases and the formation of Ti_4Fe_2O oxide phase. The increase in the value of H_c is obvious due to the increase in the particle size after annealing and the change in the volume phase fraction of synthesized phases. We optimized the composition of CoCrFeNiTi-based HEA for better soft-magnetic properties and studied the effect of variation of the composition of Fe, Co, Ni in CoCrFeNiTi- based HEA [87]. Three different non-equiatomic $Co_{35}Cr_5Fe_{20}Ni_{20}Ti_{20}$, $Co_{20}Cr_5Fe_{35}Ni_{20}Ti_{20}$, $Co_{20}Cr_5Fe_{20}Ni_{30}Ti_{20}$ HEAs were synthesized by MA with fcc, bcc, and minor intermetallic R-phase [87]. Among these HEAs, $Co_{35}Cr_5Fe_{20}Ni_{20}Ti_{20}$ HEA showed promising magnetic properties, M_s = 45.9 emu/g, H_c = 16.5 Oe in an as- synthesized state. However, the value of M_s and H_c was increased to 86.8 emu/g and 98.6 Oe for 700 ºC vacuum annealed $Co_{35}Cr_5Fe_{20}Ni_{20}Ti_{20}$ HEA. Further investigation was focused on the enhancement of the value of M_s by the variation of Fe and Ni in $Co_{35}Cr_5Fe_{20}Ni_{30}Ti_{20}$ HEA [88]. $Co_{35}Cr_5Fe_{10}Ni_{30}Ti_{20}$ HEA exhibited fcc phase with a minor intermetallic R-phase having optimized magnetic properties with M_s = 75.16 emu/g, and H_c = 12.8 Oe at as-synthesized state. Moreover, the value of M_s was increased to 78.01 emu/g, and H_c decreased to 1.75 Oe for 700 ºC vacuum annealed $Co_{35}Cr_5Fe_{10}Ni_{30}Ti_{20}$ HEA [88]. This increment in the value of M_s after annealing was due to the increase in the fcc phase volume fraction and the enhancement in the magnetic crystalline disorder. The decrement in the value of H_c was associated with the increase in particle size, decrease in lattice strain, increase in the volume phase fraction of R- phase, and precipitation of tiny particles on the large grains.

6.5.2.2 Magnetic Properties of HEOs

Mao et al. synthesized $(Co_{0.2}Cu_{0.2}Mg_{0.2}Ni_{0.2}Zn_{0.2})$ O HEO through a facile solution combustion synthesis (SCS) technique with rock-salt structure at a synthesis temperature of 1173 K [89]. The synthesized HEO showed antiferromagnetic ordering below 106 K (Neel temperature) and paramagnetic behavior at room temperature which is due to super-exchange interaction in rock-salt $(Co_{0.2}Cu_{0.2}Mg_{0.2}Ni_{0.2}Zn_{0.2})$ O HEO. In another study, $(CoCrFeMnNi)_3O_4$ HEO synthesized through the SCS technique exhibited a single spinel phase and some minor phases at other synthesis

temperatures 523 K [56]. However, a single fcc spinel phase was found for $(CoCrFeMnNi)_3O_4$ HEO synthesized at 623, 723, 823, 923, and 1123 K, with the increase in the synthesis temperature lattice constant was decreased. This HEO showed ferrimagnetic behavior and was not saturated even at the applied magnetic field of 20,000 Oe. The value of magnetization decreased up to synthesis temperature 723 K, then increased for higher synthesis temperature (shown in Fig. 5a). The value of H_c decreased with the decrease in the lattice distortion up to the synthesis temperature of 923 K and then slightly increased for the HEO synthesized at 1023 and 1123 K (shown in Fig. 5a). In another study, $(Cr_{0.2}Fe_{0.2}Mn_{0.2}M_{0.2}N_{0.2})_3O_4$ (M, N = Co^{2+}, Ni^{2+}, Zn^{2+}) HEO was synthesized at 923 K through a solution combustion synthesis technique exhibited single-phase spinel structure [90]. When Zn^{2+} was substituted for Co^{2+} the value of magnetization decreased from 9.86 emu/g for $(Cr_{0.2}Fe_{0.2}Mn_{0.2}Ni_{0.2}Co_{0.2})_3O_4$ HEO to 5.60 emu/g for $(Cr_{0.2}Fe_{0.2}Mn_{0.2}Ni_{0.2}Zn_{0.2})_3O_4$ HEO and when Zn^{2+} has substituted for Ni^{2+} the value of magnetization decreased to 8.08 emu/g for $(Cr_{0.2}Fe_{0.2}Mn_{0.2}Zn_{0.2}Co_{0.2})_3O_4$ HEO. The value of magnetization decreased due to the substitution of non-magnetic Zn^{2+} ion, which decreased the total magnetic moment of the HEO. In another study by Mao et al., they synthesized $(Al_{1/6}Co_{1/6}Cr_{1/6}Fe_{1/6}Mn_{1/6}Ni_{1/6})_3O_4$ HEO by SCS technique with single-phase spinel structure [91]. M-H curve recorded at different temperatures (50, 100, 150, 300 K) showed ferrimagnetic behavior and was not saturated at an applied field of 30,000 Oe (shown in Fig. 5b). The value of magnetization increased with decreasing temperature, whereas the value of M_r increased, and the value of H_c increased from 205.36 Oe at 300 K to 2277.59 Oe at 50 K, which is associated with the magnetic anisotropy [91]. Thus, we can tune the magnetic properties of HEO by the selection of proper cation without change in the basic structure of HEMs. The area of magnetic HEOs is quite new, and after the discovery, researchers are trying to understand the basic interaction mechanism and exploring the application of magnetic HEOs in the area of biomedical and data storage applications.

6.5.2.3 Corrosion Properties of HEAs

Corrosion is one of the most significant problems in all metals. Corrosion may occur in any of the three forms: Atmospheric corrosion, galvanic corrosion, or stress corrosion. Bolt plates, mesh, straps, and steal sets are made by most of the conventional alloys have a tendency become corrode under corrosive environments and become a cause for serious accidents and damage. Hygroscopic corrosion products at the metal surface promote moisture condensation, which can form an electrolyte onto a metal surface. Dust and gaseous pollutants are other reasons for the significant corrosion of metals and alloys. Chloride and sulfur contaminating the dust can accelerate corrosion and produce a cumulative corrosion effect on the steel. Corrosion reactions occur more rapidly in acidic solutions compared to neutral solutions. Also, dissolved solids in generally more corrosive and biological species within groundwater have a considerable effect on the corrosion of conventional alloys. HEAs can have high chromium, nickel, aluminum, molybdenum, titanium, and other passivation elements, leading

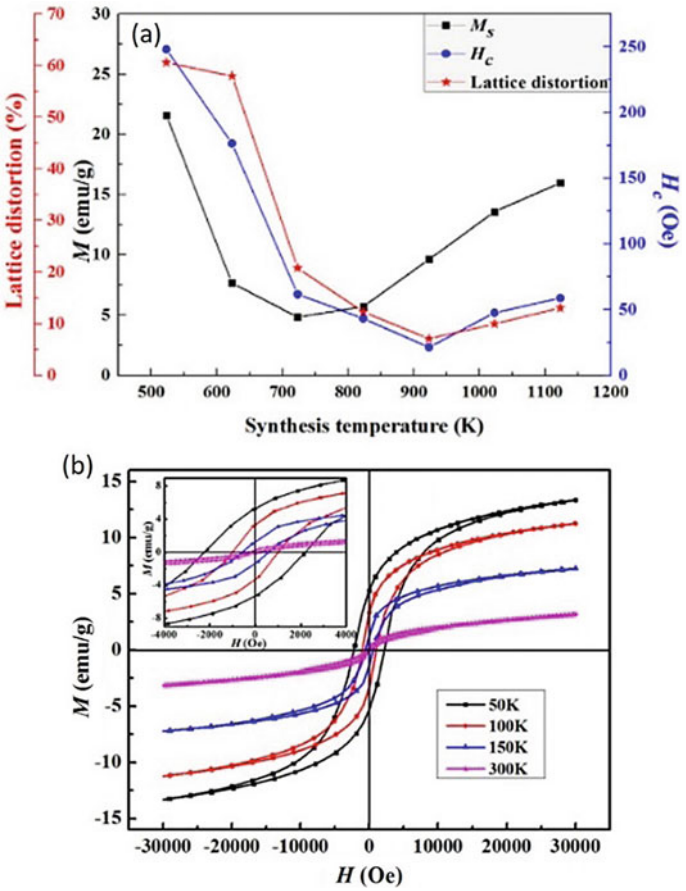

Fig. 6.5 (**a**) Variation of magnetization, H_c, and lattice distortion with synthesis temperature for $CoCrFeMnNi)_3O_4$ HEO. Adapted with permission from [56]. Copyright (2019) (Elsevier), (**b**) M-H curve of $(Al_{1/6}Co_{1/6}Cr_{1/6}Fe_{1/6}Mn_{1/6}Ni_{1/6})_3O_4$ HEO recorded at different temperatures. Adapted with permission from [91]. Copyright (2020) (Elsevier)

to superior corrosion resistance to stainless steels and Ni-based alloys [92]. In the literature, different reports on the excellent corrosion-resistant HEAs are available in various aqueous solutions, like H_2SO_4 solution, HCl, NaCl, NaOH, and $(OH)_2$ solutions [93–95]. HEAs possessed excellent corrosion resistance due to the existence of four core effects and freedom to select alloying elements. The benefits of HEAs over conventional alloys make them excellent corrosion resistance materials [92]. (i) High entropy effect of HEAs decreased the possibility of phase segregation and favored the formation of a uniform film on the surface of the HEA. Thereby improving the passive ability and pitting resistance of HEAs and avoiding galvanic corrosion. (ii) The uncertainty in occupying an atomic position in each lattice site from these distortions contributes to excess configuration entropy. This feature affects

HEAs' mechanical and chemical properties by creating an obstacle to dislocation motion and deformation, leading to a different stress corrosion cracking mechanism. Moreover, severe lattice distortion reduces HEAs' stability, which affects the passivation ability of the film on the surface of the alloys. (iii) for HEAs, the neighboring atoms of each lattice site are different than the conventional alloys. This difference in local atomic configuration leads to different bonding and, thereby, different local energies for each location. This feature is helpful in the diffusion of hydrogen and other corrosive gases and hence resistance to embrittlement at ambient temperature. (iv)The cocktail effect implies that the properties of alloys come from the combined properties of the alloying elements by the mixture rule and from the mutual interaction among all the alloying elements. These featured properties of HEAs endow us with opportunities to design and develop a synergistic system of multi-principal elements for excellent corrosion resistance with balanced mechanical properties. The studies are available for better corrosion resistance material with an element on HEAs' microstructural evolution and corrosion performance, aiming to reveal the correlation among the composition, microstructure, and corrosion resistance [96–98]. The most studied HEAs in regard to corrosion properties are FeCoCrNi-based HEAs with FCC structures. The presence of Cr, Ni, Mo, Ti, and Al makes these alloys a promising corrosion resistance alloy with balanced mechanical properties [99–103].

6.6 Advanced Functional Applications of HEAs and HEOs

6.6.1 Electrode Materials for Electrochemical Energy Storage

6.6.1.1 HEAs as Electrode Materials for Supercapacitor

Yuan et al. developed a composite electrode i.e., MnO_2 layer decorated on $FeCrCoMnNiAl_{0.75}$ HEAs metallic frame by pulse electrodeposition [104]. The HEA metallic frame was fabricated through selective phase dissolution of the fcc phase and retaining the bcc phase in 0.5 M H_2SO_4 after 2,50,60 h of immersion. The Metallic Frame (MF) was a three-dimensional cubic void with a wall of thickness 31–45 nm and a high surface area that provided excellent electronic and ionic conductivity. The morphology after MnO_2 layer is decorated on the HEAs metallic frame is shown in Fig. 6a. The MnO_2/MF composite electrode has declination in specific capacities value from 894 to 459 Fg^{-1} as the scan rate increased from 50 to 400 mVs^{-1} (shown in Fig. 6b). The specific capacity value of MnO_2/MF electrode is higher as compared to other MnO_2 based composites [105–110]. Moreover, after 6000 cycles, the electrode showed 81% of capacitance retention of initial value at 400 mVs^{-1} (shown in Fig. 6c). In another separate study. Kong et al. studied the super capacitive property of nano-porous binder-free HEA in 2 M KOH electrolytes [111]. They developed

electrodes after the selective dissolution of Al-Ni rich phase and retaining the Cr-Fe phase in H_2SO_4 solution of equiatomic AlCoCrFeNi HEA precursor. The cyclic voltammetric and Galvanostatic charge–discharge curve reveals that the electrodes have pseudo-capacitive nature (as shown in Fig. 6d, e). The electrode exhibits good voltammetry charge storage capacitance of around 700 F cm^{-3} due to the presence of interlinked conductive metal ligament of a large surface area. They found that the electrode retains 97% of initial capacitance after 3000 cycles, indicating the electrode's better stability. Shen et al. developed a new strategy for the development of electrodes by using HEA nanoparticles (HEA-NP) [112]. They deposited HEA-NP having a thin oxide layer on hyper crosslinked polymer-based carbons (HCPC) through in-situ reduction followed by a carbonization process [112]. The developed electrode with the composite mentioned above showed an excellent specific capacity of 495 F/g at 0.5 A/g current density in 1 M KOH electrolyte. Moreover, the developed electrode has 94.7% of capacity retention after 15,000 cycles. This extraordinary super capacitive behavior was observed due to the formation of a thin nanoscale layer of metal oxide. This layer act as a pseudo-capacitor. The study suggested that the storage capacity of multicomponent alloy nanoparticles can be enhanced by the deposition of particles on porous carbon. Equiatomic FeNiCoMnMg High Entropy Alloy nanoparticles (HEA) were assembled on aligned Carbon Nanofibers (CNFs) by Carbothermal Shock (CTS) (as shown in Fig. 6f) and supercapacitor performance was studied [113]. The developed (HEA-NP/ACNF) electrode has a specific capacitance of 54 F/g, 127 F/g, and 203 F/g at 20 mM,10 mM, and 5 mM percussor concentration of FeNiCoMnMg chloride solution (as shown in Fig. 6g). The developed HEA-NP/ACNF electrode showed good capacity retention of 85% after 2000 cycles and 21.7 Wh/kg energy density for 5 mM concentration due to homogenous coating for HEA-NP/ACNF electrode. The loss in capacity arises due to irreversible reduction and solvation.

6.6.1.2 HEOs as Electrode for Supercapacitor

Recently, few reports have appeared on the super capacitive applications of HEOs, and these materials also showed promising electrochemical energy storage. Liang et. al synthesized $(FeCoCrMnZn)_3O_4$ HESO through a solid state method calcined at 900 °C for 2 h [114]. The supercapacitive performance of the electrode was studied in 1 M KOH electrode in a three-electrode system. The $(FeCoCrMnZn)_3O_4$ electrode has pseudocapacitive behavior in the potential range of 0.15–0.5 V. They found redox peaks during charging and discharging due to changes in the oxidation state of transition metal cations present in the HEO. The value of specific capacitance was found to be 281.8, 301.5,287.9, and 340.3 Fg^{-1} at 10,5,2 and 1 A/g, respectively. The $(FeCoCrMnZn)_3O_4$ electrode showed capacity retention of 69% of the initial value after 1000 cycles measured at 5 A/g current density. Talluri et al. synthesized $(CoCrFeMnNi)_3O_4$ High Entropy Spinel Oxide nanoparticle with spherical morphology through reverse co-precipitation method and studied the super capacitive properties of electrode developed by HESO nanoparticles in 2 M KOH electrolyte

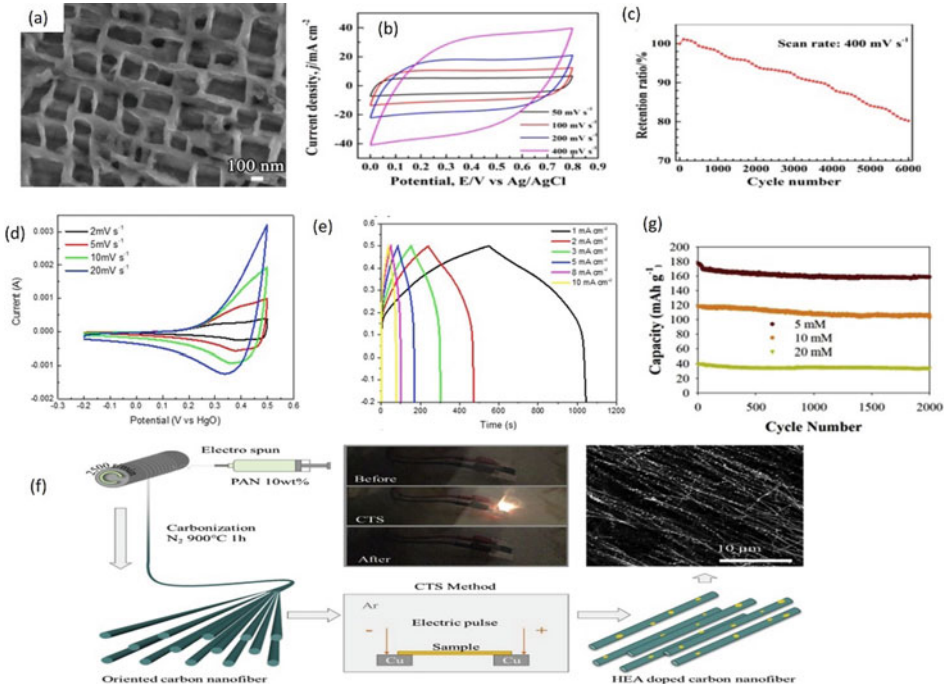

Fig. 6.6 (**a**) The surface morphology of metallic frame after MnO_2 electrodeposition, (**b**) Cyclic voltammetry curve of MnO_2/MF composite electrode at various scan rates, (**c**) Retention ratio for 6000 cycles at 400 mVs^{-1} scan rates of MnO_2/MF composite electrode. Adapted with permission from [104]. Copyright (2021) (Elsevier). (**d**) Cyclic voltammetry curve recorded at different scan rates and (**e**) Galvanostatic charge–discharge curve at different current densities of nano-porous equiatomic AlCoCrFeNi HEA precursor. Adapted with permission from [111]. Copyright (2019) (Elsevier). (**f**) The synthesis of HEA-NPs/ACNF, and (**g**) cyclability performance at different concentrations of 5 mM, 10 mM and 20 mM of precursor FeNiCoMnMg chloride solution. Adapted with permission from [113]. Copyright (2020) (Elsevier)

[58]. The developed as electrode showed pseudocapacitive nature confirmed through the C-V measurements at different scan rates (as shown in Fig. 7a). The specific capacity value was found to be 90,108,126,152,190,210,228,239 Fg^{-1} at current density of 25,20,15,10,5,3,1,0.5 Ag^{-1}, respectively. Also, the electrode showed a rate capability of 38% from 0.5 to 25 Ag^{-1}. The electrode exhibited good cyclability; after 1000 cycles, the capacity retention was 76% at 1 Ag^{-1} current density (as shown in Fig. 7b). The coulombic efficiency was 86% after 1000 cycles. The HESO electrode showed a specific capacity of 239 Fg^{-1} at a current density of 0.5 Ag^{-1} with a specific energy density of 24.1 $Whkg^{-1}$. Lal et. al developed High Entropy Oxide–Carbon Nanotubes (HEO-CNTs) composite by the growth of CNTs on HEO nanoparticles [115]. The HEO (Ni–, Fe–, Co–, Cr, and Al–) was synthesized through sol–gel auto combustion technique. The three samples, HEO, HEO-CNT, and reduced HEO-CNT were synthesized systematic manner. The schematic diagram for the synthesis of different composite materials is shown in Fig. 7c. The super capacitive performance was studied in a three-electrode system in various electrolytes. The C-V and GCD curve of HEO, HEO-CNT, and rHEO-CNT electrodes were studied in 1 M H_2SO_4 electrolyte in half cells shown in Fig. 7(d, e). The HEO, HEO-CNT, and rHEO-CNT electrodes exhibited a specific capacity of 91.5,156.0 and 170.1 F g^{-1} at the scan rate of 100 mVs^{-1}. The value of capacitance was highest for rHEO-CNT due to the high specific surface area and EDLC-like behavior of CNTs. In PVA/H_2SO_4 hydrogel electrolyte, the HEO-CNT electrode shows 100% capacitance retention for 15,000 cycles at the current density of 5 Ag^{-1} and also with 100% of coulomb efficiency with stability (as shown in Fig. 7f). Moreover, in [BMIM][TFSI] electrolyte HEO-CNT electrode showed a specific capacitance of 271 Fg^{-1} at 1 A/g specific current.

6.6.1.3 HEOs as Electrode for Battery

(Mg,Cu,Ni,Co,Zn)O HEO was synthesized by a novel and fast microwave irradiation method by Kheradmandfard et. al and used as anode material for Lithium-Ion Battery (LIB) [53] The electrochemical properties were studied in 1 M $LiPF_6$ in combination with diethyl carbonate, ethylene carbonate and 2 wt% of vinylene carbonate electrolyte. The electrode delivered a specific capacity of 250 $mAhg^{-1}$ at 5 A/g, and also it showed great rate capability from 0.1 to 5 A/g current density. They reported that the electrode showed good capacity retention of 98% after 1000 cycles at 1 A/g and concluded that high cyclic stability was achieved due to the entropy stabilized phase. Recently Xiang et al. also studied the effect of the addition of Al in $(CoCrFeMnNi)_{0.6}O_{4-d}$ nanocrystalline powder with a high concentration of oxygen vacancy synthesized by the combustion synthesis method [116]. With the addition of Al in the base materials, the capability becomes double. They concluded that lattice distortion is enhanced due to the small ionic size of Al, and hence more accommodation of Li-ion is possible for $(Al_{0.2}CoCrFeMnNi)_{0.58}O_{4-d}$ HEO. $(FeCoNiCrMnXLi)_3O_4$ Spinel HEO was synthesized by Duan et al. and investigated the effect of Cu, Mg, and Zn on the structure and electrochemical performance of

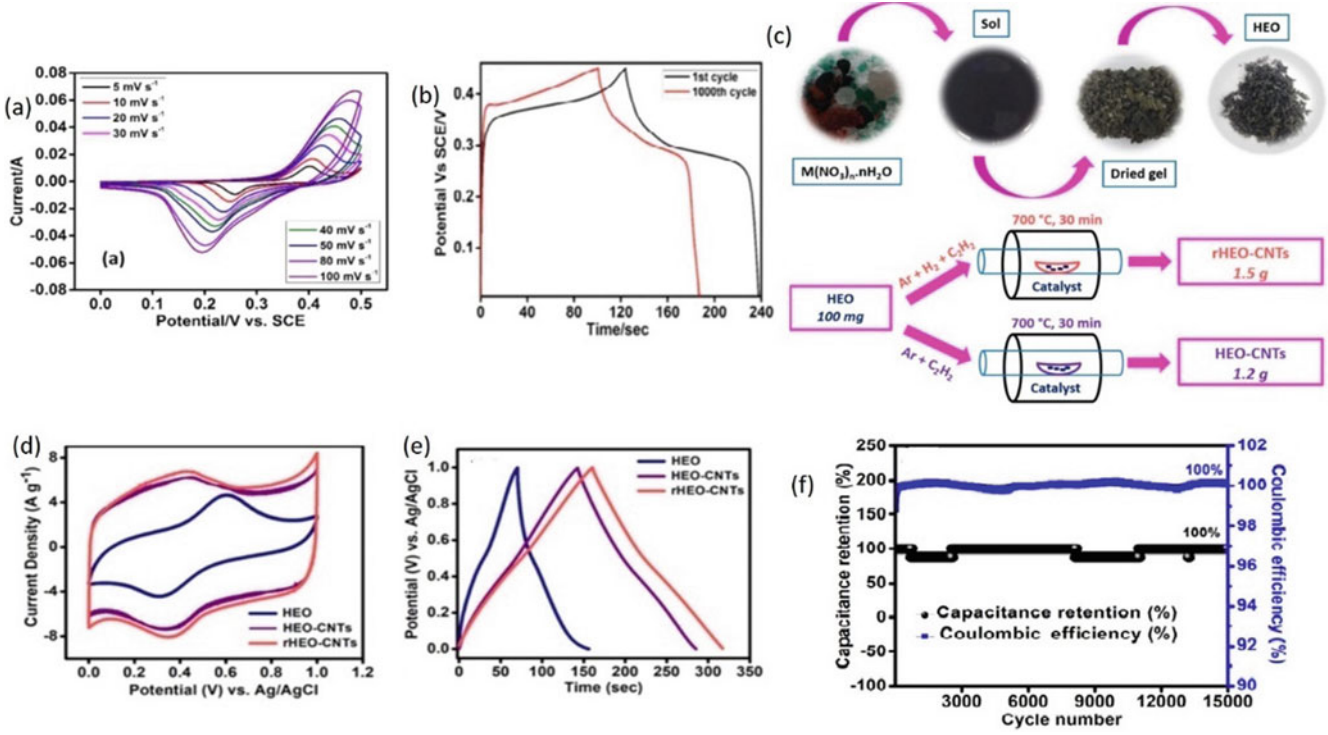

Fig. 6.7 (**a**) C-V curve recorded at different scan rate, (**b**) cyclic performance at 1 A/g with 1000 cycles for $(CoCrFeMnNi)_3O_4$ HESO. Adapted with permission from [58]. Copyright (2021) (Elsevier). (**c**) Pictorial view of synthesis route of HEO nano- particles, HEO-CNT and rHEO-CNT nanocomposite, (**d**) and (e) are C-V and GCD curve of HEO, HEO-CNT and rHEO-CNT in 1 M H_2SO_4 aqueous electrolyte, (**f**) Capacitance retention after 15,000 cycles at 5 A/g specific current in PVA/H_2SO_4 hydrogel electrolyte. Adapted with permission from [115]. Copyright (2019) (American Chemical Society)

the spinel HEO [117]. They found that $(FeCoNiCrMnZnLi)_3O_4$ spinel phase for Zn substituted HEO, and it has the best performance with a capacity of 522 mAh/g even after 100 cycles with increasing trends in the capacity observed with cycling. Similar to the study of Duan et al., Xiao et al. compared the electrochemical performance of Mg and Zn containing Spinel HEO i.e., $(FeNiCrMnZn)_3O_4$ and $(FeNiCuMnMg)_3O_4$ [118]. They also found that Zn containing Spinel HEOs had more lithium storage capacity and also having better crystallinity.

6.6.2 HEAs as Hydrogen Storage Materials

For harnessing hydrogen economy, safe and efficient hydrogen storage is a crucial issue. Till now, all hydrogen-fueled vehicles are equipped with unsafe high-pressure hydrogen cylinders (Fuel cell and combustion type). It is now well known that hydrogen can only be safely stored as a metal hydride form. For practical realization of a safe, efficient metal hydride tank, we need low density, high storage capacity, i.e., high volumetric and gravimetric storage of hydrogen, excellent thermal conductivity, high kinetics for the absorption, and desorption of hydrogen reaction [119, 120]. All the investigated conventional alloys have good gravimetric storage capacity but suffer low volumetric capacity [121]. In the past two–three years, some promising results have appeared on the hydrogen storage properties of HEAs [36]. It is now well known that several technologically important properties of HEAs are governed by their associated four core effect. These core effects of HEAs may further endow excellent hydrogen storage properties [36]. If we talk specifically, (i) the high entropy effect endows the formation of simple solid solution phases, i.e., bcc and fcc, and it is well known that the bcc phase is most favorable for better HS, (ii) the sluggish diffusion effect helps in the precipitation of nanograins these may further help to enhance the active sites for hydrogen and helps in the absorption /desorption kinetics, (iii) severe lattice distortion, it endows the large voids space for storage of hydrogen and (iv) cocktail effect will help to tune the absorption /desorption kinetics, reaction, storage capacity by the synergistic effect of each element [122]. Kao et al. reported HS properties of CoFeMnTiVZr-based HEA in 2010. This was the Ist report on the HS properties of HEA. They developed $CoFeMnTi_xVZr$, $CoFeMnTiV_yZr$, $CoFeMnTiVZr_z$ HEAs for different values of x,y and z ranges from $0.5 \leq x \leq 2.5, 0.4 \leq y \leq 3, 0.4 \leq z \leq 3$ by arc melting [123]. C_{14}-type laves phase was reported, and it was stable with hydrogenation/dehydrogenation. The higher value of the storage capacity was found for the range of x in 0.5–2 and the range of z in 0.4–2.3. Thus, this report confirmed how we could tune the HS storage properties of HEAs by a small change in the composition without changing the basic structure of HEAs. After the report of Kao et al., several research groups started work on the HS properties of HEAs [124–133]. Recently, Strozzi et al. investigated the HS properties of MgVM (M = AlCrNi) ternary, MgVAlCr, MgVCrNi, MgVAlNi quaternary, and MgVAlCrNi quinary alloy. Synthesized through High energy ball milling under 3 atm of hydrogen pressure [124]. MgAlVCrNi has a single-phase

and absorbs only 0.3 wt% of hydrogen. They also synthesized the non-equiatomic composition of Mg and V, namely $Mg_{28}V_{28}Al_{19}Cr_{15}Ni_6$ and $Mg_{26}Al_{31}V_{31}Cr_6Ni_6$ HEA. They found a low storage capacity of HS and concluded that the low value of HS was found due to the presence of a large number of elements present in the alloy that have a positive enthalpy of hydrogen. Only Ni has a negative enthalpy of hydrogen. In another study, TiZrNbFeNi and non-equiatomic $Ti_{20}Zr_{20}Nb_5Fe_{40}Ni_{15}$ HEAs were also synthesized and studied for HS behavior [126]. The PCI absorption desorption measurement was also measured and shown in Fig. 8a, b). The equiatomic HEA absorbs 1.64 wt%, and non-equiatomic HEA absorbs only 1.34 wt% after Ist absorption cycles because of the large cell volume of equiatomic TiZrNbFeNi HEA. However, non-equiatomic HEA performed better regarding the reversibility and storage capacity after the 2nd cycle. Moreover, both the HEAs did not have a well-defined plateau, confirming the hydrogenation through the solid solution mechanism. Recently, Zhang et al. found improved hydrogen desorption kinetics and significant improvement in the absorption temperature after activation of TiZrNbTa HEA synthesized through arc melting followed by suction casting [134]. The hydrogen absorption temperature was reduced to room temperature for activated HEA from 715 K (for without activation) (as shown in Fig. 8c). The significant improvement in the absorption kinetics after activation can be seen in Fig. 8d. They concluded that activated TiZrNbTa HEA followed higher nucleation rates than as-cast TiZrNbTa HEA. The improved hydrogenation behavior was observed due to the existence of a vacancy cluster in TiZrNbTa HEA and hence improved the hydrogen diffusion efficiency. They suggested that the value of δ also plays a significant role in single-phase hydride formation, larger δ promotes the formation of single-phase hydride and lower δ value promotes the formation of two steps hydrides phase [134]. High storage capacity Ti-V-Cr based bcc HEA was synthesized by Liu et al. [127]. Different compositions $V_{35}Ti_{30}Cr_{25}Fe_{10}$, $V_{35}Ti_{30}Cr_{25}Mn_{10}$, $V_{30}Ti_{30}Cr_{25}Fe_{10}Nb_5$and $V_{35}Ti_{30}Cr_{25}Fe_5Mn_5$ bcc HEA were developed through melting. Among studied compositions, $V_{35}Ti_{30}Cr_{25}Mn_{10}$ HEA confirmed the highest storage capacity. However, $V_{35}Ti_{30}Cr_{25}Fe_5Mn_5$ HEA showed the highest reversible storage capacity under hydrogen absorption measurement at 2000 kPa pressure and room temperature (shown in Fig. 8e). The trends for hydrogen absorption were found in the order of $V_{35}Ti_{30}Cr_{25}Mn_{10} > V_{35}Ti_{30}Cr_{25}Fe_5Mn_5 > V_{35}Ti_{30}Cr_{25}Fe_{10} > V_{30}Ti_{30}Cr_{25}Fe_{10}Nb_5$. This trend is the same as the order of increasing unit cell volume. However, the reverse trends have been observed in desorption pressure with increasing cell volume, i.e., $PV_{35}Ti_{30}Cr_{25}Fe_{10} > PV_{35}Ti_{30}Cr_{25}Fe_5Mn_5 > PV_{35}Ti_{30}Cr_{25}Mn_{10}$.

6.6.3 Waste Water Treatment

The production of azo dyes from different industries like textile, rubber, food, plastic etc., is one of the most severe impacts on the environment. These azo dyes are not easily degradable due to their complex stable structure, making it hard to remove

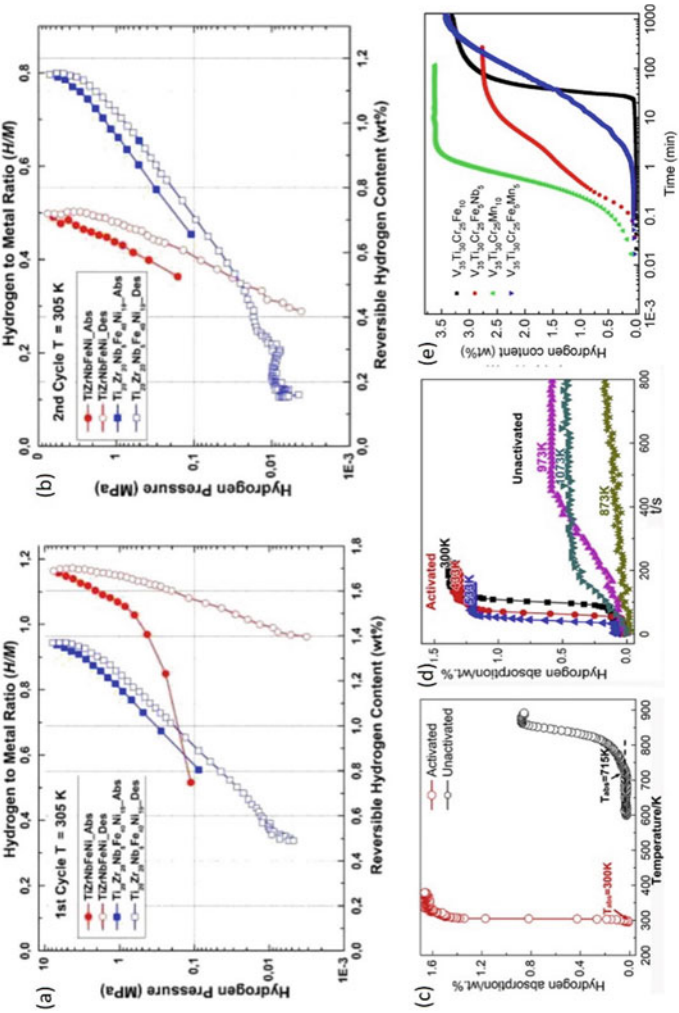

Fig. 6.8 The PCI absorption and desorption curve for (**a**) 1st absorption desorption cycle, (**b**) 2nd absorption desorption cycle for TiZrNbFeNi and non-equiatomic $Ti_{20}Zr_{20}Nb_5Fe_{40}Ni_{15}$ HEAs. Adapted with permission from [126]. Copyright (2020) (Elsevier). (**c**, **d**) Hydrogen absorption and kinetic plot for unactivated TiZrNbTa HEA. Adapted with permission from [134]. Copyright (2019) (Elsevier). (**e**) Measurement of reversible storage capacity under hydrogen absorption measurement at 2000 kPa pressure and room temperature of $V_{35}Ti_{30}Cr_{25}Fe_5Mn_5$ HEA. Adapted with permission from [127]. Copyright (2021) (Elsevier)

them from water. These azo dyes also negatively affect human and animal health [135]. The catalytic treatment is one of the conventional ways to treat these azo dyes from an aqueous solution. Transition metals Mg, Fe, Al, or Zn are used as catalysts, but these catalysts have certain limitations like Mg is easily consumed because of low corrosion resistance, and Fe can be easily agglomerated and less stable under such ambiance [136]. Thus, cost-effective, efficient, and environmentally friendly materials are required to treat this wastewater from the industry. Recently, AlCoCrTiZn HEA is used as decolorized material for azo dyes [137]. This study showed good efficiency for degradation of direct blue 6(DB6). The reported AlCoCrTiZn HEA has a lower activation barrier and more efficiently degraded azo dye than Fe-based catalyst. The authors claimed that the excellent performance of mechanically alloyed AlCoCrTiZn HEA was observed due to the high residual stress, severe lattice distortion, and favorable chemical composition of HEA. In another study, AlCoCrFeMn HEA was also synthesized through mechanical alloying and found that the decolorization rate of this HEA is 3-times faster than AlCoCrTiZn HEA [138]. Further, Wu et al. study was extended to the effect of the addition of Mg, Ti, Ni as the sixth element in AlCoCrFeMn HEA on the degradation of DB6 [139]. They concluded that the Mg and Ti both are beneficial, while Ni plays a negative role in the decolorization of DB6. Also, new AlFeMnTiCr, AlFeMnTiCo, and AlFeMnTiNi HEAs were synthesized and investigated for degradation of DB6 [140]. They found AlFeMnTiCr HEA was 19-times and 100-times more efficient as compared to Fe–Si–B alloy and commercial Fe powder, respectively. The use of HEAs to decolorize azo types of waste water opens a new area of applications of HEAs.

6.6.4 Catalyst Materials

Few reports are also available on the different catalytic applications of HEAs. $Ir_{0.19}Os_{0.22}Re_{0.21}Rh_{0.20}Ru_{0.19}$ and $Ir_{0.18}Os_{0.18}Pt_{0.16}Re_{0.17}Rh_{0.16}Ru_{0.15}$ HEA possessed excellent catalytic activity for oxidation of methanol as compared with pure metals [141]. For HEAs as a catalyst for methanol oxidation, the presence of platinum atoms absorbs the methanol molecule. However, other transition metal endows surface oxides to oxidize absorbed methanol at low potential. The electrochemical water splitting has two reactions, Hydrogen Evolution Reaction (HER) and Oxygen Evolution Reaction (OER), for hydrogen production. The poor efficiency of the cell is due to the higher practical cell voltage (1.8–2 V) as compared to the theoretical value (1.23 V) [142]. Traditionally Pt-based catalysts are used to accelerate the HER kinetics, but non-Pt-based catalysts are needed for harnessing the cost-effective hydrogen production. The multicomponent alloy may possess excellent catalytic activity due to the cocktail effect, disorder structure, metastable characteristics, tuneable composition, and partially filled d orbital [143]. Moreover, the high corrosion resistance of HEAs is another benefit to be used these materials for HER and OER [144–147]. The different nanoparticles of HEAs have been synthesized and

investigated for catalytic applications in methanol oxidation [141], Hydrogen Evolution Reaction (HER) [144, 145], Oxygen Evolution Reaction (OER) [146, 147], Oxygen Reduction Reaction (ORR) [148] and Carbon dioxide reduction reaction [149, 150]. For most of these reactions, the conventional catalyst is costly Pt-based. The use of HEA as a catalyst is cost-effective and efficient.

6.6.5 Microwave Absorbing Materials

In recent years, microwave absorbing properties of HEAs have been investigated. HEAs possessed promising microwave absorption properties due to their comprehensive properties. A flaky FeCoNiCrAl HEA was synthesized through MA, having M_s = 20.21 emu/g and H_c = 142 Oe [151]. The synthesized HEA has the value of RL_{min} = 35.3 dB at 10.35 GHz with effective absorption bandwidth of 2.7 GHz. Moreover, crystalline HEA has better microwave absorption properties than amorphous alloys [152]. For FeCoNiCrAl HEA, the increase in the content of Cr increased complex permittivity was observed [82]. HEA for microwave absorption is FeCoNiSiAl HEA [153, 154]. The studies confirmed that the crystal structure and microstructure are the two important parameters that govern the microwave absorption properties of HEAs. As we know, in the case of HEAs, the structure and microstructure of the synthesized alloys are highly sensitive to the alloying element and processing parameters. Thus, by selecting proper alloying elements and synthesis parameters, we can easily tune the microwave absorption properties of HEAs. Wu et al. developed HEA based composite for the high-performance EM wave absorption. They synthesized $FeCoNiCrCuAl_{0.3}$ HEA as core and Ni-NiO as shell, i.e., core–shell microspheres, by hydrothermal method [155]. This composite's adequate absorption bandwidth was found to be 4 GHz with an ultra-thin thickness (1.3 mm). Through this strategy, they combined two components with no EM wave absorption property independently to realize a composite material with extraordinary EM wave property.

6.7 Conclusions and Future Outlooks

In conclusion, we can say HEAs and HEOs are emerging materials with extraordinary properties compared to conventional alloys and ceramics. These are multi-principal alloys, and their compounds have excellent physical and chemical properties. HEAs and HEOs provide us vast freedom to select elements for the balance properties in a single material. We can easily tune the multiple properties simultaneously by selecting proper alloying elements and their compositions. Thus, these materials can be considered technologically vital materials. In this chapter, we briefly describe the four core effects of HEAs responsible for these materials' extraordinary properties. Also, we summarized different synthesis methods for synthesizing nanocrystalline HEAs and HEOs and briefly discussed their merits and demerits. The properties of

the materials are susceptible to the alloying elements, composition, synthesis method, and processing routes.

Moreover, we summarized the different properties of these materials and discussed the correlation of these properties with the alloying elements and processing parameters. Though these materials have extraordinary properties, these materials are emerging and may also have applications in different advanced areas. Here, we also summarized the advanced functional application of these materials in electrochemical energy storage, hydrogen storage, the catalyst for methanol oxidation, OER, HER, wastewater treatment, and microwave absorbing materials. For the future development of these materials in, depth structural investigations of core effect detail atomic level characterization and synthesis approach for the single-phase materials are needed for the more feasible applications of these emerging materials.

Acknowledgements The authors are thankful for receiving the financial support from the SERB and UGC- DAE CSR through collaborative research scheme project no. CRS/2021-22/01/381.

References

1. B. Cantor, I.T.H. Chang, P. Knight, A.J.B. Vincent, Mater. Sci. Eng. A **375–377**, 213–218 (2004).
2. M.H. Tsai, J.-W. Yeh, Materials Research Letters **2**(3), 107–123 (2014).
3. V.E. Gromov, S. v Konovalov, Y.F. Ivanov, K.A. Osintsev, Springer Nature Switzerland 107, 1–110 (2021).
4. M.H. Tsai, Entropy **18**, 252 (2016).
5. M.C. Gao, J.-W. Yeh, P.K. Liaw, Y. Zhang, Springer International Publishing Switzerland, pp. 516 (2016).
6. P. Kumari, A.K. Gupta, R.K. Mishra, M.S. Ahmad, R.R. Shahi, J. Magn. Magn. Mater. **554**, 169142 (2022).
7. J.W. Yeh, Ann Chim-Sci Mat. **31**, 633–648 (2006).
8. J.W. Yeh, JOM **65**, 1759–1771 (2013).
9. Y. Zhang, X. Yang, P.K. Liaw, JOM **64**, 830–838 (2012).
10. M. Feuerbacher, M. Heidelmann, C. Thomas, Mater. Res. Lett. **3**, 1–6 (2015).
11. X. Wang, W. Guo, Y. Fu, J. Mater. Chem. A **9**(2), 663–701 (2021).
12. K.H. Cheng, C.H. Lai, S.J. Lin, J.W. Yeh, Ann Chim-Sci Mat. **31**, 723–736 (2006).
13. J.W. Yeh, S.-K. Chen, S.J. Lin, J.-Y. Gan, T.S. Chin, T.-T. Shun, C.H. Tsau, S.Y. Chang, Adv. Eng. Mater. **6**(5), 299–303 (2004).
14. Z. Lei, X. Liu, Y. Wu, H. Wang, S. Jiang, S. Wang, X. Hui, Y. Wu, B. Gault, P. Kontis, D. Raabe, L. Gu, Q. Zhang, H. Chen, H. Wang, J. Liu, K.e. An, Q. Zeng, T.-G. Nieh, Z. Lu, Nature **563** (7732), 546–550 (2018).
15. M.H. Tsai, **15**, 5338–5345 (2013).
16. S. Ranganathan, Curr. Sci. **85**, 1404–1406 (2003).
17. Y. Zhang, Y.J. Zhou, J.P. Lin, G.L. Chen, P.K. Liaw, Adv Eng Mater. **10**, 534–538 (2008).
18. S. Guo, C.T. Liu, Prog Nat Sci. Mater Int. **21**, 433–446 (2011).
19. S. Guo, C. Ng, J. Lu, C.T. Liu, J Appl Phys. **109**, 103505 (2011).
20. C.M. Rost, E. Sachet, T. Borman, A. Moballegh, E.C. Dickey, D. Hou, J.L. Jones, S. Curtarolo, J.P. Mar, Nat. Commun. **6**, 8485–8492 (2015).
21. A. Sarkar, Q. Wang, A. Schiele, M.R. Chellali, S.S. Bhattacharya, D. Wang, T. Brezesinski, H. Hahn, L. Velasco, B. Breitung, Adv Mater. **31**, 1806236–1806244 (2019).

22. A. Sarkar, B. Breitung, H. Hahn, Scr Mater. **187**, 43–48 (2020).
23. Q. Wang, A. Sarkar, D. Wang, L. Velasco, R. Azmi, S.S. Bhattacharya, T. Bergfeldt, A. Düvel, P. Heitjans, T. Brezesinski, H. Hahn, B. Breitung, Energy Environ. Sci. **12**, 2433–2442 (2019).
24. A. Sarkar, R.Kruk, H. Hahn Dalton Trans., 50, 1973–1982 (2021).
25. A. K, Gupta, A. Prakash and R.R. Shahi. Material Science:Future aspects, Nova publication (2022).
26. S.J. McCormack, A. Navrotsky, Acta Mater. **202**, 1–21 (2021).
27. P. B. Meisenheimer, J. T. Heron, MRS Adv., 1–18 (2020).
28. N. Dragoe, D. Bérardan, Science **366**, 573–574 (2019).
29. Z. Fu, W. Chen, H. Xiao, L. Zhou, D. Zhu, S. Yang, Mater. Des. **44**, 535 (2013).
30. L. Zendejas Medina, L. Riekehr, U. Jansson, Surface and Coatings Technology **403**, (2020).
31. C.Z. Yao, P. Zhang, M. Liu, G.R. Li, J.Q. Ye, P. Liu, Y.X. Tong, Electrochim. Acta **53**, 8359 (2008).
32. Y. Yao, Z. Huang, P. Xie, S.D. Lacey, R.J. Jacob, H. Xie, F. Chen, A. Nie, T. Pu, M. Rehwoldt, D. Yu, M.R. Zachariah, C. Wang, R. Shahbazian-Yassar, J. Li, L. Hu, Science **359**, 1489–1494 (2018).
33. A. Mao, H. Xiang, X. Ran, Y. Li, X. Jin, H. Yu, X. Gu, J. Alloy. Compd. **775**, 1177 (2019).
34. P. Veronesi, E. Colombini, R. Rosa, C. Leonelli, M. Garuti, Chem. Eng. Process. **122**, 397 (2017).
35. B. Niu, F. Zhang, H. Ping, N. Li, J. Zhou, L. Lei, J. Xie, J. Zhang, W. Wang, Z. Fu, Sci. Rep. **7**, 3421 (2017)
36. R. R. Shahi, A. K. Gupta, P. Kumari, Int. J. Hydrog. Energy (in press) (2022).
37. M. Vaidya, G.M. Muralikrishna, B.S. Murty, J. Mater. Res. **34**, 664–686 (2019).
38. C. Suryanarayana, Prog. Mater. Sci. **46**, 1–184 (2001).
39. Y. Zhang, B. Zhang, K. Li, G.L. Zhao, S.M. Guo, J. Alloy. Compd. **734**, 220–228 (2018).
40. N. Sharma, S.N. Alam, *B* (C. Ray, Springer International Publishing, 2019), pp.21–59.
41. A. Sarkar, R. Djenadic, N.J. Usharani, K.P. Sanghvi, V.S.K. Chakravadhanula, A.S. Gandhi, H. Hahn, S.S. Bhattacharya, J. Eur. Ceram. Soc. **37**, 747–754 (2017).
42. D. Wang, Z. Liu, S. Du, Y. Zhang, H. Li, Z. Xiao, W. Chen, R. Chen, Y. Wang, Y. Zou, S. Wang, J. Mater. Chem. **7**, 24211–24216 (2019).
43. S. Vaddiraju, I. Tomazos, D.J. Burgess, F.C. Jain, F. Papadimitrakopoulos, Biosens. Bioelectron. **25**, 1553–1565 (2010).
44. M. Kheradmandfard, S.F. Kashani-bozorg, J.-S. Lee, C.L. Kim, A.Z. Hanzaki, Y.S. Pyun, S.W. Cho, A. Amanov, D.E. Kim, Alloys Compd. **726**, 941–949 (2018).
45. X.Y. Qin, J.G. Kim, J.S. Lee, NanoStruct. Mater. **11**, 259–270 (1999).
46. H. Liu, T.J. Webster, Biomaterials **28**, 354–369 (2007).
47. N. Sharma, H. Ojha, A. Bharadwaj, D.P. Pathak, R.K. Sharma, RSC Adv. **5**, 53381–53403 (2015).
48. S. Labib, S. Abdelaal, A.M. Abdelhady, E.K. Elmaghraby, Mater. Chem. Phys. **256**, 123654 (2020).
49. R. Nagahata, Y. Mori, Y. Saito, K. Takeuchi, Y. Shimizu, M. Shimizu, R. Benioub, Mater. Chem. Phys. **257**, 123744 (2021).
50. M. Kheradmandfard, A.H.N. Alfesharaki, A.Z. Kharazi, M. Kheradmandfard, S.F. Kashani-Bozorg, Ceram. Int. **44**, 18752–18758 (2018).
51. M. Kheradmandfard, S.F. Kashani-bozorg, A.H.N. Alfesharaki, A.Z. Kharazi, M. Kheradmandfard, N. Abutalebid, A.H. Noori-alfesharaki, Mater. Sci. Eng. C **92**, 236–244 (2018).
52. M. Baghbanzadeh, L. Carbone, P.D. Cozzoli, C.O. Kappe, Angew. Chem. Int. Ed. **50**, 11312–11359 (2011).
53. M. Kheradmandfard, H. Minouei, N. Tsvetkov, A. K. Vayghan, S. F. K-B, G. Kim, S. Ig Hong, D-E. Kim, Materials Chemistry and Physics **262**, 124265–124275 (2021).
54. P. Veronesi, R. Rosa, E. Colombini, C. Leonelli, Technologies **3**, 182–197 (2015).
55. B. G. Rao, D. Mukherjee, B. M. Reddy, In Micro and Nano Technologies, Elsevier,2017, pp 1–36.

56. A. Mao, F. Quan, H.-Z. Xiang, Z.-G. Zhang, K. Kuramoto, A.-L. Xia, J. Mol. Struct. **1194**, 11–18 (2019).
57. C. Burda, X. Chen, R. Narayanan, M.A. El-Sayed, Chem. Rev. **105**, 1025–1102 (2005).
58. B. Talluri, M.L. Aparna, N. Sreenivasulu, S.S. Bhattacharya, T. Thomas, J. Energy Storage **42**, 103004 (2021).
59. A.J. Gröhn, S.E. Pratsinis, A. Sánchez-Ferrer, R. Mezzenga, K. Wegner, Ind. Eng. Chem. Res. **53**, 10734–10742 (2014).
60. M.Y. Rekha, N. Mallik, C. Srivastava, Sci. Rep. **8**, 8737 (2018).
61. F. Waag, Y. Li, A.R. Ziefuß, E. Bertin, M. Kamp, V. Duppel, G. Marzun, L. Kienle, S. Barcikowski, B. Gökce, RSC Adv. **9**, 18547–18558 (2019).
62. E.P. George, W.A. Curtin, C.C. Tasan, Acta Mater **188**, 435–474 (2020).
63. Z. Wu, H. Bei, G.M. Pharr, E.P. George, Acta Mater **81**, 428–441 (2014).
64. C. Varvenne, A. Luque, W.G. Nohring, W.A. Curtin. Phys. Rev. B **93** (2016).
65. O. Shigenobu, U. Yoshitaka, K. Masanori, Model. Simul. Mater. Sci. Eng. **17**, 013001 (2009).
66. Reed Hill RE, Abbaschian R. PWS-KENT (1991).
67. C.J. Tong, M.R. Chen, S.K. Chen, J.W. Yeh, T.T. Shun, S.J. Lin, S.Y. Chang, Metall Mater Trans A **35**, 1263–1271 (2005).
68. C.Y. Hsu, Yeh JW, Chen SK. Shun TT. Metall Mater Trans A **35**, 1465–1469 (2004).
69. S.T. Chen, W.Y. Tang, Y.F. Kuo, S.Y. Chen, C.H. Tsau, T.T. Shun, J.W. Yeh, Mater Sci Eng A **527**, 5818–5825 (2010).
70. M.R. Chen, S.J. Lin, J.W. Yeh, S.K. Chen, Y.S. Huang, C.P. Tu, Mater Trans. **47**, 1395–1401 (2006).
71. M.R. Chen, S.J. Lin, J.W. Yeh, S.K. Chen, Y.S. Huang, M.H. Chuang, Metall Mater Trans A **37**, 1363–1369 (2006).
72. M.H. Chuang, M.H. Tsai, C.W. Tsai, N.H. Yang, S.Y. Chang, J.W. Yeh, S.K. Chen, S.J. Lin, J Alloys Compd. **551**, 12–18 (2013).
73. M.H. Chuang, M.H. Tsai, W.R. Wang, J.W. Yeh, S.J. Lin, Acta Mater. **59**, 6308–6317 (2011).
74. J.M. Wu, S.J. Lin, J.W. Yeh, S.K. Chen, Y.S. Huang, Wear **261**, 513–519 (2006).
75. C.Y. Hsu, T.S. Sheu, J.W. Yeh, S.K. Chen, Wear **268**, 653–659 (2010).
76. M.H. Tsai, C.W. Wang, C.W. Tsai, W.J. Shen, J.W. Yeh, J.Y. Gan, W.W. Wu, J Electrochem Soc. **158**, H1161–H1165 (2011).
77. P.K. Huang, J.W. Yeh, Scr Mater. **62**, 105–108 (2010).
78. V. Chaudhary, R. Chaudhary, R. Banerjee, R.V. Ramanujan, Mater. Today **49**, 231–252 (2021).
79. P.F. Yu, L.J. Zhang, H. Cheng, H. Zhang, M.Z. Ma, Y.C. Li, G. Li, P.K. Liaw, R.P. Liu, Intermetallics **70**, 82 (2016).
80. W. Ji, W. Wang, H. Wang, J. Zhang, Y. Wang, F. Zhang, Z. Fu, Intermetallics **56**, 24 (2015).
81. F. Alijani, M. Reihanian, K. Gheisari, J. Alloy. Compd. **773**, 623 (2019).
82. Y. Duan, X. Wen, B. Zhang, G. Ma, T. Wang, J. Magn. Magn. Mater. **497**, 165947 (2020).
83. R. F. Zhao, B. Ren, G. P. Zhang, Z. X. Liu, B. Cai, J. jian Zhang, Journal of Magnetism and Magnetic Materials **491**,165574 (2019).
84. R.K. Mishra, P.P. Sahay, R.R. Shahi, J. Mater. Sci. **54**, 4433 (2019).
85. R.K. Mishra, R.R. Shahi, J. Magn. Magn. Mater. **442**, 218–223 (2017).
86. R.K. Mishra, R.R. Shahi, Mater. Today: Proceedings **18**, 1422–1429 (2019).
87. R. K. Mishra, R. R. Shahi, J. Alloy. Compd. **821**, (2020).
88. R.K. Mishra, P. Kumari, A.K. Gupta, R.R. Shahi, J. Alloy. Compd. **889**, 161773 (2022).
89. A. Mao, H.Z. Xiang, Z.G. Zhang, K. Kuramoto, H. Yu, S. Ran, J. Magn. Magn. Mater. **484**, 245–252 (2019).
90. A. Mao, H. Z. Xiang, Z.G. Zhang, K. Kuramoto, H. Zhang, Y. Zia, J. Magn. Magn. Mater. 497, 165884 (2020).
91. A. Mao, H.X. Xie, H.Z. Xiang, Z.G. Zhang, H. Zhang, S. Ran, J. Magn. Magn. Mater. **503**, 166594 (2020).
92. Y. Fu, J. Li, H. Luo, C. Du, X. Li, J. Mater. Sci. Technol. **80**, 2017–2233 (2021).
93. H. Luo, S. Zou, Y. Chen, Z. Li, C. Du, X. Li, Corros. Sci. **163**, 108287 (2020).
94. X. Shang, Z. Wang, F. He, J. Wang, J. Li, J. Yu, Sci. China Technol. **61**, 189–196 (2018).

95. C.S. Raju, D. Venugopal, P. Srikanth, K. Lokeshwaran, M. Srinivas, C. Chary, A. Kumar, Mater. Today: Proc. **5**, 26823–26828 (2018).
96. X. Qiu, Y. Zhang, C. Liu, J. Alloys Compd. **585**, 282–286 (2014).
97. J. Yang, J. Wu, C. Zhang, S. Zhang, B. Yang, W. Emori, J. Wang, J. Alloys Compd. **819**, 152943 (2020).
98. Y. Zhao, M. Wang, H. Cui, Y. Zhao, X. Song, Y. Zeng, X. Gao, F. Lu, C. Wang, Q. Song, J. Alloys Compd. **805**, 585–596 (2019).
99. C. Lee, C. Chang, Y. Chen, J. Yeh, H. Shih, Corros. Sci. **50**, 2053–2060 (2008).
100. R. Kalsar, R. Ray, S. Suwas, Mater. Sci. Eng. A **729**, 385–397 (2018).
101. Q. Wang, A. Amar, C. Jiang, H. Luan, S. Zhao, H. Zhang, G. Le, X. Liu, X. Wang, X. Yang, J. Li, Intermetallics **119**, 106727 (2020).
102. C. Wu, S. Zhang, C. Zhang, H. Zhang, S. Dong, J. Alloys Compd. **698**, 761–770 (2017).
103. B. Ren, R. Zhao, Z. Liu, S. Guan, H. Zhang, Rare Met. Mater. Eng. **33**(2014), 149–154 (2014).
104. Y. Yuan, Z. Xu, P. Han, Z. Dan, F. Qin, H. Chang, J. Alloy. Compd. **870**, 159523–159532 (2021).
105. C.F. Xue, Y.N. Hao, Q. Luan, E.Y. Wang, X.L. Ma, X.G. Hao, Electrochim. Acta **296**, 94–101 (2019).
106. R. Li, X.J. Liu, H. Wang, Y. Wu, Z.P. Lu, Electrochim. Acta **182**, 224–229 (2015).
107. J. Yan, Z.J. Fan, T. Wei, J. Cheng, B. Shao, K. Wang, L.P. Song, M.L. Zhang, J Power Source **194**, 1202–1207 (2009).
108. C. Wu, Y. Zhu, M. Ding, C.K. Jia, K.L. Zhang, Electrochim. Acta **291**, 249–255 (2018).
109. M. Li, H.G. Park, Electrochim. Acta **296**, 676–682 (2019).
110. Z.F. Wang, J.Y. Liu, C.L. Qin, L. Liu, W.M. Zhao, A., Intermetallics **56**, 48–55 (2015).
111. K. Kong, J. Hyun, Y. Kim, W. Kim, D. Kim, J. Power Sources **437**, 226927–226936 (2019).
112. E. Shen, X. Song, Q. Chen, M. Zheng, J. Bian, H. Liu, ChemElectroChem **8**(1), 260–269 (2021).
113. X. Xu, Y. Du, C. Wang, Y.Guo, J. Zou, K. Zhou, Z. Zeng , Y.Liu L. Li, J. Alloy. Compd. **822**, 153642–153650 (2020).
114. B. Liang, Y. Ai, Y. Wang, C. Liu, S. Ouyang, M. Liu, Materials **13**(24), 5798 (2020).
115. M.S. Lal, R. Sundara, A.C.S. Appl, Mater. Interfaces **11**, 30846–30857 (2019).
116. H.-Z. Xiang, H.-X. Xie, Y.-X. Chen, H. Zhang, A. Mao, C.-H. Zheng, J. Mater Sci. **56**, 8127–8142 (2021).
117. C. Duan, K. Tian, X. Li, D. Wang, H. Sun, R. Zheng et al., Ceram. Int. **47**, 32025–32032 (2021).
118. B. Xiao, G. Wu, T. Wang, Z. Wei, Y. Sui, B. Shen et al., Ceram. Int. **47**, 33972–33977 (2021).
119. M. Hirscher, V.A. Yartys, M. Baricco, J.B.V. Colbe, D. Blanchard, R.C. Bowman, D.P. Broom, C.E. Buckley, F. Chang, P. Chen, Y.W. Cho, J.C. Crivello, F. Cueva, W.I.F. David, P.E.D. Jongh, R.V. Denys, M. Dornheim, M. Felderhoff, C. Jalotea, J. Alloy. Compd. **827**, 153548 (2020).
120. B.P. Tarasov, P.V. Fursikov, A.A. Volodin, M.S. Bocharnikov, Y.Y. Shimkus, A.M. Kashin, Int. J. Hydrogen Energy **46**, 13647–13657 (2021).
121. I.A. Hassan, H.S. Ramadan, M.A. Saleh, D. Hissel, Renew. Sustain. Energy Rev. **149**, 111311 (2021).
122. F. Marques, M. Balcerzak, F. Winkelmann, G. Zepon, M. Felderoff, Energy Environ. Sci. **14**, 5191–5227 (2021).
123. Y.F. Kao, S.K. Chen, J.H. Sheu, J.T. Lin, W.E. Lin, J.W. Yeh, S.J. Lin, T.H. Liou, C.W. Wang, Int. J. Hydrogen Energy **35**, 9046–9059 (2010).
124. R.B. Strozi, D.R. Leiva, J. Huot, W.J. Botta, G. Zepton, Int. J. Hydrogen Energy **46**, 2351–2361 (2021).
125. S.K. Dewangan, V.K. Sharma, P. Shahu, V. Kumar, Int. J. Hydrogen Energy **45**, 16984–16991 (2020).
126. R. Floriano, G. Zepon, K. Edalati, G.L.B.G. Fontana, A. Mohammadi, Z. Ma, H.W. Li, R.J. Contieri, Int. J. Hydrogen Energy **45**, 33759–33770 (2020).
127. J. Liu, J. Xu, S. Sleiman, X. Chen, S. Zhu, H. Cheng, J. Huot, Int. J. Hydrogen Energy **46**, 28709–28718 (2021).

128. B.H. Silva, C. Zlotea, Y. Champion, W.J. Botta, G. Zepon, J. Alloys Compd. **865**, 158767 (2021).
129. G. Ek, M.M. Nygàrd, A.F. Pavan, J. Montero, P.F. Henry, M.H. Sorby, M. Witman, V. Stavila, C. Zlotea, B.C. Hauback, M. Sahlberg, Inorg. Chem. **60**(2), 1124–1132 (2020).
130. H. Shen., J. Hu, P. Li, G. Huang, J. Zhang, J. Zhang, Y Mao, H. xiao, X. zhou, X. Zu, X. Long and S. J. Peng. Mater. sci. Technol., **55**, 116–125 (2020).
131. K.R. Cardoso, V. Roche, A.M. Jorge, F.J. Antiqueira, G. Zepon, Y. Champion, J. Alloy. Compd. **858**, 158357 (2021).
132. J. Montero, G Ek, M. Sahlberg, C. Zlotea. Scripta Materialia;194: 113699 (2021).
133. F. Marques, H.C. Pinto, S.J.A. Figueroa, F. Winkelmann, M. Felderhoff, W.J. Botta, G. Zepon, Int. J. Hydrogen Energy **45**, 19539–19552 (2020).
134. C. Zhang, Y. Wu, L. You, X. Cao, Z. Lu, X. Song, J. Alloy. Compd. **781**, 613–620 (2019).
135. J. H.Ramirez, F.J. M. Hodar, A.F. P. Cadenas, C. M. Castilla, C.A. Costa, L.M. Madeira, Appl. Catal. B-Environ. **75**. 312–323 (2007).
136. J.Q. Wang, Y.H. Liu, M.W. Chen, G.O. Xie, D.V.L. Luzgin, A. Inoue, J.H. Perepezko, Adv Func Mater. **22**, 2567–2570 (2012).
137. Z.Y. Lv, X.J. Liu, B. Jia, H. wang, Y. Wu, Z.P. Lu. Sci Rep., **6** 34213, (2016).
138. S. Wu, Y. Pan, N. Wang, W. Dai, J. Lu, T. Lu, RSC Adv. **8**, 41347–41354 (2018).
139. S. Wu, Y. Pan, N. Wang, W. Dai, J. Lu, T. Lu, J. Mater, Sci Technol. **35**, 1629–1635 (2019)
140. S.K. Wu, Y. Pan, N. wang, T. Lu, W.J. Dai, Int. J Min Met Mater., **26**, 124–132, (2019).
141. K.V. Yusenko, S. Riva, P.A. Carvalho, M.V. Yusenko, S. Arnaboldi, A.S. Sukhikh, M. Hanfland, S.A. Gromilov, Scripta Mater. **138**, 22–27 (2017).
142. S. Chu, A. Majumdar, Nature **488**, 294–303 (2012).
143. S.-M. Kim, S.-H. Jin, Y.-J. Lee, M.H. Lee, Electrochim. Acta **252**, 67–75 (2017).
144. G. Zhang, K. Ming, J. Kang, Q. Huang, Z. Zhang, X. Zheng, X. Bi, Electrochim. Acta **279**, 19–23 (2018).
145. Z. Jia, T. Yang, L. Sun, Y. Zhao, W. Li, J. Luan, F. Lyu, L. C. Zhang, J. J. Kruzic, J. J. Kai, J. C. Huang, J. Lu, C. T. Liu, Adv. Mater. 2000385 (2020).
146. W. Dai, T. Lu, Y. Pan, J. Power Sources **430**, 104–111 (2019).
147. H.-J. Qiu, G. Fang, J. Gao, Y. Wen, J. Lv, H. Li, G. Xie, X. Liu, S. Sun, ACS Materials Lett. **1**, 526–533 (2019).
148. H.J. Qiu, G. Fang, Y. Wen, P. Liu, G. Xie, X. Liu, S. Sun, J. Mater. Chem. A **7**, 6499–6506 (2019).
149. S. Li, X. Tang, H. Jia, H. Li, G. Xie, X. Liu, X. Lin, H.-J. Qiu, J. Catal. **383**, 164–171 (2020).
150. S. Nellaiappan, N.K. Katiyar, R. Kumar, A. Parui, K.D. Malviya, K.G. Pradeep, A.K. Singh, S. Sharma, C.S. Tiwary, K. Biswas, ACS Catal. **10**, 3658–3663 (2020).
151. P. Yang, Y. Liu, X. Zhao, J. Cheng, H. Li, Adv Powder Technol **27**, 1128–1133 (2016).
152. P. Yang, Y. Liu, X. Zhao, J. Cheng, H. Li, J Mater Res **31**, 2398–2406 (2016).
153. B. Zhang, Y. Duan, Y. Cui, G. Ma, T. Wang, X. Dong, Mater Des **149**, 173–183 (2018).
154. B. Zhang, Y. Duan, X. Wen, G. Ma, T. Wang, X. Dong, H. Zhang, N. Jia, Y. Zeng, J Alloys Compd. **790**, 179–188 (2019).
155. X. Qi, Q. Hu, H. Cai, R. Xie, Z. Bai, Y. Xiang, S. Qin, W. Zhong, Y. Du, Sci Rep **6**, 37972 (2016).

Chapter 7
Layered Chalcogenides: Evolution from Bulk to Nano-Dimension for Renewable Energy Perspectives

Ankita Singh, Jay Deep Gupta, Priyanka Jangra, and Ashish Kumar Mishra

Abstract Recently, two-dimensional (2D) transition-metal dichalcogenides (TMDCs) have gained significant attraction due to their remarkable physical and chemical properties for potential application in compact and lightweight integrated systems. To monitor their integration in various applications, it is important to probe the controllable and reliable synthesis of mono- to few-layer 2D TMDCs. Herein, an overview of the various synthesis techniques of 2D TMDCs under the top-down and bottom-up approaches are discussed, showing their own merits and demerits. Further, their electronic, optical, thermal, magnetic and mechanical properties are highlighted briefly to find their suitable application. At the end, different applications such as optoelectronics, energy generation and storage, environmental and biomedical applications of TMDCs have been discussed.

Keywords TMDCs · Synthesis · Properties · Applications

7.1 Introduction

Two-dimensional (2D) materials have stimulated recently huge research activity owing to their exotic properties, versatility and wide-ranging applications. Both experimental and theoretical investigations have revealed the exceptional properties of 2D materials that have brought a breakthrough in the world of nanomaterials and nanodevices. Among 2D materials, Graphene has been widely used for photonic, electronic and plasmonic devices due to high transparency, strong photon interactions and good electrical conductivity. It has been recognized as an alternative to highly expensive indium tin oxide, as the transparent electrode material for optoelectronic applications. The problem of zero bandgap in graphene, that limits its application for optoelectronic devices, has been solved by introducing functionalized graphene and graphene nanoribbons. Apart from graphene, new families of layered transition metal dichalcogenides (2D TMDCs) such as MoS_2, WSe_2, VS_2, etc. have been discovered

A. Singh · J. D. Gupta · P. Jangra · A. K. Mishra (✉)
School of Materials Science and Technology, Indian Institute of Technology (Banaras Hindu University), Varanasi 221005, India
e-mail: akmishra.mst@iitbhu.ac.in

D. K. Singh et al. (eds.), *Nanomaterials*,
https://doi.org/10.1007/978-981-19-7963-7_7

to accomplish more exotic features covering broad applications like sophisticated electronics, optoelectronics, spintronics, energy harvesting, personalized medicine and DNA sequencing. Layered TMDCs feature fascinating and distinct characteristics countered to their bulk ones. They exhibit an exclusive combination of favorable mechanical and electronic properties, atomic-scale thickness, variable bandgap and powerful spin–orbit coupling. Basically, 2D TMDCs are sandwich compounds of a layer of transition metal (Mo, W, V, etc.) and two chalcogen atoms (S, Se or Te) in different layers attached by weak van der Waals interaction. TMDCs feature different crystal structures with discrete characteristics. Relying upon the coordination of transition metal and chalcogen atom, monolayer TMDCs exist in H- and T- (or T') phases. The stacking sequence of the semiconducting H-phase allows the 2H (AB-stacking showing hexagonal symmetry) and 3R (ABC-stacking showing rhombohedral symmetry) stacking patterns, while the metallic T-phase exhibits octahedral coordination of transition metal atom [2]. The H-phase TMDCs find application in semiconductor-based electronic devices and other energy-related applications, while the T-phase enhances the charge transfer efficiency suitable for energy applications such as supercapacitors and batteries. The schematic of structures of different polytypes of MoS_2 is illustrated in Fig. 7.1. Over years, the phase transition in TMDCs has attracted the spotlight showing varied electronic characteristics present in the same material. These functionalities have been tuned for applications in electronic or optoelectronic devices.

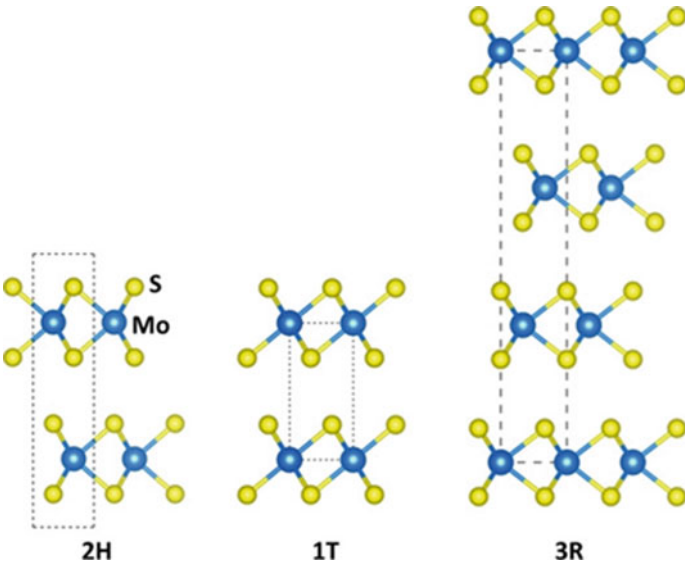

Fig. 7.1 Schematics showing different polytypes of MoS_2 (**a**) 1 T, (**b**) 2H and (**c**) 3R phases. Adapted with permission from [2]. Copyright 2018, Chemistry–A European Journal

Semiconducting nanometer-thick 2D TMDCs provide important advantages over 3D materials in electronic and optoelectronic devices [1, 2]. One of the most significant applications of TMDCs is for scaling transistors to atomically thin dimensions in digital electronics. However, the absence of short-channel effects in TMDCs hinders the device's performance. To reduce the short-channel effect and power dissipation, researchers are trying to use tunable bandgap TMDCs as ultrathin materials to fabricate FETs that allow more efficient control over switching with high on/off ratios. Recently, mechanically exfoliated mono- and few-layer TMDC-based FETs have been demonstrated for the detection of pollutant gases like CO, CO_2, NO, CH_4, Fluorinated Gas, NO_x, H_2S and other toxic gases with less than 1 ppm limit of detection [3–5].

The 2D TMDC semiconductors show direct bandgaps in the visible to near-IR region, which can provide extraordinary improvement in the performance of optoelectronic devices such as photovoltaics and light-emitting diodes (LEDs) [6]. Additionally, the absorption cross-section is higher in TMDC materials compared to other conventional semiconducting materials. Atomically and self-passivated thin TMDCs show excellent optical absorption, which makes them promising candidates for photovoltaic acceptors in solar cell applications [7, 8]. Due to the absence of dangling bonds at the free surface, it also minimizes non-radiative recombination, and near-unity photoluminescence quantum yields show an opportunity for high-efficiency LEDs. The large-scale invention of mono- and few-layer TMDCs can enable their widespread application for energy storage devices such as supercapacitors, batteries, electrochemical and light-induced catalysis processes [9–11]. Apart from this, the 2D TMDCs can also be an exceptional platform for biomedical applications, such as drug delivery. The 2D TMDCs show a high photothermal/photoacoustic conversion coefficient, which enables hopeful materials for photothermal therapy and biomedical imaging [12–15]. In the following section, we will look into different synthesis processes for TMDCs.

7.2 Synthesis and Characterization Techniques of Transition Metal Dichalcogenides

2D TMDCs are illustrated as a layer of untied nanosheets, exhibiting an elevated ratio of lateral size (nanometers to microns) to thickness (angstroms to nanometers). Various techniques for the synthesis of single to few-layer TMDCs have been developed. The two main approaches to synthesize 2D nanomaterials are top-down and bottom-up approaches. The choice of technique in both the approaches has its own merits and demerits. These growth techniques are widely applied and open a new possibility for device fabrication on an industrial scale. Here, we have discussed the most frequently applied techniques in brief. For large-area synthesis and to mark the mass production, various microscopic to spectroscopic characterization techniques of these 2D materials are employed to analyze the optical, structural, vibrational

and thermal properties of as-synthesized TMDC nanomaterials. In order to understand the quality of the film, its thickness, phase formed, grown layer number, etc. of TMDC materials, the Raman spectroscopy technique is extensively used. Group theory analysis predicts five vibrational modes for monolayer MX_2 TMDCs: $\Gamma = A_{2u}$ (IR) + A_{1g} (R) + E_{2g} (R) + E_{1g} (IR + R). As an example, 2H-MoS_2 has two Raman active modes seen at ~ 384 cm^{-1} (in-plane vibration: $E^1{}_{2g}$) and at ~ 404 cm^{-1} (out-of-plane vibration: A_{1g}), in contrast to 1 T phase having three peaks J_1, J_2 and J_3 at ~160, ~230 and ~330 cm^{-1}, respectively. The peak separation between the $E^1{}_{2g}$ and A_{1g} modes enables the approximation of the layer number. As the layers add on, interlayer coupling comes into account and results in the blue shift of A_{1g} mode, while $E^1{}_{2g}$ mode shows red shift accounted for the coulombic interlayer interactions. Annealing the sample to higher temperature leads to the transformation of the 1 T phase into the 2H phase.

To reveal the electronic behavior of TMDCs, photoluminescence (PL) spectroscopy is used. The PL signal of TMDCs is observed on moving from bulk to single layer, i.e. on the crossover from indirect to direct bandgap. For a single layer, the direct bandgap emerges from the transition of valence band maxima to conduction band minima, both situated at the same K-point, and the excitonic transitions emits photon, responsible for a strong PL signal. For example, the PL spectra of monolayer MoS_2 show two excitonic peaks (A and B) at 627 and 677 nm, respectively. It is due to the d–d transitions to the degenerated d_{xy} and $d_x{}^2{}_{-y}{}^2$ orbitals from the filled d_x orbital, splitted due to spin–orbit coupling. As the layer number increases, the PL signal intensity decreases and diminishes in bulk cases. Microscopic characterization techniques like scanning electron microscopy (SEM), atomic force microscopy (AFM) and transmission electron microscopy (TEM) techniques are extensively used for characterizing TMDCs. The surface morphology of the material can be understood by SEM, while estimation of the thickness of a variety of 2D materials and their topographic images can be obtained using AFM. TEM elucidates the structure by scaling the image of the direct atomic-scale lattice of 2D material. To access the structural properties of TMDCs, the X-ray diffraction (XRD) technique is also used. It is based on the diffraction pattern and depicts the nature and structural composition of the nanomaterial. The XRD pattern of TMDCs is affected by different synthesis conditions like pH, temperature and pressure. In the following section, we will specifically discuss different synthesis methods and characterization of TMDCs prepared with those methods.

7.2.1 Top-Down Methods

In this approach, the crafting of the 2D nanomaterials from layered bulk into a single or few layers is achieved via physical or chemical processes. The physical process exfoliates the layered structures by using the mechanical force or ultrasonic wave, while the chemical processes are solution-based processes including ion exchange,

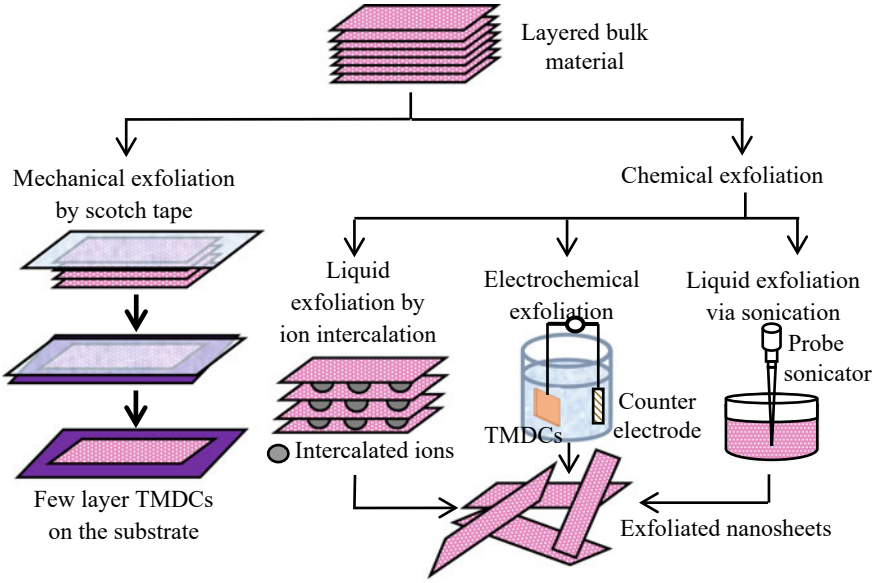

Fig. 7.2 Schematic showing mechanical exfoliation via Scotch tape, liquid phase exfoliation and electrochemical exfoliation steps to obtain 2D exfoliated TMDC nanosheets from bulk material

heat, etc. Figure 7.2 shows the schematic of the various routes of synthesizing 2D nanomaterials via a top-down approach.

7.2.1.1 Mechanical Exfoliation

The Scotch tape exfoliation technique is considered as the representative mechanical exfoliation method. In this method, the nanosheets are peeled off from their bulk layered crystals by applying mechanical force, and it works on the mechanism of weakening the van der Waals interaction present between layers by using adhesive scotch tape. These cleaved nanosheets are then transferred onto the desired substrate. After the removal of Scotch tape, single to few-layer nanosheets are left over the substrate. This method is recognized as the Scotch-tape method and was first developed by Novoselov in 2004 by detaching a single graphene layer from graphite [16]. Later, this technique was applied to 2D TMDC nanomaterials like MoS_2, $MoSe_2$, $MoTe_2$, WS_2, WSe_2, TiS_2, TaS_2, ReS_2, $TaSe_2$, $NbSe_2$, etc. [17–19].

This method is one among the simplest, cleanest and cost-effective ways to obtain high crystalline nanosheets but is not scalable, is time-consuming and has no control over the nanosheet thickness. The problem of randomness in layer thickness was overcome by developing the nanomechanical cleavage technique. The nanomechanical cleavage of MoS_2 from monolayer to up to 23 atomic layers with in situ transmission electron microscopy was successfully demonstrated [20]. In this technique, a sharp

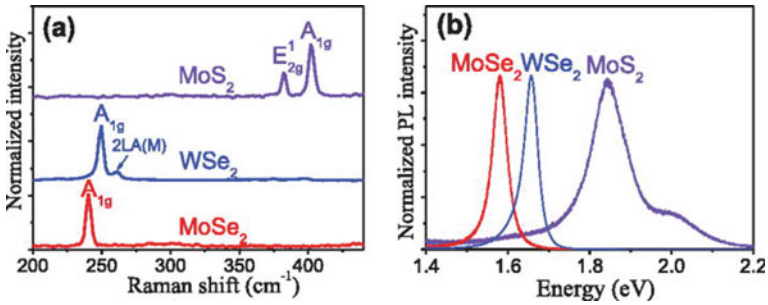

Fig. 7.3 (**a**) Raman and (**b**) PL spectra of exfoliated single-layer MoS_2, $MoSe_2$ and WSe_2. Adapted with permission from [21]. Copyright 2017, American Institute of Physics

tungsten tip (~10 nm) with a piezoelectric motor is brought in contact with a bulk MoS_2 crystal hooked up on a support with an edge-on orientation. Then the tip is bent in order to detach the layers. Yang et al. characterized the mechanically exfoliated different TMDC samples on SiO_2(300 nm)/Si substrate [21]. Figure 7.3 illustrates the Raman and PL spectra of single-layer MoS_2, $MoSe_2$ and WSe_2. The peak separation of 19.8 cm^{-1} is observed in the Raman signal with strong PL emissions: A exciton at ~1.88 eV and B exciton at ~2.04 eV, confirming the monolayer growth. The Raman spectra of TMDCs are affected by the incident excitation, applied strain and temperature. With the decrease of incident energy, more peaks are observed like 2LA(M) at ~2.04 eV, indicating a double resonance process. With uniaxial strain, $E^1{}_{2g}$ peak starts splitting due to the breaking of the in-plane symmetry of monolayer MoS_2, while the A_{1g} mode remains unaffected. With the rise of temperature of monolayer MoS_2, both the $E^1{}_{2g}$ and A_{1g} mode red shift and A_{1g} mode undergo broadening. Similar behavior is observed for other TMDCs as well.

7.2.1.2 Chemical Exfoliation

This method is a solution-based synthesis process suitable for the mass production of nanomaterials at a large scale. This method includes solvent-based exfoliation and ion intercalation methods. The schematic of the liquid exfoliation by sonication, liquid exfoliation by ion intercalation and electrochemical lithiation process is illustrated in Fig. 7.2. In the solvent-based exfoliation method, the bulk precursors are dissolved in solvents like dimethylformamide and N-methyl-2-pyrrolidone for sonication. Sonication provides mechanical forces to the solvent to overcome the weak van der Waals interaction of the layered material. Coleman et al. applied this process for the synthesis of MoS_2, $MoSe_2$, $MoTe_2$, WS_2, $TaSe_2$, $NbSe_2$, $NiTe_2$, BN and Bi_2Te_3 [22]. In the ion intercalation method, the cations like Li^+, K^+, Na^+, etc. intercalate in between layers and reduce the interlayer van der Waals interaction of bulk crystal. Many times, intercalated ions interact with water to form hydrogen gas that helps in departing the adjacent layers. Li^+ ion is mostly considered owing to its

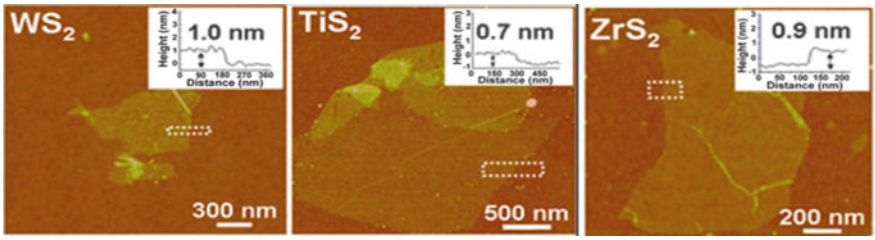

Fig. 7.4 AFM images and corresponding height profile of (**a**) WS_2 nanosheets with average thickness of ~1.0 nm, (**b**) TiS_2 nanosheets with average thickness of ~0.7 nm and (**c**) ZrS_2 nanosheets with average thickness of ~ 0.9 nm, deposited on SiO_2 substrate, confirming the single layer. Adapted with permission from [24]. Copyright 2011, Wiley

high mobility and reduction potential. In the lithium intercalation method, N-Butyl lithium is used as the lithiation agent and hexane as the solvent. Monolayer WS_2, MoS_2 and $MoSe_2$ have been obtained by lithium intercalation [23]. Lithium ion incomplete insertion produces low yield while its over-intercalation produces Li_2S. To control the intercalation process, the electrochemical ion intercalation method was designed by Zeng et al. [24]. They applied a voltage between anodic Li foil and cathodic MoS_2 in ethylene carbonate and dimethyl carbonate as an electrolyte (under a 0.05 mA current) and exfoliated different TMDCs. Figure 7.2 shows the schematic for the electrochemical Li-intercalation and exfoliation process for the production of various TMDC nanosheets: MoS_2, WS_2, TiS_2, TaS_2, ZrS_2 and $NbSe_2$. Bulk TMDCs coated on a Cu foil were taken as the cathode and lithium foil as an anode. Then the intercalation was carried out followed by the dispersion of nanosheets via sonication in water. AFM images of WS_2, TiS_2 and ZrS_2 nanosheets on SiO_2/Si substrates are shown in Fig. 7.4, indicating the formation of monolayer WS_2, TiS_2 and ZrS_2 nanosheets.

This Li intercalation method has few demerits like the complete removal of Li that gives a doping effect, and also the lithium ions have extra charges and to accommodate these charges, the 2H phase is transformed into 1 T phase, which is undesirable for semiconducting applications. To sort this, Liu et al. introduced the intercalation of SO_4^{2-} anions in a bulk MoS_2 crystal [25]. In this method, a voltage is applied between the working electrode (MoS_2) and the counter electrode (Pt wire) in 0.5 M Na_2SO_4 solution for 0.5–2 h. The radicals (-OH, -O) and SO_4^{2-} anions intercalate between the MoS_2 layers which declines the strength of van der Waals interactions. Oxidation of radicals and anions releases O_2 and SO_2 gases that detaches the flakes of MoS_2 from the bulk.

7.2.2 Bottom-Up Methods

To integrate TMDCs in electronic devices, it is obligatory to have a layer-controlled (single to few layers), enhanced-quality (absence of defects, grain boundaries) and scalable crystal growth. The top-down approach has limitations over this. Therefore, other methods with a bottom-up approach were explored. In the bottom-up approach, atomic or molecular precursors are made to react to form nanomaterials by direct chemical reaction and this involves processes like chemical vapor deposition (CVD), wet-chemical synthesis methods, molecular-beam epitaxy, atomic layer deposition (ALD), pulsed laser deposition, sputtering, etc.

7.2.2.1 Chemical Vapor Deposition (CVD)

It is one of the most preferred techniques to grow wafer-scale uniform high-quality TMDC nanomaterials of controlled thickness. Synthesis of 2D-TMDCs via the CVD technique is a cutting-edge research field nowadays. In this method, the volatile precursors decompose at high temperatures on the desired substrate in the presence of an inert atmosphere. After the growth of graphene [26], subsequently, this technique was applied to the growth of other 2D nanomaterials [27]. For TMDC growth, mainly two types of CVD setups can be employed: Thermal CVD and metal oxide CVD (MOCVD).

Thermal CVD: In the thermal CVD process for TMDC synthesis, a chemical reaction occurs between the transition metal salt and chalcogen powders as precursors at high temperatures in an inert atmosphere. First, the transition metal oxide gets adsorbed on the surface of the substrate, followed by its chalcogenization to produce TMDCs. Hydrogen gas may also help in reducing the transition metal oxide producing better chalcogenization. By optimizing the growth parameters like the amount of precursors, flow rate of inert gas, reaction temperature, reaction time, etc. the thickness, edge structure and shape evolution can be changed. Wang et al. illustrated the formation of 2D WSe_2 flakes with triangular and hexagonal shapes on the SiO_2/Si substrate by optimizing the Se flux [28]. Meng et al. synthesized 1 T-$CrTe_2$ single crystals on SiO_2/Si substrates at 983 K by the CVD technique using $CrCl_2$ and Te precursors [29]. When the growth temperature was varied in the range of 973–993 K, the thickness of the sample was observed to increase from 1.2 nm (bilayer) to 47.9 nm. Wang et al. have discussed the impact of the ratio of transition metal (M) to chalcogen (X) on the evolution of different shapes of the CVD-grown MX_2 depending upon the M:X ratio, as shown schematically in Fig. 7.5a [30]. Yang et al. further studied the shape-evolution behavior of MoS_2 flakes with growth temperature in addition to the M:X ratio and observed three-point star-, triangular- and hexagonal-shaped MoS_2 flakes in the temperature range 620–720 °C [31].

MOCVD: It is a well-recognized technique for the growth of thin films. In this technique, transition metal (M) and chalcogen (X) containing organic gases are decomposed by thermal energy on the substrate to get a thin film of TMDCs.

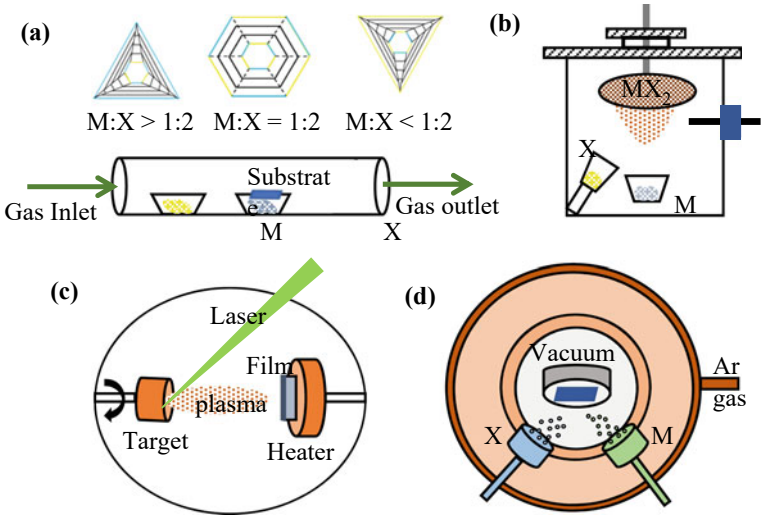

Fig. 7.5 (**a**) Schematic of the (**a**) CVD setup for the growth of MX_2. The ratio of M:X will determine the shape evolution of the domain. (**b**) MBE showing the co-evaporation of high-purity elemental source materials, (**d**) PLD and (**e**) sputtering

Kang et al. reported the deposition of single to few layers of MoS_2 and WS_2 on SiO_2/Si utilizing $Mo(CO)_6$, $W(CO)_6$, $(C_2H_5)_2S$ and H_2 [32]. Eichfeld et al. reported the formation of Wse_2 on various substrates (sapphire, graphene and amorphous boron nitride) and have controlled its thickness by changing the ratio of W:Se during growth [33]. Although this method synthesizes wafer-scale uniform monolayer films of controlled thickness, it requires toxic precursors and also high-cost equipment.

7.2.2.2 Wet-Chemical Synthesis

This method promises great controllability and reproducibility for all types of 2D nanomaterials. In this method, chemical reactions occur using precursors in the solution phase. The solvothermal/hydrothermal approach is one of the simplest as well as scalable techniques for the production of 2D materials. Its advantage over other methods is the low reaction temperature. Many 2D materials like MoS_2, $MoSe_2$, WS_2, WSe_2, etc. have been synthesized using this method. Some of the reported precursors for Mo are molybdenum trioxide (MoO_3), molybdenum pentachloride ($MoCl_5$), sodium molybdate (Na_2MoO_4), ammonium heptamolybdate ($(NH_4)_6Mo_7O_{24}$), etc. while S precursors include thiourea (NH_2CSNH_2), L-cysteine ($C_3H_7NO_2S$), dibenzyl disulfide ($C_{14}H_{14}S_2$), potassium thiocyanate (KSCN), thioacetamide (C_2H_5NS), etc. Single precursor for both Mo and S used is ammonium tetrathiomolybdate ($(NH_4)_2MoS_4$). Adding NaOH and HCl governs the pH value, while some reducing agents like N_2H_4 and $NaBH_4$ are also used. Synthesized MoS_2 may have a variety

of morphologies like nano-sized sheets, flakes, flowers, dots, rods, spheres and core–shell structures, with nanosheets being more popular among all. Chung et al. synthesized MoS_2 nanospheres and nanosheets via the hydrothermal method using Na_2MoO_4 and L-cysteine as Mo and S precursors, respectively [34]. After dropping HCl (till pH <1), the reaction occurs at 220 °C for 36 h. For MoS_2 nanosheets, they applied the same procedure except for the replacement of S precursor L-cysteine with thiourea. Srivastava et al. synthesized WS_2 quantum dots (QDs) via the hydrothermal method by using Sodium tungstate dihydrate ($Na_2WO_4{\cdot}2H_2O$) and L-cysteine ($HO_2CCH(NH_2)CH_2SH$) as precursors [35]. Both the solutions were mixed and HCl was added to them. Then the solution was poured into stainless steel lined Teflon autoclave maintained at 120 °C for 2–3 h and then kept at 190 °C for 46 h. The obtained yellow colloidal solution of WS_2 was filled into dialysis, and left for 3–4 days in ideal condition to obtain WS_2-QDs. Shelke et al. hydrothermally produced WS_2 using WCl_6 and thioacetamide as precursors [36]. The precursors were dissolved in DI water, followed by 1 h stirring. Then the solution in stainless steel autoclave was set at 265 °C for 24 h to obtain WS_2. The VS_2 was hydrothermally synthesized by taking sodium orthovanadate ($Na_3VO_4.12H_2O$) and thioacetamide as precursors at 160 °C for 24 h in an autoclave [37].

7.2.2.3 Molecular-Beam Epitaxy (MBE)

It is the most advanced, scalable and controllable growth technique for TMDC synthesis. The deposition is achieved in an ultra-high vacuum (10^{-8}–10^{-12} Torr) that gives the highest purity of the film. During growth, the heated molecular source or the gas source was controlled by an effusion cell, and the chemical reaction occurs at the substrate (Fig. 7.5b). Wafer-scale single-layer TMDCs can be synthesized via this method but it takes a longer duration, i.e. ~10 h for growing a 2-inch monolayer of MoS_2 and also requires expensive effusion equipment. He et al. demonstrated the wafer-scale growth of atomically thin 2H-$MoTe_2$ monolayers on SiO_2 substrate by co-evaporating Mo from an electron-beam evaporator and Te from an effusion cell [38]. The different phases of $MoTe_2$ depend upon the temperature of the substrate. A variety of TMDCs have been synthesized via the MBE technique like $MoSe_2$, WSe_2, WTe_2, $HfSe_2$, $HfTe_2$, $SnSe_2$, etc. [39–44].

7.2.2.4 Atomic Layer Deposition (ALD)

This method enables the formation of an atomically thin layer of nanomaterials via a gas phase chemical reaction. Materials like MoS_2, WS_2, TiS_2, etc. have been successfully synthesized via ALD by a few research groups. Song et al. synthesized wafer-scale WS_2 nanosheets by sulfurizing ALD-grown WO_3 film via H_2S annealing [45]. The layer number can be tuned by controlling the number of ALD cycles. Krbal et al. demonstrated the ALD synthesis of 2D $MoSe_2$ structures by taking $Mo(CO)_6$ and $MoCl_5$ as the Mo precursors and $((CH_3)_3Si)_2Se$ as the Se precursor at deposition temperatures of 167 and 300 °C, respectively [46]. $MoSe_2$ structures prepared via

$MoCl_5$ are crystalline 2H nanoflakes, while those prepared via $Mo(CO)_6$ have some MoO_x content.

7.2.2.5 Pulsed Laser Deposition (PLD)

In this method, a focused high-energy pulsed laser is bombarded on the target material, raising the temperature of the small area to ten thousand degrees in small time interval, thus converting the solid material into the plasma state (Fig. 7.5c). Chen et al. fabricated the high-quality, large-scale, single-crystalline WTe_2 films on mica substrates by a two-step synthesis process: PLD and the post-annealing process [47]. However, this technique is time-taking and has the possibility of impurities during the annealing process. Vermeulen et al. demonstrated the single-step method for the growth of single crystal WTe_2 films at 210 °C using PLD [48]. This technique is useful for growing high-melting-point materials, and the grown film shows homogeneity with high quality. Also, it has control over the thickness of the grown film by controlling the number of laser pulses.

7.2.2.6 Sputtering

This technique is widely used for thin film production on industrial scale. In this method, glow discharge is produced in an inert environment to form energetic electrons and ions that collide and create secondary electrons and more ions. These ions bombard on the target giving kinetic energy to the sputtered species to get deposited on the substrate. The schematic of the sputtering technique for the growth of TMDCs is shown in Fig. 7.5d. This technique has high deposition rate along with wafer-scale production. Huang et al. demonstrated the deposition of large area, crystalline, few-layer 2H-$MoTe_2$ on SiO_2 substrate by sputtering a $MoTe_2$ target [49]. To enhance the crystallinity of the deposited film, it was annealed at 650 °C in nitrogen atmosphere. Researchers have also reported the co-sputtering technique to produce 1 T' $MoTe_2$ films [50, 51]. The Mo and Te atoms were co-deposited onto graphene surface and their sticking coefficient depends upon the substrate temperature. Moreover, ex situ thermal processing in Te atmosphere improves the stoichiometry of $MoTe_2$ films. Several reports confirmed the enhanced crystallization and stoichiometry with post-annealing process.

7.2.2.7 Other Methods

Apart from the above-mentioned methods, researchers have developed many new methods to grow 2D TMDC nanostructures. It includes electrodeposition, microwave induced-plasma-assisted technique, laser pyrolysis, lithography, microemulsion, electron beam evaporation, etc. Devadasan et al. reported the electrodeposition of WS_2 on conducting glass plates in an electrolyte of 1:1 mixture of tungstic acid

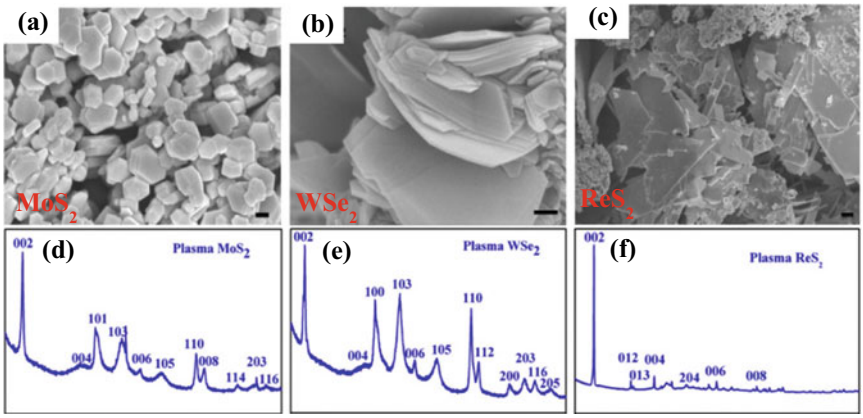

Fig. 7.6 (**a-c**) SEM images and (**d-f**) corresponding XRD pattern of as-grown samples of MoS_2, WSe_2 and ReS_2, showing hexagonal morphology. Adapted with permission from [53]. Copyright 2016, Elsevier

and Na_2SO_3 aqueous solution [52]. Films were formed at different current densities, bath temperature and bath pH. The electrodeposited film at current density of 30 mA/cm^2 and bath temperature 40 °C was of high thickness and exceedingly opaque to light. The film degrades if the current density is increased beyond and pin hole formation starts in the film if temperature is increased beyond 40 °C. Chaturvedi et al. synthesized few-layer thin crystals of WS_2, MoS_2, WSe_2, $MoSe_2$ and ReS_2 by using microwave-induced-plasma-assisted method [53]. The morphology of the synthesized product was examined via SEM images, as shown in Fig. 7.6a–c, indicating almost micrometer-sized stacked flakes of hexagonal TMDCs. The phase and thickness of the produced samples were confirmed by powder XRD and AFM. Figure 7.6d–f shows the powder XRD pattern of different TMDCs assuring the formation of desired phases. Many other techniques have been developed but presently, it is still a challenging task to fabricate high-quality TMDC film for industrial application.

Based on the synthesis process, TMDCs show variation in their physical properties. In the following section, we will look into some of the general physical behaviors of different TMDCs.

7.3 Properties of Transition Metal Dichalcogenides

7.3.1 Electronic Properties

The 2D TMDCs with many interesting phases like superconducting phase, charge density wave phase, mott insulating and topological insulating phase show unusual electronic properties [1]. The 1 T' crystal structure and nanoribbons mostly exist

in topological insulating phases. Some other topological phases possible at room temperature have been predicted by using first principles study. In addition to theoretical predictions of 2D phases, experimentalists have also demonstrated these topological phases credibly. In the basal plane, absence of dangling bonds allows the stability of TMDCs in air and liquids and no reactivity with ambient chemicals. This stability is also maintained in the lateral dimension. The 1 T phase shows metallic and paramagnetic behavior. The basic properties of both 2H and 3R phases are the same, i.e. both exist in diamagnetic and semiconducting phases with different band structures. But the 2H phase is more stable and abundant and that's why most of the studies are based on the 2H phase of TMDCs. The electronic bandgap of the 2H phase of TMDCs vary with thickness. Mostly, the bulk TMDCs are indirect bandgap semiconductors but when reduced to monolayer, they are converted into direct bandgap semiconductors. The bandgap of PtS_2 also varies with layer number, but it exhibits an indirect bandgap even up to monolayer. The electronic band structure for one-, two- and bulk WS_2 is shown in Fig. 7.7.

In case of monolayer, both conduction band (CB) minima and valence band (VB) maxima are located at K-point of the Brillouin zone, showing direct bandgap transition. The direct transitions remain relatively unchanged with the variation in layer number [54]. For bulk WS_2, bandgap transition is indirect at G-point. The 2D confinement in single layer reduces the dielectric screening caused by strong many-body effects facilitated by Coulomb interactions [55]. In few-layer TMDCs, the bound state of excitons show large binding energy of around hundreds of meV, which makes them stable at room temperature. The valence band splitting leads to the existence of low-energy A exciton and high-energy B exciton. Excitonic transition is the

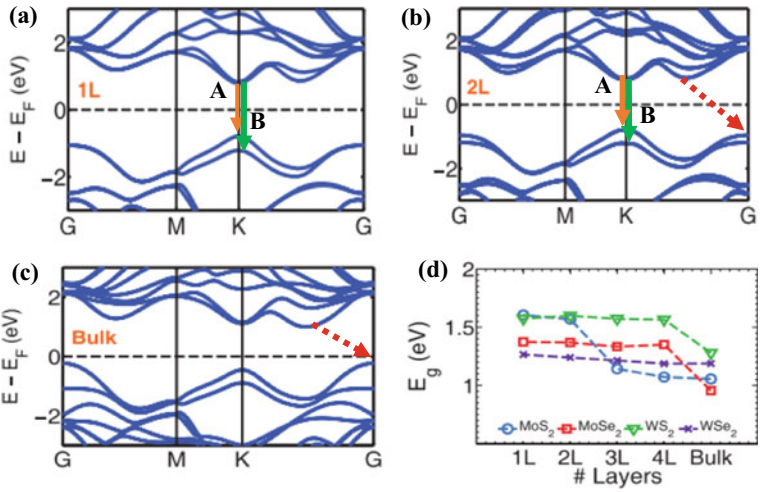

Fig. 7.7 Band structures of WS_2, calculated using DFT: (**a**) 1L, (**b**) 2L and (**c**) bulk, and (**d**) shows the variation of the bandgap of the TMDCs with number of layers. Adapted with permission from [54]. Copyright 2014, American Institute of Physics

radiative transition which is dominant in few layers of TMDCs and is not observed in bulk cases due to dominance of non-radiative transition. The band structure variation with the number of layers occurs due to quantum confinement and variation in hybridization of p_z orbitals of chalcogen atoms and d orbitals of transition metal atoms. Density functional theory (DFT) calculation of TMDCs like MoS_2, WS_2, $MoSe_2$ and WSe_2, etc. shows that the conduction band at K-point is due to localized d-orbitals of metal atom. These K-point states are comparatively unaffected by interlayer interactions. The states near the Γ-points are the combination of antibonding p_z orbitals of chalcogen atoms and d-orbitals of transition metals. Hence, the interlayer coupling at this point is very strong and effective. That's why with the variation of layer number, electronic states near the K-point remain unchanged but states near G-point vary significantly from indirect to direct transition on reducing from bulk to monolayer. It was further studied that the optical bandgap decreases with increasing external applied mechanical stress or electric field until metallic conductivity for various TMDCs like MoS_2, WSe_2, $CrTe_2$, etc. was achieved [56]. Some TMDCs like ZrS_2, $ZrSe_2$, HfS_2 and $HfSe_2$ show an increment in bandgap with the application of external stress up to $6 \pm 8\%$ and then it decreases. In tellurium-based compounds, $ZrTe_2$ and $HfTe_2$, the bandgap does not change under mechanical stress until 4% and 2%, respectively, and then it increases.

7.3.2 Optical Properties

The interaction of direct bandgap semiconducting TMDCs with light covers a wide field of light absorption and emission technologies. When incident photon energy is less as compared to the material's bandgap, the material seems to be transparent for that light. As the transparency decreases, the light absorption capability of the material increases. Absorption of any material is the percentage of light that is neither transmitted nor reflected and depends upon the energy of the incident photons. In semiconductors, light absorption as a function of thickness is considered as the absorption coefficient. The absorption coefficient increases for light with higher energy than the bandgap. Ullah et al. studied that the absorption coefficient of single and multi-layer MoS_2 is comparatively high near the visible spectrum (400–500 nm) with sharp decay after 500 nm, indicating that the MoS_2-based photodetector is good at detecting light below 500 nm [57]. Tang et al. showed the maximum value of absorptance for single-layer TMDCs: MoS_2, $MoSe_2$, WS_2 and WSe_2 on a silicon substrate as 98.81% (1.58 eV), 98.2% (1.61 eV), 99.92% and 99.84% (1.73 eV), respectively. The maximum values of absorptance for the above bulk TMDCs were found to be 98.6%, 97.6% (1.62 eV), 99.87% and 99.44% (1.90 eV), respectively [58].

7.3.3 Thermal Properties

Thermal properties of TMDCs play a vital role from the application point of view. Phonon transport phenomena are responsible for the thermal conductivity of 2D nanostructured materials. These materials exhibit a large potential for thermal management in electronic and optoelectronic devices. The thermal conductivity of 2D TMDCs changes with layer number, and its value decreases with an increasing number of layers. If some defects exist in 2D material such as phonon defects, scattering occurs that reduces thermal conductivity. When the material is supported on a substrate, then the thermal conductivity reduces. The thermal conductivity of CVD-grown pristine bilayer MoS_2 over SiO_2/Si substrate was found around 42 Wm^{-1} K^{-1} by Majee et al. using the optothermal Raman technique [59]. Majee et al. also demonstrated thermal transport behavior of a few layers of vertically grown MoS_2 over Si substrate and showed high thermal conductivity of around 100 Wm^{-1} K^{-1}. They showed that due to the vertical architecture of MoS_2, the substrate effect was minimized, and high thermal conductivity was obtained [60]. Thermal conductivity of MoS_2 was also measured by the suspended pad method for 4 and 7 layers and was observed to be in the range of 44–50 and 48–52 Wm^{-1} K^{-1}, respectively [61]. The cross plane thermal conductivity of disordered nanosheets of layered WSe_2 crystal, calculated by the time-domain thermos-reflectance method, was found to be 0.05 Wm^{-1} K^{-1} [62]. Thermal conductivities of different TMDC MX_2 (M = Mo, W; X = S, Se, Te) were also calculated by the first principles study, and it was observed that monolayer WTe_2 possesses the lowest lattice thermal conductivity (33.66 Wm^{-1} K^{-1}), while monolayer WS_2 shows highest thermal conductivity (113.97 Wm^{-1} K^{-1}) at room temperature among the family of TMDCs [63].

7.3.4 Magnetic Properties

It is one of the crucial properties of low-dimensional spintronic devices. Unfortunately, most of the 2D TMDCs don't show novel magnetic properties despite their versatile electronic structures. The absence of magnetic behavior in TMDCs greatly hampers their applications in spintronic devices. For tuning the magnetic properties of these materials, there is a great desire to develop new techniques like vacancy and impurity doping in bulk material, however uniform doping and precise manipulation of defects are very typical and challenging. The few layers of Vanadium dichalcogenides VX_2 (X = S, Se, Te) are found magnetic in nature having interesting spintronic and optomagnetic properties. The Vanadium-based TMDCs are expected to be ferromagnetic when reduced from bulk to monolayer regimes. According to DFT, this ferromagnetic behavior is due to the presence of V^{4+} ions having an electronic structure $[Ar]3d^1$. This unpaired d electron is responsible for the magnetic behavior of these Vanadium based TMDC materials [64]. Researchers venture their work in this field to determine magnetic properties based on phase fluctuations. It was confirmed by theoretical studies that VS_2 exists in H- and T- phase VS_2. The

magnetic moment of monolayer H-VS_2 is (1.00 mB) more than T-VS_2 (0.51 mB), which clearly depicts that the magnetic properties are structurally dependent.

7.3.5 Mechanical Properties

Mechanical properties of TMDCs are appropriate for their prospective applications in flexible and stretchable electronics and photonics. One of the simple techniques to estimate the mechanical behavior of 2D TMDCs is the buckling metrology method. Iguiñiz et al. used this method to find Young's modulus of various exfoliated TMDCs like MoS_2, $MoSe_2$, WS_2 and WSe_2 with varying thicknesses [65]. They acquired the values of Young's modulus for MoS_2 (3–11 L), $MoSe_2$ (5–10 L), WS_2 (3–8 L) and WSe_2 (4–9 L) as 246 ± 35, 224 ± 41, 236 ± 65 and 163 ± 39 GPa, respectively. They found that Young's modulus of metal disulphides is higher than that of metal diselenides. Another basic parameter that determines the mechanical properties of any material is the elastic modulus. Bertolazzi et al. showed the in-plane elastic modulus of 180 ± 60 and 260 ± 70 Nm^{-1} for exfoliated monolayer and bilayer MoS_2, respectively [66]. They showed the effective Young's modulus of 270 ± 100 and 200 ± 60 GPa for monolayer and bilayer MoS_2, respectively. The obtained high Young's modulus of single-layer MoS_2 is comparable to stainless steel, proving it as a flexible and strong material. Liu et al. reported the elastic modulus of CVD-grown single-layer MoS_2 ($\sim$171 Nm^{-1}) and WS_2 ($\sim$177 Nm^{-1}) and their bilayer heterostructures ($\sim$314 Nm^{-1}) [67]. The lower value of moduli for MoS_2/WS_2 heterostructures compared to the sum of each layer indicates excellent mechanical interaction between layers.

As we observed that different TMDCs show a variation of electronic behavior from metal to semiconductor, magnetic to non-magnetic, good to bad thermal conductor and so on, hence, these TMDCs can be applied for various applications by choosing suitable ones. In the following section, we will highlight some of the key applications of different TMDCs.

7.4 Application of TMDCs

The bandgap value of 2D TMDC materials can be varied by the variation of the composition of the element, and their properties can be expanded without surface modification. Due to their tunable bandgap, thickness-dependent photoelectric effect and photoacoustic signal of 2D TMDCs, these materials can be used in a variety of optoelectronic devices, such as transistors, photodetectors, photoelectric modulators, etc. The TMDC nanostructures show unique properties like strong piezoelectric coupling which makes them suitable materials for piezoelectric nanoenergy generator applications [68–70]. Additionally, due to the porous nature and good conductivity of TMDCs, they can be used as electrodes for electrochemical applications such as capacitors, batteries, hydrogen production, etc. [11]. The 2D TMDC nanostructured

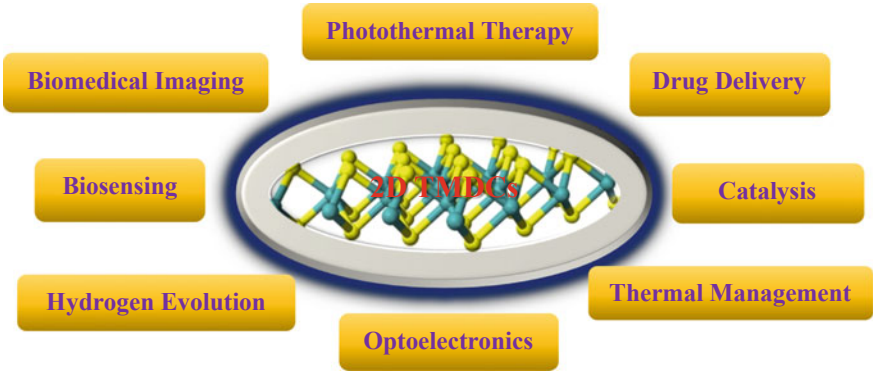

Fig. 7.8 Schematic diagram showing applications of 2D TMDC materials in various fields

materials can also provide a platform for biomedical applications like biosensing, biomedical imaging and drug delivery [12]. A schematic representation of the application of 2D TMDC materials is shown in Fig. 7.8, and examples of their different applications have been discussed in the following sections.

7.4.1 Application of 2D TMDCs as Photodetectors

Optical sensors are key in monitoring and imaging applications. These sensors basically utilize the optical and electronic properties of TMDC nanostructures to transform one form of signal into another form. As an example, photodetectors are used to detect different electromagnetic signals and convert those signals into electrical signals by utilizing optical absorption and bandgap characteristics. The photodetectors can detect weak signals as an indication of unwanted movement and can act as an alert system for defense and security. As the temperature of the object increases, the emitted electromagnetic radiation falls into the IR spectrum. In recent years, TMDCs based on visible near-infrared (Vis–NIR) photodetectors are being rapidly investigated due to their tunable bandgap, high photoresponsivity and flexibility suitable for Vis–NIR imaging, night vision, thermal sensing, etc. Recently, our research group performed the photodetection application of an interconnected network of horizontally grown few-layer n-type MoS_2 over p-type Si substrate with photoresponsivity of 0.1413 AW^{-1} under low-power white light (~0.15 $mWcm^{-2}$) illumination at − 2 V [71]. Good responsivity can be associated with the development of a better-quality p–n junction and effective charge carrier separation. Our group also successfully demonstrated the vertically oriented few-layer (VFL)-MoS_2 grown over Si substrate in a large dimension as a p–n junction photodetector for the detection of green light [60]. We found excellent photodetection under a laser intensity of 0.15 $mWcm^{-2}$ illumination with responsivity around 7.37 A W^{-1} at − 2 V bias (Fig. 7.9). The high photoresponsivity and outstanding optoelectronic behavior of VFL-MoS_2 can be attributed to the enhanced light trapping by multiple reflections of light with a high aspect ratio and vastly exposed edges.

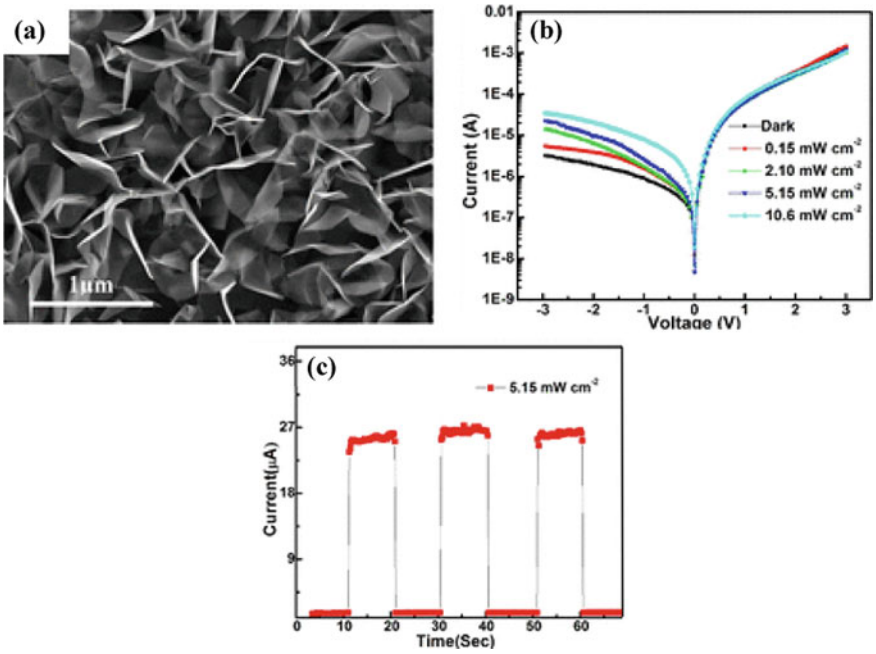

Fig. 7.9 (**a**) SEM image of vertically oriented few-layer MoS_2. (**b**) Current–Voltage (I-V) characteristics curves for vertical MoS_2/Si photodiode under 532 nm laser illumination. (**c**) Switching behavior of photodiode at − 3 V. Adapted with permission from [60]. Copyright 2020, American Chemical Society

These studies suggest that few-layer MoS_2 can be utilized for photodetection purposes in the visible region. These MoS_2 nanostructure-based photodetectors can be used in sensors, night vision devices, surveillance, optical communications, etc. Li et al. [72] fabricated an ultraband antenna-assisted photodetector based on Vanadium diselenide (VSe_2) nanosheets for the visible to terahertz (THz) region signal detection. In the near-visible infrared (NIR) region, they showed the photoresponse which is triggered by photoexcited electron–hole (e–h) pairs and a photothermal effect with an external bias voltage. They demonstrated the photoresponsivity under different wavelength illumination ranges of around 1.57 AW^{-1} at 635 nm, 0.63 AW^{-1} at 808 nm, 0.34 AW^{-1} at 980 nm and 1.18 AW^{-1} at 1550 nm.

7.4.2 Application of 2D TMDCs for Gas Sensing

Currently, in cities and most populated areas, pollution is commonly produced by harmful gases such as CO, CO_2, NO, CH_4, fluorinated Gas, NO_x, H_2S and other toxic gases. These poisonous gases are responsible for ozone pollution, climate change and even menace food security. Further, these pollutant gases have reduced the performance of photosynthesis, caused acid rain and increased the chances of respiratory

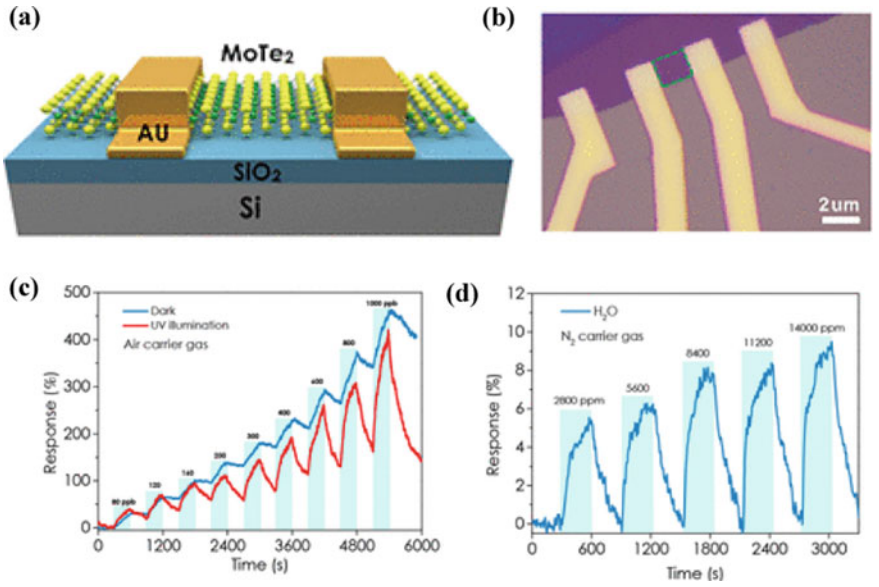

Fig. 7.10 (**a**) Schematic diagram of $MoTe_2$-based transistor on SiO_2/Si substrate. (**b**) Optical image of the fabricated $MoTe_2$ transistor. (**c**) Dynamic response of $MoTe_2$-based sensor to detect NO_2 gas in the air at different concentrations of NO_2 from 80 ppb to 1 ppm under both dark and UV light illumination. (**d**) Dynamic response of the $MoTe_2$-based sensor to H_2O in N_2 environment from 2800 to 14,000 ppm. Adapted with permission from [4]. Copyright 2018, American Chemical Society

diseases. In recent years, TMDCs have been used for gas sensing and removal via adsorption which helps in the reduction of pollution in the air. In TMDC-based gas sensing devices, the basic working mechanism is the transfer of charge that occurs by gas adsorption on TMDC surface which changes the resistivity and electrical signals that can be used for sensing. The MoS_2 is one of the most widely used TMDCs for gas sensing, and it is the most popular material for NO_2 detection. Liu et al. [73] demonstrated the gas detection of NO_2 and NH_3 by using CVD-grown triangular-shaped MoS_2 with a range of limits of detection down to parts per billion (ppb) with a long recovery time. Wu et al. [4] developed a $MoTe_2$-based gas sensor for the detection of NO_2 under UV light with a detection limit of 252 ppb (Fig. 7.10).

7.4.3 Application of 2D TMDCs in Green Energy Harvesting

In our society, natural fossil energy sources are very limited, so green energy is a very hopeful option to provide sustainable development for the world society and economy. The nanogenerators are devices that can provide self-sustainable power. The 2D TMDCs are the prominent material for the green energy generator due to their piezoelectric properties. Piezoelectric materials generate electricity due to

their non-centrosymmetric structure by applying mechanical stress or strain on the materials. Wu et al. have demonstrated the piezoelectric properties of nanostructured 2D TMDC crystals [68]. They prepared a flexible device based on the monolayer MoS_2, which produces piezoelectricity by inducing polarization of opposite charge polarity. The output of piezoelectric is generated due to altering polarity by stretching and releasing the substrate. They also demonstrated the dependency of piezoelectric on different layer numbers in MoS_2 nanostructures, which showed that by increasing the number of odd layer flakes, the piezoelectric output decreases. Similarly, TMDCs are also being investigated for solar energy harvesting. Currently, layered 2D TMDCs are used in photovoltaic applications due to their large surface area, dangling free bond surface and good sunlight absorption behavior. In solar cells, these materials are used to make Schottky or p–n junction to work as charge carrier separation at the interface. Shanmugam et al. prepared a MoS_2-based solar cell using the CVD technique and demonstrated a photo-conversion efficiency (PCE) of around 0.7% and 1.8% for 110 nm and 220 nm thick MoS_2, respectively [7]. In another work, they demonstrated WS_2/graphene-based solar cell, which shows very good photon absorption in the visible light region and demonstrated PCE of around 3.3% [74]. Park et al. observed the photovoltaic effect in few-layer ReS_2/WSe_2 heterostructure with a high fill factor of about 0.56, an external quantum efficiency of about 15.3% and power conversion efficiency of about 1.5% [75].

7.4.4 Application of 2D TMDCs in Green Electronics for Low-Power and High-Performance Integrated Circuits

Green electronics is an emergent field of electronic devices, where the use of eco-friendly materials is preferred over the cost factor. The 2D TMDCs are suitable materials for integrated circuits due to the availability of large bandgap value, high on/off ratio and high charge carrier mobility compared to other conventional semi-conducting materials. Their atomically thin structure decreases the short-channel effect in electrical circuits. Radisavljevic et al. demonstrated the first single-layer n-type MoS_2-based top-gated FET showing a high on/off ratio of around 10^8 with high charge carrier mobility of around 200 $cm^2V^{-1}\ s^{-1}$ [76]. Liu et al. fabricated WSe_2-based FET device showing an excellent current of 210 $\mu A{\cdot}\mu m^{-1}$ with high electron mobility of 142 $cm^2V^{-1}\ s^{-1}$ and a high on/off ratio of around 10^6 [77].

7.4.5 Application of 2D TMDCs in Electrochemical Energy Conversion and Storage Application

Hydrogen is known as a clean energy source with high energy density and can be used as an alternative to fossil fuels to reduce global warming effects. Water electrolysis is one of the major techniques to produce hydrogen for renewable energy.

The basic mechanism for hydrogen production is that catalysis can boost chemical reactions and accomplish high conversion efficiency with low overpotential. Due to their large fraction of active sites compared to other materials, atomically thin 2D TMDCs can be used as an electrode for hydrogen production. Recently, Mishra et al. synthesized MoS_2 nanoflowers as electrocatalysts for hydrogen production [78]. They evaluated the low overpotential of about 0.193 V with a Tafel slope of 69 $mV{\cdot}dec^{-1}$ and excellent stability for more than 2500 cycles for electrochemical hydrogen production. Ling et al. demonstrated a plasma-treated semi-metallic WTe_2-based microcell device for hydrogen evolution reaction (HER) application [79]. They showed that the catalytic activity of WTe_2 for HER can be enhanced by plasma treatment, which induces atomic defects and substitution of new elements to form a new chemical bond on the basal plane and the edges of WTe_2. The local HER measurement at edges in the microcell device which is treated by plasma exhibited active electrocatalytic activity with a Tafel slope (96 $mV{\cdot}dec^{-1}$), compared with pristine WTe_2 having Tafel slope of 145 $mV{\cdot}dec^{-1}$.

For the purpose of storing the produced energy, supercapacitors exhibit remarkable development due to their high-power density, long cycle life and ultrafast charge–discharge rate. During the past few years, TMDC nanostructures were proposed as a new class of hopeful materials for energy generation and storage. Mishra *et. al* fabricated solid-state supercapacitor (SSC) electrodes based on the hexagonal 2H phase of 3D MoS_2 nanoflowers [80]. They reported the highest specific capacitance of 382 Fg^{-1} at a current density of 1 Ag^{-1} by measuring a three-electrode system in a 1 M Na_2SO_4 aqueous electrolyte. This 2H phase MoS_2 SSC device shows a high energy density of 16.4 $Wh{\cdot}kg^{-1}$ at a constant current density of 0.2 Ag^{-1} (Fig. 7.11). The selection of catalyst materials is a very important step in the fabrication of batteries which can improve the capacity of the battery to store and provide power. Recently, researchers incorporated different TMDC materials that can be utilized as catalysts in the fabrication of alkali metal-ion batteries. Zhong et al. synthesized N-doped $MoSe_2$ with porous carbon microspheres ($MoSe_2$@N-HCS) by spray drying method at high-temperature calcination and selenization [81]. $MoSe_2$@N-HCS shows exceptional potassium storage properties, a higher rate performance of around 113.7 $mAhg^{-1}$ at current density of 10 Ag^{-1}, and long cycle life of around 16,700 cycles. The superior electrochemical performance can be ascribed to the N-doping which gives more active sites and decreases the migration energy barrier of K^+. These outstanding properties of $MoSe_2$ provide a new platform for anode material for potassium ion batteries.

7.4.6 Application of 2D TMDCs for Wastewater Treatment

The major cause of water pollution arises from many sources like industrial waste, oil leakage, sewage, chemical fertilizer and pesticides. This pollutant requires more oxygen molecules for decomposition through oxidation, which decreases the oxygen level in the water leading to health hazards and damaging the ecosystem. The 2D

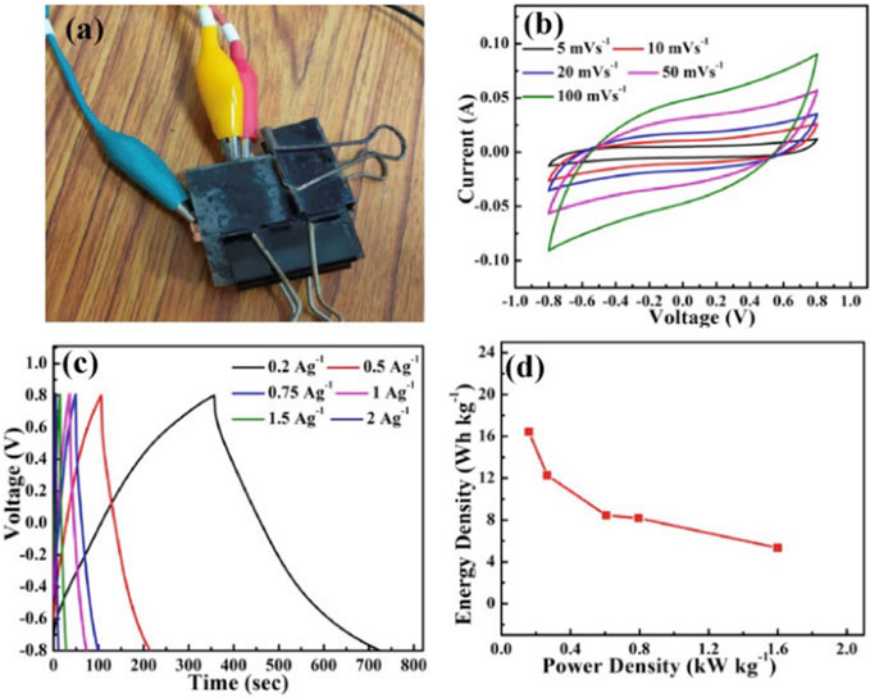

Fig. 7.11 Electrochemical measurements for MoS_2 nanoflowers-based SSC device with PVA-Na_2SO_4 as solid electrolyte (**a**) Image of SSC, (**b**) CV curves at various scan rates, (**c**) galvanostatic charge–discharge curves at various discharge current densities and (**d**) Energy density versus power density plot. Adapted with permission from [80]. Copyright 2020, Elsevier

TMDC-based nanostructured materials are being investigated for wastewater treatment. Li et al. proposed a model that is based on the adsorption technology, which provides a unique strategy for partial oxidation by removing the Rhodamine B (RhB) from wastewater by using WS_2/WO_3 [82]. Wan et al. developed a sponge with melamine–formaldehyde coated on MoS_2 (MF@MoS_2) with high adsorption capacity that shows superhydrophobic and superhydrophilic characteristics [83]. The MF@MoS_2 shows high adsorption for organic solvent, oil and water-soluble dye. They also developed the apparatus to collect and separate insoluble oils and organics and adsorbed soluble dyes from water. This prepared sponge pumping system provides a new technique to separate oil–water and remove soluble dyes from contaminated wastewater. Along with treatment, detection techniques like SERS are also key for wastewater management. Majee et al. demonstrated the CVD-grown vertically oriented few-layer MoS_2 nanosheets over Si as SERS substrate for the ultra-sensitive surface-enhanced Raman spectroscopy (SERS) detection of Rhodamine 6G and Methyl Orange at 10^{-10} M concentration [88].

7.4.7 Biomedical Application of 2D TMDCs

Recently, 2D TMDCs have shown promise in the area of biological applications, where health and protection are of great concern. The 2D TMDCs are applicable in biosensors applications, and interact with various anticancer drugs and biomolecules owing to their absence of dangling bonds, large surface area as well as high stability in liquid and air [84]. They also show high NIR absorbance, photothermal effects, surface chemistry and low toxicity. They have also been used as a photothermal mediator for photothermal therapy of cancer disease treatment with hopeful therapeutic results. Prismatic edges and basal surfaces of nanoflakes can be modified by some reported techniques to initiate bio reactions to target specific biomaterials [85]. The 2D TMDCs offer a large surface area that can enhance biological interactions. Moreover, the plasmonic properties with photoluminescence of these materials permit optical observations of cells by biosensing. The most important property of 2D TMDCs is their capability to intercalate ions with organic molecules that help to detect or persuade cellular responses [13]. The 2D TMDCs have been utilized for making biosensors with high-quality conductometric and field effect-based sensing for effective bioimaging. Also, 2D TMDCs exhibit unique mechanical properties, which can be utilized for using necessary backgrounds for tissue engineering and for establishing nanoscale acoustic transducers. Nanostructured 2D TMDCs can be utilized for imaging and tagging by functionalizing these materials. Fluorescent 2D TMDCs based on Mo, W and Zr dichalcogenide composites are used for imaging and identifying cell organs and targeting chemicals around the cells [12]. Further, 2D TMDCs can be used in sensing, depending on electron exchange and quenching processes by successfully binding to other fluorophores. With small lateral dimensions (<50 nm), they can be occupied by the cell and used for high-contrast cell tagging. This method may be embattled for positive cells when the 2D TMDC is functionalized to display a suitable cell-specific ligand. Additionally, the thermal behavior of both metallic and semiconducting TMDCs can be subjugated in optical applications including photothermal therapeutics [12, 13].

Most of the 2D TMDCs show near-infrared (NIR) absorbance, like MoS_2 exhibits higher absorbance than other 2D materials like graphene. This absorbance in the NIR region makes them suitable materials for the treatment of cancer by photothermal ablation. The drug-carrying and photothermal characteristics of 2D TMDC nanostructured materials can be employed to transport NIR-triggered treatment with chemotherapeutic agents. Yin et al. gave a model to treat pancreatic cancer by injecting 2D MoS_2 loaded with doxorubicin (DOX) as nanocarriers to NIR radiation [86]. Yang et al. show exciting physical properties of WS_2/iron oxide/polyethylene glycol (PEG) for a chemotherapy drug, DOX, whose intercellular release afterward may be triggered by NIR-induced photothermal heating for enhanced cancer cell killing [15]. Currently, most of the 2D TMDC-based sensors are made by field-effect and electrochemical transducing templates. These devices have been used to identify proteins and DNA (Fig. 7.12a–d). In redox systems, 2D TMDC-based electrochemical devices are suitable for sensing ionic species of the biomolecule. The PL

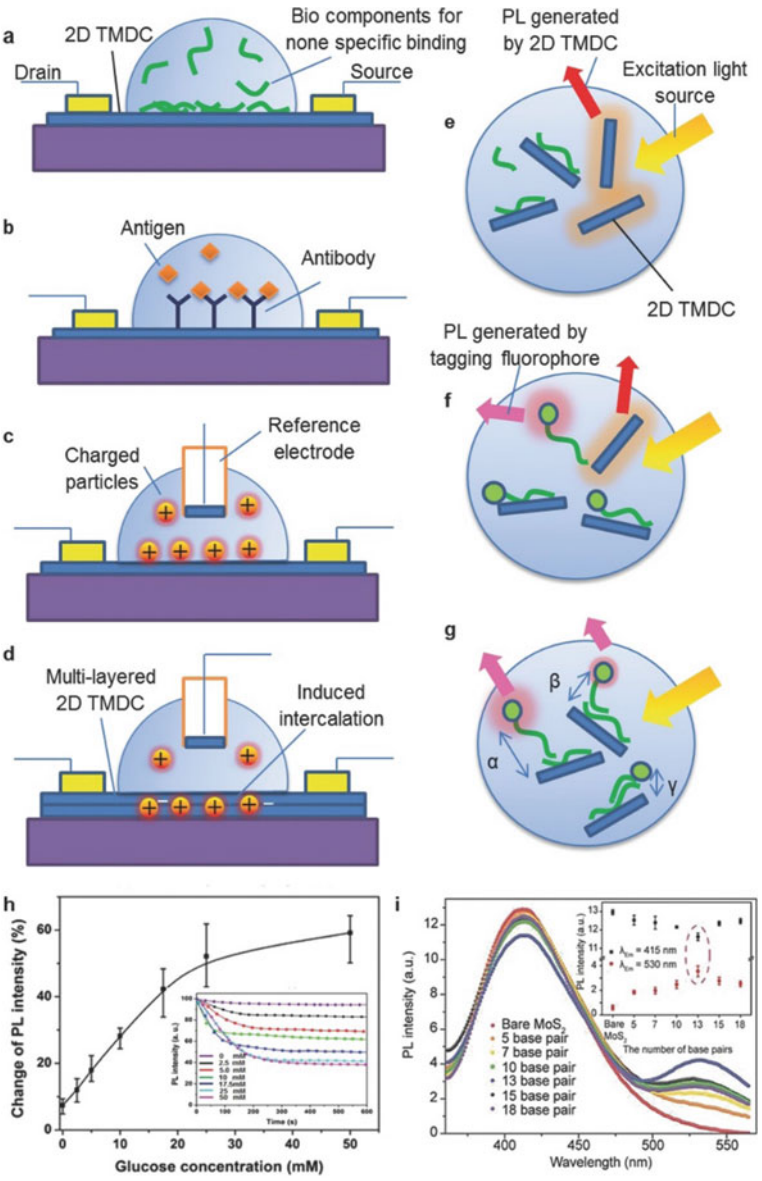

Fig. 7.12 (**a**) Schematics diagram of 2D TMDC device for biosensing systems, (**b**) Mechanism of lock and key concept of antibody–antigen, (**c**) Production of electrical double layer on 2D TMDC nanostructure with a reference electrode, (**d**) Schematic diagram of biosensing systems based on 2D TMDC suspensions with a reference electrode, (**e**) Non-specific immobilization of bio components with the PL of 2D TMDCs, (**f**) Bio components with fluorophore is quenched after immobilization, (**g**) The probability of energy transfer and PL with the combination of fluorophores and 2D TMDCs, (**h**) Characterization of the 2D TMDC glucose oxidize system with change of PL intensity glucose concentration and (**i**) PL spectra at different concentrations of glucose with fixed voltage –1.5 V. Adapted with permission from [13]. Copyright 2015, Wiley

of semiconducting 2D TMDCs can be reduced or enhanced upon interactions with biomolecules or the ligation of biomolecules on the surface of TMDCs (Fig. 7.12e–i). To date, different types of 2D TMDCs have been revealed for sensing based on PL including $MoSe_2$, MoS_2, WS_2, TiS_2 and TaS_2 [13, 87].

7.5 Conclusions and Future Outlook

In summary, we have briefly discussed various synthesis methods of 2D TMDCs from top-down to bottom-up approaches with their exciting structural–morphological orientation. The top-down approach includes the synthesis of TMDCs from bulk layered material by different techniques mainly categorized under mechanical exfoliation and chemical exfoliation. This method produces large-size and high-quality TMDCs but is not suited for application in electronics and optoelectronic devices due to a lack of controllability over growth techniques. Comparatively, the bottom-up approach could overcome this shortage, which includes chemical vapor deposition (CVD), wet-chemical synthesis, molecular-beam epitaxy (MBE), atomic layer deposition (ALD), pulsed laser deposition (PLD), sputtering, etc. techniques. The key physical properties and corresponding application of different TMDCs have also been discussed in this chapter. The thickness-dependent tunable bandgap of TMDCs makes them applicable in various electronic and optoelectronic devices like transistors, photodetectors, photoelectric modulators, etc. The porous nature and good conductivity of TMDCs make them suitable for capacitors, batteries, hydrogen production, etc. The 2D TMDC nanostructured materials can also provide a platform for biomedical applications like biosensing, biomedical imaging and drug delivery. Therefore, it is imperative to develop more and more technologically advanced synthesis techniques. In the future, scientists should put more efforts into the controlled synthesis of high-quality 2D TMDCs that still remains a challenge to obtain the desired morphology and crystal structure for relevant applications.

Acknowledgements The authors are thankful to the support of IIT (BHU), SERB and DST, India for helping financially. The authors are also thankful for some of the research works related to this field.

References

1. M. Bernardi, C. Ataca, M. Palummo, J.C. Grossman, Nanophotonics **6**, 479–493 (2017)
2. W. Zhao, J. Pan, Y. Fang, X. Che, D. Wang, K. Bu, F. Huang, Chem. Eur. J. **24**, 15942–15954 (2018)
3. J. Baek, D. Yin, N. Liu, I. Omkaram, C. Jung, H. Im, S. Hong, S. M. Kim, Y. K. Hong, J. Hur, Y. Yoon, S. Kim 10, Nano Res. **10**, 1861–1871 (2017)
4. E. Wu, Y. Xie, B. Yuan, H. Zhang, X. Hu, J. Liu, D. Zhang, ACS Sens. **3**, 1719–1726 (2018)

5. T. Venanzi, H. Arora, A. Erbe, O. Pashkin, S. Winnerl, S. Helm, H. Schneider, Appl. Phys. Lett. **114**, 172106 (2019)
6. Y. Q. Bie, G. Grosso, M. Heuck, M. M. Furchi, Y. Cao, J. Zheng, D. Bunandar, E. Navarro-Moratalla, L. Zhou, D. K. Efetov, T. Taniguchi, K. Watanabe, J. Kong, D. Englund & P. Jarillo-Herrero Nature Nanotechnology **12**, 1124–1129 (2017)
7. M. Shanmugam, C.A. Durcan, B. Yu, Nanoscale **4**, 7399–7405 (2012)
8. S.K. Lee, D. Chu, J. Yoo, E.K. Kim, Sol. Energy Mater. Sol. Cells **184**, 9–14 (2018)
9. X. Yu, M.S. Prévot, N. Guijarro, K. Sivula, Nat. Commun. **6**, 1–8 (2015)
10. H. Li, Y. Shi, M.H. Chiu, L.J. Li, Nano Energy **18**, 293–305 (2015)
11. Y. Liu, X. Peng, Appl. Mater. Today **8**, 104–115 (2017)
12. X. Zhou, H. Sun, X. Bai, Front. Bioeng. Biotechnol. **8**, 236 (2020)
13. K. Kalantar-zadeh, J.Z. Ou, T. Daeneke, M.S. Strano, M. Pumera, S.L. Gras, Adv. Funct. Mater. **25**, 5086–5099 (2015)
14. M. M. Hossain, B. Shabbir, Y. Wu, W. Yu, V. Krishnamurthi, H. Uddin, N. Mahmood, S. Walia, Q. Bao, T. Alan, S. Mokkapati, 2d Mater. **8**, 045005 (2021)
15. G. Yang, H. Gong, T. Liu, X. Sun, L. Cheng, Z. Liu, Biomaterials **60**, 62–71 (2015)
16. K. S. Novoselov, A. K. Geim, S. V. Morozov, D. Jiang, Y. Zhang, S. V. Dubonos, I. V. Grigorieva, A. A. Firsov, science **306**, 666–669 (2004)
17. H. Li, Z. Yin, Q. He, H. Li, X. Huang, G. Lu, D. W. H. Fam, A. I. Y. Tok, Q. Zhang, H. Zhang, small **8**, 63–67 (2012)
18. N.E. Staley, J. Wu, P. Eklund, Y. Liu, L. Li, Z. Xu, Phys. Rev. B. **80**, 184505 (2009)
19. F. Liu, S. Zheng, A. Chaturvedi, V. Zólyomi, J. Zhou, Q. Fu, C. Zhu, P. Yu, Q. Zeng, N.D. Drummond, H.J. Fan, C. Kloc, V.I. Fal'ko, X. He, Z. Liu, Nanoscale **8**, 5826–5834 (2016)
20. D.-M. Tang, D.G. Kvashnin, S. Najmaei, Y. Bando, K. Kimoto, P. Koskinen, P.M. Ajayan, B.I. Yakobson, P.B. Sorokin, J. Lou, D. Golberg, Nat. Commun. **5**, 1–8 (2014)
21. M. Yang, X. Cheng, Y. Li, Y. Ren, M. Liu, Z. Qi, Appl. Phys. Lett. **110**, 093108 (2017)
22. J.N. Coleman, M. Lotya, A. O'Neill, S.D. Bergin, P.J. King, U. Khan, K. Young, A. Gaucher, S. De, R.J. Smith, I.V. Shvets, S.K. Arora, G. Stanton, H.-Y. Kim, K. Lee, G.T. Kim, G.S. Duesberg, T. Hallam, J.J. Boland, J.J. Wang, J.F. Donegan, J.C. Grunlan, G. Moriarty, A. Shmeliov, R.J. Nicholls, J.M. Perkins, E.M. Grieveson, K. Theuwissen, D.W. McComb, P.D. Nellist, V. Nicolosi, Science **331**, 568–571 (2011)
23. R.A. Gordon, D. Yang, E.D. Crozier, D.T. Jiang, R.F. Frindt, Phys. Rev. B **65**, 125407 (2002)
24. Z. Zeng, Z. Yin, X. Huang, H. Li, Q. He, G. Lu, F. Boey, H. Zhang, Angew. Chem. **123**, 11289–11293 (2011)
25. N. Liu, P. Kim, J.H. Kim, J.H. Ye, S. Kim, C.J. Lee, ACS Nano **8**, 6902–6910 (2014)
26. A.J. Pollard, R.R. Nair, S.N. Sabki, C.R. Staddon, L.M.A. Perdigao, C.H. Hsu, J.M. Garfitt, S. Gangopadhyay, H.F. Gleeson, A.K. Geim, P.H. Beton, J. Phys. Chem. C **113**, 16565–16567 (2009)
27. Q. Ji, Y. Zhang, Y. Zhang, Z. Liu, Chem. Soc. Rev. **44**, 2587–2602 (2015)
28. X. Wang, Y. Li, L. Zhuo, J. Zheng, X. Peng, Z. Jiao, X. Xiong, J. Han, W. Xiao, CrystEngComm **20**, 6267–6272 (2018)
29. L. Meng, Z. Zhou, M. Xu, S. Yang, K. Si, L. Liu, X. Wang, H. Jiang, B. Li, P. Qin, P. Zhang, J. Wang, Z. Liu, P. Tang, Y. Ye, W. Zhou, L. Bao, H.-J. Gao, Y. Gong, Nat. Commun. **12**, 1–8 (2021)
30. S. Wang, Y. Rong, Y. Fan, M. Pacios, H. Bhaskaran, K. He, J.H. Warner, Chem. Mater. **26**, 6371–6379 (2014)
31. S.Y. Yang, G.W. Shim, S.-B. Seo, S.-Y. Choi, Nano Res. **10**, 255–262 (2017)
32. K. Kang, S. Xie, L. Huang, Y. Han, P.Y. Huang, K.F. Mak, C.-J. Kim, D. Muller, J. Park, Nature **520**, 656–660 (2015)
33. S.M. Eichfeld, L. Hossain, Y.-C. Lin, A.F. Piasecki, B. Kupp, A.G. Birdwell, R.A. Burke, N. Lu, X. Peng, J. Li, A. Azcatl, S. McDonnell, R.M. Wallace, M.J. Kim, T.S. Mayer, J.M. Redwing, J.A. Robinson, ACS Nano **9**, 2080–2087 (2015)
34. D.Y. Chung, S.-K. Park, Y.-H. Chung, S.-H. Yu, D.-H. Lim, N. Jung, H.C. Ham, H.-Y. Park, Y. Piao, S.J. Yoo, Y.-E. Sung, Nanoscale **6**, 2131–2136 (2014)

35. M. Srivastava, P. Tiwari, V.K. Mall, S.K. Srivastava, R. Prakash, Mikrochim Acta **186**, 1–10 (2019)
36. N.T. Shelke, B.R. Karche, J. Alloys Compd. **653**, 298–303 (2015)
37. J. Feng, X. Sun, C. Wu, L. Peng, C. Lin, S. Hu, J. Yang, Y. Xi, J. Am. Chem. Soc. **133**, 17832–17838 (2011)
38. Q. He, P. Li, Z. Wu, B. Yuan, Z. Luo, W. Yang, J. Liu, G. Cao, W. Zhang, Y. Shen, P. Zhang, S. Liu, G. Shao, Z. Yao, Adv. Mater. **31**, 1901578 (2019)
39. L. Jiao, H.J. Liu, J.L. Chen, Y. Yi, W.G. Chen, Y. Cai, J.N. Wang, X.Q. Dai, N. Wang, W.K. Ho, M.H. Xie, New J. Phys. **17**, 053023 (2015)
40. H. J. Liu, L. Jiao, L. Xie, F. Yang, J. L. Chen, W. K. Ho, C. L. Gao, J. F. Jia, X. D. Cui, M. H. Xie, 2d Mater. **2**, 034004 (2015)
41. L. A. Walsh, R. Yue, Q. Wang, A. T. Barton, R. Addou, C. M. Smyth, H. Zhu, J. Kim, L. Colombo, M. J. Kim, R. M. Wallace, C. L. Hinkle, 2d Mater. **4**, 025044 (2017)
42. R. Yue, A.T. Barton, H. Zhu, A. Azcatl, L.F. Pena, J. Wang, X. Peng, N. Lu, L. Cheng, R. Addou, S. McDonnell, L. Colombo, J.W.P. Hsu, J. Kim, M.J. Kim, R.M. Wallace, C.L. Hinkle, ACS Nano **9**, 474–480 (2015)
43. S. Aminalragia-Giamini, J. Marquez-Velasco, P. Tsipas, D. Tsoutsou, G. Renaud, A. Dimoulas, 2d Mater **4**, 015001 (2016)
44. Y. W. Park, S.-K. Jerng, J. H. Jeon, S. B. Roy, K. Akbar, J. Kim, Y. Sim, M.-J. Seong, J. H. Kim, Z. Lee, M. Kim, Y. Yi, J. Kim, D. Y. Noh, S.-H. Chun, 2d Mater **4**, 014006 (2016)
45. J.-G. Song, J. Park, W. Lee, T. Choi, H. Jung, C.W. Lee, S.-H. Hwang, J.M. Myoung, J.-H. Jung, S.-H. Kim, C. Lansalot-Matras, H. Kim, ACS Nano **7**, 11333–11340 (2013)
46. M. Krbal, J. Prikryl, R. Zazpe, F. Dvorak, F. Bures, J.M. Macak, Phys Status Solidi Rapid Res Lett **12**, 1800023 (2018)
47. Y. Chen, Y. Chen, J. Ning, L. Chen, W. Zhuang, L. He, R. Zhang, Y. Xu, X. Wang, Chin. Phys. Lett. **37**, 017104 (2020)
48. P.A. Vermeulen, J. Momand, B. J. Kooi **21**, 3409 (2019)
49. J.-H. Huang, K.-Y. Deng, P.-S. Liu, C.-T. Wu, C.-T. Chou, W.-H. Chang, Y.-J. Lee, T.-H. Hou, Adv. Mater. Interfaces **4**, 1700157 (2017)
50. K. Yumigeta, C. Kopas, M. Blei, D. Hajra, Y. Shen, D. Trivedi, P. Kolari, N. Newman, S. Tongay, Nanoscale Adv. **2**, 1443–1448 (2020)
51. D. Shi, G. Wang, C. Li, X. Shen, Q. Nie, Vacuum **138**, 101–104 (2017)
52. J.J. Devadasana, C. Sanjeevirajaa, M. Jayachandranb, J. Cryst. Growth **226**, 67–72 (2001)
53. A. Chaturvedi, A. Slabon, P. Hu, S. Feng, K.-K. Zhang, R.R. Prabhakar, C. Kloc, J. Cryst. Growth **450**, 140–147 (2016)
54. D. Wickramaratne, F. Zahid, R.K. Lake, J. Chem. Phys. **140**, 124710 (2014)
55. J. Jadczak, J. Kutrowska-Girzycka, P. Kapuściński, Y.S. Huang, A. Wójs, L. Bryja, Nanotechnology **28**, 395702 (2017)
56. L.A. Chernozatonskii, A.A. Artyukh, PHYS-USP **61**, 2 (2018)
57. M.S. Ullah, A.H.B. Yousuf, A.D. Es-Sakhi, M.H. Chowdhury, A.I.P. Conf, Proc. **1957**, 020001 (2018)
58. W. Tang, S.S. Rassay, N.M. Ravindra, Madridge J Nano Tec. Sci. **2**, 59–65 (2017)
59. B.P. Majee, J.D. Gupta, A. Sanskrityayn, A.K. Mishra, J. Phys. Chem. C **125**, 14865–14873 (2021)
60. B. P. Majee, Bhawna, A. Singh, R. Parkash, A. K. Mishra, J. Phys. Chem. Lett. **11**, 1268–1275 (2020)
61. I. Jo, M.T. Pettes, E. Ou, W. Wu, L. Shi, Appl. Phys. Lett. **104**, 201902 (2014)
62. C. Chiritescu, D.G. Cahill, N. Nguyen, D. Johnson, A. Bodapati, P. Keblinski, P. Zschack SCIENCE **315**, 351–353 (2007)
63. M. Zulfqar, Y. Zhao, G. Li, Z.C. Li, J. Ni, Sci. Rep. **9**, 1–7 (2019)
64. H. Zhang, L.M. Liu, W.M. Lau, J. Mater. Chem. A **1**, 10821–10828 (2013)
65. N. Iguiñiz, R. Frisenda, R. Bratschitsch, A. Castellanos-Gomez, Adv. Mater. **31**, 1807150 (2019)
66. S. Bertolazzi, J. Brivio, A. Kis, ACS Nano **5**, 9703–9709 (2011)

67. K. Liu, Q. Yan, M. Chen, W. Fan, Y. Sun, J. Suh, D. Fu, S. Lee, J. Zhou, S. Tongay, J. Ji, J.B. Neaton, J. Wu, Nano Lett. **14**, 5097–5103 (2014)
68. W. Wu, L. Wang, Y. Li, F. Zhang, L. Lin, S. Niu, D. Chenet, X. Zhang, Y. Hao, T.F. Heinz, J. Hone, Z.L. Wang, Nature **514**, 470–474 (2014)
69. W. Chen, H. Yin, S. Jiang, S. Liu, C. Liu, B. Wang, G.P. Zheng, Appl. Phys. Lett. **118**, 213103 (2021)
70. J. Seo, Y. Kim, W.Y. Park, J.Y. Son, C.K. Jeong, H. Kim, W.H. Kim, Appl. Surf. Sci. **487**, 1356–1361 (2019)
71. B. P. Majee, S. Mishra, R. K. Pandey, R. Prakash, A. K. Mishra, *J. Phys. Chem. C*.**123**, 18071–18078 (2019)
72. J. Li, L. Jiang, W. Ma, T. Wu, Q. Qiu, Y. Shi, W. Zhou, N. Yao, Z. Huang, A.C.S. Appl, Nano Mater. **5**, 5158–5167 (2022)
73. B. Liu, L. Chen, G. Liu, A.N. Abbas, M. Fathi, C. Zhou, ACS Nano **8**, 5304–5314 (2014)
74. M. Shanmugam, R. Jacobs-Gedrim, E.S. Song, B. Yu, Nanoscale **6**, 12682–12689 (2014)
75. C. Park, N.T. Duong, S. Bang, D.A. Nguyen, H.M. Oh, M.S. Jeong, Nanoscale **10**, 20306–20312 (2018)
76. B. Radisavljevic, A. Radenovic, J. Brivio, V. Giacometti, A. Kis, Nat. Nanotechnol. **6**, 147–150 (2011)
77. W. Liu, J. Kang, D. Sarkar, Y. Khatami, D. Jena, K. Banerjee, Nano Lett. **13**, 1983–1990 (2013)
78. S. Mishra, P.K. Maurya, A.K. Mishra, Mater. Today Commun. **25**, 101270 (2020)
79. N. Ling, S. Zheng, Y. Lee, M. Zhao, E. Kim, S. Cho, H. Yang, APL Mater. **9**, 061108 (2021)
80. S. Mishra, P.K. Maurya, A.K. Mishra, Mater. Chem. Phys. **255**, 123551 (2020)
81. F. Zhong, A. Xu, Q. Zeng, Y. Wang, G. Li, Z. Xu, Y. Yan, S. Wu, A.C.S. Appl, Mater. Interfaces **13**, 59882–59891 (2021)
82. G. Li, Y. Wang, J. Bi, X. Huang, Y. Mao, L. Luo, H. Hao, Nanomaterials **10**, 278 (2020)
83. Z. Wan, D. Li, Y. Jiao, X. Ouyang, L. Chang, X. Wang, Appl. Mater. Today **9**, 551–559 (2017)
84. E. P. Nguyen, C. d. C. C. Silva, A. Merkoçi, Nanoscale **12**, 19043–19067 (2020)
85. X. Li, J. Shan, W. Zhang, S. Su, L. Yuwen, L. Wang, Small **13**, 1602660 (2017)
86. W. Yin, L. Yan, J. Yu, G. Tian, L. Zhou, X. Zheng, X. Zhang, Y. Yong, J. Li, Z. Gu, Y. Zhao, ACS Nano **8**, 6922–6933 (2014)
87. J.Z. Ou, A.F. Chrimes, Y. Wang, S.Y. Tang, M.S. Strano, K. Kalantar-Zadeh, Nano Lett. **14**, 857–863 (2014)
88. B.P. Majee, V. Srivastava, A.K. Mishra, A.C.S. Appl, Nano Mater. **3**, 4851–4858 (2020)

Chapter 8
Recent Escalations in MXenes: From Fundamental to Applications

Jeevan Jyoti, Bhanu Pratap Singh, Manjit Sandhu, and Surya Kant Tripathi

Abstract Enormous efforts have been devoted towards the development of various advanced materials with long cycle life, high power density and high energy density for energy storage and conversion applications. From the discovery of MXene, the family of two-dimensional (2D) transition metal nitrides, carbides and carbonitrides has attained significant research focus due to their outstanding properties. MXene has drawn significant attention because they have tunable layered structures, controllable interfacial chemistry, high mechanical strength, excellent electronic conductivity, superior specific surface area, magnetic properties, hydrophilic features, multiple possible surface terminations and the ability to accommodate intercalates. In this chapter, we reported the synthesis techniques and properties of MXene and MXene-based hybrid materials and their potential applications. The MXene has been synthesized by various routes such as chemical vapor deposition (CVD), sputtering, pulse laser plasma deposition and etching techniques. Generally, etching technique has been used for the synthesis of MXene. Different etchants have been used for the synthesis of MXene such as hydrofluoric acid, lithium fluoride, hydrochloric acid, ammonium hydrazine, etc. After etching, the surface termination groups such as –F, –OH and–O presents on the MXene influence their properties. The surface termination groups on 2D MXene have been significantly used in various applications such as rechargeable batteries, supercapacitors, electromagnetic interference shielding, sensors and so on. In summary, a widespread overview of the synthesis of MXene with the current challenges and encouraging technologies for the preparation of large scale MXene and its usefulness in several applications are provided.

Keywords MAX phase · Properties · Batteries · Supercapacitors · EMI shielding

J. Jyoti (✉) · S. K. Tripathi
Centre of Advanced Studies, Physics Department, Panjab University, Chandigarh, India
e-mail: jeevanjyoti.npl@gmail.com

B. P. Singh
Advanced Carbon Products and Metrology, CSIR-National Physical Laboratory, New Delhi 110012, India

M. Sandhu
School of Mechanical Engineering Department, Indian Institute of Technology Ropar, Nangal Road, Rupnagar, Punjab 140001, India

D. K. Singh et al. (eds.), *Nanomaterials*,
https://doi.org/10.1007/978-981-19-7963-7_8

8.1 Introduction

Since 2004, graphene's outstanding mechanical strength, carrier mobility, high electrical and thermal conductivity have significant applications for 2D materials. Various 2D materials have been synthesized and investigated such as metal–organic frame work (MOF), transition metal oxide (TMOs), transition metal dichalcogenides (TMDs), h-Boron nitrides, perovskites, etc. monolayer of boron nitride and so on [1–3]. Due to their excellent intrinsic features, these 2D materials have been used in multiple promising applications. The incorporation of layered 2D advanced materials has enhanced the properties of conventional devices, like batteries, fuel cell, solar cell, biomedical devices, supercapacitors, electromagnetic interference shielding, and photothermal therapeutic applications [4–17]. The layered 2D materials reported various problems like mechanically unstable, or electrochemical inertness, or having low intrinsic electronic conductivity. Scientists and researchers are continuously developing various 2D materials which can provide good mechanical stability, excellent electronic conductivity, fast redox reaction, etc. Researchers of Drexel University in 2011, discovered the advanced material, commonly known as MXene [18, 19]. A new family of 2D materials has emerged, consisting of transition metal nitrides, carbides and carbonitrides, also known as MXene.

Their parent metal ceramic phases (MAX) are the layered structure with the formula of $M_{n+1}AX_n$ and the symbol M signifies the transition metal (TM = Zr, Ti, Mo, Ta, V, Hf, etc.), A stands for elements of group of 13 and 14 and X represents the Nitrogen/carbon atom [20, 21]. The symbol "n" can be any value that lies between 1 and 3. The layer of "A" atom is sandwiched between the transition metal layers and the X atoms position at the octahedral sites. The strong bonding between the M-X has a mixed type of ionic/metallic/covalent bond, on the other hand, M-A bonds are metallic in behavior. The bonding present between the MAX phases are too strong to be damaged using shear and another comparable mechanical means. In the MAX phase, the bonding between the M-A bonds are slightly weaker as compared to the M-X bond. Using a particular etching technique, the "A" atom can be removed from the MAX phase using the strong acids or molten salts without distortion of the M-X bond. MXene have been commonly found in three phases such as M_2X, M_3X and M_4X. Figure 8.1a shows the Ti_2AlC and Ti_3AlC_2 are structure of ternary carbides. Both crystalline in the $P6_3/mmc$ space group.

The MXene are synthesized using the selective etching technique. In the acid treatment of MAX phase, the acid damages the bonding between transition metal (TM) and "A" element. The MXene-based materials are synthesized using the etching of layers of MAX phase as shown in Fig. 8.1b. Figure 8.1b shows the X and M atoms of MAX phases arranged in hexagonal lattice, the position of X atoms occupied at the centre of the edges-shares M octahedral sites. The MAX phase exhibited in three different phases such as 211, 312 and 413 corresponds to layers of Ti atoms between Al layers i.e., 1, 2 and 3. The layers of carbon atoms are always one layer less than the Ti layer. The different structures of the MXene such as M_2AX, M_3AX_2, and M_4AX_3 phases are shown in Fig. 8.1b.

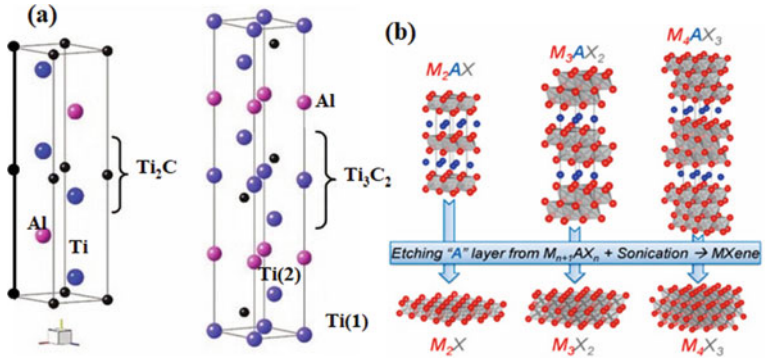

Fig. 8.1 **a** Layered structure of Ti_3AlC_2 "Adapted with permission from [22]. Copyright (2010), Elsevier **b** different phases of MXene such as M_2AX, M_3AX_2, and M_4AX_3; Adapted with permission from [23]. Copyright (2021) Elsevier

Till now, more than 80 different types of MXene have been recognized. MXene like Ti_3C_2, Ti_2AlC, Nb_2C Ti_2C $(Ti_{1/2}, Nb_{1/2})_2C$, V_2C, Ti_3CN, and Ta_4C_3 etc. are well known materials [24, 25]. The structure of Ti_2AlC phase contains four different layers of Ti–C–Ti–Al. The bi-layers of Ti atoms are packed densely. On the other side, a single layer of carbon atoms occupied the octahedral position between the Ti layers and the Al atom is placed between the Ti–C–Ti layer [26]. The octahedral arrangement of Ti_6C is similar to rock salt structure and atoms of Al are placed in trigonal sites. Generally, M-X bonds show various features of ionic, covalent and metallic characters, which provide strong binding energy as compared to M-A metallic bond. The M-A phase is less stable as compared to M-X bound layers. The "A" atom exit in M-A phase offers higher chemical reactivity. The different functional groups attached on the surface of the MXene are considered to be modified in the structural and chemical form.

With enhanced research consideration to layered 2D materials after graphene and with MXene signifying a new family of 2D material world-wide. In this book chapter, we willemphasize on their synthesis, properties and potential applications of MXene and MXene-based hybrid materials.

8.2 Preparation of MXene Such as Transition Metal Nitrides and Carbides

Commonly, MXene-based material is synthesized using the single metal carbides such as Ti_3C_2, Ti_4C_3, etc. Binary metal bases MXene materials are also synthesized such as $M_2'M''C_2$ and $M_2'M''_2C_3$ phases. B. Anasori, and his co. worker has successfully synthesised the binary phase $M_2'M''C_2$ and $M_2'M''_2C_3$ MXene, Where M' and M'' are the two different metals [27]. Most commonly binary MXene compounds are

Mo_2TiC_2 and $Mo_2Ti_2C_3$ MXenes are successive examples. Figure 8.2a displays the X-ray diffraction (XRD) pattern of Mo_2TiAlC_2 red colour signifies the before and green colour represents after etching which terminates to blue colour respectively. Mo_2TiAlC_2 indicate the layered structure and after the etching, the peak close to 62° is also seen after the delamination peak is vanished. The vanished peaks after the delamination represent the layers are restacked arbitrarily and the crystallographic axis is retained properties. The XRD plot of $Mo_2Ti_2C_3$ also shows comparable behavior, but the lattice parameter of $Mo_2Ti_2AlC_3$ powder is 23.6 Å(pink plot) and it improved upto 34.5 Å after delamination as shown in Fig. 8.2c. Figure 8.2e, j exhibits the SEM micrograph of the parent MAX phase and Fig. 8.2f, k shows their MXene. Figure 8.2b, d show confirmations of 3D to 2D conversion of both materials. Figure 8.2g, h exhibits the high-resolution scanning transmission electron microscopy (HRSTEM) images of Mo_2TiAlC_2 and $Mo_2TiC_2T_x$ respectively, Fig. 8.2g, h indicate the presence and absence of Al layer as shown in Fig. 8.2h. $Mo_2Ti_2C_3T_x$ shows analogous behavior at the presence and disappearance of the Al layers as shown in Fig. 8.2l, m. The HRSTEM gives clear confirmation for the removal of Al layers after etching. The low magnified of TEM shows the flakes like layered structure as shown in Fig. 8.2i and n.

Similar, Raman Spectroscopy is a useful tool to give information about the bonding in the MXene structure. This technique detects the molecular fingerprints and is sensitive to amorphous materials as well as traces of TMO, which are often present in the structure of MXene.

MXene has been synthesized by various techniques such as wet etching [25, 28, 29], chemical vapor deposition [30, 31], molten salts [32–34] and electrochemical etching [35]. Usually, MXene are synthesized from the MAX precursors. The Top-down and Bottom-up techniques have been used for the fabrications of MXene as shown in Fig. 8.3. The 2D materials can be prepared by using the top-down technique which contains the exfoliation of materials using mechanical or chemical methods. The second technique is bottom-up technique which uses chemical deposition on the substrate to produce the high quality of material.

8.2.1 Top-Down Technique

For the synthesis of 2D MXene using the top-down technique is generally used. It involves several steps such as etching and exfoliation. MXene-based materials are generally synthesized using this approach.

8.2.1.1 Wet Chemical Technique

This technique is generally used for the preparation of MXene, by elimination of "A" atom from a multi-layered MAX phase because the layer to layer bond is much

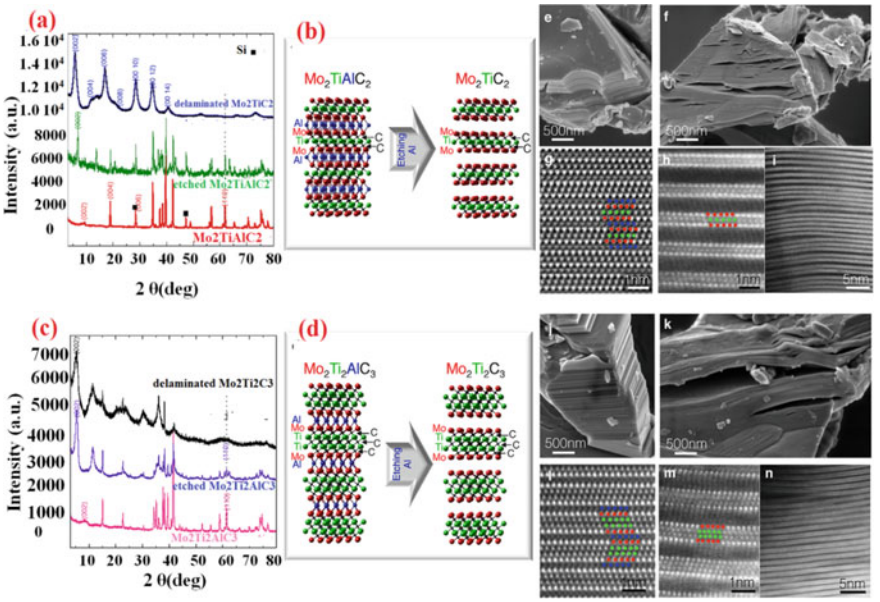

Fig. 8.2 Synthesis and structure of Binary metal MXene phase Mo_2TiC_2 and $Mo_2Ti_2C_3$, **a** XRD plots of Mo_2TiAlC_2 red (before) and green (after) the HF treatment and after delamination(blue), **c** XRD patterns of $Mo_2Ti_2AlC_3$ pink (before) and after (purple) HF treatment and after delamination black, **b** and **d** diagrams of Mo_2TiAlC_2 to $Mo_2TiC_2T_x$and $Mo_2Ti_2AlC_3$ to $Mo_2Ti_2C_3T_x$ transformation respectively, **e**, **f** SEM of Mo_2TiAlC_2 and $Mo_2TiC_2T_x$ and **g** and **h** HRSTEM micrograph of Mo_2TiAlC_2 and $Mo_2TiC_2T_x$, respectively, **i** lowered magnificent of TEM micrograph shows the layered structure through the sample, **j** and **k** SEM micrograph of $Mo_2Ti_2AlC_3$ and $Mo_2Ti_2C_3T_x$ respectively, HRSTEM micrograph of **l** $Mo_2Ti_2AlC_3$ and **m**, **n** $Mo_2Ti_2C_3$ Adapted with permission from [27]. Copyright (2015) American Chemical Society

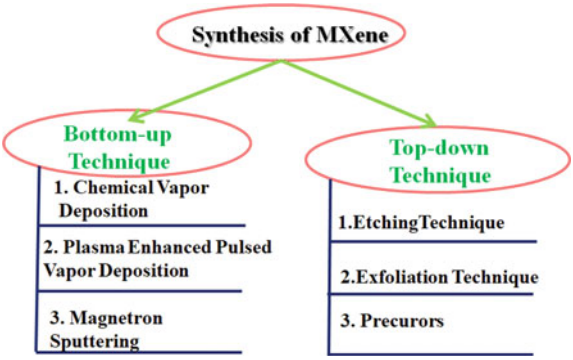

Fig. 8.3 Different techniques used for the synthesis of MXene

weaker as compared to the intra-layer one. Firstly acid soaking in the MAX phase is used to breaking the bonding between transition metals and "A" element as shown in Fig. 8.4. Commonly, acid containing fluoride solutions have been significantly used for the etching technique and it contains the stirring of MXene powder with the acid solution for the suitable time and temperature. When the reaction is completed, the surface terminations are found in the outer layers of metal of MXene because of the acid treatment [20]. These materials have a mixture of both metals and ceramics like ceramics have good strength, stiffness, brittleness and high thermal stability and like metals, they conduct electricity and heat.

The major difference of MXenes is interlayer interaction between M-A band as compared to the other layered compounds. The reaction occurs at room temperature and acid containing aqueous solution of HF is used as etching reagent

$$Ti_3AlC_2 + 3HF = Ti_3C_2 + AlF_3 + 1.5\ H_2(g) \tag{8.1}$$

$$Ti_3C_2 + 2HF = Ti_3C_2F_2 + H_2 \tag{8.2}$$

$$Ti_3C_2 + 2H_2O = Ti_3C_2(OH)_2 + H_2 \tag{8.3}$$

The main issue in using HF is that it is a dangerous solvent, so various other substitute solvents have been used to solve the problem of hazardousness. Ammonium fluoride (NH_4HF_2), HCl/LiF are commonly used for the elimination of Al layers such as

$$Ti_3AlC_2 + NH_4HF_2 = Ti_3C_2 + (NH_4)_3AlF_6 + 3/2\ H_2 \tag{8.4}$$

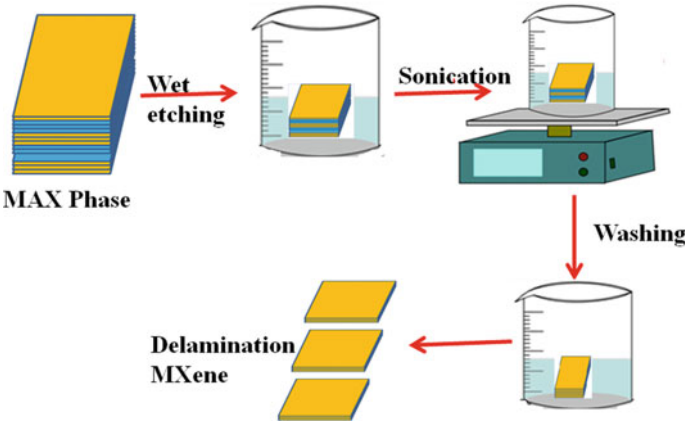

Fig. 8.4 Synthesis of MXene phase using the etching technique

$$Ti_3C_2 + 2HF = Ti_3C_2F_2 + H_2 \tag{8.5}$$

$$Ti_3C_2 + 2H_2O = Ti_3C_2(OH)_2 + H_2 \tag{8.6}$$

Reactions (8.5) and (8.6) exhibit the surface termination with fluorine/hydroxyl group on the layered of the MXene. The layered structure of Ti_3C_2 contains the two atoms of Ti in the unit cell.

8.2.1.2 Exfoliation Technique

During the synthesis of MXene using the chemical etching, multi-layered forms of MXene are obtained, then the ultra-sonication can be used to sonicate these multi-layers of MXene to get the single layer. The shaking or ultra-sonication can be used for the exfoliation of MXene [36, 37]. The dimethyl sulfoxide (DMSO) has been utilized for the exfoliation of Ti_3AlC_2 [38]. Tetrabutlammonium hydroxide (TBAOH) can also be used for the exfoliation of 2D materials, they depends upon the intercalation of TBA^+ ions in the interlayers. The multilayers consist of organic molecules or cations, to insert the suitable molecules to exfoliate the multilayers into single layer.

8.2.1.3 Precursor

The MAX phases have more than 140 family groups having the structure of octahedral MX_6 containing an interlayer of "A" elements. The common difference is the no. of M atoms layers between the A layers such as 211, 312, or 413. The structure of MXene depends upon the parent phases. In 2013 as well as mid-2017, two chemical ordered MXene phases were reported out of plane and designed as o-MAX, 312 and 413 phase and in-planed phases named as i-MAX 211 phase. In the o-MAX phase, the mono/bilayer of M elements is sandwiched between the M layers. Similarly, in the i-MAX phase, two M elements are in plane.

8.2.2 Bottom-Up Technique

The bottom-up technique uses techniques like CVD, pulse laser deposition (PLD), sputtering, and template method. In these techniques, high purity crystalline materials are obtained.

8.2.2.1 Magnetron Sputtering:

Magnetron sputtering has also been used for the synthesis of the MXene materials. Using this technique, the Ti_3AlC_2 MXene film was deposited on the substrates (sapphire) using the C, Al, and Ti targets as shown in Fig. 8.5a–c [39]. Figure 8.5b shows the schematic representation of Ti_3AlC_2 MXene after the removal of the Al element. STEM image of Ti_3AlC_2 MXene film as shown in Fig. 8.5c. For the deposition of TiC layer, a superior adhesion substrate is required. After the deposition, absorption of MXene/sapphire as etching solvent for the fabrication of MXene phase has been observed.

Ion beam sputtering is based on the direct current beam sputtering which were the low energy ions such as inert gas bombarding the target. The sputtered materials are deposited on the substrate. The main benefit of this technique is that the ion source is placed outside of the chamber, so that the development of materials using the sputtering does not affect the presence of ion source. This technique can be used for the fabrication of ultrathin layers with the pre-designed structures. The synthesis

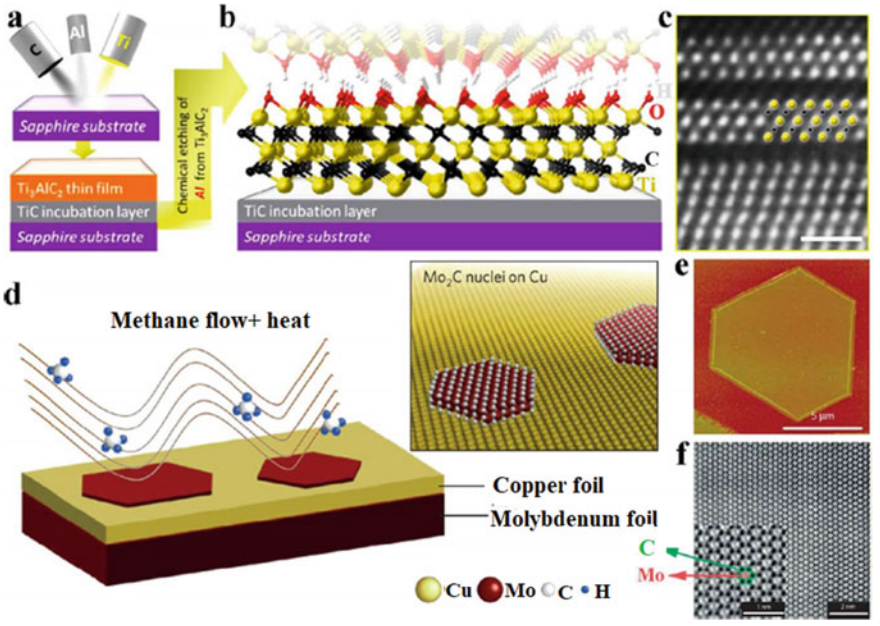

Fig. 8.5 **a** Step used for the synthesis of Ti_3AlC_2 MXene film using sputtering of Ti, Al and C on the sapphire substrate, **b** schematic representation for the preparation of Ti_3AlC_2 MXene film after the removal of Al element, **c** STEM image of Ti_3AlC_2 MXene film obtained from sputtering Adapted with permission from [40]. Copyright (2014) American Chemical Society, **d** schematic representation for the preparation of Mo_2C film on copper substrate, **e** AFM micrograph of Mo_2C film, **f** STEM image of Mo_2C sheet, Adapted with permission from [39]. Copyright (2020) American Chemical Society

of thin materials does not require a large amount of the materials as compared to the bulk materials.

The synthesis of high quality thin films depends upon various aspects such as low substrate contaminations, well control parameters for the deposition, high purity sputtering targets, high quality deposition environment etc. The deposition parameter plays a vital role in the growth and defining the quality of the synthesized film. However, the synthesis of the MAX and MXene-based thin films is quite difficult.

8.2.2.2 Chemical Vapor Deposition

Chemical vapor deposition (CVD) has been used to synthesize the MXene. Ti_3SiC_2 MXene, the first thin film, was synthesized using the CVD [41]. This technique requires a high temperature (1000–1300 °C) for synthesizing Ti_3SiC_2 MXene. The range of temperature was typically higher and purity was another issue faced by CVD. The molybdenum carbide (Mo_2C) MXene phase was synthesized using CVD in the presence of CH_4 and molybdenum [30, 31]. The temperature range of synthesized carbide was 1080 °C in the presence of precursors such as H_2 and CH_4 [31, 42–44]. Geng et al. [45] reported the control morphology of molybdenum carbide (Mo_2C) crystals by changing the concentration of the flow rate of gases. At a low flow rate of CH_4, irregular crystals were obtained; the shapes of the crystals were also transformed from triangular to polygons. Xu et al. [31] reported the synthesis of ultrathin crystals of Mo_2C using CVD with a high temperature as shown in Fig. 8.5d. Due to the high temperature, growth of Mo_2C crystals synthesized using the catalyzed CVD were reported to be orthorhombic crystal structures. The experimental conditions such as processing time and temperature affected the size and thickness of the materials. The atomic force microscopic (AFM) scanning transmission electron microscopy (STEM), bright-field STEM (BFSTEM) and atomic-level-high-angle annular dark field (HAADF) images are shown in Fig. 8.5e, f. The HAADF-STEM pattern exhibits that substantial Mo atoms are strongly packed in the hexagonal structure. The BF-STEM image clearly shows the pressure of heavy atoms such as Mo (red circle) and C (red green) clearly observed in the insert of Fig. 8.5f. The C atom occupies the central position and six Mo atoms adjoining it to form an orthogonal structure with no disorder, defects. Materials fabricated by CVD techniques had fewer defects and had large transparent size, which helped the study of intrinsic properties of the MXene.

However, the CVD approach is not an appropriate technique for the preparation of MXene because they synthesize the thin layers rather than the single layers. Also, CVD technique requires high cost and low yield of MXene which still needs to be optimized for the synthesis of high quality of MXene.

8.2.2.3 Plasma Enhanced Pulsed Laser Deposition

Zhang et al. [46] reported the fabrication of ultrathin film using the CVD and pulse laser deposition technique. The sapphire substrate was heated at 700 °C in the presence of CH_4. The CH_4 was used as a carbon source. MXene synthesized using this approach exhibited low quality of crystalline and quantities of stacking faults were existed in the films.

8.3 Properties of MXene

MXenes have attained significant focus due to their excellent properties such as mechanical, electrical, thermal, magnetic and optical as given in Fig. 8.6. Due to the hydrophilic behavior of the MXene, it exhibits excellent electrical and thermal conductivities.

8.3.1 Mechanical Properties

Mechanical properties of MXene have attracted significant attention due to the presence of strong interaction between MXene carbides (M–C) and MXene nitrides (M–N). According to theoretical calculations, the elastic modulus of MXene is at least two times higher as compared to MAX phases and lowers than the graphene. The mechanical performances of MXene depend upon the surface termination, thickness and chemical compositions. The Young's modulus of the MXene was calculated using the stress strain graph as shown in Fig. 8.7. The stress strain plot with the different strain rates is shown in Fig. 8.7a–c. The value of Young modulus of, Ti_4C_3,

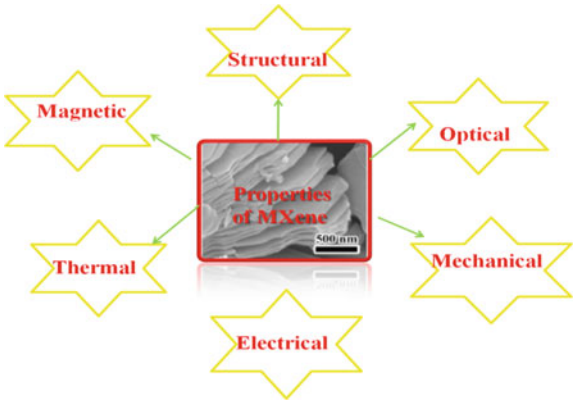

Fig. 8.6 Various properties of MXene

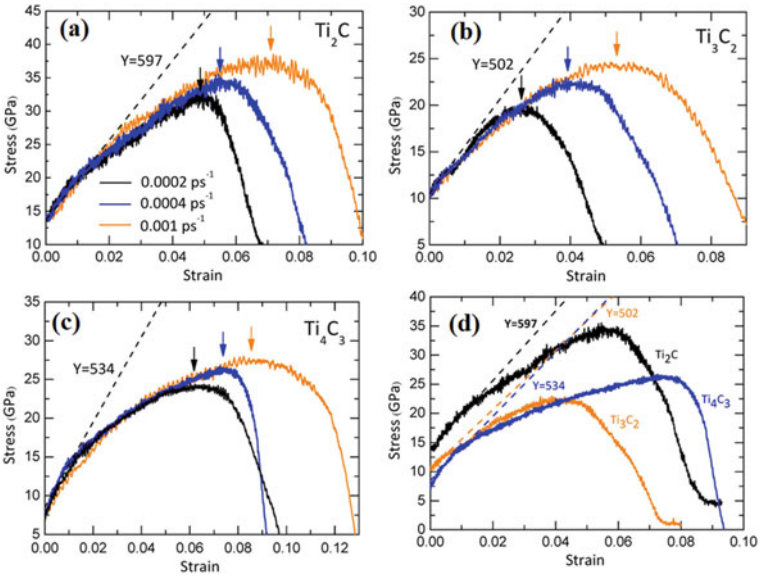

Fig. 8.7 Stress strain graph of MXene at different strain rates **a** Ti_2C, **b** Ti_3C_2, **c** Ti_4C_3 and **d** stress strain plot recorded under the tensile loading. Adapted with permission from [15] Copyright (2022) Sustainable Energy and Fuels, Royal Society of Chemistry

Ti_3C_2 and Ti_2C was observed at 534, 502 and 597 GPa, respectively as shown in Fig. 8.7d.

8.3.2 Thermal Properties

Efficient thermal management materials (TMMs) are the need of the hour for the development of next-generation electronic devices. The critical issues faced by thermal management are reliability, flexibility and the life span of electronic devices. The electronic devices essentially require a focus on heat dissipation. The TMMs not only exhibit a high value of thermal conductivity and dissipation power density but also show flexibility in structure, and are lightweight with mechanical robustness. The thermal expansion coefficient and higher thermal conductivity of MXenes are still unlimited. Theoretical models predict that the $Sc_3(CN)F_2$ and Sc_2CT_2 (T=OH,F) has lower thermal expansion coefficient and higher thermal conductivity as compared to MoS_2 and phosphorene single layer [32, 47]

According to the theoretical model, room temperature thermal conductivity of Zr_2Co_2, Ti_2CO_2 and Sc_2CF_2 MXene was analyzed and found to vary from 23 to 473 W/mK [47, 48]. MXene also exists in two high routes symmetry such as Zigzag and armchair directions. According to the top-view of MXene, the x-axis is parallel to the Zigzag direction and Y-axis overlaps with the armchair as shown in

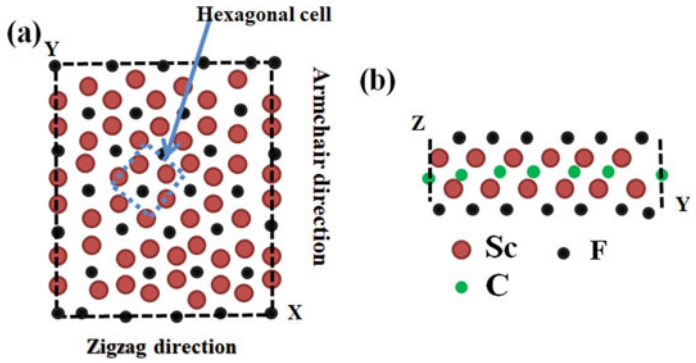

Fig. 8.8 **a** Upper and **b** side view of Sc_2CF_2 MXene

Fig. 8.8. Thermal conductivity of Sc_2CF_2 MXene enhances from 298 to 722 W/mK by increasing the size of flakes from 1 to 50 μm [47]. It concludes that the particle size and thermal conductivity of MXene depend upon the synthesis papermakers and morphology of the MXene. Thermal conductivity of $Ti_3C_2T_x$ was observed experimentally and other types of MXene should also beanalyzed.

8.3.3 Structural Properties

The 2D MXene is attained by the removal of the "A" atom from the MAX phase using etching method. The monolayer of MXene has a hexagonal lattice, equivalent to the graphene flakes. The different functional groups (such as O, OH and F) are attached to the MXene after the exfoliation of the MAX phase. OH and O terminations of MXene was more stable as compared to the F, because the F terminations will be easily substituted by other groups such as OH. Xie et al. [49] reported that at high temperature treatment and metal adsorption processes the OH functional group gets converted to O terminations. Further, O terminated MXene decomposes into pure MXene when they are in contact with other metals such as Mg, Ca, Al, etc. [50]. The attachment of the functional groups depends upon the basic requirement of MXene materials. Generally, MXene is formed with the termination of the different functional groups. Additionally, modeling is an essential requirement which gives the information regarding the complicated structure of the MXene-based materials.

8.3.4 Magnetic Properties

The magnetic behavior of the MXene depends on the spin polarization properties. The magnetic behavior of MXene also strongly depends on the covalent bonding

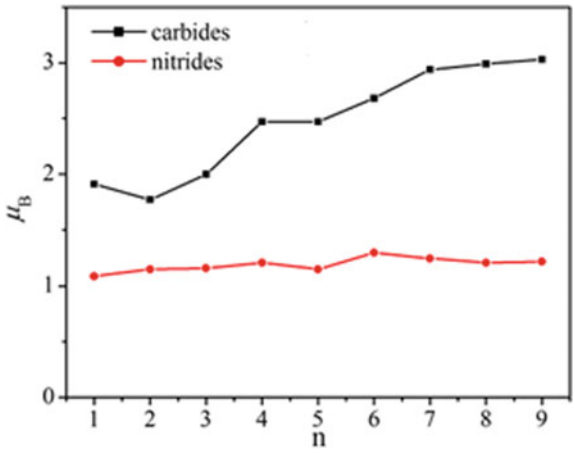

Fig. 8.9 Total magnetic moment of a monolayer of pristine nitride and carbide as a function of layer thickness; Adapted with permission from [51] copyright (2013) American Physical Society

between the TM and X element as well as the attachment of the functional groups. The single layer of the MXene ($M_{n+1}X_n$) is intrinsically magnetic. The magnetic behavior of the MXene is the result of the "d" electrons of the surface. In the Ti, 3d electron on the surface is present and the magnetic moment (μ_B) of the Ti surface and top sites carbon/nitrogen atoms are 0.619 and 0.027 μ_B per atom of Ti_2N and 0.983 and 0.065μ_B per atom of Ti_2C, respectively. The magnetic moments of MXene (nitrides/ carbides) as a function of "n" are shown in Fig. 8.9. Figure 8.9 exhibits the behavior of the carbides and nitrides, the total μ_B of the carbides enhances from 2 to 3 μ_B. On the nitrides, the μ_B varies around 1.2 μ_B [51]. The continuous enhancement of the biaxial strain, the half-metallic ferromagnetic single layer of Ti_2C changes into perfect half metal, semiconductor, and then metal. The nitride (Ti_2N) remains to be half-metallic and the biaxial strain shows a negligible effect [52].

The monolayers of V_2N and V_2C show nonmagnetic and antiferromagnetic behavior respectively. The attachment of the functional group (OH or F) on V_2C converts into an antiferromagnetic semiconductor [53]. Similarly, the Cr_2C is transformed into a semiconductor with functionalization (F, Cl, OH, or H). The magnetic behavior of the double TM carbides MXenes, $Cr_2M''C_2T_2$ (M″=V and Ti, T=O, OH, and F) have been studied. The magnetic behavior of $Cr_2M''C_2T_2$ are depending on the M″ and T. The literature shows that the magnetic behavior of $Cr_2TiC_2O_2$ is metallic, while $Cr_2TiC_2(OH)_2$ and $Cr_2TiC_2F_2$ are antiferromagnetic and $Cr_2VC_2O_2$, $Cr_2VC_2O_2$, $Cr_2VC_2(OH)_2$ are ferromagnetic [54].

8.3.5 Optical Properties

MXene can be considered as an appropriate material for the fabrication of flexible electrodes. The surface terminations on the MXene strongly influence the optical properties. In the visible range spectrum, the oxidized MXene samples exhibit strong

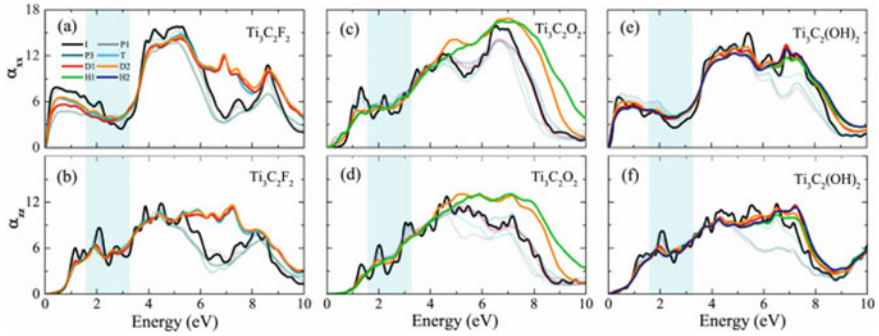

Fig. 8.10 The absorption coefficients in In-Plane (α_{xx}) and normal (α_{zz}) as a function of photon energy, **a** $Ti_3C_2F_2$, **b** $Ti_3C_2O_2$ and $Ti_3C_2(OH)_2$ respectively Adapted with permission from [57]. Copyright (2022) Elsevier

absorption properties, and the surface fluorination experiences weak absorption as compared to pure MXene. In the range of ultraviolet energy, the attachments of functional groups enhance the reflectivity and absorption properties. The thin film of $Ti_3C_2T_X$ (T = mixture of OH, O, and F) has shown 77% of transmittance at visible light. The $Ti_3C_{2.3}O_{1.2}F_{0.7}N_{0.2}$ has more than 90% transmittance, although Ti_3AlC_2 thin film has 30% transmittance. It concludes that the absorbance of $Ti_3C_2T_X$ linearly depends upon the thickness and intercalated films [55, 56].

Figure 8.10 shows the calculated absorption spectrum of MXene-based materials, for convenience the visible region is distinguished from the shaded area. The absorption regions are generally focused in the UV region with the onsets of absorption in the infrared range for these materials. The $Ti_3C_2F_2$ observed three typical absorption peaks. The peak covering 3.5–6.5 eV belongs to the UV region. The coefficient of absorption is also enhanced slightly in the Visible–UV region with photon energy from 2.5 to 3.5 eV. For $Ti_3C_2O_2$, the absorption region covers the visible and UV region. The curves of absorption exhibit anisotropy along with the normal and in-plane directions, in which the adsorption peaks showed at 4.5 and 6.5 eV respectively. The defects present in $Ti_3C_2O_2$ can significantly increase the intensity of light absorption from 4.5 eV, generally for the normal direction. The enhancement of light absorption by defect is mostly concentrated in the infrared and visible regions of $Ti_3C_2(OH)_2$. In the in-plane direction, the intensity of absorption light enhances by more than 25% for all these points.

8.3.6 Electronic Properties

According to the theoretical computations, the optical [58], thermoelectric [59], elastic [60], magnetic [51, 61, 62], electronic [63] and dielectric [64] properties of

MXene have been reported. Few experimental studies have confirmed the theoretical analysis. In this section, we will focus on the electronic properties, which have been reported thoroughly. $Ti_{n+1}X_n$ MXene are metallic in nature. As the value of "n" enhances, metallic behavior reduces, because of the additional Ti-X bond [58]. The attachment of X atom (C and N) plays an important role in the metallic behavior. Titanium nitrides show more metallicity in nature as compared to the titanium carbide, due to the N atom having a higher atomic number (1 more electron) as compared to C atom. On the other side, terminated MXene sheets have thin band gaps and they behave like metal or semiconductors, depending upon the orientation and types of the functional group [65, 66]. Indirect band gap of Zr_2CO_2, Hf_2CO_2, Ti_2CO_2, Sc_2CF_2, and Sc_2CO_2 terminated MXene sheets are also reported, though $Sc_2C(OH)_2$ with lower direct band gap [67]. Therefore, it is necessary to tune the electronic structure to attain the direct band gap, mainly in the field of optics and optoelectronic devices. Lee et al. [68] reported the band gap of Sc_2CO_2 under the effect of applied strain. As strain changes, the value of the interatomic distance within the atoms also changes. The band gap progressively reduces, as the tensile strain is enhanced.

Generally, MXene exhibit outstanding mechanical strength [69, 70], high thermal conductivity [55], and tunable bandgap [29], thus it is significantly used in the field of electromagnetic interference (EMI) shielding [71, 72], environmental protection [73, 74], sensing [75, 76], energy storage and conversion [3, 26] and so on. Similar to other 2D materials, MXene has suffered agglomeration and restacking issues because of van der Waals force of attractions, which limits its practical applications [77, 78].

8.4 Applications

In the next-generation of electronic devices (ED), electric vehicles (EV) and their hybrid EV (EHV) and smart electricity grids, demand outstanding properties in terms of high energy and power to ensure a reliable energy supply. Therefore, high-performance energy storage devices are essential requirements for renewable energy sources. In rechargeable batteries, the materials used in the electrode play a significant role in the electrochemical performance (ECP). Researchers have continuously focused on the design and synthesis of various advanced nanomaterials which improve ECP of the secondary batteries. Various nanomaterials such as 1D, 2D and 3D have been significantly used in the electrode materials. But, the layered two-dimensional (2D) advanced nanomaterials have attained significant research consideration because they exhibit unique optical, mechanical, thermal, and electrical properties, and electrochemical performance [79]. Rechargeable Secondary batteries are significantly used in energy storage applications. High storage capacity, high rate capability, good cyclability, long life, and cheapest are the basic requirements of rechargeable batteries, and they depend upon the properties of the electrode materials. Generally, a graphite based electrode is used as an anode electrode; it has a moderate specific capacity of 372 mAh/g and low rate capability properties.

8.4.1 Lithium-Ion Batteries (LIBs)

The basic mechanism of LIBs depends upon the Li-ion insertion/extraction into or from the electrodes during the charging/discharging processes. LIBs are slow in charging/discharging process (low power device) and have high energy density. The fundamental diffusion dynamics of LIBs in the solid-state electrode materials inevitably restrict the rate of intercalation/deintercalation. Ideal pure 2D MXene flakes cannot be used in practical applications, because of their low capacitance, low capacity and inferior retention properties. So, nanoengineering methods on the pure MXene materials such as surface modification, hybridization, coating, and morphology control techniques are used to enhance the ECP of energy storage applications and resolve the problem of diffusion dynamics challenges. Researchers have continuously explored various advanced materials to replace the graphite material in LIBs [80].

Since the discovery of MXene in 2011, the use of transition metal carbides and nitrides have been quickly expanded. Today, MXene and MXene-based hybrid materials are the growing materials that have been widely explored because they are similar to graphene. Similar to graphene, MXene-based materials have been used for ESCDs. Nowadays, MXene hybrid materials have been significantly used in next-generation EVs and HVs. The basic necessities of EV are high power systems, which can work under high current conditions.

According to the theoretical calculations, MXene is a capable material for energy storage applications [81, 82]. MXene-based materials are continuously used as renewable energy resources for practical applications. In recent years, Ti_3C_2 has received significant focus for its outstanding hydrophobicity and conductivity. Due to its low capacity, its practical application is restricted. So, researchers are continuously exploring hybrid materials. MXene hybrid materials have been significantly used in electrode materials for rechargeable batteries [83, 84]. Several researchers have reported improving the ECP using surface modification, lamination and intercalation [85–87]. Zhang et al. [88] studied the intercalation of Ti_3C_2 MXene with Cu_2O and slightly improved its specific capacity. Xie et al. [89] reported that intercalating of CNTs/Ti_3C_2 has significantly enhanced the electrical conductivity. Yin et al. [90] reported the synthesis of $Ti_3C_2F_X$ MXene using electrochemical etching. The electrochemical exfoliation approach was used to synthesize MXene which controls its fluorination degree. Figure 8.11 shows the SEM image of pure Ti_3AlC_2 and $Ti_3C_2F_X$ MXene. The contact layered structure of Ti_3AlC_2 MXene is shown in Fig. 8.11a. Al layer of Ti_3AlC_2 was slowly etched at low potential (3 V vs. Ag wire) and the accordion-like structure is shown in Fig. 8.11b. As the potential was increased to 5 V, the Al layer was etched sufficiently and nanosheets were formed as shown in Fig. 8.11c. Figure 8.11d exhibits that increasing potential to 7 V, the amorphous behavior was observed. $Ti_3C_2F_X$ MXene exhibited improved electrochemical properties as cycling stability. The initial discharge capacity at 329 mAh/g was 0.2 A/g and sustained at 210 mAh/g after 500 cycles.

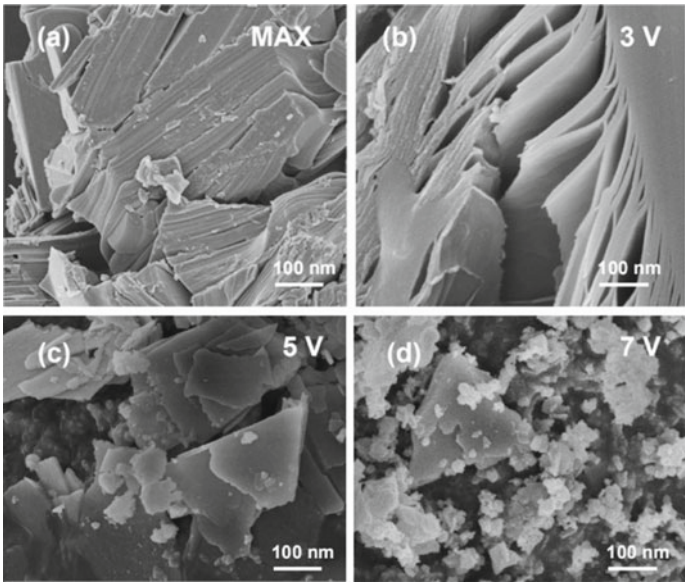

Fig. 8.11 SEM images of **a** Pure Ti_3AlC_2, and electrochemical etched $Ti_3C_2F_X$ at different potential of **b** 3 V, **c** 5 V and **d** 7 V versus Ag wire; Adapted with permission from [90]. Copyright (2021) Elsevier

Zheng et al. [91] studied the 3D sandwich structure of MoS_2 intercalated partially oxidized Ti_3C_2 (p–Ti_3C_2) was synthesized using the etching technique and consequent hydrothermal treatment to avoid the limitation of Ti_3C_2. MoS_2 behaves as the intercalation agent to reduce the restacking issue of p-Ti_3C_2 and assist the fast transportation of ions and electrons between the MXene layers. The electrochemical properties of MoS_2/p-Ti_3C_2 composites were also analyzed with different content of MoS_2 (10, 20, 30 and 40 wt.% was designed as T10, T20, T30 and T40). The charging/discharging performance of different wt.% of MoS_2 was analyzed between 0.00001 and 3Vat 50 mA/g. At 50 mA/g, initial discharge capacities of T10, T20, T30 and T40 were 434, 656, 604 and 605 mAh/g, respectively. Figure 8.12a exhibits the cycling stability of different wt.% of MoS_2 on Ti_3C_2 and Coulombic efficiency (CE) of the T20 sample. The specific capacity was increased by increasing the wt.% of MoS_2. Among all the samples, T20 shows the highest discharging capacity and best cycling stability. At the higher wt.% such as T30 and T40 showed that as increases the number of cycles, discharge capacity declined. Figure 8.12b shows the discharging capacity of the MoS_2/Ti_3C_2 electrode which was much higher as compared to Ti_3C_2. In the low current density, T30 and T40 composites exhibited a higher discharge capacity as compared to others. The increased number of cycles enhances current density and reduces the discharging capacity remarkably. A T20 sample delivers a higher specific capacity as compared to others at a high current density. The reversible capacity of 487.9 mAh/g was attained at 50 mA/g, which was 2 times higher as compared to p-Ti_3C_2. Ali et al. [92] studied the ECP of iron oxide/MXene anode

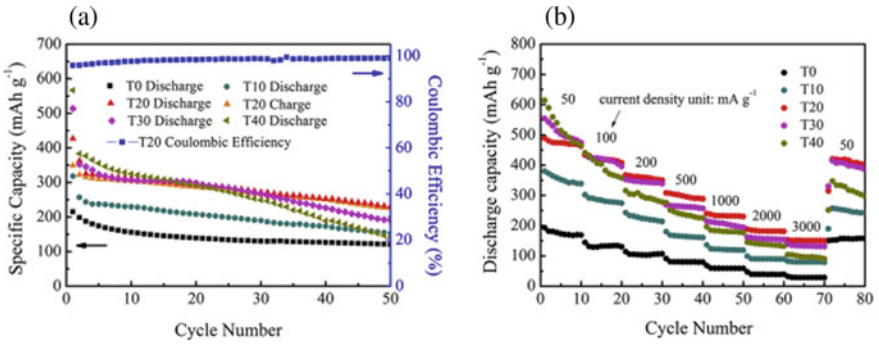

Fig. 8.12 **a** Cycling performance of all samples at 0.5 A/g with CE of T20 electrode, **b** discharging performance at various current densities; Adapted with permission from [91]. Copyright (2018) Elsevier

material for LIBs. The iron oxide/MXene hybrid material was fabricated by different concentrations of iron oxide nanoparticles into MXene using a facile and scalable dry-milling method. Composites of 25 and 50 wt.% of iron oxide/MXene synthesized using the ball milling resulted in proper dispersion of iron oxide nanoparticles and reported the ECP. The composite containing 50wt.% iron oxide/MXene shows a higher reversible capacity of 271 mAh/g at 1C and 100 mAh/g rate performance at 10C.

8.4.2 Supercapacitors (SCs)

Developments in electronic devices have significantly promoted the new flexible energy storage devices (ESD). SCs have drawn significant consideration because of their high power density, eco-friendly nature, unlimited cycle life, low charging ability, and compelling cycling performance [93, 94]. SCs are also another family of the energy storage device, which can accumulate and distribute energy at a faster rate. SCs have rapid charging/discharging, high power density, long cycle life, etc. According to the mechanism of energy storage, SCs are divided into pseudocapacitors and electrochemical-double layer capacitors (EDLCs) [95]. EDLCs can store charges by reversible electron charge transfer properties at the interface of electrode/electrolyte. In non-faradic (NF) reactions, EDLCs have long cycle life and low energy densities. The pseudocapacitors contain the fast reversible Faradic response at the surface of electrode materials, but they can have low rate capability, short cycle life and higher energy densities. The mechanism of hybrid SCs (HSCs) is based upon the different mechanisms in which non-faradic charging-discharging occurs on capacitive carbon electrodes combined with the surface redox reaction at the negative electrode [96]. The combined merits of both pseudocapacitors and EDLCs possess

high energy density with cycling stability. Electrodes and electrolytes have played an essential part in the design of supercapacitors.

Flexible electrode materials for the SCs are of significant interest due to their high flexibility, lightweight, high power density, and ease of handling [97, 98]. Free-standing films/paper can be used as electrode materials without the addition of an insulating binder and conducting fillers that provide high volumetric and gravimetric performances. Various nanomaterials such as graphene, CNTs, graphene-carbon nanotube (GCNTs), carbon black and hollow structured metal oxides/sulfides and MXene [99, 100] are widely used in electrode materials [65, 101]. The max. specific capacitance of 481 F/g at 0.005 V/s was recorded at 0.1 M sulphuric acid electrolytes with a high cyclic retention rate of 89% [102]. The MXene has also suffered from restacking issues similar to graphene, which restricts its electrochemical properties. The addition of various nanoparticles coated/doped within MXene is done to form MXene hybrid composites.

The 2D MXene possesses a high surface to volume ratio, hydrophilic surface, high electrical conductivity, structural variety etc. Free-standing MXene film has been significantly used as electrode material in SCs due to their large volumetric capacitances as compared to carbon based nanofillers [103, 104]. $Ti_3C_2T_x$ film exhibited a specific surface area (SSA) of 98 m^2/g and carried a volumetric capacitance of 340 F/cm^3 as compared to carbon based electrodes of 300 F/cm^3 [104]. Wang et al. [105] studied the synthesis of nickel cobalt oxide-metal–organic frame work (NiCo-MOF = NCM) on nickel foam using the hydrothermal technique. The Ni-Co@NiCo-MOF/NF (M-NC@NCM/NF) nanosheets were synthesized using electrodeposition. The specific capacity of the Co@NiCo-MOF/NF nanosheet reached 2138 F/g at 1A/g and the specific capacity was retained at 75%. Chen et al. [106] reported the synthesis of NiCoFe-layer double hydroxide/Ti_3C_2 composites using nano-dimension coating of NiCoFe-layer double hydroxide(LDH) on Ti_3C_2 MXene via the surface functional group. Figure 8.13a exhibits the XPS spectrum showing the presence of Ni, Co, Fe, C, Ti and F elements. Figure 8.13b shows the deconvolution spectrum of 1S carbon of Ti_3C_2 and NiCoFe-LDH/Ti_3C_2 composites. The peaks of Ti_3C_2 MXene at 286.1, 284.8 and 282.8 eV are ascribed to O-C=O, C=C, and C-Ti-Tx peaks respectively. In NiCoFe-LDH/Ti_3C_2 hybrid, C-Ti-Tx peaks are changed to C- at 281.5 eV. Figure 8.13c shows the XRD pattern of NiCoFe-LDH, Ti_3C_2 MXene and NiCoFe-LDH/MXene composites. The diffraction peaks at 2 θ values of 8.9°, 18.2° and 44° represent the (002), (004) and (200) crystal planes of Ti_3C_2 MXene. The diffraction peaks at 2 θ values of 11.7°, 26.7°, 34.5°, 39.1°, 46.6°, 59.8° and 61.1° signifies the (006), (012), (015), (018), (110) and (113) planes of NiCoFe-LDH verified that the successful synthesis of NiCoFe-LDH/MXene.

NiCoFe-LDH/Ti_3C_2 composite shows an excellent specific capacity of 1990 F/g at 1A/g in 1 M KOH and maintained the specific capacity of 85% after 500 cycles of charge/discharge at 10 A/g. Li et al. [107] reported the fabrication of graphene/MXene film by vacuum-filtration. The graphene/MXene hybrid electrodes were accumulated into flexible solid-state SCs, which presented a volumetric capacitance of 217 F/cm^3. Zhu et al. [108] reported the fabrication of foam MXene using two different techniques such as: a facile hard and a pore-forming approach. The

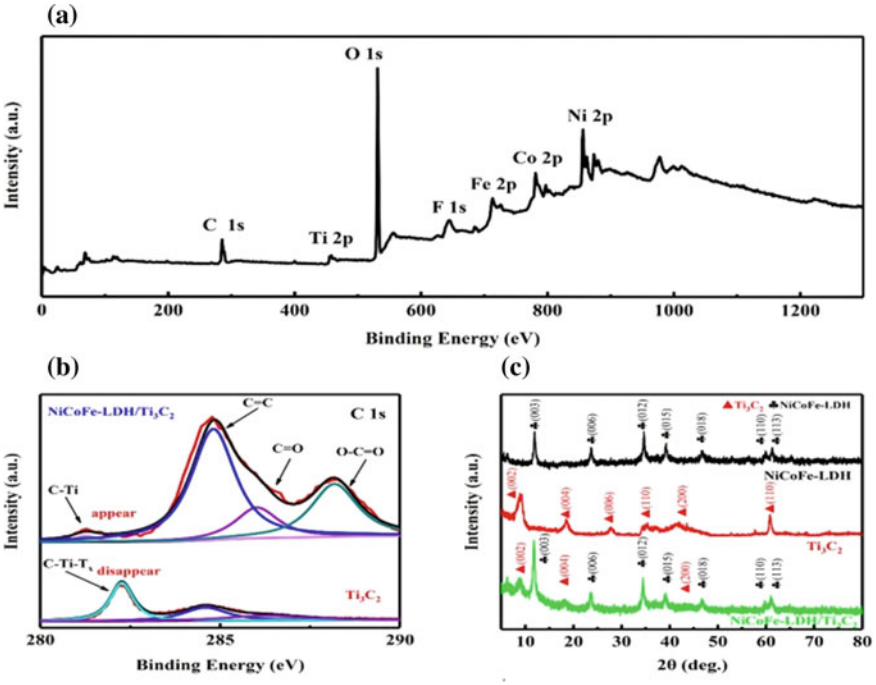

Fig. 8.13 **a** XPS spectrum of NiCoFe-LDH/Ti_3C_2 composite, **b** deconvolution and **c** XRD spectrum of Ti_3C_2 MXene, NiCoFe-LDH and NiCoFe-LDH/Ti_3C_2 composite; Adapted with permission from [106], Copyright (2021) Elsevier

sheets of MXenes were expanded using the MgO nanoparticles using hard templates showing the wrinkled flakes with open morphology. The expanded MXene used as electrode materials delivered the capacitance of 180 F/g at 1A/g. On other hand, MXene foam synthesized after the urea-MXene composites at 600 °C, displayed the various pores on the layers as shown in Fig. 8.14.

CV plots of all MXene-based composite electrodes displayed the rectangular shape plot at 5 mV/s as shown in Fig. 8.15a, and determined the pseudocapacitive behavior. Figure 8.15b shows CV plots of the MXene foam electrodes at various scan rates. Figure 8.15c shows the specific capacitance of pure MXene-based electrodes at 48 F/g at 20 A/g, expanded MXene electrodes at 70 F/g and MXene foam electrodes at 125 F/g. The cyclic stability of all electrodes was tested for 5000 cycles using galvanostatic charging/discharging at the current density of 5 A/g. At a higher scan rate, only slight distortions are observed. The foamy porous structure of MXene showed the capacitance of 203F/g at 5A/g and maintained 99% after the 5000 cycle as shown in Fig. 8.15d. Wang et al. [109] studied the ECP of self-discharging behavior of $Ti_3C_2T_X$ based SCs. They reported the self-discharge behavior of tightly bonded and loosely bonded ions corresponding to the individual self-discharge behavior.

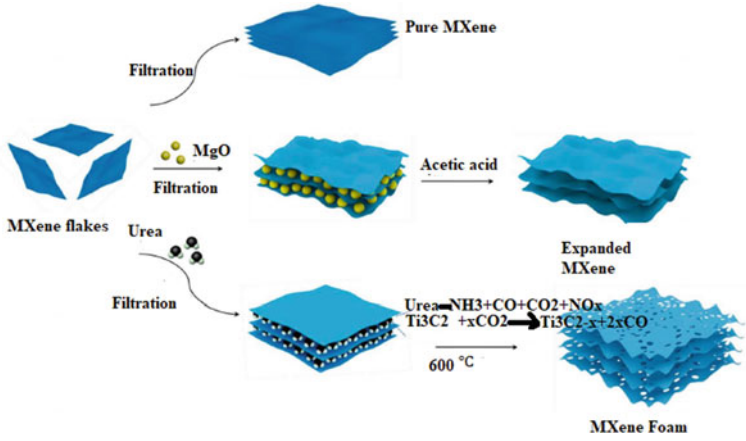

Fig. 8.14 Schematic representation for the synthesis of MXene foam, Adapted with permission from [108]. Copyright (2020) Elsevier

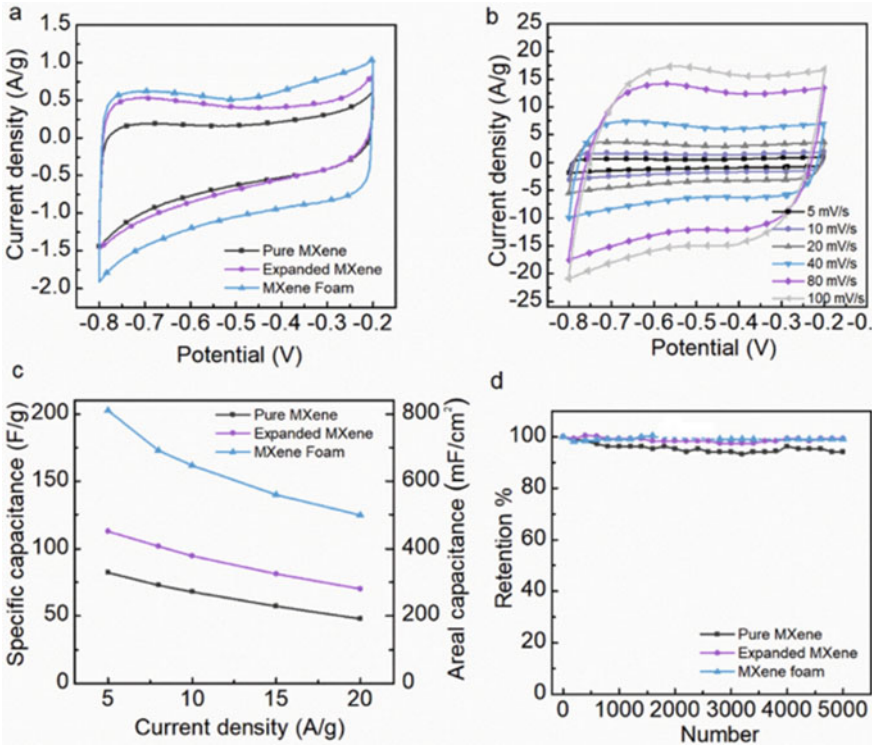

Fig. 8.15 ECP of binder free three electrodes **a** CV plot of all three electrodes at 5 mV/s scan rate, **b** CV graph of MXene foam at different scan rates, **c** relationship between the specific capacitance of all three electrodes at different current densities, **d** comparison of retention of all three electrodes at 5A/g over 5000 cycles; Adapted with permission from [108]. Copyright (2020) Elsevier

Figure 8.16a exhibits the schematic representation of the relationship between the self-discharging behavior and the mechanism of surface chemistry of $Ti_3C_2T_X$ MXene. They show that the direct interface between the electrode and ions surface indicates the tight-bond atoms. The bottom part of the image shows the loose bonding model, as the distance between the ions and electrode increases, the surface results in a weak attractive force between them. Figure 8.16b shows that two different models indicate the mixed charge behavior. It clearly shows that both loose and tightly packed bonded ions diffused out of the surface of electrode and fitted by a mixed potential model as given:

$$V \propto V_1 \times e^{-t/\tau 1} + V_1 \times e^{-t/\tau 2} \tag{8.7}$$

Here V1 represents the SC potential during self-discharge, V_1 and V_2 indicate the initial potential of the self-discharge process, $\tau 1 and \tau 2$ represents the time constant of discharging process, and t is the time. When the loose bonding ion diffuses out of the electrode, the individual potential of the self-discharge model is

$$V \propto V_1 \times e^{-t/\tau 1} \tag{8.8}$$

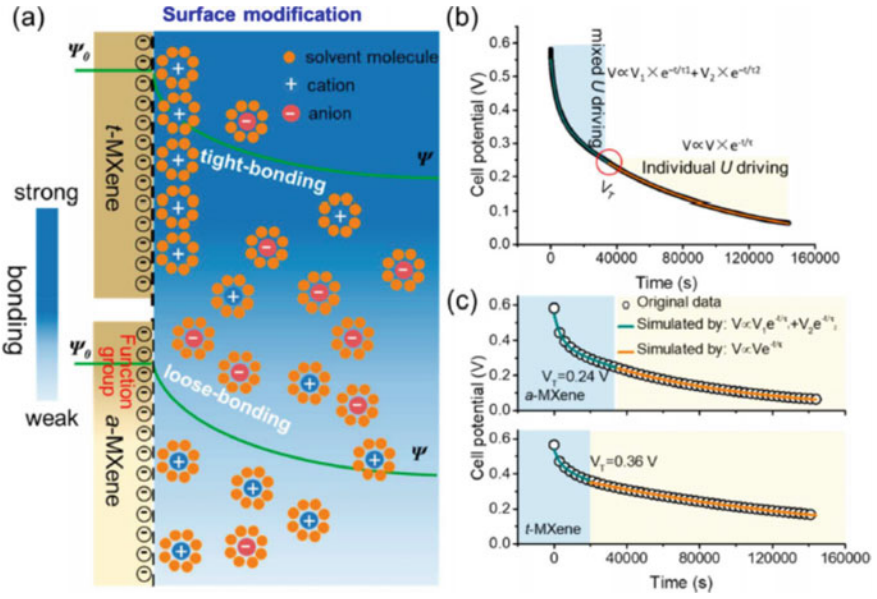

Fig. 8.16 Self-discharging effect of $Ti_3C_2T_X$ MXene **a** theoretical model of different tightly-bonding atoms, **b** mixed self–discharging mechanism of different bonding, **c** schematic of a tunable self-discharging by regulating surface chemistry; Adapted with permission from [109]. Copyright (2020) Applied Chemical Society

Figure 8.16c shows that $Ti_3C_2T_X$ t-MXene, eliminating the Fluorine (F)-rich elements (65% atoms) shared a positive apparent decline of 20% self-discharge rate in comparison to high F-containing atoms. Yan et al. [110] studied the preparation of MXene/graphene film using the electrostatic self-assembly technique. In this case, rGO nanosheets were inserted within the MXene layers to avoid the restacking issue. The volumetric capacitance of the MXene/rGO film electrode was 1040 F/cm^3 at 2 mV/s, with capacitance retention of 61% at 1 V/s. The symmetric SCs show an ultrahigh volumetric energy density of 32.6 Wh/L and power density of up to 75 kW/L, which was much higher as compared to MXene and carbon based materials in aqueous electrolytes. Huang et al. [111] studied the fabrication of MXene-based microsupercapacitors which promoted the development of portable devices. The synthesized microsupercapacitors provided a volumetric capacitance of 351 F/cm^3 at 1.2 V, representing a breakthrough volumetric energy density of 76 mWh/cm^3

8.4.3 Electromagnetic Interference Shielding

With the increasing demand of electronic devices, electromagnetic pollution has become a serious issue, which harmfully affects the performance of electronic instruments. These electromagnetic radiations are also hazardous to living beings and the surrounding environment. To avoid this problem, electromagnetic interference (EMI) shielding materials are used to solve this problem. From the past few decades, the development of smart electronic devices, nuclear reactors, aerospace and aircraft materials require lightweight, thin film EMI shielding materials [112, 113]. Conventional shielding materials like metals have suffered the problems of heaviness, bulkiness and easy to corrosion [114]. So, material science and engineering require various advanced nanomaterials for the development of new EMI shielding materials [115, 116].

Various materials such as CNT, graphene, MXene, etc. have attracted more effective materials for EMI shielding because of their low density, lightweight, high conductivity and corrosion resistance. Incorporating these fillers within polymer has been used as the feasible material for EMI shielding. MXene-based materials show excellent capability for EMI shielding. Li et al. [117] reported the preparation of novel $Ti_3C_2T_x$ MXene for high-performance EMI shielding. The EMIs shielding of $Ti_3C_2T_x$ MXene reached 70 dB in X-band at 0.8 mm. Shahzad et al.[118] reported the fabrication of $Ti_3C_2T_x$ film and $Ti_3C_2T_x$-sodium alginate (SA) film using vacuum-filtration and provided higher EMI shielding of 92 dB. Sun et al. [119] reported the fabrication of $Ti_3C_2T_x$/polystyrene composites through excellent EMI shielding of 54 dB in X-band. Li et al. [120] reported the synthesis of rGO/ $Ti_3C_2T_x$ foam with hollow core–shell architectures, showing the high value of specific electromagnetic absorption of 14,300 dB cm^2/g. Zhou et al. [121] reported the fabrication of ultrathin $Ti_3C_2T_x$ MXene/calcium alginate ($Ti_3C_2T_x$/CA) aerogel film used for EMI. The $Ti_3C_2T_x$/CA film exhibited an EMI value of 54.3 dB at a sample thickness of 26 μm. Lei et al. [122] reported the fabrication of Aramid nanofiber/$Ti_3C_2T_x$ MXene (ANF/

$Ti_3C_2T_x$) using brick and motar architecture. The ANF/ $Ti_3C_2T_x$ composites film showed the specific EMI shielding effectiveness of 8814.5 dB cm^2/g. Liu et al. [71] reported the preparation of MXene foam using the hydrazine-induced foaming technique. The MXene foam exhibited outstanding wear resistance, durability and 70 dB EMI shielding effectiveness. Ganguly et al. [123] reported the fabrication of carbon dot generated polynorepinephrine (PNE) coated MXene and Fe_3O_4 hybrid using the vacuum-assisted filtration (VAF) technique. The free-standing cellulose-based composite membrane (CM) was fabricated using the VAF approach. The different concentrations of the magnetic nanoparticles coated on the CM were also analyzed. Figure 8.17a–c shows the SEM image of uncoated CM exhibiting the entangled architecture without coated nanoparticles. Figure 8.17d–j exhibits the coating of nanoparticles on the CMs and showed that the compact morphology has increased the concentration of particle coated on CMs as compared to an uncoated surface. The cross-sectional image was used to determine the thickness of coated materials using the focused-ion beam (FIB) technique as shown in Fig. 8.17h, i. Figure 8.17j shows that the average thickness was 9.8 μm. Figure 8.17k shows that the average value of coated thickness lies between the range of 9–11.5 μm.

The image of the PNE-MXene/ Iron Oxide Nanohybrid (PMIO)-based membrane coated region is shown in Fig. 8.18a. Figure 8.18b shows the EMI shielding values

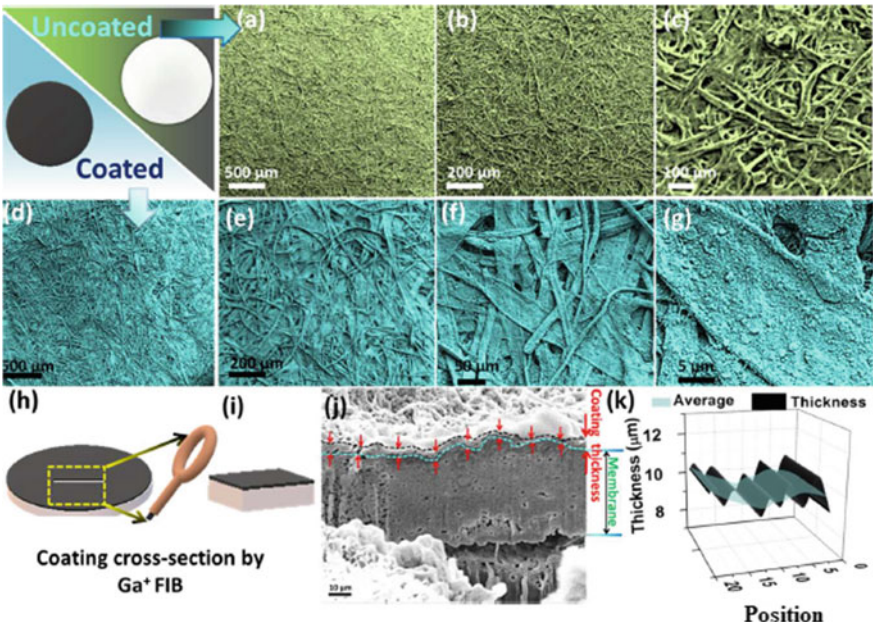

Fig. 8.17 SEM images of **a–c** uncoated FP and **d–g** coated CM of nanoparticles coated on woven fiber, **h** image of coated CM with the cross-section of Ga+ ion FIB, **i** cross-section image, **j** FIB-SEM cross-section image CM coated the thickness, **k** average thickness of coated CM nanoparticles; Adapted with permission from [123], Copyright(2020) American Chemical Society

increases with increase in concentration of nanoparticles deposited on CM. The EMI shielding value was increased from 8.5 dB (CM1) to 40 dB (CM4) by increasing the coating concentrations. The EMI shielding value was reported 40 times higher as compared to uncoated FP, due to the development of a 3D network inside the coated layer. Figure 8.18c exhibits the EM shielding of all CM and clearly shows that the SE_A values of all CM composites are comparatively higher as compared to SE_R and both values of SE_R and SE_A were increased with the coated mass. The toughness of the materials was also analyzed in their shielding effectiveness in dry and wet chemical conditions. Figure 8.18d shows that bending affects the SE values for CM4. Figure 8.18e shows the durability test of CM material under the static and water flowing test. The CM absorbed for 30 min showed no deterioration in SE values. Sun et al. [124] reported the fabrication of MXene-xanthan films for EMI shielding. The MXene-xanthan nanocomposites show shielding effectiveness of SSE/t = 24,465 and 14,491 dB cm^2/g.

Nguyen et al. [125] reported the $Ti_3C_2T_x$/graphene/PDMS composites for the EMI shielding. Fe_3O_4 nanoparticle deposited on the graphene particle- intercalated in the $Ti_3C_2T_x$ MXene sheets. The hybrid composite shows the EMI SE of 81 dB in X-band (8.2–12.4 GHz) and 77 dB in Ka-band (26.5–40 GHz). Lu et al. [126] reported the synthesis of a self-healable assembly of waterborne PU/ $Ti_3C_2T_x$ (ADWPU-T) composites for the stirring technique. The self-assembly between ADWPU and $Ti_3C_2T_x$ MXene exhibited EMI shielding of 52 dB.

8.4.4 Sensors

Recently, sensors have attained significant attention in our daily life due to the fast progress of electronic and information technology. Sensors are devices that detect/respond to some type of input from the physical phenomenon. There exist different types of sensors such as gas sensors, strain sensors, pressure sensors, photodetectors, humidity sensors, biosensors, etc. as shown in Fig. 8.19.

Various nanomaterials have been synthesized and used for sensing purposes. But, 2D layered materials have been significantly used because of their large surface area, excellent flexibility, tunable electronic structure and outstanding mechanical properties.

8.4.4.1 Strain Sensors

Strain sensors have been extensively used in numerous applications such as health care, artificial eardrum, electronic skin, robotics, motion monitoring, etc. [128, 129]. Due to the outstanding properties of MXene, it has been significantly used in strain/stress sensors. Yang et al. [130] reported the tensile strain sensor properties of $Ti_3C_2T_x$ nanosheets and nanoparticles. The change in resistance was due to the movement of nanoparticles and the bridging-network of $Ti_3C_2T_x$ nanosheets.

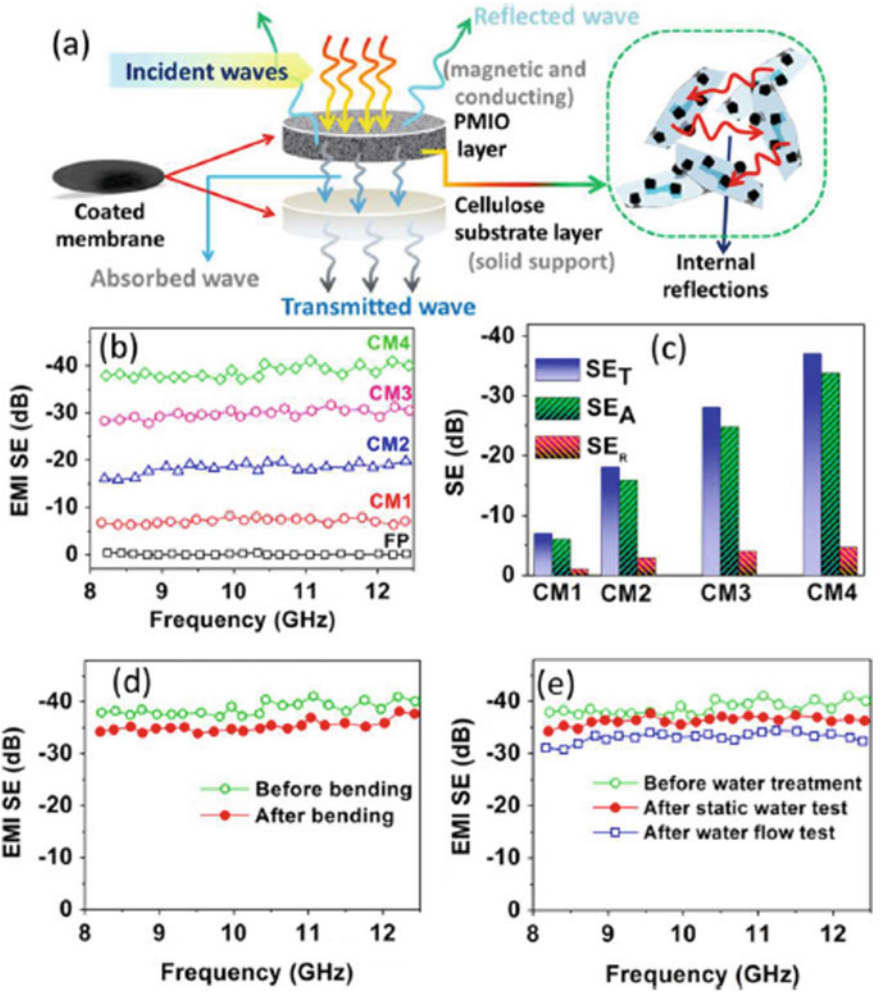

Fig. 8.18 Schematic diagram for preparation of PMIO coated CMs materials and mechanism of shielding, **b** EMI shielding value composite materials, **c** comparison value of SE_T, SE_A and SE_R for the CMs, **d** EMI SE values of CM bending and **e** durability analysis of CMs before and after water flow test; Adapted with permission from [123], Copyright (2020) American Chemical Society

The fabricated sensors showed that the gauge factor was greater than 179, sensing range lies between 0 nad 54%, and the limit of detection was observed at 0.025% with stable response under the 20% strain without degradation over 5000 cycles. Cai et al. [131] reported the tensile strain sensor of $Ti_3C_2T_x$/CNTs hybrid materials. The fabricated sensors showed the gauge factor of 773 and sensing range between 30 and 131% and detection limit of 0.1% and good consistency and stability over 5000 cycles. Zhang et al. [132] reported the self-healable and highly stretchable MXene/PVA hydrogel based wearable sensors. Hydrogels consist of

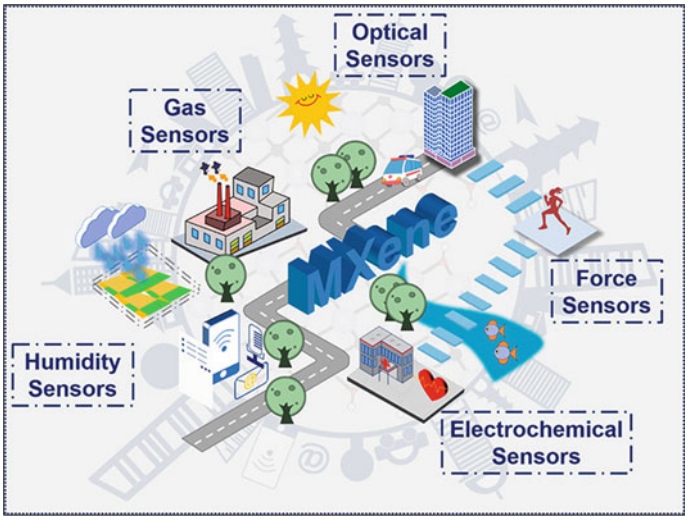

Fig. 8.19 MXene-based materials used in various types of sensor Adapted with permission from [127] copyright (2021) from American Chemical Society

3D network structures with an excess concentration of water/ionic liquid that has been proposed for electrodes for soft electronics. Figure 8.20a shows the diagram illustration for the fabrication of MXene/PVA hydrogel. Figure 8.20b shows the photograph of the cut piece of MXene/PVA hydrogel. Figure 8.20c exhibits that when the two cut pieces were joined together, self-healing instantaneously appeared in Fig. 8.20d and also retained the high stretch-ability up to 1200% as shown in Fig. 8.20e. Figure 8.20f exhibits the diagram illustration for the hydrogel electrode compressed with VHB tape. Figure 8.20g shows the stretching/releasing performance of the MXene/PVA hydrogel electrode under the different applied strains. Although the stretching/releasing process, the MXene/PVA hydrogel electrode showed the hysteresis curve at all applied strains. The change in the relative resistance in the favor of applied strain was up to 200%. The relative change resistance of 200% strain was 1 for PVA/MXene which was smaller as compared to PVAhydrogel. CNTs/PVA hydrogel based strain sensors enhanced the sensitivity. Figure 8.20h shows that the change in resistance of CNTs/PVA hydrogel at 200% was 2.4, which was more than two times higher as compared to MXene/PVA hydrogel. Therefore, they concluded that PVA/MXene hydrogel could be an excellent choice as compared to MXene/PVA for strain sensors.

8.4.4.2 Gas Sensors

The detection and concentrations of gases such as CO_2, NO_2, CO, NO, NH_3, SOx and H_2S are important requirements to measure air quality. Monitoring and identification

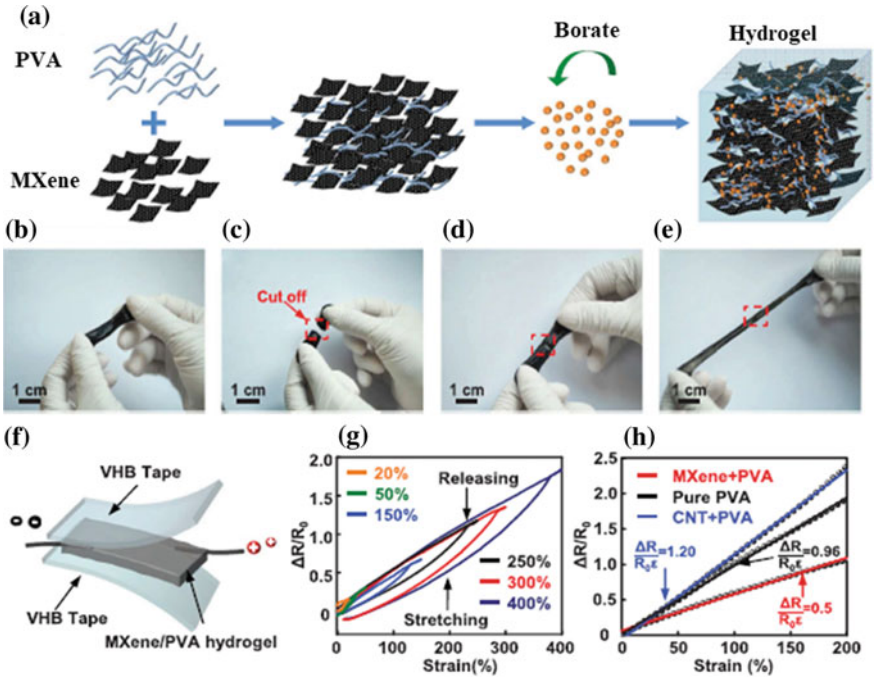

Fig. 8.20 Schematic illustration for the preparation of PVA/MXene hydrogel, **b–e** photograph of self-healing and stretch-ability of PVA/MXene hydrogel, **f** PVA/MXene electrode for analyzing the performance of strain sensor, **g** change in the resistance response of PVA/MXene electrode at different strains, **h** relative resistance change-strain plots of PVA, PVA/CNTs, PVA/MXene hydrogel electrodes Adapted with permission from [132]. Copyright (2019) Wiley

of the exhaust, toxic and flammable gases are vital for energy saving and protection of the environment [133]. Researchers are continuously putting efforts to improve sensitivity and selectivity. Various nanomaterials have been explored to enhance the gas sensing properties. The small, low power consumption, cheaper and reliable gas sensors are a significant requirement in various applications. With increasing demand for improved gas sensors, the higher sensitivity and selectivity of various materials are used to analyze and fabricate suitable materials for gas sensing properties. 2D materials have attracted significant attention in gas sensing applications due to their controlled surface chemistry, large surface area and capability of sensing selection at room temperature. Among the various 2D materials, MXene-based hybrid materials have gained significant consideration in gas sensor applications. MXene-based materials have outstanding physical and chemical properties. Lee et al. [134] reported the synthesis of $Ti_3C_2T_x$ and were combined on flexible polyimide platforms for gas sensing applications. $Ti_3C_2T_x$ MXene sensors successfully measured methanol, ethanol, ammonia gas and acetone at room temperature. The $Ti_3C_2T_x$ based sensors showed a high sensing response for ammonia because of its large energy absorption.

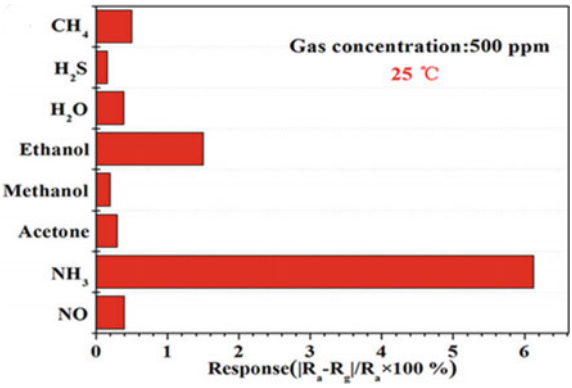

Fig. 8.21 $Ti_3C_2T_x$ MXene-based gas sensors response toward 500 rpm for H_2S, NH_3, NO, CH_4, methanol, ethanol and acetone at room temperature (25 °C) Adapted with permission from [136]. Copyright (2019) American Chemical Society

Kim et al. [135] reported the $Ti_3C_2T_x$ MXene-based gas sensors. $Ti_3C_2T_x$ MXene-based gas sensors showed a very small limit of detection of 49–100 ppb for volatile organic compounds gases at normal temperature. Wu et al. [136] reported the preparation of 2D $Ti_3C_2T_x$ MXene for gas sensing applications. The colloidal suspension of $Ti_3C_2T_x$ MXene was deposited on the surface of ceramic tubes to develop the gas sensors. At room temperature, this gas sensor was used to detect the many gases such as (H_2S, NH_3, CH_4, NO, methanol, acetone and ethanol) with a concentration of 500 ppm. $Ti_3C_2T_x$ based gas sensors have high choice for NH_3 as associated to other gases as shown in Fig. 8.21.

8.4.5 Other Sensors

8.4.5.1 Optical Sensors

MXene has a tuneable electronic structure depending upon the attachment of different surface functional groups and the number of layers shows interesting non-linear optical properties. $Ti_3C_2T_x$ MXene MX has an extensive optical absorption region from visible to infrared with high photothermal properties [137].

Electrochemical sensors are significantly used in various practical applications because of their excellent repeatability, low cost, linear output and good selectivity. Commonly, the interaction between analyser and sensing materials is critically essential to analyse the sensing performance. MXene-based materials have a large surface area, biocompatibility, good mechanical properties, good conductivity etc., allowing effective and selective interaction with target species [130, 138]. MXene hybrid materials have been significantly used as redox transducers and electrocatalysts for sensing environmental pollutants, minor molecules, biomarkers and pharmaceutical drugs.

8.4.5.2 Humidity Sensors (HS)

It is a device used to sense the humidity and commonly expressed as relative humidity. HS has been commonly used in industry, meteorology, automation, agriculture, medical health, aerospace, food storage and smart homes [139]. Researchers are putting continuous efforts in improving the performance of HS such as response value, response speed, and sensitivity of sensors. Some HS shows very quick time response (in ms) and large response values (10^6) [140–143]. The main challenge is the development of a low detection limit, high detection resolution and wide detection range of HS. The detection range of most HS lies within 10–90% relative humidity, HS shows no response for a low value of RH such as less than 5%. Several nanomaterials have been used for HS, among MXene because of their outstanding properties. Muckley et al. [144] studied $Ti_3C_2T_x$ MXene film for HS. $Ti_3C_2T_x$ MXene film showed a reproducible reversible response in the 0.1–95% RH range in a detection limit of less than 20 m Torr H_2O. Li et al. [145] reported the fabrication of high-performance HS based on $Ti_3C_2T_x$ MXene–derived TiO_2 nanowire composites. $Ti_3C_2T_x/TiO_2$ nanowire composites exhibited high sensitivity in a 7%-33%RH.

8.5 Conclusion and Outlook

We discussed the recent advancement of MXene-based hybrid materials in terms of synthesis techniques, properties and potential applications. The synthesis of MXene materials using various techniques has several limitations, followed by a summary of various techniques used for the synthesis of MXene in terms of hazardous, yield, cost, thickness, etc. The broad applications of MXene hybrid materials in terms of rechargeable batteries, supercapacitors, EMI and sensing were also reported.

Similar to other 2D materials, surface modification and morphology have an important impact on enhancing the no. of active sites. The production of defect-free and high quality MXene is very important for various applications in the field of high-performance rechargeable batteries and supercapacitors. MXene-based hybrid materials are still hindered in various potential applications. The thickness of MXene flakes is the major challenge.

- The synthesis method of MXene should be safe, high quality, cheaper and efficient materials.
- Synthesis of various advanced new materials must be explored for next-generation applications.
- Synthesis technique for MXene techniques should be improved in terms of restacking, the tendency of oxidation and difficulty in exfoliation.
- The synthesis of defect-free MXene should be explored to improve the electrochemical performances
- Easy synthesis of various advanced 2D MXene should be explored to improve stability

- The tuning porosity of MXene should be investigated.

In industrial applications, the technical issues for process integration and mass production should be examined. Hence, it is an essential requirement to know the exfoliation mechanism of the important properties and performance of MXene to the scale-up synthesis of MXene as environmentally friendly and cheap. In conclusion, MXene hybrid materials have witnessed major innovations in several fields and have important prospects. In recent years, energy storage applications of MXene-based materials have significantly focused but their applicable research is still in its beginning. Innovative investigation of MXene is still required for practical and commercial applications.

References

1. G. Wang, L. Zhang, J. Zhang, Chem. Soc. Rev. **41**, 797 (2012)
2. H. Jin, C. Guo, X. Liu, J. Liu, A. Vasileff, Y. Jiao, Y. Zheng, S.-Z. Qiao, Chem. Rev. **118**, 6337 (2018)
3. D. Han, J. Zhang, Z. Weng, D. Kong, Y. Tao, F. Ding, D. Ruan, Q.-H. Yang, Mater. Today. Energy **11**, 30 (2019)
4. P.K. Panda, A. Grigoriev, Y.K. Mishra, R. Ahuja, Nanoscale Advan. **2**, 70 (2020)
5. K. Khan, A.K. Tareen, M. Aslam, R. Wang, Y. Zhang, A. Mahmood, Z. Ouyang, H. Zhang, Z. Guo, J. Mater. Chem. C **8**, 387 (2020)
6. J. D. Gouveia, G. Novell-Leruth, P.M. Reis, F. Viñes, F. Illas, J.R. Gomes, ACS Appl. Bio Mater. (2020)
7. Y. Chen, L. Wang, J. Shi, Nano Today **11**, 292 (2016)
8. C. Dai, Y. Chen, X. Jing, L. Xiang, D. Yang, H. Lin, Z. Liu, X. Han, R. Wu, ACS Nano **11**, 12696 (2017)
9. H. Zhong, Z. Liu, P. Tang, X. Liu, X. Zhan, P. Pan, C. Tang, Sol. Energy **208**, 445 (2020)
10. K. Huang, C. Li, H. Li, G. Ren, L. Wang, W. Wang, X. Meng, ACS Appl. Nano Mater. (2020)
11. K.R.G. Lim, A.D. Handoko, S.K. Nemani, B. Wyatt, H.-Y. Jiang, J. Tang, B. Anasori, Z.W. Seh, ACS Nano **14**, 10834 (2020)
12. K. Deshmukh, T. Kovářík, S.K. Pasha, Cood. Chem. Rev. **424**, 213514 (2020)
13. A. Yang et al., Nat. Nanotech. **15**, 231 (2020)
14. Y. Li, M.-S. Chen, J. Cheng, W. Fu, Y. Hu, B. Liu, M. Zhang, Z. Shen, Langmuir **36**, 2255 (2020)
15. J. Jyoti, B.P. Singh, M. Sandhu, S.K. Tripathi, Sust. Energy Fuels (2022)
16. J. Jyoti, A. Kiran, M. Sandhu, A. Kumar, B.P. Singh, N. Kumar, J. Mech. Behav. Biomed. Mater. **117**, 104376 (2021)
17. J. Jyoti, B.P. Singh, S.K. Tripathi, J. Energy Storage **43**, 103112 (2021)
18. M. Naguib, O. Mashtalir, J. Carle, V. Presser, J. Lu, L. Hultman, Y. Gogotsi, M.W. Barsoum, ACS Nano **6**, 1322 (2012)
19. M. Naguib, M. Kurtoglu, V. Presser, J. Lu, J. Niu, M. Heon, L. Hultman, Y. Gogotsi, M.W. Barsoum, Adv. Mater. **23**, 4248 (2011)
20. M. Naguib, V.N. Mochalin, M.W. Barsoum, Y. Gogotsi, Adv. Mater. **26**, 992 (2014)
21. V.M.H. Ng, H. Huang, K. Zhou, P.S. Lee, W. Que, J.Z. Xu, L.B. Kong, J. Mat. Chem. A **5**, 3039 (2017)
22. X. Wang, Y. Zhou, J. Mat. Sci. Tech. **26**, 385 (2010)
23. S. Mallakpour, V. Behranvand, C.M. Hussain, Ceram. Int. **47**, 26585 (2021)
24. M. Naguib, J. Halim, J. Lu, K.M. Cook, L. Hultman, Y. Gogotsi, M.W. Barsoum, J. Amer. Chem. Soc. **135**, 15966 (2013)

25. M. Ghidiu et al., Chem. Comm. **50**, 9517 (2014)
26. J. Pang, R.G. Mendes, A. Bachmatiuk, L. Zhao, H.Q. Ta, T. Gemming, H. Liu, Z. Liu, M.H. Rummeli, Chem. Soc. Rev. **48**, 72 (2019)
27. B. Anasori, Y. Xie, M. Beidaghi, J. Lu, B.C. Hosler, L. Hultman, P.R. Kent, Y. Gogotsi, M.W. Barsoum, ACS Nano **9**, 9507 (2015)
28. J. Zhou, X Zha, X Zhou,G Gao, S Wang., Q. Hang, ACS Nano **11**, 3841 (2017)
29. J. Halim, S. Kota, M. Naguib, M. Zho, Adv. Funct. Mater. **26**, 3118 (2016)
30. Y. Gogotsi, Nat. Mat. **14**, 1079 (2015)
31. C. Xu, L. Wang, Z. Liu, L. Chen, J. Guo, N. Kang, X.-L. Ma, H.-M. Cheng, W. Ren, Nat. Mater. **14**, 1135 (2015)
32. M. Li, J Lu, K Luo, K Cheng, K. Chen, J. Rosen, J. Am. Chem. Soc. **141**, 4730 (2019)
33. P. Urbankowski, B. Anasori, T. Makaryan, D. Er, S. Kota, Nanoscale **8**, 11385 (2016)
34. Y. Li. H. Saho, Z. Lin, J. Lu, L. Liu, B. Duployer, Nat. Mater. **19**, 894 (2020)
35. S.-Y. Pang, Y.-T. Wong, S. Yuan, Y. Liu, M.-K. Tsang, Z. Yang, H. Huang, W.-T. Wong, J. Hao, J. Am. Chem. Soc. **141**, 9610 (2019)
36. O. Mashtalir, M. Naguib, V.N. Mochalin, Y. Dall'Agnese, M. Heon, M.W. Barsoum, Y. Gogotsi, Nat. Commun. **4**, 1 (2013)
37. M. Ghidiu, S. Kota, J. Halim, A.W. Sherwood, N. Nedfors, J. Rosen, V.N. Mochalin, M.W. Barsoum, Chem. Mater. **29**, 1099 (2017)
38. V. Natu, M. Sokol, L. Verger, M.W. Barsoum, J. Phys. Chem. C **122**, 27745 (2018)
39. L. Gao, C. Li, W. Huang, S. Mei, H. Lin, Q. Ou, Chem. Mater. **32**, 1703 (2020)
40. J. Halim, M.R. Lukatskaya, K.M. Cook, J. Lu, Chem. Mater. **26**, 2374 (2014)
41. J. Nickl, K. Schweitzer, P. Luxenberg, J. Less Common Metals **26**, 335 (1972)
42. B. Anasori, M.R. Lukatskaya, Y. Gogotsi, Nat. Rev. Mater. **2**, 1 (2017)
43. C. Zhang, Y. Ma, X. Zhang, S. Abdolhosseinzadeh, H. Sheng, W. Lan, A. Pakdel, J. Heier, F. Nüesch, Energy Environ. Mater. **3**, 29 (2020)
44. Z. Liu, C. Xu, N. Kang, L. Wang, Y. Jiang, J. Du, Y. Liu, Nano Lett. **16**, 4243 (2016)
45. D. Geng, X. Zhao, L. Li, P. Song, B. Tian, W. Liu, 2D Mater. **4**, 011012 (2016)
46. F. Zhang, Z. Zhang, H. Wang, C.H. Chan, N.Y. Chan, X.X. Chen, J.-Y. Dai, Phys. Rev. Mater. **1**, 034002 (2017)
47. X.-H. Zha, J. Zhou, Y. Zhou, Q. Huang, J. He, J.S. Francisco, K. Luo, S. Du, Nanoscale **8**, 6110 (2016)
48. X.-H. Zha, Q. Huang, J. He, H. He, J. Zhai, J.S. Francisco, S. Du, Sci. Rep. **6**, 1 (2016)
49. Y. Xie et al., J. Am. Chem. Soc. **136**, 6385 (2014)
50. Y. Xie, Y. Dall'Agnese, M. Naguib, Y. Gogotsi, M.W. Barsoum, H.L. Zhuang, P.R. Kent, ACS Nano **8**, 9606 (2014)
51. Y. Xie, P. Kent, Phys. Rev. B **87**, 235441 (2013)
52. G. Gao, G. Ding, J. Li, K. Yao, M. Wu, M. Qian, Nanoscale **8**, 8986 (2016)
53. J. Hu, B. Xu, C. Ouyang, S.A. Yang, Y. Yao, J. Phys. Chem. C **118**, 24274 (2014)
54. J. Yang, X. Zhou, X. Luo, S. Zhang, L. Chen, Appl. Phys. Lett. **109**, 203109 (2016)
55. J. Halim, M. Lukatskaya, K. Cook, J. Lu, C. Smith, Chem. Mater. **26**, 2374 (2014)
56. M. Mariano, O. Mashtalir, F.Q. Antonio, W.-H. Ryu, B. Deng, F. Xia, Y. Gogotsi, A.D. Taylor, Nanoscale **8**, 16371 (2016)
57. W. Lv, F.-N. Xue, Y. Zhang, B. Sun, Y. Lu, Y. Yang, P. Zhang, Appl. Surf. Sci. **587**, 152768 (2022)
58. H. Lashgari, M. Abolhassani, A. Boochani, S. Elahi, J. Khodadadi, Solid State Commun. **195**, 61 (2014)
59. M. Khazaei, M. Arai, T. Sasaki, M. Estili, Y. Sakka, Phys. Chem. Chem. Phys **16**, 7841 (2014)
60. S. Wang, J.-X. Li, Y.-L. Du, C. Cui, Computat. Mater. Sci. **83**, 290 (2014)
61. S. Zhao, W. Kang, J. Xue, Appl. Phys. Lett. **104**, 133106 (2014)
62. I. Shein, A. Ivanovskii, Superlatt. Microstruct. **52**, 147 (2012)
63. A. Enyashin, A. Ivanovskii, J. Solid State Chem. **207**, 42 (2013)
64. V. Mauchamp, M. Bugnet, E.P. Bellido, G.A. Botton, P. Moreau, D. Magne, M. Naguib, T. Cabioc'h, M.W. Barsoum, Phys. Rev. B **89**, 235428 (2014)

65. Q. Tang, Z. Zhou, P. Shen, J. Am. Chem Soc. **134**, 16909 (2012)
66. A.N. Enyashin, A.L. Ivanovskii, J. Phys. Chem. C **117**, 13637 (2013)
67. M. Khazaei, M. Arai, T. Sasaki, C.Y. Chung, N.S. Venkataramanan, M. Estili, Y. Sakka, Y. Kawazoe, Adv. Funct. Mater. **23**, 2185 (2013)
68. Y. Lee, S.B. Cho, Y.-C. Chung, ACS Appl. Mater. Interface **6**, 14724 (2014)
69. V.N. Borysiuk, V.N. Mochalin, Y. Gogotsi, Nanotechnology **26**, 265705 (2015)
70. X. Zhang, X. Zhao, D. Wu, Y. Jing, Z. Zhou, Nanoscale **7**, 16020 (2015)
71. J. Liu, H.B. Zhang, R. Sun, Y. Liu, Z. Liu, A. Zhou, Z.Z. Yu, Adv. Mater. **29**, 1702367 (2017)
72. X. Zhang, X. Wang, P. Sha, B. Wang, Y. Ding, S. Du, Comp. Sci. Tech. **189**, 108020 (2020)
73. L. Wang et al., Environ. Sci. Tech. **53**, 3739 (2019)
74. Q. Peng, J. Guo, Q. Zhang, J. Xiang, B. Liu, A. Zhou, R. Liu, Y. Tian, J. Am. Chem. Soc. **136**, 4113 (2014)
75. C. Jiang, X. Li, Y. Yao, L. Lan, Y. Shao, F. Zhao, Y. Ying, J. Ping, Nano Energy **66**, 104121 (2019)
76. Y. Ma, Y. Yue, H. Zhang, F. Cheng, W. Zhao, J. Rao, ACS Nano **12**, 3209 (2018)
77. D. Xiong, X. Li, Z. Bai, S. Lu, Small **14**, 1703419 (2018)
78. X. Xie, M. Zhao, B. Anasori, K. Maleski, C. Ren, J. Li, B. Byles, Nano Energy **26**, 513 (2016)
79. J. Jyoti, A.K. Arya, S. Chockalingam, S.K. Yadav, K.M. Subhedar, S. Dhakate, B.P. Singh, J. Poly. Res. **27**, 1 (2020)
80. J. Jyoti, T.K. Gupta, B.P. Singh, M. Sandhu, S.K. Tripathi, J. Energy Storage **50**, 104235 (2022)
81. J. Nan, X. Guo, J. Xiao, X. Li, W. Chen, W. Wu, H. Liu, Small **17**, 1902085 (2021)
82. I. Persson, J. Halim, H. Lind, T.W. Hansen, Adv. Mater. **31**, 1805472 (2019)
83. M. Naguib, M. Kurtoglu, V. Presser, J. Lu, J. Niu, M. Heon, L. Hultman, Y. Gogotsi, M.W. Barsoum, Adv. Mater. **23**, 4207 (2011)
84. X. Zhan, C. Si, J. Zhou, Z. Sun, Nanoscale Horiz. **5**, 235 (2020)
85. F. Wang, C. Yang, M. Duan, Y. Tang, J. Zhu, Biosens. Bioelectron. **74**, 1022 (2015)
86. J. Come et al., Nano Energy **17**, 27 (2015)
87. Y. Liu, W. Wang, Y. Ying, Y. Wang, X. Peng, Dalton Trans. **44**, 7123 (2015)
88. H. Zhang, H. Dong, X. Zhang, Y. Xu, J. Fransaer, Electrochim. Acta **202**, 24 (2016)
89. X. Xie, M.Q. Zhao, B. Anasori, K. Maleski, C.E. Ren, J. Li, Nano Energy **26**, 513 (2016)
90. T. Yin, Y. Li, R. Wang, O.A. Al-Hartomy, A. Al-Ghamdi, S. Wageh, X. Luo, X. Tang, H. Zhang, Ceram. Interface **47**, 28642 (2021)
91. M. Zheng, R. Guo, Z. Liu, B. Wang, L. Meng, F. Li, T. Li, Y. Luo, J. Alloys Compounds **735**, 1262 (2018)
92. A. Ali, K. Hantanasirisakul, A. Abdala, P. Urbankowski, M.-Q. Zhao, B. Anasori, Y. Gogotsi, B. Aïssa, K.A. Mahmoud, Langmuir **34**, 11325 (2018)
93. B.E. Conway, *Electrochemical Supercapacitors: Scientific Fundamentals and Technological Applications* (Springer Science & Business Media, 2013)
94. Y. Wang, Y. Song, Y. Xia, Chem. Soc. Rev. **45**, 5925 (2016)
95. M. Vangari, T. Pryor, L. Jiang, J. Energy Eng. **139**, 72 (2013)
96. M. Zhi, C. Xiang, J. Li, M. Li, N. Wu, Nanoscale **5**, 72 (2013)
97. Y. Han, Y. Ge, Y. Chao, C. Wang, G.G. Wallace, J. Energy Chem **27**, 57 (2018)
98. C. Wang, G.G. Wallace, Electrochim. Acta **175**, 87 (2015)
99. Z. Fan, Q. Zhao, T. Li, J. Yan, Y. Ren, J. Feng, T. Wei, Carbon **50**, 1699 (2012)
100. X. Huang, Z. Zeng, Z. Fan, J. Liu, H. Zhang, Adv. Mater. **24**, 5979 (2012)
101. S. Murali, N. Quarles, L.L. Zhang, J.R. Potts, Z. Tan, Y. Lu, Y. Zhu, R.S. Ruoff, Nano Energy **2**, 764 (2013)
102. R. Syamsai, A.N. Grace, J. Alloys Comp. **792**, 1230 (2019)
103. B. Anasori, M. Lukatskaya, Y. Gogotsi, Nat. Rev. Mater. 1–17 (2017)
104. M.R. Lukatskaya et al., Science **341**, 1502–1505 (2013)
105. J. Wang, J. Gong, H. Zhang, L. Lv, Y. Liu, Y. Dai, J. Alloys Comp. **870**, 159466 (2021)
106. J. Chen, Y. Ren, H. Zhang, J. Qi, Y. Sui, F. Wei, Appl. Surf. Sci. **562**, 150116 (2021)
107. H. Li, Y. Hou, F. Wang, M.R. Lohe, X. Zhuang, L. Niu, X. Feng, (2017)

108. Y. Zhu, K. Rajouâ, S. Le Vot, O. Fontaine, P. Simon, F. Favier, Nano Energy **73**, 104734 (2020)
109. Z. Wang, Z. Yu, M. Das, L. Huang, ACS Nano **14**, 4916 (2020)
110. J. Yan, C.E. Ren, K. Maleski, C.B. Hatter, B. Anasori, P. Urbankowski, A. Sarycheva, Y. Gogotsi, Adv. Funct. Mat. **27**, 1701264 (2017)
111. H. Huang, K. Kim, G. Lee, M. Kang, H. Chang, A.R. Jang, ACS Nano **16**, 3776 (2022)
112. C.J. Von Klemperer, D. Maharaj, Comp. Struct. **91**, 467 (2009)
113. J. Jyoti, S. Basu, B.P. Singh, S. Dhakate, Comp. Part B Eng. **83**, 58 (2015)
114. M.H. Al-Saleh, W.H. Saadeh, U. Sundararaj, Carbon **60**, 146 (2013)
115. S.H. Ryu, Y.K. Han, S.J. Kwon, T. Kim, B.M. Jung, S.-B. Lee, B. Park, Chem. Eng. J **428**, 131167 (2022)
116. J. Jyoti, A.K. Arya, Poly. Testing **91**, 106839 (2020)
117. X. Li, X. Yin, S. Liang, M. Li, L. Cheng, L. Zhang, Carbon **146**, 210 (2019)
118. F. Shahzad, M. Alhabeb, C.B. Hatter, B. Anasori, S. Man Hong, C.M. Koo, Y. Gogotsi, Science **353**, 1137 (2016)
119. R. Sun, H.B. Zhang, J. Liu, X. Xie, R. Yang, Y. Li, S. Hong, Z.Z. Yu, Adv. Funct. Mat. **27**, 1702807 (2017)
120. X. Li, X. Yin, C. Song, M. Han, H. Xu, W. Duan, L. Cheng, L. Zhang, Adv. Funct. Mat. **28**, 1803938 (2018)
121. Z. Zhou, J. Liu, X. Zhang, D. Tian, Z. Zhan, C. Lu, Adv. Mater. Interfaces **6**, 1802040 (2019)
122. C. Lei, Y. Zhang, D. Liu, K. Wu, Q. Fu, ACS Appl. Mater. Interfaces **12**, 26485 (2020)
123. S. Ganguly, P. Das, A. Saha, M. Noked, A. Gedanken, S. Margel, Langmuir **38**, 3936 (2022)
124. Y. Sun, R. Ding, S.Y. Hong, J. Lee, Y.-K. Seo, J.-D. Nam, J. Suhr, Chem. Eng. J. **410**, 128348 (2021)
125. V.-T. Nguyen, B.K. Min, Y. Yi, S.J. Kim, C.-G. Choi, Chem. Eng. J. **393**, 124608 (2020)
126. J. Lu, Y. Zhang, Y. Tao, B. Wang, W. Cheng, G. Jie, L. Song, Y. Hu, J, Colloid Interface Sci. **588**, 164 (2021)
127. Y. Pei, X. Zhang, Z. Hui, J. Zhou, X. Huang, G. Sun, W. Huang, ACS Nano **15**, 3996 (2021)
128. Z. Hui et al., ACS Appl. Mater. Interfaces **12**, 12155 (2020)
129. T.-S. Dinh Le, J. An, Y. Huang, Q. Vo, J. Boonruangkan, T. Tran, S.-W. Kim, G. Sun, Y.-J. Kim, ACS Nano **13**, 13293 (2019)
130. Y. Yang, L. Shi, Z. Cao, R. Wang, J. Sun, Adv. Funct. Mater. **29**, 1807882 (2019)
131. Y. Cai, J. Shen, G. Ge, Y. Zhang, W. Jin, W. Huang, J. Shao, J. Yang, X. Dong, ACS Nano **12**, 56 (2018)
132. J. Zhang, L. Wan, Y. Gao, X. Fang, T. Lu, L. Pan, F. Xuan, Adv. Electron. Mater. **5**, 1900285 (2019)
133. M. Zhang, Z. Yuan, J. Song, C. Zheng, Sens. Actuators B Chem. **148**, 87 (2010)
134. E. Lee, A. VahidMohammadi, B.C. Prorok, Y.S. Yoon, M. Beidaghi, D.-J. Kim, A.C.S. Appl, Mater. Interfaces **9**, 37184 (2017)
135. S.J. Kim, S.Y. Cho, B. Anasori, C.K. Kim, Y.K. Choi, J. Kim, ACS Nano **12**, 986 (2018)
136. M. Wu, M. He, Q. Hu, Q. Wu, G. Sun, L. Xie, Z. Zhang, Z. Zhu, A. Zhou, ACS Sens. **4**, 2763 (2019)
137. Y. Zuo, Y. Gao, S. Qin, Z. Wang, D. Zhou, Z. Li, Y. Yu, M. Shao, X. Zhang, Nanophotonics **9**, 123 (2020)
138. B.E. Scheibe, J.K. Wychowaniec, M. Scheibe, B. Peplinska, M. Jarek, G. Nowaczyk, Ł. Przysiecka, ACS Biomat. Sci. Eng. **5**, 6557 (2019)
139. Z. Duan et al., Sens. Actuators B Chem. **339**, 129884 (2021)
140. J. Yang, R. Shi, Z. Lou, R. Chai, K. Jiang, G. Shen, Small **15**, 1902801 (2019)
141. M.A. Haque, A. Syed, F.H. Akhtar, R. Shevate, S. Singh, K.-V. Peinemann, D. Baran, T. Wu, A.C.S. Appl, Mater. Interfaces **11**, 29821 (2019)
142. L. Sun, A.A. Haidry, Z. Li, L. Xie, Z. Wang, Q. Fatima, Z. Yao, J. Mater. Sci. Mater. Elect. **29**, 18502 (2018)

143. R. Kumar, R.N. Jenjeti, S. Sampath, Adv. Mater. Interfaces **6**, 1900666 (2019)
144. E.S. Muckley, M. Naguib, I.N. Ivanov, Nanoscale **10**, 21689 (2018)
145. N. Li, Y. Jiang, C. Zhou, Y. Xiao, B. Meng, Z. Wang, D. Huang, C. Xing, Z. Peng, A.C.S. Appl, Mater. Interfaces **11**, 38116 (2019)

Chapter 9
Nanocomposite Ceramics for Energy Harvesting

Raghvendra Pandey and Prabhakar Singh

Abstract A nanocomposite material is composed of a number of phases, each of which has at least one, two, or three dimensions that are in the nanoscale regime. As the dimensions of a material are reduced to the nanoscale size, phase interfaces are created which are crucial for improving the characteristics of materials. The structure and property of nanocomposite ceramics directly depend on the ratio of reinforced material volume to surface area employed in the creation of nanocomposites. In the field of medical, pharmaceutical, food packaging, electronics, and energy industries, nanocomposites provide possibilities on entirely new dimensions. Additionally, ceramic nanocomposites can be broadly classified as either a nanophase ceramic in a ceramic matrix, a ceramic matrix carbonaceous nanophase, or as a ceramic matrix with metal as the additional component. Oxides, carbides, and nitrides combined with metallic and non-metallic components produce ceramic nanocomposites. The ceramic nanocomposites have been widely used in a number of applications in electronics and structural components because of their better mechanical, electrical, and magnetic properties. Developing innovative processing methods that allow for the fabrication of products ranging from laboratory research to commercial level is increasingly using ceramic nanocomposites. Nowadays, the ceramic nanocomposite is widely used in electrochemical devices as an electrode or electrolyte for energy conversion or storage purpose. This chapter describes the key concepts behind nanocomposite ceramics and explores various classes of nanocomposite ceramics. The purpose of this chapter is to provide a basic introduction to nanocomposites, their types, material fabrication technique that is most appropriate for the preparation and processing of nanocomposites ceramics, physical properties, applications, benefits, and flaws of these nanocomposites and their uses in energy harvesting.

Keywords Nanocomposite · Ceramics · Matrix · Reinforcement · Energy harvesting

R. Pandey (✉)
Department of Physics, ARSD College, University of Delhi, New Delhi 110021, India
e-mail: raghvendra@arsd.du.ac.in; raghvendra.sspl@gmail.com

P. Singh
Department of Physics, Indian Institute of Technology (BHU), Varanasi 221005, India
e-mail: psingh.app@iitbhu.ac.in

D. K. Singh et al. (eds.), *Nanomaterials*,
https://doi.org/10.1007/978-981-19-7963-7_9

9.1 Introduction

The development of innovative nanocrystalline ceramic powders with multifunctional potentials has sparked study into the progress of multifunctional engineering materials using nanoscale structural design [1–4]. The evolution of nanocomposite is the prominent fast-growing field in composite research which has been pushed by the increasing interest in nanotechnology [5–7]. When a functional material with at least one dimension on the nanoscale range (less than 100 nm) is disseminated in a matrix such as ceramic, polymer, or metal, nanocomposites are formed [8, 9]. Carbon nanotubes (CNTs), nanocellulose, graphene, ceramics, inorganic nanowires, layered double hydroxides, layered silicates, and many other inorganic nanoparticles are examples of functional materials [9–11]. A composite material with multifunctional abilities can be created by translating the numerous distinctive and outstanding features of such functional materials for example thermal conductivity, electrical conductivity, high current density, stiffness, strength, optical and magnetic to the matrix material [12]. The concept behind nanocomposites is to design and produce new materials with outstanding flexibility and improvements in their physical attributes by using building blocks with sizes in the nanometer range. Nanoscale material reduction results in interaction phase interfaces, which are crucial for improving the characteristics of materials [12, 13]. The nanocomposite will have significantly different electrical, mechanical, electrochemical, thermal, catalytic, and optical properties from its components. These size constraints effects are crucial and are listed below [12–14]:

- Size <5 nm is suitable for catalytic activity
- Size <20 nm is appropriate for making a hard magnetic material into soft material
- Size <50 nm to change the refractive index
- Size <100 nm is apt for getting the mechanical strength, super-magnetism, etc (Fig. 9.1).

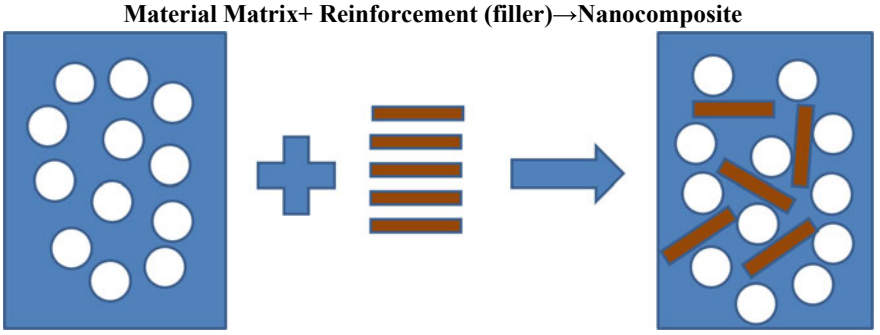

Fig. 9.1 Formation of nanocomposite materials

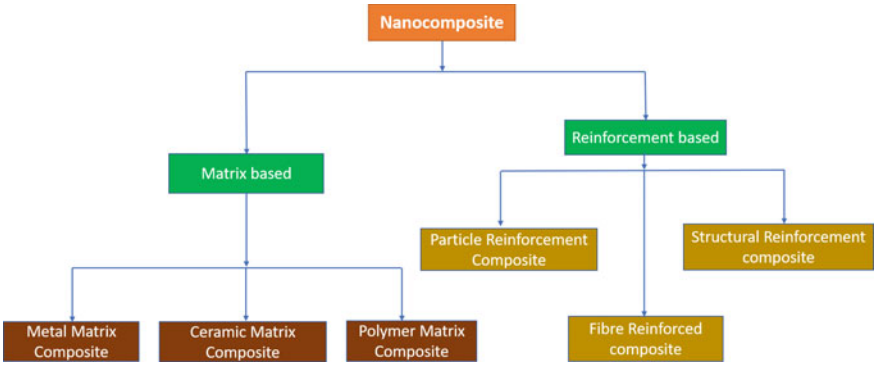

Fig. 9.2 A broad classification of nanocomposite materials

Understanding the relationship between structure and property is directly influenced by the surface area to volume ratio of the reinforced material employed during the fabrication of nanocomposites. The basic characteristics of the non-metallic, metallic, and polymeric materials are retained in the nanocomposite material (at least one component of nanometric scale (10^{-9} m), which offers the added benefit of overcoming flaws and exhibiting some new characteristics [7, 14]. These materials embody a multiphase crossover of matrix material and reinforcing material as classified in Fig. 9.2. The matrix material is a continuous phase that comprises metallic, inorganic, non-metallic, and polymer matrix materials. The reinforcing material is a dispersed phase that typically consists of fibrous materials like glass fibre, organic fibre, etc [6–14].

According to their matrix materials, nanocomposite materials can be broadly categorized into three groups: (a) metal matrix Nanocomposites (MMNCs), (b) polymer matrix Nanocomposites (PMNCs), and (c) ceramic matrix Nanocomposites (CMNCs). Based on the application requirement, these different types of nanocomposites may be used [15]. A few examples of all three types of matrix-based nanocomposite materials are listed in Table 9.1.

Among all other matrix composites, ceramic matrix nanocomposites (CMNCs) have received attention owing to their enhanced physical properties as compared to conventional or traditional ceramics. In ceramic matrix nanocomposite, the main components, i.e. matrix is generally a ceramic material and other components may

Table 9.1 Types of nanocomposites on the basis of matrix

Class	Examples
Metal	Ni/Al_2O_3, Fe–Cr/Al_2O_3, Fe/MgO, Co/Cr, Mg/CNT, Al/CNT, Ni/YSZ, Ni/SDC, etc.
Polymer	Polymer/layered silicates, thermoplastic/thermoset, polymer/CNT, polyester/TiO_2, polymer/layered double hydroxides, etc.
Ceramic	ZrO_2/Al_2O_3, Al_2O_3/TiO_2, Al_2O_3/SiO_2, SiO_2/Ni, Al_2O_3/CNT, Al_2O_3/SiC, etc.

be either ceramic, metal or polymer. The ceramic component is generally occupied by oxides, nitrides, borides, silicides, carbides, etc. as a major volume. CMNCs were designed to address the single-phase ceramic materials' inefficiency. In order to get superior characteristics, ceramic reinforcement is used in ceramic matrix composites. Ceramic particle dispersion tends to inhibit dislocation motion and contributes to the dispersion strengthening mechanism, improving a number of attributes including increased hardness, thermal conductivity, thermal shock resistance, electrical conductivity, etc [7, 16–19]. Here are a few common examples of nanocomposite ceramic materials as given below:

- *Alumina-based nanocomposites*: Alumina matrix materials with increased mechanical properties (hardness, fracture toughness, wear resistance, and higher corrosion resistance) have been produced with the inclusion of a number of nano reinforcements.
- *Alumina/silicon carbide nanocomposites*: Wear resistance is increased by adding SiC nanoparticles to an alumina matrix.
- *Alumina/zirconia nanocomposites*: They are also known as zirconia-toughened alumina (ZTA) nanocomposites and are made of zirconia particles bonded to a fine-grained alumina matrix. The purpose of the zirconia nanoparticles is to make the alumina matrix more resilient.
- *Alumina/titania nanocomposites*: There has been an increase in hardness, fracture toughness, and fracture resistance.
- *Zirconia/alumina nanocomposites*: They are also referred to as alumina-toughened zirconia (ATZ) and are made of a zirconia matrix that has been strengthened by alumina nanoparticles. They exhibit great hardness and resistance.
- *Silicon nitride/silicon carbide nanocomposites*: Due to residual compressive thermal stresses within the nanocomposites, intragranular SiC particles increase strength and fracture toughness.
- *Ceramic/carbon nanofibre composites*: Mostly used to improve the mechanical properties of ceramic materials by reinforcing them with carbon nanofibers.
- *Ceramic/polymer composites*: specific to applications involving tissue engineering and biomedical applications.
- *Ceramic/carbon nanotube (CNT) composites*: improved thermal, mechanical, and electrical properties.

A few examples of ceramic matrix nanocomposite and their characteristic features are given in Table 9.2.

Ceramic nanocomposites exhibit better strength, toughness, hardness, and creep resistance compared to traditional ceramic matrix composites. Because of their outstanding properties, such as resistance to corrosion, high-temperature oxidation, and better wear resistance than that of metals in high-temperature conditions, they have been used in numerous industrial applications. However, these ceramic nanocomposites' primary goal is to increase fracture toughness and prevention from thermal shock [22, 23].

Table 9.2 Examples of ceramic matrix nanocomposite and their properties [20, 21]

Matrix/Reinforcement	Properties/Characteristics
Metal oxides/metal	Sensors, catalysts, optoelectronic devices, electrochemical electrodes
$BaTiO_3$/SiC, PZT/Ag	High-performance ferroelectric devices and electronic industry
SiO_2/Co	Optical fibres
SiO_2/Ni	Chemical sensors
ZrO_2/$MoSi_2$, Al_2O_3/ZrO_2	Improved mechanical properties, toughness, strength
B_4C/TiB_2	Improved mechanical properties, toughness, strength
Al_2O_3/$NdAlO_3$ and Al_2O_3/$LnAlO_3$	Phosphors, photoluminescence, optical amplifiers, solid-state laser media
TiO_2/Fe_2O_3	High-density magnetic recording media, ferrofluids, and catalysts
Al_2O_3/Ni	Engineering parts
$PbTiO_3$/$PbZrO_3$	Microelectronic and micro-electromechanical systems
Al_2O_3/SiC, Si_3N_4/SiC	Structural materials
TiO_2/C nanofibre	Electrospinning
SiO_2/Fe	High-performance catalysts, data storage technology
ZnO/Co	Field effect transistor for the optical femtosecond study of interparticle
YSZ/Ni, SDC/Ni	Mixed conducting anode materials for solid oxide fuel cells
SDC/Na_2CO_3, SDC/Al_2O_3	Ion conducting electrolyte for SOFCs
TiO_2/CNT, ZrO_2/CNT	Improved fracture toughness, strength
Ceramic Si_3N_4/MWCNT	High durability, thermoelectric attributes, high electrical conductivity

Benefits and drawbacks of the Nanocomposite

Nanocomposites are the next generation of materials because they offer a new alternative to the current limitations of micro composites and monolithics. The following are the primary benefits of nanocomposites over other composite materials [23]:

- high surface to volume ratio allows small filler size and separation between the fillers;
- improved mechanical properties;
- high ductility retaining high strength and scratch resistance;
- better optical properties (the transmission of light depends on the particle size).

The main drawbacks of using nanocomposites are their impact performance and toughness due to the integration of nanoparticles into the bulk matrix.

– Inadequate comprehension of the link between formulation, property, and structure, simpler particle exfoliation and dispersion process is required.
– Expensiveness.

9.2 Classification of Nanocomposites Ceramics

As depicted in Fig. 9.3, Niihara [24] categorizes nanocomposites into four groups: intergranular, intragranular, hybrid, and nano/nanocomposites. The nano-size particles are mainly dispersed within the grains or at the grain boundaries of the matrix, respectively, in the intra- and intergranular nanocomposites, as schematically depicted in this figure. Their objective is to improve both mechanical properties at high temperatures, such as hardness, strength, creep, and fatigue fracture resistances, as well as mechanical properties at room temperature, such as hardness, fracture strength, toughness, and durability [25, 26]. On the other hand, the dispersoids and nanometer-sized matrix grains comprise the nano/nanocomposites. The main objective of this composite is to provide ceramics with new properties similar to metals, such as machinability and superplasticity [24].

The magnitude and distribution of the resultant phase obtained as well as the synthesis procedure used all affect the properties of CMNCs. According to the

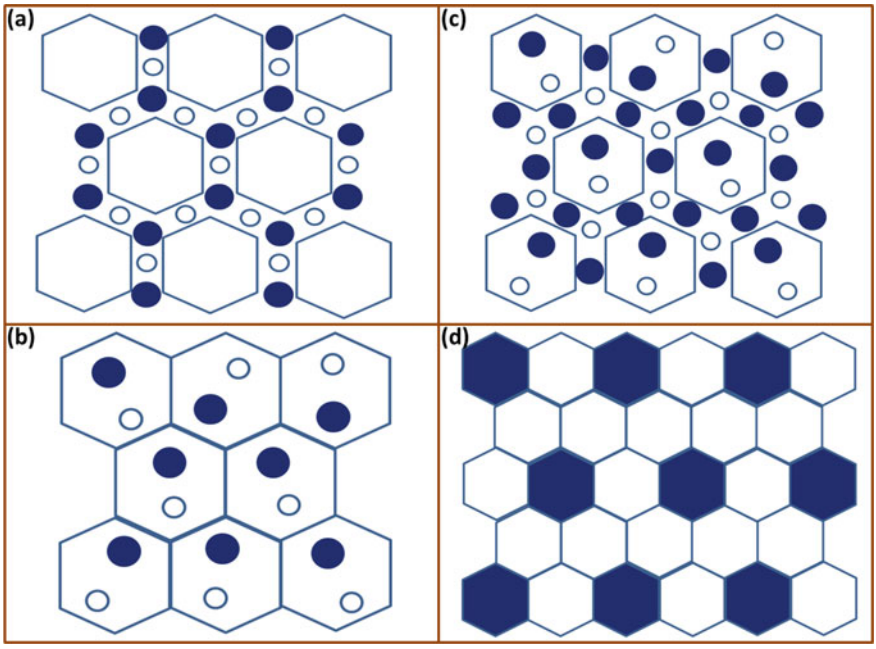

Fig. 9.3 Schematic categorization of ceramic nanocomposite. **a** Inter type, **b** Intra type, **c** Hybrid (inter/intra) type, and **d** Nano-nano type

desired area of application, several ceramic matrix nanocomposite systems have been developed through a variety of synthesis techniques (shown in Table 9.3) [6, 17]. Sol–gel synthesis was used by D. Sarkar et al. to produce the powder of the Al_2O_3–ZrO_2 nanocomposites [27–29]. Due to their unique characteristics, such as particularly improved toughness, high wear resistance, and enhanced room temperature strength, synthetic materials have been found to have applications in cutting tools and as components of implants. Al_2O_3–ZrO_2 nanocomposite powder was synthesized and characterized by the sucrose process, according to Beitollahi et al. [30]. This method is a modified chemical pathway in which metal nitrates, sucrose, and polyvinyl alcohol (PVA) were used to prepare powder, which was then subjected to post-calcinations. ZrO_2–Al_2O_3 nanocomposite powder was synthesized by J. Kishan et al. by changing the alumina content from 3 to 8% [31]. In their investigation, they used the aqueous combustion synthesis technique to produce nanopowder. Al_2O_3-13wt% TiO_2 plasma sprayed coatings made from nanocrystalline powders have been prepared by Goberman et al. [32]. It was observed that the final microstructure had a bimodal distribution with two distinct zones. One had a fully melted zone, whereas the other had a microstructure with a partially melted portion. A parameter known as the critical plasma spray parameter (CPSP) can be used to adjust the ratio of the completely melted region to the partially melted region (CPSP). This bimodal distribution of nanostructured Al_2O_3-13wt% TiO_2 has improved a number of attributes including mechanical strength, wear resistance, spalling resistance, and others. Dejang et al. [33] have fabricated Al_2O_3/TiO_2 nanocomposite coatings via plasma spray method and studied their properties by adding varying amount of nano-sized TiO_2. They found that with excess addition of TiO_2 nanoparticle, the hardness of the nanocomposite decreases while fracture toughness increased. Surface morphology of nanocomposite revealed that lamellas of TiO_2 were well separated and dispersed homogeneously among lamellas of Al_2O_3. By using a hydrothermal synthesis technique at a relatively low temperature, Kaya et al. synthesized pure zirconia nanostructures with mullite, boehmite, and other materials [34]. In this study, a porous morphology with almost hexagonal particle shapes was attained. The generated nanostructured materials are used in ceramic composites with fibre reinforcement and ceramic fibre coating, among several other things. Recently, green synthesis of TiO_2/MWCNTs nanocomposites was performed by Khasan et al. [35] via pulsed laser ablation in liquid. Zeta potential fallouts of these nanocomposites displayed a rise as the concentration ratios of MWCNTs increased.

As was already discussed, there are several processing methods for the production of ceramic matrix composites. These techniques include the co-precipitation route, the solid-state route, the sol–gel route, plasma spraying, laser synthesis, and many others. Co-precipitation and hydrothermal approaches are the most cutting-edge methods for obtaining nanoparticles and a uniform microstructure in composite materials. Utilizing polymer as a surfactant during synthesis has also helped in further improvement. The following section covers various processing methods for the synthesis of CMNCs.

Table 9.3 Processing methods of nanocomposite ceramics and their examples [6]

Synthesis route	Type of composite	Nanocomposite compositions	References
Mechanochemical/solid state synthesis	Oxide/oxide Oxide/non-oxide Non-oxide/non-oxide	HA/$MgTiO_3$/MgO; β-CP/MgTiO3/MgO Al_2O_3/TiB_2, $Al_2O_3/ZrB_2/ZrO_2$ NbC/NbB_2, B_4C/SiC	[43–48]
Polymer precursor route	Oxide/non-oxide Non-oxide/non-oxide	Mullite/SiC, Al_2O_3/SiC ZrC/SiC; Si_3N_4/SiC	[49–58]
Vapour phase reaction	Oxide/oxide Non-oxide/non-oxide	ZrO_2/SiO_2; TiO_2/V_2O_5 Si_3N_4/SiC	[21, 59, 60]
SHS	Oxide/non-oxide Non-oxide/non-oxide	Al_2O_3/SiC; Mullite/TiB_2 Si_3N_4/TiN;$Si_3N_4/MoSi_2$; Si_3N_4/SiC; TiN–SiC–Si_3N_4; ZrB_2–SiC–ZrC–ZrSi	[61–68]
Sol–gel route	Oxide/oxide Oxide/non-oxide Non-oxide/non-oxide	Al_2O_3/ZrO_2;$Al_2O_3/Y_3Al_5O_{12}$; La_2O_3/TiO_2, TiO2/Al_2O_3; $Al_2O_3/SiO_2/ZrO_2$ Al_2O_3/SiO_2; TiO_2/Fe_2TiO_5, $NdAlO_3/Al_2O_3$; Mullite/ZrO_2; Mullite/TiO_2; Al_2O_3/SiC, ZrO_2/SiC; Mullite/SiC; AlN/BN	[69–78]
Co-precipitation method	Oxide/oxide	Al_2O_3/ZrO_2;$Al_2O_3/Y_3Al_5O_{12}$;ZrO_2/Gd_2O_3; $Al_2O_3/LaAl_{11}O_{18}$; $Ca_{10}(PO_4)_6(OH)_2$]/Fe_2O_3/Mullite/Al_2O_3	[79–82]
Solution combustion/spray decomposition	Oxide/oxide Metal/Oxide	Al_2O_3/ZrO_2; FeO/SiO_2; CeO_2–MxOy; MOx–ZnO; γ-Fe_2O_3–TiO_2; $Al_2O_3/ZrO_2/MgAl_2O_4$ Cu/NiO_2	[83–86]
Surface modification route	Oxide/oxide Non-oxide/oxide	Al_2O_3/SiO_2; $ZrO_2/MgAl_2O_4$; $ZrO_2/Al_2O_3/SrAl_{12}O_{19}$; $Al_2O_3/ZrO_2/Y_3Al_5O_{12}$; SiC/$Al_2O_3$; SiC/$Y_2O_3$	[87–91]
Plasma phase	Oxide/Oxide	$LaCeO_{2-x}$/$CuCeO_{2-x}$, ZrO_2/Al_2O_3	[92, 93]
Chemical vapour deposition	Non-oxide/non-oxide	SiC/TiC/C, SiC/$TiSi_2$, SiC/TiC, SiC/C	[94, 95]
Electrospinning method	Oxide/Non-oxide	TiO_2/C nonofibre	[96]

9.3 Synthesis and Processing Techniques of Nanocomposite Ceramics

There are several theories that can be used to synthesize different ceramic matrix composites. The method of synthesis utilized to make the ceramic matrix composite material influences the structural, thermal, and mechanical properties. As a result, choosing the right processing route is crucial to getting the intended results. Researchers have employed a variety of traditional and cutting-edge processing methods to produce different types of CMNCs [36]. A few of them are described below.

9.3.1 Solid-State Route

The traditional method for obtaining various ceramic matrix composites is via solid state [37]. This method involves mixing several oxide powders in a stoichiometric ratio to obtain the desired composition. A high-energy ball mill is used for wet milling of the prepared powder mixture. Several hours are spent doing this to create a homogeneous nanomixture. To obtain a fine and uniform powder mixture, grinding media is typically utilized during mixing. The ball to powder ratio and milling time depends on the desired powder size. For improved homogeneity, wet milling is favoured over dry milling, which is carried out in the appearance of any fluid phase like acetone or ethyl alcohol or propanol. For the elimination of moisture and organic matter, as well as the phase transition, the prepared mixed powder is dried and calcined at the desired temperature. To achieve the desired shape, the synthesized powder is mixed with a very little amount of binder and then compressed to a certain pressure to form pellets. The manufactured pellet is ultimately dried before being sintered at a high temperature for a short time duration in order to develop its microstructure, undergo a phase change, and achieve densification. A number of characterizations were performed on the obtained calcined powders and sintered pellets.

9.3.2 Sol–Gel Method

In this method [38], a stoichiometric mixture of two or more precursor solutions is used. With constant stirring at room temperature, this solution is stabilized. Drop by drop, ammonium hydroxide solution is added to this stirred mixture. The hydroproduction gel causes a constant rise in the viscosity of the solution. Finally, when a sufficiently high viscosity is reflected, pH is maintained at 7–8. The received gel is aged for a short while at room temperature. The precipitation that has formed is removed using distilled water. The filtered precipitate is washed to remove any remaining acidic and basic ions, and it is then dried for a short period of time at a

temperature below 100 °C. Following that, the obtained powder is examined utilizing several characterization techniques.

9.3.3 Pechini Method

This technique generates a metal nitrate solution by combining metal isopropoxide with nitric acid. In the Pechini process [39], metallic ions from metal nitrate nonahydrate and -hydroxy carboxylic ions combine to produce polybasic quelates. The final solution's pH is kept at a somewhat lower level, around 2. The solution is polyesterized by heating it to a temperature below 100 °C and stirring it with polyfunctional alcohol. A resin with a high viscosity is produced by further heating to a higher temperature of around 175 °C. The glassy gel that results from this transformation of the viscous resin is rigid and transparent. This dehydrated gel is put through an attrition mill for a few hours to turn it into powder. To obtain the desired powder particle size, the milled powder is sieved. By heating it at a higher temperature, the precursor oxide can eventually be formed.

9.3.4 Laser Synthesis Route

For laser synthesis, conditions of the vapour/plasma non-equilibrium, that are produced at the surface by a strong laser pulse, are one of the basic requirements [40]. In the laser synthesis process, a powder mixture including various oxides is compacted into pellet form under a specific load. This compact is laser-treated utilizing continuous-action laser light at a wavelength of 1064 nm. Irradiation causes the surfaces of specimens to develop concave channels (tracks). Their production is linked to high temperatures inside the irradiation zone, where melting and sintering processes occur before solidification. These tracks might be readily taken out of the compact discs. The loose, somewhat sintered powder was removed from the lower sides of the tracks. During the irradiation process, phase formation also takes place. Different characterization, procedures are used to examine synthesized materials.

9.3.5 Melt Synthesis Route

The first oxide particles are weighed and mixed in an ethanol medium as part of the melt synthesis process [41]. The mixture is first dried and then melted in an arc furnace. A small amount of graphite is added to the melt in order to absorb radiation. To assure complete melting, a second melting is performed and then cooled to room temperature. For the purpose of making powder grounding is done. With the help of various characterization techniques, more studies may be conducted.

9.3.6 Co-precipitation Route

The co-precipitation route [42] involves homogeneously mixing various metal salts, which are subsequently precipitated with the aid of any basic media, often ammonia solution. After preparation, the precipitate is washed to eliminate excess basic and acid ions. To make powder, the washed product is dried, calcined, and then ground. Two distinct approaches can be used to achieve co-precipitation. The first method of precipitation is called direct precipitation, while the second is called inverse precipitation, where the salt solution is poured into the precipitator and stirred to produce a precipitate. Compared to the precipitate produced by the first method, the precipitate obtained by the second method is more finely scattered. The co-precipitation method has the following benefits:

- A quick and easy method of preparation.
- The ability to easily alter particle size and content.
- Several choices for changing the particle surface state and overall homogeneity.
- Using the co-precipitation technique, the smallest size particles with rounded shapes can be produced.

9.3.7 Hydrothermal Synthesis

By employing the initial precursor powder in the hydrothermal process [34], fine powders can be produced. These precursors are put into an autoclave that is lined with Teflon. For various reaction periods, the reactor is heated to a temperature between 100 and 150 °C under certain uniaxial pressure. After being thoroughly dried in a hot air oven for a few hours to eliminate all hygroscopic water, the obtained product is rinsed with distilled water to flush out any soluble components. The dry powder is sinterized for a short period of time at a high temperature. Hydrothermal synthesis depends heavily on the control of pH and solubility. According to reports, a higher pH level aids in de-agglomerating the powder and lowering particle size. During sintering, small particles with a higher solubility have a tendency to form big crystals. This morphological shift aids in densification, which leads to an improvement in mechanical behaviour. Utilizing a polymer as a surfactant during the hydrothermal synthesis process has resulted in recent advancements. The employment of a surfactant in tandem with a hydrothermal method results in the following benefits:

- The produced powder has nanoscale (less than 100 nm) sized particles.
- The finished sintered product has a homogenous and fine-grained microstructure.
- A lower synthesis temperature and a faster reaction.
- Well-crystallized solid solution that does not require additional thermal processing.

Ceramics materials are usually grouped into two types: (i) Oxide Ceramics and (ii) Non-oxide Ceramics (which include carbides, borides, nitrides, silicides, etc.). Therefore, the ceramic-ceramic nanocomposite may be of four types: (i) Oxide/oxide ceramic, (ii) oxide/non-oxide ceramic, (iii) non-oxide/oxide ceramics, and (iv) non-oxide/non-oxide ceramics [5, 6]. Apart from as described above, there are many other recent and advanced synthesis routes available to fabricate nanocomposite ceramics [15, 22, 23]. A few synthesis routes and the type of ceramic nanocomposite along with a few examples are provided in Table 9.3.

9.4 Characterization of Nanocomposites Ceramics

The phase formation of the nanocomposite ceramics can be done by the X-Ray Diffraction (XRD)/Neutron diffraction techniques. Composite phases may be identified and indexed by the various crystallographic databases and matching programme software's. Rietveld's refinement of X-ray/Neutron data gives the exact phase information of the synthesized system. Scanning electron microscopy (SEM), transmission electron microscopy (TEM), wide-angle X-ray diffraction (WAXD), and small-angle X-ray scattering are the primary methods used to examine the macroscopic morphology and surface texture of nanocomposites (SAXS). The most popular application for SEM is morphological analysis because it is so simple. Although many researchers consider TEM to be a crucial tool for qualitative analysis, structural defect analysis, and spatial distribution studies, it takes a lot of time and doesn't yield quantitative data. The position, character, and strength of basal reflections are frequently seen using WAXD to examine the structure. DSC/TGA is used to analyse the thermal behaviour of nanocomposites. Numerous methods, including nuclear magnetic resonance, Fourier transform infrared, SAXS, and optical birefringence can be used to determine the molecular structure of nanocomposite materials [2, 5, 23]. Chemical characteristics can be examined using methods like water contact angle measurement and X-ray photoelectron spectroscopy. An analytical method called inductively coupled plasma (ICP) spectroscopy is used to quantify and identify the elements in a sample matrix based on how they ionize. Many other characterization tools like STM, AFM, UV, PL, RAMAN, etc. are also used to characterize the nanocomposite powder samples.

9.5 Physical Properties of Ceramic Nanocomposite

Depending on the morphology and interfacial properties of the component materials, nanocomposite materials may exhibit unique chemical and physical properties. The features of the nanocomposite ceramics depend on the composition of the matrix and reinforcement, the properties of the ceramics and nanofiller, and the structure of the final composite. The nanocomposite ceramics possess perceptible variances in

their thermal, mechanical, optical, magnetic, electrical, and textural properties when collate with traditional ceramic composites.

9.5.1 Mechanical Properties

The surface morphology and the materials used to make nanocomposites play a significant role in their mechanical properties, such as tensile strength, elongation, and modulus. Due to the high stiffness and high aspect ratio of the nanofillers, as well as their good affinity with the ceramic, ceramic nanocomposite's mechanical properties have improved. It has been suggested that classic ductile metals can be made hard and robust by reducing grain size [5, 23]. Conventional ceramics, on the other hand, are capable of plastic deformation. Few reports on the ductility of nanoceramics have been published. The research is a result of processing challenges, particularly densification of nanoceramics without any grain formation. Fabricating test specimens is a difficult task because mechanical tests need specimens with specific dimensions. As a result, the majority of the data were collected utilizing an indentation technique, which calls for a straightforward fixture and a small sample size. The fact that pre-cracking is not necessary is another benefit. These tests can also provide Young's modulus, hardness, toughness, and strain-rate sensitivity. A nanoindenter can be used as a probe to analyse the qualities in the nanoscale size range since it is particularly well suited for measurements in the nanometer range. A hot hardness tester can be used to measure the fluctuation in mechanical properties (such as hardness with temperature). By altering the indenter's loading rate, one can generate strain-rate-sensitivity rates, which provide a formability indication. There are numerous publications that cover various elements of toughening and strengthening mechanisms in ceramic nanocomposites. In contrast to intragranular types of composites, which have very similar microstructures, Bhaduri et al. obtained mechanical property data for nano/nano types of composites [17]. The Al_3O_3-SiC nanocomposites, in which SiC particles are found at intragranular regions of the massive Al_2O_3 grains, have been studied by Niihara's group [24, 53, 54]. According to Carroll et al.'s [97] findings, their nanocomposites have a smaller critical flaw size. Finally, a model predicting the mechanical behaviour of such nanocomposites was brought forward by Levin et al. Powders that had just been synthesized were used to form Al_2O_3–ZrO_2 nano/nanocomposites [98]. Provided that both phases are nanocrystalline, this structure is truly nano/nano. This substance is modestly tough and has a moderate hardness [99]. Properties at high temperatures were investigated by Hirano and Niihara to determine how bend strength varied with temperature for monolithic Si_3N_4 and Si_3N_4/SiC nanocomposite materials [53, 54]. As the temperature increased up to 1,200 °C, where abrupt degradation was observed, the strength of Si_3N_4 gradually reduced. However, nanocomposites demonstrated nearly the same strength up to 1,400 °C. The increased high-temperature strength may be the result of the intergranular SiC particles' obstruction of grain-boundary

sliding. Kennedy et al. [100] examined the high-temperature mechanical characteristics of an Al_2O_3–SiC nanocomposite with 550 MPa strength at 1,250 °C. Even after 96 hours at 1,350°C, the oxidation behaviour of such composites showed that very little oxidation had taken place. In additional studies, the relationship between hardness and temperature was examined for both monolithic and nanocomposite materials. At 1,200 °C and 1,400 °C, the fracture strengths were 1,200 MPa and 800 MPa, respectively. Si_3N_4/SiC nanocomposites' R curve behaviour was studied at high temperatures (1,500–1,650 °C). With a maximum crack-growth resistance, almost twice as high as the beginning value, rising R curves were obtained. Near the ductile area, it was found that the rate of fracture propagation consistently and significantly decreases. Ohji et al. [101] conducted creep measurements on monolithic alumina and an Al_2O_3–SiC nanocomposite at 1,200–1,300 °C. 50, 100, and 150 MPa of applied loads were used for the creep experiments at 1,200 °C, and 50 MPa at 1,300 °C. The creep resistance of nanocomposites was superior to that of monolithic alumina. In a given stress range, the minimum creep rate of the composite was found to be about three orders of magnitude lower than that of the monolithic. The nanocomposites have a tenfold longer creep life. This extraordinary creep resistance is thought to be the result of the strong interface bonding between Al_2O_3 and SiC. Nano/nanocomposites may have accelerated creep as opposed to inhibited creep in intragranular nanocomposites, which may be advantageous in the formation of superplastic materials. Fine and equiaxed microstructures and the suppression of grain development during deformation are necessary microstructural conditions for micrograin superplasticity. The fine-grained microstructures were maintained after consolidation, grain expansion was minimal due to the duplex structures of Si3N4 and SiC grain, and the nucleation of elongated -Si3N4 grains was restricted. These factors were satisfied in Si_3N_4/SiC nanocomposites. Si_3N_4/SiC nanocomposites were tested for tensile strength by researchers [23]. In contrast to prior studies, where strain rates varied from 2×10^{-5} to 1.6×10^{-4}/s with an elongation of 110%, the compositions displayed superplastic elongation larger than 150% at 1,600 °C.

9.5.2 Thermal Properties

The thermal behaviours like heat flow, weight loss, and expansion coefficient of nanocomposite ceramics can be analyzed by DSC/TGA and dilatometry techniques. The thermal stability of nanocomposites can be estimated from the weight loss on heating material at higher temperatures. The heat resistance of nanocomposites may be measured by the Heat Deflection Temperature (HDT) Technique. The application of ceramic materials depends significantly on their thermal conductivity. In a certain range, improving the thermal conductivity of ceramic materials using particular techniques can enhance their capacity for heat conduction, heat convection, and heat radiation, hence broadening their use range [23]. Polycrystalline diamond ceramics, aluminium nitride, beryllium oxide, silicon nitride, and silicon carbide are examples of materials with a high thermal conductivity that are mostly made of oxides,

nitrides, carbides, and borides. The nanocomposite with good thermal conductivity has multiple applications, such as thermal interface materials, printed circuit boards (PCBs), heat sinks, connectors, and systems for thermal management. The diffusivity of nanocrystalline/nanocomposite materials is expected to be increased compared to that of their traditional counterparts. Low impurity concentration at the grain boundary, faster diffusion along the triple junctions, various boundary structures, and a multitude of charged defects in ionic ceramics all contribute to the enhancement of diffusivity. Superior mechanical qualities could result from this improved diffusivity. Further advancements in thermal shock resistance are required in order to use ceramic nanocomposites in a larger variety of high-temperature applications. One of the most crucial factors for advancement in this field is fracture strength, which is well established. Thermal shock resistance in Si_3N_4/SiC nanocomposites was reported by Hirano and Niihara [55]. The bend strength of the water-quenched sample was used to determine thermal shock resistance, while the thermal expansion coefficient and thermal conductivity were determined using the laser-flash technique and dilatometer, respectively. When Si_3N_4 with 32 vol.% SiC nanocomposites was mixed, the thermal expansion coefficient increased from $3.4 \times 10^{-6}\ K^{-1}$ for monolithic Si_3N_4 to $4.2 \times 10^{-6}\ K^{-1}$. As the SiC content increased, the thermal conductivity initially increased, then marginally decreased.

9.5.3 Optical Properties

A little research has been done so far on optical properties. During the consolidation of nanocomposites, certain intriguing optical characteristics have been obtained by regulating porosity. Granqvist demonstrated in the early 1980s that the codeposited oxide film exhibited spectral selectivity, making it suitable for effective photoconversion of PV energy [102]. All potential electrochromic materials, which typically consist of crystals of electrochromic metal (Me) oxides, were studied by Granqvist in his report. Under the influence of a voltage pulse, electrochromic devices can change their optical characteristics in a persistent and reversible manner. The quantity of mobile ions in the materials affects the optical modulation. There are many uses for these kinds of materials. Kundu et al. [103], and Huber et al. [104], have examined the optical characteristics of glass ceramics Cu–SiO_2 and GaSb–SiO_2, respectively.

9.5.4 Magnetic Properties

In the literature, the magnetic characteristics of nanocomposites have been documented [105]. The magnetocaloric effect is connected to the most beneficial magnetic property provided by nanoceramics/composites. The decline in magnetic-spin alignment that follows the removal of a magnetic field from a substance raises spin entropy. When the field is reduced adiabatically, the lower lattice entropy is brought about

by the higher spin entropy. The temperature of the substance falls as a result of the reduction in lattice entropy. The magnetocaloric effect is the name given to this shift in temperature. Shull and his colleagues conducted significant research on these phenomena and speculated that low fields and high temperatures would intensify the magnetocaloric effect. $Gd_3Ga_{3.25}Fe_{1.75}O_{12}$ (x <25 K for the current paramagnetic refrigerant $Gd_3Ga_5O_{12}$) is one of the materials utilized for this purpose [106]. By Shull et al. [107] and Roy et al. [108], the magnetic characteristics of glass-metal nanocomposites were assessed. Ultrafine ferromagnetic particles have recently been the subject of a large body of literature, either as separate systems or as nanocomposites. Maya et al. [109] investigated the magnetic characteristics of films made of CoN/BN or CoN/Si_3N_4. A promising field of research is ferromagnetic nanocomposites as data-recording media. Most of the time, by adjusting the particle size and volume fraction, enhanced magnetic performance may be designed. The ferromagnetic component of the film has dimensions that fall within the range of a single magnetic domain, which means that depending on temperature, it may exhibit super magnetic behaviour or a variable level of coercivity. Various scientists investigated the properties of glass-metal nanocomposites (such Ni–SiO_2 or Fe–SiO_2) [110]. The majority of the time, nanocomposites (such as the Ni/SiO_2 and Fe/SiO_2 systems) were found to have increased coercivity. Another area of interest is magnetic nanometal inclusion in a nonmagnetic matrix, such as oxides. The presence of super magnetic iron oxide grains in a metallic silver matrix raises the possibility that these samples may experience enormous magnetoresistance [105].

9.5.5 Electrical Properties

In Nanocomposites, electrical properties depend upon many factors, for example, aspect ratio, dispersion, and conformation of the conductive nanofillers/reinforcement materials in the structure. The electrical properties of the CNT-containing nanocomposites exhibit high energy densities and low driving voltages [5, 23]. The ionic conductivity of the ether/clay nanocomposite is many orders of magnitude greater than that of the comparable clay. With a very low loading of nanotubes, the electrical conductivity is enhanced by several orders of magnitude without affecting other properties like optical clarity, mechanical strength, or low melt flow viscosities. Application of conductive nanocomposite is found in many areas such as electrostatic painting, electromagnetic interference (EMI) shielding, electrostatic dissipation, printable circuit wiring, and transparent conductive coating [17]. Ables et al. [111] provide an overview of the composition and characteristics of granular metal films. Due to their high resistivity, granular metals—which are combinations of metals and insulators—are utilized as electrical resistors. Ables and his team studied Ni–SiO_2, Pt–SiO_2, and Au–Al_2O_3 films in detail. By varying the size of the metal particles and the space between them, a broad range of resistivity can be formed in glass-metal nanocomposites. It is clear that altering the metal phase

or its size can change resistivities by up to four orders of magnitude. Both the classical percolation contribution to electrical conduction and the electron tunnelling contribution to it can be used to explain the fluctuation in resistivity with temperature. As the size of the metal particle is decreased, another significant effect is a fall in the Debye temperature. Phonon softening is the term used to describe a drop in the Debye temperature of this kind [10, 12, 17]. This results from the alteration of an ultrafine particle's phonon spectrum from that of bulk metal. Between 235 and 340 K, these nanocomposites frequently exhibit semiconductor-like properties. Nanocomposites made of polymer and glass are another area of study. $NiONi(OH)_2$ nanocomposites have been suggested for use as humidity sensors by Hwang et al. [112]. The electrical properties of Al_2O_3–SiC were reported by Sawaguchi et al. [113]. Resistivity of the order of 10^{13} ohm cm was found in the composite with SiC below 10 vol.%, but it quickly dropped to 10^6 ohm cm with the addition of 20 vol.%. Therefore, this type of composite can be employed as either insulators or semiconductors by adjusting the volume percent of SiC. A new class of electrically conductive diamond-like nanocomposites with conductivities ranging from 2–4 $\times$ 10^{-4} ohm cm to 10^{14}–10^{16} ohm cm was developed by Dorfman et al. [114]. Applications such as microelectronics and battery technologies are made possible by this material.

9.6 Applications of Nanocomposite Ceramics

Ceramic nanocomposites with their unprecedented property combinations and exceptional design possibilities are establishing themselves as high-performance materials of the twenty-first century and are used in multifarious cutting-edge technologies [1–6]. A schematic diagram is provided in Fig. 9.4 listing out various applications of nanocomposite ceramics.

Recently ceramic–ceramic, ceramic–polymer, and Ceramic–graphene-based nanocomposite and hybrid materials have gained much attention due to their application in many different areas such as energy production, conversion, and storage like solar cells, Fuel Cells, batteries, supercapacitors, and other electrochemical energy devices, sensors, energy harvesting, electromagnetic interference (EMI) shielding, thermal management, biomaterials, catalysts, engineering components, etc [17, 23].

9.7 Nanocomposite Ceramics for Energy Conversion and Storage

Nowadays, ceramic nanocomposites are extensively used in the area of energy conversion storage and sensing.

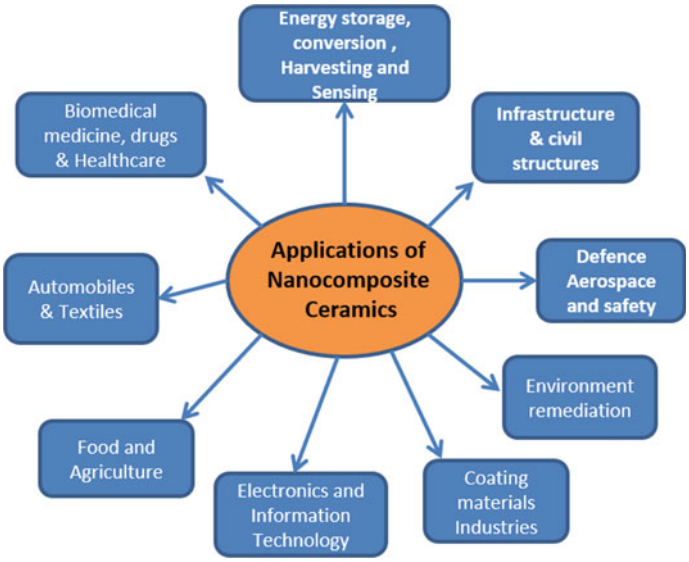

Fig. 9.4 Application area of nanocomposite ceramics

9.7.1 Nanocomposite Ceramics for Fuel Cells (NANOCOFC)

A functional nanocomposite material for fuel cells (NANOCOFC) is being developed using a scientific approach to run SOFCs at low temperatures (300–600 °C). For the purpose of producing electrical power, the synthesized nanocomposite materials can also be used in numerous other electrochemical devices. The main criteria for the development of advanced fuel cell nano-architectures are flexibility and viability [5, 23, 115]. These nanocomposite materials are two-phase materials (TPM), which exhibit some distinctive properties and serve a wide range of functions.

(i) TPM materials have an interface between their two structural phases; this two-phase interfacial area (core–shell structure) is responsible for the material's functionality. The interfacial functionalities of TPM composites eliminate conventional structural constraints.
(ii) In two-phase nanocomposite electrolytes, the ionic transport process is not viable and varies from the bulk structure. The functions and electrical properties of composite materials can be revealed at the interfaces by interfacial superionic conduction (SIC) and its associated mechanisms.
(iii) At low temperatures (300–600 °C), source ions (O_2, H+) and SIC cooperate to improve device performance.
(iv) Fast ion conduction mechanism at interfaces assists in the development of functional composite materials.

(v) Interfacial and surface redox reactions both can provide new opportunities for the advancement of the development of functional nanocomposite for LTSOFCs.

(vi) Nowadays, a variety of Nanocomposite ceramic anode, cathode, and electrolytes are being developed for SOFC applications [115, 116]. For example, for the anode, YSZ/Ni, or YSZ/NiO, SDC/Ni, $La_{0.2}Sr_{0.24}Ca_{0.45}TiO_3$-SDC, etc., For Cathode, LSCF–GDC, LSC-SDC, LSM-YSZ, etc., for electrolyte, SDC-Na_2CO_3, SDC-Al_2O_3, SDC-$SrTiO_3$, LSGM-YSZ, YSZ-SDC, LSGM-SDC nanocomposites, etc., are widely used in SOFCs [117, 118].

9.7.2 Nanocomposite Ceramics for Solar Cells

Nanocomposites have numerous uses in renewable energy sectors, including solar energy conservation. Thin film organic solar cells have been successfully constructed using organic and inorganic nanocomposites, either to boost solar energy harvesting or to assist with charge transport processes [119]. The use of highly absorbent materials with very short photogenerated charge carrier drift or diffusion lengths in solar cells was made possible by nanocomposite absorbers. In perovskite solar cells,

- In order to facilitate the development of perovskite lattice structures, nanoparticles, and nanocomposites serve as useful nucleation sites.
- Increase perovskites' crystallinity and assist in obtaining high grain sizes.
- Enhancement in the absorption of light due to plasmonic effects.
- The distribution of nanoparticles at the grain boundary passivates the perovskite layer, reducing nonradiative recombination.
- enhancing charge transport characteristics through the doping of metal nanoparticles.

TiO_2-based nanocomposites (like GO/TiO_2, etc.) are widely applicable in solar cell as it's having good photocatalytic and photo-electrochemical properties. TiO_2/ZnO is an excellent composite for DSSCs for application in heterogeneous photocatalysis owing to the superior properties of ZnO compared to TiO_2 [23, 120].

9.7.3 Nanocomposite Ceramics for Batteries

In today's information-rich and mobile culture, rechargeable batteries are one of the most important technologies. The cathode, anode, binder, and separator of Li-ion batteries are being developed using nanocomposite materials. Li-ion battery safety, cycle life, rate capability, and specific capacity can all be improved with nanocomposite materials. Carbon nanotubes (CNTs), which have a high surface area and are excellent electronic conductors, can improve the overall electrical and ionic conductivity of active cathode/anode materials by linking their inert "dead" zones [121].

At both low and high C rates, the performance of the $LiFePO_4$-CNT composite was noticeably superior to that of the pure $LiFePO_4$. Due to close contact between the nonaqueous electrolyte and the $LiFePO_4$ active materials and better charge and mass transfer, using graphene in $LiFePO_4$ nanocomposite enabled the attainment of near theoretical specific capacity, extraordinary rate capability, and improved life cycle [122].

9.7.4 Nanocomposite Ceramics for Supercapacitor

Supercapacitors (SCs) find one of the most important places among the energy storage system due to their quick energy storage capacity, enhanced cycle stability, high-power density, and environmental friendliness. A variety of materials have been developed for supercapacitor electrodes, including carbon-based materials (activated carbon, CNTs, GO, conducting polymers) oxides, hydroxides, sulphides, carbides, nitrides, MOF, and MXene. By carefully etching a layer from the MAX phase, a two-dimensional transition metal carbide/nitride ceramic material called MXene is formed [123]. MXene is frequently used as a supercapacitor electrode material. Nanocomposites, MnO_2-MWCNT, NiO/YSZ, etc. are also used as electrode materials in supercapacitors. Advanced nanocomposite for supercapacitor applications was made by combining graphene with metal oxides such as CeO_2, SnO_2, RuO_2, V_2O_5, and Nb_2O_5. CNTs coated with transition metal oxide nanoparticles have proven to be a great electroactive material for supercapacitor applications [124].

Nanocomposite ceramics are also used in many electrochemical devices like electrochromic windows, various kinds of sensors, displays, detectors and optoelectronic devices.

9.8 Nanocomposite Ceramics Applications in Energy Harvesting

Researchers have been looking at alternative energy systems that can harness ambient energy as a result of the global energy crisis and environmental pollution brought on mostly by increased usage of nonrenewable energy sources [125]. Energy harvesting can be understood as a process of converting ambient energy from the environment into electrical energy for use in autonomous electronic devices or circuits. Energy harvesting technologies include thermoelectric energy harvesting, photovoltaic energy harvesting, piezoelectric energy harvesting, pyroelectric energy harvesting, Electromagnetic energy harvesting, Electrochemical Energy Harvesting, wind energy harvesting, vibration-based energy harvesting, etc. Nanocomposite materials can be used in different energy harvesting techniques. Some few are described hereunder.

9.8.1 Multifunctional Materials for Energy Harvester and Sensor

One of the most crucial components of an energy harvester and related systems is energy conversion materials. The efficiency of energy harvesters is significantly impacted by the functionality of such materials, which also dictates the input energy sources. Energy harvesting research typically makes use of materials that exhibit piezoelectric, photovoltaic, pyroelectric, thermoelectric, electromagnetic, magnetostrictive, or electro-caloric characteristics. They are frequently utilized for sensing as well. The simultaneous use of a harvester as a sensor offers a workable solution for multifunctional integrations. Hybrid energy harvesters manufactured from various materials/structures are currently the focus of extensive research in an effort to increase the quantity of input energy sources and the overall capability/effectiveness of energy harvesting processes. Additionally, monolithic and composite materials can be used to produce multifunctional features, such as piezoelectric and pyroelectric, and piezoelectric and photovoltaic. These hybrid and multifunctional materials and devices are also advantageous replacements for the integration of harvester-sensors. Recently, nanocomposites are used as cutting-edge hybrid energy conversion materials and in equipment with multi-source or multifunctional harvesting or harvesting-sensing capabilities. A nanostructured cerium oxide and multiwall carbon nanotube composite (CeO_2/MWCNT) has been successfully formed by Jixing et al. for use in an electrochemical sensor for the measurement of nitenpyram (NIT) [126].

9.8.2 Piezoelectric, Mechano-Magneto-Electric, and Triboelectric Energy Harvesting

Piezoelectric materials are currently among the most promising building blocks for sensing, actuation, and energy harvesting systems. In our surroundings, on a range of platforms, mechanical vibrations and low-amplitude magnetic fields are readily available [125]. These mechanical and magnetic fields might be efficiently converted into electricity to produce a source of energy that is available everywhere. For instance, the infrastructure for electricity transmission creates parasitic magnetic noise at 50/60 Hz all around us. Recent research on MME generators has demonstrated the potential to harness this magnetic field with a high-power density. Low-power electric gadgets, wireless charging systems, and wireless sensor networks can all run on this MME generator. Multiferroic magnetoelectric (ME) composites are attractive building blocks for dual-phase harvesters and MME generators. Numerous study areas, including piezoelectric and triboelectric energy harvesting, have shown increasing interest in low-dimensional materials, such as nanowires, nanotubes, nanofibres, and nanomaterials. Low-dimensional materials have a variety of interesting mechanical, electrical, and electromechanical characteristics that are barely noticeable at macroscales, making them an excellent choice

for energy-harvesting applications. For instance, the theoretically anticipated properties of piezoelectricity or triboelectricity in two-dimensional materials having a non-centrosymmetric structure have been empirically validated. The MgO/$BaTiO_3$ nanocomposite exhibited piezoelectricity after poling. However, the magnitude of the planar piezoelectric coupling factor was reduced to 5% even in MgO/80 vol% $BaTiO_3$ composite [125, 127].

9.8.3 Thermoelectric Energy Harvesting

Thermoelectric energy harvesting (THE) is primarily governed by the function of the thermoelectric generator (TEG) or modules. Thermoelectric systems modules are solid-state devices with direct heat-to-electricity and electricity-to-heat conversion capabilities [125]. These nanocomposites are promising for use in thermal energy harvesting because they have improved thermoelectric properties. In recent years, rapid advancements are seen in the discovery, conceptualization, and practical use of thermoelectric materials and devices. In thermoelectric materials, factors such as mechanical characteristics, thermal stability, and oxidation resistance should be taken into account in addition to the high peak and average ZT of the materials [128]. The design of thermoelectric modules and devices, as well as the materials used for joints and brazing, as well as the manufacturing methods, are all areas where the thermoelectric society has to put more effort since, more than the performance of the individual components, it is the overall performance of the device that drives investment and research efforts and results in practical applications for energy harvesting and cooling. Investigating micro and nanoscale methods enables the integration of low-dimension materials and the production of micromodules for small footprint devices. Recently, Hinterding et al. have investigated the thermoelectric behaviour of ceramic nanocomposites containing undoped $Ca_3Co_{4x}O_{9+}$ and La_2NiO_{4+} in various ratios for enhancing the average ZT value [129]. Apart from high thermoelectric efficiency, alloys such as Bi_2Te_3, $Si_{1-x}Ge_{x,}$ and PbTe, a few nanoceramic oxides, and composite materials are also explored because of their high stability and nontoxic nature. These materials often have a lower figure of merit than alloys, but they have higher thermal and chemical stability. Aluminium incorporated ZnO with other ceramics nanocomposite is also reported as a good n-type thermoelectric ceramic oxide material.

9.9 Conclusions and Future Perspective

Nanotechnology advancements are associated with the future of modern technology. With the development of engineering techniques based on nanocomposite materials, the goal of producing sustainable energy is becoming a reality. These nanocomposite ceramics have demonstrated outstanding outcomes which lead the innovative

types of solar and hydrogen fuel cells, served as effective catalysts for water splitting, and demonstrated good hydrogen storage capabilities. Nanocomposites Ceramics are very important in the field of material science for the past two decades. These ceramic nanocomposites have great potential, marking them as an exciting area in recent years. With the use of nanoparticles, properties like mechanical strength, hardness, and electrical or thermal conductivity significantly improved. In this study, a thorough analysis of several processing techniques used to fabricate ceramic matrix composites is conducted. The mechanical and thermal behaviour of composite has been found to be enriched by the reinforcement of a second ceramic phase in a few ceramic matrixes. Nanocomposite ceramics are being used in many areas like medical and health sector, Energy generation and storage, sensing, infrastructure development, aerospace and defence sector, beauty products, coating materials, paints, electrocatalyst, food, and agriculture, electronics and Information Technology sector, environmental remediation, automobiles, and textiles, etc. Recently, the usage of nanocomposite ceramics in energy harvesting has increased due to its wide application in energy conversion and storage devices.

Acknowledgements Authors acknowledge the funding support of SERB, DST.

References

1. F.J. Heiligtag, M. Niederberger, Mater. Today **16**, 262–271 (2013)
2. B.S. Murty, P. Shankar, B. Raj, B.B. Rath, J. Murday, Springer Berlin, Heidelberg (2013)
3. S. Zhu, H. Meng, Z. Gua, Y. Zha, Nano Today **39**, 101233 (2021)
4. E. Roduner, Chem. Soc. Rev. **35**(7), 583–592 (2006)
5. P.M. Ajayan, S.S. Linda, V.B. Paul, Wiley (2006)
6. P. Camargo, K. Satyanarayana, F. Wypych, Mater. Res. **12**(1), 1–39 (2009)
7. E. Omanović-Mikličanin, A. Badnjević, A. Kazlagić et al., Health Technol. **10**, 51–59 (2019)
8. M. Vinyas et al., Mater. Res. Express **6**, 092002 (2019)
9. J.A. Arsecularatne, L.C. Zhang, Recent Pat. Nanotechnol. **1**(3), 176–185 (2007)
10. I. Ahmad, B. Yazdani, Y. Zhu, Nanomaterials **5**(1), 90–114 (2015)
11. N.P. Padture, Adv. Mater. **21**, 1767–1770 (2009)
12. M. Sen, Nanocomposite materials, in *Nanotechnology and the Environment* (IntechOpen, London, United Kingdom, 2020)
13. S.-M. Choi, H. Awaji, Sci. Technol. Adv. Mater. **6**(1), 2–10 (2005)
14. I. Khan, K. Saeed, I. Khan, Arab. J. Chem. **12**(7), 908–931 (2019)
15. M. Hafeez, Recent progress and overview of nanocomposites, in *Nanocomposite Materials* (IntechOpen, London, United Kingdom, 2022)
16. K.K. Chawla, Ceramic matrix composites, in *Composite Materials* (Springer, New York, NY, 2012), pp. 249–292
17. S. Bhaduri, S.B. Bhaduri, JOM **50**, 44–51 (1998)
18. J. Cho, A.R. Boccaccini, M.S.P. Shaffer, J. Mater. Sci. **44**(8), 1934–1951 (2009)
19. N.P. Bansal, L. Jacques, *Ceramic Matrix Composites: Materials, Modeling and Technology* (Wiley, 2014)
20. P. Palmero, Nanomaterials (Basel) **5**(2), 656–696 (2015)
21. M. Sternitzke, J. Eur. Ceram. Soc. **17**, 1061–1082 (1997)

22. J. Parameswaranpillai, N.H. Kurian, Y. Yu, *Nanocomposite Materials, Synthesis, Properties and Applications* (CRC Press, Taylor & Fransis Group, LLC, 2017)
23. R. Banerjee, I. Manna, *Ceramic Nanocomposite*, vol. 46 (Woodhead Publishing Ltd., 2013)
24. K. Niihara, J. Ceram. Soc. Japan **99**, 974–982 (1991)
25. S. Komarneni, J. Mater. Chem. **2**(12), 1219–1230 (1992)
26. D. Sarkar, S. Adak, N.K. Mitra, Compos. A Appl. Sci. Manuf. **38**(1), 124–131 (2007)
27. D. Sarkar, D. Mohapatra, R. Sambarta, S. Bhattacharyya, S. Adak, N. Mitra, Ceram. Int. **33**(7), 1275–1282 (2007)
28. D. Sarkar, D. Mohapatra, S. Ray et al., J. Mater. Sci. **42**, 1847–1855 (2007)
29. D. Sarkar, S. Adak, S.J. Cho, M.C. Chu, N.K. Mitra, Ceram. Int. **33**(2), 255 (2007)
30. A. Beitollahi, H. Hosseini-Bay, H. Sarpoolaki, J. Mater. Sci. Mater. Electron. **21**(2), 130–136 (2010)
31. J. Kishan, V. Mangam, B.S.B. Reddy, S. Das, K. Das, J. Alloys Compd. **490**, 631–640 (2010)
32. D. Goberman, Y.H. Sohn, L. Shaw, E. Jordan, M. Gell, Acta Mater. **50**(5), 1141–1152 (2002)
33. N. Dejang, A. Watcharapasorn, S. Wirojupatump, P. Niranatlumpong, S. Jiansirisomboon, Surf. Coat. Technol. **204**, 1651–1657 (2010)
34. C. Kaya, J.Y. He, X. Gu, E.G. Butler, Microporous Mesoporous Mater. **54**, 37–49 (2002)
35. K.S. Khashan, A.A. Hadi, I.F. Hasan, Appl. Phys. A **128**, 835 (2022)
36. N. Singh, R. Mazumder, P. Gupta, D. Kumar, J. Mater. Env. Sci. **8**, 1654–1660 (2017)
37. B.S.R. Reddy (ed.), *Advances in Nanocomposites: Synthesis, Characterization and Industrial Applications* (Intechopen, 2011)
38. M. Guglielmi, G. Kickelbick, A. Martucci, *Sol-Gel Nanocomposites* (Springer, NY, 2014)
39. M.Y. Nassar, A.A. Alia, A.S. Amina, RSC Adv. **7**, 30411–30421 (2017)
40. E.V. Barmina et al., Materials (Basel) **13**(18), 4086 (2020)
41. A.V. Rane, K. Krishnan, V.K. Abitha, S. Thomas, Methods for synthesis of nanoparticles and fabrication of nanocomposites, in *Synthesis of Inorganic Nanomaterials* (Woodhead Publishing, 2018), pp. 121–139
42. P.K. Rao, P. Jana, M.I. Ahmad, P.K. Roy, Ceram. Int. **45**, 16054–16061 (2019)
43. S.Z. Khalajabadi, M. Rafiq A. Kadir, S. Izman, M. Zamri, M. Yusop, Appl. Surf. Sci. **324**, 380–392 (2015)
44. A. Fahamin, B. Nasiri-Tabrizi, R. Ebrahimi-Kahrizsangi, Ceram. Int. **38**, 6729–6738 (2012)
45. M.A. Khaghani-Dehaghani, R. Ebrahimi-Kahrizsangi, N. Setoudeh, B. Nasiri-Tabrizi, Int. J. Refract. Metals Hard Mater. **29**(2), 244–249 (2011)
46. B.J. Abbasi, M. Zakeri, S.A. Tayebifard, Mater. Res. Bull. **49**, 672–676 (2014)
47. O. Torabi, S. Naghibi, M.H. Golabgir, H. Tajizadegan, A. Jamshidi, Ceram. Int. **41**(4), 5362–5369 (2015)
48. S.M. So, W.H. Choi, K.H. Kim, J.S. Park, M.S. Kim, J. Park, Y.-S. Lim, H.S. Kim, **46**(7), 9575–9581 (2020)
49. B. Su, M.A. Sternitzke, in *Fourth Euro-Ceramics*, ed. by A. Bellosi (Gruppo Editoriale Faenza Editrice S.p.A., Faenza, Italy, 1995), pp. 4109–4116
50. D. Galusek, J. Sedláček, P. Švančárek, R. Riedel, R. Satet, M. Hoffmann, J. Eur. Ceram. Soc. **27**, 1237–1245 (2007)
51. R. Riedel, L. Toma, C. Fasel, G. Miehe, J. Eur. Ceram. Soc. **29**, 3079–3090 (2007)
52. D. Pizon, L. Charpentier, R. Lucas, S. Foucaud, A. Maître, M. Balat-Pichelin, Ceram. Int. **40**, 5025–5031 (2014)
53. R. Riedel, K. Strecker, G. Petzow, J. Am. Ceram. Soc. **72**, 2071–2077 (1989)
54. J. Wan, R.G. Duan, M.J. Gasch, A.K. Mukherjee, Mater. Sci. Eng. A **424**, 105–116 (2006)
55. T. Hirano, K. Niihara, Mater. Lett. **22**, 249–254 (1995)
56. K. Niihara, T. Hirano, A. Nakahira, K. Izaki, K. Ishizaki, K. Niihara, M. Isotani, R.G. Ford (eds.) *Elsevier Applied Science* (London, UK, 1992), pp. 103–111
57. R. Riedel, M. Seher, J. Mayer, D.V. Szabo, J. Eur. Ceram. Soc. **15**, 703–715 (1995)
58. J. Mayer, D.V. Szabo, M. Rtihle, M. Seher, R. Riedel, J. Eur. Ceram. Soc. **15**, 717–727 (1995)
59. S. Choi, M.S. Lee, D.W. Park, Ceram. Int. **33**, 379–383 (2007)
60. A.W. Weimer, R.K. Bordia, Compos. B Eng. **30**, 647–655 (1999)

61. S. Kim, Met. Mater. Int. **8**, 455–458 (2002)
62. Z.I. Zaki, E.M.M. Ewais, M.M. Rashad, J. Alloy. Compd. **467**, 288–292 (2009)
63. K.V. Manukyan, S.L. Kharatyan, G. Blugan, J. Kuebler, Ceram. Int. **33**, 379–383 (2007)
64. S.L. Kharatyan, K.V. Manukyan, H.H. Nersisyan, H.L. Khachatryan, Int. J. SHS **12**, 19–34 (2003)
65. J.C. Han, Q.C. Chen, S.Y. Du, Y.V. Wood, J. Eur. Ceram. Soc. **20**, 927–932 (2000)
66. H. Wanbao, Z. Baolin, Z. Hanrui, L. Wenlan, Ceram. Int. **8**, 2211–2214 (2004)
67. H.Y. Ryu, H.H. Nersisyan, J.H. Lee, Int. J. Refract. Metals Hard Mater. **30**, 133–138 (2012)
68. D.D. Jayaseelan, D.A. Rani, T. Nishikawa, H. Awaji, F.D. Gnanam, J. Eur. Ceram. Soc. **20**, 267–275 (2000)
69. S.M. Naga, E.M. Abdelbary, M. Awaad, Y.I. El-Shaer, H.S. Abd-Elwaha, Ceram. Int. **39**, 1835–1840 (2013)
70. A. Towata, H.J. Hwang, M. Yasuoka, M. Sando, K. Niihara, Compos. A **32**, 1127–1131 (2001)
71. W. Wang, D. Weng, X.D. Wu, Progr. Nat. Sci. Mater. Int. **21**, 117–121 (2001)
72. S.M. Naga, A. El-Maghraby, Mater. Charact. **6**, 174–180 (2011)
73. G. Urretavizcaya, J.M. Porto Lopez, A.L. Cavalieri, Mater. Lett. **43**, 281–285 (2000)
74. Y. Xu, A. Nakahira, K. Niihara, J. Ceram. Soc. Jpn. **102**, 312–315 (1994)
75. L. Gao, H.Z. Wang, J.S. Hong, H. Miyamoto, K. Miyamoto, Y. Nishikawa, S. Torre, J. Eur. Ceram. Soc. **19**, 609–613 (1999)
76. H.Z. Wang, L. Gao, J.K. Guo, Ceram. Int. **26**, 391–396 (2000)
77. K.G.K. Warrier, G.M. Anilkumar, Mater. Chem. Phys. **67**, 263–266 (2001)
78. P.R. Strutt, T.D. Xiao, K.E. Gonsalves, R. Boland, **2**, 347–353 (1993)
79. P.R. Rana, S.K. Pratihar, S.J. Bhattacharyya, Mater. Process. Technol. **190**, 350–357 (2007)
80. M.L. Balmer, F.F. Lange, V. Jayaram, C.G. Levi, J. Am. Ceram. Soc. **78**, 1489–1495 (1995)
81. X. Han, Z. Liang, L. Feng, W. Wang, J. Chen, C. Xue, H. Zhao, Ceram. Int. **41**, 505–513 (2015)
82. H. Wang, L. Gao, Z. Shen, M.J. Nygren, Eur. Ceram. Soc. **21**, 779–783 (2001)
83. H. Wang, H. Huang, J. Liang, J. Liu, Ceram. Int. **40**, 3995–3999 (2014)
84. Y.Q. Wu, Y.F. Zhang, W.S. Wang, J.K. Guo, J. Eur. Ceram. Soc. **21**, 919–923 (2001)
85. D.L. Trandafir, C. Mirestean, R.V.F. Turcu, B. Frentiu, D. Eniu, S. Simon, Ceram. Int. **40**, 11071–11078 (2014)
86. M. Zhou, J.M.F. Ferreira, A.T. Fonseca, J.L. Baptista, J. Eur. Ceram. Soc. **18**, 495–500 (1998)
87. J. Chandradass, M.H. Kim, D.S. Bae, J. Alloys Compd. **470**, L9–L12 (2009)
88. S. Bhaduri, S.B. Bhaduri, E.J. Zhou, Mater. Res. **13**, 156–165 (1998)
89. K. Tahmasebi, M.H. Paydar, J. Alloys Compd. **509**, 1192–1196 (2011)
90. L.H. Reddy, G.K. Reddy, D. Devaiah, B.M. Reddy, Appl. Catal. A **445–446**, 297–305 (2012)
91. D. Li, H. Haneda, N. Ohashi, S. Hishita, Y. Yoshikawa, Catal. Today **93**, 895–901 (2004)
92. J. Harra, J.P. Nikkanen, M. Aromaa, H. Suhonen, M. Honkanen, T. Salminen. S. Heinonen, E. Levänen, J.M. Mäkelä, Powder Technol. **243**, 46–52 (2021)
93. M. Khoshkalam, M.A. Faghihi-Sani, Mater. Sci. Eng. **A587**, 336–343 (2013)
94. J.J. Kingsley, K.C. Patil, Mater. Lett. **6**, 427–432 (1988)
95. P. Cortesi, H.K. Bowen, Ceram. Int. **15**, 173–177 (1989)
96. Y. Xiong, J. Qian, Y. Cao, X. Ai, H. Yang, ACS Appl. Mater. Interfaces **8**, 16684–16689 (2016)
97. L. Carroll, M. Sternitzke, B. Derby, Acta Mater. **44**, 4543–4552 (1996)
98. I. Levin, W.D. Kaplan, D.G. Brandon, T. Wieder, Acta Metall. Mater. **42**, 1147–1154 (1994)
99. I. Koltsov, J.S. Koziorowska, M.P. Welenc, M. Małysa, G. Kimmel, J. McGlynn, A. Ganin, S. Stelmakh, Materials **11**, 829 (2018)
100. T. Kennedy, M. Poorteman, F. Cambier, S. Hampshire, J. Eur. Ceram. Soc. **17**, 1917–1923 (1997)
101. T. Ohji, A. Nakahira, T. Hirano, K. Niihara, J. Am. Ceram. Soc. **77**, 3259–3262 (1994)
102. C.G. Granqvist, Mater. Sci. Eng. **20**, A168 (1993)
103. D. Kundu et al., J. Am. Ceram. Soc. **77**, 1110 (1994)
104. C.A. Huber et al., J. Phys. Codens. Matter. **5**, A337 (1993)

105. G. Barrera et al., Appl. Sci. **9**(2), 212 (2019)
106. R.D. Shull, J. Iron Steel Res. Int. **14**, 69–74 (2007)
107. R.D. Shull et al., IEEE Trans. Magn. **37**(4), 2576 (2001)
108. S. Roy, D. Das, D. Chakravorty, D.C. Agrawal, J. Appl. Phys. **74**, 4746–4749 (1993)
109. L. Maya, M. Paranthaman, J.R. Thompson, T. Thundat, R.J. Stevenson, J. Appl. Phys. **79**, 7905–7910 (1996)
110. D. Chakravorty, Bull. Mater. Sci. **15**, 411–420 (1992)
111. B. Ables et al., Adv. Phys. **24**, 407 (1975)
112. Kim, Hwang et al. Bull. Korean Chem. Soc. **26**, 1881–1884 (2005)
113. A. Sawaguchi, K. Toda, K. Niihara, J. Ceram. Soc. Japan. **99**, 510 (1991)
114. V.F. Dorfman et al., Thin Solid Films **212**, 274 (1992)
115. B. Zhu, J. Nanosci. Nanotechnol. **11**, 8873–8879 (7) (2011)
116. H.H. Lim et al., in *Sol-Gel Based Nanoceramic Materials: Preparation, Properties and Applications*, ed. by A. Mishra (Springer, 2019)
117. Raghvendra, P. Singh, Ceram. Int. 43(15), 11692–11698 (2017)
118. Raghvendra, R.K. Singh, P. Singh, J. Mater. Sci. **49**, 5571–5578 (2014)
119. S. Saadi, B. Nazari, J. Compos. Compd. **1**(1), 41–50 (2019)
120. B. Boro, B. Gogoi, B.M. Rajbongshi, A. Ramchiary, Renew. Sustain. Energy Rev. **81**, 2264–2270 (2018)
121. J. Wan et al., Mater. Today Nano **4**, 1–16 (2018)
122. W. Dua et al., Phys. Chem. Chem. Phys. **22**, 1953–1962 (2020)
123. X. Zeng et al., J. Materiomics **7**(6), 1198–1224 (2021)
124. D. Yang, Application of nanocomposites for supercapacitors: characteristics and properties, in *Nanocomposites—New Trends and Developments* (IntechOpen, London, United Kingdom, 2012)
125. A.E. Shalan et al., *Advances in Nanocomposite Materials for Environmental and Energy Harvesting Applications* (Springer, 2022)
126. J. Ai, X. Wang, Y. Zhang et al., Appl. Phys. A **128**, 831 (2022)
127. T. Nagai, J. Korean Phys. Soc. **32**, S1271–S1273 (1998)
128. C. Jeong et al., Int. J. Precis. Eng. Manuf.-Green Technol. **7**(1), 247–267 (2020)
129. R. Hinterding, Z. Zhao, M. Wolf, M. Jakob, O. Oeckler, A. Feldhoff, Open Ceram. **6**, 100103 (2021)

Chapter 10
Polymeric Nanocomposites: Synthesis, Characterization, and Recent Applications

Saurabh Shivalkar, Sneha Ranjan, and Amaresh Kumar Sahoo

Abstract Nanomaterials have been extensively studied over the last few decades owing to their unique physicochemical properties. Recent advancement in the field of nanoengineering also provides the opportunity for easy and precise modifications in the structural aspects of these nanomaterials to get exceptional functional advantages over their bulk counterpart. Polymeric nanocomposites are one such modification, where nanoparticles or nanofillers are dispersed homogeneously in the polymer matrix to get better physicochemical properties, which are apt for various applications and thus offer significant scientific as well as industrial interest. Moreover, the kin association of nanotechnology with polymer chemistry provides several new synthesis routes and formulation protocols, which are favorable for the large-scale production of nanocomposites. The opportunity of modulating the ratios of polymer matrix and inorganic components (e.g., nanoparticles) provides the benefits to control its properties including greater resistance towards moisture and gases, better electrical and thermal conductivity, tunable surface charge, and surface chemistry. Additionally, due to low toxicity and biocompatibility, the polymeric nanocomposites indeed gain an edge over pure nanomaterials and thus become an intrinsic part of several advanced applications in various sectors such as healthcare, medicine, microelectronics, chemical engineering, and mechanical engineering. Therefore, the present chapter specifically focuses on the various synthesis methods, techniques commonly used for characterization, suitable functionalization to tune the properties, and recent advancements in the applications of polymer nanocomposites.

Keywords Polymer nanocomposites · Biopolymeric nanocomposites · Drug delivery · Cancer therapeutics · Microelectronics applications

S. Shivalkar · A. K. Sahoo (✉)
Department of Applied Sciences, Indian Institute of Information Technology, Allahabad, Prayagraj, UP 211015, India
e-mail: asahoo@iiita.ac.in

S. Ranjan
Department of Biotechnology, Babasaheb Bhimrao Ambedkar University, Lucknow, UP 226027, India

D. K. Singh et al. (eds.), *Nanomaterials*,
https://doi.org/10.1007/978-981-19-7963-7_10

10.1 Introduction

Nanotechnology provides a unique scope of developing materials, devices, architecture, and designs having at least one dimension sized from 1 to 100 nm (one nanometer is one-billionth of a meter) that has become a boon to many fields since its inception owing to its remarkable physicochemical properties. Recent progress in this line of interest offers precise engineering at the 'atomic level' for developing materials of any size, and shape, and with the desired functionalization to develop advanced smart materials [1–5]. Moreover, the incorporation of nanoscale materials along with suitable polymers, which are commonly known as polymeric nanocomposites (PoNc) expands the utilities and functionalities of these modalities. Generally, PoNc is made up of polymer (major component) and nanoscale materials (minor component) that exhibit several benefits because of their exceptional properties such as ease of functionalization, better mechanical properties, high thermal stability, biodegradability, and many more. The PoNc exhibit synergistic physicochemical properties that are difficult to get from a single component [6]. The natural and derived forms of polymers have been considered a crucial material for the development of PoNc and deeply tied with human society for a long time. Polymers are abundant in the natural world and can be obtained from a wide range of sources, such as plants, animals, and microorganisms. For the design of suitable polymer composite, primary attention is given to selecting a proper polymer as its characteristics determine the overall properties and function of composite. Several polymers have been proposed by various research teams globally; however, biodegradable and biocompatible polymers offer significant prospects as it's very useful particularly in the field of biomedical. For this, both natural, as well as synthetic polymers, are found to be very useful. A few natural polymers are chitosan, alginate, polysaccharides, hyaluronic acid, dextrin, poly-glycolic acid, and poly-lactic acid. Likewise, examples of a few synthetic polymers are poly-ethylenimine, poly-2-hydroxyethyl methacrylate, poly-lactic-co-glycolic acid, poly-N-isopropyl acrylamide, and dendritic polymers. Also, there are several biopolymers like protein, nucleic acids, and lipids that showed promising outcomes in the design of polymer nanocomposites [7]. Apart from the biomedical applications, the polymer nanocomposites have shown huge prospects in various fields such as energy storage, food, automobiles, and so on [2, 8, 9].

This would be mentioned here that natural polymeric materials have several interesting properties such as unique mechanical strength, high bending and stretching (e.g., rubber) and some of them are extremely hard (e.g., epoxides) [10]. However, quite often natural polymers offer several limitations also as a higher level of structural variability while extracted from natural sources, and demands time-consuming processes of purification and not able to withstand harsh physical as well as chemical treatments. Also, its intrinsic complex structures show the issues of solubility in the desired solvent that hinders its scope of applications [11]. To overcome these, a wide range of synthetic polymers have been developed by various research groups, which are having exceptional advantages over natural polymers, that essentially open up a

spectrum of applications ranging from optoelectronic to biomedical [12]. However, synthetic polymers are generally costly, and involve multiple steps in the synthesis process. On the other hand, polymer composites, which are homogeneous mixtures of inorganic materials and polymers offer significant opportunities to develop advanced hybrid materials. More importantly, the polymer composites provide unique opportunities for crafting and developing a whole new spectrum of materials, where the properties of the materials could be easily tuned as per the demand of the users. These polymer composites are having several benefits like being lightweight, less toxicity, better mechanical properties, easy processing, and economical [13]. Therefore, products that involve the use of polymer composite, which are designed as multicomponent systems by adding different materials such as ceramics, metals, etc., to obtain unique physical properties are gaining huge popularity for scientific as well as industrial applications. For instance, the addition of fillers in polypropylene can significantly enhance the performance of thermoplastic [80]. Similarly, the use of metal and metal oxide nanoparticles (size less than 100 nm) along with polymer showed huge promises to formulating biocompatible polymer composites useful for various biomedical applications like drug/gene delivery, tissue engineering, biosensors, and prosthetic and implants [14]. However, judicious choice of a suitable polymer is very important during the formulation of the nanocomposite as physicochemical and mechanical characteristics of the composite material greatly rely on ratios of hydrophobicity and hydrophilicity groups, Young's Modulus, and biocompatibility of the polymers.

Therefore, researchers are primarily focusing on the development of advanced PoNc materials by combining a specific polymeric matrix with various types of nanoscale materials including metal and metal oxide nanoparticles, carbon nanotubes (CNTs), graphene, graphene oxide, ceramic, glass, etc. It's worth mentioning that the use of nanoscale materials added value to the composite as nanoscale materials have a large surface-to-volume ratio that leads to changes in physical and chemical properties as well as the dominance of atomic behavior on the surface of nanocomposites [15]. Moreover, the higher surface area indicates more interaction within the mixture, which increases the strength, thermal conductivity, heat resistance, crystallinity, and mechanical properties. The present chapter focuses on the synthesis, properties, and characterization techniques of polymeric nanocomposites along with their recent applications in various domains such as biomedical sciences, microelectronics, sensors, optoelectronics, and semiconductor devices.

10.2 Synthesis of Polymeric Nanocomposite

Synthesis of polymeric nanocomposites has been done to develop a more organized structure that shows better properties than pure polymer or polymer composites. Since these composites were made in nano-range for enhancing their physical, chemical, and mechanical properties, therefore it is important to understand how these nanocomposites were synthesized. For this purpose, different methods were

employed for developing PoNc. Some of the most frequently used techniques are solution casting, melt blending, in situ polymerization, and exfoliation adsorption process.

10.2.1 Solution Casting

Solution casting is one of the oldest, simplest, and most versatile techniques for the synthesis of PoNc in the lab. In this case, a polymer is dissolved in a suitable volatile organic solvent or simply aqueous solution followed by the addition of nanoscale materials that are allowed to mix thoroughly using mechanical/magnetic stirring or ultra-sonication. However, the most common method of stirring and mixing the components is ultra-sonication. The ultra-sonication techniques involve ultrasonic tools and an ultrasonic agitator that assist in the development of cavitation (i.e., generation of vapor-filled bubbles in a liquid at low pressures) of the molecules. The ultrasonic tool is kept on top of the ultrasonic agitator and vibrates at around 20 kHz with a small amplitude of 60 to 90 μm resulting in the formation of a large cavity [29, 30]. This cavity keeps moving towards the top, which further results in the dispersion of nanoscale materials (e.g., nanoparticles). When cavitation of molecules breaks, then there is a place for nanoparticles to mix thoroughly which leads to the formation of a homogenous composite. The solvent in the mixture gets evaporated leaving behind nanoparticles which are then placed inside the dryer to obtain polymeric nanocomposite. The steps of solution casting are given below (Fig. 10.1).

One of the most widely used materials is rubber nanocomposites that are developed by the above-mentioned method. For this, the rubber matrix is mixed with carbon-based nanoscale materials (e.g., graphene, graphene oxide, CNTs) as nanofillers in suitable solvents followed by vigorous mixing with the polymer solution through mechanical/magnetic stirring or ultra-sonication. Once the mixing is done, the film casting and solvent evaporation are performed. Also, this is one of the most preferred methods that is used in the development of various elastomer-based nanocomposites. The reinforcing effect of the nanofillers is increased due to hydrodynamic interactions between rubber and nanoscale materials. These nanocomposites have several exceptional properties over pure rubber such as better uniformity of thickness and good mechanochemical response [16]. The use of suitable nanofillers materials improves the compatibility and performance of the polymer nanocomposite that eventually depends on (i) the uniform and homogeneous dispersion of the nanofillers within a polymer matrix, (ii) weight ratio of the nanofiller and polymers, (iii) Aspect ratio of nanofiller shape (like CNTs, Nano-rods), (iv) hydrophilicity and hydrophobicity ratio of nanofiller and polymers, (v) non-covalent interactions between the nanofiller–polymer matrixes. However, one of the prominent issues of solution casting is that solute components (e.g., elastomers/rubber/polymers) must be soluble in a volatile solvent or water and form a stable solution with a reasonable minimum solid content and viscosity, several cases it was found that solute component is not forming a stable

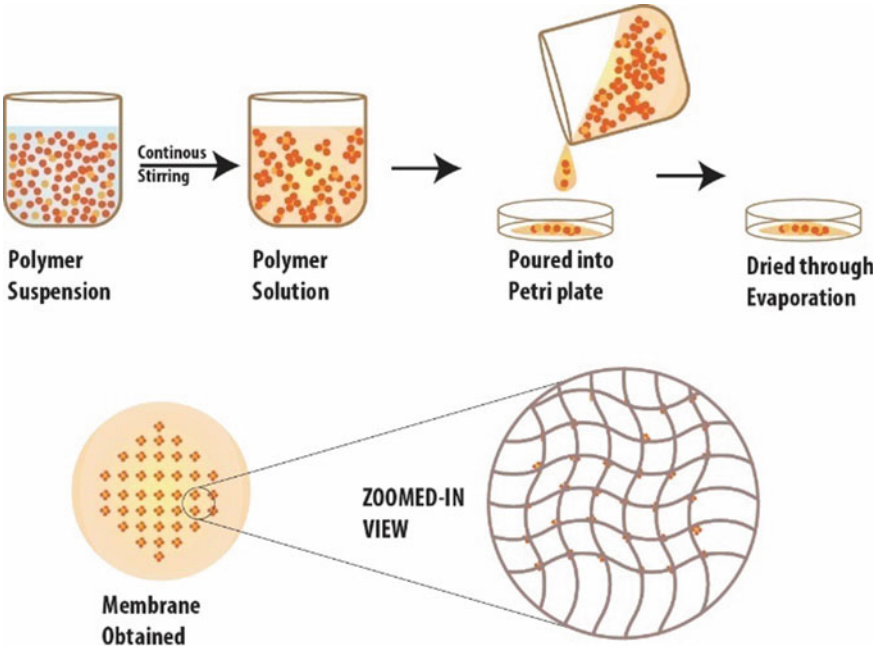

Fig. 10.1 Schematics of synthesis of PoNc using solution casting technique

solution. The method is also costly as compared to the other method of castings such as vacuum die casting and centrifugal casting [16].

10.2.2 Melt Intercalation

Melt intercalation is considered a standard approach for the synthesis of several PoNc materials. It involves annealing of the polymer matrix at a high temperature followed by thoroughly mixing it with the desired amount of fillers or nano-sized reinforcement (mostly intercalated clay) (Fig. 10.2). Finally, kneading is done to the mixture to obtain the uniformly distributed desired PoNc materials [20]. The intercalation is formed as the polymer slowly moves into the filler interlayers due to weak electrostatic forces between the polymer matrix and filler interlayers. The melt intercalation technique is better than solvent casting as it does not rely on solvent to break apart nanomaterials, instead, it uses heat and kinetic energy to disperse nanomaterials into individual nanoparticles. This method is generally ecofriendly compared with solution casting that mostly requires biologically and environmentally harmful solvents for the synthesis of PoNc [19]. Therefore, melt intercalation is preferred for various industrial processes like extrusion and injection molding. This method meets the criteria for large-scale industrial processes and is economical too.

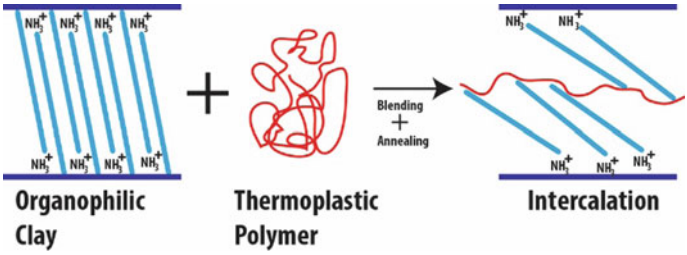

Fig. 10.2 Synthesis of PoNc from organophilic clay as nano-sized reinforcement and thermoplastic polymer using melt intercalation method

As mentioned earlier melt intercalation uses kinetic energy to disperse nanoparticles. This kinetic energy is usually provided by extruders which is a screw pump where the screw rotates (single-screw extruders) or two (twin-screw extruders) in a tightly fitting stationary barrel. However, the drawback is that sometimes surface modifications performed by this method may be damaged during the synthesis process due to very high processing temperature (190–220 °C) [18]. For instance, alkyl ammonium-modified organo-clays usually degrade at the temperature of 140 °C. Therefore, to obtain uniformly dispersed and better exfoliation the processing conditions must be properly optimized, such as lowering the operating temperature or replacing reinforcement with thermally stable alternatives to prevent any degradation during the synthesis process [19].

One of the examples of this method is the development of nylon 6/clay nanocomposites. The nylon 6/clay nanocomposites exhibit superior properties in terms of strength and heat distortion temperature than only the nylon 6 matrix. To prepare nylon 6/clay nanocomposite using the melt intercalation process a dispersed phase is prepared by mechanically mixing high molecular weight polar nylon 6 matrix and organoclay (formed when organic amine salts were ion-exchanged with sodium montmorillonite). Twin-screw extruder is then used to extrude the mixture at the rotational speed of around 30 rpm while maintaining the temperature of the mixing barrel in the range of 180–230 °C. Later, at injection molding temperature and pressure, i.e., 220 °C and 13.5 MPa respectively extrude was pelletized followed by dying and injected into the standard sample [19]. Organoclay was melt-mixed with a high molecular grade of nylon 6 using a twin-screw extruder; here, Organoclay was acting as nanofillers.

10.2.3 In-Situ *Polymerization*

In-situ polymerization involves the mixing of liquid monomer/monomer solution with the nanofillers/nanoparticles. The addition of monomer causes swelling that creates small openings between layers of nanoparticles [20]. The reason being monomers have low molecular weight, are more mobile and can diffuse easily into

the nanofiller interlayers (Fig. 10.3). During this process the reaction temperature such as polymerization time, temperature, and swelling time for better polymerization [18]. Different factors such as temperature, radiation, or diffusion of appropriate initiator/catalyst via cation exchange are responsible for polymerization. Finally, the monomers polymerize in between the interlayers to yield exfoliated or intercalated PoNc. This approach is considered better in comparison to melt intercalation methods. However, recently the focus has been shifted to graphene-based conducting polymer nanocomposites.

Furthermore, thermoplastic and thermoset-based nanocomposites can also be synthesized using in situ polymerization. It would be mentioned here that thermoplastic is a class of polymers that become flexible (i.e., plastic) on heating and harden on cooling and this can be processed many times without any chemical alterations. Some examples are polystyrene, polythene, polyamide, nylon, and polypropylene. On the other hand, thermosets are polymers, which exhibit permanent chemical changes during heating/curing which causes irreversibly hardening, for example, epoxy resins, and phenol–formaldehyde resins. These thermosets and thermoplastics polymers are further grafted on the suitable nanofillers surface to fabricate superior quality nanocomposites [20].

Recently, graphene oxide-epoxy nanocomposites (thermoset-based nanocomposites) were synthesized where graphene oxide nanofillers were dispersed using ultrasonication followed by adding epoxy matrix in a vacuum oven at around 50 °C. While approximately 80% of the solvent was evaporated then a curing agent, m-Phenylenediamine was added with vigorous stirring. Later, these were transferred to a steel mold and kept for drying for 5 h at around 60 °C that removing residual solvents. Finally, pre-cured in an oven for 2 h at around 80 °C followed by post-curing for 2 h at around 120 °C. When visualized under the high-resolution transmission

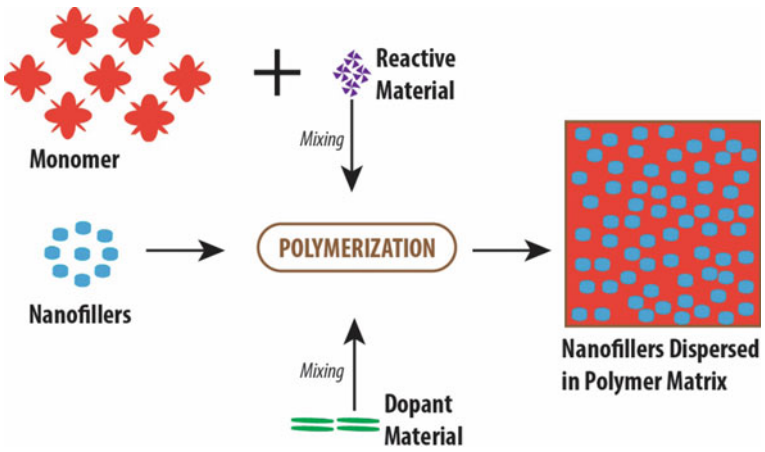

Fig. 10.3 Schematics of in situ polymerization technique for PoNc synthesis

electron microscopy (TEM), uniformly distributed bundles of epoxy functionalized graphene oxide nanocomposites were observed [18–20].

10.2.4 Template Synthesis

Template synthesis is a sol–gel technology that employs the synthesis of several PoNc. This technique involves the preparation of an aqueous solution of the inorganic nanofillers (sol) or a gel with suitable polymer and building blocks made of fillers under the influence of high temperature [21]. Herein, the polymer acts as a nucleating agent that helps in the formation and further growth of the inorganic nanofiller lyotropic liquid crystals. The nanocomposites are formed when the polymer gets trapped within the interlayers of the nanofillers during the growth of these crystals [19]. However, this technique is rarely applied recently due to the use of high temperature for synthesis causing polymer damage. For example, template CNT membrane is annealed at temperature >2000 °C to convert into partially graphitized CNT. Therefore, it is mainly restricted to double-layered hydroxide nanocomposite synthesis only.

10.2.5 Exfoliation Adsorption Process

In this process, the layered clay is exfoliated into monolayer in a solvent that can potentially dissolve the polymer. These polymers enter into the delaminated layer due to the weak forces of the clay layers. The residual solved is evaporated to obtain PoNc. For example, this method was used to synthesize Magnesium–Aluminum layered double hydroxide (Mg, Al-LDH) and poly(methyl methacrylate) (PMMA).

10.3 Properties of Polymeric Nanocomposites

The properties of polymer nanocomposites, as well as structure, are mainly dependent on the characteristics of the used nano-reinforcement and polymer matrix. These hybrid PoNc possess significantly better mechanical, thermal, electrical, and gas barriers compared with the conventional composites. Different combinations of nanofillers and polymer matrices to synthesize PoNc for desired properties and their probable area of applications are given in Table 10.1 [6, 7, 11, 12]. In this section, detailed properties of PoNc are presented.

Mechanical Properties: The material composition and surface morphology of the PoNc translates their mechanical properties such as Young's Modulus, tensile strength, and stiffness. For instance, on the introduction of the polymers into the

Table 10.1 Different combinations of nanofillers and polymer matrices to synthesize PoNc for desired properties and their probable area of applications

S.No.	Nanofillers	Polymer matrix	Acquired properties	Applications
1	Carbon nanotubes	Epoxy	Stiffness and strength	Microelectronics, optoelectronics, and sensors; sports rackets
2	Layered silicates/exfoliated clay	Nylon 6 or thermoplastic polyolefins	Stiffness and strength	Automotive body elements
3	Multiwalled CNT	Different types of polymers	Thermal and electrical conductivity	Semiconductor devices
4	Silver nanoparticles	Chitosan	Antimicrobial effects	Drug delivery; wound dressing
5	Exfoliated clay/Carbon Black	Polyisobutylene/natural rubber/polybutadiene	Strength and permeability barrier	Tires; tennis and soccer balls
6	Silver/Silica	Natural rubber	Antimicrobial and viscosity control	Latex gloves

nanofillers, Young's Modulus of the PoNc varies as a function of its particle concentration, resultantly improving strength and durability. The mechanical properties of PoNc can be significantly improved by opting for the nanofillers of high aspect ratio and high rigidity along with excellent affinity towards the incorporated polymer matrix. Apart from this the composite materials show better friction resistance, durability, and wear performance. For example, layered silicates or exfoliated clay used with nylon 6 or thermoplastic polyolefins provide excellent strength and stiffness to the PoNc that are generally used in automotive industries as body elements [22].

Thermal Properties: Differential Scanning Calorimetry (DSC) technique is generally used to determine the thermal properties of the PoNc. In this method, the thermal stability of the PoNc is analyzed by calculating the total loss of the PoNc material when subjected to uniform heating at a specific temperature known as heat distortion temperature (HDT). The HDT is a material-dependent quantity. For instance, a copolymer of polypropylene has an HDT value range of 50–60 °C. On the other hand, glass fiber reinforced polypropylene has more than double HDT, i.e., 125–140 °C. Therefore, HDT can also be used to calculate the heat resistance properties of the PoNc. The PoNc possessing excellent thermal properties can be used in high-performance thermal management systems, thermal interface material, printed circuit boards, and heat sinks [23].

Electrical Properties: Nano-filler in polymer composites are key material that determines their electrical properties because most polymers are not having good

electric properties. The conductive nanofillers with a high aspect ratio, better dispersion, and alignment provide good electrical properties to the PoNc. For example, nanofillers made of carbon nanotubes (CNT) are considered to provide superior electrical properties to the PoNc as they have low driving voltage and high energy densities. Similarly, organically modified clay, i.e., ether-clay provides enhanced ionic conductive the conventional clay. Additionally, incorporating a very small amount of the CNT (up to 0.1% of weight) can enhance the electrical conductivity of the PoNc to several folds without impacting their existing properties like mechanical or optical. PoNc with good electrical conductivity can be widely used in areas such as electromagnetic interference (EMI) shielding, electrostatic dissipation, conductive transparent coating, printable circuit wiring, and electrostatic wiring [24].

Barrier Properties: The polymer nanocomposite provides excellent gas barrier property due to the high aspect ratio and tortuous dispersion of the nanofillers in the polymer matrix. It would be mentioned here that tortuosity ($\tau = L_t/L$) is the measurement of the ratio of the actual lengths (L_t) to the straight distance (L) between the ends of the fluid pathways of the porous medium. Therefore, an intrinsic structural characteristic restricts the movement of several gas molecules through the PoNc and significantly reduces their permeability. The gas barrier properties of a composite can be monitored significantly by changing the ratios of nanofiller, which are served as an impermeable inorganic material. The addition of nanofiller in permeable polymer matrix leads to (i) reduced available diffusion area, and (ii) tortuous pathway increases the gas diffusion pathways. For example, layered silicate/polyamide PoNc are known to have barrier properties against multiple gases like nitrogen, helium, carbon dioxide, oxygen, and ethyl acetate vapors, thus offering potential applications in various areas [25].

Rheological Properties: Rheological properties suggest the flow behavior of the material. In polymer nanocomposite, the structure and viscoelastic behavior of its matrices (i.e., polymer) and dispersion of the nanofillers play a key role in determining the flow behavior. Matrices of polycaprolactone/nylon 6-based PoNc was found to have improved the flow behavior of polymer matrices [26].

10.4 Characterization of Polymeric Nanocomposites

The polymer nanocomposites are having unique properties and structural aspects. The minute change in structural parameters leads to a change in their properties hugely that ultimately affects the performance of the composite materials. Thus, characterization is a very important aspect for not only understanding their internal structure and composition but also analyzing structural defects and impurities that are compromising the properties of the polymeric nanocomposites. Different characterization techniques such as X-ray diffraction (XRD), scanning electron microscopy (SEM), infrared (IR) spectroscopy, thermal analysis, etc., are performed to understand internal and surface structure. Along with this surface, functional groups and surface chemistry also play a useful role in their altered characteristics. The advanced

characterization tools and techniques offer the scope of detailed characterization at molecular and even electronic levels too. However, in the subsequent section, we have incorporated only commonly used techniques/tools employed for routine characterization of any polymer nanocomposites.

10.4.1 X-Ray Diffraction (XRD)

The XRD is generally used for obtaining the structural information of the material. The working principle lies in the identification of the X-ray diffraction pattern of the short-range and long-range order of crystalline arrangements from the amorphous substances. While X-ray falls on crystalline materials the crystal atoms scatter (i.e., elastic scattering) incident X-rays, due to interaction with atoms' electrons. The intensities and scattering angles of the X-rays changes that are used to produce a specific diffraction pattern via destructive and constructive interference by following Bragg's law [27]:

$$2d \sin\theta = n\lambda \tag{10.1}$$

where d is the spacing between diffracting planes of the crystalline lattice, n is an integer, and θ and λ are the incident angle and wavelength of the X-ray. Therefore, the XRD pattern of the crystalline material will be having highly sharp and intense peaks; no such peaks can be seen in the amorphous material. For example, y-Fe_2O_3/natural rubber-based PoNc show a highly sharp and intense peak due to the presence of dispersed y-Fe_2O_3 nanoparticles in the natural rubber matrix [28]. This is also suitable for determining the deviation of the intrinsic structure of a material due to internal stresses and defects. Apart from this, XRD analysis is found to be very useful for finding lattice parameters, grain size, phase composition, and diameter of the nanoparticles. The XRD samples are generally powder or thin film. Predominantly, powder samples are used for the same; thus it is also known as powder X-ray diffraction (PXRD).

10.4.2 Electron Microscopy

The electron microscopy is technique for obtaining high-resolution images of the biological or non-biological specimens of sizes below micro-range. Basically, there are two different types of electron microscopy namely Transmission Electron Microscopy (TEM) and Scanning Electron Microscopy (SEM). Instead of light, beam of electrons is used for the generation of images in case of electron microscope. The wavelength of electrons is much smaller than visible light, thus resolution of the electron microscopes is far better than that of a light microscope. These are very powerful imaging modalities that can have up to 2 million times magnification than regular

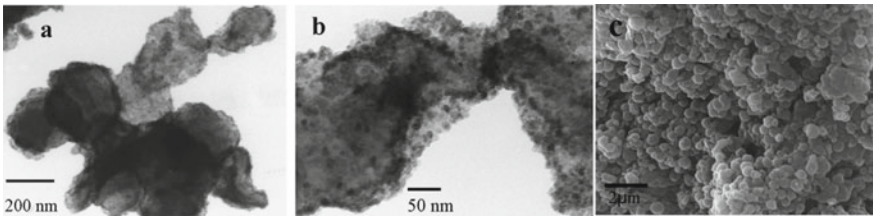

Fig. 10.4 Comparative electron microscopy image; **a** and **b** TEM images of iron oxide-polymethyl methacrylate PoNc in high resolution (**a**) and lower resolution (**b**); **c** SEM images of iron oxide-polymethyl methacrylate PoNc showing 3D morphology (Adapted with permission from [29]. Copyright, 2008, Elsevier)

light microscope. However, the working principle of both the electron microscopes are different, the TEM constructs images based on transmitted electrons (electrons that pass through the sample), and SEM images are formed by detecting reflected or scatter electrons. Thus, TEM provides internal structure of the sample whereas SEM provides information about surface morphology (Fig. 10.4).

In case of TEM, a particle beam of high energy electrons (~60–300 kV) passes through very thin samples that use to focus via electromagnetic lenses for generation of 2D projection images. The magnifications (50 million times) and resolution (<50 pm) of TEM images are better than SEM images. Thus, TEM is very suitable for imaging particle having diameter of less than 10 nm. Additionally, TEM is very useful in observing the physical properties of the nanomaterials such as size, shape, homogeneity, interaction, distribution, crystal structure, internal defects, and degradation. For example, TEM image of iron oxide-polymethyl methacrylate PoNc in high resolution (200 nm) and lower resolution (50 nm) clearly shows the presence of the iron oxide nanoparticle in within the polymethyl methacrylate matrix (Fig. 10.4a, b). However, for the TEM analysis, the sample has to be very thin (preferably less than 150 nm) so that electrons are able to pass through it [29].

On the other hand, the SEM assists in determining the detailed information on surface morphology, conductivity, and fractures of the PoNc. Generally, SEM provides the 3D image of an object, thus found to be a very effective visualization technique of surface characteristics. Additionally, a wide range of mechanical properties of the nanocomposites, i.e., from shape information by the movement of individual molecules of the polymers to more complex structural forms can be obtained from SEM. It can also be used to identify the sites of interface boundary, which is commonly known as grain size and grain boundary. For example, iron oxide-polymethyl methacrylate PoNc can be seen as uniform size granular structure in Fig. 10.4c. The resolution of SEM images of nanocomposites depends on the acceleration voltage of the electron beam. The resolution of the SEM is also reached up to a few nanometers only and the operating voltage generally varies from 2–20 kV. Nowadays, the low-voltage mode of operation is also possible that is essential for recording the image of the non-conductive polymer and/or biological specimens. Low acceleration voltage (LAV) primarily shows the surface information

of the composites, while at high acceleration voltage (HAV) sub-surface features can also be obtained. Therefore, LAV is mostly used for obtaining topological information on the PoNc while the HAV showing the sub-surface features are generally used for testing the conductivity of the PoNc [29]. Moreover, before analysis, the SEM sample was coated with plasma gold, which is very crucial for obtaining high-quality SEM images while working with a beam-sensitive and non-conductive material.

10.4.3 Infrared Spectroscopy

Infrared (IR) spectroscopy is an analytical technique used to determine chemical information such as functional groups in the materials. The interaction of the IR light with a molecule induces the vibrations in the bonds. Each functional group in a molecule is having its characteristic vibrations depending on atomic masses and bond strength. While the energy of the IR light matches with the corresponding energy necessary to initiate molecular vibrations that leads to absorption of light (i.e., IR band). Thus, each band obtained in the IR spectrum is the representation of specific functional groups. This is also considered a fingerprint of the sample. The present IR spectroscopy technique uses an IR light source that passes through an interferometer consisting of a beam splitter, a fixed mirror, and a moving mirror. The arrangement of the interferometer separates the spectral components of the IR light in time, which then passes through the sample. Finally, the detector records an interferogram as a function of time, which is processed via a mathematical operation (Fourier transform) to translate the interferogram into the actual spectrum in the frequency domain. Thus, this is also known as Fourier transform infrared spectroscopy (FTIR). The infrared absorption frequency range varies from 400 to 4000 cm^{-1} wave number, which is suitable for recording of vibration of organic and inorganic molecules. This technique requires minimum steps of sample preparation, as well as provides a fast and reliable data recording option. Additionally, FTIR analysis is suitable for recording qualitative as well as quantitative data of the samples. It is also found to be suitable for the identification of unknown samples via the signature of the presence of various functional groups. Therefore, this is frequently used in organic chemistry such as characterization of polymeric materials and coordination chemistry. In PoNc, the presence of nanomaterials and polymers can be identified at different wavelength [28]. For example, the FTIR spectrum of polystyrene shows the characteristic peaks over 2800–3100 cm^{-1}, while the addition of Titanium Oxide in higher concentration shows the characteristics peaks of Titanium Oxide in the spectrum of polystyrene/Titanium Oxide PoNC film [81].

10.4.4 Thermal Analysis

Physical and chemical properties of the nanocomposites as a function of temperature are known to be thermal analyses of the composites [30]. Two different techniques are involved in thermal analysis, i.e., thermogravimetric analysis (TGA) and differential thermal analysis (DTA). The TGA is the measurement of change in PoNc weight as a function of temperature. On the other hand, in DTA an inert reference material is introduced to measure the difference between the temperature of PoNc and inert material as a function of time. Differential scanning calorimetry (DSC) is an almost similar technique as DTA but it involves quantitative measurement of change in enthalpy of the PoNc as a function of temperature or time. DSC is frequently used to determine the thermal behavior of the PoNc. The underlying principle of DSC is that it assists in finding the glass transition temperature (Tg) of polymer and its PoNc. Higher Tg values show the presence of inorganic materials in the polymer matrix of the PoNc [28].

10.5 Applications of Polymeric Nanocomposites

Polymeric nanocomposite has turned out to be a very promising material that can potentially apply diverse areas. The schematic representation of the promising areas of applications of the polymeric nanocomposites is given in Fig. 10.5.

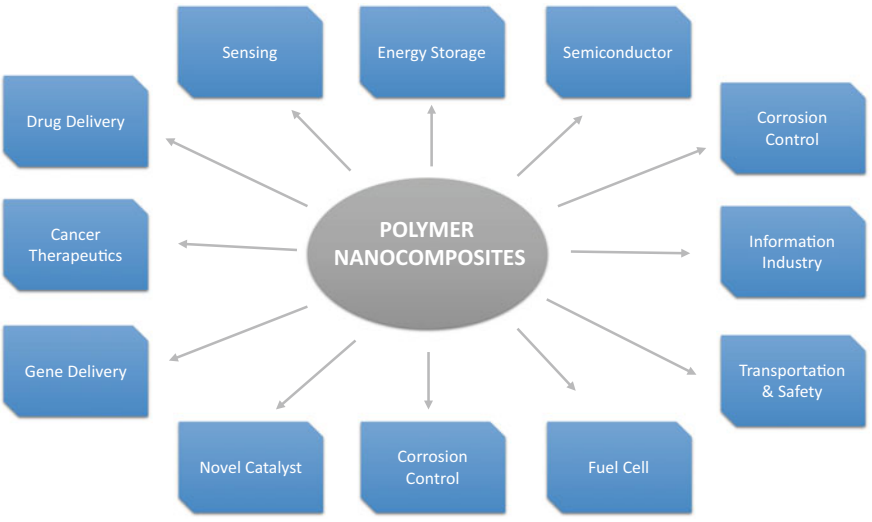

Fig. 10.5 Schematic representation of various areas of applications of polymeric nanocomposites

10.5.1 Biomedical Applications: Drug Delivery; Cancer Therapeutics; Gene Delivery

Interest in polymeric nanocomposite has been growing around the globe day by day owing to its remarkable characteristics and the prospect of a wide range of applications. Particularly, the healthcare-related applications are prioritized by various research groups due to their unique features like (i) easy functionalization with suitable cell targeting ligands like an antibody, aptamer, peptides, etc., (ii) biodegradable and biocompatible, (iii) economical as compared to other drug/gene delivery cargos, (iv) less chance of immunogenic and inflammatory response, (v) generally, non-allergenic and environmentally friendly [7].

Various polymeric nanocomposites (PoNc) were developed to apply in various biomedical applications, especially in drug/gene delivery to the tumor site (Fig. 10.6). Nanocarriers mediated delivery systems over several limitations of present drug delivery systems like insufficient bioavailability, short half-life, instability in blood circulation, and cytotoxicity. Moreover, the nanocarriers designed by using polymer nanocomposite are ably performed both active targeting via receptor-ligand interactions and passive targeting depending on the size of the nanocarriers that permeate via leaky vasculature of the tumor sites only. It would be mentioned here that active targeting via conjugation of specific ligands provides better selectivity; however, this requires tedious steps of chemical conjugation followed by purification. Also, it demands sophisticated and costly laboratory setups. On the other hand, passive targeting by nanocarriers is easy as well as results enhanced permeability and retention (EPR) effect as nanoparticles of certain sizes (around 200 nm) accumulate more near tumor tissue as compared to normal tissues. Therefore, nanocarriers mediated 'on target' drug delivery got huge attention over the conventional route of drug administration that leads to 'off target' drug accumulation that raises side effects and cost of treatment [6, 7].

Another important aspect of the polymeric nanocarriers is that it provides the scope of sustained (i.e., over a specific period) and controlled release (specific amount) of payloads. Sustained release is very important as a slow release of payloads over some time (i.e., more than a few weeks) eventually reduces the frequency of the drug uptakes. The conventional method of drug uptake greatly relies on the frequent uptake of drugs after a particular time interval for a specific period, which is indeed painstaking and challenging for persons with certain medical conditions or infants. On the other hand, sustained and controlled drug release from engineered nanocarriers may overcome these concurrent limitations as it releases a prescribed amount of drugs (i.e., therapeutic dose of the drug) from the nanocarriers for a 'programmable time period'. Hence, the proper managing of the release profile of therapeutics over time in correlation with drug concentration is a very promising feature of the polymer nanocarriers. Along with this, release profiles can be monitored via external and/or internal stimuli. Various external stimuli like light, heating, magnetic field, ultrasound, etc., are commonly explored as promising non-invasive means to induce the

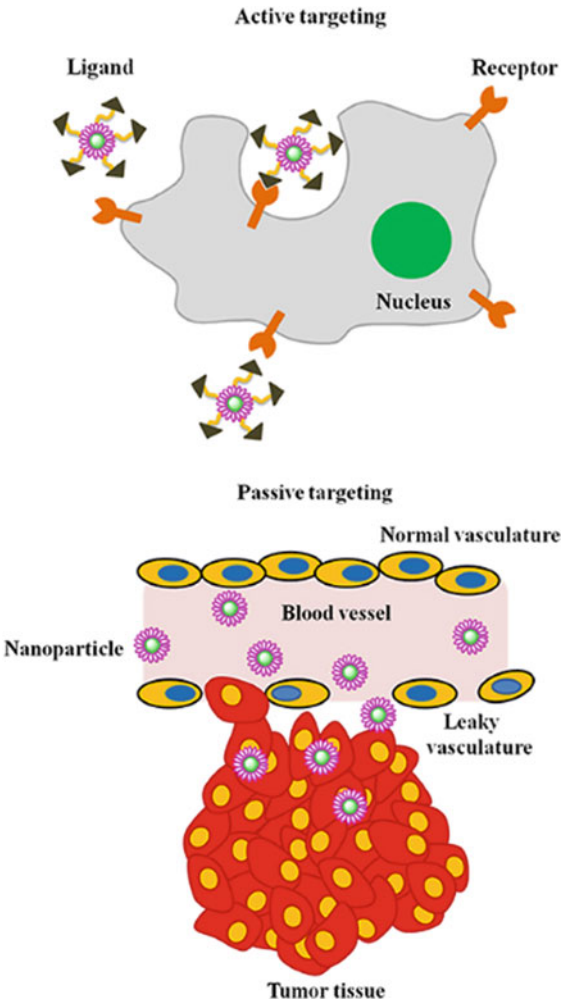

Fig. 10.6 Illustration of active and passive drug delivery mechanism for PoNc to the tumor cells (Adapted with permission from [32]. Copyright, 2014, Frontiers)

release of the drugs from the nanocarriers. Likewise, pH, ionic concentration, and enzymes are served as intra-cellular stimuli to modulate the drug release [31].

The use of polymer nanocomposites is not only limited to this, but numerous other biological applications are also possible by using such engineering materials. To add to this list, polymer nanocomposites are found to be very useful for tissue engineering, the development of biosensors, and the construction of prosthetics and implants. However, in the subsequent sections, we'll mainly focus on the drug/gene delivery via polymer nanocomposite. As integral components, various nanoscale materials including metal NPs (e.g., Au NPs, Ag NPs, Cu NPs), metal oxide NPs (ZnO NPs, TiO_2, Fe_3O_4 NPs) NPs, carbon-based nanomaterials (CNTs, graphene, graphene oxide, C-dots), hydroxyapatite, clay, etc., have been employed

with polymer to prepare PoNc for the above-mentioned applications [31]. Moreover, some biopolymer-based drug carriers were also developed from mixed nanocomposites like yolk-shell, core–shell, and coupled/impregnated nanostructured compounds embedded in a suitable polymer matrix [32, 33]. These drug carriers are found to have the potential to transport various types of pharmaceutical compounds and supplements required during the treatment process.

Chitosan-based PoNc: Chitosan (CS) is a cationic linear polymer made up of N-acetyl-d-glucosamine and D-glucosamine units. This is commonly derived by deacetylation from chitin present in shells of shrimp, prawns, crabs, and other crustaceans. Chitosan has several interesting properties such as pH-responsive solubility, antimicrobial activity, and low immunogenicity. Moreover, due to its positive surface charge, chitosan is preferred as suitable drug/gene delivery material through various routes of administration (e.g., intra-cellular, oral, and subcutaneous, etc.). Several studies demonstrated that chitosan might serve as a penetration enhancer by facilitating the opening of the tight junctions of the epithelial cells. This also helps both paracellular transport (i.e., passing through the intercellular space) and transcellular transport (i.e., substance moves through a cell) of drugs. Reports also demonstrated that chitosan makes non-covalent interactions with mucus which is also negatively charged.

Additionally, the chitosan polymer can be easily converted to chitosan nanoparticles (CS NPs) with suitable ionotropic agents like tripolyphosphate (TPP), nucleic acids, polyphosphoric acid (PPA) and hexametaphosphate (HMP), etc. The positively charged CS NPs facilitate strong interactions with the negatively charged cell membrane and hence facilitates cellular localization as well as retention. Besides, the CS NPs protect the payload from enzymatic or environmental effects. Thus, it becomes one of the widely used biodegradable materials for developing pH-dependent delivery cargo [34].

For example, recently a PoNc was developed from layered self-assembly of chitosan/sodium alginate (CS/SA) functionalized with graphene oxide nanosheets loaded magnetic iron oxide nanoparticles (GOmNP) for the targeted delivery of anticancer drug doxorubicin hydrochloride (DOX). The diameter and average thickness of GOmNP-CS/SA bio-PoNc was approximately 0.5 μm and around 50 nm, respectively. This bio-PoNc is superparamagnetic, therefore was used for magnetically targeted cellular uptake. The DOX was loaded to GOmNP-CS/SA bio-PoNc through electrostatic and π–π stacking interactions. The drug loading capacity of GOmNP-CS/SA bio-PoNc was extremely noteworthy as it loads up to 137% (w/w) [35]. Thus, pH-responsive drug release and dispersion of GOmNP-CS/SA-DOX bio-PoNc were significantly improved.

Chitosan nanocarriers showed great prospects for the delivery of nucleic acids (DNA, siRNA, miRNA, etc.) inside the cells. These cationic polymer/polymer composites can easily form polyplex with nucleic acids via electrostatic interactions. Moreover, the chitosan nanocarriers not only increase the gene loading efficiency but also protect the genetic materials from exogenous nuclease activity. A nanocomposite of chitosan and gold nanocluster (Au NCs) was developed for delivery of a cytosine deaminase uracil phosphoribosyl transferase (CD-UPRT) suicide gene. The

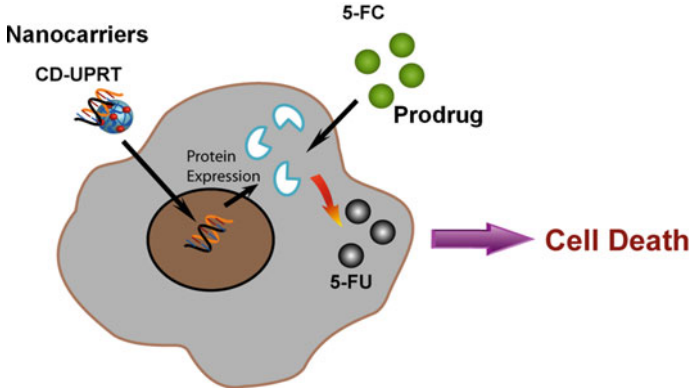

Fig. 10.7 Schematics of PoNc synthesized from gold salt and biopolymer chitosan with mercaptopropionic acid (MPA) at room temperature. The suicide gene (pCD—UPRT) was added to PoNc to form stable polyplex formation that led to apoptosis in the transfected cells. Fluorescent gold nanocluster of PoNc was also used for the imaging of cells

gene produces CD-UPRT enzyme after transcription and translation that converts a nontoxic prodrug 5-fluorocytosine (5-FC) to 5-fluorouracil (5-FU) and other toxic metabolites that inhibit DNA replication and transcription, thus destroying transfected cancer cells. The gold nanocluster used was highly fluorescent that was employed for tracking the nanocarriers by microscopic imaging. (Fig. 10.7) [36]. The study showed that chitosan-based nanocarriers protect the genetic material from nuclease degradation.

In another study, the in situ polymerization technique was used to prepare a silver-chitosan polymer composite by crosslinking the chitosan with silver nanoparticles via sodium tripolyphosphate. The study demonstrated that silver nanoparticles (Ag NPs) enhanced the swelling ability of the chitosan beads resulting in the prolonged release, otherwise encapsulated drugs in normal chitosan beads are released immediately upon swelling. The composite also exhibited excellent antibacterial activity against *Staphylococcus aureus* and *Escherichia coli* [37].

Silver-based PoNc: Among various types of metal and metal oxide nanoparticles, silver nanoparticles (Ag NPs) got special attention owing to their strong antimicrobial as well as cytotoxic activity. The cellular activity of Ag NPs/its composites becomes stronger depending on the size of the NPs, and it was demonstrated that the smaller the size better the activity. Apart from this, the shape of the Ag NPs also plays a very vital role in its biological activity. Several anisotropic NPs showed better activity as compared to spherical NPs. Thus, the overall cellular activity of the Ag NPs depends on the various factors (i) size, (ii) shape, (iii) surface charge as positively charged NPs showed better activity as compared it's the counterparts, (iv) surface functional groups, (v) Types of cell lines used in the study, and (vi) Cell division stage, i.e., cell cycle. After cellular uptakes, Ag NPs influence several events like oxidative stress, destabilization of the cell membrane, cell cycle arrest, DNA damage, and apoptosis.

Also, several in-vivo studies were performed that stated that Ag NPs may cause inflammatory responses and genotoxicity [38].

There are reports, which demonstrated that Ag NPs alone or in combination with other agents were able to show strong anti-cancer activity by causing apoptosis-mediated cell death. The primary cause of silver-based cytotoxicity is the generation of a high level of reactive oxygen species (ROS). A study developed chitosan nanocarriers to deliver silver NPs (size 10 nm) to human colon cancer cells (HT 29). The cell viability assay showed the IC50 dose (i.e., cell viability reduced by 50%) of Ag NPs was 0.33 μg/mL. The Ag NPs caused apoptosis via a mitochondria-dependent pathway as depolarization of mitochondrial membrane potential ($\Delta\Psi(m)$) was evident. Corresponding SEM images also showed the formation of apoptotic bodies. It was also proposed that elevated levels of ROS accelerated apoptosis in addition to the classical caspase signaling pathway [39].

To get synergistic activity combination therapy of Ag NPs was performed with suitable anti-cancer agents like recombinant protein. Poly(lactic-co-glycolic acid) nanocarriers (PLGA NCs) were used to encapsulate both Ag NPs and recombinant interferon-gamma (IFN.γ) protein that was used for the imaging and treatment of the two different types of cancer cells namely, cervical cancer (HeLa cells) and breast cancer (MCF-7 cells) (Fig. 10.8). It would be mentioned here that IFN.γ acts as tumoricidal and antiviral agents [40]. The combination therapy showed apoptosis-mediated cell death. Another study was conducted where folic acid was chemically conjugated with nanocarriers for targeted delivery of silver nanocluster (Ag NCs) and drugs. The metal nanoclusters (size less than 2 nm) are the smallest class of the nanomaterials. In this size, realm nanoparticles do not show surface plasmon resonance (SPR) rather it exhibits luminescence due to discreet energy levels. It was demonstrated that while silver nanocluster was delivered with paracetamol dimer that was selectively showing better cell killing activity against folic acid receptor overexpressed cancer cells (HeLa cells) as compared to folic acid receptor downregulating lungs cancer cell lines (A_{549} cells). This combination therapy synergistically caused apoptosis for selective cancer cell lines [41].

Alginate-based PoNc: Sodium alginate is a naturally occurring polysaccharide obtained from brown algae and soil bacteria. These polysaccharides can easily be crosslinked with calcium (Ca) ions to prepare a microsphere with 3D networks. This polymer is readily available at low cost and biocompatible. Therefore, it is frequently used as a suitable material for food thickener, bone tissue engineering, and drug delivery [42] systems. For example, a microsphere-shaped hydroxyapatite nanoparticles-sodium alginate-chitosan (H–S-C) polymer composite was developed by emulsion (oil/water) crosslinking procedure in presence of Ca ions as a crosslinker. The morphology and dispersion of the hydroxyapatite nanoparticles in the H–S-C polymer composite are dependent on the concentration of sodium alginate, rotation speed, and ratio of oil to water in the emulsion. This composite was loaded with an anti-cancer drug (DOX) drug and their release profile was examined at different pH. The DOX-loaded H–S-C microsphere showed pH-sensitive drug release [43]. Similarly, hydrogel beads of curcumin-loaded sodium alginate crosslinked with zinc oxide nanoparticles (CUR-S-ZNP) were prepared for the prolonged release of curcumin.

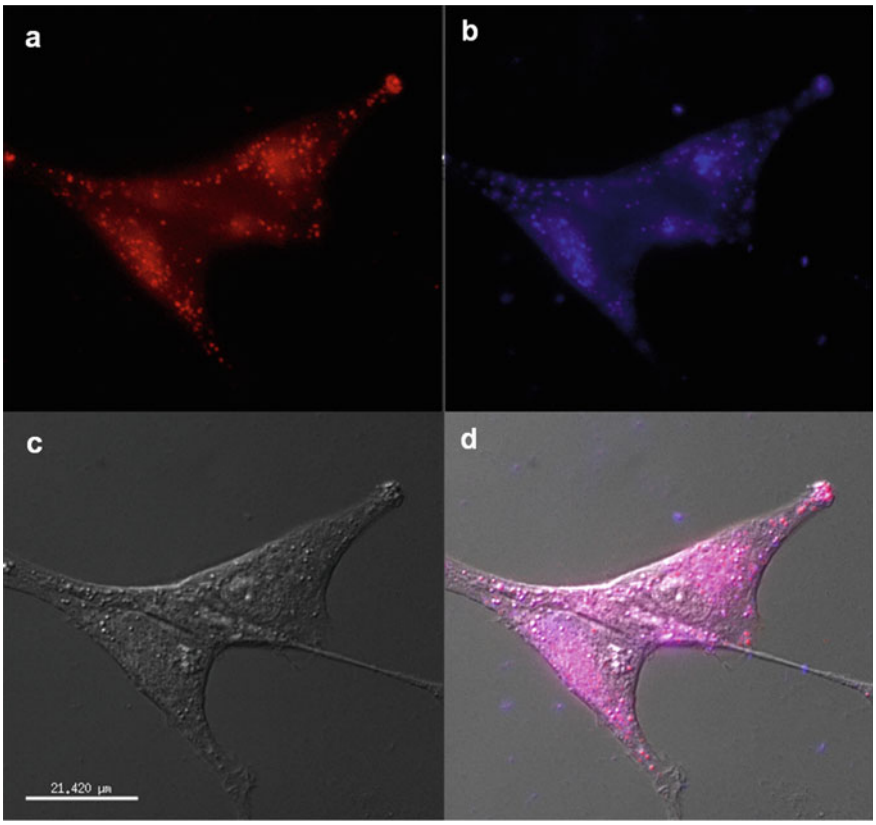

Fig. 10.8 **a–d** Fluorescence microscopy images of *HeLa* cells with silver nanocluster-paracetamol dimer PoNc. **a** and **b** are showing the red and blue emission, respectively due to silver nanoclusters and paracetamol dimer when excited under ultra-violet light **c** phase contrast image **d** merged images of **a** and **b** is showing magenta color due to presence of both paracetamol dimer and silver nanoclusters inside the cells (Adapted with permission from [40]. Copyright, 2014, RSC)

Generally, pure hydrogels undergo burst release, whereas the as-synthesized CUR-S-ZNP hydrogels provided sustained release that essentially decreased the chances of immediate physiological clearance of curcumin [44].

Cellulose-based PoNc: Cellulose is a polysaccharide of β-1,4-linked anhydrous-D-glucose repeating units, synthesized via acid hydrolysis. The nanocrystals of cellulose, cellulose nano-whiskers, and cellulose nanoparticles are nano-sized counterparts of cellulose. These nano-sized (diameter: 10 to 100 nm; length: 0.025–2 μm) counterparts can potentially undergo hydrophilic interaction and H-bond formation, thus can modulate the physiological efficiency of the drug delivery system. Other than hydrophilicity, nano-sized cellulose has low density, high modulus, high surface area, and a high aspect ratio. This is also biocompatible, non-irritant, and biodegradable thus widely employed in the area of biomedical. The properties have made

cellulose a better reinforcement material in PoNc, hydrogels, scaffolds, etc., for a wide range of applications [45, 46]. For example, PoNc prepared by combining iron oxide nanoparticles with cellulose nanocrystals (Fe@CNc) and loaded with curcumin works as drug carriers. These Fe@CNc drug carriers were magnetically triggered and used in-vitro for the treatment of colon cancer. The drug loading efficiency of the Fe@CNc was approximately 99.35% and stabilized using a Pickering emulsion. The application of a magnetic field of 0.7 T causes the curcumin to release from the Fe@CNc drug carrier and inhibited the growth of human colon cancer cells (HCT116) [47].

Hybrid lipid polymer enveloped matrix PoNc: Another interesting class of polymer is lipids, which are biodegradable also, so it has been already applied in several biomedical applications. However, the hydrophobic nature of lipid restricts its application in quite a few cases. To address this, the development of a hybrid composite of polymer with other suitable agents like proteins, showed immense scope to monitor its physicochemical properties. Both materials have their advantages and disadvantages in terms of chemical properties, cost, and availability. The hybrid lipid polymer material would result in several benefits and thus be found to be suitable for various biological applications. Additionally, this hybrid lipid-polymer PoNc (HPL-PoNc) would create a possibility of an improved multifaceted drug delivery system that may overcome several challenges [48] like improved drug availability and therapeutic index. Moreover, a judicious choice of combination of HPL-PoNc can be employed for nucleic acid delivery also. There are various types of hybrid protein-lipid polymer composites available like lipid-hydrogel nanocomposites, lipid-mesoporous silica nanoparticles, and lipid-polyester nanocomposites [49].

Effectively delivery of sparingly water-soluble drugs is a very crucial challenge while the use of this hybrid polymer composite facilities the transport of such drug molecules in biological fluids. This hybrid composite is also suitable for the delivery of multiple drugs which are having different hydrophobicity and hydrophilicity by a single drug delivery module. For example, a lipid-based drug delivery system was used to encapsulate amphiphilic chemotherapeutic drugs paclitaxel (hydrophobic) and gemcitabine hydrochloride (hydrophilic) into lipid-coated poly(lactic-glycolic) acid (PLGA) nanocomposite using nanoprecipitation. This drug combination showed improved cytotoxicity in a human pancreatic carcinoma cell line. Therefore, the study proposed that delivery of multiple drugs having different polarities could be transported effectively by this hybrid cargo. Similarly, encapsulated hydrolysable paclitaxel–cisplatin drug conjugate in HPL-PoNc provided an improved therapeutic effect against ovarian cancer cells [34]. In another approach, chemotherapy and radiotherapy (yttrium90) were synchronized using HPL-PoNc to perform chemo-radiation therapy. To avoid the interference of radioisotopes with docetaxel (drugs), the HPL-PoNc was integrated with phospholipids that were modified with the chelator diethylene triamine pentaacetate, in the PEGylated lipid monolayer of the PLGA core. Later, A10 RNA aptamer was tagged with HPL-PoNc for selective delivery of docetaxel and yttrium90 (90Y) to prostate-specific membrane antigen overexpressing prostate cancer cells. This combination therapy showed the synergistic killing of prostate cancer cells [50, 51].

Clay-based PoNc for controlled drug delivery: The clay (a soft, earthy material having a grain size <4 μm) materials are gaining attention from the pharmaceutical industry due to its unique physical and mechanical properties. Some examples of pharmaceutical-grade clay are kaolinite, fibrous clay, and smectites. These are generally chemically inert, and cost-effective [52]. Studies showed that the presence of a very less amount of clay (less than 5%) in a composite increases its heat resistance, and mechanical strength, and reduced gaseous permeability significantly [53, 54]. Additionally, pharmaceutical-grade clay possesses excellent intercalation properties thus preferred in sustained drug release applications [55–57]. The clay material also easily interacts with organic materials (drugs) and cell surfaces. Moreover, polymer–clay composite is useful for the development of nanocarriers having a size range of 1–1000 nm [58].

Collagen-based PoNc: Collagen is a naturally occurring fibrous protein present in the extracellular membrane of mammalians. The size of the collagen fibers usually ranges from 50 to 500 nm; therefore, these are inherently suitable for the development of the polymer nanocomposite which is suitable for various biomedical applications [59]. For example, hydrolyzed collagen was reinforced with polycaprolactone-based semi-conductive polymer composite to form an electrically actuated controlled drug delivery cargo. Herein, the in situ polymerization technique was followed to produce conductive nanofibers with the matrix of a hydrogel synthesized through radical copolymerization of acrylic acid. These hydrogels did not cause any cytotoxicity and were used for hydrocortisone drug release under electrical stimuli [60].

Moreover, gene delivery was also executed by using a hybrid nanocomposite. For this purpose, PoNc was developed by complexing DNA-polyethyleneimine-silica nanoparticles and fibroblasts in collagen hydrogel matrices. The transfection efficiency was monitored by altering the particle size and molecular weight of the polyethyleneimine. The study proposed that transfection efficiency was remarkably affected by the cell proliferation in collagen hydrogel matrices [61].

10.5.2 Corrosion Control

Clay-based polymer composite is now of great interest for the development of anti-corrosive material. The PoNc structure and its interfacial characteristics greatly influence the anti-corrosion efficiency. Clay-based PoNc coating over the metallic surfaces creates an effective physical barrier that prevents corrosion due to the presence of chemicals. These physical barriers generally protect metals against the corrosion caused due to the presence of aggressive species such as O_2 and H^+ ions. For example, clay-based PoNc was prepared when inorganic nanolayers of montmorillonite (MMT) clay dispersed in the organic poly-(methylmethacrylate) (PMMA) using *an* in situ polymerization technique. Furthermore, 1% (w/w) of MMT-PMMA composite was applied to the cold-rolled steel to observe its anti-corrosive property. Generally, the anti-corrosive property is estimated from the values of corrosion

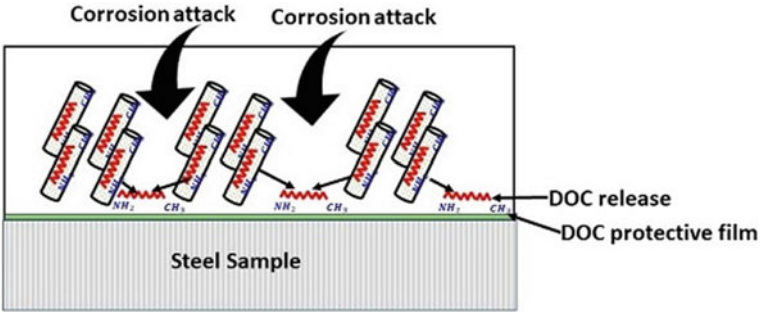

Fig. 10.9 Schematics of epoxy matrix reinforced titanium nanotubes loaded dodecylamine (DOC) was used for corrosion control by coating over the steel surface (Adapted with permission from [82]. Copyright, 2019, MDPI)

potential (E_{corr}), polarization resistance (Rp), corrosion current (I_{corr}), and corrosion rate (Record). Experimentally, polymer nanocomposite coated cold-rolled steel showed a higher E_{corr} value as compared to its uncoated counterpart [62]. Similarly, epoxy matrix reinforced titanium nanotubes loaded dodecylamine (DOC) was used for corrosion control by coating over the steel surface (Fig. 10.9). Spectroscopic analysis confirmed the release of the inhibitor (DOC) in response to pH change over the steel surface. It was also found that anti-corrosion properties can be controlled more effectively when pH was dropped to 2 as it supported improved release of DOC from the PoNc [82].

10.5.3 Fuel Cell Applications

Fuel cells require the polymer-based proton exchange membrane (pPEM), electrodes binder, and matrices for bipolar plates. Conventionally, electrodes possess polymer nanocomposite having carbon black particles (0.5–1.0 mm) with platinum catalyst particles (2–5 nm) and Nafion polymeric binder. However, when platinum nanoparticles are functionalized with carbon nanotubes (mostly single-walled) having Nafion as a binder increases the efficiency of the electrodes as compared with carbon black particles electrodes [63]. Furthermore, the incorporation of the nanoparticles or PoNc in pPEM can improve electron conductivity as well as mechanical properties. Therefore, nanoparticles were added to direct methanol fuel cells to prevent methanol crossovers [64]. The conductivity and mechanical properties of the proton exchange membrane can be improved at higher temperatures by adding nano-sized particles of Heteropoly-acids (such as $H_3PW_{12}O_{40}$; $H_3PMo_{12}O_{40}$) [65]. Titanium oxide, zirconium hydrogen phosphate, and zirconium phosphate nanoparticles in pPEM showed promising results in direct methanol fuel cells [66–68].

10.5.4 Semiconductor

A semiconductor is a material that has the interim value of electrical conductivity of the conductor and insulator. Generally, the semiconductor has a band gap range of 1–1.5 eV such as MoS_2-polyvinylidene fluoride PoNc, MnO_2-paraffin, and CdSe-paraffin PoNc, while there are also semiconductors with wide band gaps, i.e., from 2–4 eV such as MoO_3—paraffin PoNc, $BaTiO_3$—polyaniline PoNc, TiO_2—paraffin PoNc and ZnO—poly(vinyl alcohol), and $SrTiO_3$-epoxy PoNc [69]. These semiconductor nanocomposites are reinforced with multi-walled carbon nanotubes (MWCNTs) to incorporate highly semiconducting layers into high-voltage electrical power cables. For this purpose, a homogenous mixture of MWCNT is reinforced into the semiconducting nanocomposites. The thermal, mechanical, and electrical properties depend on the type of polymer matrix used. Therefore, the volume resistance of MWCNT-based PoNc can be altered up to several folds just by modulating the polymer matrix. For example, an increase in the degree of crystallinity of the polymer matrix can linearly increase the volume resistance of the MWCNT-based PoNc. Therefore, modified MWCNT-based PoNc can have promising applications in creating semiconducting layers of high-voltage electrical power cables [70].

10.5.5 Thermal Conductive

Thermally conductive polymer nanocomposites can be used to replace several metal parts associated with the function of thermal conductions in generators, electric motors, power electronics, heat exchanges, etc. Recently, several polymer nanocomposites are developed that possess high thermal conductivity and mechanical properties. Carbon-based nanomaterials (like nanotubes, graphene, and graphene oxide) are found to best material for this purpose. Although, the thermal conductivity of PoNc based on carbon nanotubes possesses low thermal conductivity in comparison with the thermal conductivity of the carbon nanotubes only. This is due to the thermal resistance offered by the surrounding polymer matrix. Apart from carbon nanotubes, the thermal conductivity of the PoNc can be enhanced by the incorporation of other types of fillers, and ceramics like aluminum nitride, boron nitride or silicon carbide, carbon black, carbon fibers, and metal particles such as copper, silver, aluminum, or nickel [71]. These materials are thermally conductive, although the degree of conductivity is dependent on the size, crystallinity, or purity of the materials.

The thermal conductivity of the polymers and their nanocomposites-based specimen can be measured using steady-state and non-state methods. In steady-state methods, the temperature difference across the specimen was measured in response to applied heat. On the other hand, non-steady methods involve sub-techniques like temperature wave, hot wire and plate and laser flash thermal diffusivity techniques [72]. Herein, mostly laser flash technique is used where specimen surface is heated using a short laser pulse and increase in temperature is measured at opposite sides of

the specimen. This allows the measurement of thermal diffusivity of the PoNc using the expression given in Eq. 10.1. This method is considered relatively simple and quick.

$$k = \alpha C_p \rho \tag{10.2}$$

where k, α, C_p, and ρ are the thermal conductivity, thermal diffusivity, heat capacity, and density, respectively [71].

10.5.6 Microelectronics, Optoelectronics, and Sensors

Today nanotechnology has become the root of advanced electronics and optoelectronic devices. Therefore, these devices now mostly had components in the nanorange. The introduction of PoNc will create a viable option for developing smart applications. Recently, conjugated polymers and CNT are receiving considerable attention in the PoNc category. Potential applications of PoNc in this category include supercapacitors, photodiodes, photovoltaic cells, light-emitting diodes, sensors, and field-effect transistors [6].

The electrical conductivity of the CNT we have already seen in a previous application. Based on this property of CNT they are also employed in electrostatic dissipation, transparent conductive coatings, supercapacitors, electromagnetic interference shielding, electromechanical actuators, and other electrode-based applications. For example, MWCNT-epoxy PoNc has a percolation threshold of 0.0025 wt% for electrical conductivity, which is comparatively lower than dispersed carbon black particles [73]. Exfoliated graphene sheets have been used for synthesizing polystyrene-graphene PoNc which has almost a similar percolation threshold as the CNT. Recently, considerable interest in graphene for the application in microelectronics and optoelectronics is nothing less than the CNT [74].

The basic structure of the PoNc-based photovoltaic cells and LED devices is shown in Fig. 10.10. However, actual devices do not contain all the potential layers. The major difference between these two devices is the light-harvesting layer (LHL) and light-emitting layer (LEL). Anode, hole injection layer (HIL), LEL, and LHL are mostly made of PoNc. However, a transparent substrate may be made from PoNc from different polymers depending upon the requirement of barrier properties to oxygen or water permeability and flexibility for the transparent substrate. For example, the application of silicon-conjugated polymer-based PoNc in photovoltaic devices can provide high flexibility, stability, efficiency, and cost-effectiveness [6].

Moreover, PoNc based on conjugated polymers can also be used for sensor applications such as chemical sensors, gas sensors, and biosensors. The nanofillers used in PoNc based on conjugated polymers can be of CNT, gold nanoparticle/nanoclusters, metal oxide nanowires, etc. For example, CNT-conjugated polymers PoNc are used as gas sensors due to their electrical resistance in presence of nitrogen dioxide and ammonia [6]. Similarly, SWCNT/polypyrrole PoNc were also used as gas sensors.

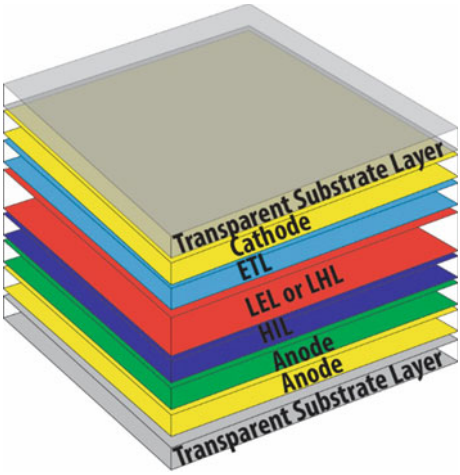

Fig. 10.10 The basic construction of LEV and PV devices

Therefore, the sensing potential of PoNc is dependent on the change in their conductivity upon exposure to specific gases. This change in conductivity in the PoNc can be due to the interaction of gases with nanofillers or polymers, electro-optical property changes, catalytic activity, chemiluminescent property or biomolecules recognition or pH change [75]. For example, poly-(aniline boronic acid)/CNT PoNc and polyaniline/gold PoNc can be used as dopamine sensors [76, 77].

10.5.7 Magnetic Storage

In the last two decades, the capacities of the storage media have significantly increased while on the contrary side the storage media is significantly reduced. This is due to applications of polymers, nanocomposites, and nanomaterials in electronics and the increasing necessity of such types of storage media to blend in with the lifestyle of the people. Nowadays, PoNc is frequently studied as potentially high storage capacity magnetic media alongside nanoscale spintronics. Materials like iron oxide nanoparticles based PoNc are preferred due to their superparamagnetic property. Later, the nanomaterial size, shape, temperature, and concentrations of the components of PoNc can be altered to regulate the magnetic media and their storage capacity. Moreover, in situ polymerization technique was used to prepare PoNc of ferromagnetic iron oxide nanoparticles reinforced in a polyvinyl alcohol (PVA) matrix. These ferromagnetic particles may interact either via magnetic dipole–dipole interactions or exchange forces due to strong interacting forces between the particles in direct contact. Consequently, the whole PoNc will possess ferromagnetic behavior. The coupling and breaking of magnetic momentum to provide long-range (coupling) or fluctuating (breaking) magnetic order switches the behavior of the PoNc from ferromagnetic (long-range) to superparamagnetic (fluctuating). In a magnetic

storage device, each nanoparticle can store information up to ca. 1017 bit/cm^2 = 10,000 Gbit/cm^2 [78]. This is a very impressive number but still, has several obstacles such as the reliability of information stored and the formation of well-organized 2D arrays in the PoNc matrix. However, ferromagnetic nanocomposites have paved a way for developing magnetic random access memory in future [79].

10.6 Conclusion and Future Outlook

Polymer nanocomposite has become part of cutting-edge modern technology, however major achievements are yet to come. There are tremendous possibilities in terms of technical and scientific advances where these PoNc may lead to groundbreaking leaps in different areas. The basic understanding of the polymers, nanomaterials, and micro and macromolecules will always be the foundation of the PoNc that may lead to the development of advanced nanocomposites. Recently, commercial, industrial and scientific communities are focusing more on the use and development of environmentally friendly and biocompatible materials with excellent physical, chemical, and biological properties. Biopolymer such as collagen, cellulose, chitosan, etc., and carbon-based nanomaterials reinforced nanocomposites can be applied in different areas of biomedical that not only requires applications associated with delicate cells, tissues, or organs but also requires low modulus and high strength for mechanically associated applications. For example, to increase the modulus and strength of nanocomposites the matrix phase of the carbon nanotubes was modified at a lower-dimensional scale while higher scale of dimensions for carbon nanofibers.

The future outlook of the potential of the PoNc relies on overcoming the challenges related to smaller filler sizes and their ability to intercalate with the polymer matrices. Furthermore, looking from a cost-effective point of view, carbon black and montmorillonite with SWCNT-based PoNc are potential markets in the future as they are relatively more feasible with today's requirements of ecofriendly, biocompatible and biodegradable materials. Replacing these materials with the traditional filler plastics will be a common strategy in diverse medical and electronic applications. However, the uniqueness of the PoNc will lead to the development of shape-memory materials for morphing aircraft, self-passivating films for satellites, and piezoresistive materials for MEMs-based sensors. Moreover, the PoNc having spatially controlled morphology will become a viable option for critically designed components for devices like fuel cell membranes, sensors, actuators, photovoltaics, and batteries.

References

1. J. Hulla, S. Sahu, A. Hayes, Hum. Exp. Toxicol. **34**, 1318 (2015)
2. S. Shivalkar et al., J. Environ. Manage. **297**, 113322 (2021)
3. P.K. Gautam, S. Shivalkar, S. K. Samanta, in *Handbook of Nanomaterials and Nanocomposites for Energy and Environmental Applications*. ed. by O.V. Kharissova, L.M. Torres-Martínez, B.I. Kharisov (Springer International Publishing, Cham, 2021), pp.1163–1181
4. S. Shivalkar et al., J. Environ. Manag. **281**, 111750 (2021)
5. P.K. Gautam, S. Shivalkar, S. Banerjee, J. Mol. Liq. **305**, 112811 (2020)
6. D.R. Paul, L.M. Robeson, Polymer **49**, 3187 (2008)
7. J.H. Lee et al., J. Colloid Interface Sci. **205**, 323 (1998)
8. M. Majumdar et al., in *Biotechnological Production of Bioactive Compounds* (Elsevier, 2020), pp. 433–466
9. S. Shivalkar et al., in *Nanotechnology in Medicine* (John Wiley & Sons, Ltd., 2021), pp. 259–280
10. L. Gasperini, J.F. Mano, R.L. Reis, J. R. Soc. Interface **11**, 20140817 (2014)
11. J.-E. Potaufeux et al., Polym. Chem. **11**, 5914 (2020)
12. R. Song et al., DDDT **12**, 3117 (2018)
13. K.P. Matabola et al., J. Mater. Sci. **44**, 6213 (2009)
14. M. Muhammed Shameem et al., Mater Today Proc. 45, 2536 (2021)
15. K.I. Winey, R.A. Vaia, MRS Bull. **32**, 314 (2007)
16. K. Shikinaka et al., Langmuir **26**, 12493 (2010)
17. J. Shojaeiarani, D. Bajwa, G. Holt, Nanocomposites **6**, 41 (2020)
18. S. Abedi, M. Abdouss, Appl. Catal. A **475**, 386 (2014)
19. M. Alexandre, P. Dubois, Mater. Sci. Eng. R. Rep. **28**, 1 (2000)
20. V. Mittal, Materials **2**, 992 (2009)
21. S. Shivalkar, S. Singh, Tissue Eng. Regen. Med. **14**, 187 (2017)
22. A.J. Crosby, J. Lee, Polym. Rev. **47**, 217 (2007)
23. A. Kumar, K. Sharma, A.R. Dixit, J. Mater. Sci. **54**, 5992 (2019)
24. N. Hu et al., Nanotechnology **19**, 215701 (2008)
25. B. Tan, N.L. Thomas, J. Membr. Sci. **514**, 595 (2016)
26. R. Hsissou et al., Heliyon **6**, e04187 (2020)
27. J. Epp, in *Materials Characterization Using Nondestructive Evaluation (NDE) Methods*, ed. by G. Hübschen et al. (Woodhead Publishing, 2016), pp. 81–124
28. A. Lagashetty, A. Venkataraman, Reson. **10**, 49 (2005)
29. S. Gyergyek et al., Colloids Surf. A **317**, 49 (2008)
30. S.-Y. Fu, X. Hu, C.-Y. Yue, Compos. Sci. Technol. **59**, 1533 (1999)
31. D. Feldman, J. Macromolecular Sci. Part A **53**, 55 (2016)
32. M. Sivasubramanian, Y. Hsia, L.-W. Lo, Front. Mol Biosci **1** (2014)
33. K. Raemdonck et al., Chem. Soc. Rev. **43**, 444 (2014)
34. M. Ahmad et al., Int. J. Pharm. **529**, 200 (2017)
35. M. Xie et al., Colloids Surf. B **176**, 462 (2019)
36. A.K. Sahoo et al., ACS Appl. Mater. Interfaces **6**, 712 (2014)
37. M. Yadollahi, S. Farhoudian, H. Namazi, Int. J. Biol. Macromol. **79**, 37 (2015)
38. F. Song et al., J. Biomed. Nanotechnol. **11**, 40 (2015)
39. P. Sanpui, A. Chattopadhyay, S.S. Ghosh, A.C.S. Appl, Mater. Interfaces **3**, 218 (2011)
40. N. Chaubey et al., Biomater. Sci. **2**, 1080 (2014)
41. A.K. Sahoo et al., ACS Biomater. Sci. Eng. **2**, 1395 (2016)
42. R. Ma et al., Compos. B Eng. **167**, 396 (2019)
43. Y. Bi, Z. Lin, S. Deng, Mater. Sci. Eng. C **100**, 576 (2019)
44. H. Wang et al., Int. J. Biol. Macromol. **121**, 1118 (2019)
45. D. Jeong et al., Cellulose **23**, 2609 (2016)
46. W.Y. Tong et al., Cellulose **25**, 631 (2018)
47. L.E. Low et al., Int. J. Biol. Macromol. **127**, 76 (2019)
48. B. Mandal et al., Nanomedicine **9**, 474 (2013)

49. R. Ghosh Chaudhuri, S. Paria, Chem. Rev. **112**, 2373 (2012)
50. C. Zheng et al., Biomaterials **33**, 5603 (2012)
51. M.T. Stephan et al., Nat. Med. **16**, 1035 (2010)
52. C.J. Pérez, V.A. Alvarez, A. Vázquez, Mater. Sci. Eng. A **480**, 259 (2008)
53. M.-Y. Chang, R.-S. Juang, Biochem. Eng. J. **35**, 93 (2007)
54. M.-Y. Chang, H.-C. Kao, R.-S. Juang, Int. J. Biol. Macromol. **43**, 48 (2008)
55. J.P. Zheng et al., React. Funct. Polym. **67**, 780 (2007)
56. E. Günister et al., Carbohyd. Polym. **67**, 358 (2007)
57. E.P. Giannelis, Adv. Mater. **8**, 29 (1996)
58. S. Puttipipatkhachorn, T. Pongjanyakul, A. Priprem, Int. J. Pharm. **293**, 51 (2005)
59. L. Yao et al., Mol. Pharmaceutics **16**, 846 (2019)
60. A. Pourjavadi, M. Doroudian, Polymer **76**, 287 (2015)
61. X. Wang, C. Hélary, T. Coradin, A.C.S. Appl, Mater. Interfaces **7**, 2503 (2015)
62. C.-J. Weng, C.-H. Chang, J.-M. Yeh, in *Corrosion Protection and Control Using Nanomaterials*, ed. by V.S. Saji, R. Cook (Woodhead Publishing, 2012), pp. 330–356
63. A. Kongkanand et al., Langmuir **22**, 2392 (2006)
64. N.W. DeLuca, Y.A. Elabd, J. Polym. Sci., Part B: Polym. Phys. **44**, 2201 (2006)
65. Y.S. Kim et al., J. Membr. Sci. **212**, 263 (2003)
66. R. Jiang, H.R. Kunz, J.M. Fenton, J. Membr. Sci. **272**, 116 (2006)
67. M.L. Hill et al., J. Membr. Sci. **283**, 102 (2006)
68. P. Bébin, M. Caravanier, H. Galiano, J. Membr. Sci. **278**, 35 (2006)
69. K. Sushmita, G. Madras, S. Bose, ACS Omega **5**, 4705 (2020)
70. M. Lu et al., Nanotechnology **27**, 065702 (2015)
71. Z. Han, A. Fina, Prog. Polym. Sci. **36**, 914 (2011)
72. W. Nunes dos Santos, P. Mummery, A. Wallwork, Polym. Testing **24**, 628 (2005)
73. J.K.W. Sandler et al., Polymer **44**, 5893 (2003)
74. Y.S. Kim, J.B. Wright, J.C. Grunlan, Polymer **49**, 570 (2008)
75. J. Kong et al., Science **287**, 622 (2000)
76. S.R. Ali et al., Anal. Chem. **79**, 2583 (2007)
77. X. Feng et al., Langmuir **22**, 4384 (2006)
78. S.W. Song, Y. Jeong, S. Kwon, IEEE J. Sel. Top. Quantum Electron. **21**, 324 (2015)
79. D.Y. Godovsky, in *Biopolymers PVA Hydrogels, Anionic Polymerisation Nanocomposites* (Springer, Berlin, Heidelberg, 2000), pp. 163–205
80. A. Graziano, S. Jaffer, M. Sain, J. Elastomers Plast. **51**, 291 (2019)
81. B. Jaleh, P. Fakhri, in *Spectroscopy of Polymer Nanocomposites* (Elsevier, 2016), pp. 112–129
82. M. Nawaz et al., Polymers **11**, 852 (2019)

Chapter 11
Nanotechnology for Biomedical Applications

Shashank Reddy Pasika, Raviteja Bulusu, Balaga Venkata Krishna Rao, Nagavendra Kommineni, Pradeep Kumar Bolla, Shabari Girinath Kala, and Chandraiah Godugu

Abstract Nowadays, promising era for stepping towards the rapid development of the novel nanomedicine using nanotechnology to address various difficulties facing our human systems by treating and diagnosing. But before the great promise of nanotechnology for biological or biomedical applications can be completely realized, a number of issues need to be effectively resolved. This chapter will provide you with a summary of contemporary research results that explain the use and applications of various nanotechnologies and modified nanomaterials, which have created a possibility in the positive shift toward diagnosis and therapy. In addition to that, this chapter covers a wide range of nanoparticles as well as their applications in

S. R. Pasika
Department of Biotechnology, National Institute of Pharmaceutical Education and Research – Raebareli (NIPER-R), Raebareli, India

R. Bulusu
College of Pharmacy and Pharmaceutical Sciences, Florida A&M University, Tallahassee, FL 32307, USA

B. V. K. Rao
Department of Pharmaceutical Sciences & Technology, Birla Institute of Technology, Mesra, Ranchi 835215, Jharkhand, India

School of Pharmacy, Suresh Gyan Vihar University, Mahal Road, Jagatpura, Jaipur 302017, Rajasthan, India

N. Kommineni
Center for Biomedical Research, Population Council, New York, NY 10065, USA

P. K. Bolla
Department of Biomedical Engineering, College of Engineering, The University of Texas at El Paso, 500 W. University Ave, El Paso, TX 79968, USA

S. G. Kala
Department of Pharmaceutical Sciences, Jawaharlal Nehru Technological University, Ananthapuramu 515002, Andhra Pradesh, India

C. Godugu (✉)
Department of Regulatory Toxicology, National Institute of Pharmaceutical Education and Research (NIPER), Balanagar, Hyderabad 500037, Telangana, India
e-mail: chandra.niperhyd@gov.in

D. K. Singh et al. (eds.), *Nanomaterials*,
https://doi.org/10.1007/978-981-19-7963-7_11

the field of biomedicine. In this chapter, the fundamental ideas behind the design of nanoparticle delivery systems, the interactions and movement of nanoparticles inside biological systems, and lastly, the potential applications of nanoparticles in industry and clinical practice are discussed in great detail. The primary focus of this discussion is on the biomedical application of inorganic (metal and metal oxide) and organic (carbon nanotubes and liposomes) nanoparticles and surfaces with nanopatterns in diagnostics, biosensing, and bioimaging devices, as well as drug delivery systems, theranostic systems, and bone-replacing implants.

Keywords Nanoparticles · Biomedical application · Drug delivery · Tissue engineering · Scaffolds

11.1 Introduction

The term "nano" comes from a Greek word that means "dwarf" or "something exceedingly small." Today, this term refers to a measurement that is one thousand millionth of a meter. More recently, this word has been used to describe the development and application of substances, machines, and systems that use matter smaller than a nanometre or at the atomic, molecular, and supramolecular levels. In other words, it refers to the study of matter at the atomic, molecular, and supramolecular levels. Nanotechnology can be put to a wide variety of uses and can be defined in a few different ways. Nevertheless, the development of highly ordered and nanostructured materials that react in a predetermined manner to a predetermined set of stimuli is emphasized across all classifications [1].

The most significant agents of transformation in the world of pharmaceutical sciences include nanotechnology and nanomaterials. According to the United States National Nanotechnology Initiative, nanotechnology is the process of determining and optimizing numerous aspects of materials in order to develop nanoscale particles that have unique features due to their size [2]. The properties of materials at the nanoscale are distinct from those of bulk materials. This is typically the result of attributes related to the greater surface-to-volume ratio of nanoscale materials, which causes shifts in chemical reactivity and quantum confinement effects.

For biological systems, the size range of nanometers can be excellent for a number of different activities, including circulating in the bloodstream, traveling through tissues, and entering cells [3]. The development of effective imaging methods for the diagnosis and treatment of a wide range of conditions has been a driving force behind recent advancements in the field of nanoscience. The peculiar physicochemical properties that can be achieved by nanosizing materials have piqued the curiosity of professionals in the biomedical field, which led to the development of the concept of nano-pharmaceuticals. "mediations created at the nanoscale, i.e., medications in which the nanomaterial fulfills the key therapeutic role or adds functionality to the currently active component" is how nano-pharmaceuticals have been defined [4].

Richard Feynman, an American physicist who later won the Nobel Prize, is credited with introducing the notion of nanotechnology in the year 1959. Feynman was well aware of the possibility that the new technology he was advocating for could have applications in the medical field. According to Feynman's point of view, it is quite probable that nanomedicine, which is a multidisciplinary discipline that encompasses biology, chemistry, physics, engineering, and materials science, will play a significant role in the process of bettering the living conditions of humans. Later on, it was discovered that Feynman's theories were accurate, and his ground-breaking insights displayed new ways of thinking at the time. As a result of his work, he is generally acknowledged as the founder of contemporary nanotechnology [5]. After fifteen years, a Japanese scientist named Norio Taniguchi was the first to adopt and define the term "nanotechnology" in 1974. He stated that "nanotechnology largely consists of the processing of separation, consolidation, and deformation of materials by one atom or one molecule" [6].

Nanotechnology has the potential to lessen our reliance on traditional forms of energy while also paving the way for improved pharmaceutical solutions to pressing medical issues. It will lead to goods with lower costs and more functionality, as well as reduced consumption of energy and raw materials [7].

This chapter will provide you with a summary of contemporary research results that explain the use and applications of various nanotechnologies and modified nanomaterials, which have created a possibility in the positive shift toward diagnosis and therapy. In addition to that, this chapter covers a wide range of nanoparticles as well as their applications in the field of biomedicine. In it, the fundamental ideas behind the design of nanoparticle delivery systems, the interactions and movement of nanoparticles inside biological systems, and lastly, the potential applications of nanoparticles in industry and clinical practice are discussed in great detail. The primary focus of this discussion is on the application of inorganic (metal and metal oxide) and organic (carbon nanotubes and liposomes) nanoparticles and surfaces with nanopatterns in diagnostics, biosensing, and bioimaging devices, as well as drug delivery systems, theragnostic systems, and bone-replacing implants.

11.2 Nanotechnology Explored in the Biomedical Field

11.2.1 Polymeric Nanoparticles

Polymer-fabricated nanoparticles have attracted a lot of interest in recent years because of the many advantages associated with their diminutive sizes [8–10]. They are frequently utilized as carrier molecules that encapsulate therapeutic payload, and they allow the regulated release of the active component while stabilizing and avoiding undesired exposure, which improves the overall effectiveness of the molecule [8, 9]. Polymeric nanoparticles appear to have a number of advantages over other colloidal carriers, including stability, processability, and the possibility of

altering the surface properties of particles. This drug delivery method appears to be the most efficient method accessible to formulation scientists for the targeted delivery of chemotherapeutic drugs [11, 12]. Biodegradable polymers for drug delivery have gained popularity in recent years since they do not need to be eliminated from the body like non-biodegradable polymers do. Polyesters such as poly(glycolic acid) (PGA), poly(lactic acid) (PLA), and their copolymer poly(lactide-co-glycolic acid) (PLGA) are non-toxic, biocompatible, and biodegradable polymeric materials that have been authorized by the FDA for a variety of biomedical uses [13]. However, these polymers are hydrophobic in nature, and nanoparticles made with them have a hydrophobic surface, which attracts plasma proteins when administered in vivo, triggering recognition and uptake by the mononuclear phagocytic system (MPS), also known as the reticuloendothelial system (RES), and resulting in rapid clearance from the circulation [14–16]. The interaction of nanoparticles with blood proteins called opsonin's causes phagocytosis, which is referred to as opsonization. This feature affects how nanoparticles and encapsulated drugs are distributed throughout the body. Surface modification with hydrophilic polymers is being investigated as a way to shield nanoparticles from MPS absorption. Polyethylene glycol (PEG) is a common hydrophilic polymer used to limit MPS absorption. Surface modification of nanoparticles can be accomplished in two ways: physically coating or by utilizing PEG copolymers. PEG-modified biodegradable polymers produced stealth nanoparticles have superior stability than PEG-coated nanoparticles. The term nanoparticle is frequently used to refer to both nanocapsules and nanospheres, despite the fact that their morphological characteristics are distinct from one another [17]. The medicine is often dissolved in an oily core that is surrounded by a polymeric matrix when it is contained in nanocapsules. The term "nanospheres" refers to the formation of polymers into a continuous network, which allows for the medicine to be disseminated throughout [17–19]. To put it another way, nanospheres can be thought of as a matrix structure, whereas nanocapsules essentially function as a reservoir for medicine. Dendrimers [20], polymeric conjugates [21], micelles [22], and nanocomposites [23] are just some of the examples of common types of polymeric nanoparticles [13]. Table 11.1 provides a list of examples of applications of nanomaterials for different diseases.

11.2.2 Lipid Nanoparticles

11.2.2.1 Solid Lipid Nanoparticles

Solid lipid nanoparticles, often known as SLNs for short, are a type of nanosized lipid-based nanoparticle that have a solid lipid core at ambient temperature. In most cases, these encase the active ingredient within a solid lipid matrix, which is further stabilized by a surfactant [24]. Their dimensions typically range from 100 to 200 nm; however, this might change depending on the fabrication method that is used [25]. The use of a surfactant enhances the stability, and the lipophilic character contributes

Table 11.1 Examples of applications of nanomaterials for different diseases

Drug	Nanostructure	Disease	Reference
Celecoxib	Polymeric nanoparticle	Lung cancer	[69]
Glucocorticoids	Polymeric nanoparticle	Systemic lupus erythematosus	[70]
Saquinavir	Polymeric nanoparticle	AIDS	[71]
Doxorubicin	Dendrimers	Non-small cell Lung cancer	[72]
Terpinene-4-ol	Solid lipid nanoparticles	Candidiasis	[73]
Saquinavir	Solid lipid nanoparticles	AIDS	[74]
Ciprofloxacin	Solid lipid nanoparticles	Cystic fibrosis, folliculitis	[75]
Ivacaftor	Nanostructured lipid carrier	Cystic fibrosis	[76]
Procaterol	Liposomes	Asthma and COPD	[77]
Chloroquine	Liposomes	Malaria	[78]
Methotrexate	Liposomes	Rheumatoid arthritis	[79]
Stavudine	Liposomes	AIDS	[80]
Simvastatin	Niosomes	Breast cancer	[81]
Vancomycin	Transferosome	Microbial infections	[82]
Acetazolamide	Cubosome	Glaucoma	[83]

to an increase in both the solubility and the permeation of the substance [26]. The fact that the medicine is encased in the matrix ensures that it will have a prolonged release and that it will be protected from unfavorable environmental conditions. Because the SLN has various benefits, such as a larger payload capacity [27], and an appropriate carrier for encapsulating both lipophilic and hydrophilic medicines, they have become the preferred carrier [27, 28]. In addition, the surface can be functionalized with molecules such as antibodies, pH-sensitive polymers, and magnetic nanoparticles, all of which have the ability to further modulate targeting [29]. SLN usually addresses problems like chemical instability, poor solubility and permeability, and first-pass metabolism, making them a suitable carrier for drug delivery and other broad biomedical applications [30, 31].

11.2.2.2 Nanostructured Lipid Carriers

SLNs were successful as a carrier molecules, addressing various obstacles that were presented by conventional drug delivery methods; nonetheless, they were ineffective in addressing problems such as polymorphic transitions, leakage of medication, unexpected gelation tendency, and many more [32]. In many cases, nanostructured lipid carriers, also known as NLCs, are considered to be the second generation of lipid nanoparticles, with SLN representing the first generation. NLCs were developed in response to the difficulties presented by SLN [33]. NLCs are fabricated using the emulsifiers and biodegradable compatible lipids [34]. The incorporation of lipids in liquid state creates structural imperfections of solid lipids, creating a less ordered crystalline arrangement. This modification averts drug leakage from the carrier, maintaining a higher drug load [35, 36]. These NLCs can be classified into three classes/models depending upon the site of drug incorporation. Type 1 NLC also termed as imperfect crystal model incorporates drug as amorphous clusters as it contains many disordered void spaces. These are produced as a result of the inclusion of sufficient quantities of both solid lipids and liquid lipids; the fact that the chain lengths of these lipids vary results in the production of a highly disordered structure. The major drawback with this model is that it offers the least entrapment efficiency. The multiple type NLC is referred to as the type II NLC, and it is predicated on the concept that the solubility of pharmaceuticals varies depending on the medium in which they are dissolved. For example, lipophilic medications dissolve more easily in liquid lipids as opposed to solid lipids. These offer numerous advantages like high entrapment efficiency, low drug leakage, and regulated drug release. In the type III model, the lipid matrix can be found in a state that is both homogeneous and amorphous. It is formulated by carefully mixing the lipids in order to avoid leakage, which is typically the result of crystallization. This is done in order to preserve the integrity of the product [37].

11.2.2.3 Vesicular Systems

In the 1900s, vesicular systems came to the forefront of many people's minds, despite the fact that their biology has just been the subject of research in recent decades. Both natural/biological/extracellular vesicles and synthetic vesicles can be distinguished from one another by examining their points of origin. Both of these are able to enclose and move cargo around within of the biological system [38]. Rothman, Schekman, and Südhof were awarded the nobel prize in 2013 in physiology or medicine for their discoveries in the machinery regulating vesicle traffic, a major transport system in our cells. Synthetic vesicles can be further classified into lipoidal vesicular systems comprising of liposomes, enzymosomes, emulsomes, ethosomes, sphingosomes, transferosomes, pharmacosomes, exosomes [39, 40], and colloidosomes. Among the several non-lipoidal vesicular systems are things like noisomes, bilosomes, aquasomes, and polymersomes. Some of the properties that attributed to the broad success of these systems in numerous biomedical applications

include surface morphology, coupled with the tunability of various structural properties, such as size, polydispersity, permeability, surface characteristics, adhesion properties, and elasticity. Some of the vesicular systems commonly used for broad biomedical applications are discussed briefly in this section [41].

11.2.2.4 Liposomes

Gerald Weissman developed the term "liposome" to describe a structural arrangement consisting of "microscopic vesicular structure containing lipid bilayers (one or more) [42, 43]". The phospholipids in the liposomes form a bag-like shape and are now exploited as drug delivery methods as they mimic biological cells, hence liposomes are the focus of the majority of research [43, 44]. Liposomes are vesicular systems that are composed of lipid molecules and have a spherical form. They have a hydrophilic hollow core that is surrounded by a lipid bilayer. Phospholipids that have been dried out typically, upon hydration, will tend to form a liposome. These vesicles can be categorized as small unilamellar vesicles, large unilamellar vesicles, or multilamellar vesicles depending on the number of bilayers that are produced [45]. While unilamellar vesicles are made up of just one lipid bilayer each, multilamellar vesicles are made up of numerous lipid bilayers that are separated from one another by a hydrophilic core [46]. Because the outer layer is lipophilic, it interacts with the cell membrane and aids in the process of delivering the therapeutic payload straight into the cytoplasm. This process is called transcytosis. Liposomes are similar to biological components; hence they could be used to deliver medications intracellularly. They have the ability to combine with cell components. Liposomes' unique ability to encapsulate pharmaceuticals in both an aqueous and a lipid layer makes them ideal for both hydrophilic and hydrophobic medications [47]. Lipophilic drugs are generally encased in liposomes' lipid bilayers, while hydrophilic drugs are found in the aqueous core. The poorly water-soluble substance had issues with entrapment and storage stability [48]. Furthermore, they are commonly utilized as a cell model for the penetration of various medicines. These have the ability to encapsulate a wide range of therapeutic payloads while simultaneously enhancing their bio circulation and targeting. In addition to this, the surface of it can also be altered by employing certain polymers [49]. Additionally, liposomes are nontoxic, biocompatible, non-irritant, easy to produce, sustain and trigger the release of payload, capable of self-assembly, and targeted drug delivery [50]. Due to the fact that the lipid components of liposomes are degraded by the body's own enzymes, they are one of the most biocompatible nano transporters accessible [51]. Liposomes can be functionally altered to meet our needs by adding PEGylated lipids, additional functional lipids, and surface-active molecules [51]. Because of all of these benefits, they are the perfect candidate for use as a carrier in drug delivery and therapeutic diagnostic applications, particularly in the treatment of neurodegenerative and cancerous disorders.

11.2.2.5 Niosomes

Niosomes are one type of recently discovered nanocarrier. Researchers working in the cosmetic sector were the ones who initially documented the formation of these in the late 1970s. They are produced when non-ionic surfactants assemble themselves into vesicles through a process known as self-assembly. Microscopic lamellar structures known as non-ionic surfactant vesicles are created following hydration. These structures are often produced when a non-ionic surfactant known as an alkyl or dialkyl polyglycerol ether interacts with cholesterol [52] Because they are amphiphilic, when they come into contact with aqueous media, they create some energy by physically agitating themselves, and then form a bilayer vesicular structure. The hydrophobic components will position themselves away from the aqueous medium, whereas the hydrophilic components will continue to be in touch with the aqueous medium. These newly generated vesicles have a wide range of possible configurations due to the fact that their composition, as well as their size, lamellarity, surface charge, and concentration, may all be modified [53]. Their effect in vivo is comparable to that of liposomes in that they extend the amount of time an encapsulated therapeutic payload is in circulation, which improves the pharmacokinetic properties of the payload [54]. In the same way that the properties of liposomes are dependent on their composition, the properties of these particles are also influenced by the various process parameters that are used in their production. For example, the intercalation of cholesterol in the bilayer reduces the drug's encapsulating efficiency, which further lowers the particle's efficiency [55]. In spite of the fact that niosomes and liposomes share a great number of similarities, there are some distinguishing characteristics between the two types of particles. Niosomes are made from uncharged single-chain surfactants and cholesterol, whereas liposomes are made from double chains of phospholipids [53].

11.2.2.6 Transferosomes

A transferosome is a lipid vesicle that was initially developed in 1991 by Cevc and Blume with the purpose of transporting medicinal payload across the skin via the transdermal route [56]. Despite the fact that it has been available in the market for close to thirty years, very few products have been developed and brought to market. Transferosomes are lipid-based vesicular carriers that are highly elastic, ultra-deformable, and stimuli-sensitive [57]. They have properties that are easily deformable, which allows them to be easily squeezed out from the stratum corneum. The mechanism for penetration is the generation of a "osmotic gradient," which is caused by the evaporation of water while applying the lipid suspension (transferosomes) on the surface of the skin [58]. Transferosomes can access the stratum corneum through either the intracellular or the transcellular pathway [58, 59]. These are usually fabricated by employing the use of amphipathic molecules, surfactants, and water [60]. Because they are manufactured from natural phospholipids, which are comparable to those found in liposomes, they are biocompatible and biodegradable. They have a high entrapment efficiency, which in the case of lipophilic drugs

is close to 90%. They prevent the encapsulated medicine from being broken down by the body's metabolic processes [61, 62]. They perform the function of a depot, releasing their contents in a measured and staggered fashion. They have use in the systemic as well as the topical administration of pharmaceuticals. Therefore, the complex lipid molecules known as transferosomes have the potential to enhance the site specificity of bioactive compounds, raise the transdermal flux, and extend the release.

11.2.2.7 Cubosomes

Recently, there has been a lot of interest in the use of cubosomes as delivery vehicles. Cubosomes are liquid crystals that are in a bicontinuous cubic liquid crystalline phase [63] as a novel structure at the nanoscale scale that is optically transparent and extremely viscous. The lipid bilayer has been twisted into a space-filling structure, creating a barrier between the two continuous but non-intersecting aqueous zones, hence the term "bicontinuous." Polymers and surfactants are extensively used for modifying drug delivery systems. They offer numerous advantages and can form supra-assemblies when used appropriately. For instance, polymers can form cross-link structures (hydrogels), whereas surfactants can form aggregates like liposomes and cubosome [64]. The formation of a lipid bicontinuous cubic phase is essential to the manufacturing process of cubosomes, which is based on the fundamental idea that the lipid mixture, in addition to the stabilizer molecule and the medication or potential molecule of interest, can self-assemble [65]. Using different lipid combinations, it is possible to generate a wide variety of other phases in addition to the cubosome, such as the hexagonal phase [66], the micellar cubic phases, and the sponge phase [67]. Applications for these materials include therapeutic delivery, artificial cells, membrane bioreactors, and biosensors. They can be engineered in vitro in both bulk and nanoparticle versions [68].

11.2.3 Metallic Nanoparticles

Metallic nanoparticles (NPs) are those whose metallic origin allows them to demonstrate substantial optical absorption as a result of a localized surface phenomenon known as plasmon resonance. This phenomenon is primarily being explored for potential novel uses in biomedicine. The fact that metal NPs such as gold, silver, and copper have a broad absorption band in the visible part of the electromagnetic spectrum is the foundation for a diverse set of applications [84].

Metallic NPs have recently been recognized as the most advantageous and suitable nanomaterials for usage in biological research applications. Due to the unique optical, physical, and electrical properties that metallic nanoparticles (NPs) possess, they have found widespread application in a wide range of biological applications, such as imaging, sensing, drug administration, and gene targeting [85].

11.2.3.1 Silver Nanoparticles

Nanoparticles of silver, also known as AgNPs, typically consist of 20–15,000 atoms of silver and have a size of less than 100 nm. Silver nanoparticles have attracted a lot of attention and are finding important applications in a variety of fields, including optics, electronics, and medicine, due to the specific physical, chemical, and biological properties that they possess. Given all of the advantages that come with using nanoparticles made of noble metals in biological applications, silver nanoparticles have also attracted a lot of attention recently. Several biosensing applications are based on the spectrum shifts that are caused by aggregated particles [86]. Guidelli et al. conducted research on a large number of AgNPs and reported that the production of AgNPs is straightforward due to the fact that their size can be easily manipulated and that they can be simply incorporated into a wide variety of materials [87, 88].

In published work, it is explained how silver can be used as a coating in materials for central venous catheters, cardiovascular implants, and neurosurgical catheters [89]. Polymers that were employed as bone cement and wound dressing were also loaded with AgNPs, and the antibacterial response of these polymers was compared with that of conventional antibiotics and silver salts [90]. In comparison to silver salt and gentamicin bone cement, only AgNPs bone cement exhibits a high level of antibacterial activity while exhibiting a low level of cytotoxicity [90, 91]. According to the publications that were cited, in order to effectively manufacture biocompatible AgNPs with improved stability and considerable antibacterial activity [45], they used bovine serum albumin as a stabilizing agent and glucose as a reducing agent [89]. Both of these agents were used in the manufacturing process. It has been established that silver nanoparticles have considerable antibacterial activity and boost the efficiency of standard antibiotics [92] (Fig. 11.1).

11.2.3.2 Gold Nanoparticles

Although gold nanoparticles (AuNPs) have been known for more than two thousand five hundred years, the twenty-first century has witnessed a substantial increase in interest in the possibility that they could have medical applications [94]. The use of gold nanoparticles is continuing to be critical to the development of nanoscale devices and nanosensors that are particular to tumor [95].

Recent research conducted on animals suggests that in order to identify the molecular hallmarks of cancer using optical imaging, a dielectric silicon core combined with hybrid AuNPs that have been coated with cancer markers may be the most effective combination to use. For instance, optical imaging tests conducted on animals have successfully demonstrated the ability to target and identify even the tiniest of breast cancers by utilizing gold/silicon nanoparticles coupled with the biomolecule Her-2, which is unique to breast cancer [96]. These tests were successful because the nanoparticles were coupled with the biomolecule. Despite the fact that the penetration of nanotechnology in biomedicine (for diagnostic and therapeutic reasons) has been restricted, the synergistic advantages of nanoparticle-mediated imaging and

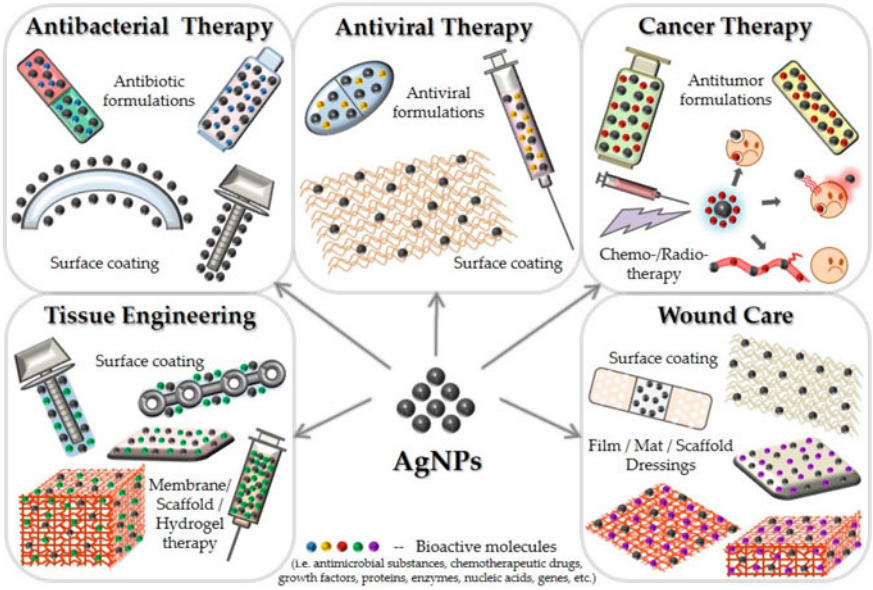

Fig. 11.1 Application of silver nanoparticles in biomedicine and tissue engineering. Adapted from [93]. Copyright 2020 by the Multidisciplinary Digital Publishing Institute

therapy for the field of oncology are opening new possibilities in clinical modalities of cancer treatment [97]. These advantages are opening the door to new possibilities in clinical modalities of cancer treatment. Clinical and biomedical applications of gold nanoparticles (Fig. 11.2).

11.2.4 Non-metallic Nanoparticles

These nanoparticles are also referred to as inorganic nanoparticles despite the fact that they are non-metallic. Non-metallic and inorganic nanoparticles have also been widely utilized for a number of biological applications in addition to metals. This is mostly because of the superior imaging and drug-delivery capabilities that these nanoparticles provide [99]. Carbon is the nonmetal that is used in biomedical applications such as drug delivery, bioimaging, tissue engineering, and biosensing more frequently than any other nonmetal. Single- and multi-walled carbon nanotubes (CNTs), which were not metallic when they were first discovered, have found utility in applications such as tissue engineering, drug delivery, and biosensors. In this chapter, we went through a few different nanoparticles that have received the greatest research attention for their potential use in biomedical settings.

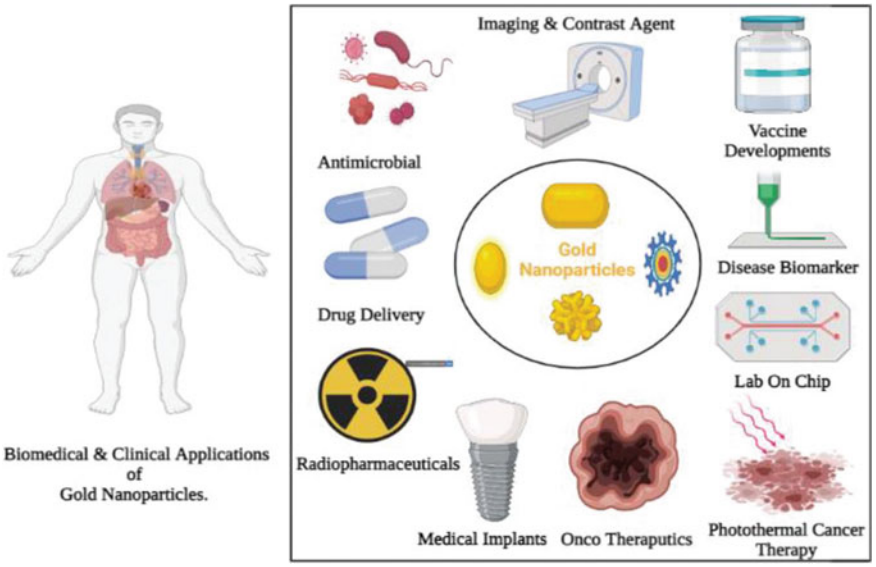

Fig. 11.2 Clinical and biomedical application of gold nanoparticles. Adapted from [98]. Copyright 2022 by the Wiley–VCH GmbH (Wiley Online Library)

11.2.4.1 Quantum Dots

Semiconductor nanocrystals are known as quantum dots. These nanocrystals have excited states that are restricted in space. Their coating with other materials is necessary for their biological applications because it promotes aqueous dispersion and prevents dangerous heavy metal leakage. This is crucial for the use of these materials. In the past ten years, researchers have identified two primary methods for the production of quantum dots (QDs): (1) the production of nanosized semiconductor particles through the use of colloidal chemistry [100–102] and (2) the use of epitaxial growth and/or nanoscale patterning, which refers to the utilization of technology that is based on lithography [103, 104]. This interest stems from inorganic particles' distinctive optical, electrical, and magnetic characteristics, which may be changed by adjustments to their size, composition, geometry, and structure. The creation of semiconductor nanoparticles may be accomplished using two main techniques [105]. Quantum dots are frequently used for a variety of imaging and labeling applications, both in vitro and in vivo. Quantum dots have been successfully utilized in the measurement of fluorescence in a variety of applications, including in situ hybridization signals, charge transfer-based biosensors, drug delivery, and photodynamic therapy [85]. In addition, quantum dots (QDs) are an excellent option for real-time in vivo imaging. This is due to the fact that QDs are 100–1000 times more intense than ordinary organic fluorophores, and they also enable multiphoton imaging using only a single wavelength of illumination [106].

11.2.4.2 Carbon Nanotubes

Carbon nanotubes are a novel class of nanomaterials that entered the field of nanomedicine only a few years ago. Since their introduction to the nanoplatform, their unique characteristics, such as high aspect ratio, ultralight weight, easy drug loading via pie-pie stacking interactions, and photoacoustic effect, have made them promising candidates for the targeted delivery of chemotherapeutics [107]. Depending on the configuration of the individual carbon atoms, carbon nanotubes (also known as CNTs) can take on a wide variety of properties. Carbon nanotubes (CNTs) are well-composed materials, which means that in addition to having a larger surface area, higher strength, and superior chemical and thermal stability features, they also have a larger surface area. CNTs are excellent choices for a wide range of applications [108]. Because of the unique physical and chemical properties that carbon nanotubes (CNTs) possess, their application in a wide range of scientific fields has recently become increasingly common. Surface modification and molecular functionalization with biological molecules have led to an increase in the application of these particles in nanobiotechnology. Studies of the toxicity of oxidized, pegylated CNTs in vitro and in vivo have shown that they are highly water soluble, stable in serum, biocompatible, nontoxic, and might be useful for biomedical applications. Further studies in this regard have further established that functionalized CNTs (f-CNTs) [109, 110] can easily cross the cell membrane facilitating the internalization of various cargos inside the cells (e.g. fluorescein, plasmid DNA, proteins, etc.) that would not otherwise be taken up, without any apparent side effects. CNTs are able to trigger internalization of cells because they engage with receptors on the cell surface. This is made possible by the presence of a [111] a large number of functional components. Because these receptor-mediated systems allow for selective cell loading, it is feasible to reduce the amount of a medication that is taken [112]. Tovani et al. have proposed the use of calcium carbonate nanotubes modified with collagen as an innovative form of tubular structure for bone regeneration [113]. Nanoparticles taken up by the reticuloendothelial system (RES) are cleared slowly via the biliary pathway and end up in faeces, without showing any systematic toxicity [109, 111, 114].

11.2.4.3 Dendrimers

Dendrimers are high-branched nanocarriers that have their own characteristic structural architecture. They were first developed in 1978 with the purpose of delivering drugs [115]. These are structured nanocarriers that have layers that are referred to as "generations," a molecular weight that falls between 5000 and 50,000 g/mol, and a polydispersity index that is relatively low. They divide into a central core and radially interconnected branches, each of which is tied to a different set of functional categories. The chemical synthesis of dendritic structures can take place through two distinct methods, either divergent or convergent. In the divergent method, the dendrimer is first synthesized from the core, which serves as the starting point, and is then constructed generation after generation. The alternate convergent method

that was established by Hawker and Frechét [116, 117] begins at the surface and works its way all the way down to the core, where the dendrimer segments are joined together to form dendrons. It is essential to get chemotherapeutic drugs to the area that needs treatment in order to reduce the likelihood that the pharmaceuticals may cause unwanted side effects. Dendrimer surfaces were modified by attaching various components, such as folic acid, antibodies, and peptides, in order to achieve this goal. By encasing the medication within dendrimers, both its solubility and its release in vitro were enhanced. Because of their robust branching, ability to encapsulate many active compounds with diverse chemical compositions, and high level of biological compatibility, dendrimers are the ideal carriers for use in biomedical applications [84]. In addition, dendrimers may be made in high purities with very few structural faults, and they are simple to analyze using conventional techniques such as mass spectrometry, infrared spectroscopy, and nuclear magnetic resonance spectroscopy. Dendritic polymers are distinguished from linear polymers in a number of ways, including the following: (i) they have well-defined structures that are comprised of a finite number of functions in a single molecule.; (ii) they are a system that is both unitary and monodisperse; (iii) they feature a high density of functional groups and are water soluble at the same time; (iv) the functional groups are located near to one another yet do not entangle with one another's chains; (v) they make it possible for the functional groups to be easily accessible, which may result in cooperative substrate binding to receptors; (vi) it is possible to load medications in a number of different methods, such as through encapsulation, complexation, and conjugation; additionally, they can be loaded into a matrix or nanogel structure.; (vii) dendrimers are highly malleable in terms of their size, charge, type, and the number of functional groups they contain.; and (viii) the spherical structure is suitable for entrapment of host and guest molecules and improves the stability of the encapsulated drug molecules. A wide variety of pharmacological chemicals, including as targeting ligands, solubilizing agents, and imaging agents, can be included into dendrimers. This allows the dendrimers to perform a multitude of functions inside the biological system [118].

11.3 Biomedical Applications of Nanomaterials

In the topic of nanomedicine, one can find examples of how nanomaterials might be useful in the study of various medical conditions. The primary goals of nanomedicine are the same as they have always been in medicine: to diagnose a condition with as much accuracy and promptness as is practical, to treat a condition with as much efficacy as is possible while minimizing adverse effects, and to evaluate the effectiveness of a treatment regimen in a way that does not involve the patient. A summary of applications of nanomaterials in drug delivery is provided in Table 11.2. The advent of nanotechnology has opened the door to a plethora of opportunities, some of which include the creation of whole new tools and skills as well as the enhancement of those that already exist [85].

Table 11.2 Applications of nanomaterials in drug delivery

S. No.	Type of nanomaterial	Applications
1	Liposomes	Drug carriers for anti-cancer agents [12, 120], antibiotics, antigens, and targeted drug delivery system [120–122]
2	Dendrimers	Cancer treatment [123], gene transfection, diagnostic tool of brain tumor [124], kidney diseases, etc., and disorders of the brain, blood vessel, heart, and skin diseases [122, 125]
3	Polymeric micelles	Gene delivery, multiple functional targets, and micelles with attached ligands [126]
4	Fullerenes	Free radicle scavenger in cancer therapy, Anti-tubercular [127], transporter of antiviral drugs, and anti-cancer agents [128]
5	Carbon-based nanocarriers	Targeted drug delivery, gene delivery [129], siRNA delivery [130], small protein delivery [131]

11.3.1 Drug Delivery

The majority of nanomedicine research focuses on the use of nanomaterials in drug—delivery systems (DDS). The use of nanoparticles in drug delivery aims to achieve precise drug targeting and distribution, biocompatibility during application and treatment processes, and quicker manufacture. NPs can deliver a diverse range of drugs to various locations such as the brain, artery walls, lymph vessels, liver, spleen, lungs, or systemic circulation for both short-term and long-term dosages, while metallic and non-metallic NPs have been widely employed in biomedicine, nanoparticles composed of lipids and proteins, such as liposomes and micelles, are progressively being considered as drug delivery nanocarriers along with some other prominently used nanomaterials are dendrimers, polymeric nanoparticles, carbons based nanocarriers, fullerenes [119], etc., diagrammatic representation of the morphology of different nanomaterials is illustrated in Fig. 11.3.

11.3.2 Gene Delivery

Gene therapy emerged in 1980s as a new approach for the treatment of monogenic diseases. It involves modification of the genetic content of the cell through the introduction of genes using delivering integrative or non-integrative vectors [134]. Different applications of gene delivery are listed below.

Viral vectors: The first success in gene therapy was obtained in Italy in a clinical trial that was carried out on a boy with "bubble boy disease" suffering from X chromosome-linked severe combined immunodeficiency (SCID-X1). The therapeutic transgene was introduced into bone marrow stem cells ex vivo using a modified gamma retroviral vector. These modified cells were then infused into the patients.

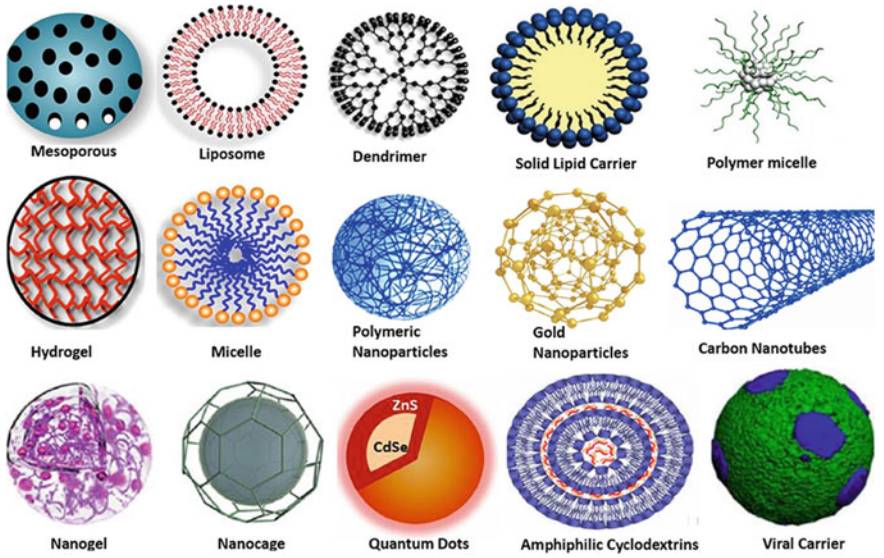

Fig. 11.3 Morphology of different types of nanomaterials. Adapted from [132, 133]. Copyright 2020 by Frontiers and Copyright 2022 by the Multidisciplinary Digital Publishing Institute

After a few months, the patients became immunocompetent, demonstrating that the therapy can constitute a definitive cure [135, 136].

Magnetofection: It is a process involving the combination of genetic material with nanoparticles and the application of a magnetic field. Polymers can serve as a connection between particles and nucleic acid [137, 138].

Iron Oxide Nano bioconjugates: The nanoparticles employed were commercial ultrasmall superparamagnetic iron oxide nanoparticles (USPIO). As the authors employed a covalent strategy, both the nanoparticle and the virus capsid were required to be functionalized [139]. Transduction tests on HepG2 cell lines revealed that USPIO coating of the avidin-displaying baculovirus enhanced both transduction efficiency and transgene expression [140].

Gold Nano bioconjugates: In this the adenoviral vectors (Ad) which are widely used for gene transfer are conjugated with smaller gold nanoparticles and allowed the complex to penetrate the plasma membrane directly in the presence of a magnetic field which results in an improvement in gene transfer efficiency [141].

11.3.3 Diagnosis and Imaging

Nanomaterials used in the diagnosis and imaging of various cancers and other diseases for effective treatment initially. Metallic nanomaterials are used as biomedical-based imaging systems. gold nanoparticles [142] when coupled with

a certain oligonucleotide, it can identify complementary DNA strands (leading to color change) [142, 143]. Nanoparticle-based agents are used in regular biomedical imaging techniques, such as fluorescence imaging, MRI [144], CT, US, PET, and SPECT. Nanoparticle fluorescence mapping has been employed in gene identification, protein assessment, enzyme activity evaluation, element tracing, cell tracking, early-stage disease diagnosis [145], tumor research, and real-time therapeutic activity monitoring [146]. Metal containing magnetic properties conjugated with high-density lipoproteins used for imaging and diagnosis of atherosclerotic plaque in the arterial wall [147]. Additionally, DNA-AuNP enriched with Gd3+ has been used in MRI imaging of genes after endocytosis [148] and poly (cholesteryl carbonate γ-butyrolactone-propylene oxide) nanoparticles have tumor identification properties used for tumor imaging [149].

11.3.4 Biosensors

Biosensors are devices that combine a biologically active component with a physicochemical signal transducer and an electrical signal processor in close proximity to one another [150]. This combination was devised with the intention of exploiting the sensitivity and selectivity of biological sensing for the purpose of analytical work in a number of different scientific and technological domains. Nanomaterial-based biosensors have significant benefits over conventional biosensors, such as enhanced detection sensitivity and specificity and have great potential in applications such as the detection of DNA, RNA, glucose, proteins, pesticides, and certain other small molecules from clinical samples, food industrial samples, and environmental monitoring [151].

11.3.4.1 Carbon-Based Nanomaterials (CBNs)

Researchers have become interested in carbon-based nanomaterials (also known as CBNs) because of the unique chemical and physical properties that they possess. Because of its exceptional mechanical, electrical, and structural diversity, it possesses superior strength, flexibility, and electrical conductivity toward a wide variety of biological entities. As a result, it can be utilized for sensing, medical diagnosis, and the treatment of a number of different diseases. CBNs, which are comprised of carbon nanotubes (CNT), graphene oxide (GO), and graphene quantum dots (GQDs), have been extensively used for biosensing includes, CNT-glucose biosensors have been designed based on the conjugation of glucose oxidase-impregnated polyvinyl alcohol solution [152], Graphene nanoparticles have been widely employed for single- and double-stranded DNA selective electrochemical sensing [153] because of the possibility of simple functionalization, a greater number of functional groups have been enriched on its surface. This, in turn, makes the specific and selective detection of a

variety of biological segments simpler [154]. In addition to this, it has an extraordinarily wide surface area, is chemically pure, and has free pi electrons, all of which make it a perfect choice for drug administration [155].

11.3.4.2 Magnetic Nanoparticles

Magnetic nanoparticles (MNP) have been the subject of extensive research in a variety of applications due to the distinctive magnetic properties that they possess. Some of these applications include hyperthermia, the contrast agent for magnetic resonance imaging (MRI), tissue healing, immunoassay, drug/gene delivery, cell separation, and GMR-sensor. Because nanomaterials have vast surface areas and an environment that is biocompatible, they are excellent candidates for enzyme loading. Several iron magnetic nanoparticles (MNPs) have proved to be an excellent nanomaterial for electrochemical biosensing applications as key material [156]. This is due to their electroconductivity, biocompatibility, and availability of fabrication. Iron and oxides of iron nanoparticles have been investigated as signal amplification components for biosensors used for the identification of glucose, ethanol, acetaminophen [156, 157], and gold along with iron have been used for dual detection of carcinoembryonics antigens and have correctly shown the presence of antigens [158]. Nanozymes, also known as magnetic metal–organic frameworks, have been shown to be effective at detecting hydrogen peroxide [159].

11.3.5 Tissue and Implant Engineering

Tissue engineering is an emerging multidisciplinary field that combines the study of biology, engineering, materials science, and medicine in order to construct biological substitutes for the purpose of repairing, replenishing, retaining, or enhancing the function of tissues and organs. Within tissues, cells are surrounded by a substance known as extracellular matrix (ECM), which is characterized by a natural network of nanofibers that are structured hierarchically. This fundamental nanoarchitecture is essential because it provides support for cells and directs cell function by way of interactions between cells and extracellular matrix [16, 160].

Nanotechnology has the potential to enable the design and fabrication of biocompatible scaffolds at the nanoscale, as well as control the spatial and temporal release of biological factors in a manner that closely resembles native extracellular matrix [16], to direct cell behaviors, and, ultimately, to create implantable tissues [161].

11.3.5.1 Nanofabricated Scaffolds

A framework that resembles extracellular matrix that can be manufactured using nanopatterning, electrospinning, self-assembly, conjugating adhesion motifs to the

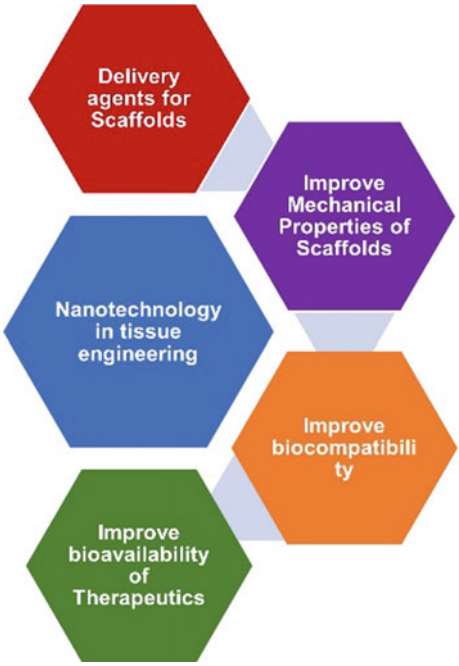

Fig. 11.4 Schematic representation of importance if nanotechnology in tissue engineering

matrix backbone, or sulfating the matrix backbone. Nanomaterials, such as carbon nanotubes, nanowires, and nanoparticles 95, can be inserted into a framework that resembles an extracellular matrix, and this can cause the properties of the framework to be altered [162].

The fabrication of a conductive hybrid hydrogel scaffold on the basis of gold nanoparticles generated homogeneously over a polymer template gel [163]. Newly generated cardiomyocytes cultivated on this scaffold showed an increase in the expression of connexin-43, which is evidence that an electrically active gold-impregnated scaffold can improve cardiomyocyte function [164]. There is a significant possibility that fibrous nanocomposites of hydroxyapatite (HA) and biodegradable polymers that are able to replicate the fundamental building units of mineralized collagen nanofibers can be used to make functioning natural bone-like analog [165]. Applications in tissue engineering, medication administration, and gene delivery are just a few of the areas that have seen extensive research into nanomaterials based on lignin [166]. Schematic representation of the importance if nanotechnology in tissue engineering is illustrated in Fig. 11.4.

11.3.5.2 Delivery Agents for Scaffolds

Pre-loaded nanomaterials incorporated with growth mediators like nano polymers, lipids, and dendrimer-based nanocarriers play an important role in the field of

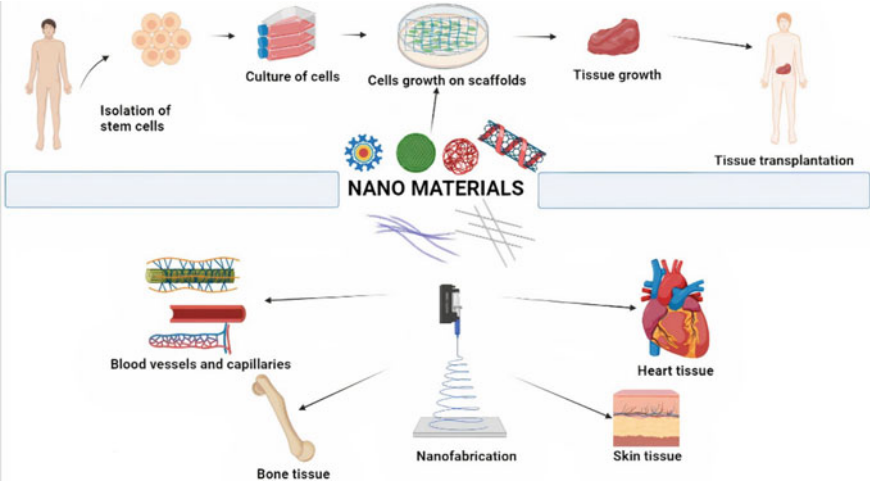

Fig. 11.5 Schematic illustration of various applications of nanomaterials in tissue engineering

tissue engineering. The goal of tissue engineering is to achieve the delivery of specific growth factors and biological molecules for the development of scaffolds. Specifically, polymer-based sustained release of angiogenic factors, such as vascular endothelial growth factors and basic fibroblast growth factors, can promote vascularization, which is essential for ensuring a constant blood supply to growing tissues [167]. Delivery of biological materials (DNA and siRNA) incorporated with nano polymer(β-amino esters) for enhanced angiogenesis for scaffolds including stem cells [167]. In point of fact, the release of numerous components in conjunction with environmental changes such as pH, temperature, light, and mechanical stress together with signaling molecules allows immobilized scaffolds to be transported for the purpose of improving cell adhesion and guided cell migration. Nanotechnology has been found to play an important role in achieving successful transplants for people who are at risk of chronic rejections by delivering immunosuppressive medications in a targeted and regulated manner [168]. Schematic illustration of various applications of nanomaterials in tissue engineering has been represented in Fig. 11.5.

11.3.6 Therapeutic Potential of Nanomaterials

In comparison to traditional pharmaceuticals, the therapeutic potential of nanomaterials is far higher. The goal of therapeutic nanoparticles is to increase the local concentration and rate of medication release at the site of disease, boost therapeutic efficacy, and reduce exposure to healthy tissues, hence reducing the likelihood and severity of side effects [169].

11.3.6.1 Treatment of Auto Immune Diseases

Autoimmune disorders are chronic, severe illnesses that can result in functional impairment and organ failure. Even though there have been significant improvements in the variety of therapeutic agents, especially biologicals, limitations in the routes of administration, the need for frequent dosing, and inadequate targeting options mostly result in undesirable effects, adverse reactions, and lack of patient compliance. By addressing several of the limitations of conventional immunosuppressive and biological therapy, nanotechnology offers promising prospects for augmenting and optimizing the treatment of autoimmune diseases [170]. Cationic liposomes with TNFα targeting siRNA suppress inflammatory cytokines used for the treatment of rheumatoid arthritis and psoriasis [125, 171]. Mycophenolic acid, when delivered via nanogels and drug-loaded PLGA, suppresses inflammation by lowering cytokine production, making it useful in the treatment of systemic lupus erythematous [172].

11.3.6.2 Nanomaterials to Overcome Multidrug Resistance

Nanomaterials may be useful against multidrug-resistant organisms like bacteria, which are becoming increasingly resistant to drugs. Due to the fact that unlike conventional medications, nanoparticles can target a wide variety of diseases, many nanomaterials were discovered to have antibacterial activity based on the zone of inhibition on an agar plate for test pathogens after incubation for 24 h. Manufactured inorganic NPs are distinct from natural or synthetic biocides in their potential to lessen bacterial resistance [173].

Metallic nanoparticles have progressively developed for multidrug resistance pathogens silver conjugated with chitosan natural polymer have antimicrobial activity again drug-resistant pathogen [173]. Nano compost formulated from Ag/TiO_2/graphene can release silver ions, oxides, and superoxides which is used for altering cell surface and physiology [174].

11.3.6.3 Cancer Therapy

Nanoparticles have been employed in a variety of applications, including preclinical studies for cancer therapy, diagnostics, anticancer drug carriers [175], and cancer biomarkers. NPs used in cancer treatment have a variety of methods, but most of them aim to increase the efficacy of the medicine when it reaches the tumor site by a combination of radiation or other external impacts such as heat and laser beam [176]. Tumor pathophysiology is distinct, including hallmarks such as excessive angiogenesis, improper vascular architecture, and poor lymphatic drainage. These characteristics are used by NPs to target tumor tissue. NPs are efficiently maintained due to decreased venous return in tumor tissue and inadequate lymphatic clearance. This is referred to as EPR. Similarly, tumor-targeting can be performed by targeting nearby tissues [177]. Cryo surgery is an advanced technique developed causes freezing of

tumour cells and subsequently damage. Nanoparticles having freezing ability have been employed in this process [178].

11.3.6.4 Neurodegenerative Diseases

Nanoscale treatments have been investigated in this scientific literature and are the most modern strategies to neurological diseases. Due to the complication such as entry restriction across the blood–brain barrier, many therapeutical medications fail to show their activity. Hence nanomaterials-based therapeutical molecules are potentially used for the treatment of neurodegenerative diseases. AuNPs modified by poly ethylene glycols have more neuro-protective role compared with AuNPs itself [179]. A study states that transcytosis might be used to transport nanoparticles that interact with the LDLr via a particular apolipoprotein E (ApoE) amino acid sequence across the BBB, avoiding lysosomal breakdown used for the delivery of curcumin which has therapeutic properties for neurodegenerative diseases [180]. Polymer containing polyaspartic acid backbone have shown activity toward upregulation of amyloid plague aggregates by inducing the cellular autophagy where this polymeric nanomaterial interacts with cell via lipid raft endocytosis at perinuclear region where the protein oligomer/aggregate primarily localizes, clears aggregated protein from the cell, and increases the cell's survival against toxic protein aggregates [181].

11.4 Theranostic Applications of Nanomaterials

Nanoparticles like many other materials have also profound applications in theragnostic. The word "theragnostic" refers to the simultaneous application of both therapy and diagnosis (Tables 11.3 and 11.4). When nanoparticles are used for theranostic applications, it is referred to as nanotheranostic. Nanotheranostic can yield promising results in fatal diseases such as cancer, which further is beneficial in saving humongous number of resources and time, improving the quality of life [182].

11.4.1 Recent Developments in Theragnostic Applications Using Nanomaterials

Zhang et al. describe the injection of the nanotheranostic agent via various drug particles, which, when reaching the target area of the body, tend to breakdown, resulting in the release of the agents. This aids in targeting the molecules or neurons responsible for or contributing to the illness [199]. Han et al. describe that using different metal nanoparticles makes it easy to turn electromagnetic waves into processes that are useful in medicine at the nanoscale (NPs). So, this chemical effect is combined

Table 11.3 Highlights of theragnostic nanomedicines

Theragnostic nanomedicine	Therapeutic agent	Diagnostic agent	Improvement over conventional forms
Carbon nanotubes	NA	NA	Self photolumines-cent and photothermal property [183]
Gold nanoparticles (AuNPs)	Doxorubicin	AuNPs	Stimuli responsive drug release [184]
Micelles	Iron oxide nanoparticles	Iron oxide nanoparticles	Delivery of Theragnostic agent [185]
Liposomes	Docetaxel	Quantum dots	Co-delivery of docetaxel and quantum dots [186]
Dendrimers	Phthalocyanines	Phthalocyanines	Delivery of Theragnostic agent [187]
Solid lipid nanoparticles	Paclitaxel	Quantum dots	Multimodal therapy [188]
Polymeric nanoparticles	Docetaxel	Quantum dots	Co-delivery of docetaxel and quantum dots [189]
Drug-polymer conjugates	64Cu	64Cu	Cancer imaging and radiochemo-therapy [190]

NA Not available

Table 11.4 Theragnostic application of nanoparticles in neurodegenerative diseases

S. No.	Type of nanomaterial	Drug	Disease/Location	Reference
1	Crosslinked nanogels	Oligonucleotides	BBB	[191]
2	Polyether-copolyester dendrimers	Rhodamine B	BBB	[192]
3	SLN	Nitrendipine	BBB	[193]
4	Liposomes	Cisplatin	Brain tumors	[194]
5	n-butyl-cyanoacrylate nanoparticles	Clioquinol	BBB	[195]
6	Iron oxide nanoparticles	Monocrystalline iron oxide	Alzheimer's disease	[196]
7	Hydrogel nanoparticles	Phenytoin	Epilepsy	[197]
8	Quantum dots	Graphene	Parkinsons disease	[198]

with laser technologies that can help the agents get deeper into the body's tissues. This makes the process easier and much more effective [200]. Ramanathan et al. describe that Mice were injected with conjugated AuNPs and an RGD-peptide to determine the effects of the elements on the animal. The application and injection of NPs in mice resulted in increased tumor accumulation, giving a successful strategy for treating tumors and NDs such as AD [201]. Niu et al. created a silicon model of

the cells of Parkinson's disease (PD) patients, in which DA transporter cells were modeled. The aggressive and intrusive nature of the nanotheranostic method using NPs on the model led to the stimulation of these transporter cells, resulting in the production of more dopamine, which is responsible for aiding motor functions in humans [202].

11.5 Recent Advancements in Nanotechnology

Jiagen Li et al. report regulation of drug release performance using mixed doxorubicin-doxorubicin dimer nanoparticles with high drug content as a pH-triggered drug self-delivery system by adjusting dimer feeding ratios [203]. Omar et al. used nanocellulose crystalline/hexadecyltrimethylammonium bromide, respectively)/EDC-N-hydroxysuccinimide (NHS) as an injectable dosage form for early detection of dengue virus E-protein using surface plasmon resonance [204]. Tan et al. discovered a method to regulate the peroxidase activity of molybdenum-based quantum dots that functioned as "nanozymes" (small artificial enzymes) in a study. In the presence of a certain medicine, these nanozymes induced a color shift, the intensity of which indicated the concentration of the drug [205]. Exosomes, which are produced naturally by human cells, are emerging as a new class of highly protective nanoplatforms for effective drug delivery. Not only can they transport medicines, but also molecular imaging agents for application in diagnostics and precision treatments. Exosomes are a suitable nanoplatform for loading both hydrophilic and lipophilic drugs due to their unusual structure, which consists of an aqueous core and a lipid-rich membrane [206, 207]. Tuan et al. developed a "nano-needle" with a tip approximately one-thousandth the width of a human hair is used to puncture a living cell, causing it to briefly quiver. Once removed from the cell, this nanosensor from ORNL detects early DNA damage that can lead to cancer. The team believes that the nanosensor can monitor the presence of proteins and other biomedically significant species in a living cell by employing antibodies specific to a wide range of cell chemicals [208].

11.6 Limitations of Nanoparticles for the Biomedical Application

Indrasekara et al. discovered the use of nanotheranostic techniques to treat neurodegenerative diseases has limitations due to the fact that each patient's genome, neurological functioning, and characteristics are unique; therefore, no single treatment strategy can be applied to all patients. Individually diagnosing and treating these neurodegenerative diseases is a challenging task that hinders the development of a single approach or treatment plan that is effective for everyone [209, 210]. Kim et al. emphasized the limitation that if the injection is not delivered properly, the NPs used

in this method may be absorbed by the blood or other bodily tissues, rather than the intended target site. If the medication is not injected properly, it will not be absorbed or used to treat the intended area for neurodegenerative diseases such as Alzheimer's and Parkinson's. Due to the fact that only a little amount of the medication reaches its intended destination, some have argued that the therapy has not been proven to be 100% effective [211, 212]. The development of nanoparticles that target specific brain cells is an important issue that warrants additional research. The most effective NP formulations for brain delivery accumulate widely in other organs, including the spleen, the liver, and the kidneys. Therefore, it is essential to develop nanoformulations that are only triggered when they reach the brain and not when they reach other organs [213]. Inorganic nanoparticles such as TiO_2 and HAP were able to activate the NF-B signaling pathway and cause inflammation-related iNOS (inducible nitric oxide synthase). All evaluated NPs produced, to varying degrees, the accumulation of pro-inflammatory chemicals. It was demonstrated that these inorganic NPs could activate microglial cells and cause potential pathogenic modifications in the olfactory bulb, striatum, and hippocampi of mice, hence leading to dysfunction and cytotoxicity in PC12 cells [214].

11.7 Conclusions and Future Perspectives

This is a promising era for stepping towards the rapid development of the novel nanomedicine using nanotechnology to address various difficulties facing our human systems by treating and diagnosing. But before the great promise of nanotechnology for biological or biomedical applications can be completely realized, a number of issues need to be effectively resolved. So far, the focus has been on cancer diagnosis and treatment. However, the greatest challenge is to apply the newly acquired information and technological advances to infectious diseases, which are the main cause of death. Although nanoparticles have special qualities that are exploited for their advantageous benefits, it is equally important to research any potential negative side effects. To ensure the safety of nanomedicine and its potential to improve human health, significant in vitro and in vivo toxicological research is required. The wide range of multimodal diagnostic platforms and therapy applications made possible by nanotechnology has the potential to drastically alter the current state of human health. As a result of these scientific breakthroughs, efforts are currently underway to construct a new biomedical paradigm.

References

1. V.S. Saji, H.C. Choe, K.W. Yeung, Int. J. Nano Biomater. **3**, 119 (2010)
2. L. Leon, E.J. Chung, C. Rinaldi, *Nanoparticles for Biomedical Applications* (Elsevier, 2020), p. 1

3. V. Gote, A.R. Nookala, P.K. Bolla, D. Pal, Int. J. Mol. Sci. **22**, 4673 (2021)
4. P.R. Gil, D. Hühn, L. Loretta, D. Sasse, W.J. Parak, Pharmacol. Res. **62**, 115 (2010)
5. H. Brune et al., *Nanotechnology: Assessment and Perspectives*, vol. 27 (Springer Science & Business Media, 2006)
6. N. Taniguchi, *Proceeding of the ICPE* (1974)
7. S. Sahoo, S. Parveen, J. Panda, Nanomed. Nanotechnol. Biol. Med. **3**, 20 (2007)
8. A. Cano et al., J. Control Release **301**, 62 (2019)
9. A. Cano et al., Nanomedicine (Lond.) **15**, 1239 (2020)
10. P.K. Bolla, V. Gote, M. Singh, M. Patel, B.A. Clark, J. Renukuntla, Pharmaceutics **12**, 798 (2020)
11. P.K. Bolla, V. Gote, M. Singh, V.K. Yellepeddi, M. Patel, D. Pal, X. Gong, D. Sambalingam, J. Renukuntla, J. Microencapsul. **37**, 502 (2020)
12. N. Kommineni, S. Mahira, A.J. Domb, W. Khan, Pharmaceutics **11**, 141 (2019)
13. C. Sarkar, N. Kommineni, A. Butreddy, R. Kumar, N. Bunekar, K. Gugulothu, Nanoeng. Biomater. 217 (2022)
14. W. Liu, A. Yang, Z. Li, H. Xu, X. Yang, J. Wuhan Univ. Technol.-Mater. Sci. Ed. **22**, 112 (2007)
15. M.-F. Zambaux, B. Faivre-Fiorina, F. Bonneaux, S. Marchal, J.-L. Merlin, E. Dellacherie, P. Labrude, C. Vigneron, Biomaterials **21**, 975 (2000)
16. E. Muntimadugu, N. Kommineni, W. Khan, Pharmacol. Res. **126**, 109 (2017)
17. S.R. Schaffazick, A.R. Pohlmann, T. Dalla-Costa, S.S. Guterres, Eur. J. Pharm. Biopharm. **56**, 501 (2003)
18. C.I.C. Crucho, M.T. Barros, Mater. Sci. Eng. C Mater. Biol. Appl. **80**, 771 (2017)
19. S.S. Guterres, M.P. Alves, A.R. Pohlmann, Drug Target Insights **2**, 147 (2007)
20. H.J. Hsu, J. Bugno, S.R. Lee, S. Hong, Wiley Interdisc. Rev. Nanomed. Nanobiotechnol. **9** (2017)
21. H. Ringsdorf, *Journal of Polymer Science: Polymer Symposia* (Wiley Online Library, 1975), p. 135
22. M. Ghezzi, S. Pescina, C. Padula, P. Santi, E. Del Favero, L. Cantù, S. Nicoli, J. Control Release **332**, 312 (2021)
23. Y. Tahara, K. Akiyoshi, Adv. Drug Deliv. Rev. **95**, 65 (2015)
24. P.K. Bolla, R.S. Kalhapure, V.A. Rodriguez, D.V. Ramos, A. Dahl, J. Renukuntla, J. Drug Deliv. Sci. Technol. **49**, 6 (2019)
25. M.B. de Jesus, I.S. Zuhorn, J. Control Release **201**, 1 (2015)
26. T.M. Amis, J. Renukuntla, P.K. Bolla, B.A. Clark, Pharmaceutics **12**, 892 (2020)
27. J. Ezzati Nazhad Dolatabadi, H. Valizadeh, H. Hamishehkar, Adv. Pharm. Bull. **5**, 151 (2015)
28. S. Doktorovova, E.B. Souto, A.M. Silva, Eur. J. Pharm. Biopharm. **87**, 1 (2014)
29. E. Rostami, S. Kashanian, A.H. Azandaryani, H. Faramarzi, J.E. Dolatabadi, K. Omidfar, Chem. Phys. Lipids **181**, 56 (2014)
30. S. Weber, A. Zimmer, J. Pardeike, Eur. J. Pharm. Biopharm. **86**, 7 (2014)
31. Y. Luo, Z. Teng, Y. Li, Q. Wang, Carbohydr. Polym. **122**, 221 (2015)
32. S. Mukherjee, S. Ray, R.S. Thakur, Indian. J. Pharm. Sci. **71**, 349 (2009)
33. S. Selvamuthukumar, R. Velmurugan, Lipids Health Dis. **11**, 159 (2012)
34. P. Sathe, R. Saka, N. Kommineni, K. Raza, W. Khan, Drug Dev. Ind. Pharm. **45**, 826 (2019)
35. P. Jain, P. Rahi, V. Pandey, S. Asati, V. Soni, Egypt. J. Basic Appl. Sci. **4**, 89 (2017)
36. R. López-García A. Ganem-Rondero, J. Cosmet. Dermatol. Sci. Appl. **5**, 62 (2015)
37. S. Selvamuthukumar, R. Velmurugan, Lipids Health Dis. **11**, 1 (2012)
38. K. Kostarelos, T.F. Tadros, P. Luckham, Langmuir **15**, 369 (1999)
39. A. Butreddy, N. Kommineni, N. Dudhipala, Nanomaterials **11**, 1481 (2021)
40. A. Gebeyehu, N. Kommineni, D. Meckes, M. Sachdeva, *Critical Reviews™ in Therapeutic Drug Carrier Systems* (2021)
41. W.T. Wickner, Proc. Natl. Acad. Sci. **110**, 18349 (2013)
42. G. Sessa, G. Weissmann, J. Lipid Res. **9**, 310 (1968)

43. U. Bulbake, N. Kommineni, W. Khan, *Handbook of Materials for Nanomedicine* (Jenny Stanford Publishing, 2020), p. 121
44. M.N. Jones, Adv. Colloid Interface Sci. **54**, 93 (1995)
45. J. Buse, A. El-Aneed, Nanomedicine **5**, 1237 (2010)
46. H. Daraee, A. Etemadi, M. Kouhi, S. Alimirzalu, A. Akbarzadeh, Artif. Cells Nanomed. Biotechnol. **44**, 381 (2016)
47. U. Bulbake, S. Doppalapudi, N. Kommineni, W. Khan, Pharmaceutics **9**, 12 (2017)
48. V.G.S. Jyothi, R. Bulusu, B.V.K. Rao, M. Pranothi, S. Banda, P.K. Bolla, N. Kommineni, Int. J. Pharm. **12**, 2022 (2022)
49. A. Gabizon, R. Catane, B. Uziely, B. Kaufman, T. Safra, R. Cohen, F. Martin, A. Huang, Y. Barenholz, Cancer Res. **54**, 987 (1994)
50. L. Sercombe, T. Veerati, F. Moheimani, S.Y. Wu, A.K. Sood, S. Hua, Front. Pharmacol. **6**, 286 (2015)
51. G. Shim, M.-G. Kim, J.Y. Park, Y.-K. Oh, Asian J. Pharm. Sci. **8**, 72 (2013)
52. M. Malhotra, N. Jain, Indian Drugs-Bombay **31**, 81 (1994)
53. K.M. Kazi, A.S. Mandal, N. Biswas, A. Guha, S. Chatterjee, M. Behera, K. Kuotsu, J. Adv. Pharm. Technol. Res. **1**, 374 (2010)
54. M. Azmin, A. Florence, R. Handjani-Vila, J. Stuart, G. Vanlerberghe, J. Whittaker, J. Pharm. Pharmacol. **37**, 237 (1985)
55. F. Szoka Jr., D. Papahadjopoulos, Annu. Rev. Biophys. Bioeng. **9**, 467 (1980)
56. G. Cevc. G. Blume, Biochimica et Biophysica Acta (BBA)-Biomembr. **1104**, 226 (1992)
57. R. Rajan, S. Jose, V.B. Mukund, D.T. Vasudevan, J. Adv. Pharm. Technol. Res. **2**, 138 (2011)
58. P. Verma, A. Ram, A. Jha, A. Mishra, A. Thakur, Int. J. Pharm. Sci. Res. **1**, 1 (2010)
59. R. Langer, Adv. Drug Deliv. Rev. **56**, 557 (2004)
60. T. Jiang, T. Wang, T. Li, Y. Ma, S. Shen, B. He, R. Mo, ACS Nano **12**, 9693 (2018)
61. Y. Chien, *Novel Drug Delivery Systems*, 149
62. A. Nanda, S. Nanda, M. Dhall, R.T. Rao, Drug Deliv. **5**, 395 (2005)
63. V. Luzzati, F. Reiss-Husson, E. Rivas, T. Gulik-Krzywicki, Ann. N. Y. Acad. Sci. **137**, 409 (1966)
64. G. Garg, S. Saraf, S. Saraf, Biol. Pharm. Bull. **30**, 350 (2007)
65. H.M. Barriga, M.N. Holme, M.M. Stevens, Angew. Chem. **131**, 2984 (2019)
66. I.D. Azmi, S.M. Moghimi, A. Yaghmur, Ther. Deliv. **6**, 1347 (2015)
67. J. Barauskas, M. Johnsson, F. Tiberg, Nano Lett. **5**, 1615 (2005)
68. H.M. Barriga, M.N. Holme, M.M. Stevens, Angew. Chem. Int. Ed. **58**, 2958 (2019)
69. R. Said-Elbahr, M. Nasr, M.A. Alhnan, I. Taha, O. Sammour, Eur. J. Pharm. Biopharm. **103**, 1 (2016)
70. E. Moallem, E. Koren, R. Ulmansky, G. Pizov, M. Barlev, Y. Barenholz, Y. Naparstek, Lupus **25**, 1209 (2016)
71. L.K. Shah, M.M. Amiji, Pharm. Res. **23**, 2638 (2006)
72. L.M. Kaminskas, V.M. McLeod, G.M. Ryan, B.D. Kelly, J.M. Haynes, M. Williamson, N. Thienthong, D.J. Owen, C.J. Porter, J. Control. Release **183**, 18 (2014)
73. L.-M. Sun, C.-L. Zhang, P. Li, J. Agric. Food Chem. **60**, 6150 (2012)
74. S.S. Dodiya, S.S. Chavhan, K.K. Sawant, A.G. Korde, J. Microencapsul. **28**, 515 (2011)
75. G.A. Shazly, BioMed Res. Int. **2017** (2017)
76. O. Garbuzenko, N. Kbah, A. Kuzmov, N. Pogrebnyak, V. Pozharov, T. Minko, J. Control. Release **296**, 225 (2019)
77. K. Tahara, H. Tomida, Y. Ito, S. Tachikawa, R. Onodera, H. Tanaka, Y. Tozuka, H. Takeuchi, Int. J. Pharm. **505**, 139 (2016)
78. N. Aditya, P. Vathsala, V. Vieira, R. Murthy, E. Souto, Adv. Coll. Interface. Sci. **201**, 1 (2013)
79. W. Foong, K. Green, J. Pharm. Pharmacol. **40**, 464 (1988)
80. M. Garg, A. Asthana, H.B. Agashe, G.P. Agrawal, N.K. Jain, J. Pharm. Pharmacol. **58**, 605 (2006)
81. I. Akbarzadeh, A. Saremi Poor, S. Yaghmaei, D. Norouzian, H. Noorbazargan, S. Saffar, R. Ahangari Cohan, H. Bakhshandeh, Drug Dev. Ind. Pharm. **46**, 1535 (2020)

82. R. Maji, C.A. Omolo, Y. Jaglal, S. Singh, N. Devnarain, C. Mocktar, T. Govender, Int. J. Pharm. **607**, 120990 (2021)
83. H.E. Teba, I.A. Khalil, H.M. El Sorogy, Drug Deliv. **28**, 2177 (2021)
84. S. Bharathala, P. Sharma, *Nanotechnology in Modern Animal Biotechnology* (Elsevier, 2019), p. 113
85. S.K. Singh, P.P. Kulkarni, D. Dash, *Bio-Nanotechnology: A Revolution in Food, Biomedical and Health Sciences*, 1 (2013)
86. H. Liao, C.L. Nehl, J.H. Hafner, Nanomedicine (Lond.) **1**, 201 (2006)
87. E.J. Guidelli, A.P. Ramos, M.E. Zaniquelli, O. Baffa, Spectrochim. Acta. A Mol. Biomol. Spectrosc. **82**, 140 (2011)
88. E.J. Guidelli, A.P. Ramos, M.E. Zaniquelli, P. Nicolucci, O. Baffa, Nanoscale **4**, 2884 (2012)
89. K. Chaloupka, Y. Malam, A.M. Seifalian, Trends Biotechnol. **28**, 580 (2010)
90. J. Tian, K.K. Wong, C.M. Ho, C.N. Lok, W.Y. Yu, C.M. Che, J.F. Chiu, P.K. Tam, ChemMedChem **2**, 129 (2007)
91. V. Alt, T. Bechert, P. Steinrücke, M. Wagener, P. Seidel, E. Dingeldein, E. Domann, R. Schnettler, Biomaterials **25**, 4383 (2004)
92. A.M. Fayaz, K. Balaji, M. Girilal, R. Yadav, P.T. Kalaichelvan, R. Venketesan, Nanomed. Nanotechnol. Biol. Med. **6**, 103 (2010)
93. O. Gherasim, R.A. Puiu, A.C. Bîrcă, A.-C. Burduşel, A.M. Grumezescu, Nanomaterials **10**, 2318 (2020)
94. M.-C. Daniel, D. Astruc, Chem. Rev. **104**, 293 (2004)
95. I. Tokareva, S. Minko, J.H. Fendler, E. Hutter, J. Am. Chem. Soc. **126**, 15950 (2004)
96. L.R. Hirsch, R.J. Stafford, J. Bankson, S.R. Sershen, B. Rivera, R. Price, J.D. Hazle, N.J. Halas, J.L. West, Proc. Natl. Acad. Sci. **100**, 13549 (2003)
97. R. Kannan, K.V. Katti, Biomed. Appl. Nanotechnol. **7** (2007)
98. M.I. Anik, N. Mahmud, A. Al Masud, M. Hasan, Nano. Select. **3**, 792 (2022)
99. J. Conde, J.T. Dias, V. Grazú, M. Moros, P.V. Baptista, J.M. de la Fuente, Front. Chem. **2**, 48 (2014)
100. B. Mahler, P. Spinicelli, S. Buil, X. Quelin, J.-P. Hermier, B. Dubertret, Nat. Mater. **7**, 659 (2008)
101. Y. Shi, P. He, X. Zhu, Mater. Res. Bull. **43**, 2626 (2008)
102. D. Bodas, C. Khan-Malek, Sens. Actuators B Chem. **128**, 168 (2007)
103. H. Mattoussi, G. Palui, H.B. Na, Adv. Drug Deliv. Rev. **64**, 138 (2012)
104. H. Yokota, K. Tsunashima, K. Iizuka, H. Okamoto, J. Vac. Sci. Technol. B Microelectron. Nanometer Struct. Process. Measure. Phenom. **26**, 1097 (2008)
105. E.C. Cho, C. Glaus, J. Chen, M.J. Welch, Y. Xia, Trends Mol. Med. **16**, 561 (2010)
106. U. Resch-Genger, M. Grabolle, S. Cavaliere-Jaricot, R. Nitschke, T. Nann, Nat. Methods **5**, 763 (2008)
107. A. Bianco, K. Kostarelos, C.D. Partidos, M. Prato, Chem. Commun. 571 (2005)
108. V. Raphey, T. Henna, K. Nivitha, P. Mufeedha, C. Sabu, K. Pramod, Mater. Sci. Eng. C **100**, 616 (2019)
109. Z. Liu, W. Cai, L. He, N. Nakayama, K. Chen, X. Sun, X. Chen, H. Dai, Nat. Nanotechnol. **2**, 47 (2007)
110. M. Bottini, F. Cerignoli, M.I. Dawson, A. Magrini, N. Rosato, T. Mustelin, Biomacromol **7**, 2259 (2006)
111. M.L. Schipper, N. Nakayama-Ratchford, C.R. Davis, N.W.S. Kam, P. Chu, Z. Liu, X. Sun, H. Dai, S.S. Gambhir, Nat. Nanotechnol. **3**, 216 (2008)
112. A.P. Ramos, M.A. Cruz, C.B. Tovani, P. Ciancaglini, Biophys. Rev. **9**, 79 (2017)
113. C. Tovani, D. Zancanela, A. Faria, P. Ciancaglini, A. Ramos, RSC Adv. **6**, 90509 (2016)
114. X. Deng, G. Jia, H. Wang, H. Sun, X. Wang, S. Yang, T. Wang, Y. Liu, Carbon **45**, 1419 (2007)
115. E. Buhleier (1978)
116. C.J. Hawker, J.M. Frechet, J. Am. Chem. Soc. **112**, 7638 (1990)
117. K. Wooley, C. Hawker, J. Pochan, J. Frechet, Macromolecules **26**, 1514 (1993)

118. A.P. Sherje, M. Jadhav, B.R. Dravyakar, D. Kadam, Int. J. Pharm. **548**, 707 (2018)
119. J.A. Zhang, G. Anyarambhatla, L. Ma, S. Ugwu, T. Xuan, T. Sardone, I. Ahmad, Eur. J. Pharm. Biopharm. **59**, 177 (2005)
120. S. Bhatia, *Natural Polymer Drug Delivery Systems: Nanoparticles, Plants, and Algae* (Springer, 2016)
121. A.A. Kadry, S.A. Al-Suwayeh, A.R. Abd-Allah, M.A. Bayomi, J. Antimicrob. Chemother. **54**, 1103 (2004)
122. D. Shcharbin, B. Klajnert, M. Bryszewska, Biochem. Mosc. **74**, 1070 (2009)
123. T. Sun, Y. Li, Y. Huang, Z. Zhang, W. Yang, Z. Du, Y. Zhou, Oncotarget **7**, 43095 (2016)
124. C. Kojima, B. Turkbey, M. Ogawa, M. Bernardo, C.A. Regino, L.H. Bryant Jr, P.L. Choyke, K. Kono, H. Kobayashi, Nanomed. Nanotechnol. Biol. Med. **7**, 1001 (2011)
125. P. Pandi, A. Jain, N. Kommineni, M. Ionov, M. Bryszewska, W. Khan, Int. J. Pharm. **550**, 240 (2018)
126. S. Movassaghian, O.M. Merkel, V.P. Torchilin, Wiley Interdisc. Rev. Nanomed. Nanobiotechnol. **7**, 691 (2015)
127. S. Bosi, T. Da Ros, S. Castellano, E. Banfi, M. Prato, Bioorg. Med. Chem. Lett. **10**, 1043 (2000)
128. Z. Markovic, V. Trajkovic, Biomaterials **29**, 3561 (2008)
129. J. Wang, R. Liu, B. Liu, Mini. Rev. Med. Chem. **16**, 905 (2016)
130. K.S. Siu et al., Bioconjug. Chem. **25**, 1744 (2014)
131. T. Nirosa, A. Roy, Carbon **5**, 1765 (2013)
132. N. Krasteva, M. Georgieva, Pharmaceutics **14**, 1213 (2022)
133. A.A. Yaqoob, H. Ahmad, T. Parveen, A. Ahmad, M. Oves, I.M. Ismail, H.A. Qari, K. Umar, M.N. Mohamad Ibrahim, Front. Chem. **8**, 341 (2020)
134. F. Herranz, E. Almarza, I. Rodríguez, B. Salinas, Y. Rosell, M. Desco, J.W. Bulte, J. Ruiz-Cabello, Microsc. Res. Tech. **74**, 577 (2011)
135. M. Cavazzana-Calvo et al., Science **288**, 669 (2000)
136. S. Hacein-Bey-Abina et al., N. Engl. J. Med. **346**, 1185 (2002)
137. J.M. Bryson, K.M. Fichter, W.-J. Chu, J.-H. Lee, J. Li, L.A. Madsen, P.M. McLendon, T.M. Reineke, Proc. Natl. Acad. Sci. **106**, 16913 (2009)
138. S.W. Kamau, P.O. Hassa, B. Steitz, A. Petri-Fink, H. Hofmann, M. Hofmann-Amtenbrink, B. Von Rechenberg, M.O. Hottiger, Nucleic Acids Res. **34**, e40 (2006)
139. K. Airenne, M. Hiltunen, M. Turunen, A. Turunen, O. Laitinen, M. Kulomaa, S. Ylä-Herttuala, Gene Ther. **7**, 1499 (2000)
140. J.K. Räty et al., Mol. Ther. **9**, 282 (2004)
141. I. Kovesdi, D.E. Brough, J.T. Bruder, T.J. Wickham, Curr. Opin. Biotechnol. **8**, 583 (1997)
142. D.K. Yi et al., Bioconjug. Chem. **21**, 2173 (2010)
143. C. Loo, A. Lin, L. Hirsch, M.-H. Lee, J. Barton, N. Halas, J. West, R. Drezek, Technol. Cancer Res. Treat. **3**, 33 (2004)
144. J.C. Frias, Y. Ma, K.J. Williams, Z.A. Fayad, E.A. Fisher, Nano Lett. **6**, 2220 (2006)
145. Y. Wei, Q. Chen, B. Wu, A. Zhou, D. Xing, Nanoscale **4**, 3901 (2012)
146. T. Muthukumar, M. Chamundeeswari, S. Prabhavathi, B. Gurunathan, J. Chandhuru, T.P. Sastry, Eur. J. Pharm. Biopharm. **88**, 730 (2014)
147. Y. Song, X. Xu, K.W. MacRenaris, X.Q. Zhang, C.A. Mirkin, T.J. Meade, Angew. Chem. **121**, 9307 (2009)
148. H.S. Min et al., Biomaterials **108**, 57 (2016)
149. M. Goldberg, R. Langer, X. Jia, J. Biomater. Sci. Polym. Ed. **18**, 241 (2007)
150. C.R. Lowe, Trends Biotechnol. **2**, 59 (1984)
151. M.S. Pinho, M.L. Gregori, R.C.R. Nunes, B.G. Soares, Polym. Degrad. Stab. **73**, 1 (2001)
152. L. Tang, Y. Wang, J. Li, Chem. Soc. Rev. **44**, 6954 (2015)
153. N. Zahin, R. Anwar, D. Tewari, M. Kabir, A. Sajid, B. Mathew, M. Uddin, L. Aleya, M.M. Abdel-Daim, Environ. Sci. Pollut. Res. **27**, 19151 (2020)
154. S. Pattnaik, K. Swain, Z. Lin, J. Mater. Chem. B **4**, 7813 (2016)
155. H. Zhang, G. Gruener, Y. Zhao, J. Mater. Chem. B **1**, 2542 (2013)

156. L. Lou, K. Yu, Z. Zhang, R. Huang, J. Zhu, Y. Wang, Z. Zhu, Nano Res. **5**, 272 (2012)
157. G.K. Kouassi, J. Irudayaraj, G. McCarty, J. Nanobiotechnol. **3**, 1 (2005)
158. J. Lu, Y. Hu, P. Wang, P. Liu, Z. Chen, D. Sun, Sens. Actuators B Chem. **311**, 127909 (2020)
159. A.I. El-Batal, N.E. Al-Hazmi, F.M. Mosallam, G.S. El-Sayyad, Microb. Pathog. **118**, 159 (2018)
160. M.M. Stevens, J.H. George, Science **310**, 1135 (2005)
161. D.H. Kim, H. Lee, Y.K. Lee, J.M. Nam, A. Levchenko, Adv. Mater. **22**, 4551 (2010)
162. T. Dvir, B.P. Timko, D.S. Kohane, R. Langer, Nano-Enabled Med. Appl. 351 (2020)
163. J.D. Kretlow, A.G. Mikos, Tissue Eng. **13**, 927 (2007)
164. J.-O. You, M. Rafat, G.J. Ye, D.T. Auguste, Nano Lett. **11**, 3643 (2011)
165. J. Shi, A.R. Votruba, O.C. Farokhzad, R. Langer, Nano Lett. **10**, 3223 (2010)
166. R. Kumar et al., Int. J. Nanomed. **16**, 2419 (2021)
167. F. Yang et al., Proc. Natl. Acad. Sci. **107**, 3317 (2010)
168. T.G. Kim, H. Shin, D.W. Lim, Adv. Func. Mater. **22**, 2446 (2012)
169. M. Abd Elkodous et al., Colloids Surf. B Biointerfaces **180**, 411 (2019)
170. P. Serra, P. Santamaria, Clin. Immunol. **160**, 3 (2015)
171. M. Khoury, V. Escriou, G. Courties, A. Galy, R. Yao, C. Largeau, D. Scherman, C. Jorgensen, F. Apparailly, Arthritis Rheum. Offic. J. Am. Coll. Rheumatol. **58**, 2356 (2008)
172. M. Look, E. Stern, Q.A. Wang, L.D. DiPlacido, M. Kashgarian, J. Craft, T.M. Fahmy, J. Clin. Investig. **123**, 1741 (2013)
173. D.D. Divakar, N.T. Jastaniyah, H.G. Altamimi, Y.O. Alnakhli, A.A. Alkheraif, S. Haleem, Int. J. Biol. Macromol. **108**, 790 (2018)
174. Z. Noreen, N. Khalid, R. Abbasi, S. Javed, I. Ahmad, H. Bokhari, Mater. Sci. Eng. C **98**, 125 (2019)
175. N. Kommineni, R. Saka, U. Bulbake, W. Khan, Chem. Phys. Lipid. **224**, 104707 (2019)
176. M. Yang, T. Yang, C. Mao, Angew. Chem. Int. Ed. **58**, 14066 (2019)
177. L. Zhang, F. Gu, J. Chan, A. Wang, R. Langer, O. Farokhzad, Clin. Pharmacol. Ther. **83**, 761 (2008)
178. Y. Hou, Z. Sun, W. Rao, J. Liu, Nanomed. Nanotechnol. Biol. Med. **14**, 493 (2018)
179. S. Mittal, M.U. Ashhar, F.F. Qizilbash, Z. Qamar, J.K. Narang, S. Kumar, J. Ali, S. Baboota, Curr. Pharm. Des. **26**, 2291 (2020)
180. F. Re et al., Nanomed. Nanotechnol. Biol. Med. **7**, 551 (2011)
181. K. Debnath, N.R. Jana, N.R. Jana, ACS Biomater. Sci. Eng. **5**, 390 (2018)
182. N. Ahmed, H. Fessi, A. Elaissari, Drug Discov. Today **17**, 928 (2012)
183. J.T. Robinson, K. Welsher, S.M. Tabakman, S.P. Sherlock, H. Wang, R. Luong, H. Dai, Nano Res. **3**, 779 (2010)
184. W.-H. Chen, X.-D. Xu, H.-Z. Jia, Q. Lei, G.-F. Luo, S.-X. Cheng, R.-X. Zhuo, X.-Z. Zhang, Biomaterials **34**, 8798 (2013)
185. P. Chandrasekharan, D. Maity, C.X. Yong, K.-H. Chuang, J. Ding, S.-S. Feng, Biomaterials **32**, 5663 (2011)
186. M.S. Muthu, S.A. Kulkarni, A. Raju, S.-S. Feng, Biomaterials **33**, 3494 (2012)
187. O. Taratula, C. Schumann, M.A. Naleway, A.J. Pang, K.J. Chon, O. Taratula, Mol. Pharm. **10**, 3946 (2013)
188. A.J. Shuhendler, P. Prasad, M. Leung, A.M. Rauth, R.S. DaCosta, X.Y. Wu, Adv. Healthcare Mater. **1**, 600 (2012)
189. J. Pan, Y. Liu, S.-S. Feng, Nanomedicine **5**, 347 (2010)
190. J. Yuan, H. Zhang, H. Kaur, D. Oupicky, F. Peng, Mol. Imag. **12**, 7290. 2012. 00038 (2013)
191. S.V. Vinogradov, A.D. Zeman, E.V. Batrakova, A.V. Kabanov, J. Control. Release **107**, 143 (2005)
192. R.S. Dhanikula, A. Argaw, J.-F. Bouchard, P. Hildgen, Mol. Pharm. **5**, 105 (2008)
193. K. Manjunath, V. Venkateswarlu, J. Drug Target. **14**, 632 (2006)
194. T. Anda, H. Yamashita, Drug Deliv. Syst.-Osaka Tokyo **10**, 425 (1995)
195. C. Roney et al., J. Control. Release **108**, 193 (2005)
196. Y.Z. Wadghiri et al., Magn. Reson. Med. Offic. J. Int. Soc. Magn. Reson. Med. **50**, 293 (2003)

197. X. Ying et al., Angew. Chem. **126**, 12644 (2014)
198. D. Kim et al., Nat. Nanotechnol. **13**, 812 (2018)
199. P. Zhang et al., Adv. Mater. **30**, 1705350 (2018)
200. L. Han, X.-Y. Zhang, Y.-L. Wang, X. Li, X.-H. Yang, M. Huang, K. Hu, L.-H. Li, Y. Wei, J. Control. Release **259**, 40 (2017)
201. S. Ramanathan, G. Archunan, M. Sivakumar, S.T. Selvan, A.L. Fred, S. Kumar, B. Gulyás, P. Padmanabhan, Int. J. Nanomed. **13**, 5561 (2018)
202. S. Niu et al., Theranostics **7**, 344 (2017)
203. J. Li, X. Li, P. Xie, P. Liu, J. Pharm. Anal. **12**, 122 (2022)
204. N.A.S. Omar, Y.W. Fen, J. Abdullah, C.E.N.C.E. Chik, M.A. Mahdi, Sens. Bio-Sens. Res. **20**, 16 (2018)
205. J. Tan, S. Wu, Q. Cai, Y. Wang, P. Zhang, J. Pharm. Anal. **12**, 113 (2022)
206. H.M. Soliman et al., Int. J. Mol. Sci. **22**, 10794 (2021)
207. P.H. Tran et al., Adv. Mater. **32**, 1904040 (2020)
208. G.G. Tuan Vo-Dinh, B. Cullum, ThoughtCo (2022)
209. A.S.D. Indrasekara, R.C. Wadams, L. Fabris, Part. Part. Syst. Charact. **31**, 819 (2014)
210. L. De Lau, P. Koudstaal, J. Witteman, A. Hofman, M. Breteler, Neurology **67**, 315 (2006)
211. J.-W. Kim, E.I. Galanzha, D.A. Zaharoff, R.J. Griffin, V.P. Zharov, Mol. Pharm. **10**, 813 (2013)
212. M. Rahman, S. Akhter, M.Z. Ahmad, J. Ahmad, R.T. Addo, F.J. Ahmad, C. Pichon, Nanomedicine **10**, 2405 (2015)
213. W. Li et al., Biomaterials **65**, 76 (2015)
214. Y. Xue, J. Wu, J. Sun, Toxicol. Lett. **214**, 91 (2012)

Chapter 12
Nanomaterials in Animal Nutrition and Disease Treatment: Recent Developments and Future Aspects

Stuti Bhagat, Divya Mehta, and Sanjay Singh

Abstract Raise in the human population requires increased demand for animal-derived food products. The quality of animal-derived food depends on the livestock's health and nutrition levels. Globally, every possible effort to make livestock disease accessible and health is in high demand. Supplementing food with essential minerals, vitamins and amino acids has been one of the easiest ways to improve livestock health. Recently, the intrinsic properties of nanoparticles (such as small size (1–100 nm), easy surface functionalization and high surface-to-volume ratio) have made them a potential candidate for different biomedical applications including nutrition. In the livestock sector, nanoparticles have been studied for their nutritional effect as well as its antibacterial, anti-parasitic and anti-helminthic properties. Only a handful of nanoparticles, such as ZnONPs, CuONPs, SeNPs, Fe_2O_3 NPs and AgNPs, have been studied for different applications using livestock models. Apart from this, liposomes, polymeric micelles and SiO_2NPs are being widely learned as vaccine adjuvants because they can improve antigen presentation, target delivery, stimulate innate immunity and induce strong T cell responsiveness, which makes them ideal for vaccine adjuvants. This book chapter has been designed to comprehensively present nanomaterials' application for animal nutrition, therapeutic agents against various disease-causing microbes, parasites and fungi and as a vaccine adjuvant.

Keywords Livestock nutrition · Viral disease · Parasitic disease · Bacterial disease · Nanovaccine

S. Bhagat · D. Mehta · S. Singh (✉)
DBT-National Institute of Animal Biotechnology (NIAB), Opposite Journalist Colony, Near Gowlidoddy, Extended Q-City Road, Gachibowli, Hyderabad 500032, Telangana, India
e-mail: sanjay@niab.org.in

DBT-Regional Centre for Biotechnology (RCB), Faridabad 121001, Haryana, India

D. K. Singh et al. (eds.), *Nanomaterials*,
https://doi.org/10.1007/978-981-19-7963-7_12

12.1 Introduction

The last few decades have witnessed enormous research in nanoscience and nanotechnology, mainly hovering over the precise control of nanoparticle size, shape, composition, surface modification and associated biomedical applications. Nanoparticles (average diameter of 1–100 nm) display significantly altered properties than their bulk counterparts, chiefly novel optoelectronic, physicochemical and catalytic properties. Some notable applications of nanomaterials are drug/gene delivery, anticancer and antibacterial agents. Certain redox-active nanomaterials are also reported as antioxidants due to their ability to scavenge various free radicals. The use of nanomaterials to develop novel biosensors to detect the disorder or disease-specific biomarkers is another area of recent interest. However, limited efforts have been devoted to addressing the concerns of the nutritional domain. A recent report by the Food and Agricultural Organization (FAO) has witnessed ~10% growth in the global population with the concurrent surge in food demand, thus necessitating the matching food production [1]. According to the Statista Global Consumer Survey, in 39 countries, including major global economies, ~86% of respondents' diets contained meat [2]. Therefore, it is expected that in the near future, the demand for meat will be fulfilled by the livestock industry.

Further, needless to mention that the possible efforts to make the livestock disease free and healthy would be in high demand. One of the health aspects of keeping the livestock is to supplement their food with essential minerals, vitamins and amino acids. Among various efforts, specific nanoparticles are reported to be used as a supplement to promote growth [3] the quality and quantity of eggs [4], meat [5], and milk [6]. Improved reproductive ability and immunity are other factors that are seldom studied [7, 8]. Concerning livestock nutrition, zinc oxide nanoparticles (ZnONPs) [9], selenium nanoparticles (SeNPs) [10], and copper oxide nanoparticles (CuONPs) [11] are some of the major nanoparticle types that are tested in livestock to study the antioxidant levels and improvement in growth performance. Livestock also suffers from various bacterial (mastitis, brucellosis, leptospirosis, listeriosis, borreliosis), viral (foot and mouth disease, swine fever, rift valley fever), and parasitic diseases (tick fever, toxoplasmosis, theileriosis, trypanosomiasis) [12]. So far, there is no suitable treatment to eradicate these diseases that leads to the culling of animals to control the spread of the diseases, thus causing significant economic and production loss. Nanomaterials could be important in developing novel therapeutics for addressing livestock diseases. For example, several nanoparticles are reported to exhibit the antibacterial ability to kill drug-resistant pathogens selectively. In doing so, nanoparticles have shown promising results, either alone or in combination with antibacterial drugs. Similarly, nanoparticles are also being explored as vaccine adjuvants to deliver multiple epitopes/antigens. In the context of the above-discussed applications of nanomaterials for various sectors of livestock health and nutrition, this chapter comprehensively covers the use of nanoparticles as a nutrient supplement, health and disease monitoring, and immunity of livestock.

12.2 Animal Health: General Aspect

Good health can be disease-free and perform normal metabolic functions by animals or humans. Livestock is considered healthy when it produces an optimum quantity and quality of milk, meat, egg, or wool and disease-free offspring. Poor livestock health may be associated with several issues broadly categorized into three parts: (i) Economic loss: The common diseases may affect livestock viability, leading to production loss and interference in the good management of the farms leading to substantial economic loss. (ii) Loss of public health: concerning zoonoses, parasites casuing infectious diseases are transmitted from diseased animals to humans, causing public health issues. (iii) Environmental pollution is related to agricultural activity and dumping of medicinal waste on land, causing antibiotic resistance in pathogenic microbes and spreading diseases from domestic to wildlife. Currently, these are considered issues of prime concern and therefore being addressed by the World Health Organization (WHO), World organization for Animal Health (OIE), and FAO. To maintain the optimum health of livestock, a balanced diet is required. Minerals, amino acids and vitamins are provided as supplements to achieve the necessary nutrition. Various minerals are essential in synthesizing key enzymes and biochemical processes that facilitate proper body functioning. For example, Zn ions participate in biochemical functions as Lewis acids and help to maintain the structure and stability of various proteins [13]. Additionally, "Se" is a part of the glutathione peroxidase system and located at the enzyme's active site. "Fe" acts as an inorganic cofactor and helps in collagen cross-linking (functions as a cofactor for proline and lysyl hydroxylases), DNA synthesis (helicases, nucleases, glycosylases, demethylases), and synthesis of hemoglobin. Magnesium (Mg) also works as a cofactor for more than 300 enzymatic biochemical reactions, such as ATPase, creatine kinase, alkaline phosphatase and enolase. It also helps in cell adhesion, muscle contraction, and neurotransmitter release [14]. Manganese (Mn) can function as a redox switch; therefore, it plays an essential role as a cofactor of metalloenzymes, antioxidant enzymes (mitochondrial superoxide dismutase, MnSOD), carbohydrates (glucose) and lipid metabolism [15]. Usually to balance the nutrition, ionic minerals are provided as a supplement; however, a high concentration of minerals is required in the diet due to poor absorption. To overcome this challenge, researchers have come up with nanotechnology-based strategies. Recent progress has enabled researchers to develop nanomaterials of precise size, shape and composition, methods to enhance biocompatibility which has further added the potential. For example, nanoparticles of essential mineral ions are being studied for their nutritional value in livestock. ZnONPs and SeNPs are studied by different research groups and tested in a few animal models [3, 10]. Upon administration, these nanoparticles showed promising results as evidenced by enhanced production of milk, egg, or wool quality and quantity, improved reproductive potential and prevention of various infections.

12.3 Use of Nanomaterials as a Nutritional Supplement

Mineral nanoparticle supplement is expected to provide optimum nutrition by avoiding mineral ions deficiency and related diseases in livestock. Research has been done in this aspect that revolves around estimating the reproductive ability, growth performance and the quality of animal products (Egg, meat, milk and wool). Therefore, based on nanoparticle types, the following sections provide a comprehensive discussion on reports offering nanomaterials as nutrition to livestock.

12.3.1 Zinc Oxide Nanoparticles

ZnONPs is one of the livestock's most studied nanoparticle types and are investigated for their nutritional benefits. The result suggests that feeding ZnONPs improved reproductive ability, enhanced milk or egg production, and increased immunity against common infections. In a study, ZnONPs (80 ppm) were administered to male sheep and investigated their effects on reproductive ability [7]. Results revealed that the ZnONPs-based diet increased the semen volume, sperm motility (74.83%), and viability rate (76.90%), and significantly reduced sperm abnormality (28.3%). ZnONPs also increased the total antioxidant capacity of semen plasma compared to control groups (without ZnONPs diet). 67 mg/kg of ZnONPs (75 days) fed Japanese quail showed better fertility rate and egg quality, thus enhancing egg production of high weight and eggshell surface compared to the control group [4]. In another study, Zn-coated chitosan nanoparticles (ZnChNPs), chitosan nanoparticles containing Ca (CaChNPs), and chitosan nanoparticles containing Cu, Fe_2O_3, Mg, Co, TiO_2, and Zn (Multi-ChNPs) were sprayed on eggs for 35 days to increase egg hatchability and help in egg preservation [16]. Among different formulations, Multi-ChNPs improved egg hatchability by 11.6%, and the contamination rate was significantly decreased (99.7%) than untreated eggs. Additionally, a few research groups have also worked on the effects of ZnONPs-based feed on the quality and quantity of milk and meat. Rajendran et al. reported that lactating Holstein Friesian cow fed on a ZnONPs-based diet (for 75 days) resulted in increased milk production with a lower number of somatic cells [17]. Alkhatib et al. tested methionine (Met) coated ZnONPs-based feed on broiler chicken [5]. About 50 g of the zinc-Met mixture, ZnONPs and Met-ZnONPs were mixed per ton of feed and broiler chicken was fed on it for 21 days. Interestingly, Met-ZnONPs fed chicken showed high tibia strength and increased overall weight compared to control groups. Additionally, Xu et al. used the pasteurization technique with ZnONPs combined with radio frequency [18]. ZnONPs combined with radio frequency techniques were explored to improve the chicken meat quality. It was observed that 20 min ZnONPs combined radio frequency exposure to chicken thigh meat retained water and improved meat quality. Compared with high-pressure steam, ZnONPs combined with the radio frequency technique improved the color, moisture, flavor, texture and pH value. ZnONPs are also known for their antibacterial activity.

In a study, ZnONPs were tested against *C. jejuni* in chicken meat [19]. The ZnONPs treated meat had increased chicken meat shelf-life when stored at 4 °C. ZnONPs (6–8 mM) exposure to meat was reported to reduce the risk of growth of different pathogenic bacteria such as *L. monocytogenes*, *E. coli*, *B. cereus,* and *S. aureus* [20]. ZnONPs feeding also improves the immunity of livestock. For example, Fazaeli and co-workers fed Holstein calves with ZnONPs (30 nm) containing diet for ~100 days (considering the weaning period) [21], and results reported improved rumen fermentation by decreasing rumen ammonia which further reduced the incidence of diarrhea. In another study, a 75 nm-sized ZnONPs-based diet showed increased high fiber digestibility and rumen fermentation in goats [9]. In pigs, decreased incidence of diarrhea was observed when a ZnONPs-based diet was administered for 21 days [3]. Efficient absorption of Zn was further confirmed by their presence in the kidney, liver, spleen, heart and blood serum. Decreased concentration of IgM and increased levels of IL-6 and TFN-α suggest improved immunity in pigs after feeding on a ZnONPs-based diet. ZnONPs are also found to promote wound healing in livestock. In a goat model, Jabbar and co-worker orally administered about 75 mg/kg ZnONPs (once a week, a total of ten doses) [22] and observed a quick narrowing of the wound area (within five weeks) than the control group.

12.3.2 Selenium Nanoparticles

Se is an essential mineral element required for various biochemical functions within humans and animals. Se concentration in milk is directly proportional to the Se content in livestock feed. Se requirement in livestock can be supplemented by sodium selenite or selenate. Concerning the poor bioavailability, Se content in livestock is significantly reduced; therefore, some alternate form, such as nanoparticles of Se, is expected to be better absorbed. For example, the effects of sodium selenite, selenomethionine and SeNPs (mixed in the diet) were evaluated during the final stage of pregnancy in goat [23]. SeNPs showed evident alterations in the serum concentration of other minerals such as Zn, Fe and Cu. Zn levels were found to be decreased, whereas Cu and Fe levels were found to be increased in the blood serum. In another study, the glycine-coated SeNPs (G-SeNPs)-based diet was studied in finishing pigs [24]. The results showed an accumulation of G-SeNPs (0.50 mg/kg) in different tissues (Loin, Heart, Liver, Pancreas and Kidney). The Se-chitosan conjugate was reported to improve the wool yield from the sheep (Chinese merino) [25]. About 60 mg of Se-chitosan conjugate (once/month) was given to the sheep with an essential diet showed increased RBC count and hemoglobin content within five days. SeNPs-based diet (0.3 mg/kg) showed an increased level of Se content in serum and glutathione peroxidase in the milk of lactating cows [10].

12.3.3 Copper Oxide Nanoparticles

Copper is an essential mineral element required to protect cells from oxidative stress and gut microbiota and an important component of antioxidant enzymes [26]. Copper-containing enzymes prevent free radical-mediated damage and maintain the structural integrity of the tissues (lysyl oxidase) and energy production (cytochrome C oxidase). Further, Cu-SOD (present in the cytosol) facilitates the dismutation of superoxide radicals and hydrogen peroxide [27]. The sustained release of Cu ions from copper oxide nanoparticles (CuONPs) is also expected to serve as a long-term supply to support the vital biochemical functions of the body. Therefore, CuONPs have been tested to protect livestock from infection and oxidative stress. CuONPs-based diet (0.040 mg/kg, 12 month) reported to increase in the weight of Holstein young cattle (~355 kg) than control (310 kg) [28]. The blood formation was also increased with increasing red blood cell count and hemoglobin by 14.7% and 11.2%, respectively. It was suggested that the nutritional value of 5 mg/kg CuONPs was comparable to the 10 mg/kg inorganic Cu-powder. In another study, the effect of CuONPs on oocytes (bovine) was studied using in vitro maturation technique [29]. Here, 0.7 μg/mL CuONPs was given to oocytes that showed reduced DNA fragmentation and increased glutathione level. CuONPs containing a standard diet were reported to improve antioxidant activity and induce immune defense in broiler chicken [11]. In this study, 12 mg CuONPs/chicken was given for six weeks. Results revealed that MDA content was decreased in the blood and lipid peroxidation level was also maintained. A CuONPs-based diet also stimulated catalase activity, IL-6, IgM and IgA expression.

12.3.4 Other Nanomaterials

There have been few more nanomaterials [calcium (CaNPs), manganese (MnNPs), magnesium (MgNPs), polymeric NPs and nanoliposomes] that are recently reported to improve the nutrition among livestock; however, much literature is not available. For example, a MnNPs-based diet was fed to the turkey and analyzed the effects on oxidative stress [30]. MnNPs-based diet (50 mg/kg) increased antioxidant activity; however, there was no significant alteration in glutathione peroxidase, glutathione and SOD enzyme expression. Additionally, AuNPs were fed to chickens and their interaction with the immune system was observed [8]. A diet containing 1 mg/kg of AuNPs induced proinflammatory events, as confirmed by increasing ceruloplasmin and IL-6 activity. The inflammation caused due to AuNPs feeding was also found to depend on the duration of the administration and concentration, where 1 mg/kg AuNPs was found safe to be mixed in feed and given up to 38 days. Zhao et al. synthesized gelatine-cellulose-coated MgONPs (GC-MgONPs) and used them to preserve eggs [31]. The developed GC-MgONPs were biodegradable with small pore size, and when used as a thin film coating, they retained the water of the eggs

and unaltered pH conditions. To increase the calcium content in the milk, Kwak and co-workers mixed Zn-containing CaNPs (CaNPs isolated from oyster shrimp) and stored them at 4 °C for 16 days [32]. Results revealed that for up to 16 days, no sedimentation of the nanoparticles was observed, and physicochemical properties were also maintained. Although more experimental work has to be performed, such results suggest that exogenous supplementation of inorganic Ca and other minerals in milk would be possible in the near future. Table 12.1 comprises a list of nanoparticles that are tested to improve livestock nutrition.

12.4 Strategies to Treat Animal Diseases Using Nanoparticles

12.4.1 Bacterial Infections

Majority of the bacterial infections in livestock are caused by different species of *Staphylococcus, Salmonella, Streptococcus, Escherichia, Aracanobacterium, Pasteurella*, etc. Bacterial diseases can be localized or systemic based on the causing agent and site of infection and symptoms include inflammation or pus formation, compressions or fractures in the spinal cord, and axon degeneration leading to weakness, paralysis and spasticity. Damage to the central nervous system (CNS) via the gastrointestinal tract (GIT) or osteocytes via the umbilical region of lambs and calves are a few other major symptoms [38]. Some of the major bacterial diseases of livestock are discussed below.

12.4.1.1 Brucellosis

Brucella represents the genus of Gram-negative coccobacilli (short rods) measuring about 0.6 to 1.5 μm × 0.5 to 0.7 μm. These bacteria are non-spore-forming, non-motile, non-encapsulated, aerobic, or microaerophilic (may require CO_2). Brucellosis is a severe acute febrile disease that causes relapses and focal lesions in bones, joints and the genitourinary tract. Different species of the organism can be characterized and differentiated by the production level of urease and H_2S, sensitivity toward dyes, cell wall antigens, phages, etc. [39]. Different species of *Brucella* cause infection in specific livestock, such as *B. melitensis*, *B. abortus and B. suis* cause pathogenesis in goats, cattle and pigs, respectively. Some common symptoms of Brucellosis include muscle and joint pain, enhanced sweating, headache, inflammation in lymphoid organs (mainly the spleen), etc. The pathogen exhibit camouflage to mask itself within macrophages of the reticuloendothelial system (spleen, lymph nodes, bone marrow and liver) and blood monocytes. The infection is considered one of the ancient infections and is known by various names, such as Malta fever, Mediterranean fever, undulant fever and gastric remittent fever [38]. Brucellosis is

Table 12.1 Organic nanomaterials tested to improve animal nutrition

Nanoparticle type	Test animal model	Results/Observations	References
Liposome encapsulated α-linolenic acid (Lipo-ALA) and α-lipoic acid (α-LA)	Cow	Cow milk treated with α-LA and Lipo-ALA showed 236.16 mg and 719.52 mg α-LA and Lipo-ALA in one serving of milk (240 mL)	[33]
Chromium picolinate NPs	Broiler chicken	Decreased Zn and Cr retention time was observed. Improved egg quality and mineral accumulation (Cr, Ca and P) in eggshells, liver, and yolk	[34]
Carboxymethyl chitosan-loaded reduced glutathione NPs	Cow	The cow was fed NPs for ten days to treat subclinical ketosis. Post-administration, the reduction in ketogenesis and enhanced gluconeogenesis was observed	[6]
Matrix metalloproteinase-9-based protein NPs	Holstein cows	1.2 mg NPs (one week) improved immunity and enhanced mammary glands during the cow's dry period	[35]
Chromium nanoparticles (CrNPs)	Finishing pig	A 35 days administration of CrNPs showed increased finishing pig weight with improved meat quality	[34]
Modified *Spirulina maxima* Pectin nanoparticles (SpiNPs)	Porcine oocytes	Reduced reactive oxygen species (ROS) level, high maturation and cleavage rate, improved blastocyte development, and total cell count	[36]
Alginate NPs	Egyptian Nubian goats	Better immunity (increased IFN-γ, TNFα, IL1β, IL-6, Ig-A and Ig-G) was observed in alginate NPs fed goats	[37]

classified under zoonotic infections, which usually spreads in humans through raw food (meat) or non-pasteurized milk from extremely infected animals or due to close contact with the secretions [40].

Several formulations have been developed to treat the infection of Brucellosis. Among them, liposomal formulations of different antibiotics are some standard methods that have yielded positive results. Hernandez et al. developed a liposomal

formulation (positive and negative charged) containing Gentamicin (1 μg/mL) and tested it against *B. melitensis* infected mice [inoculated intraperitoneally (0.1 mL solution of 10^3 bacteria/mL)]. Liposomes (with and without Gentamicin) and free Gentamicin were injected on the 2nd, 5th and 8th day after *Brucella* infection in mice, and the effects were followed in the spleen and liver. Interestingly, free Gentamicin showed less efficacy than liposomal formulation towards inhibition of *B. melitensis.* The complete inhibition of the pathogen was observed with liposome-encapsulated Gentamicin with a dose of 500 μg of Gentamicin/mice. Also, the positively charged liposomes exhibited better inhibition than those negatively charged in terminating the disease [41]. Hosseini et al. also compared the efficiency of free doxycycline (DOX) and DOX-encapsulated (91.3–97.4% loading efficiency) solid lipid NPs (DOX-SLN) against *B. melitensis* inside the macrophages [42]. The study reported that DOX-SLN reduced the bacterial population inside macrophages (3.5 Log) more effectively than the free DOX. Alizadeh et al. studied the antibacterial effects of AgNPs by considering the minimum inhibitory concentration (MIC) and minimum bactericidal concentration (MBC) against *B. abortus* 544, which were noted as six ppm and eight ppm, respectively. The effect of AgNPs was checked on peritoneal macrophages of mice by incubating 0–4000 ppm of AgNPs with the bacterial suspension (5×10^5 CFU/mL). The AgNPs were efficient in penetrating macrophages and killing bacteria, thus producing the highest efficacy (at 8–10 ppm of AgNPs exposure) [43].

12.4.1.2 Listeriosis

L. monocytogenes is considered the main agent for causing Listeriosis in livestock. Several serotypes are virulent for livestock, such as 1/2a, 1/2b and 4b. The most common example is *L. ivanovii* (also known as *L. bulgaricus* or *L. monocytogenes* serotype 5), which causes reproductive abnormalities and abortion in cows and sheep [44]. Common routes of entry of this pathogen are via nasal passage [45]. Encephalitis is a neurological disease caused by *L. monocytogenes* in sheep, goats and cattle. It is also known as "circling disease," as animal heads get turned or twisted to one side after attaining the infection and prefer to walk in circles. Infection also leads to unilateral paralysis in facial nerves causing drooping eyelids and ears, flaccid lips and deviated muzzle, loss of sensation and depression in animals. Pharyngeal paralysis causes saliva drooling in animals and due to severe infection, lesions are formed in the cerebellum region of the brain in sheep and goats, causing death. *L. monocytogenes* are susceptible to penicillin G (oxytetracycline), ceftiofur, erythromycin and trimethoprim. These drugs are required in very high doses (22,000 U/kg body weight, every 12 h for 1–2 weeks for penicillin and 16.5 mg/kg per day for oxytetracycline) to be effective. The administration of dexamethasone was controversial as it depresses cell-mediated immunity and causes abortion in sheep and cattle, and also induces antimicrobial resistance in pathogens [46]. In nanoparticle-based treatments, Markowska et al. used AgNPs against *L. monocytogenes* and results revealed that AgNPs showed high efficacy with low doses than free antibiotics. The MIC was determined against *L. monocytogenes* (2×10^6 CFU/mL) in a range from 0.5

μg/mL to 12 μg/mL of AgNPs. At a concentration of 0.25 μg/mL of AgNPs, cell lysis was enhanced 1000-fold than lysozyme or Triton X-100 treatment. AgNPs were assumed to enhance the activity of autolysins (peptidoglycan hydrolyzing enzymes) that cause polymer destruction and pore formation in the cell envelope to enhance cell permeability, which was further confirmed by DNA and protein efflux [47]. 1 h treatment of AgNPs (0.50 μg/mL) showed enhancement in DNA, and protein efflux was noted as 48% and 30%, respectively, compared to lysozyme treatment. Additionally, curcumin nanoparticles (CNPs) coated with different surfactants [sodium dodecyl sulfate (SDS), Tween 20, and Cetrimonium bromide (CTAB)] showed antimicrobial activity against *L. monocytogenes*. The antimicrobial efficiency was found to be dependent on the surface charge and size of the NPs. NPs coated with CTAB (positively charged) showed enhanced antimicrobial activity than other surfactants, possibly due to the opposite charge between NPs and *L. monocytogenes*. 1 μg/mL of CNP-CTAB completely inhibited the growth of the *L. monocytogenes*, whereas a slight reduction in growth was observed in the case of CNP-SDS (500 μg/mL) [48]

12.4.1.3 Mastitis

Bovine mastitis causes ~$147/ cow/annum income loss in milk production [49]. Annual economic losses due to sub-clinical and clinical mastitis were estimated to be one billion dollars. Mastitis is the inflammation of the mammary glands of animals caused by the infection of a group of microorganisms and sometimes due to physical trauma. Among microbes, bacterial pathogens are predominantly causative agents, including *P. multicida, S. aureus, S. pyogenes, E. coli*, etc. Considering the levels of inflammation, bovine mastitis can be categorized into three classes: clinical, sub-clinical and chronic mastitis. Swelling and redness in the udder region, fever, weight loss, lack of appetite, sunken eyes and diarrhea are some acute symptoms of mastitis-affected cows. Under severe conditions, the appearance of milk is changed to watery or released as a brown discharge with a foul smell and clots. Under extreme situations, mastitis may be fatal [50]. Like other bacterial diseases, mastitis can be treated by antibiotics such as penicillin, intramuscular, ampicillin, tetracycline, gentamycin, etc., via administration through intra-mammary infusion, intramuscular and intravenous antibiotics. However, overuse of antibiotics led to their release in milk poses a significant concern. Antibiotics may retain the animal body for longer, causing health issues in animals. Although vaccines may be a suitable alternative for treating bovine mastitis, they face a lack of efficiency and the multi-etiological nature of bovine mastitis.

Alternatively, nanoparticle-based strategies have been tested against the causative organisms of mastitis. Several examples report the development of a nanotechnology-based formulation of the traditional drugs/agents used to treat mastitis. Taking this into account, Han et al. used hydrogenated nanoforms as carriers to modulate tilmicosin release based on castor oil-solid lipid to smoothen the delivery and enhances the stability of the drug within the animal body from 5 h (without nanocarrier) to 8 days (with nanocarrier) [51]. Nanotechnology also aids in ensuring milk quality is safe

for consumption through innovative techniques of foodborne pathogen detection. Nanocomposites (AuNPs and Fe_2O_3NPs) were developed by Sung et al. carrying anti-*S. aureus* antibodies utilized to test *S. aureus* in milk samples [52]. The antibody is an intriguing aspect of these nanocomposites as they might be changed to capture a range of diseases based on specificity and selectivity. Another similar technique was developed by Wang et al. to test existing toxins in milk in 10 min by applying polyclonal antibodies along with AuNPs immune chromatographic strips (e.g., aflatoxin M1, carcinogenic) [53].

12.4.1.4 Borreliosis

Borreliosis (also known as Lyme disease or Lyme borreliosis) is an acute and persistent zoonotic infection caused by spirochete *B. burgdorferi* and spread by ixodid ticks. Borrelia is an obligate parasite, a spirochete, long, wide and helical in shape. The parasite possesses a linear chromosome and linear and circular plasmids, which is the unique feature of this organism and essential for growth and survival [54]. These organisms persist in the environment usually for a short duration; however, they depend on vertebrate reservoirs, host and arthropod vectors for long-duration survival. Upon entering the host body, this organism multiplies and disseminated throughout the body to cause infection. Persistent infection in the host body leads to the induction of cytokines, which may form lesions. Only certain species (such as *B. burgdorferi*) of this pathogen have been reported infectious. In sheep and cattle, *B. burgdorferi* causes lameness, arthritis, weight loss, and abortion are common in cows. A limited number of antibiotics, such as ceftriaxone and DOX, are effective against this pathogen [55]. Among nanoparticle-based treatments, AgNPs have been tested by Nelson et al. against *Hyalomma anatolicum* ($LC_{50} = 0.78$ μg/mL). AgNPs showed 100% mortality when exposed to 2.5 μg/mL concentration [56]. AgNPs act as a catalyst to cripple the enzyme and make bacteria suffocate (without oxygen). Other suited mechanisms of AgNPs to impart antibacterial potential follow interference with replication, transcription and translation, cell membrane disruption, ROS generation, interference in cell wall synthesis, etc. (Fig. 12.1) [57]. AgNPs are also reported to enhance drug delivery and combat drug-resistance issues faced by antibiotics in microbes.

12.4.2 Viral Diseases

Viruses are microscopic infectious agents (of size 20–200 nm) and obligate intracellular parasites; hence can exist as potentially active inside the cell but act as an inert entity outside cells [58]. They either contain DNA or RNA as genetic material in single- or double-stranded form. They require host cellular machinery to multiply via sophisticated mechanisms operating by incorporating their genome into the host genome and synchronizing with their life cycle. Also, antibiotics are ineffective

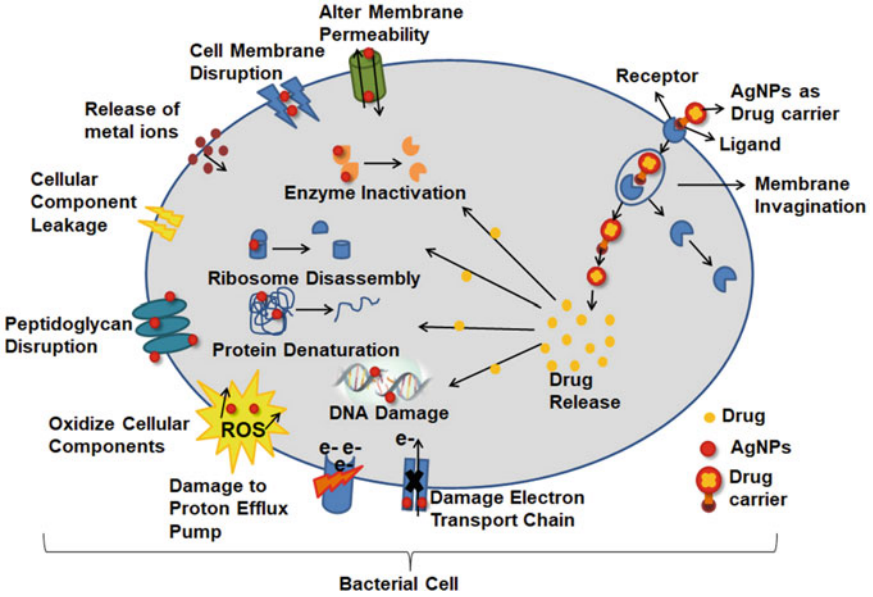

Fig. 12.1 Schematic diagram showing the possible interference caused by AgNPs to exhibit antibacterial activity and drug delivery mechanism

against viruses as they steal host machinery [59]. Viral diseases are of great concern worldwide as they are extremely difficult to control after an outbreak. Several viruses are known to cause infections in livestock, such as Foot and Mouth Disease (FMD), Rift Valley Fever (RVF), and African Swine Fever. Some common symptoms of viral infections are anorexia, excessive salivation, conjunctivitis, nasal congestion and discharge, coughing, fever, warts on the head and neck, depression, loss of appetite and abortion in severe cases [60]. Some common methods to control viral pathogenesis include immune prophylaxis (mass immunization by vaccines) and active and passive prophylaxis to provide immune protection. Other basic methods include culling, sanitation and vector control that reduce exposure and spread of viral infection [61].

12.4.2.1 Foot and Mouth Disease

FMD is considered one of the highly infectious viral diseases of cloven-hoofed animals, including cattle, sheep, pigs and goats [62]. FMD virus mainly has seven serotypes: A, O, C, Asia1, SAT1, SAT2, and SAT3 [60]. Some common symptoms include salivation, fever and vesicle formation in the mouth, muzzle, feet, and tongue. Breakage of these vesicles leads to swelling in the coronary band, depression, lameness and abortion [63]. This disease has been prevalent in many countries, including U.S., Mexico, U.K., Taiwan, China, Japan, Korea and Indonesia, for over 100 years.

Reports suggest that the first outbreak occurred in the U.S., and ~3,500 livestock herds were infected, leading to the culling of 1,09,000 animals. In the U.K., about 2000 cases were identified in 2001 [64], leading to the culling of six million sheep and cattle to halt the disease [65]. As of recent reports, there is no specific treatment for FMD; however, two methods are followed to control the spread of this infection, culling and vaccination or sometimes both. Often vaccination does not provide an effective solution. The available vaccines are developed by heat-killed pathogens; therefore, they are ineffective in protecting against other viruses and hence seek booster doses. The detection of this disease faces poor progress as real-time RT-PCR, ELISA and neutralization tests are the only methods. Hamdy et al. have developed an AuNPs-based RT-PCR nano-sensor for FMD detection that specifically recognizes FMDV RNA. It was designed by using thiol-linked primers that resulted in enhanced specificity (100% with rT-PCR), efficacy (94.5% with rT-PCR), and sensitivity [66]. Another study by Hafashjani et al. revealed that AuNPs possess good antiviral activity and may be used as an upcoming treatment option for FMD. The anti-FMDV activity by plaque retardation assay displayed ~50% cytotoxicity at 10.4 μg/mL concentration using MTT assay. Such initiatives may be regarded as possible anti-FMDV agents [67].

12.4.2.2 Rift Valley Fever

RVF comes under one of the most important zoonotic infections caused by the RVF Virus, which infects cattle, sheep and other livestock animals. This pathogen generally attacks young animals more than mature ones and causes fever, loss of appetite, weakness, diarrhea, abortion and death [62]. As of now, there is no specific treatment available for RVF. Mohamed et al. aimed to assess the use of AuNPs as immune boosters for the RVF vaccine. Male albino rats were used for testing and divided into several groups, including the negative control group, immunized with non-adjuvant RVF vaccine group and immunized with RVF vaccine in combination with 40 μM rod-shaped AuNPs and 40 μM spherical AuNPs (two groups). The groups treated with vaccines in combination with rod and spherical AuNPs expressed elevations in enzymatic markers of the liver (alanine transaminase, aspartate aminotransferase), bilirubin, TNFα, CD-68 positive cells than untreated and the group treated with the non-adjuvant vaccine. These elevations for enzymatic markers and bilirubin depended on AuNPs morphology, where spherical AuNPs induced more than rod-shaped AuNPs [68]. Borrego et al. conducted an in vitro study in Vero cells and analyzed the effectiveness of AgNPs in pre-incubated with RVFV MP-12 strain. A small amount (about 30–300 pfu) of RVFV MP-12 strain pre-incubated with AgNPs (1.5–12 μg/mL) and observed that AgNPs at 1.2 to 2.4 μg/mL showed ~50% whereas 12 μg/mL exposure showed ~98% effectiveness against RVF. In vivo experiments in 8–10 weeks old transgenic mice infected with RVF (about 30–300 pfu) showed ~80% and ~40% survival rates after AgNPs (6 mg/kg) administration in undiluted and diluted (½) forms, respectively, while 100% mortality rate was observed in the untreated group [69].

12.4.2.3 African Swine Fever

It is a highly contagious and deadly disease of swine caused by an unclassified virus and localized to domestic and feral pigs of all ages. The clinical symptoms include fever, vomiting, red blotchy skin, coughing, diarrhea, cyanosis (blue skin), necrosis in the skin, loss of appetite and abortion. So far, no vaccine or treatment is available for this disease, and the only way to control it is the depopulation of the affected swine. The current detection method is PCR-CRISPR-based or immunoassay-based (ELISA). Lateral flow assay (LFA) is one of the methods used to detect African Swine Fever viruses (ASFV) by several groups. Zhu et al. described a double-antigen sandwich LFA formulated on AuNPs-conjugated ASFV capsid protein (p-72) to detect ASFV antibodies from serum samples with high specificity and sensitivity within 10 min. Also, the result can be seen with the naked eye. These LFA strips could detect 10,000 times diluted serum samples [70]. Dung et al. have shown that non-toxic AgNPs of 14 nm in size (0.78 ppm) could inhibit the virus titer and a 25 ppm exposure completely reduced the viral load. It was observed that AgNPs interact with viral capsid (particularly with gp120) to inhibit viral entry into host cells. Further, inhibition of intracellular RNA synthesis in virions was observed. The effect of AgNPs size on antiviral efficacy has also been investigated by several groups [71]. Galdiero et al. reported that AgNPs produced from fungal species *Alternaria* and *Phoma* with a mean diameter of 47 and 45 nm, respectively, showed low viral inhibition (0–40%), while AgNPs produced by *Fusarium oxysporum* (24 nm size) showed high inhibitory response (~80%) [72].

12.4.3 Protozoan Diseases

The infection in animals due to protozoan parasites raises important concerns because they affect many animals, are easy to transmit and are deadly. Some most common protozoan diseases include toxoplasmosis, theileriosis and trypanosomiasis. They usually infect cattle, sheep, goats, buffalo, chickens and pigs.

12.4.3.1 Toxoplasmosis

This disease is caused by *Toxoplasma gondii*, a tick-borne pathogen. Cat acts as a definite host of this disease because, after ingestion, the parasite is released into the digestive tract and thus, feces further cause infection in other animals in contact [73]. The common symptoms include fever, diarrhea, cough, seizures, lethargy, loss of appetite, abortion and death in severe cases. Sulfadiazine, combined with pyrimethamine (targets active stage), pyrimethamine, clindamycin, atovaquone and clarithromycin, are given as a treatment for toxoplasmosis. However, none of these drugs are effective at the bradyzoite stage of the parasite [74]. In a study by Gaafar et al., *Toxoplasma gondii*-infected mice treated with chitosan combined AgNPs (200

μg/mL) showed a significant reduction in parasite infection than only AgNPs (200 μg/mL) followed by the control group. Although complete eradication of the infection was not observed, a significant reduction in the population of toxoplasma was found [75]. In another study, Keyhani et al. studied the effect of SeNPs (~130 nm size and spherical shape) on the *Toxoplasma gondii*-infected mice [76]. A dose of 10 mg/Kg of SeNPs exposed to mice showed reduction in the number of cysts in the brain, increased inflammatory cytokines and immune response by enhancing the expression of IFN-γ, TNF-α and IL-12. Atovaquone was developed as a nanoemulsion using grape seed oil to increase the bioavailability and efficacy of the drug. The oral administration of Atovaquone-loaded nanoemulsion in BALB/C mice showed improved tissue distribution, reduction in parasites, increased mice survival time and a low number of brain cysts [77].

12.4.3.2 Theileriosis

It is a bovine disease commonly caused by a protozoan *Theileria annulata* and transmitted by *Hyalomma* tick species (Ixodid ticks). Some common symptoms of infection include fever, leukopenia, anorexia, lymph node enlargement, diarrhea, anemia, conjunctivitis, difficulty in respiration, cough and abortion. In cattle, proliferative tissue is infected by *Theileria* species and causes morbidity. Routine diagnosis is performed by careful examination of the clinical symptoms however, suffers from false negative results [78]. Oxytetracycline has shown some positive responses and is considered one of the therapeutic options for this disease. Parvaquone and buparvaquone are the only two drugs reported to act against this disease. Soni et al. used solid lipid nanoparticles (~230 nm) with high drug loading efficiency (~85%) to deliver the hydrophobic drug buparvaquone in *Theileria*-infected Holtzman rats. Within 24 h of treatment, the drug was found to be distributed in the spleen (major organ for localization of theileria parasite) (~35%), liver and lungs [79].

12.4.3.3 Trypanosomiasis

It is commonly called "Surra" because of multi-organ dysfunction due to hyperglycemia after the infection. The causing agent of this disease is *Trypanosoma evansi* in bovines. Some common symptoms include fever, circular motion, anorexia, maniacal behavior, discoloration of the eyeball and death in severe cases. Isometamidium chloride, Diminazine aceturate, Quinopyramin sulfate or chloride and Melarsomn dihydrochloride (Cymerlasan) are the common drugs used for the treatment of trypanosomiasis. These treatments are effective; however, the administration of drugs is difficult due to hydrophobicity. In a study by Adeyemi et al., AuNPs, AgNPs and Platinum NPs (PtNPs) were investigated against different species of *Trypanosoma.* Among these NPs, 1 to 10 μg/mL AuNPs and AgNPs showed efficacy against *Trypanosoma brucei* (~95% reduction in the number of ticks), AgNPs reduced *Trypanosoma congolense* and *Trypanosoma evansi* by >70%, AuNPs, AgNPs and

PtNPs moderately reduced *Trypanosoma gondii* viability by 60%. The activity of these NPs was found to be very selective. Also, the LD_{50} was noted as more than 500 mg/kg when these NPs administered orally [80]. In another study, Arias et al. developed PEG-PLGA [poly ethylene glycol-poly(D, L-lactide-co-glycolide acid)] nanoparticles coated with heavy chain antibody (against *Trypanosoma brucei,* NbAn3) and first-line drug pentamidine for the treatment of the African trypanosomiasis [81]. This formulation showed specificity towards *Trypanosoma brucei* due to the coating of NbAn3 and delivered pentamidine specifically to infected cells. The in vitro assay showed a sevenfold decrease in the IC_{50} value of PEG-PLGA nanoparticles (1.37 μg/mL) compared to the free drug (9.8 μg/mL). Additionally, Hernández et al. reported the CNP-based therapy of trypanosomiasis [82], where 25 mg/Kg of CNPs loaded with benznidazole (drug against *Trypanosoma cruzi*) was orally given to *Trypanosoma cruzi* infected mice (for 130 days). The formulation showed high effectiveness against *Trypanosoma* and downregulated the expression of proinflammatory cytokines (IL-6, TNFα, IL-1β, CCL5).

12.4.4 Others

A long list of pathogens causing various diseases in livestock leads to severe morbidity and mortality. Some of the notable diseases that are caused by pathogenic fungi include Aspergillosis (caused by *Aspergillus flavus)*, Candidiasis (by *Candida albicans*), and Fusarium mycosis (by *Fusarium oxysporum)* [83]. The common antifungal agents used are Itraconazole, Fluconazole, Voriconazole and Amphotericin B, possessing an active site that binds with the heme moiety of the binding pocket of the fungal enzyme (14α-demethylase), causing inhibition and thus disrupting the sterol synthesis of the cell membrane [84]. Fungal pathogens develop resistance to the antifungal drugs and therefore cause side effects in tested animals. A study by Atef et al. revealed that AgNPs could inhibit the growth of *Aspergillus flavus* by altering the aflatoxin biosynthesis process. Also, AgNPs have shown better efficacy in drug-resistant pathogens with the least possible side effects than common antifungal drugs. Hassan et al. used ZnONPs (2 to 10 μg/mL) on mycotoxins produced by various *Aspergillus* species (*Aspergillus flavus*, *Aspergillus parasiticus*, *Aspergillus ochraceus* and *Aspergillus niger*) present in milk and dairy products. Results revealed that 8 and 10 μg/mL of ZnONPs were enough to diminish the Aflatoxins and Ochratoxins, respectively, from the contaminated samples. ZnONPs were found to disrupt the membrane of Aspergillus conidial cells and pits and pore formation in the fungal cell membrane (10 μg/mL) [85]. Hosseini et al. have also studied the MIC of ZnONPs against *Candida albicans* and reported MIC-50 and MIC-90 as 5 μg/mL and 11.3 μg/mL, respectively [86].

Apart from fungal infections, helminths are also prevalent in causing livestock diseases across the globe. Some common infections in livestock include gastrointestinal nematodes, liver fluke and lungworms [87]. Khan et al. studied the effect of ZnONPs (16.7 nm size) against *the Gigantocotyle explanatum* parasite, which resides

in buffalo's (*Bubalus bubalis*) liver. Exposure of 0.012% ZnONPs significantly terminated the antioxidant system (SOD and Glutathione-S-transferase) of *Gigantocotyle explanatum*. The study concluded that ZnONPs reduced the infection by generating free radicals that disrupt nucleic acids, lipids and proteins, ultimately the termination of functional cellular machinery [88]. Zahir et al. studied the effect of AgNPs against cattle tick (*Haemaphysalis bispinosa*) and haematophagus fly (*Hippobosca masculata*) and obtained LC_{50} values as 2.30 ppm and 2.55 ppm, respectively [89]. About 100% mortality was noted against *Hippobosca bispinosa* and *Hippobosca masculata* after 24 h of treatment of 10 mg/mL AgNPs (average size 52.4 nm), and no side effects were observed when administered in Kangayam cattle (*Bos indicus*). Table 12.2 shows various livestock diseases and developed nanoparticles for the therapy.

12.5 Nanotechnology-Enabled Vaccines for Animal Diseases

According to the WHO, 2–3 million child lives are saved annually due to the vaccination program [97]. Several fatal diseases, such as smallpox, tetanus, polio, yellow fever, measles, influenza, and diphtheria, are almost (~99%) eradicated due to vaccination. Typically, a vaccine represents essential fragments of single or multiple protein antigens, which induce an immune response against infection. However, a few polysaccharide-based antigens have also induced immune responses against pneumonia and meningitis [98]. Vaccines are classified into two categories: (1). *Whole-agent vaccine*: This type of vaccine contains an attenuated replicating strain of the pathogenic organism (Whole killed organism and live attenuated). There are several vaccines licensed using this technology, such as measles, BCG, mumps, typhoid, polio, smallpox, Japanese encephalitis, and hepatitis-A. (2). *Subunit vaccine*: This type of vaccine contains only important biomolecules such as protein/DNA/RNA/polysaccharides, which help for inducing an immune response. The licensed vaccine includes tetanus, diphtheria, pertussis, hepatitis B, etc. Figure 12.2 shows the classification of vaccines and clinically available vaccines [99]. Despite successfully developing a vaccine against infection/disease, it causes unwanted side effects (such as fever, fatigue, headache, joint pain, chills, nausea, etc.). Until now, first-generation vaccines (whole organism vaccines) are more efficient for livestock [99]. However, another conventional vaccine suffers from low immunogenicity, activation of an oncogene (caused by a DNA-based vaccine), expensive production, low yield, etc.

To overcome these issues, nanoparticle-based vaccines (Nanovaccine) are being considered. The development of nanovaccines offers several opportunities, such as protecting antigens against degradation, carrying multiple hydrophilic/hydrophobic antigens, controlling antigen release, increasing cellular uptake and better immune response [100, 101]. In a study, Singh et al. developed PLGA-based nanoparticles encapsulating rL7/L12 proteins against Brucella antigen. This nanovaccine induced

Table 12.2 List of common diseases of livestock, associated parasites, and developed nanoparticles for the treatment

Nanoparticles (size in nm)	Disease	Animal model	Pathogen	Route of administration	Results	References
Recombinant B. anthracis protective antigen (rPA) mixed in Water-in-oil Nanoemulsion (NE) with an adjuvant (<400 nm)	Anthrax	Mice, Guinea pig (14 days observation)	*B. anthracis*	Intranasal, intradermal	Inducing serum anti-PA immunoglobulin G (IgG) and bronchial anti-PA IgA and IgG antibodies. Enhanced immune response	[90]
ChNPs (250–300 nm)	Leishmaniasis	Mice (21 days observation)	*Leishmania donovani*	Subcutaneous	Increased immunogenicity	[91]
Polyisohexylcyanoacrylate NPs (183 ± 13 nm)	Salmonellosis	Mice (10 days observation)	*Salmonella typhimurium*	Intravenous	Enhanced therapeutic index, reduced mortality	[92]
Oil core Diminazene (DMZ) NPs ($_{70}$DGNP+) (74 nm)	African trypanosomiasis	Mice	*Trypanosoma brucei*	Intraperitoneal	Enhanced drug degradation	[93]
Mesoporous silica nanoparticles (MSNPs) (96.9 ± 15.9 nm)	Hemorrhagic enterititis	Mice	*E. coli* O157:H7	Oral, subcutaneous	Immunization of joined MSNPs with EspA protein enhance immune response	[94]
AgChNPs (276.1 ± 36.3 nm)	Chlamydial infection	Mice (52 days observation)	*Chlamydia psittaci*	Intranasal, intramuscular	Enhanced drug delivery, crossing mucosal membrane efficiently	[95]
Liposome (–)	Q fever	Mice (7 days observation)	*Coxiella burnetii*	Intranasal	Reduced bacterial count, enhanced antibiotic uptake	[96]

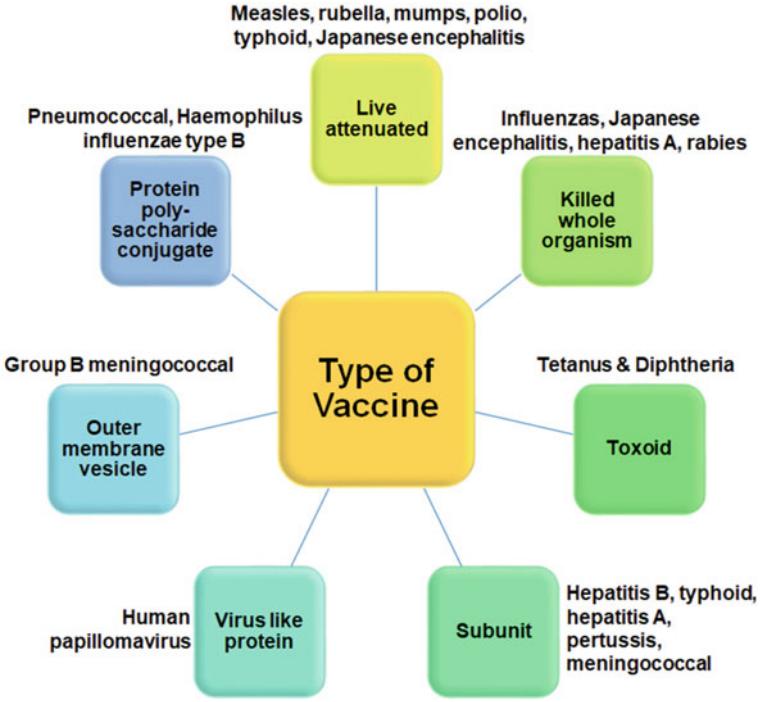

Fig. 12.2 Schematic classification of clinically available vaccines for various animal diseases

the expression of IFN-γ and IgG1 with a high Th_1/Th_2 ratio. This formulation delivered the entrapped vaccine candidate in mice to elicit specific humoral and cellular responses due to the entrapped Brucella antigen. In India, there are several licensed vaccines available for various livestock diseases such as FMD (Bovillis® Clovax, Raksha), Brucellosis (Bruvax), Haemorrhagic Septicemia (Raksha HS), Anthrax (Sterne vaccine, Raksha-anthrax) and Rabies (Raksharab) [102].

12.5.1 Viral Diseases

Viral diseases cause major economic losses (~20,000 crores per year) in India's dairy and meat industry [103]. Major viral diseases of livestock include bovine viral diarrhea virus (BVDV), bovine respiratory syncytial virus (BRSV), bovine parainfluenza 3 (BPF3), adenovirus, herpesvirus-1, bovine respiratory disease complex virus, ASF, RVF and FMD, etc. BVDV causes gastrointestinal, reproductive, and respiratory infections in sheep and cattle. Unlike the plant and bacteria virus, the livestock virus does not penetrate the cell wall to access the host cell. The naked or non-enveloped virus may enter the host cell by two routes: (1). Receptor-mediated endocytosis

or fusion and (2). Capsid protein undergoes shape changes to bind with the host cell receptor and penetrate inside the cell [104]. Graham and co-workers developed biomimetic poly-(D, L-lactic-co-glycolic acid) (PLGA) nanoparticles containing BVDV-1 NS3 protein (target for T cells) and poly (I: C) adjuvant to induce NS-3 specific T cell response in calves against BVDV-1. Figure 12.3a shows the typical construction of PLGA nanoparticles containing BVDV-1 NS3 protein and poly (I: C) adjuvant (Control-NP) coated with E2 glycoprotein (Vaccine-NP). Control-NPs were smaller in hydrodynamic size -~300 nm with negative zeta potential (~−20 mV) (Fig. 12.3b, c). In contrast, the coating of E2 glycoprotein on Vaccine-NPs increased the zeta potential by +1.0 mV and size by ~500 nm. 87.5% of Vaccine-NPs were coated with E2 glycoprotein, which was confirmed using a flow cytometer using an anti-mouse IgG1-APC antibody against E2 glycoprotein (Fig. 12.3d). In this graph, the Control-NPs and Vaccine-NPs denoted with a red and blue line, respectively. This nanovaccine showed significant virus-neutralizing activity after the booster dose (at 21 days). It showed high IFN-γ response (Fig. 12.3e, f) and BVDV antigen response in the blood (Fig. 12.3g, h) and was comparable to the inactivated BVDV vaccine [105]. Mesoporous silica nanoparticles (MSiNPs) coated with the BVDV-1 E2 glycoprotein vaccine have also been developed against BVDV-1. The MSiNPs were 60 nm in size with a 6 nm thick wall and 16 nm average pore size. The 500-μg concentration of the MSiNPs containing recombinant BVDV-E2 glycoprotein induced T cells mediated IFN-γ secretion and induced IgG level in sheep. The cellular immunity against BVDV-1 was sustained till four months post-MSiNPs vaccination [106]. Wang and co-workers synthesized chitosan-coated PLGA nanoparticles encapsulating plasmid DNA (for capsid protein and bovine IL-6), viral protease 3C protein, and P1-2A against the FMD virus [107]. The nasal route administered this vaccine to deposit the vaccine in the lungs. The IL-6 effectively worked as mucosal adjuvants in Guinea pigs and developed a systematic humoral immune response by enhancing the IFN-γ, IgG, and IgA expression levels. Table 12.3 shows different viral nanovaccine tests for livestock.

12.5.2 Bacterial Diseases

Nanovaccine has been developed for inducing immunity against various bacterial diseases of livestock, including Johne's disease, Brucellosis, Leptospira, etc. Johne's disease is caused by *M. avium* and its subspecies *paratuberculosis*. It is a highly contagious and chronic disease that targets the small intestine of ruminants and causes diarrhea and chronic gastroenteritis. There has been no treatment for this disease and culling infected animals is common. Currently, only one vaccine is available against this disease that includes inactivated bacteria in an oil base. However, this vaccine is ineffective and rarely controls the disease [108, 109]. Recently, a few nanotechnology-based formulations have been developed to efficiently deliver functional vaccines for several bacterial diseases in livestock. In an attempt by Thukral et al., polyanhydride nanoparticles were used to encapsulate mycobacterial antigens

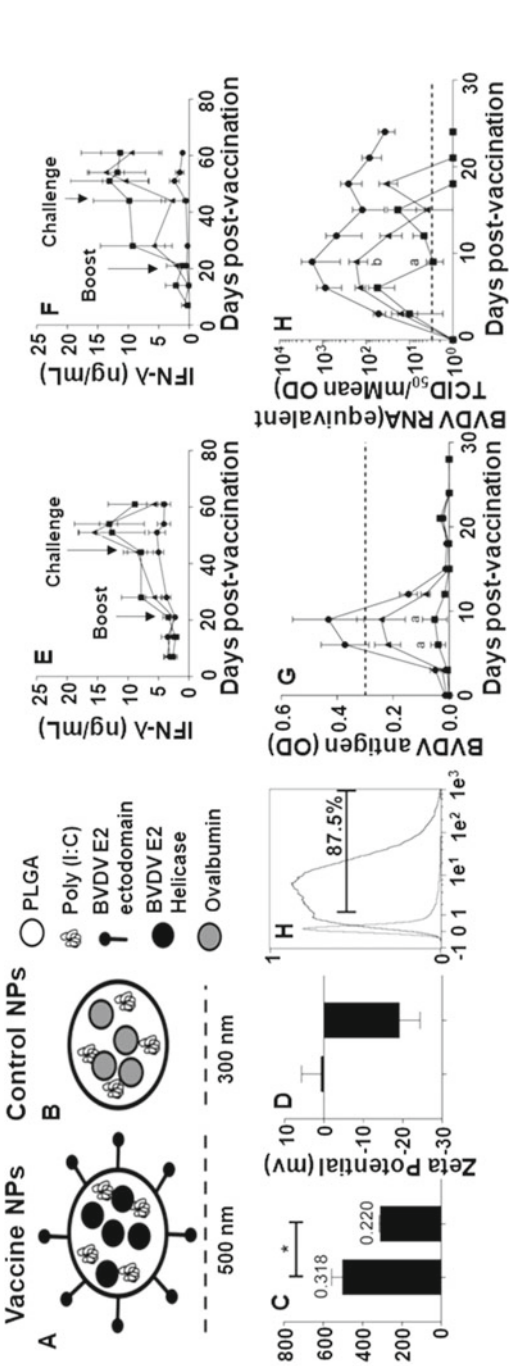

Fig. 12.3 A schematic representation of vaccine-NP and control-NPs (**a**). Dynamic light scattering to evaluate the size (**b**) and charge (**c**) of the NPs. BVDV-E2 surface coating was determined by flow cytometry where Control-NP and Vaccine-NP showed in the red and blue lines, respectively (**d**). The course of vaccination and BVDV challenge stimulated with recombinant BVDV-E2 (**e**) or NS3 helicase (**f**) proteins. BVDV antigen measurement in blood samples from vaccinated calves was assessed by BVDV-E antigen by ELISA (**g**) and BVDV RNA by quantitative RT-PCR (**h**). Vaccine-NP, Control-NP, and inactivated BVDV vaccine triangle, circle and squares, respectively. Adapted with permission from [105]. Copyright, 2017, Springer Nature

Table 12.3 List of nanovaccines developed to prevent various livestock and poultry diseases

Nanoparticles	Disease	Animal model	Pathogen/Subunit	Route of administration	Results	References
PLGA nanoparticles	BPF3	Calves	BPF3 antigen	Intranasal	Increased antigen-specific IgA response and CD4 mediated IFN-γ	[134]
Nucleoprotein nanorings	BRSV	Holstein male calves	BRSV-F and -G epitopes	Intramuscular	Induced mucosal and systemic antibody response. Increased cellular immunity and antigen-specific humoral responses	[135]
Mannosylated chitosan nanoparticles	Brucellosis	Mice	FliC protein	Subcutaneous	Induced level of IFN-γ and IL-2 and low-level IL-10 cytokines. Nanovaccine showed protection from protection against *Brucella melitensis 16M* and *Brucella abortus 544* infections	[136]
Poly(diaminosulfide) Microparticle	Leptospirosis	Bovine	Whole lysate of *Leptospira borgpetersenii* (Hardjo strain HB15B203 (L203-PNSN)	Subcutaneous	Increased population of L203-specific $CD3^+$ T cells and $CD21^+$ B cells to levels. Also, stimulate the humoral immune response	[137]
Chitosan nanoparticles	Salmonellosis	Broiler	Outer membrane proteins and flagellin protein	Oral (through drinking water and feed)	Enhanced TLRs and Th1 and Th2 cytokines mRNA expression	[138]

(continued)

Table 12.3 (continued)

Nanoparticles	Disease	Animal model	Pathogen/Subunit	Route of administration	Results	References
Chitosan nanoparticles	Swine influenza virus	Pigs	Whole inactivated influenza virus	Intranasal	Increased Th1 (IFNγ, IL-6 and IL-2) and Th2 (IL-10 and IL-13) cytokines mRNA expression	[139]

[culture filtrate (PAN-Cf) and whole cell lysate (PAN-Lysate) of *M. paratuberculosis*] and tested in mice model [110]. The scanning electron microscope was used to study the morphology of PAN-Lysate (Fig. 12.4a), PAN-Cf (Fig. 12.4b), and empty (Fig. 12.4c) polyanhydride nanoparticles (~200 nm diameter and spherical shape). Animal studies suggested that mice that received PBS only showed high bacterial load after 12 weeks of the challenge; however, nanovaccine-treated mice showed significantly lower CFU in the spleen (Fig. 12.4d), liver (Fig. 12.4e), small intestine (Fig. 12.4f) and mesenteric lymph node (Fig. 12.4g) than different vaccine (Mycopar®, lipN and PAN-Lysate). The tested nanovaccine showed no inflammation at the site of administration however, induced the production of IL-2, INF-α and IFN-γ by $CD8^+$ T cells.

Sadeghi et al. tested calcium-phosphate nanoparticles bearing *Brucella* antigens (FliC, 7α-HSDH) and poly B-Poly T epitope to develop immunity against Brucellosis in mice [111]. The nanovaccine was found to be ~90 nm in diameter, spherical in shape and smooth surface. Exposure of this nanovaccine induced humoral and cellular immune responses as evidenced by an increased specific ratio of IgG2a (Th1 cells) to specific IgG1 (Th2 cells) than the control group. The nanovaccinated mice showed protection against the *Brucella melitensis 16M* and *Brucella abortus 544*, similar to commercially available vaccines. Leptospirosis is another zoonotic disease with 250 pathogenic serovars. In dairy and goat farms, Hardjo serovar from *Leptospira borgpetersenii* is well known to cause infection and affect the genital and urinary tract. Umthong et al. developed a DNA plasmid (expressing LipL32 and Loa22—Leptospira specific serovar) encapsulated in chitosan nanoparticles and developed a vaccine [112]. Administration of this nanovaccine induced the production of total IgG and IgG1 (due to LipL32) and IgG1 (due to Loa22) and showed no effect on $CD4^+$ T cells. IL-2 and IFN-γ production was also increased due to the co-administration of the two antigens. Table 12.3 shows different nanovaccine tests against the bacterial diseases of livestock.

12.5.3 Parasitic Diseases

Unlike viruses and bacteria, parasites have a complex system with multiple proteins, increasing the difficulties in studying and developing vaccines. For example, malaria is a well-known disease; however, only one vaccine (RTS, S/AS01) is used for the pilot test on children [113]. Livestock also suffers from parasitic diseases such as bovine anaplasmosis (tick fever), toxoplasmosis, theileriosis, trypanosomiasis, etc. Zhao et al. tested MSiNPs containing VirB9-1 and VirB9-2 (proteins of the *Anaplasma marginale*) to induce immunity against bovine anaplasmosis in mice. MSiNPs were ~50 nm in size with 6 nm wall thickness and 5.8 nm pore size [114]. The nanovaccine resulted in high antibody titers (~10^7), increased IFN-γ spot forming cells and T-lymphocyte proliferation. Bissati et al. developed self-assembling protein

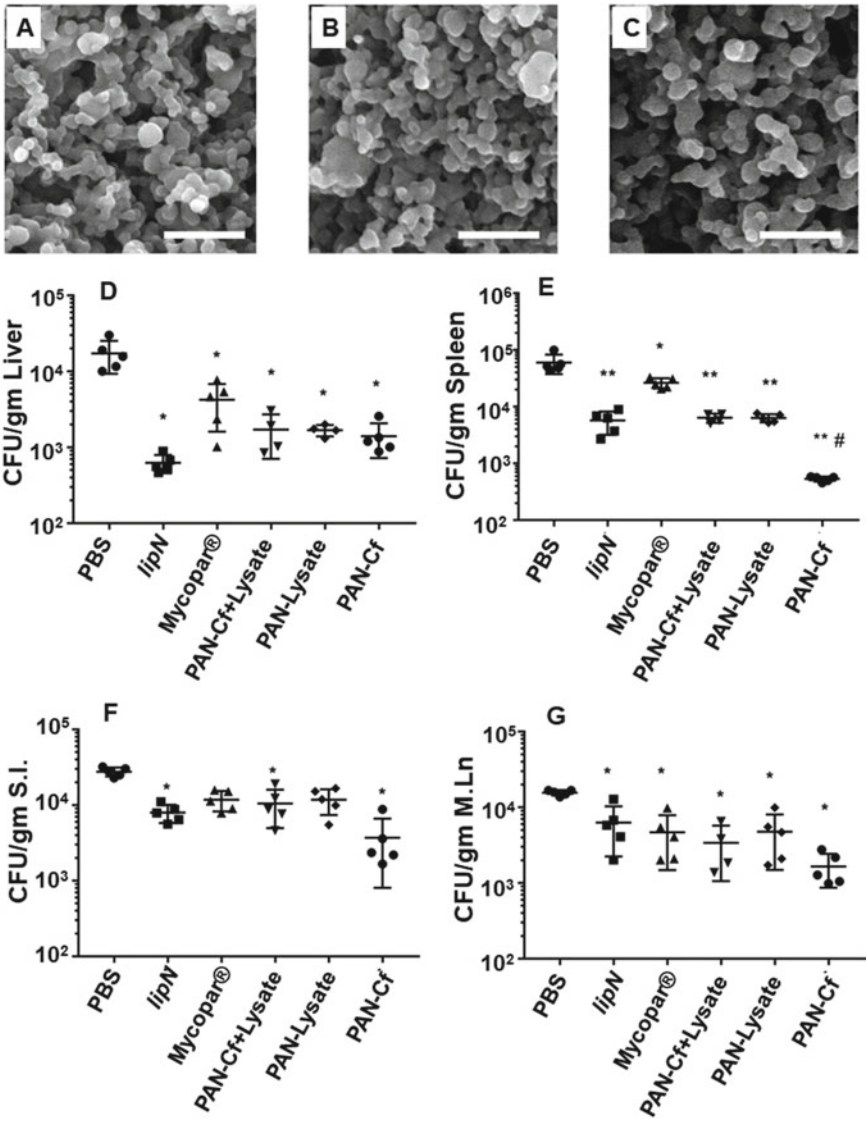

Fig. 12.4 Scanning electron micrographs of 20:80 CPTEG: CPH NPs loaded with 2.5% whole cell lysate (**a**) and 2.5% culture filtrate (**b**) and empty NPs (**c**). Scale bar = 1 μm. The total colony of M. paratuberculosis for each animal for each vaccine group is shown in the spleen (**d**), liver (**e**), small intestine (**f**), and mesenteric lymph node (**g**). Error bars indicate standard deviation. * $p < 0.05$; ** $p < 0.001$. Adapted with permission from Ref. [110]. Copyright, 2020, Springer Nature

nanoparticles containing *toxAll* (five $CD8^+$ HLA-A*11:01 epitopes, four $CD8^+$ HLA-A*02:01, one $CD8^+$ HLA-B*07:02 and MIC1 B cell epitope) to induce immunity against *Toxoplasma gondii* [115]. Tested mice showed protection from HLA-A*11:01, HLA-B*07:02, and HLA-A*02:01 by inducing the expression of $CD8^+$ T cells, $CD4^+$ helper cells, and IgG2b antibodies. It also activated TLR4 and TLR5 innate immunity pathways and reduced the parasite load by 87%. In another study, Mody et al. tested an MSiNPs-based vaccine containing Bm86 antigen from the *Rhipicephalus microplus* (cattle tick) [116]. It did not show any significant adverse effects on the tissues and was found to be highly distributed in the lymph node, liver, and kidney. Robust Th2 antibody, IgG1, and IgG2a response were generated against Bm86 antigen in mice on the 28^{th} day of administration.

12.6 Nanomaterial-Based Nutraceuticals

Nutraceutical products are isolated from food and usually sold as a medicine to improve health, prevent chronic diseases, delay the aging process, support the structure of the body and expand life expectancy [117]. Ginseng, Echinacea, green tea, glucosamine, omega-3, lutein, folic acid, cod liver oil, etc., are popular examples of nutraceuticals [117]. It is expected that the worldwide nutraceutical market will reach $650.5 billion by the year 2030 [118]. Recent studies showed the beneficial effects of nutraceuticals against diabetes [119], cardiovascular diseases [120], cancer [121], atherosclerosis [122] and neurological disorder [123], etc. In ruminants, probiotics, prebiotics, symbiotics, dietary lipids, algae and secondary metabolites are administered as nutraceuticals [124]. Nutraceuticals also help in livestock disease control, reduction in methane production, improve growth performance and reduce the risk of metabolic diseases (Fig. 12.5).

Nanotechnology-based nutraceutical products showed a growing interest in the food industry and pharmaceuticals. Nano or microencapsulation of nutraceuticals helps for the protection of the compound of interest from degradation (undesired interaction or during processing or storage), prolongs the release of the product, improves its oral bioavailability, etc [125]. Various nanocarriers (such as micelles, liposomes, nanodispersions, nanoemulsions, polymeric micelles and nanoparticles) are used for the fabrication of nutraceuticals [125]. The food-grade NPs can be synthesized using different building blocks such as proteins, vitamins, carbohydrates, flavonoids, minerals, etc., using various methods (ultrasonication, precipitation, emulsifications, homogenization and coacervation) [125]. Among these strategies, the nanoemulsion-based technique is widely studied for the delivery of a variety of nutraceutical products. Guttoff et al. formulated the nanoemulsion of cholecalciferol (vitamin D_3) to improve the bioavailability of vitamin by simulating the gastrointestinal tract of mice models [126]. Recently, essential oil-based food preservation techniques have gained the attention of researchers due to their antimicrobial properties. Thymol, carvacrol, limonene and cinnamaldehyde are essential oils

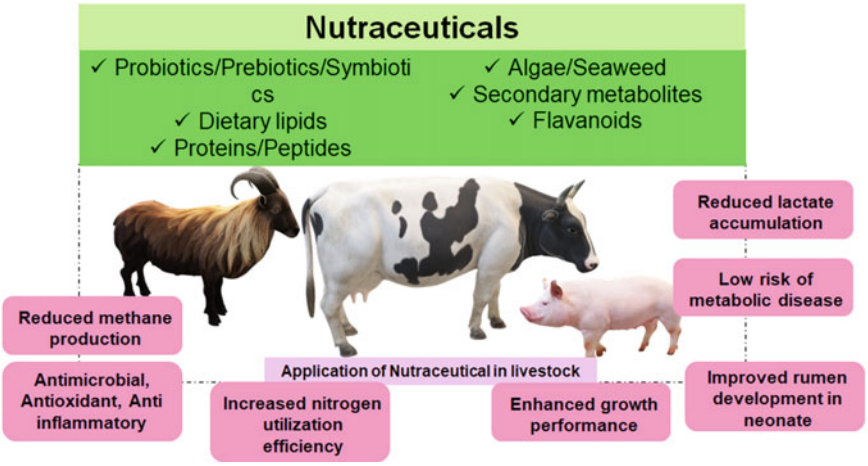

Fig. 12.5 Effect of nutraceutical products on livestock

used for food preservation. In a study, peppermint oil (PO) containing nanoemulsion showed prolonged food protection against the *L. monocytogenes* and *S. aureus* compared to bulk PO [127]. Metal nanoparticles have also demonstrated applications in the field of nutraceuticals. For example, Lydia et al. formulated functional yogurt containing pomegranate seed oil-coated AuNPs. The pomegranate oil coated AuNPs spiked yogurt exhibited antioxidant and anticancer properties by scavenging H_2O_2 (62.8 ± 1.8%) and inhibiting the growth of lung (~75%) and colon cancer cells (~73%) (in vitro), respectively [128]. In another study, AgNPs coated with quercetin and afzelin (plant nutraceutical) showed antibacterial effects against *P. aeruginosa* and *S. typhi* [129]. This nanoformulation showed 50% inhibition of the biofilm of *S. typhi.* The SEM images confirmed the inhibition of the biofilm formation after quercetin and afzelin-treated AgNPs (Fig. 12.6a–c). Also, *S. typh*e infected zebrafish model showed a reduced burden of infection by 3 log fold (Fig. 12.6d). There are very few nanoparticle-based products available commercially as sweetening agents (TiO_2NPs and SiO_2NPs) and as health supplements (CaNPs, Fe_2O_3NPs and ZnONPs) [130], etc. Nanotechnology-based nutraceutical products for livestock are unavailable commercially.

12.7 Limitations of Using Nanoparticles for Animal Health and Nutrition and Way Forward

In animals, the mineral requirement is fulfilled by supplementing salts of multi-mineral elements chelated with amino acids or vitamins. Generally, a high concentration of ionic salts is required to meet minerals' optimum absorption, thus suffering toxicity [131]. Nanoparticle-mediated delivery of desired mineral elements and

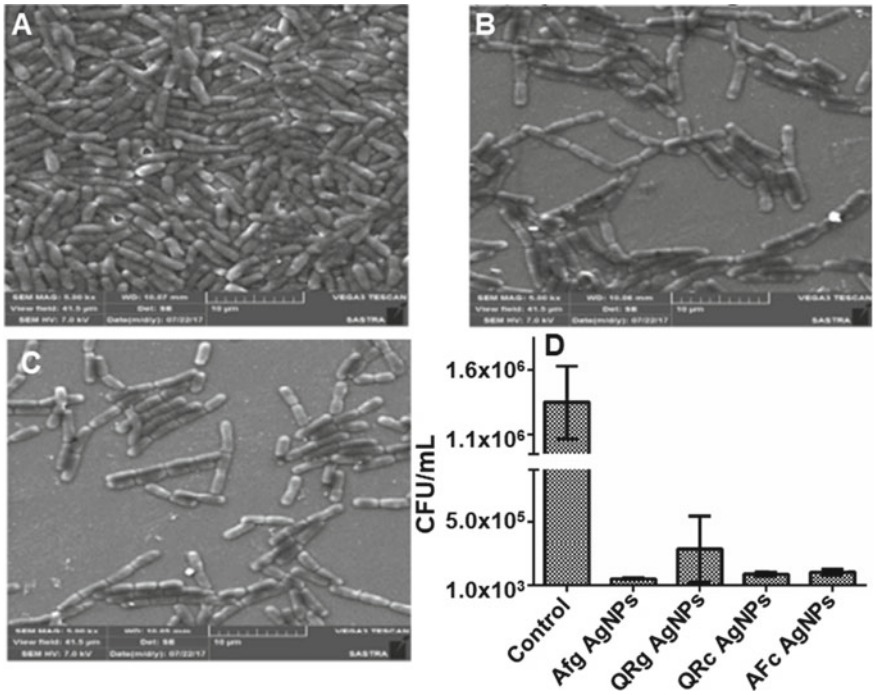

Fig. 12.6 Scanning electron micrographs show *S. typhi* biofilm formation over the coverglass (**a**) and treated with Quercetin-AgNPs (**b**) and Afzelin-AgNPs (**c**). The bar graph (**d**) represents the reduction in *S. typhi* infection in the zebrafish model upon treatment of green synthesized Quercetin and Afzelin-coated AgNPs. Adapted with permission from [129]. Copyright, 2018, Elsevier

nutrient materials is considered safe. Therefore, biocompatible nanoparticles of essential mineral elements can be further explored for feed supplement purposes. Although, the bare nanoparticles (without any surface coating) are known to cause toxicity due to the interference with the normal biochemistry of the cells/tissues [132]. In this context, the most significant limitation is the development of nanoparticles of all the essential mineral elements and making them biocompatible [132]. The surface modification of the nanoparticles with different biomolecules (ascorbic acid, thiamine, PEG, dextran, glucose, chitosan, etc.) is reported to reduce the observed toxicity [133]. Easy surface modification of nanomaterials further facilitates the targeted delivery of nanominerals or encapsulated nutrient materials. Such tissue/organ-specific delivery would also be beneficial in avoiding off-targeted accumulation and toxicity. So far, only limited nanoparticles (ZnONPs, SeNPs, CuONPs) have been studied in livestock nutrition [140]; therefore, more nanoparticle types may be tested for their utility as nutrient material. The availability of suitable animal models is another concern because most studies involve mouse/rat models for experiments; however, the inclusion of larger farm animals would be essential for extending the use of nanominerals in animals.

12.8 Conclusion and Future Prospects

Recent developments in nanoscience and nanotechnology have enabled this area to be successfully applied to various fields of nutrition and health. For nutrition, nanomaterials may be used directly or through surface grafting essential vitamins and amino acids to further aid the product's nutritional value. Nanocomposites of various mineral elements could also be designed to consider the required ratio of multiple micronutrients. Sustained release and longer duration circulation in blood could also be achieved to facilitate the assimilation of mineral elements in functional enzymes. Although preliminary, a few nanomaterials (ZnONPs, SeNPs and CuONPs) are tested among livestock, and results revealed the beneficial health effects. Specific notable parameters included better growth performance, immunity and reproductive ability. Few nanomaterials exhibit excellent antibacterial and antiviral agents; therefore, they hold tremendous potential to combat multi-drug resistant microbial species. Several studies have included nanomaterials (for example, ZnONPs, CuONPs and AgNPs) combined with antimicrobial peptides, essential oils and several other natural products, etc., as potent growth inhibitors of pathogenic microbes and parasites. Use of nanomaterials to deliver the vaccine candidates or as adjuvants are also being explored to overcome the common drawbacks of conventional vaccines (for example, storage condition and multiple-dose requirement). Nanovaccines offer to encapsulate multiple antigens/epitopes in a single unit, which could build immunity against various species of parasite-causing disease. Despite the significant advances in the field, several bottlenecks hinder the complete realization of nanotechnology applications in multiple health and nutrition sectors. A collaborative effort from material scientists and veterinarians will be required to address some concerns. Developing suitable cell culture and animal models, toxicity concerns of nanomaterials and nanotechnology-based rapid animal disease diagnosis methods are some critical areas to be explored in the near future.

Acknowledgements S. Singh acknowledges the core funding received from the DBT-National Institute of Animal Biotechnology, Hyderabad, India (Grant no: C0046). S. Bhagat thanks the Indian Council of Medical Research (ICMR), India, for providing a Senior Research Fellowship. D. Mehta thanks the Department of Biotechnology, India, for providing a Junior Research Fellowship.

References

1. How will population growth and more westernised diets affect demand for meat products? (Global Ag Media) https://www.thepoultrysite.com/news/2020/02/how-will-population-growth-and-more-westernised-diets-affect-demand-for-meat-products. Accessed 21 July 2022
2. Eating meat is the norm almost everywhere (Statista). https://www.statista.com/chart/24899/meat-consumption-by-country/. Accessed 21 July 2022
3. X. Pei, Z. Xiao, L. Liu, G. Wang, W. Tao, M. Wang, J. Zou, D. Leng, J. Sci. Food Agric. **99**, 1366–1374 (2019)

4. M. Abbasi, B. Dastar, N. Afzali, M.S. Shargh, S.R. Hashemi, Biol. Trace Elem. Res. **200**, 2338–2348 (2022)
5. A. Alkhtib, D. Scholey, N. Carter, G.W.V. Cave, B.I. Hanafy, S.R.J. Kempster, S. Mekapothula, E.T. Roxborough, E.J. Burton, Animals **10**, 1482 (2020)
6. C. Zhao, Y. Bai, S. Fu, L. Wu, C. Xia, C. Xu, J. Vet. Intern. Med. **34**, 2787–2799 (2020)
7. M.H. Abaspour Aporvari, M. Mamoei, S. Tabatabaei Vakili, M. Zareei, N. Dadashpour Davachi, Arch. Razi Inst. **73**, 121–129 (2018)
8. I. Sembratowicz, K. Ognik, J. Trace Elem. Med. Biol. **47**, 98–103 (2018)
9. P.S. Swain, S.B.N. Rao, D. Rajendran, N.M. Soren, D.T. Pal, B.S. Karthik, Anim. Nutr. Feed Technol. **18**, 297 (2018)
10. L. Han, K. Pang, T. Fu, C.J.C. Phillips, T. Gao, Biol. Trace Elem. Res. **199**, 113–119 (2021)
11. K. Ognik, I. Sembratowicz, E. Cholewinska, J. Jankowski, K. Kozlowski, J. Juskiewicz, Z. Zdunczyk, Anim. Sci. J. **89**, 579–588 (2018)
12. Z. Hubálek, I. Rudolf, in *Microbial Zoonoses and Sapronoses*, ed. by Z. Hubálek, I. Rudolf (Springer Netherlands, Dordrecht, 2011), pp. 129–297
13. K.A. McCall, C. Huang, C.A. Fierke, J. Nutr. **130**, 1437S-1446S (2000)
14. M.F. Ryan, Ann. Clin. Biochem. **28**, 19–26 (1991)
15. L. Li, X. Yang, Oxid. Med. Cell Longev. **2018**, 7580707 (2018)
16. O. Chekh, O. Bordunova, V. Chivanov, E. Yadgorova, L. Bondarchuk, Open Agric. **6**, 573–586 (2021)
17. D. Rajendran, G. Kumar, S. Ramakrishnan, T.K. Shibi, Res. J. Biotechnol. **8**, 11–17 (2013)
18. J. Xu, M. Zhang, P. Cao, B. Adhikari, LWT **134**, 110168 (2020)
19. M.J. Hakeem, J. Feng, A. Nilghaz, L. Ma, H.C. Seah, M.E. Konkel, X. Lu, E.G. Dudley, Appl. Environ. Microbiol. **86**, e01195–01120 (2020)
20. M. Mirhosseini, V. Arjmand, J. Food Prot. **77**, 1599–1604 (2014)
21. M. Abdollahi, J. Rezaei, H. Fazaeli, Arch. Anim. Nutr. **74**, 189–205 (2020)
22. A.-Z.R. Mahmood, A.K. Mahmood, A.-K.N. Jabbar, Plant Arch. **20**, 1267–1276 (2020)
23. R. Kachuee, H. Abdi-Benemar, Y. Mansoori, P. Sanchez-Aparicio, J. Seifdavati, M. Elghandour, R.J. Guillen, A.Z.M. Salem, Biol. Trace Elem. Res. **191**, 389–402 (2019)
24. Y. Zheng, W. Dai, X. Hu, Z. Hong, Anim. Feed Sci. Technol. **260**, 114345 (2020)
25. Q. Zhang, Y. Han, Y. Yang, P. Zhou, X. Shen, *Biological Trace Element Research* (2022)
26. E.B. Kurutas, Nutr. J. **15**, 71 (2016)
27. M.A. Johnson, J.G. Fischer, S.E. Kays, Crit. Rev. Food Sci. Nutr. **32**, 1–31 (1992)
28. I.A. Stepanova, A.A. Nazarova, M.V. Arisov, World's Vet. J. **10**, 492 (2020)
29. B.R. Abdel-Halim, W.A. Moselhy, N.A. Helmy, Asian Pac. J. Reprod. **7**, 161 (2018)
30. K. Ognik, K. Kozlowski, A. Stepniowska, R. Szlazak, K. Tutaj, Z. Zdunczyk, J. Jankowski, Animal **13**, 1137–1144 (2019)
31. Y. Wang, W. Luo, Y. Tu, Y. Zhao, Coatings **11**, 39 (2021)
32. Y.K. Lee, S.I. Ahn, Y.H. Chang, H.S. Kwak, J. Dairy Sci. **98**, 5841–5849 (2015)
33. P. Choudhary, S. Dutta, J.A. Moses, C. Anandharamakrishnan, J. Food Process. Preserv. **n/a**, e16082
34. N. Sirirat, J.-J. Lu, A.T.-Y. Hung, T.-F. Lien, J. Agric. Sci. **5**, 150 (2013)
35. L. Gifre-Renom, J.V. Carratala, S. Pares, L. Sanchez-Garcia, N. Ferrer-Miralles, A. Villaverde, A. Bach, E. Garcia-Fruitos, A. Aris, Sci. Rep. **10**, 11299 (2020)
36. P.-K. Roy et al., Animals **11**, 2483 (2021)
37. A. Hegazi, A. El-Houssiny, W. Sadek, F. Al-Guthami, A. Al-Gethami, A. Sadik, T. Farag, Adv. Anim. Vet. Sci. **9**, 280–288 (2021)
38. A. Kessell, J. Finnie, P. Windsor, Aust. Vet. J. **89**, 289–296 (2011)
39. G.G. Alton, J.R.L. Forsyth, in *Medical Microbiology*, ed. by S. Baron (Galveston, TX, 1996)
40. S.K. Khurana et al., Vet. Q. **41**, 61–88 (2021)
41. T. Hernandez-Caselles, A. Vera, F. Crespo, J. Villalain, J.C. Gomez-Fernandez, Am. J. Vet. Res. **50**, 1486–1488 (1989)
42. S.M. Hosseini, R. Abbasalipourkabir, F.A. Jalilian, S.S. Asl, A. Farmany, G. Roshanaei, M.R. Arabestani, Antimicrob. Resist. Infect. Control **8**, 62 (2019)

43. H. Alizadeh, M. Salouti, R. Shapouri, **7**, e9039 (2014)
44. I.V. Wesley, Food science and technology-New York-Marcel Dekker, pp. 39–74 (1999)
45. J.C. Low, W. Donachie, Vet. J. **153**, 9–29 (1997)
46. Listeriosis in Animals (MSD Manual Veterinary Manual). https://www.msdvetmanual.com/generalized-conditions/listeriosis/listeriosis-in-animals#v54241316. Accessed 21 July 2022
47. K. Markowska, A.M. Grudniak, B. Milczarek, K.I. Wolska, Pol. J. Microbiol. **67**, 315–320 (2018)
48. D.S. No, A. Algburi, P. Huynh, A. Moret, M. Ringard, N. Comito, D. Drider, P. Takhistov, M.L. Chikindas, J. Food Saf. **37**, e12353 (2017)
49. H. Hogeveen, W. Steeneveld, C.A. Wolf, Annu. Rev. Res. Econ. **11**, 289–312 (2019)
50. W.N. Cheng, S.G. Han, Asian-Australas. J. Anim. Sci. **33**, 1699–1713 (2020)
51. C. Han, C. Qi, B. Zhao, J. Cao, S. Xie, S. Wang, W. Zhou, J. Vet. Pharmacol. Ther. **32**, 116–123 (2009)
52. Y.J. Sung, H.-J. Suk, H.Y. Sung, T. Li, H. Poo, M.-G. Kim, Biosens. Bioelectron. **43**, 432–439 (2013)
53. J.-J. Wang, B.-H. Liu, Y.-T. Hsu, F.-Y. Yu, Food Control **22**, 964–969 (2011)
54. Ş. Kirkan, G. Erbaş, U. Parin, in *Livestock Science* (IntechOpen, 2017)
55. G.P. Wormser, I. Schwartz, Clin. Microbiol. Rev. **22**, 387–395 (2009)
56. N. Durán, M. Durán, C.E.d. Souza, J. Braz. Chem. Soc. **28**, 927–932 (2017)
57. L.Z. Flores-López, H. Espinoza-Gómez, R. Somanathan, J. Appl. Toxicol. **39**, 16–26 (2019)
58. H.R. Gelderblom, in *Medical Microbiology*, ed. by S. Baron (Galveston, TX, 1996)
59. P. Colson, D. Raoult, Int. J. Antimicrob. Agents **48**, 349–352 (2016)
60. P. Murcia, W. Donachie, M. Palmarini, in *Encyclopedia of Microbiology*, 3rd edn., ed. by M. Schaechter (Academic Press, Oxford, 2009), pp. 805–819
61. K.L. Goldenthal, K. Midthun, K.C. Zoon, in *Medical Microbiology*, ed. S. Baron (Galveston, TX, 1996)
62. A.S. Mweene, G.S. Pandey, P. Sinyangwe, A. Nambota, K. Samui, H. Kida, Jpn. J. Vet. Res. **44**, 89–105 (1996)
63. D.W. Gakuya, C.M. Mulei, S.B. Wekesa, Afr. J. Tradit. Complement. Altern. Med. **8** (2011)
64. A.E. Segarra, J.M. Rawson, S. Resources, I. Division (Library of Congress, Congressional Research Service, 2001)
65. E.C. Melo A. Lopez, Rev. Sci. Tech. **21**, 695–698, 689–694 (2002)
66. M.E. Hamdy, M. Del Carlo, H.A. Hussein, T.A. Salah, A.H. El-Deeb, M.M. Emara, G. Pezzoni, D. Compagnone, J. Nanobiotechnol. **16**, 48 (2018)
67. S. Rafiei, S.E. Rezatofighi, M.R. Ardakani, S. Rastegarzadeh, IEEE Trans. Nanobiosci. **15**, 34–40 (2015)
68. A.A.A. Elqasem, A.F. Mohamed, Egypt. J. Pediatr. Allergy Immunol. (The) **19**, 37–49 (2021)
69. B. Borrego et al., Nanomed. Nanotechnol. Biol. Med. **12**, 1185–1192 (2016)
70. W. Zhu, K. Meng, Y. Zhang, Z. Bu, D. Zhao, G. Meng, Front. Chem. **9** (2022)
71. M.A. Raza, Z. Kanwal, A. Rauf, A.N. Sabri, S. Riaz, S. Naseem, Nanomaterials (Basel) **6** (2016)
72. T.T.N. Dung, V.N. Nam, T.T. Nhan, T. T.B. Ngoc, L.Q. Minh, B.T.T. Nga, V.P. Le, D.V. Quang, Mater. Res. Express **6**, 1250g1259 (2020)
73. R.R. Ben-Harari, Expert Rev. Anti Infect. Ther. **17**, 911–917 (2019)
74. I.R. Dunay, K. Gajurel, R. Dhakal, O. Liesenfeld, J.G. Montoya, Clin. Microbiol. Rev. **31**, e00057–00017 (2018)
75. M.R. Gaafar, R.F. Mady, R.G. Diab, T.I. Shalaby, Exp. Parasitol. **143**, 30–38 (2014)
76. A. Keyhani, N. Ziaali, M. Shakibaie, A.T. Kareshk, S. Shojaee, M. Asadi-Shekaari, M. Sepahvand, H. Mahmoudvand, J. Med. Microbiol. **69**, 104–110 (2020)
77. S.J. Azami, A. Amani, H. Keshavarz, R. Najafi-Taher, M. Mohebali, M.A. Faramarzi, M. Mahmoudi, S. Shojaee, Eur. J. Pharm. Sci. **117**, 138–146 (2018)
78. B.R. Maharana, A.K. Tewari, B.C. Saravanan, N.R. Sudhakar, Vet. World **9**, 487–495 (2016)
79. M. Soni, N. Shelkar, R. Gaikwad, G. Vanage, A. Samad, P. Devarajan, J. Pharm. Bioallied Sci. **6**, 22–30 (2014)

80. O.S. Adeyemi et al., Artif. Cells Nanomed. Biotechnol. **46**, S86–S94 (2018)
81. J.L. Arias, J.D. Unciti-Broceta, J. Maceira, T. del Castillo, J. Hernández-Quero, S. Magez, M. Soriano, J.A. García-Salcedo, J. Control. Release **197**, 190–198 (2015)
82. M. Hernández, S. Wicz, E. Pérez Caballero, M.H. Santamaría, R.S. Corral, Parasitol. Int. **81**, 102248 (2021)
83. A.A. Hassan, R.M. Sayed-Elahl, N.H. Oraby, A.M.A. El-Hamaky, in *Nanomycotoxicology*, ed. by M. Rai, K.A. Abd-Elsalam (Academic Press, 2020), pp. 251–269
84. D.W. Denning, W.W. Hope, Trends Microbiol. **18**, 195–204 (2010)
85. A. Hassan, M. Howayda, H. Mahmoud, J. Stud. Chem. Process Technol. (SCPT), Am. Soc. Sci. Eng. **1**(3) 16–25 (2013)
86. S.S. Hosseini, H. Joshaghani, T. Shokohi, A. Ahmadi, Z. Mehrbakhsh, Infect. Drug Resist. **13**, 385 (2020)
87. J. Vercruysse, E. Claerebout, Vet. Parasitol. **98**, 195–214 (2001)
88. Y.A. Khan, B.R. Singh, R. Ullah, M. Shoeb, A.H. Naqvi, S.M.A. Abidi, PLoS ONE **10**, e0133086 (2015)
89. A.A. Zahir, A.A. Rahuman, Vet. Parasitol. **187**, 511–520 (2012)
90. S. Challenge, Infect. Immun. **75**, 4020 (2007)
91. M.A. Danesh-Bahreini, J. Shokri, A. Samiei, E. Kamali-Sarvestani, M. Barzegar-Jalali, S. Mohammadi-Samani, Int. J. Nanomed. **6**, 835 (2011)
92. E. Fattal, M. Youssef, P. Couvreur, A. Andremont, Antimicrob. Agents Chemother. **33**, 1540–1543 (1989)
93. M. Kroubi, S. Daulouede, H. Karembe, Y. Jallouli, M. Howsam, D. Mossalayi, P. Vincendeau, D. Betbeder, Nanotechnology **21**, 505102 (2010)
94. A. Hajizade, A.H. Salmanian, J. Amani, F. Ebrahimi, A. Arpanaei, Artif. Cells Nanomed. Biotechnol. **46**, S1067–S1075 (2018)
95. Y. Li, C. Wang, Z. Sun, J. Xiao, X. Yan, Y. Chen, J. Yu, Y. Wu, Int. J. Nanomed. **14**, 8179 (2019)
96. I.H. Norville et al., Antimicrob. Agents Chemother. **58**, 5510–5518 (2014)
97. Child mortality and causes of death. https://www.who.int/data/gho/data/themes/topics/topic-details/GHO/child-mortality-and-causes-of-death. Accessed 21 July 2022
98. C.C. Daniels, P.D. Rogers, C.M. Shelton, J. Pediatr. Pharmacol. Ther. **21**, 27–35 (2016)
99. A.J. Pollard, E.M. Bijker, Nat. Rev. Immunol. **21**, 83–100 (2021)
100. N. Marasini, K.A. Ghaffar, M. Skwarczynski, I. Toth, in *Micro and Nanotechnology in Vaccine Development*, ed. by M. Skwarczynski, I. Toth (William Andrew Publishing, 2017), pp. 221–239
101. K. Kettler, K. Veltman, D. van de Meent, A. van Wezel, A.J. Hendriks, Environ. Toxicol. Chem. **33**, 481–492 (2014)
102. Vaccination schedule in cattle and buffalo. https://vikaspedia.in/agriculture/livestock/cattle-buffalo/vaccination-schedule-in-cattle-and-buffalo. Accessed 21 July 2022
103. Annual Report (Government of India). https://dahd.nic.in/sites/default/filess/Annual%20Report%20English.pdf. Accessed 21 July 2022
104. S. Payne (2017), pp. 1–11
105. V. Riitho et al., Sci. Rep. **7**, 13743 (2017)
106. D. Mahony, K.T. Mody, A.S. Cavallaro, Q. Hu, T.J. Mahony, S. Qiao, N. Mitter, PLoS ONE **10**, e0141870 (2015)
107. G. Wang, L. Pan, Y. Zhang, Y. Wang, Z. Zhang, J. Lü, P. Zhou, Y. Fang, S. Jiang, PLoS ONE **6**, e27605 (2011)
108. R.R. Marquardt, S. Li, Anim. Front. **8**, 30–37 (2018)
109. Y. Phanse, C.W. Wu, A.J. Venturino, C. Hansen, K. Nelson, S.R. Broderick, H. Steinberg, A.M. Talaat, Microorganisms **8** (2020)
110. A. Thukral, K. Ross, C. Hansen, Y. Phanse, B. Narasimhan, H. Steinberg, A. M. Talaat, npj Vaccines **5**, 15 (2020)
111. Z. Sadeghi, M. Fasihi-Ramandi, S. Bouzari, Int. J. Nanomed. **15**, 3877–3886 (2020)

112. U. Supawadee, B. Arun, J. Alain, S. Noppadol, K. Ruthairat, P. Kanitha, P. Tanapat, J. Microbiol. Biotechnol. **25**, 526–536 (2015)
113. M.B. Laurens, Hum. Vaccin. Immunother. **16**, 480–489 (2020)
114. L. Zhao et al., PLoS ONE **11**, e0154295 (2016)
115. K. El Bissati et al., Sci. Rep. **10**, 16984 (2020)
116. K.T. Mody et al., Front. Bioeng. Biotechnol. **8** (2021)
117. H. Nasri, A. Baradaran, H. Shirzad, M. Rafieian-Kopaei, Int. J. Prev. Med. **5**, 1487–1499 (2014)
118. Nutraceuticals Market by Type, (Functional Beverage, Functional Food, and Dietary Supplements), Form (Capsules and Tablets, Liquid, Powder, Others), and Sales Channel (Hypermarkets/Supermarkets, Specialty Stores, Pharmacies, and Online Channels): Global Opportunity Analysis and Industry Forecast, 2021–2030, (Allied Market Research). https://www.alliedmarketresearch.com/nutraceuticals-market. Accessed 4 Sept 2022
119. G. Derosa, C.P. Limas, P.C. Macias, A. Estrella, P. Maffioli, Arch. Med. Sci. **10**, 336–344 (2014)
120. B. Sosnowska, P. Penson, M. Banach, Cardiovasc. Diagn. Ther. **7**, S21–S31 (2017)
121. M. Calvani, A. Pasha, C. Favre, Int. J. Mol. Sci. **21** (2020)
122. J.W.E. Moss, J.O. Williams, D.P. Ramji, Biochim. Biophys. Acta. Mol. Basis Dis. **1864**, 1562–1572 (2018)
123. R. Makkar et al., Int. J. Mol. Sci. **21** (2020)
124. B. Yurdakok-Dikmen, A. Filazi, in *Nutraceuticals in Veterinary Medicine*, ed. by R.C. Gupta, A. Srivastava, R. Lall (Springer International Publishing, Cham, 2019), pp. 637–648
125. A.R. Singh, P.K. Desu, R.K. Nakkala, V. Kondi, S. Devi, M.S. Alam, H. Hamid, R.B. Athawale, P. Kesharwani, Drug Deliv. Transl. Res. **12**, 485–499 (2022)
126. M. Guttoff, A.H. Saberi, D.J. McClements, Food Chem. **171**, 117–122 (2015)
127. R. Liang, S. Xu, C.F. Shoemaker, Y. Li, F. Zhong, Q. Huang, J. Agric. Food Chem. **60**, 7548–7555 (2012)
128. D.E. Lydia, A. Khusro, P. Immanuel, G.A. Esmail, N.A. Al-Dhabi, M.V. Arasu, J. Photochem. Photobiol. B Biol. **206**, 111868 (2020)
129. R. Lotha, N.S. Sundaramoorthy, B.R. Shamprasad, S. Nagarajan, A. Sivasubramanian, Microb. Pathog. **120**, 109–118 (2018)
130. Nanotechnology products database (Nanotechnology products database). https://product.statnano.com/. Accessed 22 Feb 2022
131. J.P. Goff, J. Dairy Sci. **101**, 2763–2813 (2018)
132. X.Q. Zhang, X. Xu, N. Bertrand, E. Pridgen, A. Swami, O.C. Farokhzad, Adv. Drug. Deliv. Rev. **64**, 1363–1384 (2012)
133. L. Yan, F. Zhao, J. Wang, Y. Zu, Z. Gu, Y. Zhao, Adv. Mater. **31**, 1805391 (2019)
134. F. Mansoor, B. Earley, J.P. Cassidy, B. Markey, S. Doherty, M.D. Welsh, BMC Vet. Res. **11**, 220 (2015)
135. S. Riffault et al., Vaccines (Basel) **8** (2020)
136. Z. Sadeghi, M. Fasihi-Ramandi, M. Azizi, S. Bouzari, J. Biotechnol. **310**, 89–96 (2020)
137. E.I. Wafa, J.H. Wilson-Welder, R.L. Hornsby, J.E. Nally, S.M. Geary, N.B. Bowden, A.K. Salem, Biomacromolecules **21**, 534–544 (2020)
138. S. Renu et al., Carbohyd. Polym. **243**, 116434 (2020)
139. S. Renu, N. Feliciano-Ruiz, S. Ghimire, Y. Han, J. Schrock, S. Dhakal, V. Patil, S. Krakowka, G.J. Renukaradhya, Vet. Microbiol. **242**, 108611 (2020)
140. S. Bhagat, S. Singh, Food Res. Int. **160**, 111703 (2022)